

Amalia Martínez-García · Cosme Furlong
Bernardino Barrientos · Ryszard J. Pryputniewicz *Editors*

Emerging Challenges for
Experimental Mechanics in
Energy and Environmental
Applications, Proceedings of the
5th International Symposium on
Experimental Mechanics and 9th
Symposium on Optics in Industry
(ISEM-SOI), 2015



Conference Proceedings of the Society for Experimental Mechanics Series

Series Editor

Kristin B. Zimmerman, Ph.D.
Society for Experimental Mechanics
Bethel, CT, USA

Amalia Martínez-García • Cosme Furlong • Bernardino Barrientos
Ryszard J. Pryputniewicz
Editors

Emerging Challenges for Experimental
Mechanics in Energy and Environmental
Applications, Proceedings of the 5th
International Symposium on Experimental
Mechanics and 9th Symposium on Optics
in Industry (ISEM-SOI), 2015

Editors

Amalia Martínez-García
Senior Researcher
Centro de Investigaciones en Óptica
Leon, Mexico

Cosme Furlong
Mechanical Engineering Department
Worcester Polytechnic Institute
Worcester, MA, USA

Bernardino Barrientos
Senior Researcher
Centro de Investigaciones en Óptica
Leon, Mexico

Ryszard J. Pryputniewicz
Science and Technology (NEST)
Worcester Polytechnic Institute
Worcester, MA, USA

ISSN 2191-5644 ISSN 2191-5652 (electronic)
Conference Proceedings of the Society for Experimental Mechanics Series
ISBN 978-3-319-28511-5 ISBN 978-3-319-28513-9 (eBook)
DOI 10.1007/978-3-319-28513-9

Library of Congress Control Number: 2016940959

© Springer International Publishing Switzerland 2017

This work is subject to copyright. All rights are reserved by the Publisher, whether the whole or part of the material is concerned, specifically the rights of translation, reprinting, reuse of illustrations, recitation, broadcasting, reproduction on microfilms or in any other physical way, and transmission or information storage and retrieval, electronic adaptation, computer software, or by similar or dissimilar methodology now known or hereafter developed. The use of general descriptive names, registered names, trademarks, service marks, etc. in this publication does not imply, even in the absence of a specific statement, that such names are exempt from the relevant protective laws and regulations and therefore free for general use.

The publisher, the authors and the editors are safe to assume that the advice and information in this book are believed to be true and accurate at the date of publication. Neither the publisher nor the authors or the editors give a warranty, express or implied, with respect to the material contained herein or for any errors or omissions that may have been made.

Printed on acid-free paper

This Springer imprint is published by Springer Nature
The registered company is Springer International Publishing AG Switzerland

Preface

This volume contains a series of technical papers presented at the Fifth International Symposium on Experimental Mechanics and Ninth Symposium on Optics in Industry (ISEM-SOI2015) organized by the Society for Experimental Mechanics (SEM), Academia Mexicana de Óptica, and Centro de Investigaciones en Óptica (CIO) and held in Guanajuato, Guanajuato, Mexico, August 17–21, 2015.

Symposia were dedicated as part of the celebrations of the International Year of Light 2015 and the XXXV anniversary of the founding of the CIO and having a general topic relating to the emerging challenges for experimental mechanics in energy and environmental applications.

This collection of papers presents early findings of experimental and computational investigations on important areas of Experimental Mechanics. Symposia were intended to be interdisciplinary forums for engineers, technicians, researchers, and managers involved in all fields of Optics, Opto-mechatronics, Mechanics, and Mechanical Engineering. Overall, papers were assigned to the following relevant tracks:

Non-destructive methods

Dynamic and static structure and substructure testing

Multi-scale fields

Advanced new materials and their characterization

Environmental measuring techniques

The organizers thank the authors, presenters, and session chairs for their participation, support, and contribution to these Symposia.

Leon, Mexico
Worcester, MA
Leon, Mexico
Worcester, MA

Amalia Martínez-García
Cosme Furlong
Bernardino Barrientos
Ryszard J. Pryputniewicz

Contents

1	Optical Imaging Through Horizontal-Path Turbulence: A New Solution to a Difficult Problem	1
	William T. Rhodes, Nishantha Randunu Pathirannehelage, Diego Pava, and Yezid Torres Moreno	
2	Aluminum Strain Measurement by Beam Propagation	7
	Alonso Saldaña Heredia, Pedro A. Márquez Aguilar, and Arturo Molina Ocampo	
3	The Technique of Laser-Induced Breakdown Spectroscopy for Determination of Heavy Metals in the Receiving Body of Water	19
	A. Frías, A.E. Villarreal, F.G. Rendón Sauz, T. Flores, L. Ponce, R. Ortega, and M. Domínguez	
4	Applications of Laser Induced Breakdown Spectroscopy in the Identification of Bacteria	29
	F.G. Rendón Sauz, T. Flores Reyes, R. Ortega Izaguirre, A.K. Frias, A.E. Villarreal, and L. Ponce	
5	Residual Stresses Measurement by the Hole-Drilling Technique and DSPI Using the Integral Method with Displacement Coefficients	35
	Armando Albertazzi Jr, Filipe Zanini, Matias Viotti, and Celso Veiga	
6	On the Separation of Complete Triaxial Strain/Stress Profiles from Diffraction Experiments	43
	H. Wern	
7	Quantification of Slow Mechanical Displacements in Metal Samples by Optical Polarization Phase Shift DSPI	49
	Darwin Mayorga Cruz, José Antonio Marbán Salgado, Víctor Manuel Juárez Núñez, and Álvaro Zamudio Lara	
8	Comparative Analysis of Optoelectronic Properties of Glucose for Non-invasive Monitoring	55
	Jesús García-Guzmán, Naara González-Viveros, and Héctor H. Cerecedo-Núñez	
9	Phase Shifting Interferometry Using a Coupled Cyclic Path Interferometers	65
	L. García Lechuga, N.I. Toto-Arellano, V.H. Flores Muñoz, Amalia Martínez-García, and G. Rodríguez Zurita	
10	Identification of Microorganisms Using Digital Holographic Microscopy	71
	S. Muñoz Solís, M. del Socorro Hernández-Montes, and F. Mendoza Santoyo	
11	Noise Reduction in Off-Axis Digital Holography Reconstruction from Two Reconstruction Distances Based on Talbot Effect	75
	Miguel León-Rodríguez, Raúl R. Cordero, Juan A. Rayas, Amalia Martínez-García, Adrián Martínez-Gonzalez, Fernando Labbe, and Victor Flores-Muñoz	
12	Study of Temperature Distribution Over a Stirling Engine by Using the Schlieren Technique	85
	C. Alvarez-Herrera, A.R. Moreno-Nieto, and J.G. Murillo-Ramírez	
13	On Axis Fringe Projection	93
	Analía Sicardi-Segade, J.C. Estrada, Amalia Martínez-García, and Guillermo Garnica	

14 Instrument for Recording Purkinje Images	101
I.U. Cosme-Cisneros, G.A. Escamilla-Ruiz, D. Flores-Montoya, G. Hernández-Gómez, and A. Gómez-Vieyra	
15 Ultrasonic Arc Maps and Its Potential Application in Non-destructive Testing	111
Fabio Tomás Moreno Ortiz, Antonio Hernández Zavala, Alejandro Gómez Hernández, and Noé Emir Rodríguez Olivares	
16 Phase-Shifting Generated by Wavelength Modulation by Means of Switching On-Off a Laser Diode	117
Uriel Rivera-Ortega and Joris Dirckx	
17 Index of Refraction Measurements in Liquid Substances of Full Field Using Holographic Interferometry	123
Carlos Guerrero-Mendez, Tonatiuh Saucedo-Anaya, M. Araiza-Esquivel, Enrique De la Rosa, and Carlos Olvera-Olvera	
18 Geometrical Thickness Measurement of Thin Films by a Transmitted Gaussian Beam	131
Moisés Cywiak, Octavio Olvera-R, and Joel Cervantes-L	
19 Topography and Color Study of an Object Using Fringe Projection and Colorimetry Techniques	135
Y. Yanet López D., Amalia Martínez-García, and Julián Gómez S.	
20 Temperature Measurement of a Synthetic Jet Produced by a Helmholtz Cavity	145
Alan D. Blanco M., Bernardino Barrientos G., Andrew J. Moore, and Carlos Mares C.	
21 Gates' Interferometer as Fringe Projection System for Recovering 3D Shapes	153
J.A. Rayas, M. León-Rodríguez, Amalia Martínez-García, and R.R. Cordero	
22 Development of an Automated Laser Induced Breakdown Spectroscopy System for Compositional Mapping of Surfaces	159
E. Ponce Flores, J.R. Domínguez Torres, R. Galindo Del Valle, and A.E. Villarreal	
23 Artificial Visual System Used for Dental Fluorosis Discrimination	165
Miguel Mora-González, Evelia Martínez-Cano, Francisco J. Casillas-Rodríguez, Francisco G. Peña-Lecona, Carlos A. Reyes-García, Jesús Muñoz-Maciel, and H. Ulises Rodríguez-Marmolejo	
24 Inspection of Laser Ablated Transparent Conductive Oxide Thin Films by a Multifunction Optical Measurement System	173
Chi-Hung Hwang, Ming-Hsing Shen, Shih-Feng Tseng, Wen-Tse Hsiao, I-Feng Cheng, and Wei-Chung Wang	
25 LIBS Technique for Identification of Crude Oils	181
F.G. Rendón, A.K. Frías, A.E. Villarreal, T. Flores, L. Ponce, and G. Vázquez-Bautista	
26 3D Displacement Distribution Measurement Using Sampling Moire Method with Multiple Cameras	187
Daiki Tomita, Yorinobu Murata, and Motoharu Fujigaki	
27 Automatic Generation of Codes for Routine of CNC Machining Based on Three-Dimensional Information Obtained by Fringe Projection	195
S. Bustos, C. Aguilera, and Amalia Martínez-García	
28 Automatic Generation of Movement Sequences to Robotic Arm Based on Three-Dimensional Data Obtained Through Fringe Projection Technique	203
S. Bustos, C. Aguilera, and Amalia Martínez-García	
29 Application of Optomecatronics Load Cell for Measuring Work Force and Efforts in Industrial Machinery	211
A.A. Camacho and F.J. Martínez-Serrano	

30 ASE Noise Attenuation for Signal at 1548.4 nm Through a Sagnac Interferometer Using High-Birefringence Fiber Which Is Subjected to Temperature Changes	215
Manuel May-Alarcón, Héctor H. Cerecedo-Núñez, Aarón Flores-Gil, Miguel A. García-González, Francisco Méndez-Martínez, Marco A. Rodríguez-Blanco, and Víctor Golikov	
31 Single-Shot Phase Shifting Interferometry for Microscopic Measurements of Non-Birefringent Transmissive Phase Samples	221
V.H. Flores Muñoz, B. López Ortiz, N.I. Toto-Arellano, Amalia Martínez-García, and G. Rodríguez Zurita	
32 Design of a Customized Myoelectric Hand Prosthesis	227
A.A. Silva-Moreno and E. Lucas Torres	
33 Finite Element Static Analysis Simulation for a Grain Dispenser Mechanism	233
J.E. Valtierra, A.A. Silva, B.L. Vargas, and E.A. Ruelas	
34 Controlling Bounce of Vacuum Circuit Breakers' Contacts	241
Masao Narita, Naoki Yaegashi, Minoru Kobayashi, and Shigeru Inaba	
35 Experimental and Numerical Investigation of Effects of Fiber Orientation of Wood Stiffness	249
Tzu-Yu Kuo and Wei-Chung Wang	
36 Auto-Calibration and Micro-Flow Injection Procedure Based on Automated Hydrodynamic System for Spectrophotometric Determination of Cobalt	255
R.M. Camarillo E., J.A. Padilla M., J.A. García M., C.A. Ocón D., Ch. Reyes C., J.M. Camarillo E., and R. Rodríguez R.	
37 Mathematical Model to Predict the Stress Concentration Factor on a Notched Flat Bar in Axial Tension	265
F.J. Ortega-Herrera, A. Lozano-Luna, J.P. Razón-González, J.M. García-Guzmán, and F. Figueroa-Godoy	
38 Mechanical Implementation of Kinematic Synergy for Multi-Point Grasping	273
M.A. Trejo Letechipia, J.A. Cortes Ramírez, and H. Aguayo Téllez	
39 Cascaded Ultra-Low Reflective Fiber Points for Distributed Sensing	281
Rodolfo Martinez Manuel and H.E. Sutherland	
40 Object Surface Representation Via NURBS and Genetic Algorithms with SBX	289
J. Apolinar Muñoz Rodríguez and Francisco Calos Mejia Alanís	
41 Photo-Oxidation of Polystyrene Film Irradiated with UV-B	295
C.G. Hernández, R. González, J.J. Soto, and I. Rosales	
42 Dynamic Analysis of Trawl Doors Applied in Bottom Trawls to Catch Shrimp	301
S. Sarmiento-Nafaté, J. Enríquez-Zárate, J. Villalobos-Toledo, and C. Pineda-García	
43 Simulator of an Adaptive Optics System Using Matlab	311
Marco A. Betanzos-Torres, Juan Castillo-Mixcóatl, Severino Muñoz-Aguirre, and Georgina Beltrán-Pérez	
44 Design, Development and Validation of an Artificial Muscle Biomechanical Rig (AMBR) for Finite Element Model Validation	319
A. Kriechbaumer, M.P. Trejo Ramírez, U. Mittag, M. Itskov, J.M. López Ramírez, and J. Rittweger	
45 Application of Laser Light on the Development of Equipment for the Study of Proteins	329
Nydia Tejeda Muñoz and Martha Robles-Flores	

46 Organic Solar Photovoltaic Cells	335
A. Nava-Vega, Mario Cerda Lemus, Denisse Makoske Ibarra, and Moisés Viloría Sánchez	
47 Fiber Bragg Gires-Tournois Interferometer Etalons as Fiber Sensor	341
A. González-García, C.I. Castañeda-Jiménez, N. Rico-Jordan, I. Urbina-Salas, G. González-García, and M.C. Wilson-Herrán	
48 Cleaning of Tantalum Capacitor Electrode Surface by Laser in Multipulse Regime	345
A.E. Villarreal, A.K. Frías, F.G. Rendón, T. Flores, L. Ponce, and G. Vázquez-Bautista	
49 High Quality Polishing Procedure of Glass Substrates: Application in Integrated Optics	355
H.E. Lazcano, J.L. Flores, A. Blanco, A. Hernández, R. Nieto, J.L. Martínez, R.A. Torres, G.V. Vázquez, and J.L. Hurtado	
Index	365

Chapter 1

Optical Imaging Through Horizontal-Path Turbulence: A New Solution to a Difficult Problem

William T. Rhodes, Nishantha Randunu Pathirannehelage, Diego Pava, and Yezid Torres Moreno

Abstract Time-average Fourier telescropy appears to provide a way to acquire diffraction-limited imagery in ground-level horizontal-path imaging through turbulence at kilometer-scale distances and with meter-scale apertures. The scheme, which has its basis in Fourier telescropy, uses separate averaging with time of the amplitude and phase of the Fourier telescropy signal to remove the effects of the turbulence. The basic method is described and preliminary results of simulations discussed.

Keywords Fourier telescropy • Imaging thorough turbulence • Super resolution • Time-average Fourier telescropy • Spatial-frequency-domain imaging

1.1 Introduction

Considerable progress has been made over the past 60 years in imaging through vertical-path atmospheric turbulence, with applications to astronomy and the imaging of earth-orbiting satellites. Over the same period there has been almost no progress made in improving our ability to obtain high-resolution images through long-horizontal-path, ground-level turbulence. Resolution obtainable at a distance of a kilometer is seldom better than 10 cm or so, the same as is achievable with a 1 cm aperture. The reasons are several: horizontal-path turbulence is much stronger than vertical-path turbulence; horizontal-path turbulence is distributed throughout the space between the object and the observer, precluding the successful implementation of a thin phase screen model; and the isoplanatic patch is quite small. It is, in fact, smaller than the point spread function itself, greatly complicating image processing.

In this paper we present basic aspects of a recently-developed method for imaging through ground-level, horizontal-path turbulence that can offer diffraction-limited performance (in some sense, even super-resolution) with large apertures over kilometer-scale distances, providing resolution at the scale of a millimeter and better [1]. In this method, image information is acquired in the spatial frequency domain rather than in the space domain: spatial Fourier components of the image are measured and an inverse 2D Fourier transform then yields the image. Characteristics of the method, referred to as time-average Fourier telescropy, are, on the basis of our preliminary studies, expected to include the following:

- (a) Large-aperture, diffraction-limited imagery in the presence of long horizontal-path, ground-level turbulence.
- (b) Extremely large isoplanatic patch.
- (c) Graceful degradation with increasing turbulence strength.

W.T. Rhodes (✉)

Department of Computer & Electrical Engineering and Computer Science, Florida Atlantic University, Boca Raton, FL 33431, USA

Division of Engineering, University of Guanajuato, Guanajuato, Mexico

e-mail: wrhodes@fau.edu

N.R. Pathirannehelage

Department of Computer & Electrical Engineering and Computer Science, Florida Atlantic University, Boca Raton, FL 33431, USA

e-mail: randunu.cid@gmail.com

D. Pava

Aventusoft LLC, 2840 N University Dr, Coral Springs, FL 33065, USA

e-mail: diegopava@gmail.com

Y.T. Moreno

GOTS, Grupo de Óptica y Tratamiento de Señales, Escuela de Física, Facultad de Ciencias, Bucaramanga, Colombia

e-mail: ytorres@uis.edu.co

The price paid for these positive attributes include the following:

- (d) Active illumination of the object/target required.
- (e) Potentially long integration times, implying slow image acquisition.
- (f) The requirement that the object not move during the image forming process.
- (g) A complicated and most likely expensive imaging system.

1.2 Fourier Domain Imaging and Fourier Telescopy

Figure 1.1 illustrates basic characteristics of space- and spatial-frequency-domain imaging. The effect of turbulence on space-domain imaging of a point source is illustrated in Fig. 1.2. The smoothing associated with long time-average exposures prevents recovery of high spatial frequency components. The short exposure point spread function (PSF) has the appearance of a random, time-varying laser speckle pattern, and in the horizontal-path imaging case varies strongly from one point on the object to another (strong space variance).

Time-average Fourier telescopy has its basis in Fourier telescopy [2], an imaging method developed in the 1990s and investigated for high-resolution, upward-path imaging of earth-orbiting satellites from ground-based stations. In its original form it is not applicable to long horizontal-path imaging. It can, however, be made so through appropriate signal processing.

The basic Fourier telescopy scheme is described here. An object with optical intensity reflectance $f(x, y)$ is illuminated by a moving sinusoidal (Young's) fringe pattern, produced by the interference of two mutually coherent laser beams offset in angular frequency by ω . A frequency offset in the tens of MHz range can easily be introduced by means of an acousto-optic cell. Light reflected by the object, assumed to be optically rough, is collected by a large-area detector, resulting in a signal of the form

$$i(t) = \int_{-\infty}^{\infty} \int_{-\infty}^{\infty} f(x, y) \{1 + \cos [\omega t - 2\pi(ux + vy)]\} dx dy, \tag{1.1}$$

Fig 1.1 In spatial-frequency-domain imaging, the Fourier transform of the object is sampled. An inverse Fourier transform produces the corresponding space-domain image

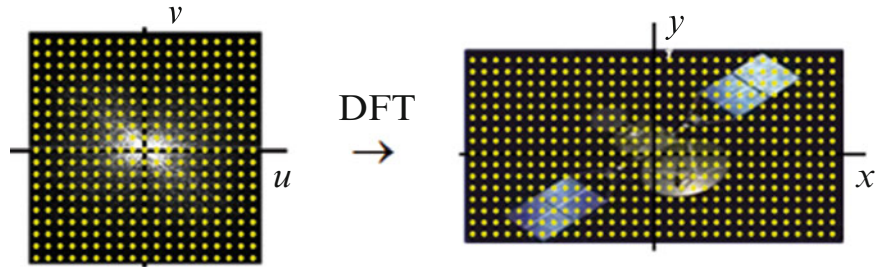
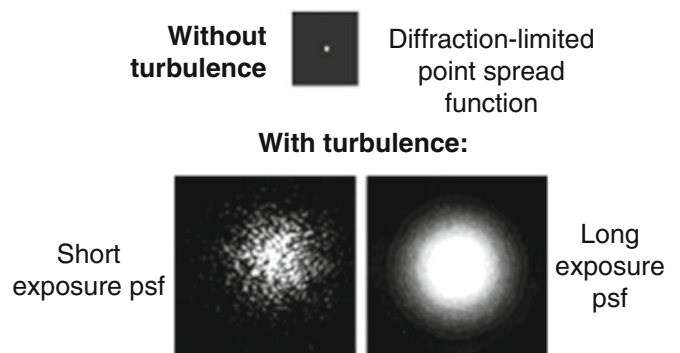


Fig. 1.2 The effect of atmospheric turbulence on the point spread function of an imaging system can be substantial



where (u, v) is the spatial frequency of the fringe pattern. For the limits of integration to be infinite, all the light must be captured by the detector. For a sufficiently large detector, however, or a satisfactorily large number of smaller detectors operating in parallel, the detector signal will be well approximated by the above expression. Evaluation of (1.1) yields

$$i(t) = B + s(t; u, v), \quad (1.2)$$

where

$$B = \iint f(x, y) dx dy \quad (1.3)$$

is a constant bias and where

$$s(t; u, v) = \iint f(x, y) \cos [\omega t - 2\pi(ux + vy)] dx dy. \quad (1.4)$$

Manipulation of this latter equation results in the time-varying signal component [1]

$$s(t; u, v) = |F(u, v)| \cos [\omega t + \psi(u, v)], \quad (1.5)$$

where the realness of $f(x, y)$ has been exploited and where

$$F(u, v) = |F(u, v)| \exp[j\psi(u, v)], \quad (1.6)$$

$F(u, v) = \mathcal{F}\{f(x, y)\}$ being the 2-D Fourier transform of $f(x, y)$. We see that $s(t; u, v)$, the time-varying component of the detected signal, conveys on a sinusoidal carrier the magnitude $|F(u, v)|$ and the phase $\psi(u, v)$ of the object Fourier transform, evaluated at the spatial frequency (u, v) of the illuminating fringe pattern. Measurements made at a suitably large number of properly chosen spatial frequencies (u, v) and an inverse discrete Fourier transform yield object function $f(x, y)$. Simple Fourier telescope experiments can be performed with the aid of a modified Michelson interferometer [3].

1.3 Time-Average Fourier Telescopy

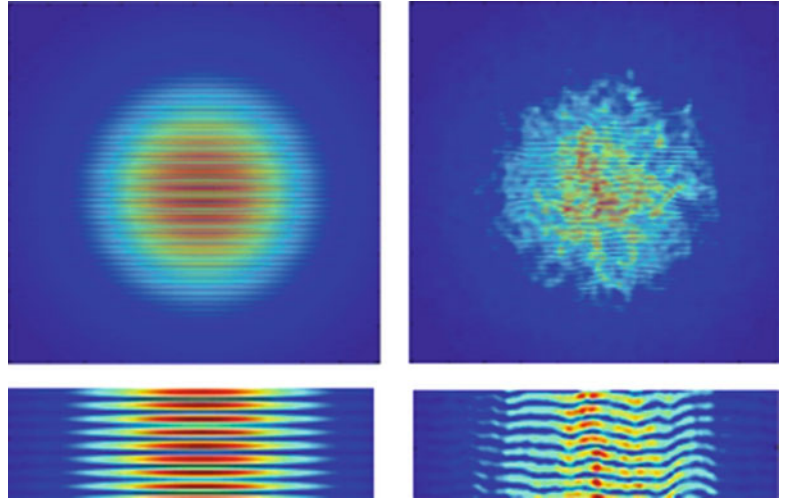
The above equations presume that there is no turbulence and that, as a consequence, the object illumination consists of straight, uniform fringes moving with constant speed. In the presence of turbulence, the illuminating fringes are distorted with spatially-varying contrast, as illustrated in Fig. 1.3, and they move and evolve in response to temporal variations in turbulent refractive-index cells in the propagation path. Signal $s(t; u, v)$ is in this case given by

$$s(t; u, v) = \int_{-\infty}^{\infty} \int_{-\infty}^{\infty} f(x, y) a(x, y, t) \cos [\omega t - 2\pi(ux + vy) + \phi(x, y, t)] dx dy. \quad (1.7)$$

For sufficiently large values of ω , $s(t; u, v)$ is a bandpass signal. Through manipulations similar to those leading to (1.5), $s(t; u, v)$ can be shown to have the form

$$s(t; u, v) = |\tilde{s}(t; u, v)| \cos [\omega t + \arg\{\tilde{s}(t; u, v)\}], \quad (1.8)$$

Fig. 1.3 Examples of numerically-calculated illuminating fringe patterns: left in the absence of turbulence, right in the presence of turbulence



where complex amplitude $\tilde{s}(t; u, v)$ is given by

$$\tilde{s}(t; u, v) = \mathbf{F}\{f(x, y)a(x, y, t)\exp[j\phi(x, y, t)]\}, \quad (1.9)$$

the Fourier transform of the product of $f(x, y)$ with the complex-valued turbulence-generated function $a(x, y, t)\exp[j\phi(x, y, t)]$. In the absence of turbulence, $s(t; u, v)$ is a pure sinusoid with constant amplitude $|F(u, v)|$ and constant phase $\psi(u, v) = \arg\{F(u, v)\}$, i.e., the desired Fourier amplitude and phase functions. In the presence of turbulence, $s(t; u, v)$ has the form of a sinusoidal carrier at frequency ω with time-varying magnitude $|\tilde{s}(t; u, v)|$ and time-varying phase $\theta(t; u, v) = \arg\{\tilde{s}(t; u, v)\}$.

The essence of time-average Fourier telemetry (TAFT) lies in the assumptions, arguably valid but yet to be verified experimentally, that under reasonably-assumed conditions, suitable time averages of $|\tilde{s}(t; u, v)|$ and of $\arg\{\tilde{s}(t; u, v)\}$ provide good estimates of the turbulence-free values, i.e., that to a good approximation

$$\langle |\tilde{s}(t; u, v)| \rangle = a|F(u, v)| \quad (1.10)$$

and

$$\langle \theta(t; u, v) \rangle = \psi(u, v), \quad (1.11)$$

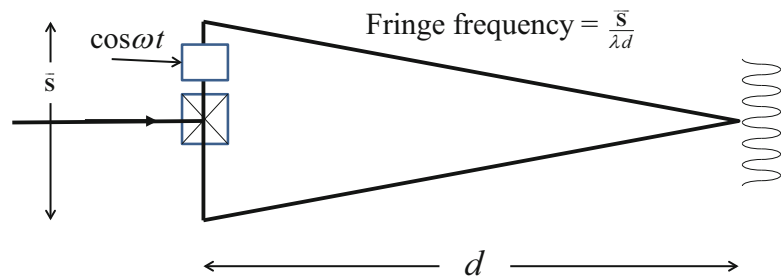
where a is a proportionality factor we expect to be less than but close to unity. Conditions under which we expect (1.10) and (1.11) to be valid are: (a) the turbulence, viewed as a random process, is stationary in time; and (b) the turbulence is homogeneous and isotropic. These conditions would appear to be well approximated in many cases of interest.

1.4 Calculating the Average Magnitude and Phase

With the aid of a lock-in amplifier, calculation of average magnitude $\langle |\tilde{s}(t; u, v)| \rangle$ is straight-forward. A local oscillator signal is available at the frequency shifter illustrated in Fig. 1.4. Calculation of the average phase $\langle \theta(t; u, v) \rangle$ is more complicated because of the need to unwrap the measured phase values. Preliminary calculations and simulations lead us to expect $\theta(t; u, v)$ to make excursions large compared to 2π radians. However, the output of the lock-in amplifier will give these phase values in the principal range $[0, 2\pi)$, i.e., modulo- 2π . Unwrapping the phase is in principle straight-forward—so long as the signal amplitude does not become too small, in which case phase tracking operation may need to begin again.

Turbulence in the atmosphere produces signal components ranging up to around 1 kHz, and we thus think that phase samples separated by ~ 1 ms will be required. (It is not necessary to sample $\theta(t)$ at its Nyquist rate or faster, since the objective is not to reconstruct $\theta(t)$, only to calculate its average value.) Samples separated by ~ 100 ms are expected to be

Fig. 1.4 Moving fringe production. Two mutually coherent laser beams offset in frequency by ω interfere at a distance to produce a moving sinusoidal fringe pattern. The frequency shifter both shifts the optical frequency of one of the interfering beams and provides a reference for the lock-in amplifier



more or less independent. Since a large number of samples of $\theta(t; u, v)$ are required for satisfactory averaging, depending on turbulence strength and distance to target, we expect to need many seconds and perhaps minutes to complete a measurement.

Given the amount of time required to obtain suitable averages of the Fourier magnitude and phase, it is desirable to record many Fourier components in parallel. This objective can be achieved through the use of spatio-temporal non-redundant source arrays, as discussed in Ref. [4]. A related approach is to produce the fringes with crossed acousto-optic cells, which can be “filled” in tens of microseconds [5]. Many measurements can thus be made in a 1 ms interval.

1.5 Concluding Remarks

We have conducted numerical simulations that we believe adequately model the effects of turbulence over kilometer paths at ground level. Preliminary results suggest strongly that the method can provide diffraction-limited performance with meter-size apertures, and we have no reason to believe that apertures extending to tens of meters and larger cannot yield diffraction-limited performance. Our findings will be published soon [6]. We note that all spatial frequency components are detected with essentially equal gain, suggesting that, unlike conventional imaging where the MTF falls off with spatial frequency, the scheme exhibits “super-resolution” characteristics. The fact that a flat MTF is inconsistent with a non-negative-real point spread function must be taken into account in the image display operation.

References

1. W.T. Rhodes, Time-average Fourier telescope: a scheme for high-resolution imaging through horizontal-path turbulence. *Appl. Opt.* **51**, A11–A16 (2012)
2. R. Holmes, S. Ma, A. Bhowmik, C. Greninger, Analysis and simulation of a synthetic-aperture technique for imaging through a turbulent medium. *J. Opt. Soc. Am. A* **13**, 351–364 (1996)
3. N. Randunu Pathirannehelage, Y. Torres Moreno, Rhodes WT, A Michelson interferometer-based system for experiments in Fourier telescope imaging, in preparation
4. D.F. Pava, W.T. Rhodes, Spatiotemporal non-redundant arrays for Fourier telescope imaging, in preparation
5. D. Feldkhun, K.H. Wagner, Doppler-encoded excitation pattern tomographic optical microscopy. *Appl. Opt.* **49**, H47–H63 (2010)
6. N. Randunu Pathirannehelage, Y. Torres Moreno, W.T. Rhodes, Time-average Fourier telescope simulation results, in preparation

Chapter 2

Aluminum Strain Measurement by Beam Propagation

Alonso Saldaña Heredia, Pedro A. Márquez Aguilar, and Arturo Molina Ocampo

Abstract In mechanics of materials it is important to know the stress–strain relation of each material in order to understand their behaviour under different loads. Optical methods are used for determine different kind of stresses and interferometry is the most used tool. In this work it is presented a new alternative to determine the stress–strain based in one beam which is reflected in the surface of the material while it is in a compression test as the ASTM indicates. It is taken the material as a reflective surface which acts as a spherical mirror and it will scatter light, the scattered area will increase as the deformation increases. The reflected beam is analysed applying beam propagation equations and Digital Image Processing for getting the increase of the scattered area. Finally it is plot the relation between the applied stress and the beam propagation. There is also presented the accuracy, sensitivity and a theoretical demonstration of the method.

Keywords Gaussian propagation • One beam strains measurement • Digital image processing • Fourier analysis • Compression test

2.1 Introduction

Stress–strain diagrams are very important in understanding the behaviour of materials under load [1]; they show the elastic, plastic and rupture part of materials. There are two methods to obtain the diagram: the invasive methods in which mechanics take advantage doing physical tests as the test-tube in which is placed a small piece of the probe and it is applied a specific load to it, then is measured the deformation in displacement [2]. Optical methods are also used as an invasive way to determine residual stress, in-field displacements and strain, in which the most used technique is the hole-drilling method, created in 1930 by Mathar [3], nowadays this technique is standardized by ASTM [4] and has many applications such as measuring in-plane residual stress [5], it was proposed the use of the interferometric speckle pattern for residual stress measurements [6–8], also it was combined with Moiré Interferometer technique, which provides more sensitivity for measuring small surfaces displacements that occur in the experimentation [9]. In the other hand, non-invasive optical methods, such as the Electronic Speckle Pattern Interferometer (ESPI) which is used with Moiré techniques [10]; another one extends conventional Moiré interferometry method to the micron-level spatial domain called micro-moiré interferometer [11]. There is also another technique called deflectometry [12–13], in which is used light passing through a fringe array in order to measure curvatures of objects which are taken as mirrors, the reflected light is observed into a CCD camera and the fringe pattern is analysed with standard phase shift techniques, the commonly analysed object has an aspherical shape. Another one uses parallel light beams to measure curvatures of surfaces [14], in which is used a collimated light beam passed through means for producing parallel light beams which are reflected off the surface to fall upon a detector that measures the separation of the reflected beams.

In this work we introduce an alternative method to determine stress–strain, in which we use one laser beam impinging our material in its cross-section during a compression test. We propose that the material (aluminium) will act as an optical spherical mirror, as the material is first completely flat and its cross-section will change as a reaction of the compression test; the laser light impacts the surface and this “mirror” will reflect and scatter light, thus the scattered area will increase as the

A.S. Heredia
Facultad de Ciencias Químicas e Ingeniería, Universidad Autónoma del Estado de Morelos,
Av. Universidad #1001 Colonia Chamilpa. C.P. 62209, Cuernavaca, Morelos, Mexico
e-mail: alonso.saldana@uaem.mx

P.A.M. Aguilar (✉) • A.M. Ocampo
Centro de Investigación en Ingeniería y Ciencias Aplicadas, Universidad Autónoma del Estado de Morelos,
Av. Universidad #1001 Colonia Chamilpa. C.P. 62209, Cuernavaca, Morelos, Mexico
e-mail: pmarquez@uaem.mx; arturo_molina@uaem.mx

deformation increases. The scattered area is studied with Gaussian beam propagation equations and it is used Digital Image Processing (DIP) in order to measure each area increasing. This is how we obtain a relation between the beam propagation and the strain, which we propose to be similar to the radius transformation of the aluminium. The scope of the present research is to determine a correlation between the radius curvature transformation and the deformation of the material with a non-invasive strain measurement method, using one beam and its propagation. Another objective is to reconstruct a strain diagram from the reflected beam using DIP. Also, we show accuracy, error and sensitivity of the method, as well as a theoretical demonstration of our phenomenological process; assessing that the present work would be a cheap technique as it only uses one laser beam.

2.2 Developments

2.2.1 Optics

The simplest beam and the most known is the Gaussian, because its characteristics and evolution are well-known [15]. The amplitude function represented from Gaussian beams could be deduced by applying boundary conditions in the optical resonator where the laser radiation is produced, this amplitude is described by

$$E(x, z) = E_0 \frac{w_0}{[W(z)]^2} \cdot \exp \left[\frac{-x^2}{[W(z)]^2} - \frac{kx^2}{2R(z)} - kz + \eta(z) \right], \quad (2.1)$$

where w_0 is the beam waist, $W(z)$ is how the beam propagates, $R(z)$ is the curvature radius of the spherical waves and $\eta(z)$ is the beam phase angle. Gaussian beams are able to pass through different media [16]; the light reflexion occurs when it arrives to the boundary separating two media of different optical densities and some of the energy is reflected back into the first medium [18], taking this outset, if a beam impinges in a mirror, the reflection can be studied as a Gaussian propagation. In our case, the metallic surface will be modelled as a convex mirror. As it is well-known, there is a relation between the focal length and the curvature radius of a mirror. Using this relation the phase of the transmitted wave is altered to

$$\varphi(x, z) = 2\eta(z) - \frac{kx^2}{z \left(1 + \frac{z_0^2}{z^2}\right)} + \frac{kx^2}{f}, \quad (2.2)$$

where z_0 is the initial Rayleigh distance, w_0 is the initial beam waist, and f is the focal length of the mirror. There are also propagation equations, in which w_0 and z_0 turns into w_1 and z_1 respectively, after a distance f and they are calculated by:

$$w_1 = \frac{w_0}{\sqrt{\left(1 + \frac{z_0^2}{f^2}\right)}}, \quad (2.3)$$

$$z_1 = \frac{f}{\left(1 + \frac{f^2}{z_0^2}\right)}. \quad (2.4)$$

This pair of equations involves how Gaussian beam propagates [19], so in order to calculate the new beam waist in the propagation axis we have:

$$W(z_p) = w_1 \sqrt{\left(1 + \frac{z_p^2}{z_1^2}\right)}, \quad (2.5)$$

where $W(z_p)$ is the new beam waist at z_p which is the propagation distance. One of the aims of the present investigation is to deduce a relation between the radius transformation of the compressed material and the real strain; all these equations are needed in order to calculate the change of the focal length of the material in every change of the compression test. Substituting (2.3) and (2.4) in (2.5) is deduced:

$$\frac{z_p^2}{z_0^4} \cdot x^2 + x \left(1 - \frac{W(z_p)^2}{w_0^2} \right) - z_0^2 = 0. \quad (2.6)$$

$W(z_p)$ is calculated doing DIP, taking 54 area increments by second during the compression test. Once is obtained the result from (2.6), the variation of the focal length is determined applying

$$\xi = \frac{f_f - f_i}{f_i}, \quad (2.7)$$

where f_f is the final focal length and f_i is the initial focal length, thus a dimensionless variable is obtained.

2.2.2 Mechanics

In mechanics of materials it is used the compression test in order to get the stress–strain diagrams of every material [2]. In the present work has been done standardized compression tests and aluminum was used with a cross-section of $1 \times 1 \times 0.9$ in.; compression tests and probes are done as ASTM E-9 indicates [19]. We are working in the elastic neighbourhood of the diagram, according to Hooke's law:

$$\sigma = E \cdot \varepsilon \quad (2.8)$$

where σ is the stress, E is the Young's module of the material (70 GPa) and ε is the dimensionless deformation. One of the objectives of this work is to obtain a relation between the focal length and the deformation; we propose an equation similar to the Hooke's law:

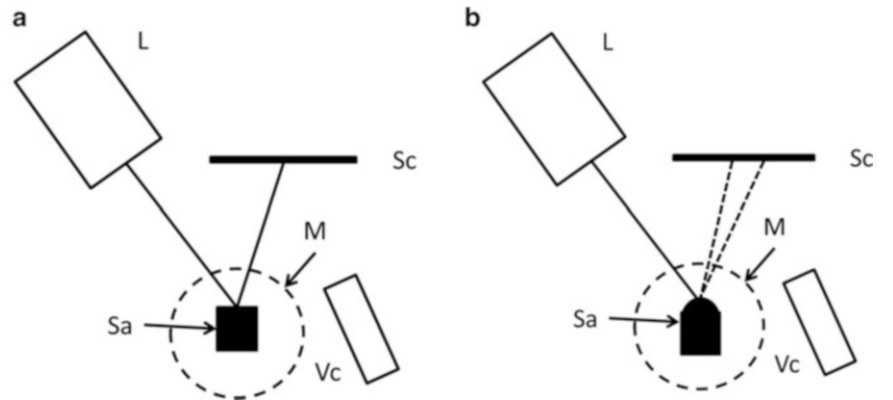
$$\sigma = E \cdot K \cdot \xi \quad (2.9)$$

where K is a dimensionless coefficient proposed in this work and ξ is the dimensionless value obtained in (2.7). The coefficient K is obtained from the relation between the slopes of both graphs of interest: stress–strain diagram and DIP plot.

2.3 Experimental Setup and Data Processing

Five probes were sanded and polished to mirror grade in the cross-section and they were placed in the machine in order to begin the compression test. A diagram of this method is shown schematically in Fig. 2.1a. The output of a He-Ne laser (L), with a wavelength $\lambda = 632$ nm and a power of 1 mW is placed in front of the sample (Sa) in order to irradiate the polished face and the reflected beam impacts a screen (Sc) which is placed aside the laser beam. The material is first completely flat and as it is compressed (M) the size of the cross-section will decrease as a reaction Fig. 2.1b. During the compression tests,

Fig. 2.1 Experimental set-up:
(a) material with no strain;
(b) the strained material will scatter light



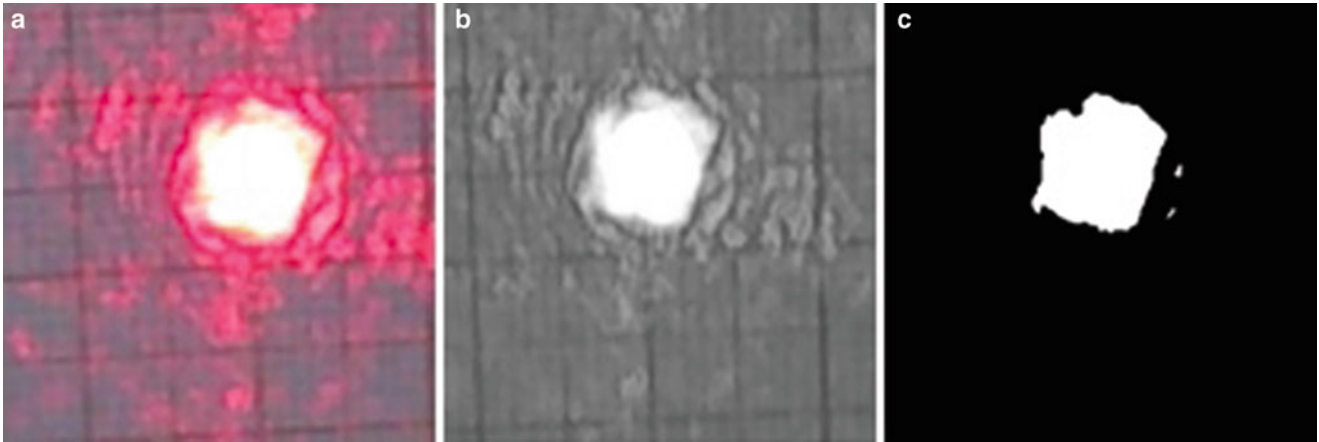


Fig. 2.2 Image processing: (a) how the image is loaded; (b) grey-scale image; (c) binary image

the speed of the compression load was 0.2 cm/s with duration of 10 min approximately and while they were taking place the reflected light was recorded with a high resolution video camera (Vc).

Once the video is recorded, it is divided into thousands of photograms in order to load each image and process it. A program is written in Matlab[®] for Digital Image Processing. The area calculation is described below: in Fig. 2.2a it is shown how the code loads the image; it is converted into a gray-scale image as it is shown in (b), the last image (c) shows how it is turned into a digital image for the processing.

There are specific functions in the program in order to do image processing: first to load the image it is needed to call the function “imread” which loads the image as a matrix, therefore, in order to convert it into a grey-scale image it is needed “rgb2gray”. Finally it is called the function “im2bw” in order to get a binary image. To get the resulting area it is used a last function “bwarea” which provides the binary area of the image. The code is programmed for doing this process iteratively for every image. From this area the $W(z_p)$ parameter is calculated. Thus (2.6) is used in order to calculate the focal length.

It is known that for every test there will be a stress–strain diagram which is given from the software of the machine and the program has also a plot which shows how the focal length increases.

2.4 Results and Discussion

In the section above, we mentioned that five samples were prepared for compression test, for each one has been obtained two graphs of interest, the stress–strain diagram is shown in Fig. 2.3 and the DIP plot which is shown in Fig. 2.4, which correspond to the first sample.

One of the aims of the present work is to rebuild a strain relation, using one beam and its propagation. From (2.8) and (2.9) are calculated the slopes of each graph, it is taken a $\Delta t = 150$ s. The slope of Fig. 2.3 is 0.0006 and for Fig. 2.4 is 0.003; the coefficient **K** between them is **5**.

In Fig. 2.5 we plot (2.8) (black) and (2.9) (red). It is seen that experimental data is close to a real stress–strain diagram. In Fig. 2.6 we plot the error of the presented method which is taken from:

$$error = \frac{v_r - v_e}{v_r} \%, \quad (2.10)$$

where V_r is the real strain value obtained from the machine; V_e is the experimental strain value obtained from (2.7). The same process is done for the next four samples, where the values of interest are **K**, the reconstructed graph and the % of error.

For the second probe these were the results: **K = 5.2**

For the third probe these were the results: **K = 4.52**

For the fourth probe these were the results: **K = 4.5**

For the fifth probe these were the results: **K = 4.54**

In Figs. 2.5, 2.7 and 2.11 the behaviour of the experimental graph is below of the real stress–strain diagram, for Fig. 2.13 the behaviour is above it and for Fig. 2.9 the graph has a different behaviour. This is mainly because of our samples surfaces,

Fig. 2.3 Strain diagram

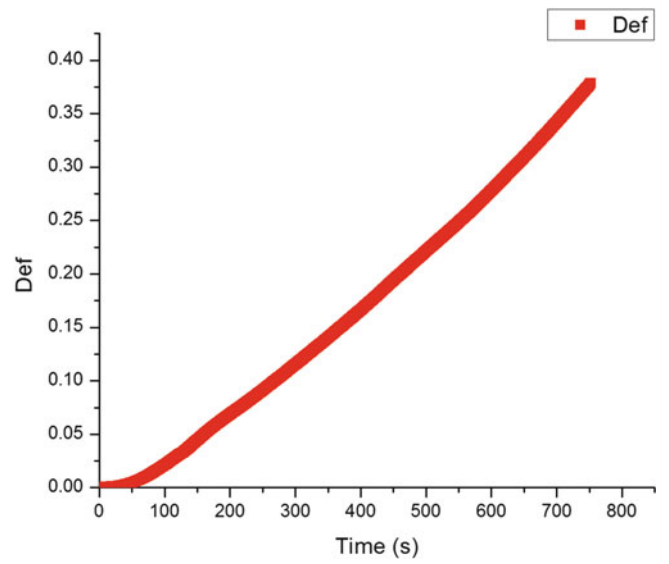


Fig. 2.4 PDI graph

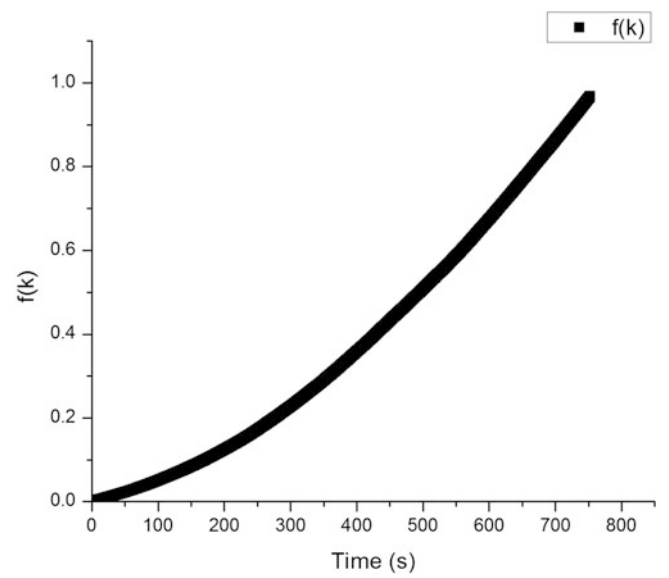


Fig. 2.5 Red, reconstructed graph; black, strain diagram

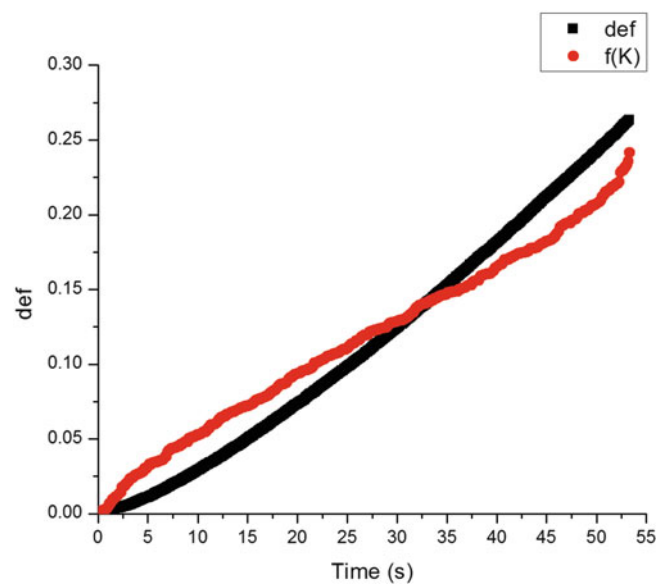


Fig. 2.6 Red part represent the error of the first test

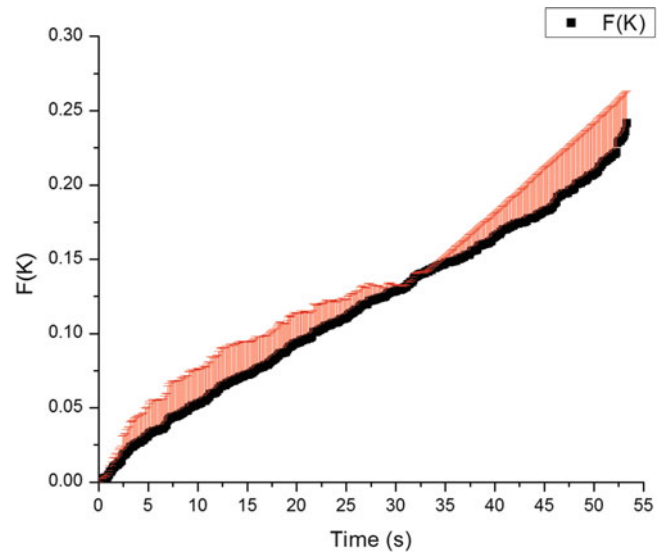
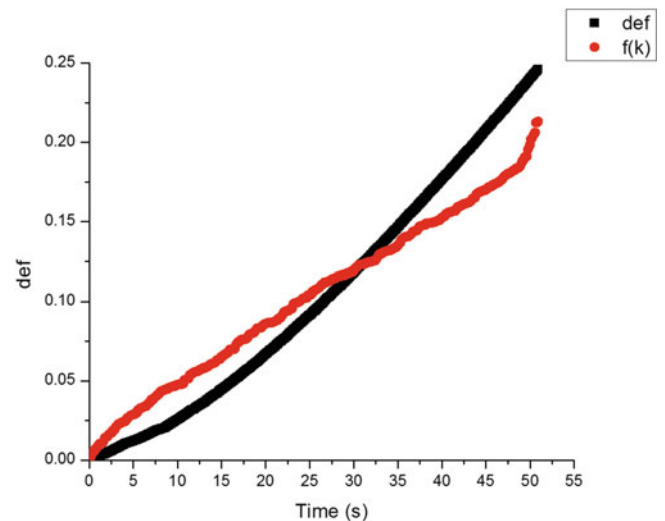


Fig. 2.7 Reconstructed graph



as they were sanded and polished, human error causes non-uniform surfaces, thus light reflection is not always the same. Figures 2.8, 2.10, 2.12 and 2.14 represent the error of each test.

In Table 2.1 we show the accuracy and mean error of each measurement, so we can assume that the mean accuracy of our method is 88 %.

By comparing the average strain determined for five different specimens with the compression stress values measured with the load cell, it was demonstrated that the present technique can measure the relative strain with an average uncertainty of 12 %.

As we mention in (2.7), there are 54 measurements per second obtained by DIP, we calculate the mean of the changes between each measure in a 10 s time interval and we obtain that the sensitivity of our method is 27 μ deformations.

2.4.1 Theoretical Demonstration

The laser used in the present work has initial parameters such as (initial intensity, beam waist and Rayleigh distance) enlisted by the manufacturer in its handbook [20].

Fig. 2.8 Second test error

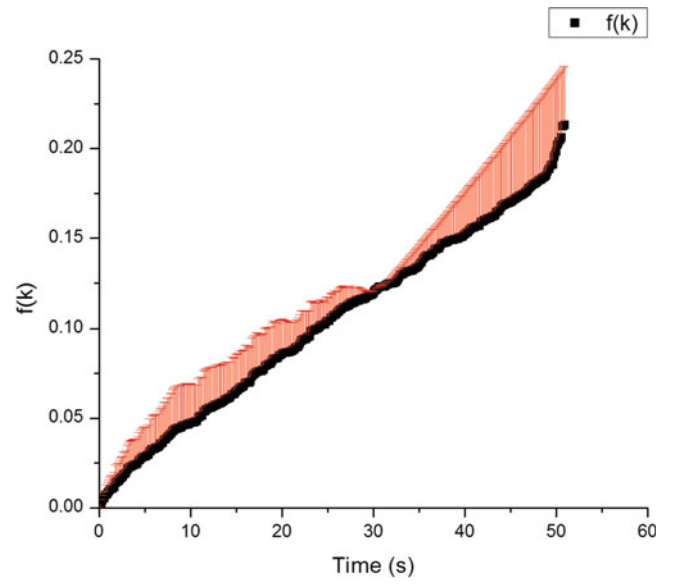


Fig. 2.9 Reconstructed graph

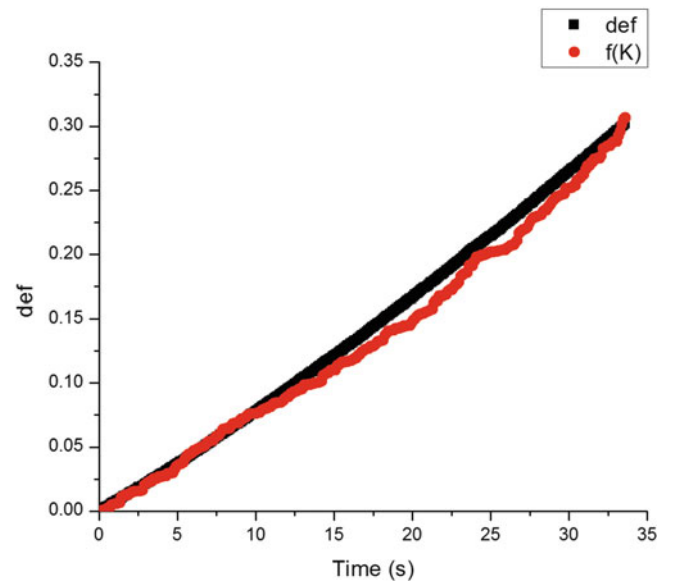


Fig. 2.10 Third test error

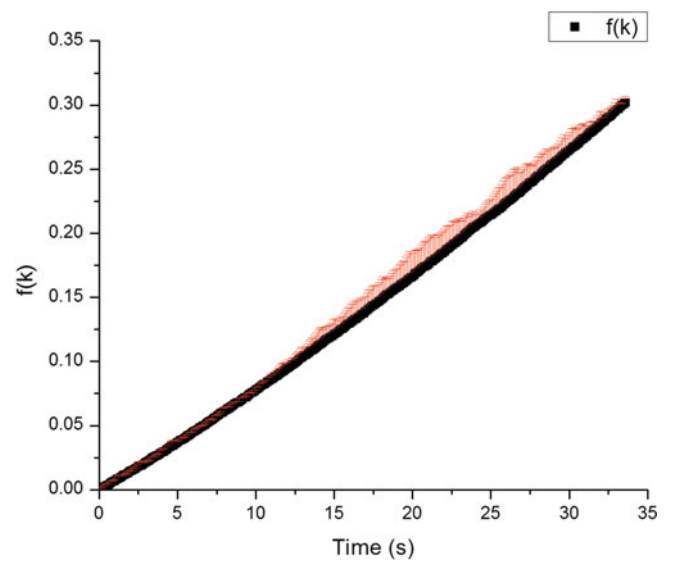


Fig. 2.11 Reconstructed graph

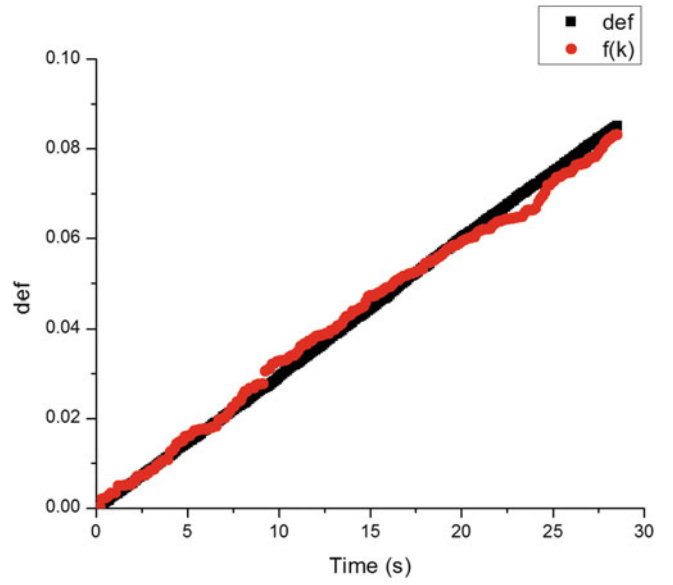


Fig. 2.12 Fourth test error

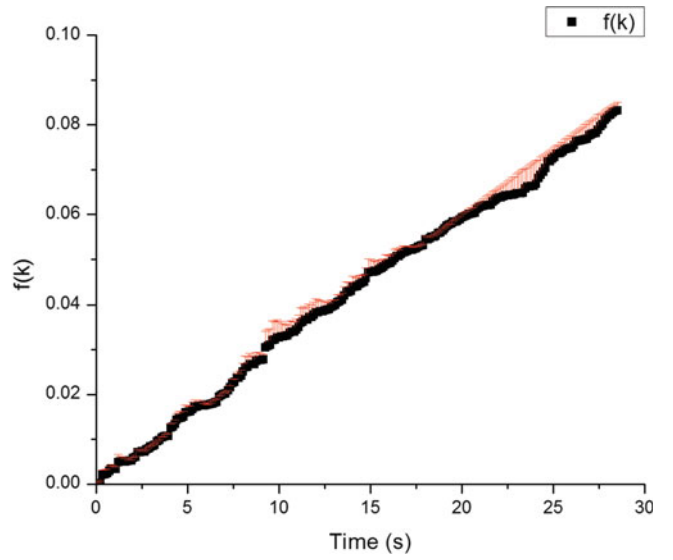


Fig. 2.13 Reconstructed graph

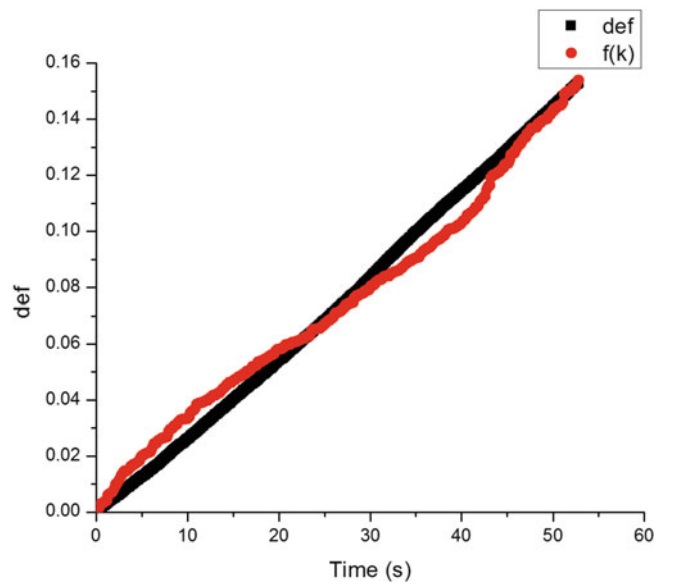
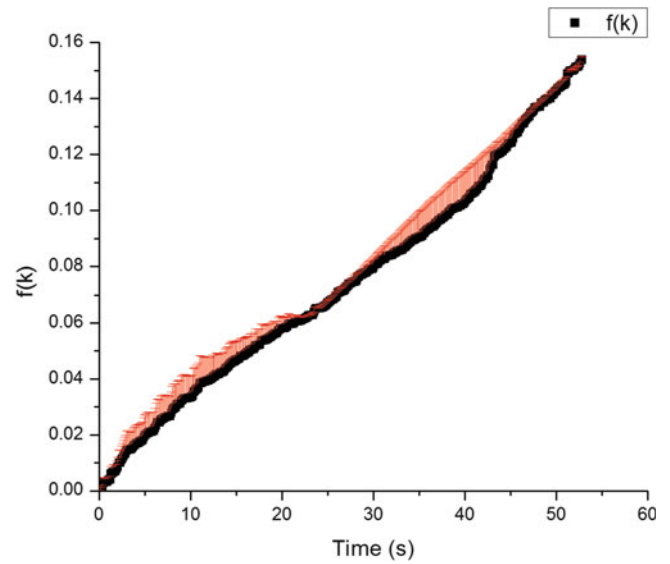
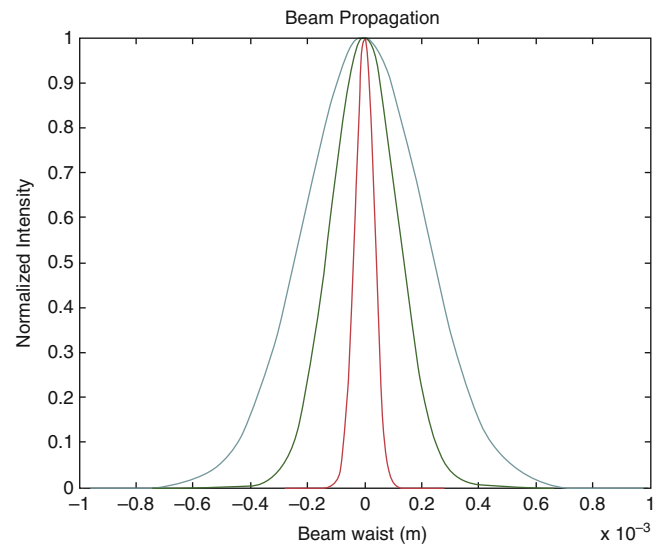


Table 2.1 Accuracy and error of the test

Probe	Accuracy (%)	Mean error (%)
1	88	12
2	89	11
3	93	7
4	92	8
5	91	9

Fig. 2.14 Fifth test error**Fig. 2.15** Gaussian propagation: Intensity profile

In Fig. 2.15 we plot (2.1) and (2.2) substituting the results from (2.7), the initial parameters of our laser and propagating formally a Gaussian beam. Using analytical expressions for numerical calculations, we show that the focal length increase is proportional to an increment of the beam waist. We assume that $\varepsilon \sim f$.

According to the Fresnel diffraction and a focal lens transmission [21] we have:

$$U_f(u, v) = \frac{\exp\left[\frac{ik}{2f}(u^2+v^2)\right]}{i\lambda f} * \iint_{-\infty}^{\infty} U(x, y) \cdot t_A \cdot \exp\left[\frac{ik}{2f}(xu+yv)\right] dx dy, \quad (2.11)$$

where

$$t_A = \exp\left[\frac{ik}{2f}(x^2+y^2)\right], \quad (2.12)$$

and

$$U(x, y) = \exp\left[-\frac{ik}{2f}(x^2+y^2)\right]. \quad (2.13)$$

Substituting (2.12) and (2.13) into (2.11), expanding formally and changing coordinates we obtain:

$$U(\rho) = \frac{i\pi}{a\lambda f} \exp\left[\left(\frac{ik}{2f} + \frac{b^2}{4a}\right)\rho^2\right], \quad (2.14)$$

where

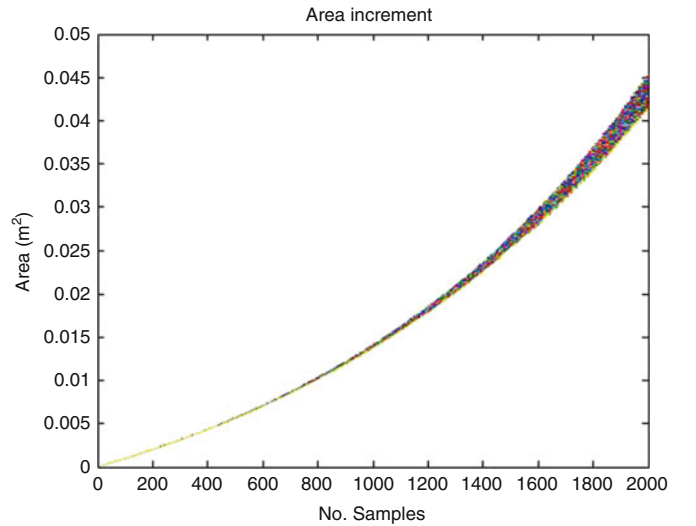
$$a = \left(1 - \frac{ik}{2f}\right), \quad (2.15)$$

$$b = \frac{ik}{f}, \quad (2.16)$$

In Fig. 2.16 we plot (2.14), substituting f by the experimentally obtained in (2.6). We can see a similar behaviour to the obtained in Fig. 2.4.

According to the present research, the initial area of the reflected laser was: $A \sim 0.0009 \text{ m}^2$. We show that the number of samples of focal lengths increase is proportional to an increment of the reflected area. We assume that $U(\rho) = W(z_p)$.

Fig. 2.16 (2.14) $U(\rho)$ distribution by f (samples)



2.5 Conclusions

It was measured the strain of a material under a compression test using one beam, its reflection and digital image processing treatment, we obtain 89 % of accuracy and micrometre resolution sensitivity. It was demonstrated theoretically that the beam waist of the laser increases as the focal length increase; also we present an analytical demonstration from Fresnel diffraction and proved that the behaviour of the area increment is similar to the obtained from reconstructed graphs.

Acknowledgement Alonso Saldaña Heredia wants to thank CONACYT for the grant No. 360140.

References

1. F. Beasley, *Theory and Design for Mechanical Measurements*, 3rd edn. (Wiley, New York, 2011)
2. J. Gere, B. Goodno, *Mecánica de Materiales*, 7th edn. (Cengage Learning, México, 2009)
3. J. Mathar, Determination of initial stresses by measuring the deformation around drilled holes. *Trans. ASME* **56**(4), 249–254 (1934)
4. ASTM, *Determining Residual Stresses by the Hole-Drilling Strain Gage Method. ASTM Standard Test Method E837-08* (American Society for Testing and Materials, West Conshohocken, PA, 2008)
5. Y. Min, D. Fulong, X. Huimin, L. Jian, Measurement of non-uniform residual stress by combined moiré interferometry and hole-drilling method: theory, experimental method and applications. *Acta Mech. Sinica* **19**(6) (2003)
6. M. Steinzig, T. Takahashi, Residual stress measurement using the hole-drilling method and laser speckle interferometry part IV: measurement accuracy. *Exp. Tech.* **27**(6), 59–63 (2003). ET occasionally features short Industry/Application articles under the title, “Technology Applications”
7. E. Ponslet, M. Steinzig, Residual stress measurement using the hole-drilling method and laser speckle interferometry part II: analysis technique. *Exp. Tech.* **27**(4), 17–21 (2003). ET occasionally features short Industry/Application articles under the title, “Technology Applications.”
8. E. Ponslet, M. Steinzig, Residual stress measurement using the hole-drilling method and laser speckle interferometry part III: analysis technique. *Exp. Tech.* **27**(5), 45–48 (2003). ET occasionally features short Industry/Application articles under the title, “Technology Applications”
9. G.S. Schajer, Advances in hole-drilling residual stress measurements. *Exp. Mech.* **50**(2), 245–253 (2010)
10. J. Ribeiro, J. Monteiro, M. Vaz, H. Lopes, P. Piloto, Measurements of residual stresses with optical techniques. *Strain* **45**(2), 123–130 (2009)
11. A.K. Asundi, Moiré Interferometric Strain Sensor (MISS) for Deformation and Strain Measurement Patent # US20070070327 A1, 2011
12. M. Knauer, J. Kaminski, G. Häusler, Phase measuring deflectometry: a new approach to measure specular free-form surfaces. *Proc. SPIE* **5457**, 366 (2004)
13. Y. Liu, E. Olesch, Z. Yang, G. Häusler, Fast and accurate deflectometry with crossed fringes. *Adv. Opt. Technol* **3**, 4 (2014). doi:[10.1515/aot-2014-0032](https://doi.org/10.1515/aot-2014-0032)
14. R. Huang, P. Su, R. Parks, G. Brusa, M. Idir, H. Burge, Measuring aspheric surfaces with reflection deflectometry. *SPIE Newsroom* (2013). doi: [10.1117/2.1201309.005087](https://doi.org/10.1117/2.1201309.005087)
15. J. Alda, Laser and Gaussian beam propagation and transformation. *Encyclopaedia of Optical Engineering* (2003)
16. A. Yariv, *Quantum Electronics*, 3rd edn. (Wiley, New York, 1990)
17. R. Wood, *Physical Optics*, 3rd edn. (Optical Science of America, Washington, DC, 1988)
18. B.E.A. Saleh, M.C. Teich, *Fundamentals of Photonics* (Wiley, New York, 1991)
19. ASTM E-9, ICS Number Code 77.040.10 (Mechanical testing of metals). doi:[10.1520/E0009-09](https://doi.org/10.1520/E0009-09)
20. JDSU Self-Contained Helium-Neon Laser Systems 1500 series Specification Sheet, JDS Uniphase Corporation 10138846 005 0512 SCHNL1500.DS.CL.AE 2012
21. J.W. Goodman, *Introduction to Fourier Optics*, 3rd ed. Roberts & Company (2005)

Chapter 3

The Technique of Laser-Induced Breakdown Spectroscopy for Determination of Heavy Metals in the Receiving Body of Water

A. Frías, A.E. Villarreal, F.G. Rendón Sauz, T. Flores, L. Ponce, R. Ortega, and M. Domínguez

Abstract Increasing human activity has highlighted the need for rapid and accurate chemical analysis of contaminants. Laser Induced Plasma Spectroscopy (LIBS) is an ideal solution because it has advantages such as in-situ analysis capable, it does not require sample preparation and the amount of sample required for analysis is minimal. This paper uses LIBS for heavy metals analysis in receiving water bodies. The LIBS system employed uses a Q: Switched multipulsed Nd:YAG laser, which favors the intensity of the emission spectra, showing sharper and improved detection limits. The obtained results are used in training a neural network to predict the elemental composition.

Keywords LIBS • Metals • Laser Nd:YAG • Multipulse • Neural networks

3.1 Introduction

An unfortunate consequence of increased human activity and industrial production is the generation and release of toxic waste that pollute the receiving bodies of water, example of which are heavy metals [1, 2]. To understand and minimize the harmful effects of these pollutants on the environment and human health, there is a great need for analysis tools to determine their presence in receiving water bodies with precision and speed [3].

Most current detection techniques are based on optical measurements and mass spectroscopy such as atomic fluorescence spectrometry [4], liquid chromatography [5], UV–Vis [6], infrared spectrophotometry [7], of inductively coupled plasma mass [8], spectroscopy [7] graphite furnace, atomic absorption spectrometry [9] and flame atomic absorption spectrometry [10]. Current standards for the analysis of contaminants in water receiving body, are based on techniques that can not deal directly with the original sample and require pretreatment to analysis. These techniques generate contaminants by using chemical reagents, besides being expensive analysis techniques and require a long time to offer the results [11].

The LIBS technique (Laser-Induced Breakdown Spectroscopy or laser ablation) is a modern technique [12], introduced about 10 years ago. It uses a high energy laser pulse to vaporize a fraction of sample under test, generating a microplasma whose emission spectrum allows spectroscopic analysis. This way you obtain a rapid method easily applicable and valid for the analysis of different kinds of sample, that may be impossible by conventional analytical techniques, being particularly useful in the analysis of complex matrices samples [13].

This technique is applied in various fields and offers the following advantages:

- Minimal or no sample preparation, which reduces analysis time and cost of reagents.
- The use of chemical reagents is not required, leading advantages of less pollution and loss.
- Allows simultaneous multi-element analysis.
- Speed, the determination is virtually instantaneous.
- Remote analysis. The presence of a person in the place where the analysis is carried out is not necessary.
- Spatial resolution, it allows to analyze different parts of the sample.

By its particular simplicity, we propose to demonstrate that the use of the technique of Laser-Induced Breakdown Spectroscopy has potential for analysis of contaminants or trace metals in receiving water bodies. It is essential to note that most applications of the LIBS technique have been used for solid samples [14]. Plasma generation in liquids presents several problems, for example the strong effect of splashing caused by shock waves generated by high intensity laser pulses

A. Frías (✉) • A.E. Villarreal • F.G. Rendón Sauz • T. Flores • L. Ponce • R. Ortega • M. Domínguez

Centro de Investigación en Ciencia Aplicada y Tecnología Avanzada (CICATA) Unidad Altamira del Instituto Politécnico Nacional (IPN), Km. 14.5 Carretera Tampico-Puerto Industrial, Altamira CP 89600, Tamaulipas, Mexico
e-mail: anykfs@hotmail.com

[15]. For lasers that emit with high pulse repetition rate, there can exist changes in the position of the surface relative to the focal point, which in turn induce adverse effects on the statistical treatment of the information [16]. Despite this, the advantages mentioned above make interesting the use of the LIBS technique for the analysis of water and this is why we propose a strategy of analysis, which is based on the use of membrane filters MF-Millipore™ as waste receivers, to capture about these the LIBS spectra. Reports on the use of the method of filter paper enriched dated back to 2008. Alamelu et al. [17] and Sarkar et al. [18] used the method of detecting liquid lanthanide series. Later, similar approaches were used to analyze heavy metals [19–22]. In the method of enrichment of graphite [23–27], in the liquid sample was dropped on the surface of a substrate of high purity graphite (99.99 %). Also can be electrochemically enriched the liquid sample to be analyzed [28, 29].

Another weakness of the LIBS technique is the matrix effect [30, 31] that influences especially in quantitative analysis. This effect is due to the high density of material in the plasma, although there can be several possible explanations to this matrix effect and how it affects the signal intensity of the analyte. In addition, the typical reproducibility is 5–20 % RSD, so that it is mandatory to work with carefully selected standards to obtain reliable results in quantitative analysis [30, 32].

Undoubtedly the recent addition of computer based signal processing techniques (chemometric algorithms) for classification and identification, has improved their ability to analyze and identify no false positives or false negatives making a very robust technique. In this work artificial neural networks were used, very suitable for nonlinear multivariate calibration. An artificial neural network model trained with a set of input data samples of known composition it is used to predict the elemental concentration of test spectra. Results in the literature that artificial neural networks are able to predict better than the traditional method in most cases [31] values are presented.

3.2 Methodological Development

3.2.1 Samples Preparation and Calibration Curve

3.2.1.1 Fortified Samples for the Calibration Curve

Selected metals include combinations of organic and inorganic nature, both dissolved and particulated. Distilled water and High-Purity Standards Cat.#ICP-200.7-6 EPA Method 200.7 Standard 6 Solution A $\mu\text{g/mL}$ in 2 % HNO_3 + Tr HF multielemental pattern, in which are contained the elements Al, Cd, Pb, P, Sr, Sb, Ca, Li, K, Tl, As, Cr, Mg, Se, Sn, Ba, Co, Mn, Si, V, Be, Cu, Mo, Ag, Zn, B, Fe, Ni Na were used. A calibration curve with 1:50, 1:20 and 1:10 dilutions, and a target in the linear range shown for each element was prepared.

To prepare dilutions were defined the following considerations:

- A minimum of 1 L of sample for generic metals mostly should be taken in a polyethylene or polypropylene container.
- For each calibration curve should be taken 4 L, a volume that allows to prepare in triplicate plus target.

For the determination of dissolved metals and / or suspended, both the field sample as the fortified targets used for reference, were filtered on a glass funnel having a base of sintered glass stopper and a clamp. A MF-Millipore Membrane composed of cellulose mixed esters, hydrophilic, with a pore size of 0.22 μ and 47 mm diameter, white color and smooth surface, is positioned in this.

3.2.1.2 Ni and Cu Fortified Samples

For samples preparation, two salts, nickel chloride and cupric nitrate solution, trademark Analytyka, based on potential contaminants that may contain a receiving body of water were used. Volumes of 3.5 mL of each solution were taken and poured onto the MF-Millipore membranes. Then it were allowed to dry 2 h under a halogen lamp of 65 W.

3.2.2 Experimental Facility

Figure 3.1 shows the general scheme of the instrumentation used in the LIBS system. The installation consists of a multi-pulse Nd:YAG equipped with a passive Q-switch of Cr:YAG, emitting at the wavelength of 1064 nm to induce plasma formation. The beam is focused on the sample of interest and the generated plasma is collected by an SR-P600-1 Ocean Optics fiber coupled to a Ocean Optics USB 4000 UV-NIR spectrometer (200–900 nm spectral range and optical resolution 0.35 nm), that processes and transmits the emission spectrum to a PC with the software SpectraSuite.

3.2.3 Application of LIBS Technique and Identification of Emission Lines

On MF-Millipore membranes, at each point of the calibration curve, were delivered Nd:YAG laser pulses with energy of 180 mJ, at a focal length of 5 cm. The fiber was positioned at an angle of 45° at a distance of 6 mm plasma.

As parameter to be optimized, the delay time is analyzed in a range from 2 to 10 ms for each point of the calibration curve. Another parameter to be optimized was the position of the light collector (fiber optic) to obtain a more defined and with less background noise spectra system, besides reducing the matrix effect due to the dispersion of the elements on the MF-Millipore membrane and the difficulty to observe their emission lines in multi element samples. For this, an arrangement was tested at 45° as shown in Fig. 3.2a and under 0° as shown in Fig. 3.2b. It was decided to implement these considerations to MF-Millipore membranes saturated with cupric chloride and nickel nitrate as well as to the membranes of the calibration curve.

For identification of the emission lines, was compared with the database that holds the Laboratory of Laser Technology, CICATA-IPN, Altamira Unit. At the same time it was matched with the database of United States Army Research Laboratory [33] and the database of the National Institute of Standards and Technology (NIST) [34]. To facilitate the work with the latter the “LIBS Analyzer” software, also developed in the laboratory of laser technology, was used.

Fig. 3.1 Block diagram of the LIBS installation

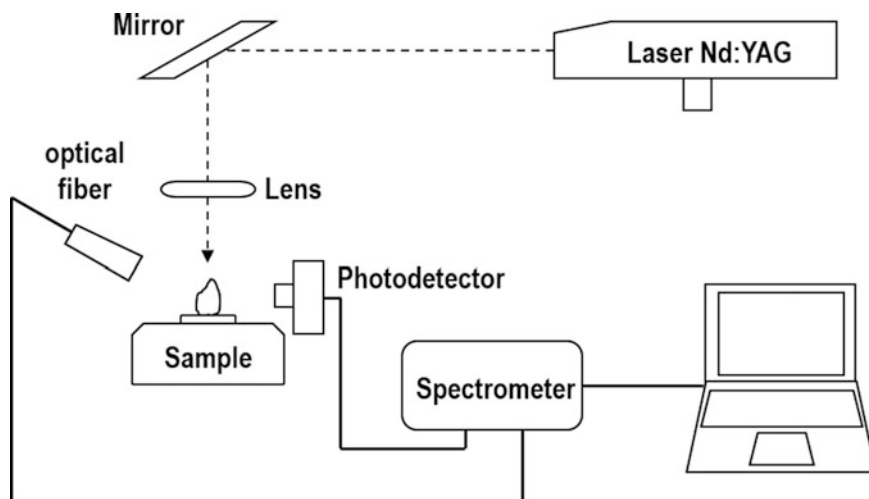
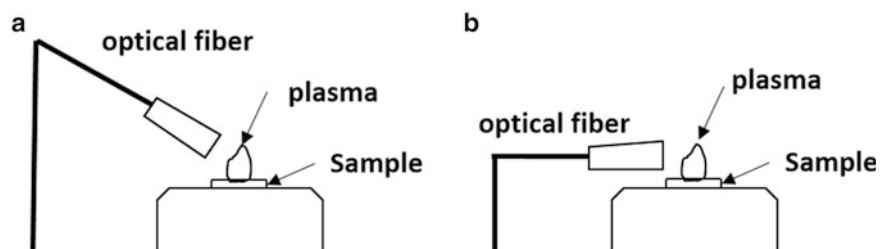


Fig. 3.2 Optical arrangement (a) 45° and (b) 0°



3.2.4 Neural Network

For each saturated MF-Millipore membrane, five spectra were obtained using the LIBS system. The ten spectra were grouped to be read and processed by the free license statistical software PAST [35]. K-means [36] method was used to classify into two groups the ten spectra. The K-means algorithm is a clustering method that aims to separate m observations x_1, x_2, \dots, x_m , where x_i is a real value in d dimensions and constructs k groups, associating the vector x_i in the j -th group. The experiment was repeated with the normalized spectra.

3.3 Results and Discussion

3.3.1 Analysis of the Spectra Obtained with the LIBS Technique

The spectra of the database of the Laboratory of Laser Technology, IPN-CICATA, Altamira Unit, were obtained by applying the LIBS technique on certified standards. In this work the following patterns were used: one of copper, from ALDRICH Chemistry brand, with purity of 99.999 %, and other of nickel, Kurt J. Lesker brand, with purity of 99.99 %. Figure 3.3 shows the spectra obtained. Table 3.1 shows their characteristic emission lines. Each emission line was confirmed using the databases of the United States Army Research Laboratory [33] and of the National Institute of Standards and Technology (NIST) [34].

Optimizing the LIBS technique it was carried out based on the spectra obtained from saturated to minimize the effect matrix membranes. Figure 3.4 shows the spectra obtained by saturating the MF-Millipore membrane with solutions of nickel nitrate and cupric chloride.

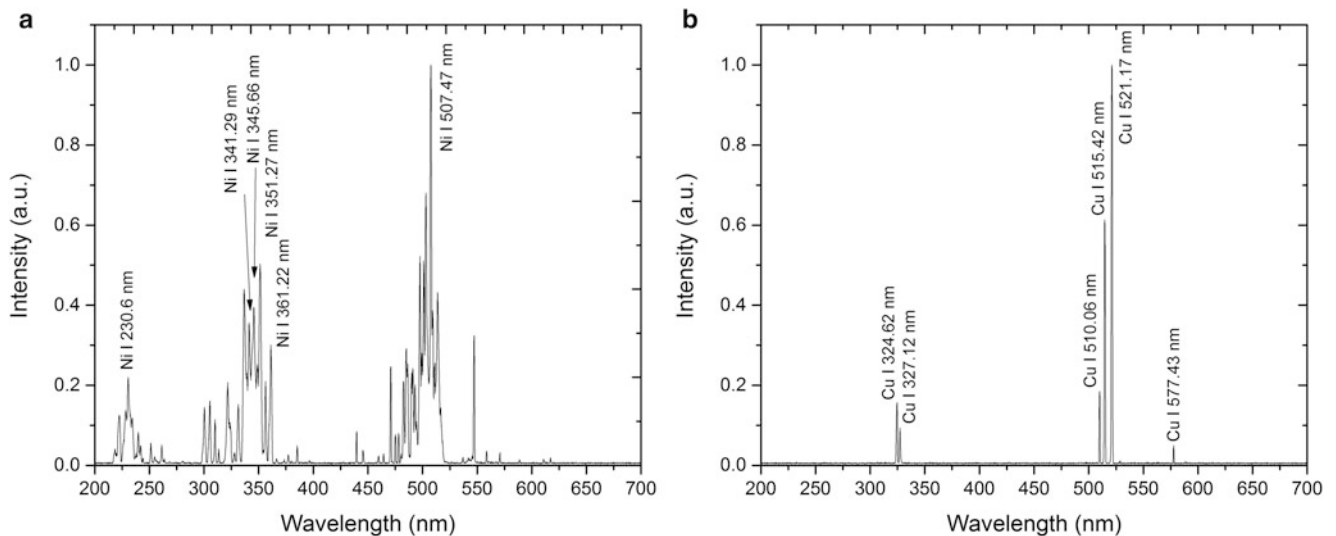


Fig. 3.3 LIBS spectra of (a) nickel and (b) copper patterns

Table 3.1 Wavelength patterns Ni and Cu

Element	Wavelength (nm) from membrana MF-Millipore	Wavelength (nm) from NIST
Ni	230.6, 341.29, 345.66, 351.27, 361.22, 507.47	231.09, 341.61, 345.84, 351.45, 361.92, 508.05
Cu	324.62, 327.12, 510.06, 515.42, 521.17, 577.43	324.75, 327.39, 510.55, 515.32, 521.82, 578.21

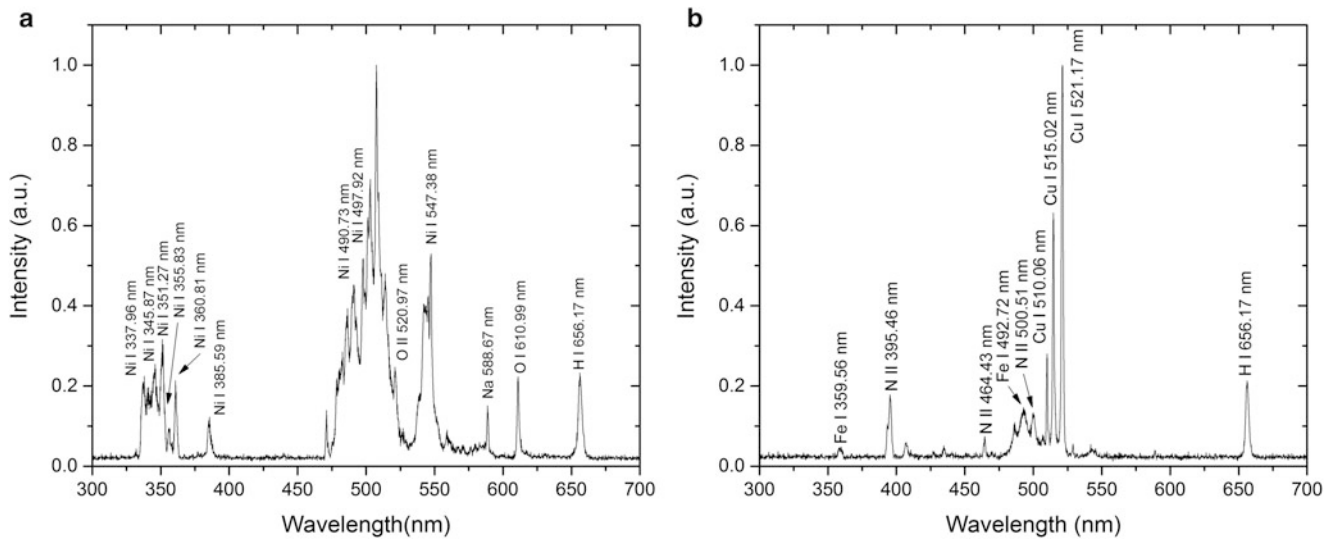


Fig. 3.4 Spectrum of (a) nickel chloride and (b) cupric nitrate

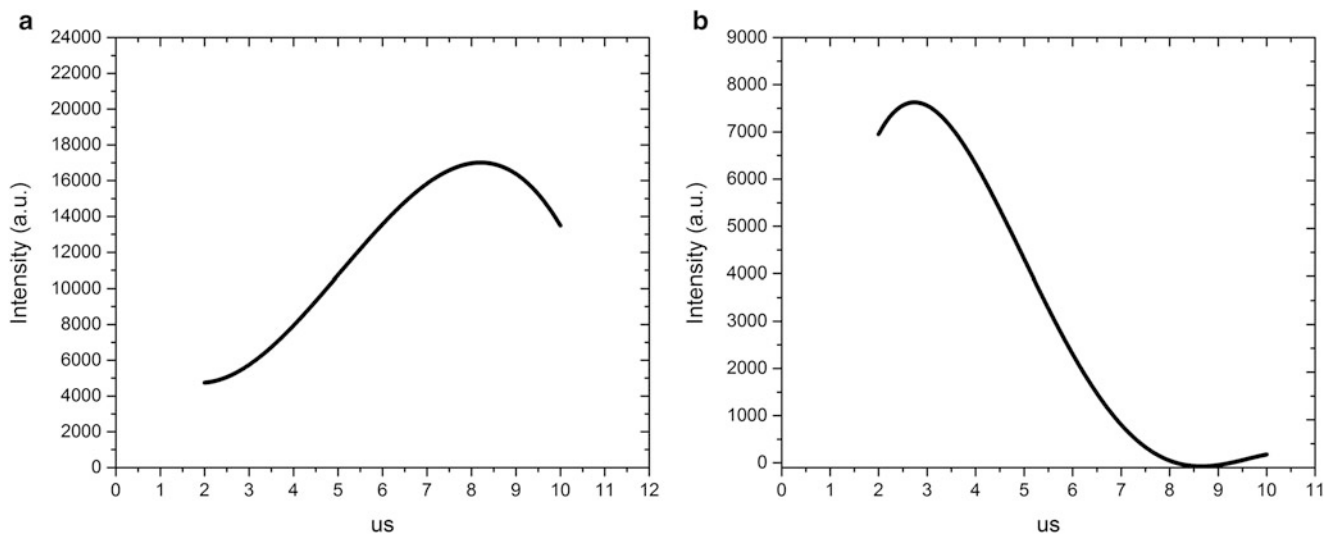


Fig. 3.5 Graphic relative intensity versus delay time characteristic curves (a) for nickel in the case of nickel chloride and (b) copper in the case of cupric nitrate

With the laser system used, the strongest signals with an energy of 180 ± 10 mJ were obtained. The focal length was set at 5 cm as a property of the focusing lens and the distance to the optical fiber is between 2 and 3 cm, at a position of 45° . The time delay of cupric nitrate based on the 521.17 nm line, is within 3 μ s, Within this time we can get the features most intense lines (Fig. 3.5b). For nickel chloride, where it was taken the baseline of 351.27 nm, it presents a linear behavior and can say that the most intense lines are obtained within 8 ms (Fig. 3.5a).

Based on the results obtained with saturated samples, we can develop a LIBS system optimized for obtaining spectra on MF-Millipore membranes with multielement pattern. A spectrum taken with this installation is shown in Fig. 3.6 where we can identify the emission lines shown in Table 3.2. According to the points set in the calibration curve the spectra shown in Fig. 3.7 is obtained, where the increase of the intensity of the lines with the increase of the characteristics concentrations of the calibration curve, it is shown.

In Fig. 3.8 we can see the calibration curves based on two elements with which we have worked. To obtain these curves were taken, for the Ni the 357.91 nm emission line, (Fig. 3.8a) and for the Cu, the 396.41 nm emission line (Fig. 3.8b).

Fig. 3.6 Spectrum MF-Millipore membrane with standard multielement

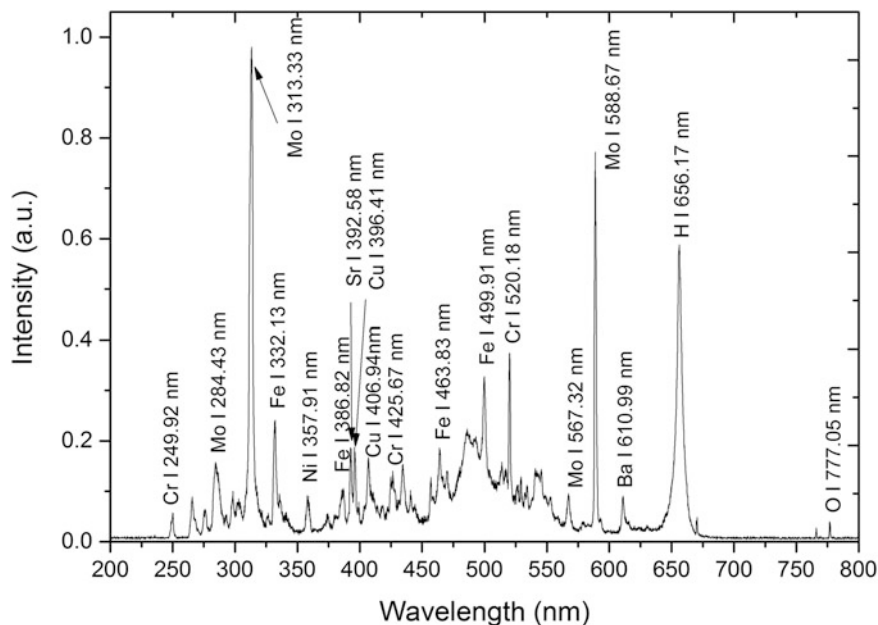


Table 3.2 Table of elements detected in the MF-Millipore membranes

Element	Wavelength (nm)
Cr I	249.92, 425.67, 520.18
Mo I	284.43, 313.33, 567.32, 588.67
Fe I	332.13, 386.82, 463.83, 499.91
Ni I	357.91
Sr I	392.58
Cu I	396.41, 406.94

3.3.2 Analysis of the Spectra of the Membranes with the PAST Software

According to the results obtained by the software PAST, it was observed that untreated spectra of cupric nitrate, shown in Fig. 3.9b had an efficiency of 0 % due to they can not be classified into one of two groups. Furthermore, the spectra of untreated nickel chloride, shown in Fig. 3.9a, had a 60 % efficiency, by classifying three of the five spectra in a group.

Table 3.3 shows the classification in groups provided by the software PAST. The group 0 is the alternative created by the software to indicate it could not be classified in any of the first two test groups. Five spectra of cupric nitrate and one of nickel chloride are in the group 0, while group 1 includes three spectra of nickel chloride correctly classified. Group 2 is which must qualify, but as noted, the spectrum that is within this group was misclassified.

Seeing this behavior, it was decided to apply a pre-treatment to normalize the data. Data were then entered into the PAST software again. The normalized spectra are shown in Fig. 3.10a, b. According to the results observed with the treatment, an improvement was observed, being classified correctly the total spectrum in their respective groups. These results are shown in Table 3.4, where each spectrum was classified correctly within a group.

3.4 Conclusions

LIBS technique, for the identification of heavy metals in receiving water bodies by using MF-Millipore membrane was used. As part of the optimization technique, spectra were previously acquired for two patterns of certified metals, one of copper and the other of nickel, to facilitate application of LIBS on nickel chloride and cupric nitrate saturated membranes. It is concluded that with an energy of 180 ± 10 mJ, the plasma emission intensity achieved was increased. Furthermore, it was

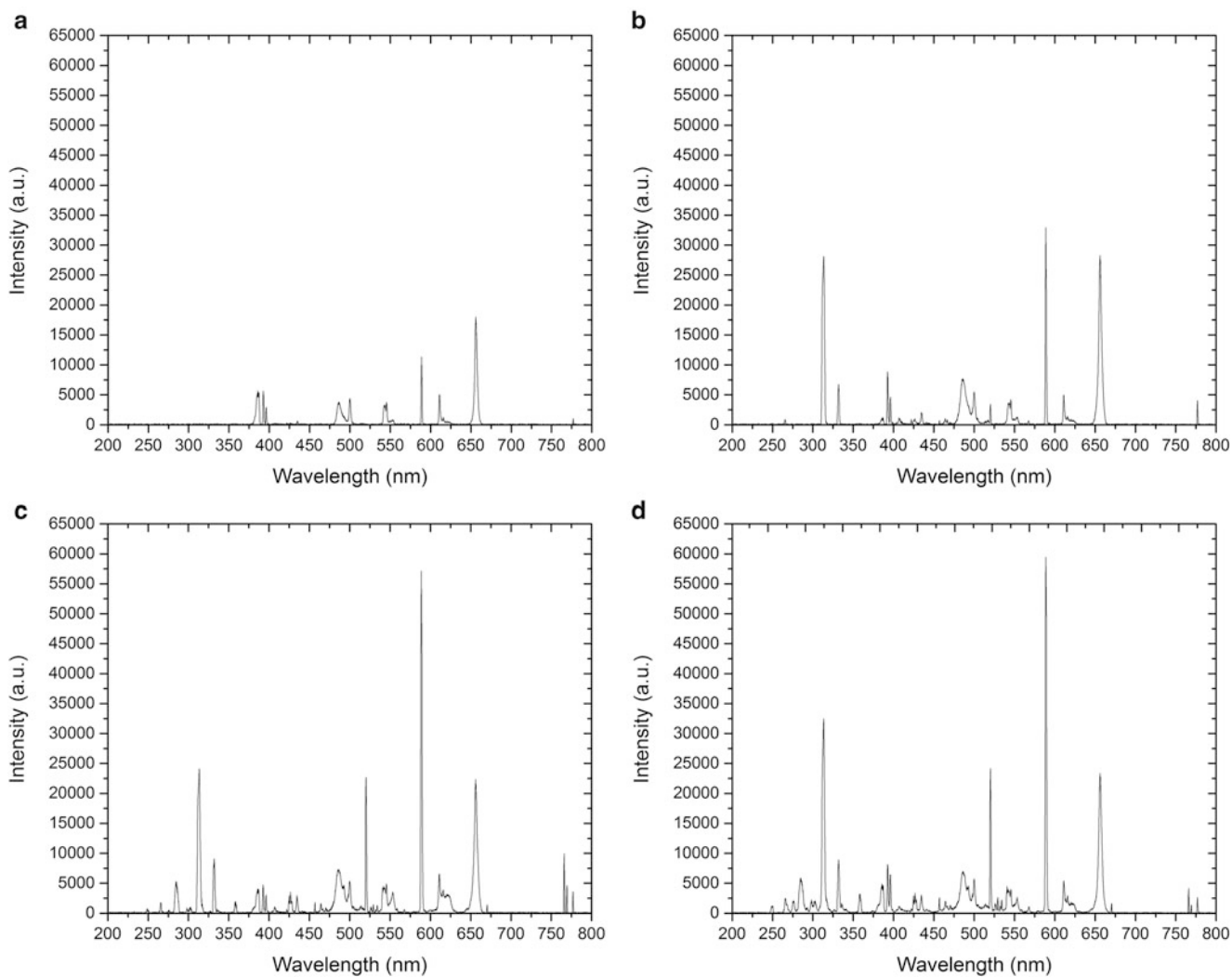


Fig. 3.7 Spectra of the calibration curve of the MF-Millipore membrane with multi elemental pattern (a) white, (b) concentration 0.4 mg/L, (c) concentration 1 mg/L, (d) concentration 2 mg/L

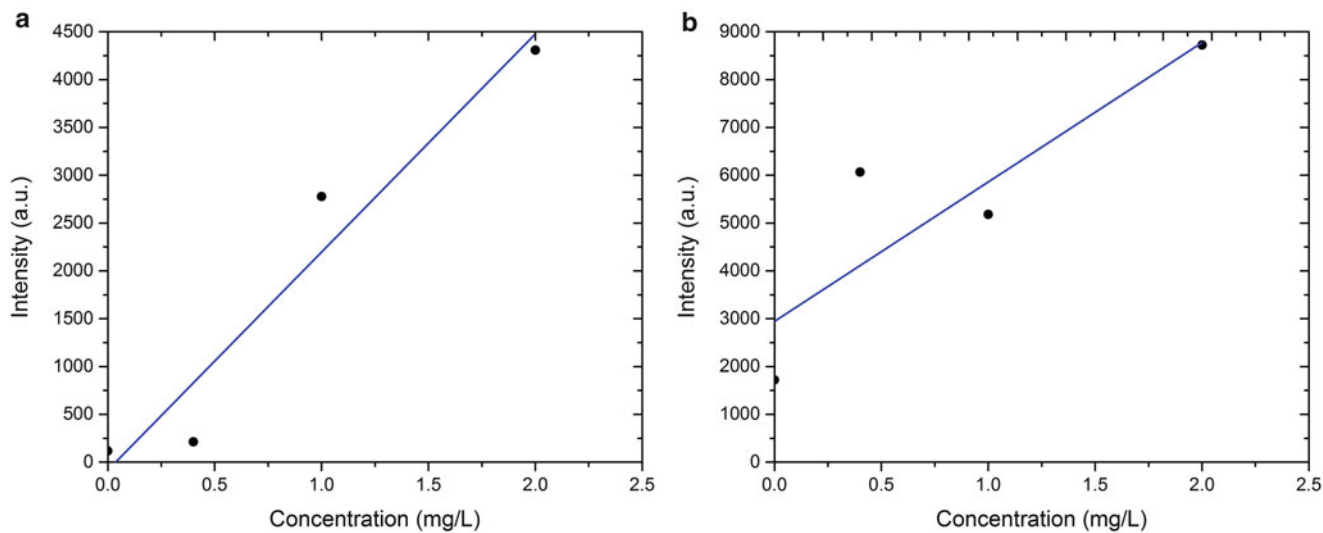


Fig. 3.8 Calibration curve of the MF-Millipore membrane with multi elemental pattern, in (a) nickel calibration curve and (b) copper calibration curve

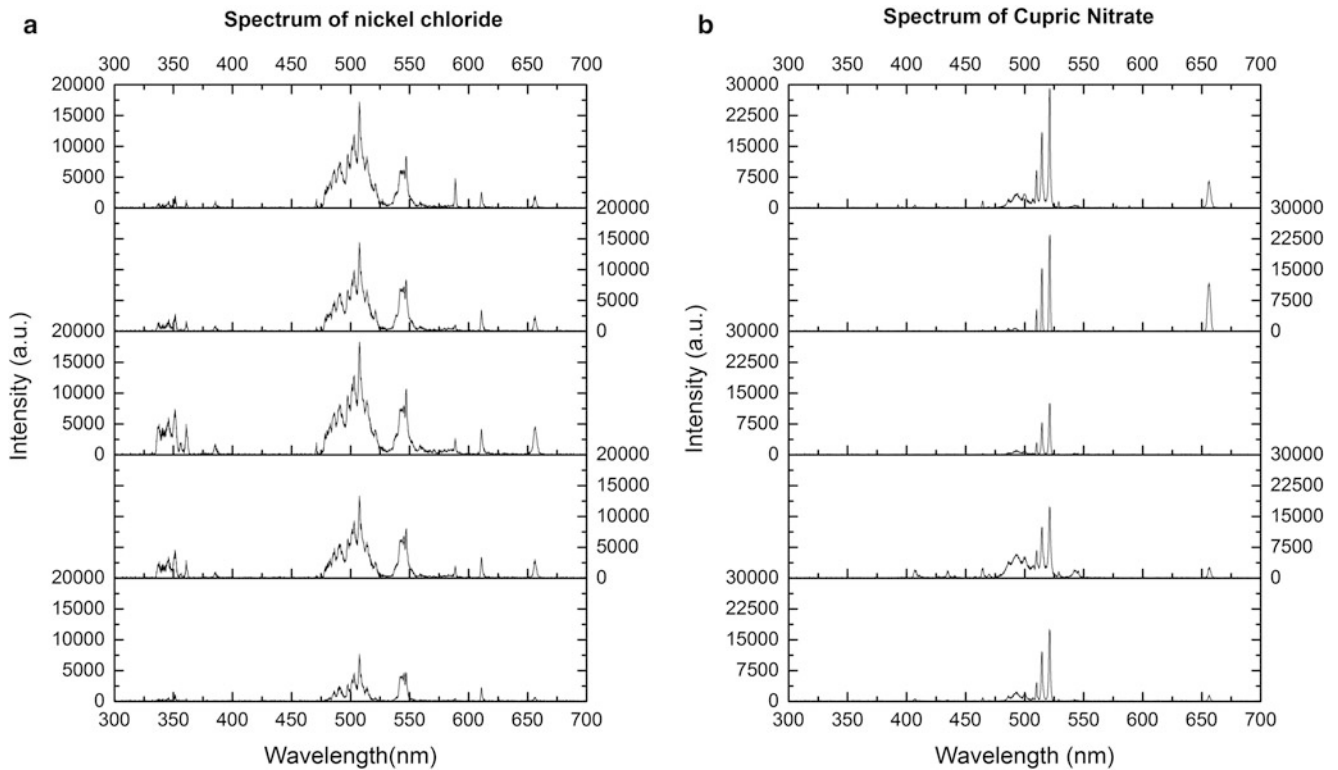


Fig. 3.9 LIBS spectra without processing (a) nickel chloride and (b) cupric nitrate

Table 3.3 Results of the classification of spectra without treatment by the K-Means method

Name	Compound	Group	Observations
E1	Cupric nitrate	0	Incorrect classification of the spectrum
E2	Cupric nitrate	0	Incorrect classification of the spectrum
E3	Nickel chloride	1	–
E4	Nickel chloride	1	–
E5	Cupric nitrate	0	Incorrect classification of the spectrum
E6	Cupric nitrate	0	Incorrect classification of the spectrum
E7	Nickel chloride	2	Incorrect classification of the spectrum
E8	Nickel chloride	1	–
E9	Cupric nitrate	0	Incorrect classification of the spectrum
E10	Nickel chloride	0	Incorrect classification of the spectrum

established that the optical fiber must be spaced a distance of 2–3 cm from the saturated sample and oriented at an angle of 45°, with no change in the focusing lens of 5 cm.

The next part of the research was the optimization of delay time, which varied from 2 to 10 ms, reaching the conclusion that, for obtain intense and defined emission lines of nickel, it should be used a delay 8 μ s. In the case of copper, it should be used a delay of 3 μ s.

With these parameters established, spectra from multielement pattern, fortified membranes were obtained. These spectra are identified and the data will be used to feed a neural network. According to experimentation with the PAST software, it is made possible by data standardization pretreatment which correctly classified 100 % of the spectra in the two groups requested.

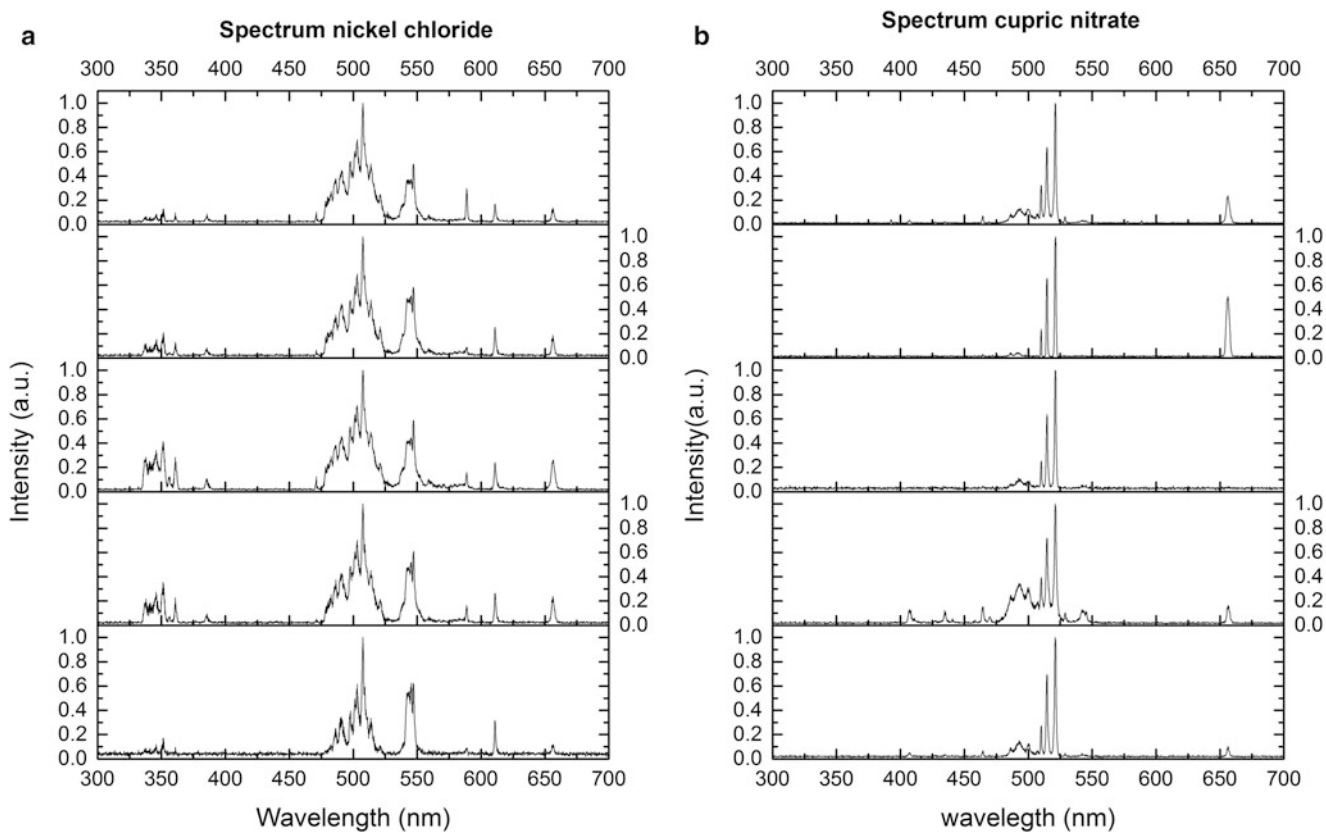


Fig. 3.10 LIBS spectra with processing (a) nickel chloride and (b) cupric nitrate

Table 3.4 Results of the classification of normalized spectra with treatment by K-means method

Name	Compound	Group	Observations
EN1	Cupric nitrate	2	–
EN2	Cupric nitrate	2	–
EN3	Nickel chloride	1	–
EN4	Nickel chloride	1	–
EN5	Cupric nitrate	2	–
EN6	Cupric nitrate	2	–
EN7	Nickel chloride	1	–
EN8	Nickel chloride	1	–
EN9	Cupric nitrate	2	–
EN10	Nickel chloride	1	–

Acknowledgement The authors thank CONACYT and COFAA-IPN for the financial support. This work was supported by project SIP-IPN 20150572.

References

1. A. Einstein, *Zur Quantentheorie der Strahlung* (Hirzel, Leipzig, 1917)
2. T.H. Maiman, *Stimulated Optical Radiation in Ruby* (Macmillan, London, 1960)
3. Y. Yu, W. Zhou, X. Su, Detection of Cu in solution with double pulse laser-induced breakdown spectroscopy. *Opt. Commun.* **333**, 62–66 (2014)
4. C.-G. Yuan, K. Lin, A. Chang, Determination of trace mercury in environmental samples by cold vapor atomic fluorescence spectrometry after cloud point extraction. *Microchim. Acta* **171**, 313–319 (2010)

5. J.R. Dean, G. Wade, I.J. Barnabas, Determination of triazine herbicides in environmental samples. *J. Chromatogr. A* **733**, 295–335 (1996)
6. A. Hosseini-Bandegharai, M. Sarwghadi, A. Heydarbeigi, S.H. Hosseini, M. Nedaie, Solid-phase extraction of trace amounts of uranium (VI) in environmental water samples using an extractant-impregnated resin followed by detection with UV-Vis spectrophotometry. *J. Chem.* **2013**, 10 (2013)
7. D. Pröfrock, A. Prange, Inductively coupled plasma-mass spectrometry (ICP-MS) for quantitative analysis in environmental and life sciences: a review of challenges, solutions, and trends. *Appl. Spectrosc.* **66**, 843–868 (2012)
8. H. Qiu, G. Luo, A simple and rapid method for determination of petroleum oils in sewage sludge samples with ultrasonic solvent extraction by infrared spectrophotometry under optimized analytical conditions. *Anal. Methods* **4**, 3891–3896 (2012)
9. D.W. Hahn, N. Omenetto, Laser-induced breakdown spectroscopy (LIBS), part II: review of instrumental and methodological approaches to material analysis and applications to different fields. *Appl. Spectrosc.* **66**, 347–419 (2012)
10. R. Gürkan, Ö. Yılmaz, Indirect quantification of trace levels cyanide in environmental waters through flame atomic absorption spectrometry coupled with cloud point extraction. *J. Iran. Chem. Soc.* **10**, 631–642 (2013)
11. N.O. Mexicana, “NMX-AA-51-1981, Análisis de agua,” *Determinación de metales. Método Espectrofotométrico de Absorción Atómica: México, Secretaría de Economía*, 1981.
12. E.F. Runge, Spectrochemical analysis using a pulsed laser source. *Spectrochim. Acta B At. Spectrosc.* **20**, 733–736 (1964)
13. T. Flores, L. Ponce, M. Arronte, E. de Posada, Free-running and Q: switched LIBS measurements during the laser ablation of Prickle Pears spines. *Opt. Lasers Eng.* **47**(5), 578–583 (2009)
14. J.O. Cáceres, J. Tornero López, H.H. Telle, A. González Ureña, Quantitative analysis of trace metal ions in ice using laser-induced breakdown spectroscopy. *Spectrochim. Acta B At. Spectrosc.* **56**, 831–838 (2001)
15. H. Sobral, R. Sanginés, A. Trujillo-Vázquez, Detection of trace elements in ice and water by laser-induced breakdown spectroscopy. *Spectrochim. Acta B At. Spectrosc.* **78**, 62–66 (2012)
16. A. De Giacomo, M. Dell’Aglio, O. De Pascale, M. Capitelli, From single pulse to double pulse ns-laser induced breakdown spectroscopy under water: elemental analysis of aqueous solutions and submerged solid samples. *Spectrochim. Acta B At. Spectrosc.* **62**, 721–738 (2007)
17. D. Alamelu, A. Sarkar, S.K. Aggarwal, Laser-induced breakdown spectroscopy for simultaneous determination of Sm, Eu and Gd in aqueous solution. *Talanta* **77**(1), 256–261 (2008)
18. A. Sarkar, D. Alamelu, S.K. Aggarwal, Determination of thorium and uranium in solution by laser-induced breakdown spectrometry. *Appl. Opt.* **47**(31), G58–G64 (2008)
19. Y. Lee, S.-W. Oh, S.-H. Han, Laser-induced breakdown spectroscopy (LIBS) of heavy metal ions at the sub-parts per million level in water. *Appl. Spectrosc.* **66**(12), 1385–1396 (2012)
20. M. Bukhari, M.A. Awan, I.A. Qazi, M.A. Baig, Development of a method for the determination of chromium and cadmium in tannery wastewater using laser-induced breakdown spectroscopy. *J. Anal. Methods Chem.* **2012**, 7 (2012)
21. D. Zhu, L. Wu, B. Wang, J. Chen, J. Lu, X. Ni, Determination of Ca and Mg in aqueous solution by laser-induced breakdown spectroscopy using absorbent paper substrates. *Appl. Opt.* **50**(29), 5695–5699 (2011)
22. M. Zheng, M. Yao, X. He, J. Ouyang, Y. Lin, W. Li, M. Liu, Improving detection sensitivity of Cu in sewage by laser induced breakdown spectroscopy using filter paper enrichment. *Laser Optoelectron. Prog.* **7**, 165–170 (2013)
23. A. Sarkar, S.K. Aggarwal, K. Sasibhusan, D. Alamelu, Determination of sub-ppm levels of boron in ground water samples by laser induced breakdown spectroscopy. *Microchimica Acta* **168**(1), 65–69 (2009)
24. Y. Wang, N. Zhao, M. Ma, C. Wang, Y. Yu, D. Meng, J. Liu, W. Liu, Chromium detection in water enriched with graphite based on laser-induced breakdown spectroscopy. *Laser Technol.* **37**(6), 808–811 (2013a)
25. H. Shi, D. Chen, Y.-J. Zhang, Study on measurement of trace heavy metal Ni in water by laser induced breakdown spectroscopy technique. *Spectrosc. Spectr. Anal.* **32**(1), 25–28 (2012)
26. C. Wang, J. Liu, N. Zhao, H. Shi, C. Lu, L. Liu, M. Ma, W. Zhang, D. Chen, Y. Zhang, W. Liu, Enrichment of trace lead in water with graphite and measurement by laser-induced breakdown spectroscopy. *Chin. J. Lasers* **38**(11), 246–250 (2011)
27. W.C.-L.L. Jian-Guo, Z.N.-J.M. Ming-Jun, W.Y.H.L.Z. Da, H.Y.Y.M. De-Shuo, Z.W.L.J.Z. Yu, J.L. Wen-Qing, Comparative analysis of quantitative method on heavy metal detection in water with laser-induced breakdown spectroscopy. *Acta Physica Sinica* **12**, 050 (2013)
28. F. Zhao, Z. Chen, F. Zhang, R. Li, J. Zhou, Ultra-sensitive detection of heavy metal ions in tap water by laser-induced breakdown spectroscopy with the assistance of electrical-deposition. *Anal. Methods* **2**(4), 408–414 (2010)
29. W. Xiong, Q. Zhang, F. Zhao, R.H. Li, High sensitive detection of trace chromium ion based on laser induced breakdown spectroscopy. *J. At. Mol. Phys.* **2**, 283–287 (2010)
30. I. Schechter, V. Bulatov, R. Krasniker, in *Laser Induced Plasma Spectroscopy and Applications*, Plasma morphology and matrix effects interrelation in LIBS analysis (Orlando, Florida, 2002), p. ThD4.
31. P. Inakollu, T. Philip, A.K. Rai, F.-Y. Yueh, J.P. Singh, A comparative study of laser induced breakdown spectroscopy analysis for element concentrations in aluminum alloy using artificial neural networks and calibration methods. *Spectrochim. Acta B At. Spectrosc.* **64**, 99–104 (2009)
32. J. El Haddad, M. Villot-Kadri, A. Ismaël, G. Gallou, K. Michel, D. Bruyère et al., Artificial neural network for on-site quantitative analysis of soils using laser induced breakdown spectroscopy. *Spectrochim. Acta B At. Spectrosc.* **79–80**, 51–57 (2013)
33. U. S. Army, United States Army Research Laboratory (ARL) (2010), <http://www.arl.army.mil/www/default.cfm?page = 250>
34. U. S. D. o. Commerce, National Institute of Standards and Technology (2010), <http://physics.nist.gov/>
35. Ø. Hammer, D.A.T. Harper, P.D. Ryan, PAST: paleontological statistics software package for education and data analysis. *Palaeontol. Electron.* **4**, 1094–8074 (2001)
36. S. Lloyd, Least squares quantization in PCM. *IEEE Trans. Inf. Theory* **28**, 129–137 (1982)

Chapter 4

Applications of Laser Induced Breakdown Spectroscopy in the Identification of Bacteria

F.G. Rendón Sauz, T. Flores Reyes, R. Ortega Izaguirre, A.K. Frias, A.E. Villarreal, and L. Ponce

Abstract LIBS technique was used to obtain spectra of *Escherichia coli* and *Staphylococcus aureus* for identifying characteristic emission lines and then they were analyzed by K-means classifier for neural network feasibility. The potential of this method for bacteria identification was demonstrated.

Keywords LIBS • Bacteria • Neural network • K-means • Spectroscopy

4.1 Introduction

LIBS technique Laser Induced Breakdown Spectroscopy (LIBS) technique (Laser Induced Breakdown Spectroscopy or Laser Induced Breakdown Spectroscopy (LIBS) technique laser ablation) involves the use of a high-energy laser radiation pulse that vaporizes a fraction of sample under analysis, generating a microplasma whose emission spectrum allows spectroscopic analysis [1–3].

LIBS is a technique capable of analyzing the atomic composition of any material regardless of its state of aggregation. In the case of solid materials, when a high power laser pulse strikes a surface, the laser energy is converted into heat and the temperature of the solid material is increased resulting in rapid melting and / or evaporation of material. A plasma is obtained due to vapour produced consisting of atoms, ions and electrons that can reach very high temperatures (in the order of 1×10^4 K). For some nanoseconds (or longer) laser pulses, a part of the laser pulse energy is absorbed by the plasma increasing its ionization and temperature. After this process known as laser ablation, a continuous emission continues (bremsstrahlung) mainly caused by collisions between free electrons, an emission by recombination of electrons and ions and spectral emission lines generated by the decay of electrons at permitted levels in the atoms composing the plasma. Because the bremsstrahlung and the recombination emission decay temporarily first that spectral lines, it is possible to identify the elements by LIBS monitoring the plasma emission spectrum in the final stage of decay of plasma [4].

Because sample preparation it is not necessary, measurement complexity is considerably reduced and there is no possibility of sample loss or cross-contamination during transportation or the complicated preparations of laboratory analysis [5].

Recent reports show that it is possible to identify bacteria by using this technique [6]. It was shown that bacteria and pollen granules can be detected and classified [7]. Guyron et al. studied the differences of spectra in bacteria for excitation with nanosecond and femtosecond lasers [8]. In reference [9] it is shown the advantage of using a multipulse laser as an excitation source, yielding a direct identification of various types of bacteria [10]. In general, in several previous studies, the motivation was to evaluate the capability of LIBS to provide quick identification compared to traditional bioanalytical methods, benefiting from the possibility of combining with chemometric methods in order to increase the performance of technique [8, 11–17]. Morel et al. [14] investigated the detection of six bacteria by using LIBS response time. They put particular emphasis on *Bacillus globigii*, which acts as a non-pathogenic substitute for *Bacillus anthracis* (Anthrax), demonstrating the ability of LIBS to detect bacteria. Baudelet et al. [16] showed a clear discrimination of various bacteria based on the concentration profile of trace elements. Recently, Rehse et al. [11, 13] studied the effect of different experimental conditions (e.g., dilution of bacteria and nutrient deprivation) on identification of bacteria by functional discriminant analysis showing a successful bacteria classification. Multari et al. [15] applied the analysis of partial regression

F.G. Rendón Sauz (✉) • T. Flores Reyes • R. Ortega Izaguirre • A.K. Frias • A.E. Villarreal • L. Ponce
Centro de Investigación en Ciencia Aplicada y Tecnología Avanzada (CICATA) Unidad Altamira del Instituto Politécnico Nacional (IPN),
Km. 14.5 Carretera Tampico-Puerto Industrial, Altamira, Altamira, Tamaulipas CP 89600, Mexico
e-mail: rfsabian12@gmail.com

of least squares to differentiate *E. coli* from *Staphylococcus aureus*. Although these studies show good results, in some cases the rate of correct identification of bacterial strains or correlation falls below 85 %.

In general, there is a clear need for more rigorous and systematic studies that include new approaches to allow this methodology to be applied in clinical environment for the diagnosis of diseases and public health. Coupled with this, the motivation behind this study is to use a mode of bacterial classification or identification using artificial intelligence algorithms such as neural networks (NN) to improve the accuracy and precision of the classification process. In a previous study Cáceres et al. [18] used artificial intelligence algorithms such as neural networks (NN) which shown to be a promising chemometric methodology to classify and to predict bacterial samples at genus level with a high degree of precision and accuracy. Complete sets of variables (intensity at each wavelength) constituting the sample spectrum are important in the process of comparison performed by the NN, which is the basis of its ability to perform discrimination. NN are able to calculate internal parameters (weights and biases) in the learning process for classifying a given set of input variables as belonging to a particular sample, with a high tolerance for noise and the presence of outliers [19].

This work was destined to broad the study to investigate the application of LIBS-NN discriminating different antibiotic resistant strains of the same bacterial species and to address its use as a diagnostic methodology potentially fast. The aim is to determine whether genetic variations among bacterial strains of the same species, even when there is a difference of a single gene can generate sufficient or significant changes in its atomic composition which can be detected by the LIBS-NN method in order to achieve their discrimination and identification.

4.2 Experimental Methodology

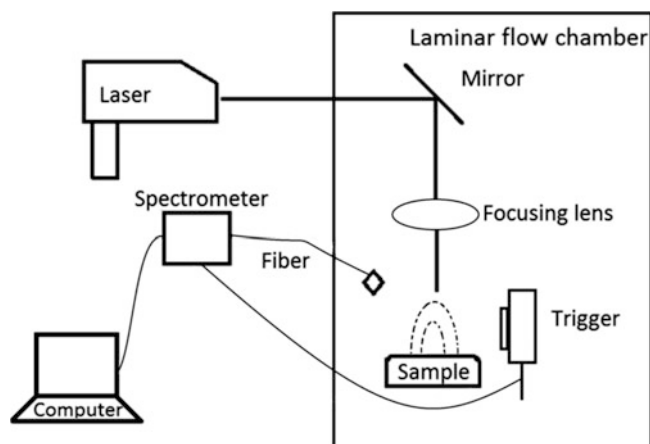
4.2.1 Samples Preparation

ATCC strains of *Staphylococcus aureus* and *Escherichia coli* developed and provided by the laboratory UNELab of Universidad del Noreste (Mexico), to obtain and classify LIBS spectra were used. Samples were kept refrigerated at 4 °C until use.

4.2.2 Experimental Installation

The scheme of the experimental setup is shown in Fig. 4.1. It includes a Nd: YAG, Q: Switched multipulse laser source emitting at 1064 nm, an optical system composed of a Thorlabs NB1-K14 (Nd: YAG 1047–1064 nm) mirror and a 5 cm focusing lens. The samples were placed at the focal length of 5 cm. By impinging on the surface, laser radiation causes the plasma emission, which is transmitted to OceanOptics USB4000 spectrometer by an optical fiber-P600-1 SR, Ocean Optics brand. The spectrometer has an optical resolution of 0.3 nm with a spectral range of 200–1100 nm and is activated when the trigger model PDA10A, Ocean Optics, sends the command. The information is transmitted and processed in a computer using the software SpectraSuite to obtain spectra, which were stored in plain text (Fig. 4.1).

Fig. 4.1 Diagram of experimental setup



4.2.3 Identification of Spectral Lines

Identifying spectral lines was performed using the “LIBS Analyzer” software, which in its database has the elemental lines from the National Institute of Standards and Technology (NIST) [20], in addition to the database United States Army Research Laboratory [21].

4.3 Results and Discussion

For each strain five spectra were obtained by using LIBS system. These spectra were averaged and plotted as shown in Fig. 4.2. Elements Ca, Na, K, O, H, were found in these spectra. Some lines associated with Fe and Mg are different for samples of *E. coli* and *S. aureus*. On the other hand, the ten spectra were grouped to be read and processed by the free licensed statistical software PAST. K-means [22] to classify into two groups the ten spectra. The K-means algorithm is a clustering method that aims to separate m variables x_1, x_2, \dots, x_m , where x_i is a real value in d dimensions and constructs k groups, associating the vector x_i is the j th group. The experiment was then repeated with the normalized spectra.

Figure 4.3 shows *E. coli* and *S. aureus* spectra untreated, where it can be observed that despite the visual similarities, they have different relative intensities, which does not prevent that may occur misclassification as shown in Table 4.1.

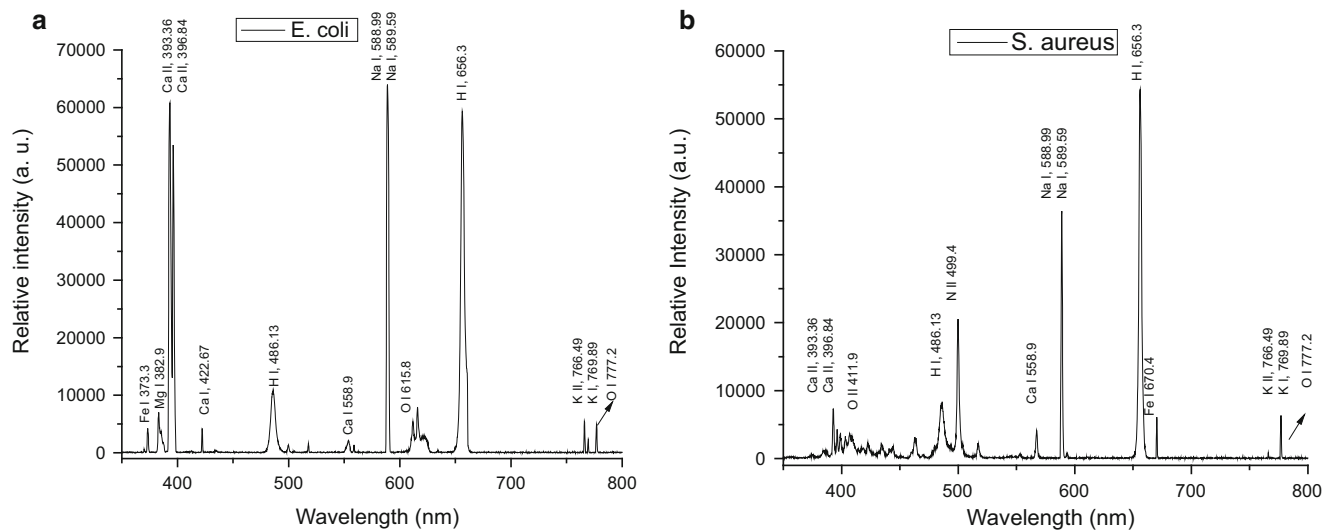


Fig. 4.2 (a) *E. coli* spectra (b) *S. aureus* spectra

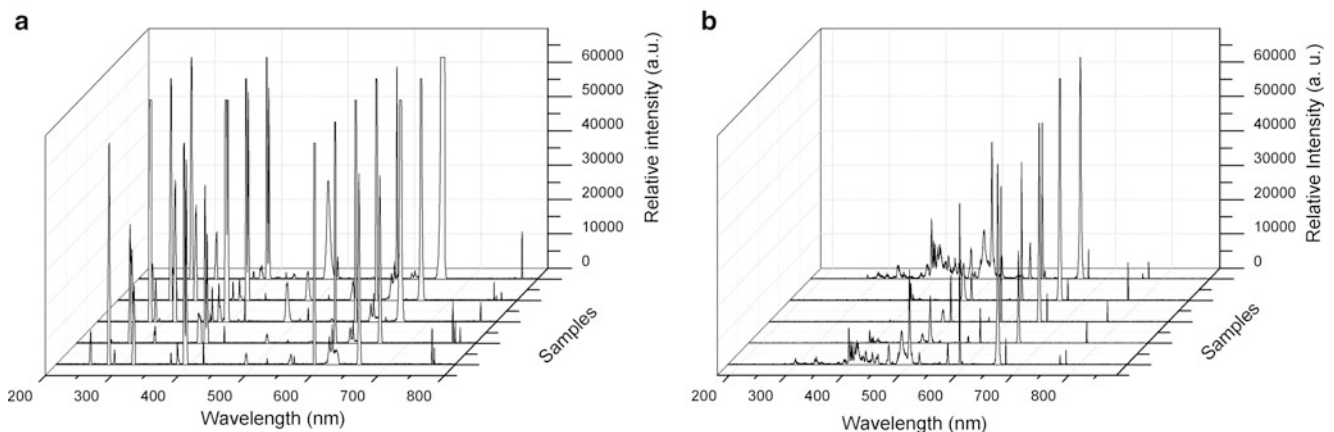


Fig. 4.3 Spectra without processing (a) *E. coli* (b) *S. aureus*

Table 4.1 Results of the classification of spectra untreated for K-Means method

Sample	Strain	Group
B1	<i>S. aureus</i>	0
B2	<i>E. coli</i>	0
B3	<i>S. aureus</i>	0
B4	<i>S. aureus</i>	1
B5	<i>E. coli</i>	0
B6	<i>E. coli</i>	0
B7	<i>E. coli</i>	2
B8	<i>S. aureus</i>	0
B9	<i>E. coli</i>	0
B10	<i>S. aureus</i>	0

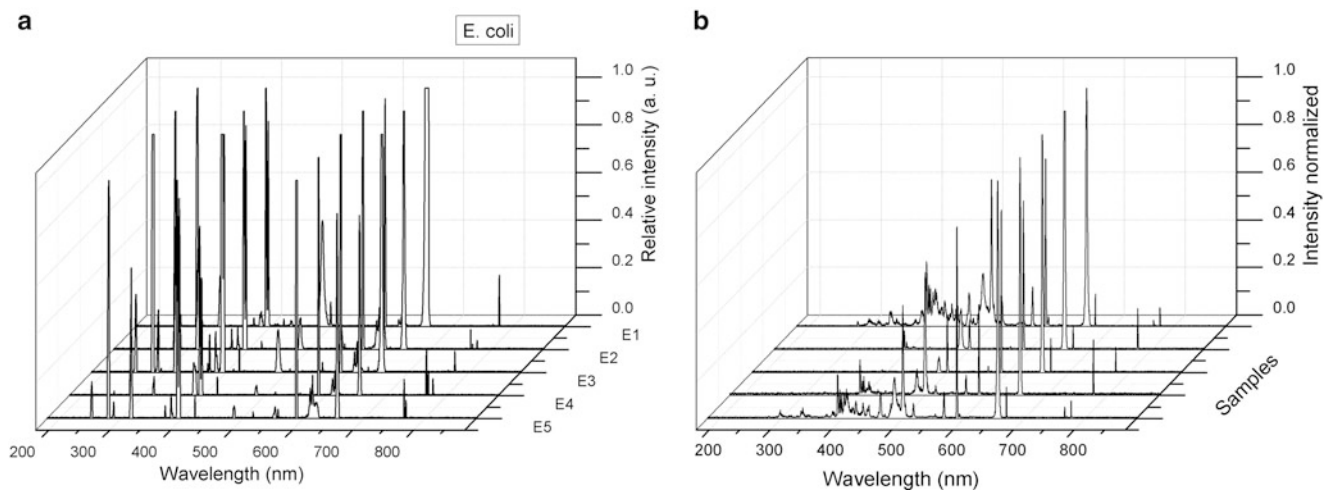


Fig. 4.4 Normalized spectra (a) *E. coli*, (b) *S. aureus*

Table 4.2 Classification results of normalized spectra by the K-Means method

Sample	Strain	Group
BN1	<i>S. aureus</i>	2
BN2	<i>E. coli</i>	1
BN3	<i>S. aureus</i>	2
BN4	<i>S. aureus</i>	2
BN5	<i>E. coli</i>	1
BN6	<i>E. coli</i>	1
BN7	<i>E. coli</i>	1
BN8	<i>S. aureus</i>	2
BN9	<i>E. coli</i>	1
BN10	<i>S. aureus</i>	2

Spectra were normalized from 0 to 1 by dividing the intensity between the higher intensity, so a standard was obtained in the maximum signal. Figure 4.4 shows the normalized spectra, where the most intense line for *E. coli* was 588.59 Na while for *S. aureus* was H 656.3. These spectra were processed by K-means whose results are shown in Table 4.2.

In Table 4.2 the results of the classification obtained from normalized spectra are observed. As can be seen, there is coherence in classification for all values.

4.4 Conclusions

According to the results obtained by the software PAST shown in Tables 4.1 and 4.2, it is observed that an unambiguous classification is obtained once normalized the spectra, providing a 100 % of efficiency, against the 20 % of efficiency obtained from untreated spectra. Thus concludes that for identification by using a classifier, a normalization pretreatment is necessary.

Acknowledgement The authors thank CONACYT and COFAA-IPN for the financial support and UNELab for providing samples. This work was supported by project SIP-IPN 20150572.

References

1. D.W. Hahn, N. Omenetto, Laser-induced breakdown spectroscopy (LIBS), part II: review of instrumental and methodological approaches to material analysis and applications to different fields. *Appl. Spectrosc.* **66**, 347–419 (2012)
2. T. Flores, L. Ponce, M. Arronte, E. de Posada, Free-running and Q-Switched LIBS Measurements During the Laser Ablation of Prickle Pears Spines, Optics and Lasers in Engineering, **47**(5), pp. 578–583 (2009)
3. L. Moreira Osorio, L.V. Ponce Cabrera, M.A. Arronte García, T. Flores Reyes and I. Ravelo, Portable LIBS system for determining the composition of multilayer structures on objects of cultural value. *Journal of Physics: Conference Series*, 274, 012093 (2011)
4. D.A. Cremers, L.J. Radziemski, in *LIBS Analytical Figures of Merit and Calibration. Handbook of Laser-Induced Breakdown Spectroscopy*, 2nd edn., pp. 123–150
5. L. Radziemski, D. Cremers, A brief history of laser-induced breakdown spectroscopy: from the concept of atoms to LIBS 2012. *Spectrochim. Acta B At. Spectrosc.* **87**, 3–10 (2013)
6. J.L. Gottfried, F.C. De Lucia, C.A. Munson, A.W. Miziolek, Standoff detection of chemical and biological threats using laser-induced breakdown spectroscopy. *Appl. Spectrosc.* **62**, 353–363 (2008)
7. J.L. Gottfried, D.A. Cremers, L.J. Radziemski, in *Chemometric Analysis in LIBS. Handbook of Laser-Induced Breakdown Spectroscopy*, 2nd edn. (Wiley, New York 2013), pp. 223–255
8. M. Baudelet, L. Guyon, J. Yu, J.-P. Wolf, T. Amodeo, E. Fréjafon et al., Femtosecond time-resolved laser-induced breakdown spectroscopy for detection and identification of bacteria: a comparison to the nanosecond regime. *J. Appl. Phys.* **99**, 084701 (2006)
9. G. Galbács, V. Budavári, Z. Geretovszky, Multi-pulse laser-induced plasma spectroscopy using a single laser source and a compact spectrometer. *J. Anal. At. Spectrom.* **20**, 974 (2005)
10. A.P. Flores, A.K.F. Sanchez, A. Villarreal, F.G.R. Sauz, L.P. Cabrera, T.F. Reyes, The potential of compact LIBS system with multi-pulse Nd: YAG laser for bacteria identification. *J. Biomed. Sci. Eng.* **8**(3), 6 (2015)
11. S.J. Rehse, Q.I. Mohaidat, S. Palchadhuri, Towards the clinical application of laser-induced breakdown spectroscopy for rapid pathogen diagnosis: the effect of mixed cultures and sample dilution on bacterial identification. *Appl. Opt.* **49**, C27–C35 (2010)
12. S.J. Rehse, N. Jeyasingham, J. Diedrich, S. Palchadhuri, A membrane basis for bacterial identification and discrimination using laser-induced breakdown spectroscopy. *J. Appl. Phys.* **105**, 102034 (2009)
13. Q. Mohaidat, S. Palchadhuri, S.J. Rehse, The effect of bacterial environmental and metabolic stresses on a laser-induced breakdown spectroscopy (LIBS) based identification of *Escherichia coli* and *Streptococcus viridans*. *Appl. Spectrosc.* **65**, 386–392 (2011)
14. S. Morel, N. Leone, P. Adam, J. Amouroux, Detection of bacteria by time-resolved laser-induced breakdown spectroscopy. *Appl. Opt.* **42**, 6184–6191 (2003)
15. R.A. Multari, D.A. Cremers, J.M. Dupre, J.E. Gustafson, The use of laser-induced breakdown spectroscopy for distinguishing between bacterial pathogen species and strains. *Appl. Spectrosc.* **64**, 750–759 (2010)
16. M. Baudelet, J. Yu, M. Bossu, J. Jovelet, J.-P. Wolf, T. Amodeo et al., Discrimination of microbiological samples using femtosecond laser-induced breakdown spectroscopy. *Appl. Phys. Lett.* **89**, 163903 (2006)
17. R.A. Putnam, Q.I. Mohaidat, A. Daabous, S.J. Rehse, A comparison of multivariate analysis techniques and variable selection strategies in a laser-induced breakdown spectroscopy bacterial classification. *Spectrochim. Acta B At. Spectrosc.* **87**, 161–167 (2013)
18. D. Marcos-Martinez, J.A. Ayala, R.C. Izquierdo-Hornillos, F.J.M. de Villena, J.O. Caceres, Identification and discrimination of bacterial strains by laser induced breakdown spectroscopy and neural networks. *Talanta* **84**, 730–737 (2011)
19. J.O. Caceres, S. Moncayo, J.D. Rosales, F.J.M. de Villena, F.C. Alvira, G.M. Bilmes, Application of laser-induced breakdown spectroscopy (LIBS) and neural Networks to olive oils analysis. *Appl. Spectrosc.* **67**, 1064–1072 (2013)
20. U. S. D. o. Commerce, National Institute of Standards and Technology (2010), <http://physics.nist.gov/>
21. U. S. Army, United States Army Research Laboratory (ARL) (2010), <http://www.arl.army.mil/www/default.cfm?page=250>
22. S. Lloyd, Least squares quantization in PCM. *IEEE Trans. Inf. Theory* **28**, 129–137 (1982)

Chapter 5

Residual Stresses Measurement by the Hole-Drilling Technique and DSPI Using the Integral Method with Displacement Coefficients

Armando Albertazzi Jr, Filipe Zanini, Matias Viotti, and Celso Veiga

Abstract The authors developed a portable optical residual stresses measurement device that combines the incremental hole-drilling method with digital speckle pattern interferometry working in polar coordinates. The device is able to measure radial in-plane displacement components around the drilled hole. A set of normalized radial displacement vectors are computed by the Finite Element Method for each hole depth increment, according to the integral method. The radial displacement field around the drilled hole is optically measured and data processed to extract the zero and second order harmonics and fitted by least squares method to the FEM coefficient vectors to quantify the amount of residual stresses in each material layer. The residual stresses profile is then determined for every 0.05 mm. A controlled experiment using a bent plate is used to experimentally evaluate the measurement performance of the developed approach. The results uncertainty are comparable to the strain gauge measurements.

Keywords Residual stresses • Integral method • DSPI • ESPI • Stress measurement

5.1 Introduction

The amount of residual stresses present into a part is very important information in most engineering applications. When combined with loading stresses, residual stresses can bring the material close, or even beyond, the acceptable limits and may result in part failure. Several residual measurement methods are already established: X-ray or neutron diffraction, relaxation, slitting, contouring are among them [1]. Perhaps the most used for in-site applications is the hole-drilling method [2], which is a particular case of relaxation methods.

The hole drilling method consists of progressively drilling a blind hole in the part with residual stresses. As the hole is drilled, a new free surface is built, which progressively releases the amount of residual stresses present in the part. The stress relaxation produces a local deformation around the drilled hole. The deformation is measured and fitted to a model to evaluate residual stresses. The ASTM E837-13a standardizes a procedure to measure residual stresses using a special strain gauge rosette [2].

The hole-drilling method using strain gauges is a time consuming approach, which can reach over 1 h for each measurement point. The authors have developed an integrated device to measure residual stresses in a very practical and faster way using a special optical interferometer in combination with a high speed drilling unit [3–5]. A brief description of the device is presented in this paper. The authors emphasize here the residual stresses calculation approach using the interferometer data.

5.2 Radial In-Plane DSPI Interferometer

The integrated portable device for residuals stresses measurement is described in details in [3–5]. The device uses a special binary diffractive optical element (DOE) to double illuminate a circular area of about 10 mm in diameter. Figure 5.1 helps to describe the working principle of the DSPI interferometer.

A. Albertazzi Jr (✉) • F. Zanini • M. Viotti • C. Veiga
Mechanical Engineering Department, Federal University of Santa Catarina, Florianópolis, SC, Brazil
e-mail: a.abertazzi@ufsc.br

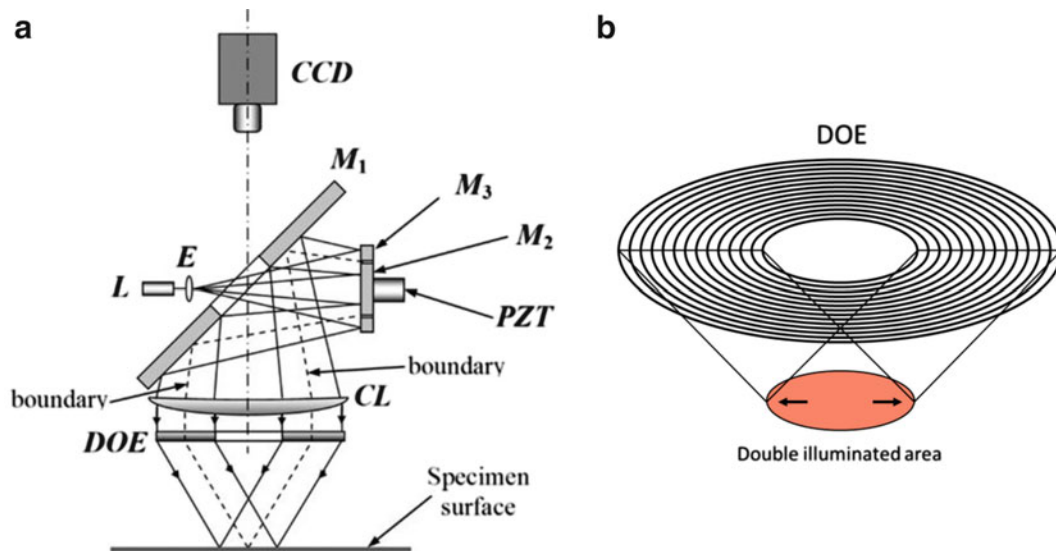


Fig. 5.1 Double illumination speckle interferometer with radial in-plane sensitivity. (a) Optical circuit configurations. (b) Double illumination by an axis-symmetrical diffractive optical element (DOE)

A plane concave lens (E) expands the light coming from a diode laser (L). It passes through the elliptical hole of the mirror M_1 , which forms a 45° angle with the optical axis of the device, illuminating mirrors M_2 and M_3 and being reflected back to the mirror M_1 . Mirror M_1 directs the expanding light to the collimating lens (CL) in order to obtain an annular collimated beam. Finally, the light is diffracted by the DOE mainly in the first diffraction order towards the specimen surface. Residual non-diffracted light or light from other diffraction orders would not be considered troublesome since they are not directed to the central measuring area on the specimen surface. Mirrors M_2 and M_3 are two special circular mirrors. The former is joined to a piezoelectric actuator (PZT) and the later has a circular hole with a diameter slightly larger than diameter of M_2 . Furthermore, mirror M_3 is fixed while M_2 is mobile. The PZT actuator moves the mirror M_2 along its axial direction generating a relative phase difference between the beam reflected by M_2 (central beam) and the one reflected by M_3 (external annular beam). The boundary between both beams is indicated in Fig. 5.1a with dashed lines. According to this figure, it is possible to see that every point over the illuminated area receives only one ray coming from M_2 and only other one from M_3 . Thus, PZT enables the introduction of a relative phase shift to calculate the optical phase distribution by means of phase shifting algorithms. Thus, the central hole placed at M_1 has several functions: (a) to allow that the light coming from the laser source reaches mirrors M_2 and M_3 , (b) to prevent that the laser light reaches directly the specimen surface having triple illumination and (c) to provide a viewing window for the camera (CCD).

Part (b) of Fig. 5.1 shows only one of the diffraction order reaching the double illuminated circular area. The special DOE is a binary circular diffraction grid with a pitch of $1.32 \mu\text{m}$, what result in a diffraction angle of about 30° at a $\lambda = 660 \text{ nm}$ wavelength laser. Since each point on the illuminated area is double illuminated in this special scheme, the sensitivity direction is radial. Therefore, only the displacement component pointing to the circular area center is measured. It is possible to demonstrate and verify that this configuration results in an achromatic interferometer [3].

The authors integrated the radial in-plane DSPI interferometer with a high-speed drilling unit in a portable residual stresses measurement device. Figure 5.2a shows an actual view of the portable device [3–5]. The device has a mechanical base that is firmly attached to the specimen surface by rare earth magnets and three legs with sharp conical tips to avoid relative motions. A motorized mechanical stage is used to automatically exchange the measuring unit and the drilling unit. A measurement software automatically control the test and acquire and process all necessary images to compute the combined stresses profile as a function of the surface depth. Figure 5.2b shows a typical phase difference image after drilling a blind hole in a part with compressive residual stresses with the principal compressive axis near horizontal.

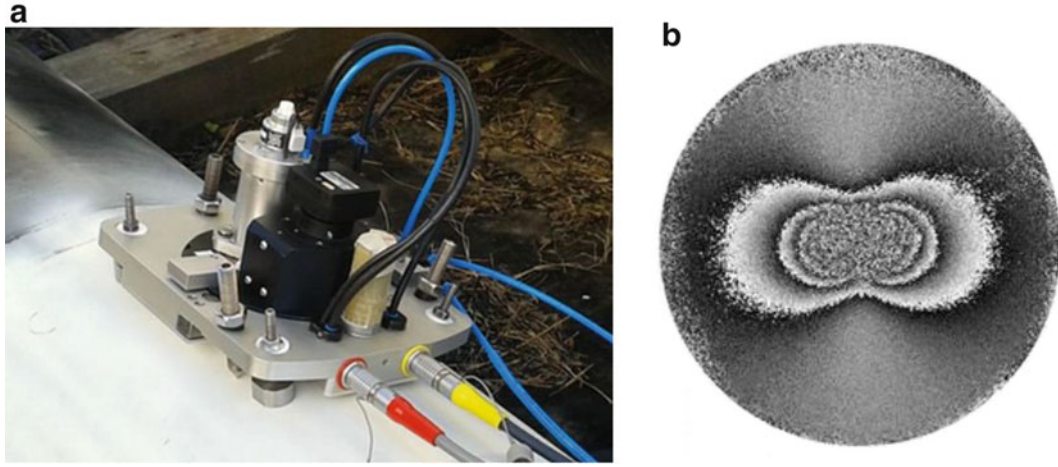


Fig. 5.2 (a) Portable radial in-plane DSPI interferometer combined with a high speed drilling unit to measure combined stresses. (b) A typical radial displacement field due to blind hole drilling measurement

5.3 Residual Stress Calculation

The relationship between the principal residual stresses σ_1, σ_2 , the principal angle β and the radial displacement field $u_r(r, \theta)$ expressed in polar coordinates (r and θ) is in the form of (5.1):

$$u_r(r, \theta) = A(r)(\sigma_1 + \sigma_2) + B(r)(\sigma_1 - \sigma_2) \cos(2\theta - 2\beta) \quad (5.1)$$

$A(r)$ and $B(r)$ are functions of: the radius r , the drilled hole radius r_0 , the hole depth h , and material properties E and ν . There is a closed form for $A(r)$ and $B(r)$ only for a thin infinity plate with uniform stresses and a through hole. For all other cases, only numerical solutions are available. Note that the residual stress sum component does not depend on the polar angle θ . Therefore, it is axially symmetrical. On the other hand, the residual stress difference component depends on the cosine of 2θ and the principal stress direction β .

To quantify the amount for residual stresses in an experiment, two vectors $A(r_k)$ and $B(r_k)$ are extracted from a phase difference map for N discrete radius values (r_k) ranging from $k = 1$ to N and compared with numerically determined reference values. After phase unwrapping, the extraction of $A(r_k)$ and $B(r_k)$ is done through Fourier analysis. The mean radial displacement value for a given radius r_k all way around 2π rad corresponds to the zero order harmonic and to $A(r_k)$. The second harmonic components in cosine $C_2(r_k)$ and the second harmonic components in sine $S_2(r_k)$ are used to compute $B(r_k)$ by $B(r_k) = \sqrt{[(C_2(r_k))^2 + (S_2(r_k))^2]}$ and $\beta_k = \text{Atan}(S_2(r_k)/C_2(r_k))/2$.

Let $a(r_k)$ and $b(r_k)$ be the radial displacement reference values for $A(r_k)$ and $B(r_k)$ respectively. They can be determined through numerical simulations by the finite element method by loading the hole cylindrical surface with an unitary stress and by setting a zero stress at the distant boundary of the object. The finite element used in this analysis belongs to a family of elements of axi-symmetric solids. For the $a(r_k)$ coefficients a uniform biaxial stress field with $\sigma_1 = \sigma_2 = 1.0$ MPa was simulated. For the $b(r_k)$ coefficients calculation the simulation used $\sigma_1 = 1.0$ MPa and $\sigma_2 = -1.0$ MPa. The radius r , ranged from $r_1 = 1.025$ to $r_N = 7.475$ mm with radial increments of 0.025 mm.

The numerical solution of the problem was evaluated by using the ANSYS software. For this reason, two dimensional eight-node elements (PLANE 83) were used. The obtained mesh, shown in Fig. 5.3, had a total of 14,722 elements and 44,601 nodes. Simulations were performed in the same way as an incremental hole-drilling test is executed by following loading recommendations presented in [2]. Hole increments were simulated by drastically reducing the modulus of elasticity at the layers removed by the hole. Twenty steps of 0.05 mm of depth were simulated reaching a final hole depth of 1.00 mm. Displacement coefficients $a_{ij}(r_k)$ and $b_{ij}(r_k)$ were exported as vectors for a future calculations, where i denotes the hole depth increment and j the stress layer count [2, 6]. As an example, Fig. 5.4 shows a plot of these coefficients for the 15th hole step.

To quantify the amount of residual stresses from the measured quantities $A(r_k)$ and $B(r_k)$ a linear behavior was assumed. Therefore, the stress values are proportional to the amount of radial displacements. As an example, let's suppose that $A(r_k)$ is P times bigger than $a(r_k)$. In this case, the sum of residual stresses will be P times bigger than $1.0 + 1.0$ MPa. Since random errors are expected in the experimental values $A(r_k)$, as well as an unexpected bias C may exists, the relationship between

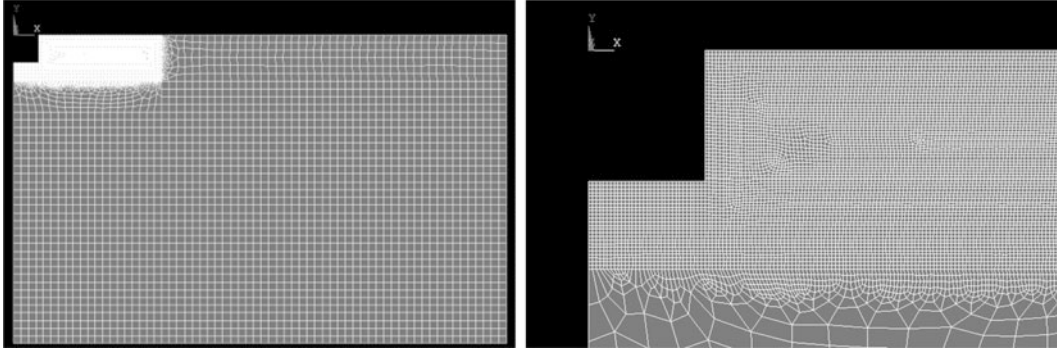
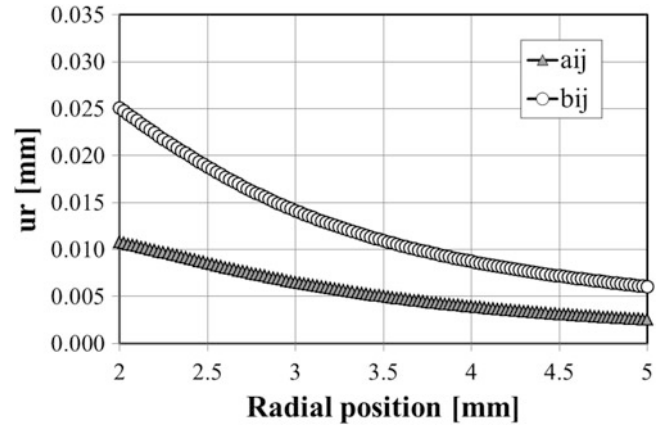


Fig. 5.3 Mesh used during simulation. *Right* part shows a detailed view of the hole region (a) Complete mesh view and (b) Enlarged view of the drilled hole region

Fig. 5.4 Example of $a_{ij}(r_k)$ and $b_{ij}(r_k)$ coefficients



$A(r_k)$ and $a(r_k)$ is in the form of (5.2), where $e(r_k)$ is a random error component. The ij sub indexes were omitted here for simplicity. A similar model is used to relate $B(r_k)$ and $b(r_k)$, but due to space limitation, it will not be described here.

$$A(r_k) = P \cdot a(r_k) + C + e(r_k) \quad (5.2)$$

A least square approach is used to determine P and C . To do that, define the square error function SE by (5.3):

$$SE = \sum_{all r_k} [P \cdot a(r) + C - A(r)]^2 \quad (5.3)$$

The minimum of SE can be found by differentiation of (5.3) to P and C and solving the resulting system of equation. The values for P and C are given by (5.4):

$$C = \frac{\sum_{all r_k} A(r) \cdot \sum_{all r_k} [a(r)]^2 - \sum_{all r_k} [A(r) \cdot a(r)] \cdot \sum_{all r_k} a(r)}{N \sum_{all r_k} [a(r)]^2 - \left[\sum_{all r_k} a(r) \right]^2} \quad \text{and} \quad P = \frac{N \sum_{all r_k} [A(r) \cdot a(r)] - \sum_{all r_k} A(r) \cdot \sum_{all r_k} a(r)}{N \sum_{all r_k} [a(r)]^2 - \left[\sum_{all r_k} a(r) \right]^2} \quad (5.4)$$

To apply the integral method for residual stresses measurement by the incremental hole-drilling technique, the accumulated experimental data for each drilling increment have to be simultaneously fitted to a series of numerical signals. Each signal is related to the hole depth (i) and the stress layer (j). Let $a_{ij}(r)$ denotes the numerical signal computed for the i -depth and j -stress layer [6]. For the first hole depth, the relationship between the experimental data and numerical signal is given by (5.5). The k sub index was omitted for simplicity.

$$A_1(r) = P_1 \cdot a_{11}(r) + C_1 + e_1(r) \quad (5.5)$$

For the second incremental hole depth, the integral method expects to relate the experimental signal to the numerical ones according to (5.6). Since (5.5) alone can determine the value of P_1 , (5.6) involves two unknowns: P_2 the stress value for depth 2 and the additive constant C_2 .

$$A_2(r) = P_1 \cdot a_{21}(r) + P_2 \cdot a_{22}(r) + C_2 + e_2(r) \quad (5.6)$$

For the third hole increment, (5.6) becomes:

$$A_3(r) = P_1 \cdot a_{31}(r) + P_2 \cdot a_{32}(r) + P_3 \cdot a_{33}(r) + C_3 + e_3(r) \quad (5.7)$$

The same idea can be extended for any number of S hole-drilling increments. A general least square solution for the simultaneous system of equations can be developed starting from the sum of the square error given by:

$$\begin{aligned} SE = & \sum_{all\ r} [P_1 \cdot a_{11}(r) + C_1 - A_1(r)]^2 + \sum_{all\ r} [P_1 \cdot a_{21}(r) + P_2 \cdot a_{22}(r) + C_2 - A_2(r)]^2 + \\ & \sum_{all\ r} [P_1 \cdot a_{31}(r) + P_2 \cdot a_{32}(r) + P_3 \cdot a_{33}(r) + C_3 - A_3(r)]^2 + \dots + \sum_{all\ r} [P_1 \cdot a_{S1}(r) + \dots + P_S \cdot a_{SS}(r) + C_S - A_S(r)]^2 \end{aligned} \quad (5.8)$$

The least squares solution for the simultaneous $2S \times 2S$ system can be formed by differentiation of (5.8) to P_1 to P_S and C_1 to C_S and setting all to zero. The $2S$ equations can be easily rearranged to solve the values of the additive constants C_1 to C_S . Since their values have no practical interest, they can be substituted in the equation system that becomes a $S \times S$ system with the S unknowns P_1 to P_S . The resulting matrix system can be written as (5.9) where the elements of the matrix $[X]$ and vectors $\{P\}$ and $\{Y\}$ are given in (5.10).

$$[X]\{P\} = \{Y\} \quad (5.9)$$

Where:

$$\begin{aligned} \{P\} &= \begin{Bmatrix} P_1 \\ \vdots \\ P_S \end{Bmatrix} \\ X_{m,n} &= \sum_{i=Q}^S \left[\sum_{all\ r} (a_{im} \cdot a_{in}) - \frac{1}{N} \sum_{all\ r} a_{im} \cdot \sum_{all\ r} a_{in} \right] \\ Y_m &= \sum_{i=Q}^S \left[\sum_{all\ r} (a_{im} \cdot A_i) - \frac{1}{N} \sum_{all\ r} a_{im} \cdot \sum_{all\ r} A_i \right] \end{aligned} \quad (5.10)$$

The quantity Q is defined as the minimum integer between m or n : $Q = \min(m, n)$.

Usually (5.9) becomes ill-conditioned when S increases. The system (9) can be solved by Tikhonov regularization by (5.11), where α is the regularization factor and $[D]$ is a tri-diagonal second derivative $S \times S$ matrix. The first and last rows of $[D]$ contain zeros; all other rows have $[-1 \ 2 \ -1]$ centered along the diagonal [2, 6].

$$\left([X] - \alpha [D]^T [D] \right) \{P\} = \{Y\} \quad (5.11)$$

Solution of (5.11) result in the principal residual stresses sum for each S drilling increment. The same approach can be applied for $b_{ij}(r_k)$ and $B_{ij}(r_k)$ to determine the principal residual stresses differences as functions of the depth. A combination of both equations allows the determination of both principal residual stresses values individually and for each drilling

increment. More details about the derivation of those equations, as well as, a set of difference equations are the focus of a detailed paper that will be submitted to *Experimental Mechanics* late 2015.

5.4 Experimental Verification

A stress free specimen was bent along a well-defined curved surface as a way to generate reference values for stresses along the specimen depth. All material treatment and geometry were carefully prepared according to recommendations of reference [7]. Figure 5.5 shows a view of the specimen. It is made by: (a) a thick aluminum base with its upper surface machined with a radius of 508 mm, and (b) a thin sheet of aluminum with a thickness of 1.6 mm. The latter part was prepared from a thicker sheet. The final thickness was achieved by machining the material of the surface. Thus, residual stresses generated by the rolling manufacturing process of the original plate were ideally removed resulting in a free-stressed material. The thin sheet was glued to the curved surface introducing a well-defined bending stress profile into the material.

A 1.6 mm diameter drill was used for incremental hole-drilling. A total of $S = 20$ drilling steps of 0.050 mm each were used. For each one a set of four phase shifted images were acquired and used to compute phase values. As a result, 20 phase differences images were obtained always involving the phase differences between the reference state (without the hole) and the actual hole depth. After phase unwrapping, the vectors $A_i(r_k)$ and $B_i(r_k)$ were extracted from each phase difference map of $i = 1$ to 20 and the residual stresses computed using (5.11) for the stresses sum and later for stresses differences. Additional residual stresses measurement were carried out by strain gauge rosettes using the conventional hole-drilling method also with 20 depth increments of 0.050 mm each. Figure 5.6 shows plots of measured residual stresses along the material thickness. S1_DSPI and S2_DSPI are standing for the optically measured principal stresses σ_1 and σ_2 respectively. S1_SG and S2_SG are the plots obtained by strain gauge rosette measurements for σ_1 and σ_2 respectively. All stress profiles were computed after using appropriate Tikhonov regularization coefficients. Figure 5.6 shows a good agreement between measurements obtained by both techniques. The total measurement time for the optical device was about 20 min. For strain gauge measurement the surface was prepared, the strain gauge cemented, wired and the measurement was done by. The total time for strain gauge measurement was about 60 min.

Fig. 5.5 View of the specimen bent over a curved surface and four holes drilled on it

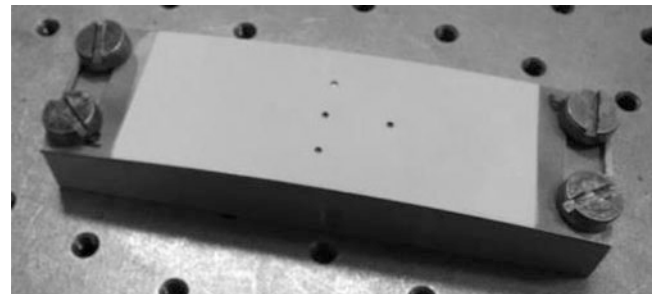
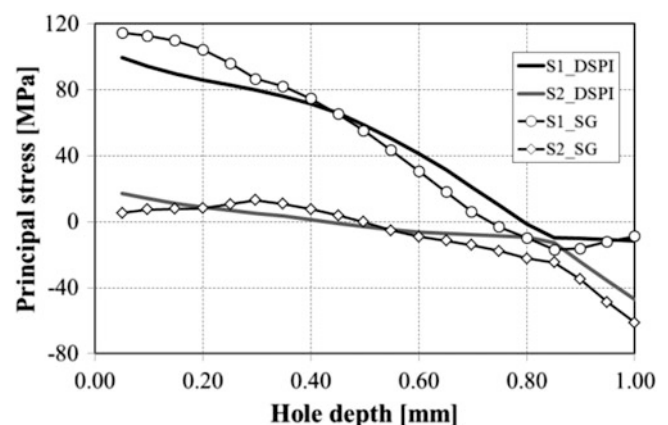


Fig. 5.6 Principal stresses profile results as functions of the hole depth for optical measurement (S1_DSPI and S2_DSPI) and for strain gauge measurement (S1_SG and S2_SG)



5.5 Conclusions

This paper presented a residual stresses calculation model using the incremental method and finite element coefficients expressed in terms of radial displacement along the radius. The measured radial displacement signal is split in two components: the zero and the second order harmonics. The residuals stresses sum is computed from the zero order harmonic using a least squares fitting algorithm with Tikhonov regularizations. The second harmonics are used to compute the residual stresses differences using the same approach, as well as, the principal directions. A bending controlled specimen was used for model validation. The principal stresses profile along the material depth were also measured using strain gauges rosettes. Both signals present a very good agreement and encourage further development of this approach. The total measurement time for the optical device was about 30 % of the time needed for strain gauge measurement.

The use of difference equations as well, as predefined residual stresses profiles, are currently under development and will be present in a paper that has been prepared to be submitted to *Experimental Mechanics* late 2015.

Acknowledgments The authors would like to thanks the financial support of PETROBRAS, CNPq, ANP/PRH 34 and CAPES. They also thanks the encouragement and help of Prof. Gary Schajer on the finite element modeling and the Labmetro team for support.

References

1. G.S. Schajer (ed.), *Practical Residual Stress Measurement Methods*, vol. 7 (Wiley, New York, 2013). ISBN 9781118342374
2. ASTM E837-13, in *Standard Test Method for Determining Residual Stresses by the Hole-Drilling Strain-Gage Method*. Annual Book of ASTM Standards (American Society for Testing and Materials, Philadelphia, 2013)
3. M.R. Viotti, W. Kapp, A. Albertazzi Jr., Achromatic digital speckle pattern interferometer with constant radial in-plane sensitivity by using a diffractive optical element. *Appl. Opt.* **48**(12), 2275–2281 (2009)
4. M.R. Viotti, A. Albertazzi Jr., W.A. Kapp, Experimental comparison between a portable DSPI device with diffractive optical element and a hole drilling strain gage combined system. *Opt. Lasers Eng.* **46**(11), 835–841 (2008)
5. M.R. Viotti, A. Albertazzi Jr., Compact sensor combining digital speckle pattern interferometry and the hole-drilling technique to measure non-uniform residual stress fields. *Opt. Eng.* **52**(10), 101905.1–101905.8 (2013)
6. G.S. Schajer, Measurement of non-uniform residual stresses using the hole-drilling method. Part I - stress calculation procedures. *J. Eng. Mater. Technol.* **110**(4), 338–343 (1988). doi:[10.1115/1.3226059](https://doi.org/10.1115/1.3226059)
7. G.S. Schajer, Hole-drilling residual stress profiling with automated smoothing. *J. Eng. Mater. Technol.* **129**, 440–445 (2007)

Chapter 6

On the Separation of Complete Triaxial Strain/Stress Profiles from Diffraction Experiments

H. Wern

Abstract The fundamental equation in X-ray diffraction relates the measured strain quantities to a superposition of six independent components: three normal and three shear components. However, the linear system of equations to solve for the six components leads to a singular matrix. The academic literature recommends regularization methods. In case of using regularization methods, non-unique solution is expected. All these methods only work if the determinant of the matrix is close to zero. In diffraction experiments it is definitely zero because of the existence of the normal component ϵ_{33} . Therefore in the past biaxial stress states have been assumed. It is shown that by a numerical differentiation the shear components can be simply resolved. Once the shear components have been subtracted from the fundamental equation, the three normal components remain. By a Taylor series development of the fundamental equation it is shown that ϵ_{33} and its first derivative at $\psi = 0$ are independent of the rotation angle φ . This requires a special structure of the matrix to analyze the data at different φ rotations. Once these two values are obtained, they serve as the initial conditions of a differential equation of second kind which is solved numerically. The unknown functions in the differential equation are approximated by a Taylor series expansion whose coefficients are determined by a nonlinear optimization procedure. Together with simulated data, first results are presented.

Keywords X-ray diffraction • Triaxial strain/stress profiles • Separation of profiles • Numerical solution of differential equation of second kind • Nonlinear least squares approach

6.1 Introduction

All measuring methods which rely on Bragg's law such as X-ray or neutron diffraction, primarily detect a strain state rather than a stress state. A strain state assigned to any point of the material under investigation is represented by a symmetric second rank tensor containing six different elements, three normal and three shear components. Because the strain state of a polycrystalline material is assumed to be the response of residual stress, the strain tensor does not have to conform with the crystal symmetry as thermal expansion does. As a consequence, no further restrictions can be made and the full triaxial tensor must always be considered. In this sense, the so called "sine-square-psi" method [1] is a restriction which can be reviewed as a first approach in the early days of X-ray stress analysis.

6.2 Goniometers

In the X-ray diffraction technique, two different types of measuring geometries are established [2]: the Ω and ψ goniometers, which are illustrated in Figs. 6.1 and 6.2.

H. Wern (✉)
HTW des Saarlandes, University of Applied Sciences, Goebenstraße 40, Saarbrücken 66117, Germany
e-mail: herald_wern@t-online.de

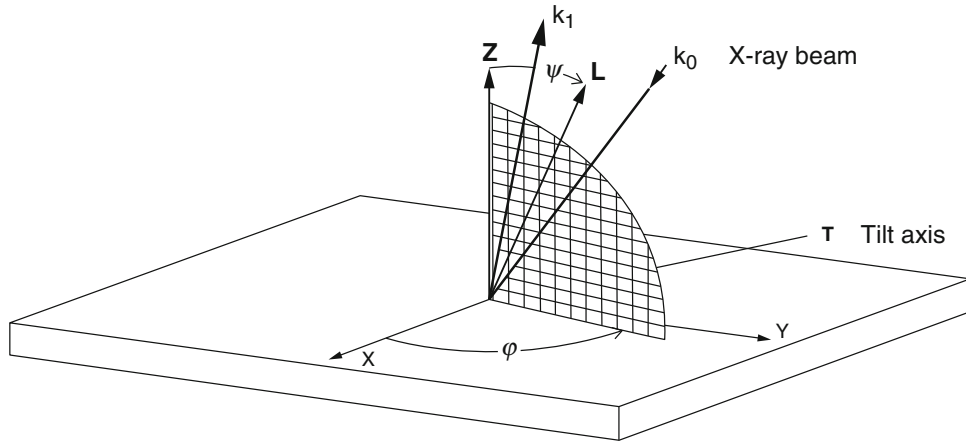


Fig. 6.1 Angular definitions of the Ω -goniometer with respect to the specimen coordinate system. The tilt axis T lies in the specimen surface and in the diffraction plane but is perpendicular to the diffraction vector (hkl), which is parallel to L

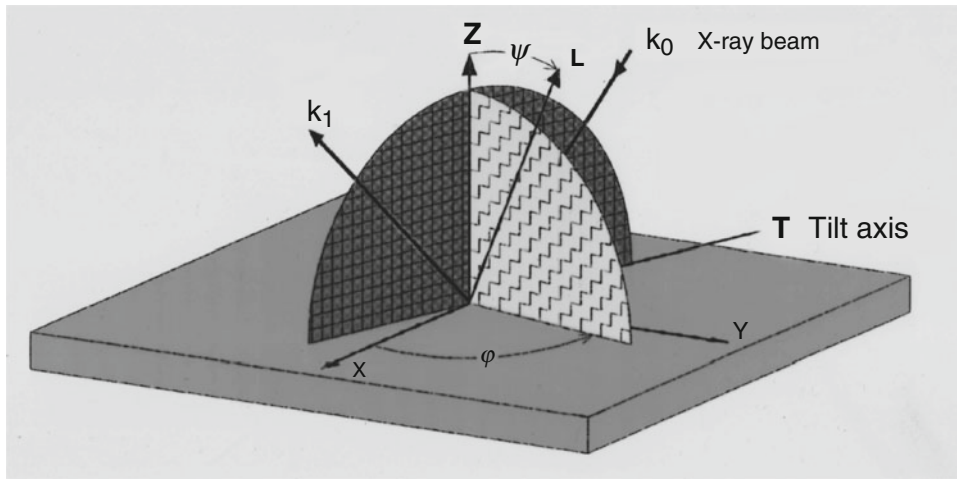


Fig. 6.2 Angular definitions of the ψ -goniometer

6.3 Fundamental Equations

A typical experimental setup uses the variation of a rotation angle φ and tilt angles ψ with respect to the sample coordinate system. The normal L refers to the measurement direction which is selected by the Miller indices (hkl). Residual strain or stress depth profiles measured with X-rays in the near surface region of polycrystalline materials are always averaged quantities because the counted intensities are averages over the diffracted volume. Therefore, the measured profiles are called τ -profiles where τ is the $1/e$ penetration depth of the X-rays. The measured profiles can be expressed as

$$\langle \varepsilon \rangle_{\varphi\psi_i}(\tau_i) = \frac{d\varphi\psi_i(\tau_i) - d0}{d0} = \frac{\int_0^D e^{-\frac{z}{\tau_i}} \varepsilon_{\varphi\psi_i}(z) dz}{\int_0^D e^{-\frac{z}{\tau_i}} dz} \quad (6.1)$$

Where ε follows from the usual transformation law of a second rank tensor ε from the laboratory system to the specimen system shown in Fig. 6.2.

$$\begin{aligned} \langle \varepsilon_{\varphi\psi}(\tau) \rangle = & \varepsilon_{11}(\tau) \cos^2\varphi \sin^2\psi + \varepsilon_{22}(\tau) \sin^2\varphi \sin^2\psi + \varepsilon_{33}(\tau) \cos^2\psi \\ & + \varepsilon_{12}(\tau) \sin 2\varphi \sin^2\psi + \varepsilon_{13}(\tau) \cos\varphi \sin 2\psi + \varepsilon_{23}(\tau) \sin\varphi \sin 2\psi \end{aligned} \quad (6.2)$$

For the ψ -goniometer τ_i is given by (6.3)

$$\tau_i = \frac{\sin\Theta_0 \cos\Psi_i}{2\mu} \quad (6.3)$$

Where μ is the absorption coefficient for the particular wavelength and the material under investigation. Θ_0 is the Bragg angle of the stress free lattice spacing d_0 . Because of the independent existence of the normal component ε_{33} at all φ -rotations the above system in (6.2) written as a linear system of equations for the six unknowns becomes always singular. Therefore a unique solution cannot be expected. This is well known in literature and the reason why several simplifications have been made such as to consider only biaxial stresses and so on [3–6].

The purpose of this paper is to find a method to separate all six and therefore triaxial components.

In order to achieve this goal, in a first step we have to use simulated data with known conditions. Therefore the left hand side of (6.2) (the measurement side) has been simulated for data in ψ geometry together with typical values for a steel specimen and $\text{CrK}\alpha$ radiation. The strains are then assumed to be converted to stresses with the corresponding X-ray elastic constants. This has the advantage that we can use a further boundary condition, namely that $\sigma_{33}(z = 0)$ at a free surface must be zero.

6.4 Simulation

With the aid of a random number generator, a total of six different stress gradients have been simulated according to the following formulae:

$$\sigma_{i,j}(z) = (a_0 + a_1z + a_2z^2)e^{-az^3} \quad (6.4)$$

The profiles of the three normal components are shown in Fig. 6.3.

These equations are put into (6.1) to produce the τ profiles. In (6.1) and (6.2) simply replace strain by stress. The results are shown in Figs. 6.4 and 6.5 respectively.

Without loss of generalization we restrict the procedure only for the case $\varphi = 0$.

Fig. 6.3 Simulated normal stress gradients versus depth from surface

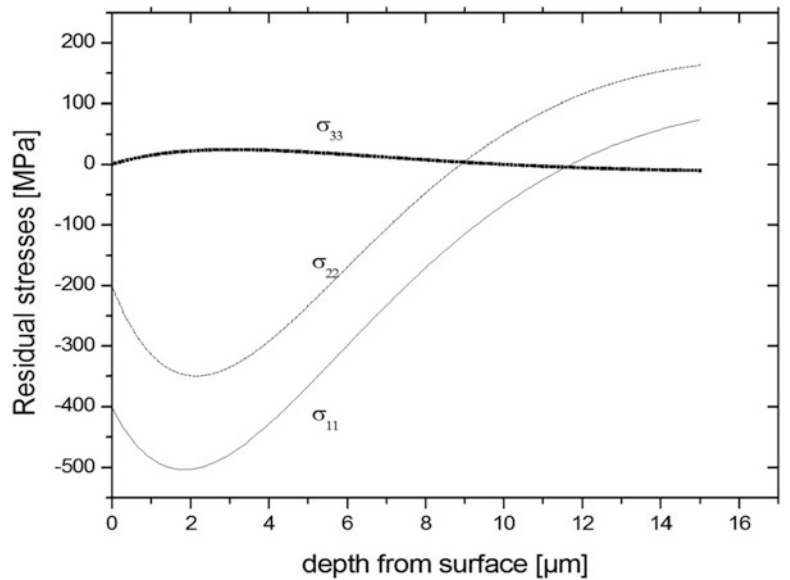


Fig. 6.4 Simulated normal stresses versus τ [μm]

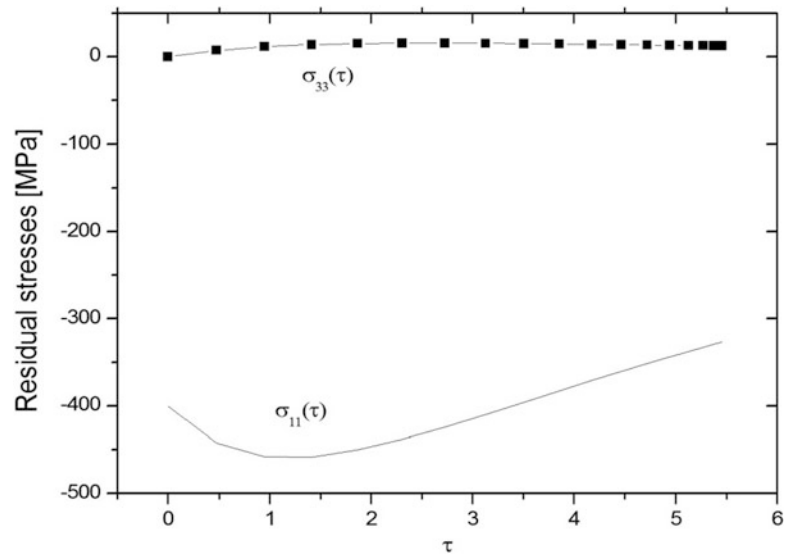
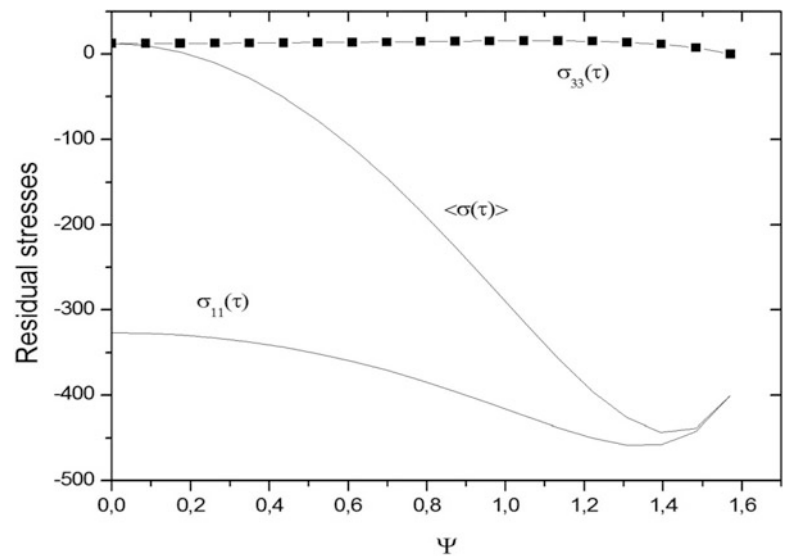


Fig. 6.5 Stress profiles as a function of ψ



The shear components are not shown because they can be exactly obtained by the following procedure: The fundamental equation (6.2) is differentiated with respect to the rotation angle φ in order to get rid of the third normal component. The left hand side is differentiated by fitting a Fourier series with respect to φ to the experimental or simulated data. In consequence, one obtains a linear system of equations for the three shear components and the difference $\varepsilon_{22}(\tau) - \varepsilon_{11}(\tau)$. The matrix is regular and therefore a unique solution is obtained. Once the shear components are separated they are subtracted from the fundamental equation with their corresponding weights. It remains the superposition of the three normal components. In order to simplify the procedure we restrict us to $\varphi = 0$. Now we start from behind, that means we plot the τ -profiles as a function of the tilt angle ψ shown in Fig. 6.5.

The curve in the middle is the superposition of both profiles which corresponds to the measuring quantity. A Taylor series expansion of the fundamental equation with respect to ψ at $\psi = 0$, exhibits the following form which reads as

$$\begin{aligned} \langle \sigma(\psi) \rangle = & \sigma_{33}(0) + \sigma_{33}'(0) + (\sigma_{33}''(0) - 2\sigma_{33}(0) + 2\sigma_{11}(0))\psi^2/2 \\ & + (\sigma_{33}'''(0) - 6\sigma_{33}'(0) + 6\sigma_{11}'(0))\psi^3/6 + \dots \end{aligned} \quad (6.5)$$

A least squares analysis of the measured data yield the corresponding coefficients of the Taylor series.

It is important to note that the first two terms are independent of the orientation angle φ . This knowledge allows us to properly perform a least squares analysis at different φ rotations. As a result, we know the exact values of σ_{33} and σ_{33}' at $\psi = 0$. The idea now was to calculate the profile as the solution of a differential equation of second kind whose initial conditions are known. Under the assumption that σ_{33}'' and σ_{33}''' at $\psi = 0$ are small we can at least obtain approximate initial conditions for σ_{11} . The two differential equations will certainly not have constant coefficients but will be rather functions of ψ . Because we do not know the functions, we again write them as a Taylor series with unknown coefficients. Let us abbreviate the superposition from the measurement as $\langle \sigma(\psi) \rangle^M$ and from the solution of the differential equations as $\langle \sigma(\psi) \rangle^{DGL}$. Then we can define an error functional which reads as $\sum_i \left(\sigma(\psi_i)^M - \sigma(\psi_i)^{DGL} \right)^2 = F^2$. Now, we minimize the error function with respect to the unknown parameters in the Taylor series of the differential equations. For that reason we need the derivatives of the $\langle \sigma(\psi) \rangle^{DGL}$ with respect to the parameters. Because they are not known analytically, we have to adopt a numerical procedure. We replace the derivatives by a symmetric difference quotient. For that reason, we have to solve the differential equations twice for each parameter. First results will be presented in the oral presentation.

References

1. E. Macherauch, P. Müller, Das $\sin^2\psi$ Verfahren der röntgenographischen Spannungsmessung. Z. Angew. Phys. **13**, 305–312 (1961)
2. U. Wolfstieg, Aufnahmeverfahren. Härterei-Tech. Mitt. **31**, 19–22 (1976)
3. A. Peiter, *Handbuch Spannungsmesspraxis* (Vieweg, Braunschweig, 1992)
4. V. Hauk, *Structural and Residual Stress Analysis by Nondestructive Methods* (Elsevier, Amsterdam, 1997)
5. H. Wern, Influence of measurement and evaluation parameters on stress distributions investigated by x-rays. J. Strain **27**, 127–136 (1991)
6. I.C. Noyan, J.B. Cohen, *Residual Stress* (Springer, New York, 1987)

Chapter 7

Quantification of Slow Mechanical Displacements in Metal Samples by Optical Polarization Phase Shift DSPI

Darwin Mayorga Cruz, José Antonio Marbán Salgado, Víctor Manuel Juárez Núñez, and Álvaro Zamudio Lara

Abstract In this work the optical polarization method applied on phase shift digital speckle interferometry (PSDSPI), was performed for measurement of slow, small mechanical out-of-plane induced displacements. A basic experimental setup was used to obtain digital specklegrams related to mechanical displacements induced during specific time intervals. A digital image processing computational analysis was applied on experimental data, combined with analysis of phase shift positions induced by a polarizer and as a result a reliable measurement of displacements was obtained. Although conventional piezoelectric phase shifting methods are well established, the optical polarization method still preserves advantages as less complex instrumentation and low cost implementation.

Keywords Optical metrology • Interferometry • Phase shifting • Polarization • Speckle patterns

7.1 Introduction

Digital Speckle Pattern Interferometry (DSPI) is a recent optical method used for deformations measured in solid objects illuminated by an interference speckle pattern formed by two beams coming from the same laser source; one of the beams is reflected from the object under analysis and the other coming directly from the source is considered as the reference beam [1]. The particular speckle feature of the optical pattern, caused by the diffused reflection of the object, is captured by means of an image acquisition device (i.e. a CCD) for digital post processing and analysis. Main interest on DSPI is its ability for detecting and monitoring of micro-deformations originated in optically rough surfaces and, as same as other interferometric techniques, is based on non-destructive procedures which means none structural modification requirement on tested object [1, 2]. Many of structural material failures on industry subjected to external forces application as stress, twisting or traction may induce strain concentrations, which also surpass acceptable limits on materials and cause micro-deformations or fractures; for such reasons the study of materials mechanical properties become of importance and application of this knowledge may be translated on practical solutions.

Optical interferometric methods provide high sensitivity and precision tools, as constructive and destructive wave interference allow ways to estimate slow displacement or slow deformation fields of analyzed objects; in particular DSPI method is useful for residual stress analysis on materials along with an automatic data analysis [3], stress-strain Young's modulus calculation on test metallic bars [4] or elastic materials like latex [5], and vibration modes measuring on materials [6]. Depending on a specific application, determination of material properties as strength, stiffness or ductility may be supported on noninvasive, high accuracy methods as optical interferometric like DSPI. As it is well known, phase shifting methods implemented on holographic interferometry allows measure of interference phase between the fringe intensity maxima and minima, as same as elimination of sign ambiguity [7–9]; introduction of phase-stepping and phase shifting on DSPI (PSDSPI) permitted then a proper calculation and comparison of optical phase distributions [10, 11].

It is also well known that a reflecting mirror mounted on a piezoelectric transducer is the most common method for introducing a phase shifting on an optical beam [12], as this is necessary on several holographic and interferometric methods like PSDSPI.

Other methods for phase shifting like moving gratings, acousto-optical modulators, glass-plate tilting, optical fiber stretching or polarizing rotating elements have been also used [9]; regarding polarization methods which introduce half-wave plates or coupled linear polarizers, although they have a lack of precision and control in comparison to other methods, they present on the other hand some advantages as less complex instrumentation and low cost in comparison with piezoelectric mirrors for example, when are implemented on experimental setups or commercial instrumentation [13–15].

D. Mayorga Cruz (✉) • J.A. Marbán Salgado • V.M. Juárez Núñez • Á. Zamudio Lara
Center for Research in Engineering and Applied Sciences (CIICAp-UAEM), Av. Universidad 1001,
Col. Chamilpa, Cuernavaca, Morelos 62209, México
e-mail: darwin@uaem.mx

7.2 Digital Speckle Pattern Interferometry

Generally all objects, metallic or synthetic, have extremely rough surfaces in the optical wavelength scale; if highly coherent light is used to illuminate them a grain structure characterized by bright and dark spots is produced as a reflected light pattern. This intensity distribution is known as *speckle light pattern* and is originated by constructive and destructive interference of optical waves emitted from large dispersion centers located on the object surface; when a coherent reference field is overlapped with a speckle pattern, correlation fringes are produced with their bright and dark regions corresponding to phase differences areas between a final and an initial state of the object which is being analyzed, similarly to interferometric holography.

There are two main setups for slow displacement measurements: in-plane configuration and out-of-plane configuration, and sensitivity will depend on illumination and observation geometries. For an out-of-plane configuration sensitivity, the optical intensity for an arbitrary point $P(x,y)$ of the object in the detection plane is given by:

$$I_1(x, y) = I_A(x, y) + I_B(x, y) + \sqrt{I_A I_B} \cos \psi \quad (7.1)$$

where (7.1) represents a speckle pattern obtained in an initial state (i.e. no displacement is applied on the object); when a phase change is applied between two wave fronts (i.e. a displacement is induced), the new optical phase distribution changes to:

$$I_2(x, y) = I_A(x, y) + I_B(x, y) + \sqrt{I_A I_B} \cos (\psi + \Delta\phi) \quad (7.2)$$

At (7.1) and (7.2), I_A and I_B are optical intensities of the two interacting beams, ψ is the random phase difference between them and $\Delta\phi$ is an additional phase difference corresponding to the object displacement or deformation. Modified speckle pattern (7.2) is compared with initial pattern by means of addition or subtraction of intensities, and as a result, correlation of these patterns is visualized as a bright and dark fringes distribution as above mentioned; generally a subtraction correlation is used in order to obtain a better visibility of the pattern and so we have:

$$I_1 - I_2 = \sqrt{I_A I_B} \sin \left(\frac{2\psi + \Delta\phi}{2} \right) \bar{n} \sin \left(\frac{\Delta\phi}{2} \right) \quad (7.3)$$

Once fringes are visualized, correlation phase $\Delta\phi$ can be calculated [5]; registration of five different intensity values $I(0)$, $I(1)$, $I(2)$, $I(3)$ and $I(4)$, each obtained for five different reference beam phase shifts 0 , $\pi/2$, π , $3\pi/2$ and 2π respectively, is then required to get $\Delta\phi$ for each pixel point. The phase shifting can be experimentally performed introducing five different positions of a polarizer on the reference beam as done in PSDSPI [13–15] (i.e. two polarizers keeping one of them fixed and rotating the other one). A five-step algorithm can now be applied on the phase-shifted frames to obtain the initial phase for reference beam with (7.4) [6, 16]:

$$\phi_r(x, y) = \tan^{-1} \left\{ \frac{2[I_i(3) - I_i(1)]}{I_i(4) + I_i(0) - 2I_i(2)} \right\} \quad (7.4)$$

After the object is deformed, five more different intensities data are taken by shifting the same phase amount as it was done for the first data set; then computation of a new speckle phase at each pixel gives:

$$\phi_r(x, y) + \Delta\phi(x, y) = \tan^{-1} \left\{ \frac{2[I_f(3) - I_f(1)]}{I_f(4) + I_f(0) - 2I_f(2)} \right\} \quad (7.5)$$

Subtraction of (7.4) from (7.5), gives the phase difference value $\Delta\phi$, which arise from the object deformation for each pixel point (7.5). The "difference of phases" method represents the most suitable approach for phase values calculation at each pixel. Then an initial phase-map is obtained and, after deformation introduction, a final phase-map is also obtained which can be unwrapped by standard phase-unwrapping methods. Phase difference $\Delta\phi$ can be finally obtained considering an out-of-plane experimental configuration [1]:

$$\Delta\phi = \frac{4\pi}{\lambda} w(x, y) \cos \theta \quad (7.6)$$

where λ is the laser wavelength, θ is the surface scattering light angle measured with respect to the object normal line, and $w(x,y)$ is the out-of-plane difference displacement component, associated in this case with the out-of-plane slow mechanical displacement or deformation.

7.3 Experimental Configuration

For quantification of slow mechanical deformations induced on a metallic sample by PSDSPI, an out-of-plane interferometric configuration was used (Fig. 7.1b). A 10 mW, 633 nm He–Ne collimated laser beam is divided in two new beams by a 50/50 beam splitter; one of these acts as the object beam as is directed by three mirrors to the metallic sample surface and its reflection is collected by a biconvex lens of 100 mm focal lens, and focused into the chip of a Genie M1280 CCD with 1200×960 pixels resolution which records and stores the obtained speckle reflected patterns. The other beam considered as the reference one is also directed by two mirrors and passed through two linear polarizers that induce a phase shifting of incoming light when the second one is rotated. A second beam splitter collects object and reference beams and the speckle interference scheme is then completed. The metallic sample is a 5×10 mm aluminum slab (Fig. 7.1a) fixed on a translation stage manually displaced by a micrometer screw, while mechanical out-of-plane deformations were slowly induced by means of a steel needle fixed out of the stage, puncturing in the center of the slab area.

7.4 Results

In order to obtain speckle interferograms formed by subtraction correlation and accordingly to (7.4), five intensity interferograms of the sample before deformation and other five intensity interferograms after deformation are needed. For initial state acquirement, phase shifts are induced rotating the second polarizer as CCD records such a rotation on a 30 frames per second, 10 s long video compound of 381×317 pixels images. Once the video is recorded, it is edited in order to get its individual images or photograms (i.e. samples); by means of digital image processing software, the mean pixels value (i.e. amplitude) for each sample is calculated for a specific zone.

For instance, the red squared zone at Fig. 7.2a indicates the chosen region to be analyzed; at Fig. 7.2b a plot of amplitude values for all samples in time domain is shown and, as it was expected, a sinusoidal dependence is obtained and $0, \pi/2, \pi, 3\pi/2$ and 2π phase shift states can be clearly identified. In order to verify our plot, $I(0)$ image of interferogram recorded at 0 phase shift state was compared with $I(4)$ image recorded at 2π phase state; both images resulted identical.

Once our five phase-shifted interferograms are identified, an initial state phase wrapped map $\phi_r(x, y)$ is obtained for each photogram pixels; Fig. 7.3 show initial state phase shifted interferograms, wrapped phase map and corresponding unwrapped phase:

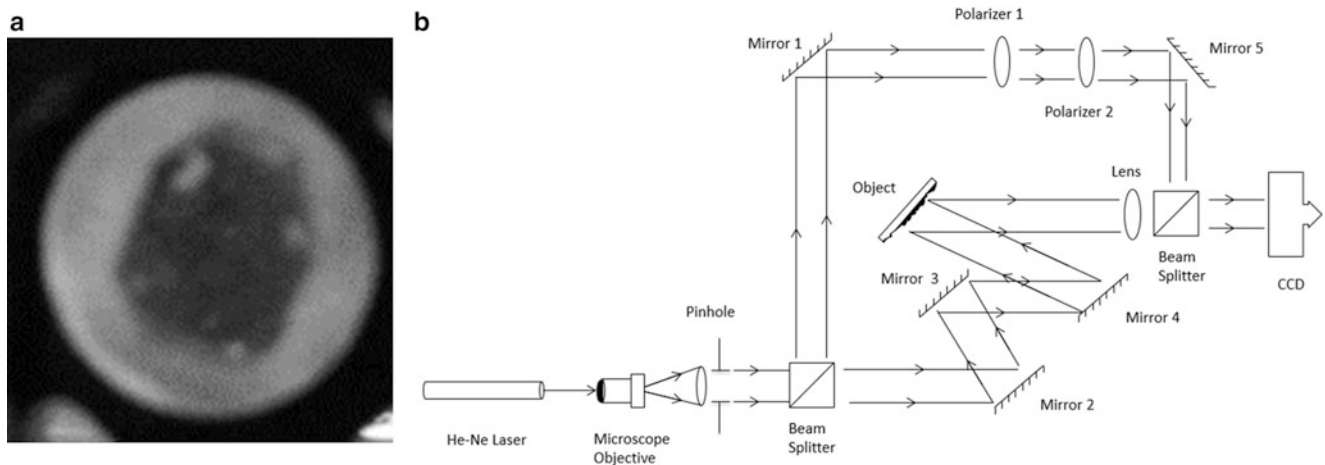


Fig. 7.1 (a) Aluminum sample; (b) Experimental setup

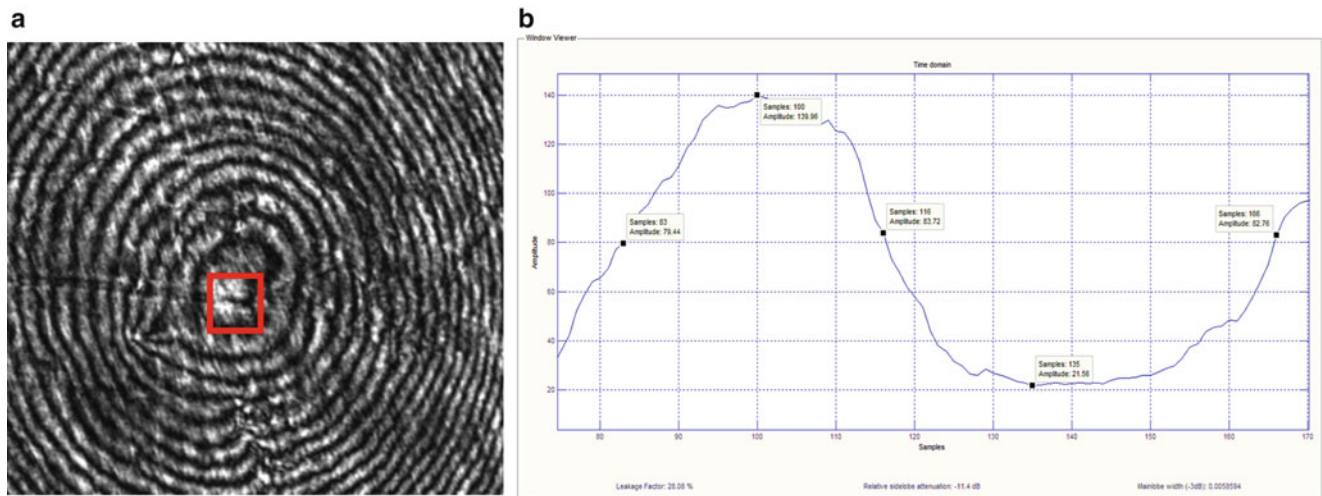


Fig. 7.2 (a) Analyzed zone for digital image processing (*red square*); (b) Plot of mean pixels values (amplitudes) vs photograms (samples) in time domain; phase shift states are clearly identified

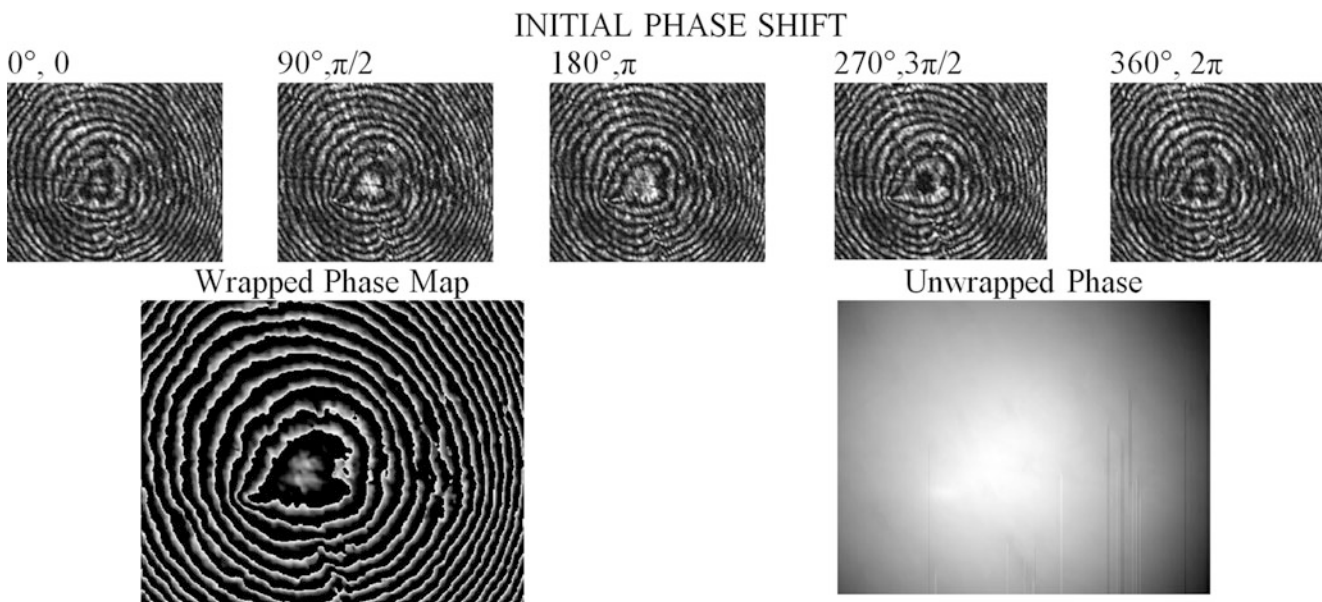


Fig. 7.3 Initial state phase shifted interferograms, wrapped phase map and unwrapped phase

After mechanical deformations are applied (performed by consecutive $10 \mu\text{m}$ screws from an initial $20 \mu\text{m}$ up to a $75 \mu\text{m}$ translational stage position), the final state phase shift $\Delta\phi(x, y)$ is calculated by using (7.6), considering $\theta = 25^\circ$, experimentally estimated. The final state phase shifted interferograms, wrapped phase map and unwrapped phase are shown at Fig. 7.4.

In order to reduce excessive speckle inherent noise in all obtained interferograms, a low-pass filtering algorithm was applied. It must be also mentioned that after initial and final states interferograms, fringes observed in following images resulted more complicated for digital processing and for this reason acquisition was stopped at $75 \mu\text{m}$ micrometer screw position, corresponding to the fifth recorded interferogram.

On Fig. 7.5 a resume of results obtained by application of (7.6) are shown; unwrapped phase used on images was obtained for a 381×317 pixels image and, as recorded pixel intensities values can be related to out-of-plane surface distortions, our system may quantified slow mechanical deformations performed by steel needle as the slab is displaced against it by micrometer screws on translational stage. The plot on Fig. 7.5a displays a record of deformations from 20 to $75 \mu\text{m}$ micrometer screws range; pixel intensities values are here plotted against lateral image pixels (i.e. x -axis). Figure 7.5b shows

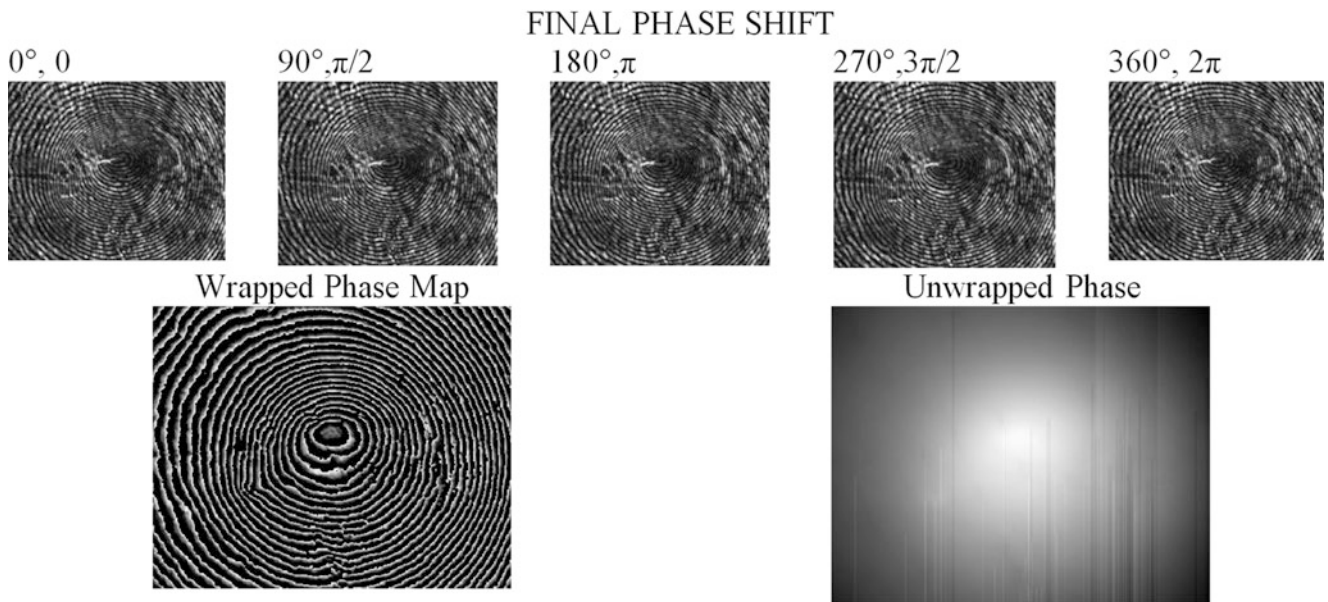


Fig. 7.4 Final state phase shifted interferograms, wrapped phase map and unwrapped phase

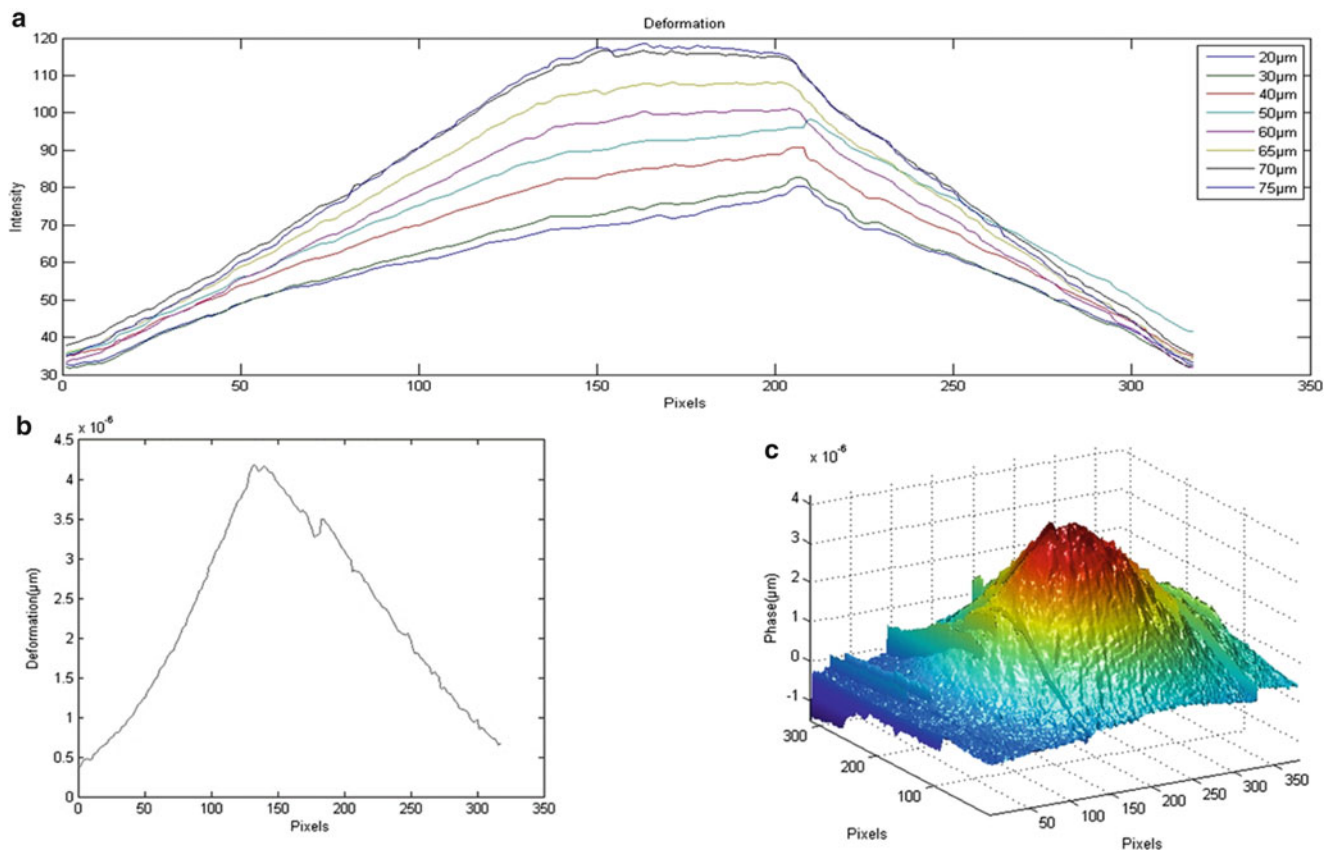


Fig. 7.5 (a) Mechanical deformations record; pixel intensities values vs. lateral image pixels plotted at specified micrometer screws; (b) slab mechanical deformation estimated by (7.6) at a single y-axis pixel value; (c) 3D representation (unwrapped phase) of induced deformation estimated on (b)

the horizontal line profile corresponding to an individual pixel intensity variation (y -axis) at a $150 = y$ -axis pixel value, plotted for the 0–381 pixels range (x -axis); accordingly to (7.4) and (7.5) a $4 \mu\text{m}$ mechanical deformation of the slab was estimated. Figure 7.5c displays a 3D representation of corresponding slab deformation estimation.

7.5 Conclusions

A measure of slow, small mechanical deformations, induced on an aluminum slab, was performed by means of a phase shift digital speckle interferometry (PSDSPI) experimental setup. The phase shift was induced by an optical polarization method implemented on reference arm, and DSPI analysis was obtained by digital image processing of video edited speckle interferograms, based on a computational interface. A quantification of out-of-plane distortions induced on the metallic slab by external puncture, gave a $4 \mu\text{m}$ approximate deformation. Further improvements on polarizing experimental method, as same as on digital procedures are necessary for better measure performance of the system, either for merely academic work or particularly for commercial purposes.

References

1. P.K. Rastogi, Measurement of static surface displacements, derivatives of displacements, and three-dimensional surface shapes-examples of applications to non-destructive testing, in *Digital Speckle Pattern Interferometry and Related Techniques*, ed. by P.K. Rastogi (Wiley, New York, 2001), pp. 141–224
2. R.S. Sirohi, Speckle Interferometry. In *Contemporary Physics*, vol. 43/3. (Taylor & Francis, London, 2002), pp. 161–180
3. F.V. Díaz, G.H. Kaufmann, G.E. Gallizzi, Determination of residual stress using hole drilling and digital speckle pattern interferometry with automate data analysis. *Opt. Lasers Eng.* **33**(1), 39–48 (2000)
4. A. Martínez, J.A. Rayas, J.C. Madrid Garay, Medición de la evolución temporal de los campos dinámicos de desplazamiento mediante interferometría de moteado para una probeta de latón. *Rev. Mex. Fís.* **56**(3), 262–267 (2010)
5. J.A. Rayas, R. Rodríguez Vera, A. Martínez, Medición del módulo de Young en el hule látex usando ESPI. *Rev. Mex. Fís.* **49**(6), 555–564 (2003)
6. J. Schwider, R. Burow, K.E. Elssner, J. Grzanna, R. Spolaczyk, K. Merkel, Digital wave-front measuring interferometry: some systematic error sources. *Appl. Opt.* **22**(21), 3421–3432 (1983)
7. B. Fischer, W. Jüptner, Automatisierte Auswertung holografischer Interferenzmuster mit dem Zeilen-Scan-Verfahren. In *Spring School of Holographic Interferometry in Technology and Medicine (Holografische Interferometrie in Technik und Medizin)*, Proceedings Frühjahrsschule 78 (1978)
8. T. Kreis, B. Fischer, W. Jüptner, G. Sepold, Automatisierte Auswertung holografischer Interferenzmuster bei der Untersuchung von Zugproben. In *Proceedings of the 5th International Congress Laser 81, Optoelektronik in der Technik/Optoelectronics in Engineering*, ed. by W. Waidelich. (Springer-Verlag, 1982), pp. 105–110
9. T. Kreis, *Handbook of Holographic Interferometry: Optical and Digital Methods* (Wiley-VCH Verlag GmbH & Co. KGaA, Weinheim, 2005)
10. K. Creath, Phase shifting speckle interferometry. *Appl. Opt.* **24**, 3053–3058 (1985)
11. K.A. Stetson, W.R. Brohinsky, Electro-optic holography and its application to hologram interferometry. *Appl. Opt.* **24**(21), 3631–3637 (1985)
12. K. Creath, Phase-shifting holographic interferometry. In *Holographic Interferometry*, ed. by P.K. Rastogi. Springer Series in Optical Sciences, vol. 68, (1994), pp. 109–150.
13. G. Jin, S. Tang, Electronic speckle pattern interferometer with polarization phase-shift technique. *Opt. Eng.* **31**(4), 857–860 (1992)
14. Y. Song, Y. Wu, R. Kulenovic, Z. Guo, M. Groll, Digital speckle pattern interferometry (DSPI) using optical polarization phase shift for measurement of temperature field in thermal flow. In *Optical Technology in Fluid, Thermal, and Combustion Flow III*, Proceedings of SPIE 3172 (1997), p. 442
15. D.I. Serrano García, A. Martínez García, N.I. Toto Arellano, Y. Otani, Dynamic temperature field measurements using a polarization phase shifting technique. *Opt. Eng.* **53**, 11220 (2014)
16. J.M. Huntley, Automated analysis of speckle interferograms, in *Digital Speckle Pattern Interferometry and Related Techniques*, ed. by P.K. Rastogi (Wiley, New York, 2001), pp. 59–139

Chapter 8

Comparative Analysis of Optoelectronic Properties of Glucose for Non-invasive Monitoring

Jesús García-Guzmán, Naara González-Viveros, and Héctor H. Cerecedo-Núñez

Abstract Among the diversity of methods for glucose level monitoring in human blood, invasive techniques are still the most commonly used. Blood samples, usually obtained with finger-pricking devices, are analysed through enzymatic reactions via electrochemical or photometric principles. In this paper, non-invasive methods for blood glucose monitoring are studied and compared, while also analysing optical and electronic properties of glucose. From this comparative analysis, proposals are made towards the design and characterisation of novel devices capable of monitoring blood-glucose levels through optoelectronic non-invasive procedures. Alteration of electrical parameters of cellular membrane, such as electric permittivity and conductivity as a function of blood glucose concentration, are observed and compared to the responses to optical stimuli. The investigation is developed by establishing a correlation between the effects of diffusion and dispersion of light on the concentration and dispersity of blood particles, and the response of electrical parameters under different glucose concentrations. As a result of the analysis, recommendations are made for the most suitable parameters and instrumental methodology, in terms of feasibility, easiness and precision, for non-invasive monitoring of blood glucose levels.

Keywords Optoelectronic measurement • Non-invasive glucose monitoring • Blood glucose monitoring • Electrical measurement • Optical measurement

8.1 Introduction

Cells need a constant supply of energy in order to perform their functions, among which mechanical work, active transport of molecules and ions, and molecular synthesis, are some of the most important ones. For most of the animal species, including man, the required type of energy for the cells is chemical energy, which is found in the nutrients consumed (carbohydrates and lipids, mainly). Glucose is the main carbohydrate present in the human body; this monosaccharide takes part in many of the chemical reactions of the metabolic process and, therefore, it is one of the foremost responsible molecules carrying energy for plants and animals [1].

Metabolism of glucose in our body starts when it is absorbed by the internal walls of the small intestine, during the digestive process, and then it is transported to the blood stream. To provide energy to cells, glucose requires the hormone insulin, which is produced, stored and released by the β -cells of the pancreas. This hormone regulates the levels of glucose in the blood, where, by a metabolic pathway called *glycolysis*, glucose is converted into *pyruvate*, releasing enough energy for the generation of two molecules of Adenosine Triphosphate (ATP), which is a high energy molecule storing the energy needed for everything we do [1, 2].

The high importance of glucose in metabolism, in the health and in the life of humans, demands that all pathologies and irregularities involving glucose are significantly addressed in biomedical research. In order to improve life quality of people suffering these conditions, knowing the level of glucose in blood is perhaps the principal issue, as this parameter indicates the

J. García-Guzmán (✉)
Facultad de Ingeniería Mecánica y Eléctrica, Universidad Veracruzana, Xalapa 91000, Mexico
e-mail: jesusgarcia@ieee.org

N. González-Viveros
Facultad de Instrumentación Electrónica y Ciencias Atmosféricas, Universidad Veracruzana, Xalapa, Mexico
e-mail: naara.gv@gmail.com

H.H. Cerecedo-Núñez
Facultad de Física, Universidad Veracruzana, Xalapa, Mexico
e-mail: hcerecedo@uv.mx

availability of the molecule for use in reactions and protein production systems. Optimal glucose levels are in the range from 70 to 100 mg/dL before breakfast for people without diabetes; the upper limit extends to 130 mg/dL for people with diabetes.

The aim of this report is to present a summary of a detailed investigation on properties of glucose from the different views that are currently used for measurement of its levels. Chemical, thermal, optical and electrical properties are discussed, together with the state of the art in blood glucose monitoring. Special attention is given to characteristics that would facilitate the non-invasive procedures, in order to propose, in a near future, a novel methodology based upon non-invasive technology.

8.2 Measuring Glucose Concentration from its Chemical Properties

Measurement of glucose concentration is often accomplished through electrochemical processes. There are three principal enzymatic reactions used in glucose meters: glucose oxidase, glucose dehydrogenase, and hexokinase [3]. In these methods, glucose is first oxidized using the enzyme, either glucose oxidase or glucose dehydrogenase, as a catalyser, producing hydrogen peroxide (H_2O_2) and glucono delta-lactone, which is then partially hydrolysed to gluconic acid. After this reaction, two approaches are used in order to determine glucose concentration.

In one of them, hydrogen peroxide reacts in a low-voltage electrode releasing two electrons per molecule. The flow of these electrons is proportional to the number of glucose molecules converted in the chemical reaction, and therefore the electronic current gives a measure of glucose concentration. Enzymatic glucose sensors, available commonly in the form of glucose sensor strips, are based on this method. In the second approach, H_2O_2 is coupled to a chromogen agent in order to use its colorimetric properties for the quantification of glucose. This can be achieved merely by visually comparing, against previously established colour patterns, the colour obtained after reacting filter paper strips. In more sophisticated procedures, spectrometric measurements on the coloured compound at a given wavelength yield to values of absorbance that are proportional to glucose concentration. Recent techniques make use of cameras and even office scanners, together with software, in order to determine the concentration of glucose [3–7].

Whatever the approach, the detection of glucose is based on the indirect measurement of the reaction products formed during a chemical transformation. Enzymes glucose oxidase and glucose dehydrogenase act as biocatalysts that accelerate the glucose conversion. Hexokinase action is slightly different; this enzyme catalyses the phosphorylation of glucose, producing glucose 6-phosphate, which is measured spectrophotometrically.

8.3 Measuring Electrical Properties of Glucose

In the human body, food turns into sugar providing energy to all the tissues and organs through the circulation of blood. It is believed that, if all the ingested food was converted into electricity, the body of an adult could generate up to 100 W, using a bio-generator [1]. While these data cannot easily be proven, it is a fact that electrical properties in the body can be measured and, particularly, changes in electrical parameters can be associated to alterations in the level of glucose concentration in the blood. Several studies have reported, for example, that the relative permittivity or dielectric constant, as well as conductivity of blood plasma, change with variations in the levels of glucose at different frequencies. However, while some studies report that these electrical parameters decrease in blood plasma with the increase of glucose levels [8, 9], it has also been observed that, when adding sugar into water, the dielectric constant decreases while conductivity is increased [8]. These variations are clearer at higher frequencies.

For the measurement of changes of glucose concentration in the blood/interstitial fluid it is also useful the relationship with the variations that are produced in the electrolyte concentration, which is observed as a change in the electrical conductivity (or resistivity) of the skin. Using this principle, the concentration of glucose in blood is measured indirectly by the physiological effect of the intracellular exchange of sodium and potassium ions mediated by glucose [4, 10–13].

Electromagnetic technology is also being used for glucose detection. Given that the transport of ions and water induced by glucose causes variations in the potential of the cell membrane, it has been shown that these changes affect its permittivity and conductivity. Therefore, electrical properties change both in the cellular and extracellular compartments. In terms of measurements, variations on capacitance and resistance of tissue near the skin surface are detected as variations in electrical impedance of the entire tissue [11, 13, 14]. Changes are detected by using an electromagnetic channel, achieved by positioning the earlobe between two electrodes in order to complete an oscillating circuit which induces voltage upon the earlobe skin and on the tissue underneath the earlobe, which acts as a dielectric [11].

8.4 Optical Properties of Glucose

Optical techniques are promissory and representative of non-invasive measurements in many medical applications. Typically, a beam of light is focused onto the part of the body under diagnostics, and light properties are modified either while being absorbed through the target zone or after being reflected by the tissue. Depending on the application and technique applied, optical procedures can determine status and levels of monitored variables. For the detection of glucose, optical technics rely on the fingerprint that chemical components in the tissue produce on the light, whose absorbance by the skin depends on the content of substances such as haemoglobin, water, melanin, fat and glucose. The concentration of glucose is associated to the changes produced in wavelength, polarization or intensity of light after being transmitted through the blood, bone, skin or any tissue, by establishing a correlation between several parameters (thickness, colour, structure, percent of fluid) and blood glucose [15].

8.4.1 Changes of Intensity

One optical way to measure levels of glucose, is through the absorption and scattering of mid-infrared or near-infrared light as a result of its interaction with chemicals in the illuminated tissue. The light that is not absorbed is reflected from the tissue or transmitted through it, before being received by optical detectors [6, 16]. Light is more intense when it propagates through greater amounts of glucose in the organs, because lesser scattering results in shorter optical paths and less absorption of light, as shown in Fig. 8.1 [17].

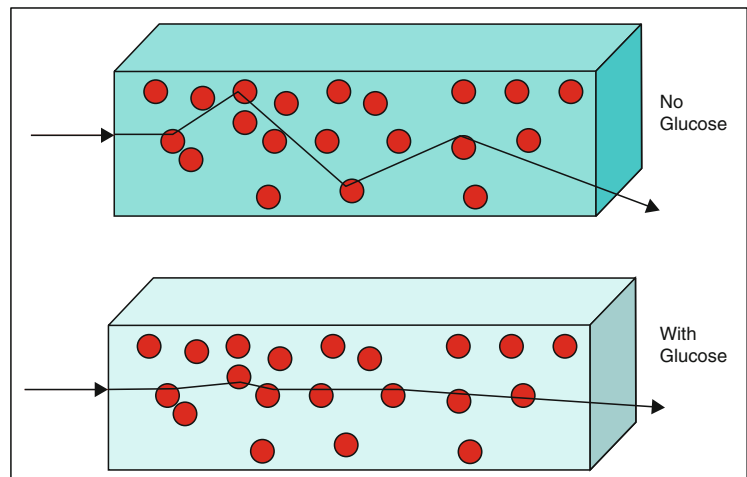
Glucose decreases the mismatch in the refractive index between scattering diffusers and the surroundings, reducing the scattering coefficient and producing, consequently, that shorter optical path. As a result, with the increasing concentration of glucose, fewer photons are absorbed and the light intensity increases [17, 18].

In Raman spectroscopy, although fundamental vibrations are monitored as changes in optical frequencies that are related to the chemical composition of the sample, these variations are also measured in terms of the intensity of the peaks. Scattered photons gain or lose energy from transitions between rotational and vibrational energy states, when incident light is scattered inelastically. These measurements, however, are difficult to make in bio-tissues, but some reports are available of *in vitro* glucose measurements made on the ocular aqueous humour [6].

8.4.2 Polarization

Polarimetry can be used to measure optical rotation of materials. Molecules of glucose in aqueous solutions have the property of rotate the plane of polarisation of light. It has been shown that the angle of rotation produced is proportional to the level of glucose contained in the sample. Therefore, the linear relation between the angle of rotation and the

Fig. 8.1 The presence of glucose causes less scattering in light, giving as a result shorter optical paths and less absorption [17]



concentration of glucose is a useful principle for the monitoring of glucose in blood, in a method known as polarimetric glucose measurement [6, 19, 20],

8.4.3 Absorption Spectroscopy

Optical absorption spectroscopy measures the absorption of light that passes through a sample, as a function of the wavelength of the beam of light. For the detection of glucose levels, light is usually restricted to the mid-infrared and near-infrared spectral regions, as it was previously mentioned. The higher the concentration of glucose, the fewer the photons that are absorbed at a given frequency, hence the spectral distribution of absorbance can be used for the determination of the levels of glucose [10, 21, 22].

8.4.4 Fluorescence

The presence of glucose causes changes in fluorescence when chemical reactions occur with other substances that are introduced to the body. Several optical methods are used for the measurement of these changes in fluorescence intensity, having all of them the advantage that sensors can be highly specific for glucose, therefore reducing the possibilities of errors or interferences that occur in other techniques. Most of the methods based on fluorescence for the detection of glucose rely in the well-known process of electroenzymatic oxidation of glucose to produce gluconolactone and hydrogen peroxide, The products of this reaction can be detected through different optical methods, several of which include the use of optical fibre acting as a glucose optrode for detection of dynamics in luminescence, with glucose oxidase being the enzymatic agent commonly used. Other techniques, also based on glucose oxidase, include other devices such as CCD cameras for the measurements, and other chemical mediators to produce specific luminescence proportional to glucose concentration [21].

An alternative to the glucose oxidase sensors are those based on fluorescent affinity-binding between glucose and other competing species. The presence of glucose introduces changes in the intensity of fluorescence either by displacement or by resonance, but all these techniques require the use of different chemical substances as reagents and more elaborate procedures. A more complete review of fluorescence methods is available in [21].

More recent approaches, based on nanotechnology, are oriented to less-invasive techniques. The use of gold nanoparticles has been proposed in order to measure the concentration of glucose as a function of the spectra resulting from the interaction. Although this method is claimed to be highly linear, non-toxic, compatible with in vivo use in humans, it still requires apparatus such as spectrophotometer and techniques available only in laboratories. Figure 8.2 shows the fluorescence spectra

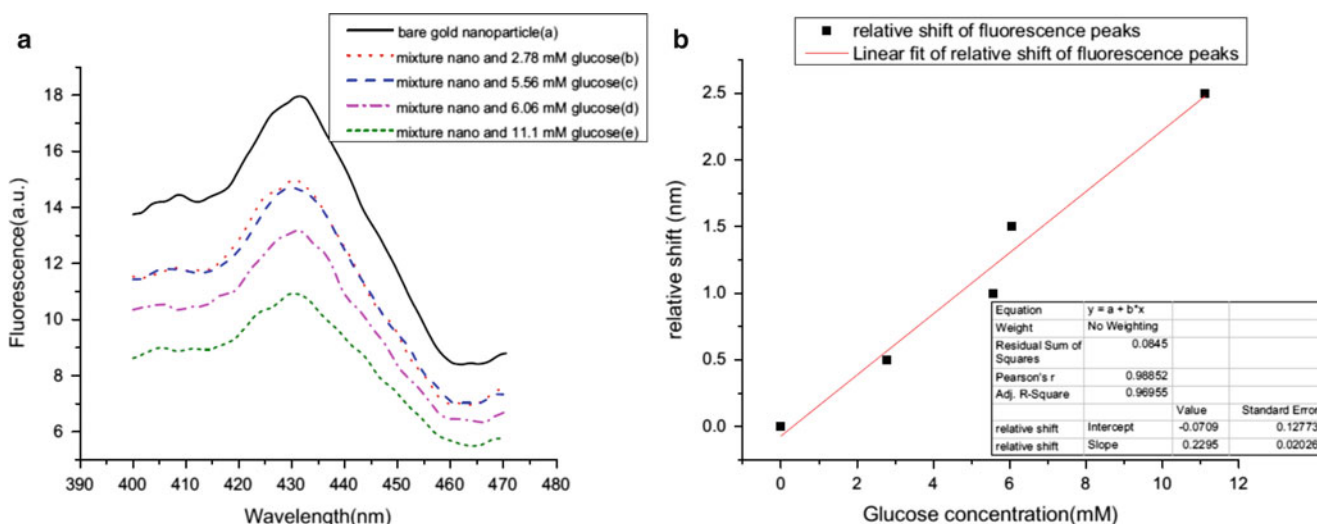


Fig. 8.2 (a) Comparison of spectra obtained from interaction of gold nanoparticles and samples with different concentrations of glucose. (b) The small shift in intensity peaks plotted as a linearized function of glucose concentration [23]

obtained with different concentrations of glucose interacting with gold nanoparticles. The relative shift in intensity peaks is a linear function of glucose concentration [23].

8.5 Other Properties of Glucose

Tissues in the human body show different physiological responses to changes in glucose. These responses can be observed through variations in a number of physical properties which include those commented above but also many others such as electric and acoustic impedance, thermal conductivity and electromagnetic response. Using a combination of sensors responding to two or more physical properties, several methods and apparatus have been developed for the measurement of glucose in blood [11, 24–26]. Thermal and acoustic properties are among the most promissory for non-invasive procedures.

8.5.1 Thermal Properties

Several studies have shown the dependence of thermodynamic properties of tissue upon variations in blood glucose. Heat transfer characteristics are affected by these variations, as it has been reported regarding heat capacity [6], density [27] and thermal conductivity [28], whose alterations are directly related to changes in glucose concentration. Both heat capacity and thermal conductivity decrease when glucose concentration increases, giving as a result higher gradients of temperature outside the tissue layers than in the internal tissues, as a response to heating [11].

Measurements made with the GlucoTrack glucose monitor, for example, rely on the application of a known amount of energy (heat) on the tissue, to produce changes in the heat transfer characteristics, obtaining indirectly the values of glucose concentration by integrating the rate and magnitude of changes in temperature [11]. Figure 8.3 shows plots of (a) the process of heating samples with different glucose concentrations and (b) the integrated thermal signal obtained as a function of glucose concentration, as it was reported by Harman-Boehm et. al after experiments with the GlucoTrack device [11].

8.5.2 Acoustic Properties

Ultrasonic technology is used for glucose measurements, given that the velocity of sound through tissue increases when so does the concentration of glucose. Therefore, higher concentrations of glucose in the tissue correspond to faster propagation of ultrasonic waves through it, with shorter times for propagation [6, 11]. The velocity of sound in fluids and soft tissue

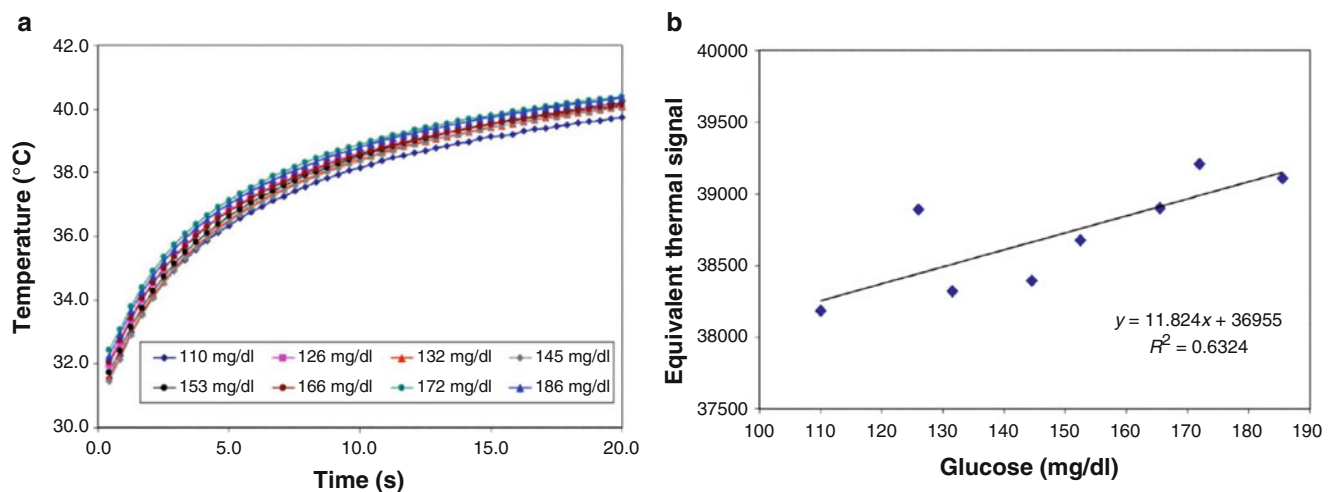
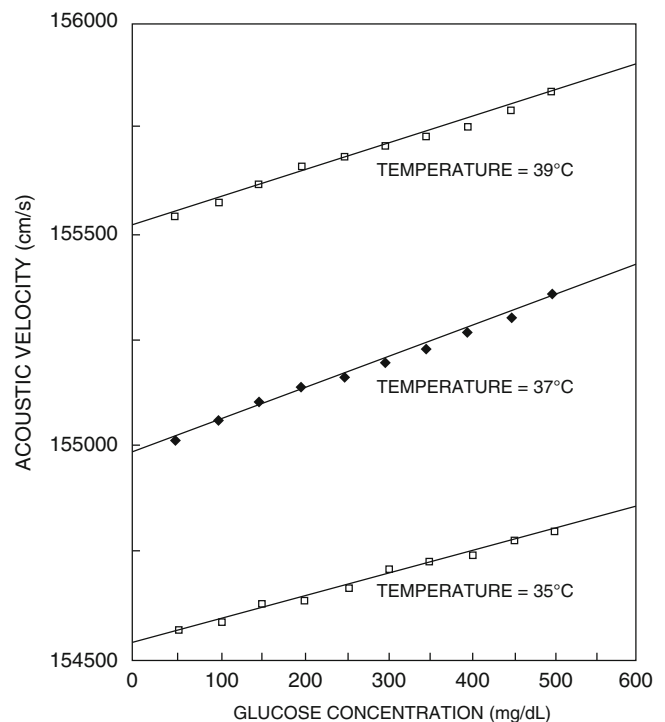


Fig. 8.3 (a) Plots of temperature while heating samples with different concentrations of glucose. (b) The thermal signal obtained after integrating the rate and magnitude of temperature changes as a function of glucose concentration [11]

Fig. 8.4 Example of the linear dependence between acoustic velocity and glucose concentration [29]



depends directly on compressibility, which is in turn determined by bonding forces between molecules. Therefore, when glucose concentration changes in the extracellular fluid, these variations are directly reflected in the velocity of acoustic waves [12, 29]. Experiments have shown changes of 0.28 % in acoustic velocity in response to a 1 % change in glucose concentration [6]. Figure 8.4 shows an example of the linear relationship between acoustic velocity and glucose concentration [29].

8.6 A Summary of Emerging Methods for Glucose Detection

After reviewing the principal optoelectronic properties of glucose that are in use for its monitoring in diabetic patients, it can be observed how advances in micro and nano electronics have been empowering the capabilities of optical methods that otherwise were not achievable for practical applications. Furthermore, current methods are in general a combination of technologies and it is sometimes difficult to establish boundaries between the fields involved. The list of technologies available today is quite extensive and it includes, apart from the ones mentioned before, fields as diverse as MIR and NIR optical absorption spectroscopy, polarimetry, reverse iontophoresis, thermal emission, electromagnetic methods, photoacoustic, Raman spectroscopy, interferometry, and fluorescence, among others. All these technologies are nowadays under intense investigation and perhaps the main trend is to create a practical and cheap non-invasive procedure for the day-to-day monitoring of blood glucose in diabetic patients.

Table 8.1 summarises the development, evolution and trends of optoelectronic technologies for the detection and monitoring of glucose. Principles of operation characteristic of the devices are allocated in four fundamental areas, namely chemical, electrical, optical and hybrid, when methodologies are based on two or more principles, such as electrochemical or electro-optical.

The summary starts with the first technology using glucose oxidase in 1956, at Miles Laboratories (later purchased by Bayer), where Alfred and Helen Free developed a dip-and-read test for glucose in urine known as Clinistix[®] [30]. This started the era of glucose sensing based on glucose oxidation, which dominated the sixties and that has evolved into different fields with the more recent development of optical and electronic technologies [30, 31]. Dextrostix[®] was developed in 1965 as a reactive strip for the measurement of glucose in blood, and in 1970 Clemens, from Ames Laboratories, developed an instrument, the Ames Reflectance Meter capable of translate the light reflected from the surface of the Dextrostix[®] strips into blood glucose values shown on analogue scales [32]. Although the instrument was heavy and expensive, it started the age of portable glucose meters, initially designed for testing in doctors' offices in the decade of 1970–1980.

Table 8.1 Classification of glucose properties used in meters, according to their principle of operation

Date	Chemical	Electrical	Optical	Hybrid
1956	First reagent strip using glucose oxidase ^a [30, 31]			
1964	Sensors based on glucose oxidation ^a [30, 31]			
1970		Ames reflectometer ^a [31, 32]		
1984	Accu-Chek and other glucometers ^a [31]			
1991	Fluorescence biosensors ^a [33]		Fluorescence biosensors ^a [33]	
1994			Polarimetry ^b [34] Fluorescence ^a [35]	
1999	Reverse Iontophoresis ^c [6, 24]			
2000			Absorption ^b [24, 39]	
			Thermal emission ^b [36]	
2001			Scattering Raman Spectrum ^b [37]	
2003		Bio-electrical impedance analysis ^b [24, 25]		
2005		Acoustic (speed of sound) with conductivity and heat capacity ^b [26]		
2006		Ultrasound (acoustic) with conductivity and heat capacity ^b [24]		
2007			Reflected light interferometry ^b [38]	

^aInvasive^bNon-invasive^cMinimally invasive

Glucometers appeared in the eighties in the United Kingdom, with names such as Glucochek and Glucoscan, introducing incipient digital technology and its poor precision problems. Glucometer I, Glucometer II, Glucometer M and Glucometer GX, based on a hexokinase method, were introduced by Ames, whereas Lifescan introduced Glucoscan II and Glucoscan 2000. In 1984 the first series of Accu-Chek was launched, and, in 1987, the meter known as OneTouch appeared [31].

The conjugation of advances in biosensor technology and digital electronics led to the development, in 1991, of a method for monitoring the glucose level in a body fluid, using an apparatus which includes a combination of glucose oxidase and a fluorescent dye coated onto an optical fibre in contact with the body fluid, a source of excitation light and a fluorescence emission detector [33]. Later, in 1994, a sensitive polarimeter was designed to measure glucose concentrations within the aqueous humour of the eye. Scatter in this fluid is smaller than in other biological tissues in the visible light spectrum, and therefore it offers an advantageous setting for optical polarimetric measurements [34]. In the same year a glucose monitor and a related method were patented, to determinate the concentration of glucose in a sample by monitoring fluorescent light produced directly by any glucose present in the sample [35]. By the end of the decade, the first version of Glucowatch® was introduced [24]. This was the first glucometer using iontophoresis, a process in which a weak electric current is employed to transport charged molecules through intact skin [6].

GluControl GC300®, based on near infrared spectroscopy, was launched in 2000. In the same year, a non-invasive infrared absorption spectrometer was patented, with capabilities for measuring intensity, wavelength and time dependence of infrared energy emanating from glucose or other substances within the human body [36]. Another non-invasive method for the detection of glucose was patented in 2001, based on the use of an excitation laser beam focused into the aqueous humour in the anterior chamber of the eye, and then detecting a Raman spectrum that was processed in order to obtain the concentration of glucose [37]. Bio-electrical impedance analysis, a technique using electrodes to apply low intensity currents in biological tissues, was the technology behind a wrist glucose monitor called Pendra, developed in 2003. The device sampled information from a LC resonant circuit, in which the skin was the capacitor dielectric [25]. A low coherence interferometer patented in 2007, measures the level of glucose in blood collecting the reflected light from within the scanned tissue and constructively interfering this reflected light. The reflection spectrum is related to glucose concentration at given wavelengths [38].

Multiparametric and hybrid methods have become common during the last decade. A patent in 2005 described a method for glucose monitoring including measurements of the speed of sound through the blood, the conductivity of the blood, and the heat capacity of the blood, obtaining thereafter a weighted average of the three calculated values of glucose concentration [26]. Also, a combination of absorption spectroscopy and complex bio-impedance measurements, with multi-parameter analysis, data treatment and neural networks processing, has been reported as an important study on non-invasive optical diagnostic [25]. GlucoTrack™ is another handheld meter based on ultrasonic measurements, using also measures of tissue conductivity and heat capacity in order to achieve more accuracy and precision [24].

8.7 Conclusions

According to our research, it is clearly observed that several properties of glucose are manifested under different phenomena, being these chemical, electrical, optical, thermal, acoustic or any combination of them. It has also been noticed that, in order to achieve greater accuracy in the determination of glucose concentration in blood, some of these properties must be used together, e.g. electrochemical reactions or an arrangement of chemical and optical properties.

Monitoring of glucose levels in diabetic patients is an important field of research, particularly for the development of non-invasive methods that can be implemented with high reliability and precision, but still at a low cost. Moreover, it is desirable that these new methods are easy to use by patients, provoking them no pain and no hassle. An analysis of the wide range of fields under study, from enzymatic reactions and pure chemical processes, up to the novel multiparametric methodologies currently developed, shows that this is not an easy challenge. However, after reviewing the intensive research that has been done for years towards the non-invasive measuring of glucose in blood, it is concluded that both optical and electrical properties are the most suitable for the realisation of this type of measurements. We aim to develop a proposal for the implementation of an optoelectronic methodology for non-invasive monitoring of glucose in blood which meets the basic requirements described above.

References

1. C. Ravariu, C. Ionescu-Tirgoviste, F. Ravariu, Glucose biofuels properties in the bloodstream, in conjunction with the beta cell electrophysiology. In *International Conference on Clean Electrical Power* (2009), pp. 124–127.
2. Facultad de Medicina Veterinaria y Zootecnia, Universidad Nacional Autónoma de México, Apuntes de Bioquímica, http://www.fm.vz.unam.mx/fmvz/p_estudios/apuntes_bioquimica/Unidad_8.pdf
3. K. Tonyushkina, J.H. Nichols, Glucose meters: a review of technical challenges to obtaining accurate results. *J. Diabetes Sci. Technol.* **3**(4), 971–980 (2009)
4. A. Soni, S.K. Jha, A paper strip based non-invasive glucose biosensor for salivary analysis. *Biosens. Bioelectron.* **67**, 763–768 (2015)
5. A. Thomas, A. Ramírez, A. Zehe, Non-invasive glucose monitoring: will nanotechnology make this dream come true? *Nanoc. Moletrón.* **12**(2), 2177–2190 (2014)
6. Z. Zhao, Pulsed photoacoustic techniques and glucose determination in human blood and tissue, Ph.D. Dissertation, University of Oulu, Finland, (2002)
7. K.L. Hermayer, A.S. Loftley, S. Reddy, S.N. Narla, N.A. Epps, Y. Zhu, Challenges of inpatient blood glucose monitoring: standards, methods, and devices to measure blood glucose. *Curr. Diab. Rep.* **15**(3), 1–10 (2015)
8. T. Yilmaz, Y. Hao, Electrical property characterization of blood glucose for on—body sensors. In *Proceedings of the 5th European Conference on Antennas and Propagation (EUCAP)*, 2011, pp. 3659–3662
9. E. Topsakal, T. Karacolak, E.C. Moreland. Glucose-dependent dielectric properties of blood plasma. In *IEEE General Assembly and Scientific Symposium*, 2011, pp. 1–4
10. K.A. Unnikrishna Menon, D. Hemachandran, A. Thekkeyil Kunnath, Voltage intensity based non-invasive blood glucose monitoring. In *4th ICCNT (IEEE)*, 2013, pp. 1–5.
11. I. Harman-Boehm, A. Gal, A.M. Raykhman, E. Naidis, Y. Mayzel, Noninvasive glucose monitoring: increasing accuracy by combination of multi-technology and multi-sensors. *J. Diabetes Sci. Technol.* **4**(3), 1–13 (2010)
12. I. Harman-Boehm, A. Gal, A.M. Raykhman, J.D. Zahn, E. Naidis, Y. Mayzel, Noninvasive glucose monitoring: a novel approach. *J. Diabetes Sci. Technol.* **3**(2), 253–260 (2009)
13. Y. Hayashi, L. Livshits, A. Caduff, Y. Feldman, Dielectric spectroscopy study of specific glucose influence on human erythrocyte membranes. *J. Phys. D: Appl. Phys.* **36**, 369–374 (2003)
14. G. Gelao, R. Marani, V. Carriero, A. Gina Perri, Design of a dielectric spectroscopy sensor for continuous noninvasive blood glucose monitoring. *Int. J. Adv. Eng. Technol.* **3**(2), 55–64 (2012)
15. R.W. Waynant, V.M. Chenault, Overview of non-invasive fluid glucose measurement using optical techniques to maintain glucose control in diabetes mellitus. *Photonics Society Newsletters*, <http://photonicsociety.org/newsletters/apr98/overview.htm>. Accessed 2 Apr 1998
16. J.T. Bruulsema, J.E. Hayward, T.J. Farrel, M.S. Patterson, L. Heinemann, M. Berger, Correlation between blood glucose concentration in diabetics and noninvasively measured tissue optical scattering coefficient. *Opt. Lett.* **22**(3), 190–192 (1997)
17. O. Amir, D. Weinstein, S. Zilberman, M. Less, D. Perl-Treves, H. Primack, A. Weinstein, E. Gabis, B. Fikhte, A. Karasik, Continuous non-invasive glucose monitoring technology based on “Occlusion Spectroscopy”. *J. Diabetes Sci. Technol.* **1**(4), 463–469 (2007)
18. K. Airat, J. Chen, G.W. Small, M.A. Arnold, Scattering and absorption effects in the determination of glucose in whole blood by new infrared spectroscopy. *Am. Chem. Soc.* **77**(14), 4587–4594 (2005)
19. L. Mor, E. Bubis, K. Hemmes, P. Schechner, Performance of a glucose AFC. In *Proceedings of the 11th IEEE International Conference on Electronics, Circuits and Systems*, 2004, pp. 278–281
20. S. Liu, E. Li, Q. Hou, Non-invasive detection system design for blood glucose based on optical rotation properties. In *3rd International Conference on Biomedical Engineering and Informatics*, 2010, pp. 1532–1535
21. R.J. McNichols, G.L. Cote, Optical glucose sensing in biological fluids: an overview. *J. Biomed. Opt.* **5**(1), 5–16 (2000)

22. V. Ashok, A. Nirmalkumar, N. Jeyashanthi, A novel method for blood glucose measurement by noninvasive technique using laser. *World Acad. Sci. Eng. Technol.* **5**(3), 484–490 (2011)
23. Z. Bagheri, R. Massudi, J. Ghanavi, Noninvasive glucose measurement by fluorescence quenching of nontoxic gold nanoparticles. *Opt. Laser Technol.* **58**, 135–138 (2014)
24. A. Tura, A. Maran, G. Pacini, Non-invasive glucose monitoring: assessment of technologies and devices according to quantitative criteria. *Diabetes Res. Clin. Pract.* **77**, 16–40 (2007)
25. C.F. Amaral, M. Brischwein, B. Wolf, Multiparameter techniques for non-invasive measurement of blood glucose. *Sens. Actuators B* **140**, 12–16 (2009)
26. D. Freger, A. Gal, A.M. Raykhman, Method of monitoring glucose level. Ashkelon, Israel Patentee U.S. 6954662 B2, 11 Oct 2005
27. M. Toubal, M. Asmani, E. Radziszewski, B. Nongaillard, Acoustic measurement of compressibility and thermal expansion coefficient of erythrocytes. *Phys. Med. Biol.* **44**(5), 1277–1287 (1999)
28. Y. Muramatsu, A. Tagawa, T. Kasai, Thermal conductivity of several liquid foods. *Food Sci. Technol. Res.* **11**(3), 288–294 (2005)
29. G.H. Thomas, R.M. Watson, Method and apparatus for non-invasive monitoring of blood glucose, U.S. Patent 5119819 A, 9 Jun 1992
30. T. Vo-Dinh, *Biomedical Photonics Handbook: Biometical Diagnostics* (CRC Press, Boca Raton, FL, 2014)
31. S.F. Clarke, J.R. Foster, A history of blood glucose meters and their role in self-monitoring of diabetes mellitus. *Br. J. Biomed. Sci.* **69**(2), 83–93 (2012)
32. E. Menéndez Torre, Self-monitoring of blood glucose in diabetes. Historical perspective and technologic evolution. *Av. Diabetol.* **26**(1), 1–4 (2010)
33. D.B. Wagner, Method for monitoring glucose. East Rutherford, New Jersey, United States Patentee U.S. 5001054 A, 19 Mar 1991
34. T.W. King, G.L. Cote, R.J. McNichols, M.J. Goetz Jr., Multispectral polarimetric glucose detection using a single Pockels cell. *Opt. Eng.* **33**(8), 2746–2753 (1994)
35. M. Stavridi, W.S. Grundfest, Glucose fluorescence monitor and method. United States Patentee U.S. 5341805 A, 30 Aug 1994
36. B.B. Sterling, J.R. Braig, D.S. Goldberger, C.E. Kramer., A.M. Shulenberg, R. Trebino, R. King, R.O. Herrera, Non-invasive infrared absorption spectrometer for measuring glucose or other constituents in a human or other body. United States of America Patentee U.S. 6025597 A, 15 Feb 2000
37. J.L. Lambert, M.S. Borchert, Non-invasive glucose monitor. California Patentee U.S. 6181957 B1, 30 Jan 2001
38. M.J. Schurman, W.J. Shakespeare, Method and apparatus for monitoring glucose levels in a biological tissue. USA Patentee U.S. 7254429 B2, 7 Aug 2007
39. M. Ahmad, M.A. Kamboh, A. Khan, Non-invasive blood glucose monitoring using near-infrared spectroscopy, *EDN Networks* (2013), pp. 1–9

Chapter 9

Phase Shifting Interferometry Using a Coupled Cyclic Path Interferometers

L. García Lechuga, N.I. Toto-Arellano, V.H. Flores Muñoz, Amalia Martínez-García, and G. Rodríguez Zurita

Abstract In this research we implemented a two-step phase shifting system based on two cyclic-path coupled interferometers for slope measurements of transparent samples. The optical system generates two π -shifted interferograms, and the phase shift between interferograms is obtained by rotating a linear polarizer, generating four interferograms with relative $\pi/2$ -phase shifts; this simplifies the number of phase steps necessary to retrieve the optical phase, since is only necessary perform a shift operating a linear polarizer. The optical phase was processed by a four-step algorithm. In order to present the capabilities of the system, results obtained for slope for transparent structures are presented.

Keywords Phase shifting • Interferometry • Polarization • Microscopy • Shearography

9.1 Introduction

The phase stepping interferometry allows the analysis and the measurement of the phase objects with high accuracy; in some cases it is necessary to obtain the phase derivative. To solve this, it has been proposed some methods [1–3] such as shearing interferometers, polarization techniques and amplitude or phase gratings, which collectively permit to reduce the number of steps to obtain the optical phase. These systems require diffractive and polarizing elements to produce the necessary phase shifts [4–6]; so, it is necessary to develop optical systems that are non-dependent on diffractive elements, where the known techniques of phase shifting using polarization can be applied to obtain the necessary interferograms to calculate the optical phase. In this work, we propose a coupled cyclic path interferometer which can generate two shearograms with π -phased shifts, with the capability of obtaining two extra interferograms by placing of a lineal polarizer at an angle of $\pi/4$. We can obtain four interference patterns with relative phase shifting of $\pi/2$ in two shots. The proposed system use a minimal of mechanical components to generate the phase shifts, and differently from others systems, the proposed setup presents stability against external vibrations because of the beams that propagate collinearly in the coupled system, so it is not required to use an holographic table for its implementation. Other advantage of this system is its ability to obtain the derivative of the phase data map in two steps, which can be associated with the partial slope of the phase object [1, 7].

9.2 Slope of Non-Birefringent Samples

In the shearography technique, the object is illuminated by a single collimated beam [8–10], then the relationship between the phase difference and the displacement is obtained as:

L.G. Lechuga • N.I. Toto-Arellano (✉)

Centro de Tecnologías Ópticas y Fotónicas, Universidad Tecnológica de Tulancingo, C.P. 43642 Tulancingo, Hidalgo, México
e-mail: noel.toto@utec-tgo.edu.mx

V.H. Flores Muñoz
Universidad Politécnica del Bicentenario, C.P. 36283 Silao, Guanajuato, México

A. Martínez-García
Centro de Investigaciones en Óptica, C.P. 37150 León, Guanajuato, México

G.R. Zurita
Benemérita Universidad Autónoma de Puebla, Puebla, Puebla, México

$$\frac{\partial \phi(x, y)}{\partial x} = \frac{2\pi}{\lambda} \cdot \left[\sin \theta \frac{\partial u(x, y)}{\partial x} + (1 + \cos \theta) \frac{\partial w(x, y)}{\partial x} \right] \Delta x \quad (9.1)$$

where $u(x, y)$ and $w(x, y)$ are the displacement field components in x and z direction respectively. The fringe pattern has contributions from the deformation $\partial u(x, y)/\partial x$ and the slope $\partial w(x, y)/\partial x$. However, when the phase object is illuminated in the normal direction, i.e. $\theta = 0^\circ$, the fringe pattern represents only the x -partial slope ($\partial w(x, y)/\partial x$) [8–12]. The phase distribution defined in (9.1) is related to the partial slope as:

$$\frac{\partial \phi(x, y)}{\partial x} = \frac{2\pi}{\lambda} \cdot \frac{\partial w(x, y)}{\partial x} \Delta x \quad (9.2)$$

where the phase change is obtained by the phase stepping algorithm of four steps [13, 14].

9.3 Four Step-Algorithm

The optical system allows obtaining two interference patterns with a relative π -phase shift, represented as:

$$\begin{aligned} I_1(x, y) &= A_0 + A_1 \cos \left[2\psi_0 + \frac{\partial \phi(x, y)}{\partial x} \right] \\ I_2(x, y) &= A_0 - A_1 \cos \left[2\psi_0 + \frac{\partial \phi(x, y)}{\partial x} \right] \end{aligned} \quad (9.3)$$

where ψ_0 represents the angle of polarizer $P(\psi_0)$ at the output of the system, considering that the amplitudes A_0 and A_1 remain constant in each step [1–3]; for the first step (Step-I) we have $\psi = 0$, obtaining:

$$\begin{aligned} I_1(x, y) &= A_0 + A_1 \cos \left[\frac{\partial \phi(x, y)}{\partial x} \right] \\ I_2(x, y) &= A_0 - A_1 \cos \left[\frac{\partial \phi(x, y)}{\partial x} \right] \end{aligned} \quad (9.4)$$

Other pair of interferograms (Step-II) will be obtained with a relative phase shift of $\pi/2$ with respect to the first capture by rotating the polarizer to an angle of $\psi_0 = \pi/4$; this can be represented as :

$$\begin{aligned} I_3(x, y) &= A_0 + A_1 \sin \left[\frac{\partial \phi(x, y)}{\partial x} \right] \\ I_4(x, y) &= A_0 - A_1 \sin \left[\frac{\partial \phi(x, y)}{\partial x} \right] \end{aligned} \quad (9.5)$$

We can obtain four interference patterns with relative phase shifting of $\pi/2$ in two shots. Phase reconstruction is performed using the four step phase shifting algorithm [13–15], so the phase can be obtained from the following equation:

$$\frac{\partial \phi(x, y)}{\partial x} = \tan^{-1} \left[\frac{I_3(x, y) - I_4(x, y)}{I_1(x, y) - I_2(x, y)} \right] \quad (9.6)$$

After removing the 2π ambiguities by means of a phase unwrapping process [14], the derivative of the optical phase can be obtained. In order to remove the background phase, the phase retrieval procedure should include a reference phase where the background is measured beforehand (the background phase is measured without the phase object).

9.4 Experimental Setup

Figure 9.1 shows the experimental setup. In Fig. 9.1a shows the diagram of the proposed system and in Fig. 9.1b the implemented arrangement.

The optical system is illuminated by a linearly polarized laser beam at 45° . The set-up consists of two coupled common path interferometers; in the first interferometer, the polarizing beams are split into perpendicular and parallel polarizing components, and their separation x_0 is controlled by the lateral movement Δx_0 of the mirror M_1 . A single shearogram is obtained from the first interferometer, which passes through the quarter wave plate (Q_1), generating the circular crossed polarization; this way the second common path interferometer will be used to obtain replicas of the first shearogram.

Due to the properties of the polarization, it is necessary to place a polarizer at an arbitrary angle at the exit of the system in order to observe the patterns. The phase shifts can be operated by placing a linear polarizer $P_1(\psi)$ to cover the two interference patterns to generate a parallel phase shifting.

Figure 9.2 shows some experimental results obtained with the proposed system. In Fig. 9.2a the reference patterns generated by the spherical wavefront with large shear are shown. Figure 9.2b shows the same wavefront with a smaller shear. The Fig. 9.2c shows the deformation of the wavefront caused by the edge of a slide. In Fig. 9.2d it is shown the phase deformation introduced by a microarthropod, Collembola.

The experimental results for all cases shown that the slope can be associated with the derivative of the phase by using this configuration, it can be seen that the fringe pattern changes around the phase object.

9.5 Experimental Results

The parallel interferograms were acquired by a 3.0 Megapixel CMOS sensor with 2048×1536 pixels. The CCD camera is adjusted to capture the images of two interference patterns simultaneously. Each pattern was filtered using a conventional low-pass filter to remove sharp edges and details. One of the advantages of the system is that diffractive elements are not included to generate the two patterns. Consequently, it is not necessary to make corrections in fringe modulation.

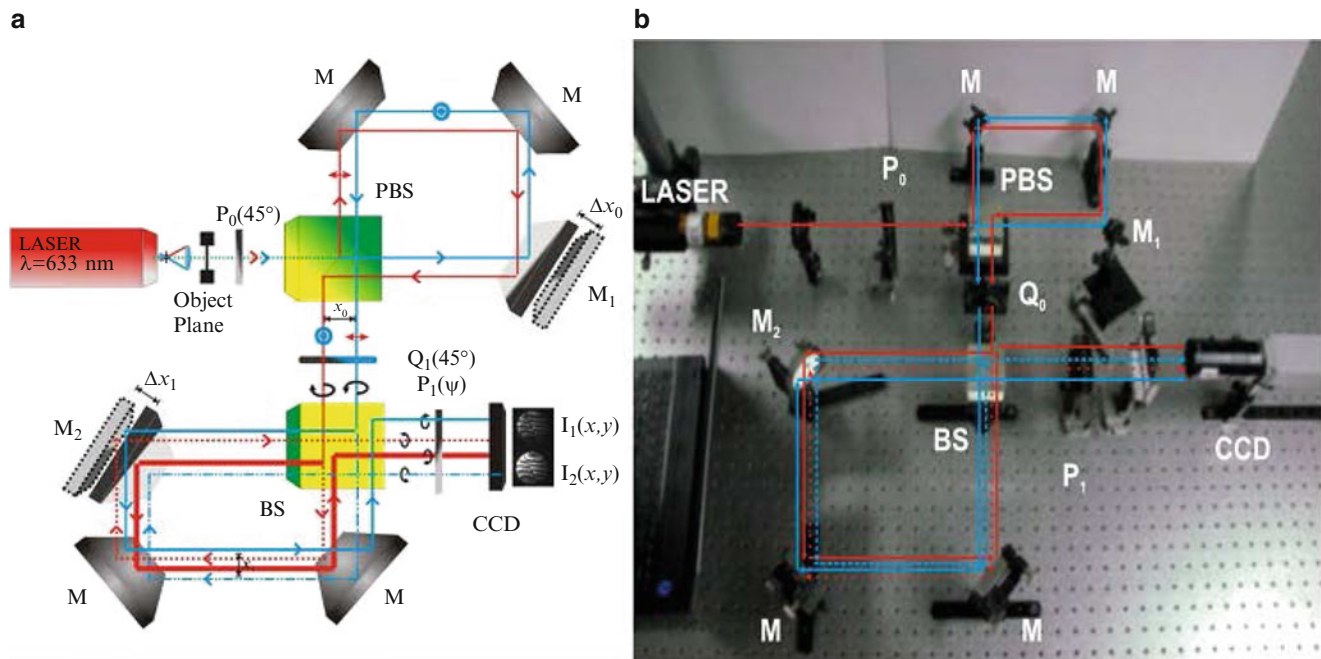


Fig. 9.1 Parallel Phase shifting interferometer. (a) Diagram of the system. (b) Experimental setup. Q_i : Quarter wave plate operating at 633 nm. P_i : polarizing filters. BS: Beam splitter; M_i : Mirrors; x_i : Beam separation

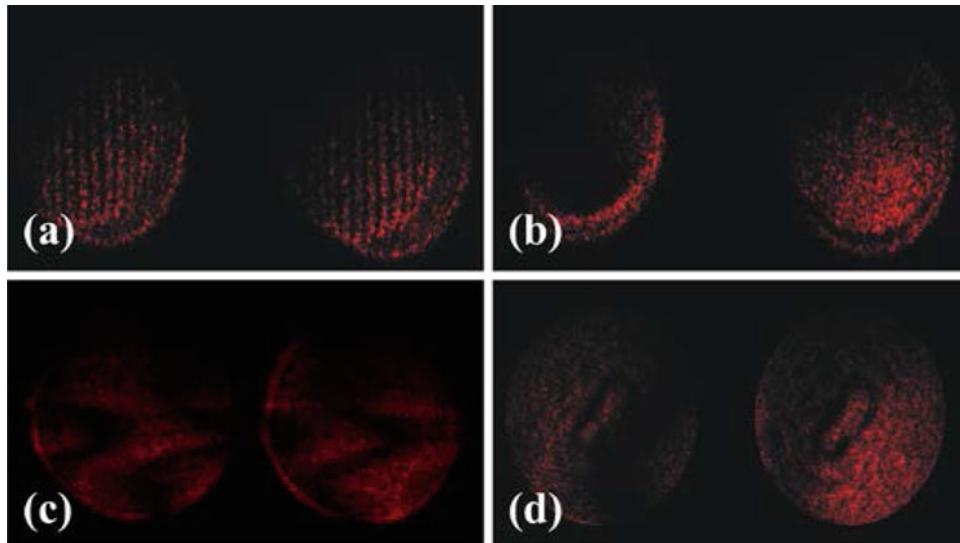


Fig. 9.2 Preliminary results. (a) Reference: spherical wavefront with large shear. (b) Reference: spherical wavefront with small shear. (c) Test object: edge of a slide (d) Test object: Microarthropod

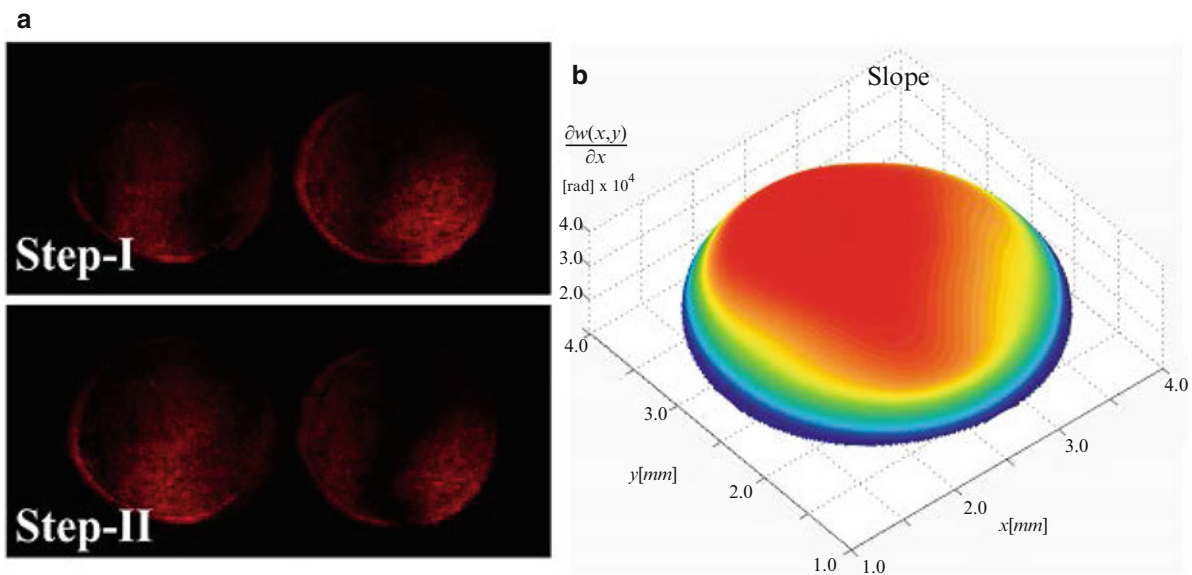


Fig. 9.3 Spherical wavefront. (a) Four shearograms generated in two steps. (b) Slope in x -direction

The experimental results presented were obtained with the proposed optical system showed in Fig. 9.1. Figure 9.3 shows the incident spherical wavefront generated by the system without the phase object; Fig. 9.3a shows the four interference patterns generated in two shots, in Fig. 9.3b the slope of the incident wavefront is shown. The diameter size of illumination beam is 2.5 mm.

The experimental results for a Microarthropod (*Collembola*) are shown in Fig. 9.4. The sample generated a phase change in the z direction. The patterns obtained in two shots are showed in Fig. 9.4a. The slope associated with the derivative of the phase is showed in Fig. 9.4b. The analyzed microorganism size is of 0.5×1.5 mm.

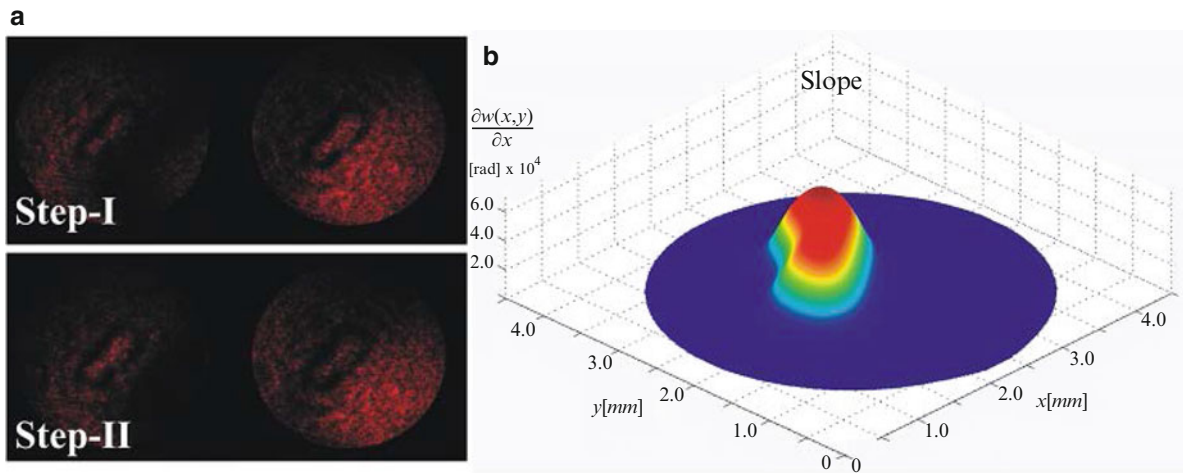


Fig. 9.4 Organic sample: Microarthropod. (a) Four shearograms generated in two steps. (b) Slope in x -direction

9.6 Conclusions

In this research we proposed a novel configuration based on two coupled common path interferometers. This optical system provides two parallel interferograms which are used to generate phase shifting by means of lineal polarizers. The technique permits to obtain the optical phase directly. Due to the use of shearography systems, the arrangement is stable to environmental or external disturbances, which leaves the interference patterns unaffected by vibrations. The experimental results show the slope associated with the changes of phase of transparent objects in shear direction.

Acknowledgments This research was supported by the Technological University of Tulancingo, according to *The Initiative* for the creation of the *First Optics and Photonics Engineering* undergraduate program in Mexico. Authors thank M. A. Ruiz for his contribution in proofreading the manuscript. Author V. H. Flores Muñoz is grateful to CONACYT for the scholarship provided (Grant. 224506) and Programa para el Desarrollo Profesional Docente (PRODEP) for grant UPBIC-PTC-022.

References

1. N.-I. Toto-Arellano, A. Martínez-García, G. Rodríguez-Zurita, J.A. Rayas-Álvarez, A. Montes-Perez, Slope measurement of a phase object using a polarizing phase-shifting high-frequency Ronchi grating interferometer. *Appl. Opt.* **49**, 6402–6408 (2010)
2. J.C. Wyant, Use of an ac heterodyne lateral shear interferometer with real-time wavefront correction systems, Reprinted from *Appl. Opt.* **14**, 2622–2626 (1975)
3. J.E. Millerd, J.C. Wyant, Simultaneous phase-shifting Fizeau interferometer, U.S. Patent 7,057,738 B2 (2006)
4. J. Vargas, J. Quiroga, C.O.S. Sorzano, J.C. Estrada, J.M. Carazo, Two-step interferometry by a regularized optical flow algorithm. *Opt. Lett.* **36**(17), 3485–3487 (2011)
5. B. Barrientos-García, A.J. Moore, C. Pérez-López, L. Wang, T. Tschudi, Transient deformation measurement with electronic speckle pattern interferometry by use of a holographic optical element for spatial phase stepping. *Appl. Opt.* **38**(28), 5944–5947 (1999)
6. B. Barrientos-García, A.J. Moore, C. Pérez-López, L. Wang, T. Tschudi, Spatial phase-stepped interferometry using a holographic optical element. *Opt. Eng.* **38**(12), 2069–2074 (1999)
7. N.I. Toto-Arellano, D.I. Serrano-García, A. Martínez-García, G. Rodríguez-Zurita, A. Montes-Perez, 4D profile of phase objects through the use of a simultaneous phase shifting quasi-common path interferometer. *J. Opt.* **13**(11), 115502 (2011)
8. W. Steinchen, L. Yang, Phase-shifting shearography, in *Digital Shearography: Theory and Application of Digital Speckle Pattern Shearing Interferometer*, vol. PM100 (SPIE Press, Washington, DC, 2003)
9. P. Hariharan, D. Sen, Radial shearing interferometer. *J. Sci. Instrum.* **38**, 428 (1961)
10. M.P. Kothiyal, C. Delisle, Shearing interferometer for phase shifting interferometry with polarization phase shifter. *Appl. Opt.* **24**, 4439–4442 (1985)
11. R.F. Horton, Design of a white light radial shear interferometer for segmented mirror control. *Opt. Eng.* **27**, 1063–1066 (1988)
12. M.V. Murty, R.P. Shukla, Radial shearing interferometers using a laser source. *Appl. Opt.* **12**, 2765–2767 (1973)
13. D. Malacara, M. Servin, Z. Malacara, C.6 in phase detection algorithms, in *Interferogram Analysis for Optical Testing* (Wiley, New York, 2005)
14. C. Ghiglia, M.D. Pritt, *C.4 in Two-Dimensional Phase Unwrapping: Theory, Algorithms, and Software* (Wiley, New York, 1998)
15. M. Servin, J.C. Estrada, J.A. Quiroga, The general theory of phase shifting algorithms. *Opt. Express* **17**, 21867–21881 (2009)

Chapter 10

Identification of Microorganisms Using Digital Holographic Microscopy

S. Muñoz Solís, M. del Socorro Hernández-Montes, and F. Mendoza Santoyo

Abstract The recognition of microorganisms is important in the diagnosing of the micro-biology. In the medical field the cell disorders can affect body tissues indirectly. In this work we use digital holographic microscopy (DHM) that can achieve high contrast images. This method permits us to obtain phase maps by means of digital reconstruction of a wavefront. Phase differences between two states allows us to realize a quantitative analysis of samples.

An off-axis layout is used to determine the morphology of different types of microorganisms. Also, we can directly examine aggregations by corresponding phase maps. The images provide information about the presence or absence of microorganisms that can be used as indicators of the physiological state of the body. By the presented results, we show that DHM may give some new perspectives within biomedical applications.

Keywords Digital holography • Morphology studies • Phase map

10.1 Introduction

The digital holographic microscopy allows us to extract information through the record of the interference of two overlapping fields; in this case, we use both the amplitude and the phase values of the recorded fields. This technique has been used in various fields and one of them is for the study biological samples where the study of cell and many biological agents play a key role [1, 2].

The optical methods and techniques used for this purpose are diverse, but the main methods are by reflection of light and by transmission of light [3–5]. This latter approach was used to inspect microorganisms from two interferograms. The phase values of the image represent differences of optical path length that arise from both the morphology of the sample and changes of the refractive index.

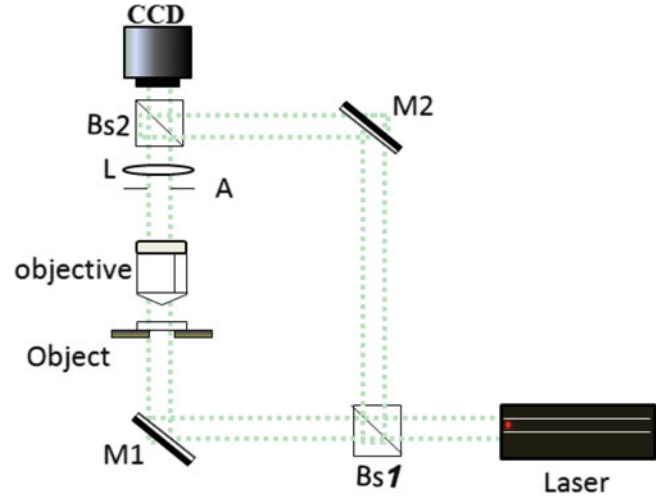
The identification of microorganisms is useful in laboratories where the diagnosis is important for detecting diseases, such as haemoparasites [6–8]. In this paper the potential of digital holography technique is explored [9, 10]. The sample is studied under coherent illumination and the intensity field of the diffracted light is recorded by a CCD camera. The recorded information is then processed by a computer to retrieve the complex field scattered by the object from which the quantitative properties of the object are reconstructed. DHM was successfully tested in two types of samples, in cells of an onion skin and cells of the bacterium *Lactobacillus casei*; the last one is important for health monitoring and for the prevention of diseases.

10.2 Determination of Phase Maps Using DHM

Figure 10.1 presents a scheme of DHM that is based on the Mach-Zehnder interferometer and operates in an off-axis holographic geometry. The light from a coherent source with $\lambda = 488$ nm first is spatially filtered using a microscope objective and a confocal-positioned pinhole, and then split into reference and object beams by beam splitter, BS1. The object beam is transmitted through the sample which it is placed at the focal length of a microscope objective (MO) whose magnification is $60\times$ and 0.85 of numerical aperture (NA). The reference beam is directed to the beam splitter, BS2, where it is combined with the object beam.

S.M. Solís (✉) • M.d.S. Hernández-Montes • F.M. Santoyo
Departamento de Metrología Óptica, Centro de Investigaciones en Óptica, A.C., León, Guanajuato, Mexico
e-mail: msolis@cio.mx; mhernandez@cio.mx; fmendoza@cio.mx

Fig. 10.1 Experimental DHM setup. M1 and M2, mirrors; Bs1, beam splitter; Bs2, beam combiner; L, lens; A, aperture



The digital holograms acquired by the camera correspond to the intensity of the superposition of the object and reference waves, and can be mathematically expressed as follows [11, 12]:

$$I(x, y) = a(x, y) + b(x, y) \cos [\varphi_0(x, y) - \varphi_r(x, y) + w(x, y)], \quad (10.1)$$

where x and y are the coordinates in the sensor, and $a(x, y)$ and $b(x, y)$ indicate unwanted irradiance variations arising from the non-uniform light reflection or transmission by the test object, $\varphi_0(x, y)$ and $\varphi_r(x, y)$ are the phase distribution of the object beam and the reference beam, respectively, and $w(x, y)$ is a spatial carrier term introduced as a reference beam tilt at the beam combiner.

Equation 10.1, using complex notation, can be written in the form:

$$I(x, y) = a(x, y) + c(x, y) + c(x, y)^*, \quad (10.2)$$

where coefficients $c(x, y)$ and $c^*(x, y)$ are:

$$c(x, y) = \frac{1}{2}b(x, y)e^{i\varphi(x, y)}, \quad c^*(x, y) = \frac{1}{2}b(x, y)e^{-i\varphi(x, y)}$$

Taking the linear and shifting properties of the Fourier transform, we can represent the Fourier transform of (10.1) with the following expression:

$$H(u, v) = A(u, v) + C(u, v) + C(u, v)^* \quad (10.3)$$

The representation of $H(u, v)$ is illustrated in Fig. 10.3a2, b2. The symmetrical lobes located around the origin, represent the Fourier spectrum of the interference term; $b(x, y) \cos [\varphi_0(x, y) - \varphi_r(x, y) + w(x, y)]$. In this way, to recover the optical phase from one interferogram, only one lobe is filtered. If we apply the inverse Fourier transform to the last result, we obtain the following complex image interferogram.

$$g(x, y) = c(x, y)e^{i\varphi(x, y)} \quad (10.4)$$

Then the optical phase of the microorganisms is found by [10–12]:

$$\varphi(x, y) = \tan^{-1} \left(\frac{\text{Im}[g(x, y)]}{\text{Re}[g(x, y)]} \right), \quad (10.5)$$

where Im and Re denote the imaginary and real parts of $g(x, y)$, respectively.

10.3 Experiments and Results by Transmission DHM

In accordance with the off-axis holographic microscopy setup shown in Fig. 10.1, the object beam contains the sample information and a microscope objective projects the magnified image of the object onto a CCD camera. The reference and object waves are offset by an angle to avoid the overlap of the reference and the twin images, resulting in a holographic interference fringe pattern caused by the interference between the diffracted object field and the off-axis reference field.

The above configuration is used to identify the epidermal cells of an onion skin. A microscope objective with a magnification of 1:60 and a numerical aperture of $\text{NA} = 0.85$ is utilized for this purpose. The obtained amplitude and phase are shown by Fig. 10.2a, b, respectively. The amplitude corresponds to shape and pattern of the onion skin cells when observed through a conventional light microscope. The phase is encoded by the optical path of the light when traveling through the cells. And as the optical path depends on the refractive index, then the structure of the cell can be retrieved.

Another test was performed in the probiotic bacterium *Lactobacillus casei* (fermented milk). This is important for the understanding of the mechanisms by which probiotic bacteria affect the immune system [13]. Figure 10.3 shows the characteristic rod shape of this bacterium. Figure 10.3a1–a4 show images of the process for obtaining the corresponding phase maps. The field of view is $\sim 10 \times 10 \mu\text{m}^2$ at 1024×1024 pixels of the CCD. Figure 10.3b1–b4 correspond to other microorganism found in the sample.

10.4 Conclusions

The viability of this method was shown for the identification of microorganisms. The observations were made in two types of samples. In cells of an onion skin as a first test, the results, obtained by calculation of optical phase maps, showed parts of the cell wall. The second sample was the bacterium *Lactobacillus casei*, because of its importance in the monitoring of health and the prevention of diseases. The understanding of the mechanisms by which probiotic bacteria affect the immune system is of great interest. The results presented show simple morphological parameters.

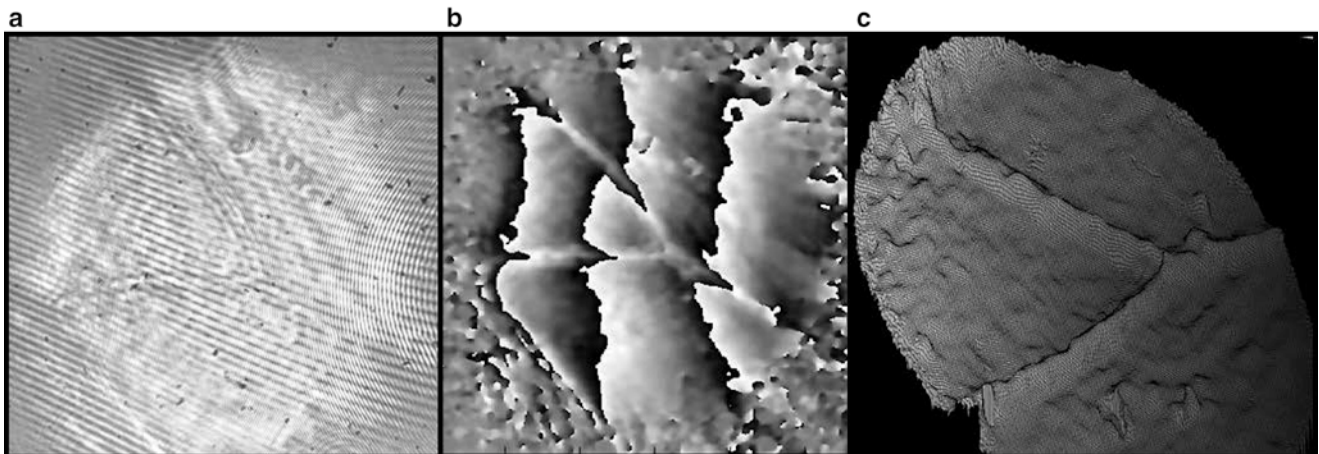


Fig. 10.2 Quantitative phase imaging using DHM: (a) amplitude of the complex transmittance of onion epidermal cells, (b) wrapped phase map and (c) unwrapped phase

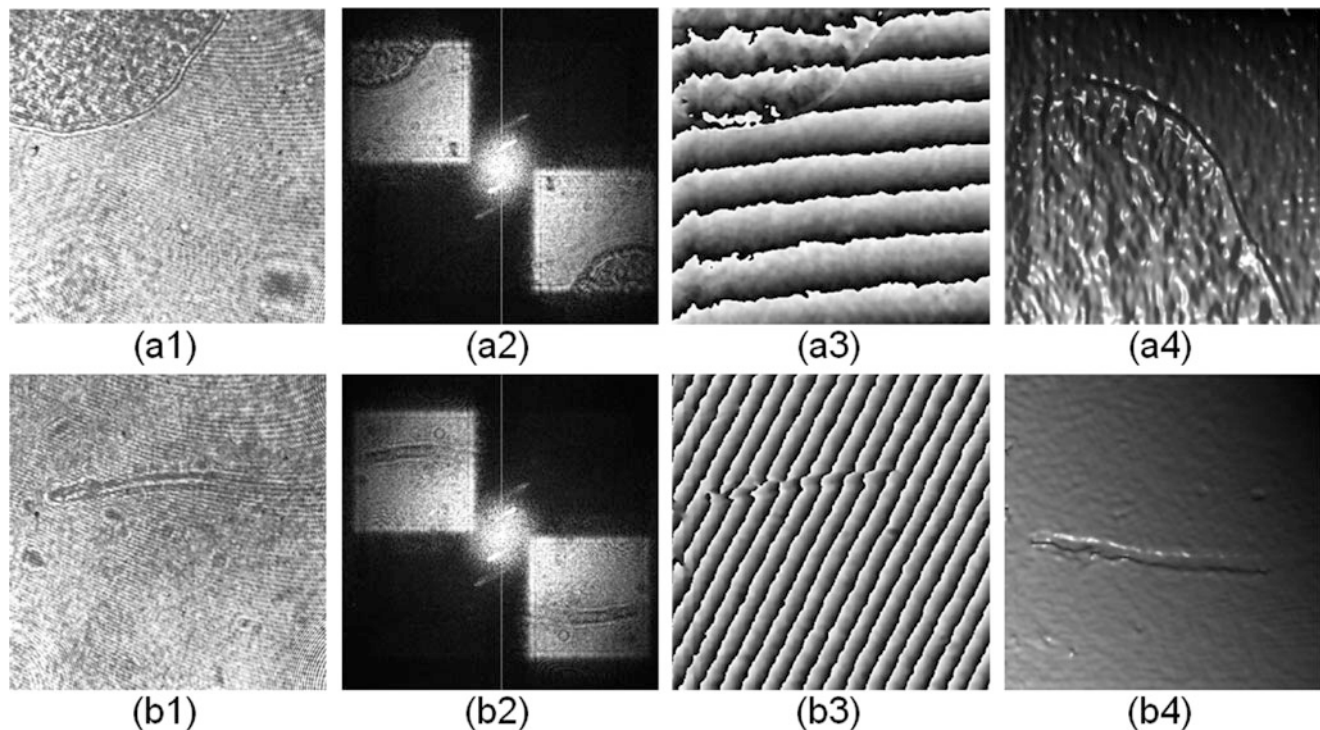


Fig. 10.3 (a-b(1)) Amplitude of the transmittance of microorganisms, (a-b(2)) Fourier spectrum, (a-b(3)) wrapped phase, and (a-b(4)) unwrapped phase

The advantage of using the microscopy technique in conjunction to holographic images for the study of microorganisms is its fullness of spatial details when compared with traditional methods of identification of bacteria.

References

1. M. del Socorro Hernández-Montes, F. Mendoza, C. Pérez, S. Muñoz, J. Esquivel, Digital holographic interferometry applied to the study of tympanic membrane displacements. *Opt. Lasers Eng.* **49**(6), 698–702 (2011)
2. S. Muñoz, F. Mendoza, M. del Socorro Hernández-Montes, 3D displacement measurements of the tympanic membrane with digital holographic interferometry. *Opt. Express* **5**(20), 5613–5621 (2012)
3. E. Cuche, P. Marquet, C. Depeursinge, Simultaneous amplitude-contrast and quantitative phase contrast microscopy by numerical reconstruction of Fresnel off-axis holograms. *Appl. Opt.* **38**(34), 6994–7001 (1999)
4. D. Gabor, Microscopy by reconstructed wave fronts. *Proc. R. Soc. A* **197**, 454–487 (1949)
5. B. Kemper, G. von Bally, Digital holographic microscopy for live cell applications and technical inspection. *Appl. Opt.* **47**(4), A52–A61 (2008)
6. C. Maldonado, G. Perdígón, The probiotic bacterium *Lactobacillus casei* induces activation of the gut mucosal immune system through innate immunity. *Clin. Vaccine Immunol.* **13**(2), 219–226 (2006)
7. J. Gerritsen, H. Smidt, G.T. Rijkers, W.M. de Vos, Intestinal microbiota in human health and disease: the impact of probiotic. *Genes Nutr.* **6**, 209–240 (2011)
8. S. Katakweba, S. Mulungu, J. Eiseb, A. Mahlaba et al., Prevalence of haemoparasites, leptospire and coccobacilli with potential for human infection in the blood of rodents and shrews from selected localities in Tanzania, Namibia and Swaziland. *Afr. Zool.* **47**(1), 119–127 (2012)
9. I. Yamaguchi, J. Kato, S. Otha, J. Mizuno, Image formation in phase-shifting digital holography and applications to microscopy. *Appl. Opt.* **40**, 6177–6186 (2001)
10. M.K. Kim, Applications of digital holography in biomedical microscopy. *J. Opt. Soc. Korea* **14**(2), 77–89 (2010)
11. T. Kreis, Digital holographic interference-phase measurement using the Fourier-transform method. *J. Opt. Soc. Am. A* **3**, 847–855 (1986)
12. M. Takeda, H. Ina, S. Kobayashi, Fourier-transform method of fringe-pattern analysis for computer-based topography and interferometry. *J. Opt. Soc. Am.* **72**, 156–160 (1982)
13. G. Perdígón, R. Fuller, R. Raya, Lactic acid bacteria and their effect on the immune system. *Curr. Issues Intest. Microbiol.* **2**, 27–42 (2001)

Chapter 11

Noise Reduction in Off-Axis Digital Holography Reconstruction from Two Reconstruction Distances Based on Talbot Effect

Miguel León-Rodríguez, Raúl R. Cordero, Juan A. Rayas, Amalia Martínez-García, Adrián Martínez-Gonzalez, Fernando Labbe, and Victor Flores-Muñoz

Abstract A simple strategy based on wavefront propagation in Fresnel regime to reduce ringing effect by using an ideal filter in off-axis digital holography is presented. In addition, we demonstrate a better focusing capacity by using this ideal filter than Butterworth and Gaussian. The reconstructed and enhanced image is obtained from the averaging operation between the image at the focused image plane ($z = z_{hd0}$) and the first Talbot distance order ($z = z_{hd1}$). This distance is determined by the periodic ringing. Reductions of 50 % of these anomalies are computed in simulation and 30 % is obtained experimentally. Numerical simulations and experimental results are carried out to validate the proposal.

Keywords Digital holography • Holography • Talbot and self-imaging effects • Microscopy • Topography

11.1 Introduction

Digital Holography (DH) has become a novel tool for reconstructing amplitude and phase information of a wave front transmitted or reflected through 3D objects, with sub-wavelength accuracy along the axial direction due to their interferometric nature [1]. DH is applied in diverse fields of knowledge, where phase quantization is related to some physical measurement. Some of those applications include the analysis and characterization of micro-electromechanical (MEMs) and micro-optical systems (MOEMs) [2], the study of biological samples [3], and the measurement of capillarity waves in micro-fluids [4], where the reconstruction distance, a unique characteristic of digital holography, plays an important role. As with classical holography the reconstructed image contains a zero order of diffraction and two images called the virtual image and the real image. In the off-axis geometry they propagate along different directions and can be observed separately. In DH, a digital hologram can be obtained from an off-axis configuration [5]. The reconstruction of this hologram results in the real image separated from the non-diffracted part of the reconstruction wave (or DC term) and the so-called ‘twin image’ (or virtual image). To eliminate the DC term and the virtual image, the frequency spectrum filtering method is applied. As a result, the wave front of the object is recovered [6]. Because a single hologram is enough for numerical reconstruction of the object’s wavefront, the technique is suitable for the acquisition and analysis of dynamic processes. The Fourier filtering method is well known in the demodulation fringe process to retrieve the phase map [7, 8]. The drawback of the filter function is a ringing effect that occurs along the edges of the filtered spatial domain image when an ideal filter is used. Furthermore, error analysis in the determination of both, the width and the location of the applied filter mask has been performed [9, 10]. Gaussian and Butterworth filters perform are the most frequently used in DH. In this manuscript, we present a

M. León-Rodríguez (✉)

Universidad de Santiago de Chile, Casilla 307 Correo 2, Santiago, Chile

Universidad Politécnica del Bicentenario, Silao-Romita Km 2, C.P. 36283 Silao de la Victoria, Guanajuato, Mexico

Centro de Investigaciones en Óptica, A.C. Loma del Bosque 115, C.P. 37150 León, Guanajuato, Mexico

e-mail: y_migue@hotmail.com

R.R. Cordero • J.A. Rayas

Universidad de Santiago de Chile, Casilla 307 Correo 2, Santiago, Chile

A. Martínez-García

Centro de Investigaciones en Óptica, A.C. Loma del Bosque 115, C.P. 37150 León, Guanajuato, Mexico

A. Martínez-Gonzalez • V. Flores-Muñoz

Universidad Politécnica del Bicentenario, Silao-Romita Km 2, C.P. 36283 Silao de la Victoria, Guanajuato, Mexico

F. Labbe

Universidad Técnica Federico Santa María, Ave. España 1680, Valparaíso, Chile

strategy to reduce the ringing effect of discontinuous surfaces in the reconstruction process in off-axis digital holography. The method is based on the natural diffraction of light (Talbot effect). In addition we show that the size of the ideal low-pass filter in the holographic reconstruction process is dependent of the focus zone. The structure of the manuscript is as follows: In Sect. 11.2 presents the optical setup, the digital holographic reconstruction method, a brief description of the Talbot effect and the filtering process. Section 11.3 numerical simulations of Talbot effect, digital holographic reconstruction and the focus capability by using ideal filter are presented. Section 11.4 we present the experimental results that support the simulations predictions given in Sect. 11.3. Finally, conclusions are given in Sect. 11.5.

11.2 Method

The digital holographic setup used in the present study for recording off-axis digital holograms is shown in Fig. 11.1. This setup is basically a Michelson interferometer. Light from a laser diode source with a wavelength of 643 nm is expanded by a beam expander system (BE). The diode also emits a low coherence (coherence length about 0.1 mm) linearly polarized plane wavefront. The beam is divided by a beam splitter (BS) into a reference wave R and an object wave O . At the exit of the interferometer a digital off-axis hologram (H) is created by the interference between the $O(x,y)$ and $R(x,y)$, after they reflect on the sample (S) and mirror (M) respectively. To obtain off-axis holograms, the orientation of M that reflects the reference wave is set such that the $R(x,y)$ reaches the CCD with an incidence angle θ while the $O(x,y)$ propagates perpendicular to the hologram plane. Then, a CCD digital camera records this interference pattern. The distance (z) between CCD camera and object is of 85 mm. The CCD camera is a standard 8 bits black and white camera with $4.4 \mu\text{m}$ pixel size.

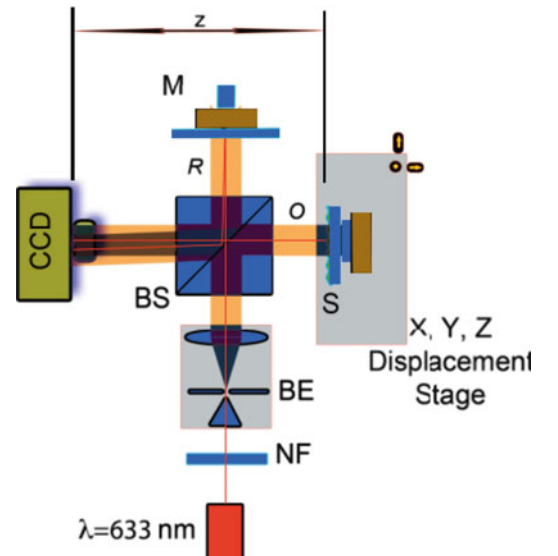
This off-axis digital hologram can be expressed as:

$$H(x, y) = |O(x, y) + R(x, y)|^2 = |O(x, y)|^2 + |R(x, y)|^2 + O(x, y)R^*(x, y) + R(x, y)O^*(x, y), \quad (11.1)$$

where the first two terms on the right of (11.1) are the intensity of the object wave and the intensity of the reference wave or the so-called the DC term, and the last ones represent the real and the virtual images respectively, while * denotes complex conjugated. A window function $W(f_x, f_y)$ is utilized to filter the term $O(x, y)R^*(x, y)$ of (11.1) in the frequency domain. On the other hand, the so-called frequency spectrum filtering method [11], is applied in order to retrieve the object wave front $O(f_x, f_y)$.

$$O(f_x, f_y) = W(f_x, f_y) \mathfrak{F}^{-1}\{H(x, y)R_D(x, y)\}, \quad (11.2)$$

Fig. 11.1 Optical system based on a Michelson interferometer. M is a mirror, NF is a neutral filter and BE is a beam expander



where R_D is a digital replica of R , and $\mathfrak{F}^{\pm 1}$ stands for the direct or inverse continuous Fourier transformation. Hence, the object $O(f_x, f_y)$ can be propagated using the paraxial approximation of the Kirchhoff-Fresnel propagation integral in convolution form [12, 13] as follows:

$$O_i(x, y, z_i) = \mathfrak{F}^{\pm 1} \left\{ \left[O(f_x, f_y) \right] \exp(jkz_i) \exp[-j\pi\lambda z_i] \left[(f_x)^2 + (f_y)^2 \right] \right\}, \quad (11.3)$$

where λ is the wavelength, k is the wave number and z_i is the reconstruction distance. The reconstructed object wavefront $O(x, y)$ provides the amplitude image $A_i(x, y) = |O_i(x, y)|^2$ and the phase image $\phi_i(x, y) = \text{tg}^{-1}(\text{imag}(O_i(x, y))/\text{real}(O_i(x, y)))$ of the object. The topography $T(x, y)$ of the specimen is computed from the reconstructed phase $\phi(x, y)$, by the reflection configuration $T(x, y) = \phi(x, y)/2k$.

11.2.1 Filtering Process

The filtering process done in this study is based on the procedure outlined by Cucho et al. in [11]. However the DC term is eliminated by the subtraction of the intensity of R and O , recorded independently, in (11.1). Edges and other sharp transitions (such as noise) in the digital hologram contribute significantly to the high-frequency content of its Fourier transform [14]. We considered three types of low-pass filters: ideal (ILPF), Butterworth (BtwLPF), and Gaussian (GLPF). These three filters cover the range from very sharp (ideal) to very smooth (Gaussian) filter functions. The Butterworth filter has a parameter, called the filter order. For high values of this parameter the BtwLPF approaches the form of the ideal filter. For lower-order values, the BtwLPF has a smooth form similar to the Gaussian filter. Thus, the Butterworth filter may be viewed as a transition between two “extremes”. When it is performed, the filtering process with an ILPF a ringing effect appears in the reconstructed image due to transfer function of W , which is a *sinc* function. The *sinc* function has a bigger central peak that is responsible for blurring. The concentric components are responsible for the ringing behavior. In addition, the filter size (cut-off frequency) directly corresponds to the frequency of the ringing, *i.e.* as we double the cut-off frequency, we double the distance between two rings and the width of the main peak decrease [14, 15]. On the other hand, as the transfer function of the Gaussian filter also is a Gaussian function will have no ringing but only blurring behavior. By using the BtwLPF of second order a ringing effect is generally imperceptible and the blurring is similar to Gaussian filter one. Ringing behavior increases as a function of filter order.

11.2.2 Talbot Effect

When a collimated monochromatic beam illuminates a linear grating of period p , multiple identical images of the original grating are observed along the path of the light. These images are formed without any lenses on integer multiples of a distance called the Rayleigh distance (z_{tdu}). This phenomenon is known as the Talbot effect (self-imaging) and it is caused by the diffraction that suffers the light when pass through the grating [16]. The Talbot planes are located at distances given by:

$$z_{tdu} = \frac{up^2}{\lambda}, \quad (11.4)$$

where $u = 1, 2, 3, \dots$ denotes the Talbot plane order (TPO) and λ is the illumination light wavelength. When u is odd the self-imaging has 180° phase shift and contrast reversal [13]. The same phenomenon can be present in a thin phase attenuated sinusoidal grating as presented in the next section.

11.3 Simulations

Numerical simulation was performing for two amplitude-phase gratings: sinusoidal and sinusoidal attenuated. The period of each grating is of 50 μm . Figure 11.2a shows the simulated Talbot carpet of amplitude distribution when the sinusoidal grating structure is illuminated by a plane wave of 633 nm wavelength. We use (11.2) for the calculation of the field

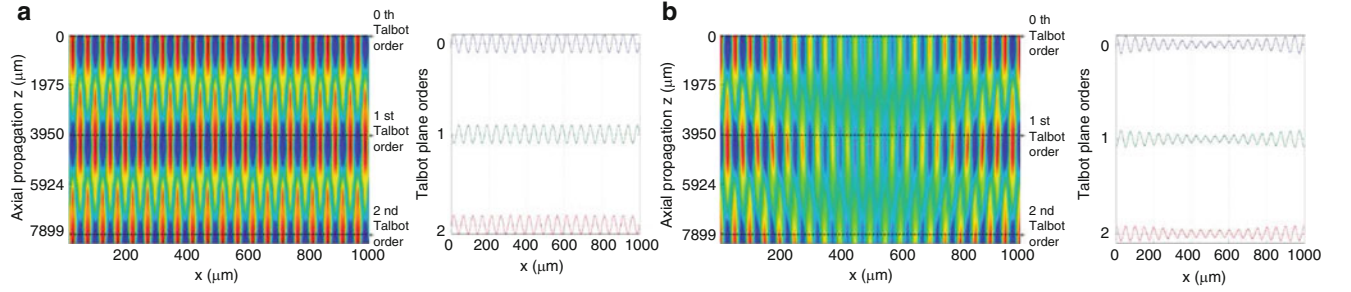


Fig. 11.2 Talbot carpet of sinusoidal gratings. (a) Sinusoidal grating amplitude and (b) sinusoidal attenuated grating amplitude

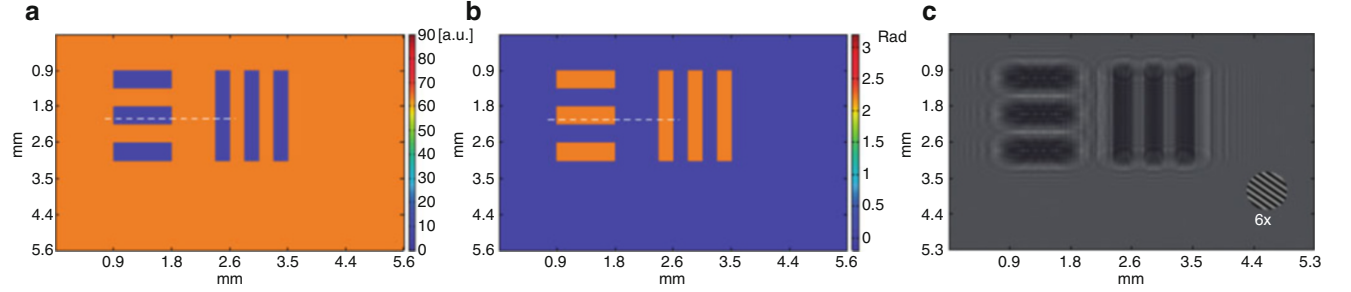


Fig. 11.3 (a) Amplitude and (b) phase test object used to perform numerical simulation. (c) Off-axis digital hologram recorded at $z = 84.4$ mm from the object test

distribution behind the gratings. Amplitude profile is plotted from the carpet at 0, 1 and 2 TPO that is at $z_{td0} = 0 \mu\text{m}$, $z_{td1} = 3949.4 \mu\text{m}$ and $z_{td2} = 7898.9 \mu\text{m}$ respectively. The distances of each Talbot order were calculated from (11.3). In this profile we can corroborate contrast reversal of the field distribution at the first TPO mentioned above. On the other hand, Fig. 11.2b shows the simulated Talbot carpet of the amplitude distribution when the sinusoidal attenuated grating structure is illuminated by the same plane wave of 633 nm wavelength. Amplitude profile is plotted from the carpet at 0, 1 and 2 TPO. In this profile also we can show the contrast reversal of the field distribution at the first TPO. So we can say that the Talbot effect also can be present in attenuated sinusoidal grating from 0 to 2 TPO.

A second simulation was carried out to create an off-axis digital hologram. According to the optical setup (Fig. 11.1), two plane waves of equal intensities have been considered to interfere in a Michelson interferometer for recording off-axis digital hologram. We use an object, which consists of three horizontal bars and three vertical bars etched on a thin chromium film (100% reflective) deposited in a glass substrate. The reflectance of each bar is of 6.25% and the thickness film correspond to a phase of 0.7π rad. (Fig. 11.3a, b). The size of this object is 1200×1200 pixels; the distance between the object under test and the CCD plane is of $z = 84.4$ mm. We assumed the working wavelength is a red laser light of 643 nm, and pixel pitch of the CCD is $4.4 \mu\text{m} \times 4.4 \mu\text{m}$ according to the real parameters. We have considered the standard deviation (STD) as a measure of the phase accuracy (axial resolution) and amplitude improvement (arbitrary unit [a.u.]) in all sections. Figure 11.3c shows the off-axis digital hologram.

First, we reconstruct the object wavefront by performing the (11.3) with a reconstruction distance ($z = z_{td0}$) of 84.4 mm. In order to suppress the DC term and the virtual image, we apply the Fourier filtering process mentioned in Sect. 11.2. Figure 11.4a, b show the amplitude and phase images, respectively, by using an ILPF with radius of 100 pixels (cut-off frequency). As we have been mentioned, Fig. 11.4a shows a plot profile of the ringing effect with a period of $u = 53 \mu\text{m}$. This profile is similar to a sinusoidal attenuated grating simulated in the previous section, according to J. Goodman [13] and confirmed in previous simulations with the 180° phase shift and contrast reversal of the field distribution at the first TPO (z_{td1}) property. A second reconstruction was performed at $z = z + z_{td1} = 84.565$ mm with the same filter. To reduce the ringing effect we can perform an averaging operation between phase and amplitude reconstructed images at different distances z_{ht0} and z_{ht1} that is:

$$\begin{aligned} \phi(x, y) &= \frac{[\phi_0(x, y) + \phi_1(x, y)]}{2} \\ A(x, y) &= \frac{[A_0(x, y) + A_1(x, y)]}{2} \end{aligned} \quad (11.5)$$

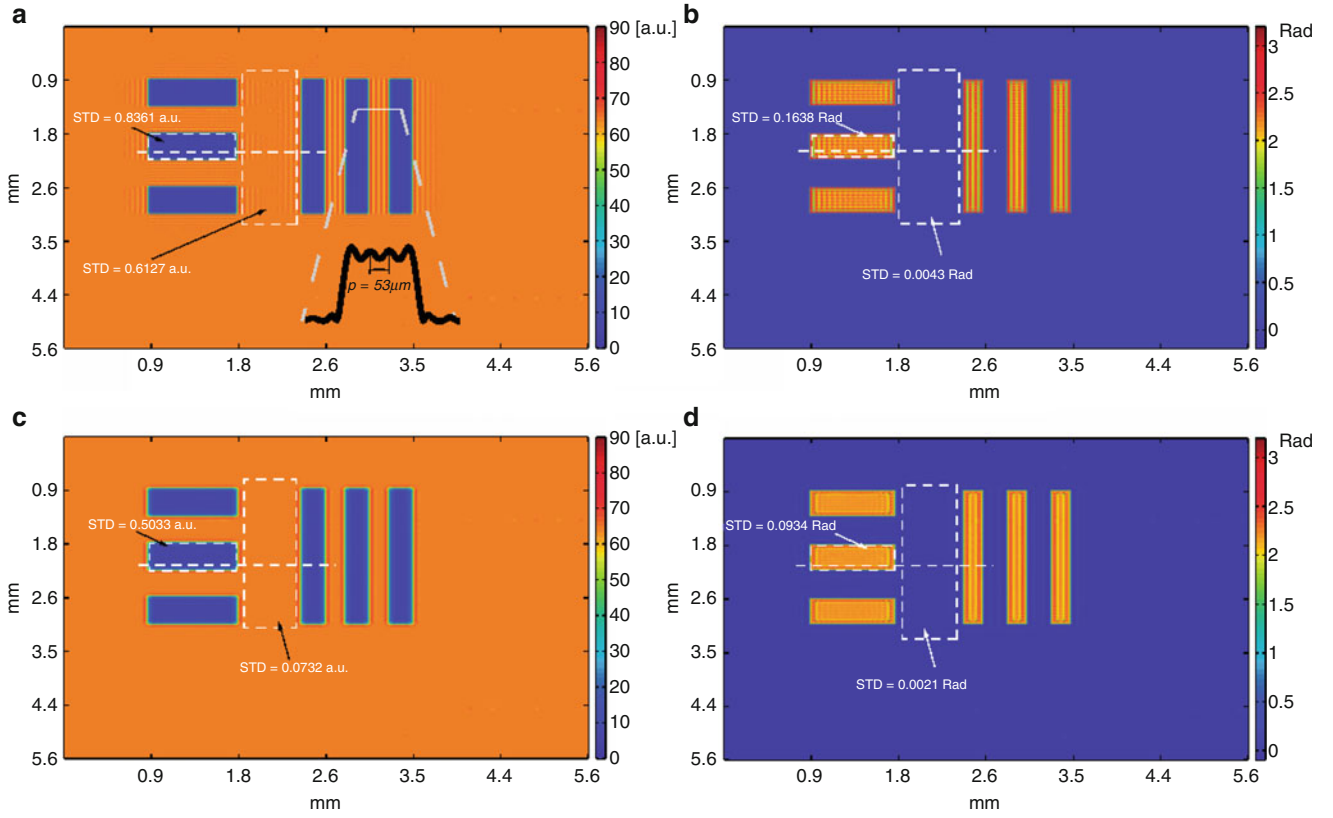


Fig. 11.4 Reconstructed images from the hologram of Fig. 11.3c. (a)–(b) Reconstructed amplitude and phase images at $z = z_{td0}$ respectively, (c)–(d) improved amplitude and phase images respectively after proposal is applied

From Fig. 11.4c, d we can see the improved images obtained with this proposal. The improved images contain nearly all the details of the original object. The improvement with this procedure is an average reduction of STD of 64 % in amplitude and 47 % in phase images. The percentage is an average between the two zones delimited by the dashed white rectangles in Fig. 11.4. The STD in each zone is clearly represented in each reconstructed images.

Figure 11.5a, b show line profiles where zone is marked with a white dashed line shown in Figs. 11.3a, b and 11.4a–d. Also we have included profiles from reconstructed images at the first TPO and profiles from reconstructed images when Gaussian and Butterworth filters were used in the filtering process. We can note the periodic component as a result of using an ideal filter not only at z_{ht0} but also at z_{ht1} . This behavior is presented in both amplitude and phase distributions. Additionally, and in agreement with simulations previously performed, we can show the shift of 180° in phase and reversal amplitude attained in the reconstruction at z_{ht1} . However usual phase and amplitude anomalies are presented in boundaries (edges) due to single diffraction order does not superpose with other diffraction orders [17]. Then when the averaging is performed between reconstructed images at z_{ht0} and z_{ht1} , we have an incomplete compensation of the ringing effect in this zone. We can observe a loss of lateral resolution in reconstructed images (principally in phase distribution) when GLPF is applied in the filtering process.

Nevertheless we can see a slight difference between proposal and the BtwLPF of second order in the profiles plot. But additional feature of ideal low-pass filter is that have the possibility to increase the focusing resolution. This property is in function of pixel size, magnification, numerical aperture of the optical imaging system as demonstrated by F. Dubois et al. [18] and (in our case) the filter size. With this, we can determine a better focus plane by using an ILPF than Gaussian or Butterworth low-pass filters. To illustrate the determination of Focus Zone (FZ), in Fig. 11.6a we have plotted the intensity evolution with the reconstruction distance on a line profile from the Fig. 11.4a, where the profile zone is marked with a white dashed line. The starting image is defocused by -10 mm to a 10 mm. We can see that the FZ is of 3.2 mm by using the ideal filter and 16 mm by using the Butterworth one. We can say that ideal filter is better to determine a focus zone than Butterworth. This result help us not only to determine the best and most accuracy reconstruction distance zone to prevent measurement errors [19], but also to adjust the refocusing capability with respect to the sample thickness to reduce the defects that can occur on either the optical component or the sample container. Additionally this feature helps us to control

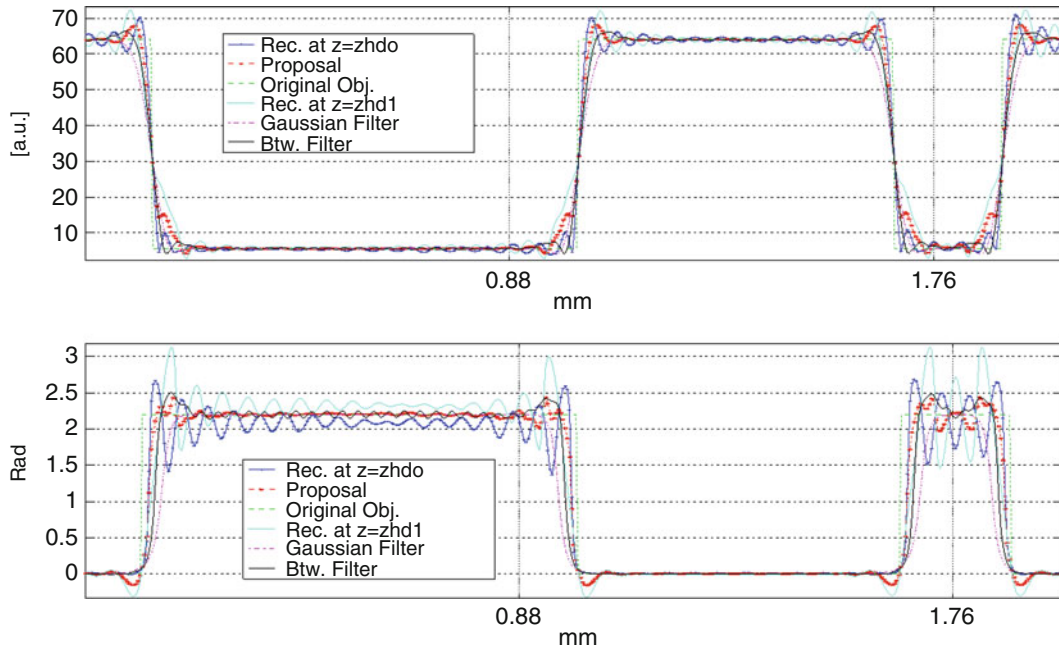


Fig. 11.5 Comparison between profiles measured a long white dashed line of Figs. 11.3a, b and 11.4a–d. (a) Profiles of amplitude distributions, (b) Profiles of phase distributions

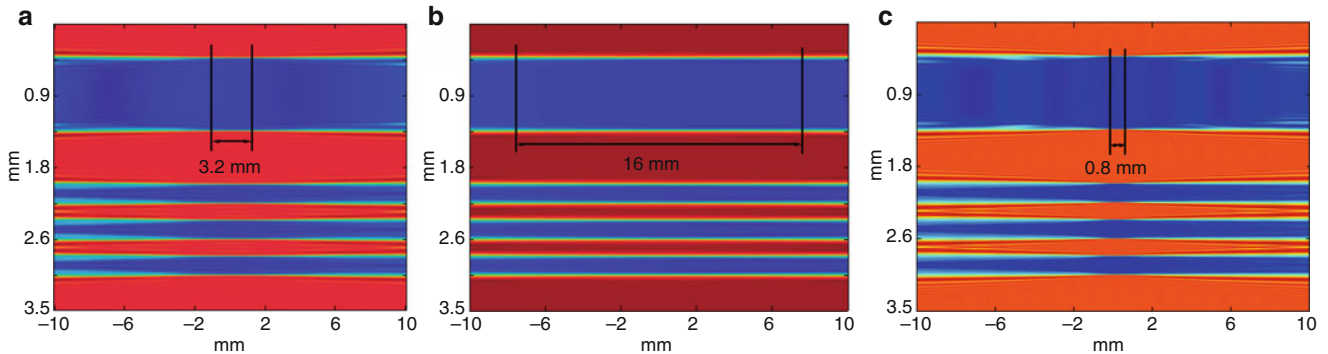


Fig. 11.6 Evolution of intensities determined on a profile line when reconstruction distance is increased. Using (a) an ILPF of 100 pixels of radius, (b) a BtwLPF of 100 pixels of radius and (c) an ILPF of 200 pixels of radius

the resolution of plane scanning in a tomographic scheme [18]. Figure 11.6c presents the intensity evolution of the line profile in the zone marked with white dashed line as Fig. 11.6a but in this case the filter size is of 200 pixels of radius. This shows a smaller focus zone than a filter size of 100 pixels of radius (Fig. 11.6a) evidencing the above mentioned.

11.4 Experimental Results

In this part, the experimental results of the recorded hologram's 1600×1200 pixels are presented. All the zones of interest are clearly depicted and defined in text and images. Figure 11.1 shows the schematic of the digital holographic setup that we used. The described investigation was carried out using a laser diode of 643 nm in wavelength. In order to prevent parasitic interference and optical noise, the diode emits a low coherence (coherence length about 0.1 mm) linearly polarized plane wavefront. The intensity hologram is recorded by a CCD Pixelink™ digital camera of 1600×1200 pixels, 8 bits, with a pixel size of $4.4 \mu\text{m} \times 4.4 \mu\text{m}$. In addition, the sample holder is attached on a x, y, z, displacement and θ rotation stage to perform the sample tilt, which is necessary for the off-axis configuration recording. We took central zones

(1200×1200 pixels) of the recorded images. In order to suppress the DC term and the virtual image, we implemented the Fourier filtering method mentioned in Sect 11.2.1. In order to reduce shot noise we performed an averaging procedure of 80 images of the hologram for the object's intensity and reference's one [20, 21]. The evaluation area to test our method is 400×300 pixels in the central zone to prevent the influence of border effects due to the discontinuity introduced by the windowing of the hologram when it is processed by the FFT calculation and the apodization function applied to the hologram. We considered the standard deviation (STD) as a measure in all sections. We used an USAF 1951 resolution test target as the object.

First, we reconstructed the object wavefront by performing the (11.3) with a reconstruction distance ($z = z_{ido}$) of 85 mm. The reconstruction distance was defined after applying the evolution profile as in simulation result. In order to suppress the DC term and the virtual image, we applied the Fourier filtering process mentioned in Sect. 11.2. Figure 11.7a, b show the amplitude and topography distributions, respectively, by using an ILPF with radius of 100 pixels (cut-off frequency). A second reconstruction was performed at $z = z + z_{idl} = 89.4$ mm with the same filter. To reduce the ringing effect we perform the averaging operation between phase and amplitude reconstructed images at different distances z_{hl0} and z_{hl1} .

From Fig. 11.7c, d we can see the improved images obtained with this proposal. The improved distributions contain nearly all the details of the original object. The improvement with this procedure is an average reduction of STD of 43.7 % in amplitude image and 23.1 % in the topography. The percentage is an average between the two zones delimited by the dashed white rectangles in Fig. 11.7. The STD in each zone is clearly represented in each reconstructed images.

Figure 11.8a, b show line profiles where zone is marked with a white dashed line shown in Fig. 11.7a–d. Also we have included profiles from reconstructed images at the first TPO and profile from reconstructed images when Butterworth filter is used in the filtering process. We can note the periodic component as a result of using an ideal filter at z_{hl0} . This behavior is presented in both amplitude and phase distributions. We assume that the percentage difference between simulation results and experimental are principally due to an additional low frequency noises coming from optical devices defects, a non-plane wave reference, aberrations non-compensated and also a non uniform thin film deposited on target.

Nevertheless we can see a slight difference between proposal and the BtwLPF of second order in the profiles plot exactly as in simulation performed in Sect. 11.3.

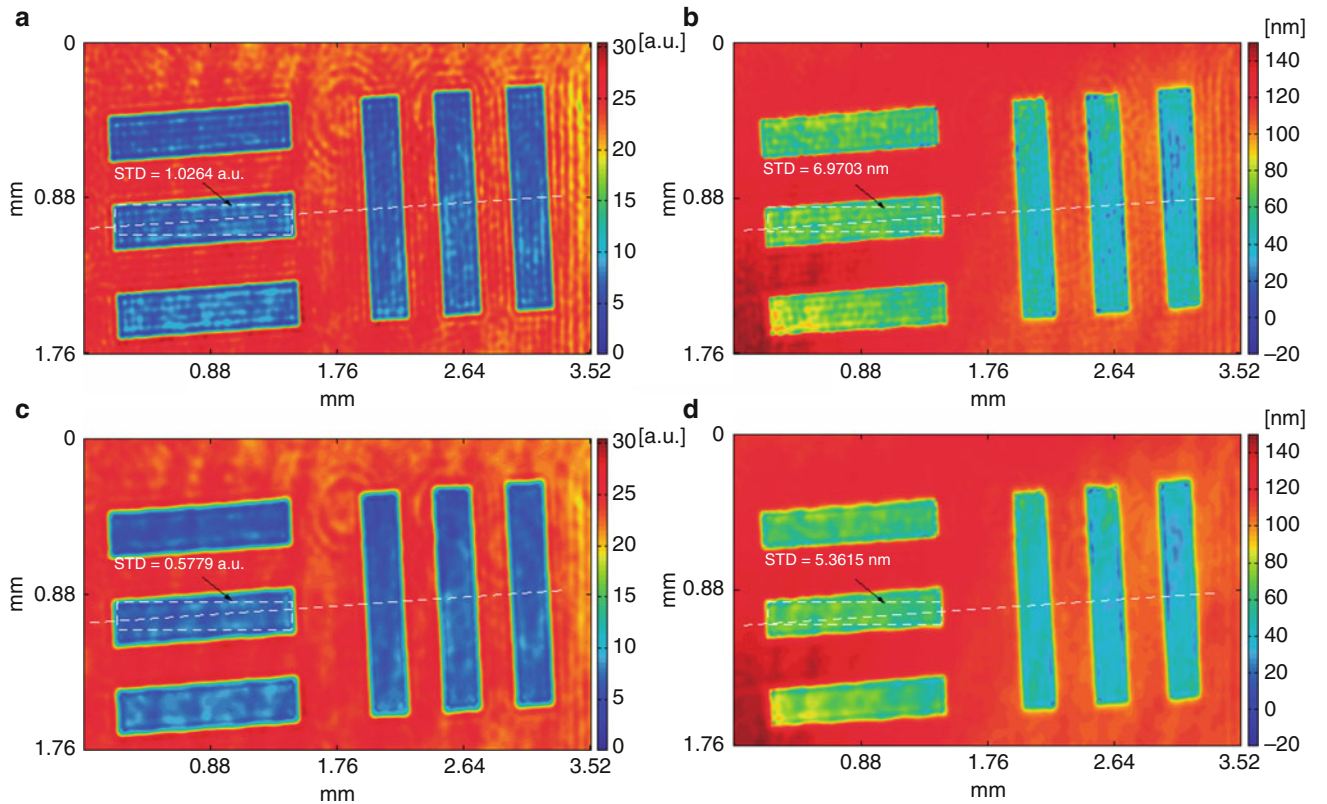


Fig. 11.7 Reconstructed images from hologram. (a–b) Reconstructed amplitude and topography distributions at $z = z_{ido}$ respectively, (c)–(d) improved amplitude and topography respectively after proposal is applied

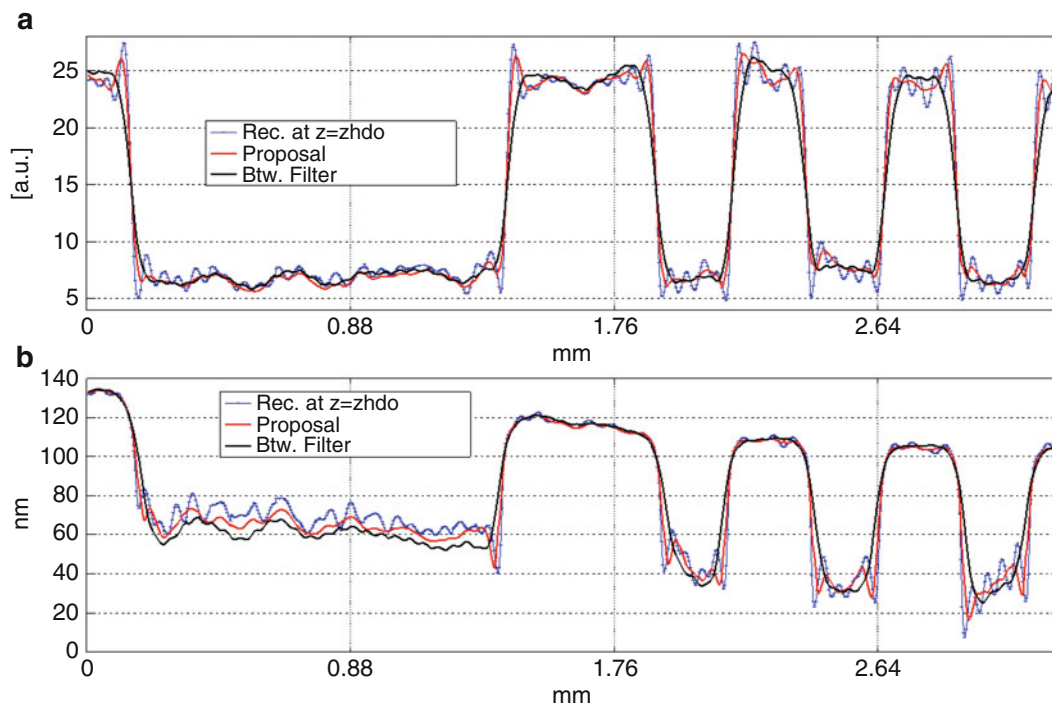


Fig. 11.8 Comparison between profiles measured a long white dashed line of Fig. 8(a, b). (a) Profiles of amplitude distributions, (b) profiles of topography distributions

11.5 Conclusion

In this work, a strategy to reduce the ringing effect of discontinuous surfaces reconstruction in off-axis digital holography was presented. The technique is based on the diffractive nature of light (Talbot effect). Experimental and numerical simulations have proved reductions of these anomalies, 50 % in simulation and 30 % experimentally. In addition, we have been demonstrated a better focusing capacity by using an ideal filter than Butterworth.

Acknowledgement The support of FONDECYT (Preis 3140076, Preis 1140239 and Preis 1120764), FONDEF (Preis IT13110034), CORFO (Preis 14BPC4-28651), USACH-DICYT ASOCIATIVO, SEP-PROMEP Preis 14146 F-38, and UTFSM- DGIP, is gratefully acknowledged.

References

1. L. Xu, J.M. Miao, A. Asundi, Properties of digital holography based on in-line configuration. *Opt. Eng.* **39**, 3214–3219 (2000)
2. M. León-Rodríguez, R. Rodríguez-Vera, J.A. Rayas, S. Calixto, Digital holographic microscopy through a Mirau interferometric objective. *Opt. Lasers Eng.* **51**(3), 240–245 (2013)
3. L. Miccio, A. Finizio, R. Puglisi, D. Balduzzi, A. Galli, P. Ferraro, Dynamic DIC by digital holography microscopy for enhancing phase-contrast visualization. *Biomed. Opt. Express* **2**, 331–344 (2012)
4. R. Guo, B. Yao, P. Gao, J. Min, M. Zhou, J. Han, X. Yu, X. Yu, M. Lei, S. Yan, Y. Yang, D. Dan, T. Ye, Off-axis digital holographic microscopy with LED illumination based on polarization filtering. *Appl. Opt.* **52**, 8233–8238 (2013)
5. E.N. Leith, J. Upatnieks, Wavefront reconstruction with defused illumination and three dimensional objects. *J. Opt. Soc. Am.* **54**, 1295 (1964)
6. P. Gao, G. Pedrini, W. Osten, Structured illumination for resolution enhancement and autofocusing in digital holographic microscopy. *Opt. Lett.* **38**(8), 1328–1330 (2013)
7. M. Takeda, H. Ina, S. Kobayashi, Fourier-transform method of fringe-pattern analysis for computer-based topography and interferometry. *J. Opt. Soc. Am.* **72**, 156–160 (1982)
8. C.A. Sciammarella, G.K. Bhat, Computer-assisted techniques to evaluate fringe patterns, in *Proceedings of SPIE 1553, Laser Interferometry IV: Computer-Aided Interferometry*, 1 January 1992, p. 252
9. M. Anguiano-Morales, A. Martínez, J.A. Rayas, R.R. Cordero, F. Labbe, Uncertainty analysis of whole-field phase-differences retrieved from ESPI fringe patterns by using the Fourier transform method (FTM). *Opt. Commun.* **282**(5), 686–691 (2009)

10. V.A. Lórenz-Fonfría, E. Padrós, The role and selection of the filter function in Fourier self-deconvolution revisited. *Appl. Spectrosc.* **63**, 791–799 (2009)
11. E. Cuche, P. Marquet, C. Depeursinge, Simultaneous amplitude-contrast and quantitative phase-contrast microscopy by numerical reconstruction of Fresnel off-axis holograms. *Appl. Opt.* **38**, 6994–7001 (1999)
12. M. Nazarathy, J. Shamir, Fourier optics described by operator algebra. *J. Opt. Soc. Am.* **70**, 150–159 (1980)
13. J.W. Goodman, *Introduction to Fourier Optics* (McGraw-Hill, New York, 1996)
14. R.C. González, R.E. Woods, S.L. Eddins, *Digital Image Processing Using Matlab* (Pearson Prentice-Hall, Upper Saddle River, NJ, 2009)
15. A.V. Oppenheim, R.W. Schaffer, *Discrete-Time Signal Processing* (Prentice-Hall, Upper Saddle River, NJ, 1999)
16. K. Patorski, *Handbook of the Moiré Fringe Technique* (Elsevier, Amsterdam, 1993)
17. M.S. Kim, T. Scharf, C. Menzel, C. Rockstuhl, H.P. Herzig, Phase anomalies in Talbot light carpets of self-images. *Opt. Express* **21**, 1287–1300 (2013)
18. F. Dubois, L. Joannes, J.-C. Legros, Improved three-dimensional imaging with a digital holography microscope with a source of partial spatial coherence. *Appl. Opt.* **38**, 7085–7094 (1999)
19. A. El Mallahi, F. Dubois, Dependency and precision of the refocusing criterion based on amplitude analysis in digital holographic microscopy. *Opt. Express* **19**, 6684–6698 (2011)
20. M. León-Rodríguez, R. Rodríguez-Vera, J.A. Rayas, S. Calixto, High topographical accuracy by optical shot noise reduction in digital holographic microscopy. *J. Opt. Soc. Am. A Opt. Image Sci. Vis.* **29**, 498–506 (2012)
21. F. Charrière, B. Rappaz, J. Kühn, T. Colomb, P. Market, C. Depeursinge, Influence of shot noise on phase measurement accuracy in digital holographic microscopy. *Opt. Express* **15**, 8818–8831 (2007)

Chapter 12

Study of Temperature Distribution Over a Stirling Engine by Using the Schlieren Technique

C. Alvarez-Herrera, A.R. Moreno-Nieto, and J.G. Murillo-Ramírez

Abstract The Schlieren technique has been used to visualize and measure some relevant physical properties in transparent media such as refractive index and some dependent variables on it such as density and temperature. This technique was implemented to visualize temperature gradients that appear from the heat applied into the hot section of a Stirling engine. Temperature gradients and temperature fields are described qualitatively and compared with temperature measurements using chromatic thermometric crayons. Furthermore, natural and turbulent heat convection was visualized from the temperature fields. The obtained results give important information about the heat transfer mechanism and its dissipation on a real engine.

Keywords Schlieren devices • Image forming • Image processing • Temperature gradients • Temperature fields

12.1 Introduction

The measurement of physical variables in the fluid flows area requires no intrusive techniques and instruments that no alters the dynamics of the fluid flows. As is well known the optical visualization techniques have high sensibility to measure these variables and do not perturb the media under study. For this reason in this research was used the Schlieren optical technique. The optical Schlieren technique is widely used in wind tunnels to visualize the fluid flows in aerodynamics devices such as airfoils, cylinders and blades just to mention some of the most usual applications. There is a wide variety of Schlieren arrangements used each one of them for different purposes. These arrangements changes in form and optical components like lenses, mirrors and grids, depending on the size of the field to resolve. Different light sources are used depending on the specific arrangement, like filaments, mercury, sodium, LEDs lamps, and laser sources. The Schlieren technique captures the changes of the refractive index of transparent media, which are linearly related with the gradient density and this last in its turn with the temperature gradient. The common Schlieren arrangements use now the setup originally introduced by Toepler, which includes two lenses a source light and a knife edge. In this research a modified Toepler's arrangement, common called the Z-type setup was used. This arrangement has a light source, a spherical mirror to collimate the light beam and a second mirror to concentrate the light beam in the focal plane of the setup. The knife edge is located at the focal plane of the setup and gives the refractive gradient in the image plane. The Z-type arrangement is used to increase the size of the field to visualize.

The fluid flow to visualize need to be transparent media as a principal characteristic to use this technique or in other words the fluid must to be an isotropic homogeneous media. The transparent media or phase object appears in different forms in science and engineering such compressible flows, convective heat transfer, mixing of two or more different fluid densities, combustion, plasma flow and stratified flow [1]. This paper focuses on the hot gases produced by a flame of the mixture of butane and atmospheric air to visualize gradient temperatures at full field from density gradients from refractive index of the hot gases with the relation of Gladstone-Dale and the ideal gas equation.

In addition, chromatic thermometer crayons were used to measure temperatures of operation in the hot surfaces changing the color surface of the crayon depending of the temperature measured.

C. Alvarez-Herrera (✉) • A.R. Moreno-Nieto
Facultad de Ingeniería, Universidad Autónoma de Chihuahua, Nuevo Campus Universitario, Circuito Universitario S/N,
31125 Chihuahua, Chihuahua, Mexico
e-mail: crwxss1@gmail.com

J.G. Murillo-Ramírez
Centro de Investigación en Materiales Avanzados S. C., Miguel de Cervantes 120, Chihuahua C.P. 31136, Chihuahua, Mexico

The test object used in this work was the cylindrical hot surface of a Stirling engine heated by a mixture of butane-air. The Stirling engine invented in 1816 by Robert Stirling was used to pump water. This engine used air as work substance and was more safety than the steam engine [2]. But with the invention of Diesel and Otto cycles the Stirling engine decayed in use. In present days with the increment of renewable energies in thermo-solar and biomass systems, the use of this old technology as Stirling engines is suitable for these purposes, this justify the importance to study this technology.

12.2 Theoretical Background

12.2.1 Optical Background

This chapter describes the procedure to measure temperature in fluid flows using the Schlieren technique, Fig. 12.1 shows the Z-type arrangement used in this research. When a phase object with refractive index $n = n(x, y, z)$, is located between the two mirrors, occurs a small displacement δx in the direction of propagation of the incident rays in the image plane as shown in Fig. 12.2 (the image formed in the camera). This variation in the deviation rays is linearly proportional to the changes of the refractive index. In the case of fluid flows this variation is related to the density changes as explained before. When a light ray passes through an isotropic and inhomogeneous medium this suffers a small angle deviation which depends on the refractive index and the width of the test object. The ray path is described by the ray equation shown next:

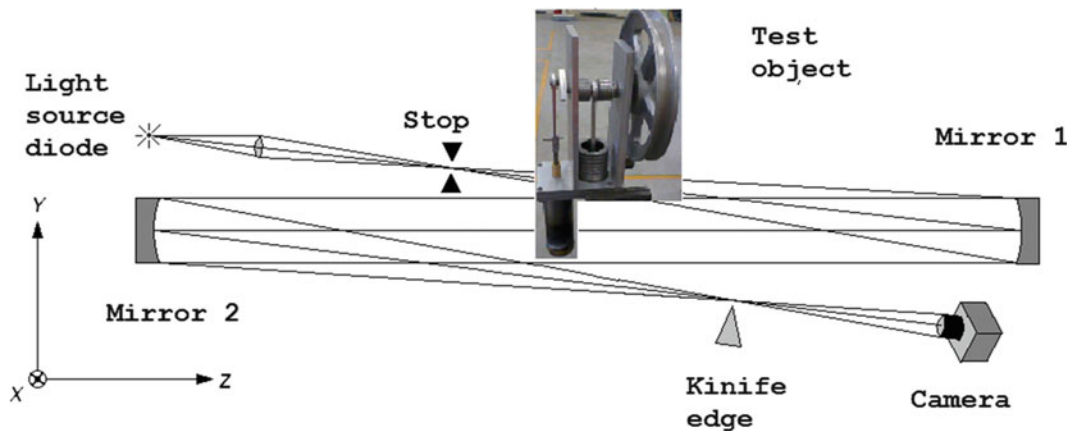
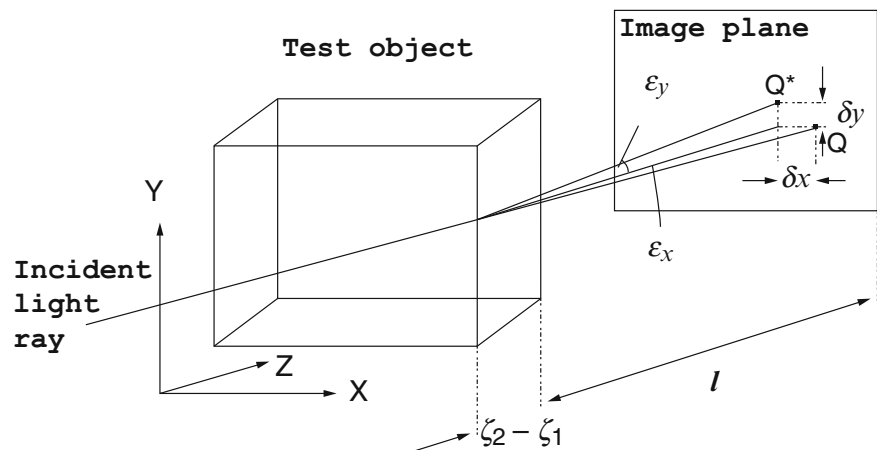


Fig. 12.1 Z-type Schlieren setup with the Stirling engine as test object located in the half position between the two mirrors

Fig. 12.2 Ray pass through a transparent media l is the distance between the test object and image plane position



$$d(n\mathbf{P}')/ds = \Delta n \quad (12.1)$$

Where $\mathbf{P} = \mathbf{P}(x, y, z)$ is a position vector, \mathbf{P}' is the derivative of \mathbf{P} with respect to ds and $ds = dx^2 + dy^2 + dz^2$ represents the arc length along the ray propagation as shown in Fig. 12.2. The ray propagation direction is in z -direction, then the ray suffers small deviation in x and y directions. For simplicity here is considered the approximation in x -direction only, which is valid for small deviation angles given by:

$$\frac{\partial}{\partial z} \left(n \frac{dx}{dz} \right) = \frac{\partial n}{\partial x}, \quad (12.2)$$

The deviation angle is represented with ε , an the measured deviation in the image plane of the setup is represented with $\delta x = f_2 \tan \varepsilon \approx f_2 \varepsilon$ where f_2 is the focal length of the second mirror included in the setup. In this approach the gradient of the deviation angle can be represented as:

$$\varepsilon_x = \int_{\zeta_1}^{\zeta_2} \frac{\partial n}{\partial x} dz \quad (12.3)$$

This equation depends on the refractive index gradient and the width of the test object defines the integration limits in z -direction $\zeta_2 - \zeta_1$, as shown in Fig. 12.2. Using the Gladstone-Dale relation $(n - 1) = K\rho$ given by Merzkirch [1] and Settles [3], where K is the Gladstone-Dale constant, the density fluid ρ can be expressed as follows:

$$\rho_x = \frac{\partial \rho}{\partial x} = \frac{\delta x}{f_2 WK} \quad (12.4)$$

After to integrating linearly (12.4) in x -direction the density takes the form:

$$\rho(x) = \rho_0 + \frac{1}{f_2 WK} \int_{x_1}^{x_2} \delta x dx \quad (12.5)$$

Where $W = \zeta_2 - \zeta_1$ is the width of the test object and ρ_0 is the fluid density at the reference temperature T_0 . For an ideal gas at constant pressure and assuming the Gladstone-Dale relation with the approach of small deviation angles, the temperature can be expressed as:

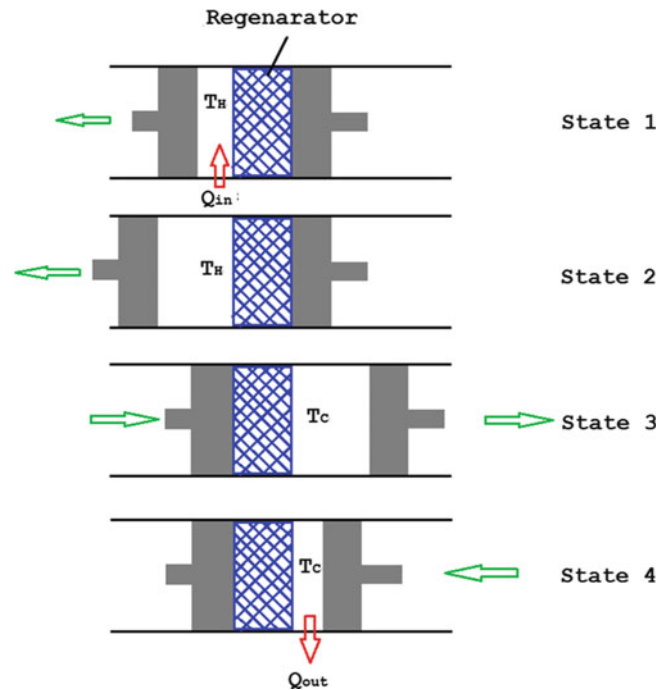
$$T = \frac{\rho_0}{\rho} T_0 = \frac{n_0 - 1}{n - 1} T_0 \quad (12.6)$$

Further details are found in [4–7].

12.2.2 Stirling Engine

The Stirling engine is a closed cycle device with the same theoretical efficiency as the Carnot cycle which has four isentropic processes given by: Isothermal expansion between states 1 and 2, isochoric process states 2–3, in this process heat at T_H is absorbed by the regenerator changing the gas temperature at T_C . Isothermal compression states 3–4 at T_C , and isochoric processes states 4–1, in this process the gas temperature is increased from T_C to T_H when gas pass through the regenerator in inverse direction as the 2–3 process as shown in the diagram depicted in Fig. 12.3, [2, 8].

Fig. 12.3 Process in the Stirling cycle



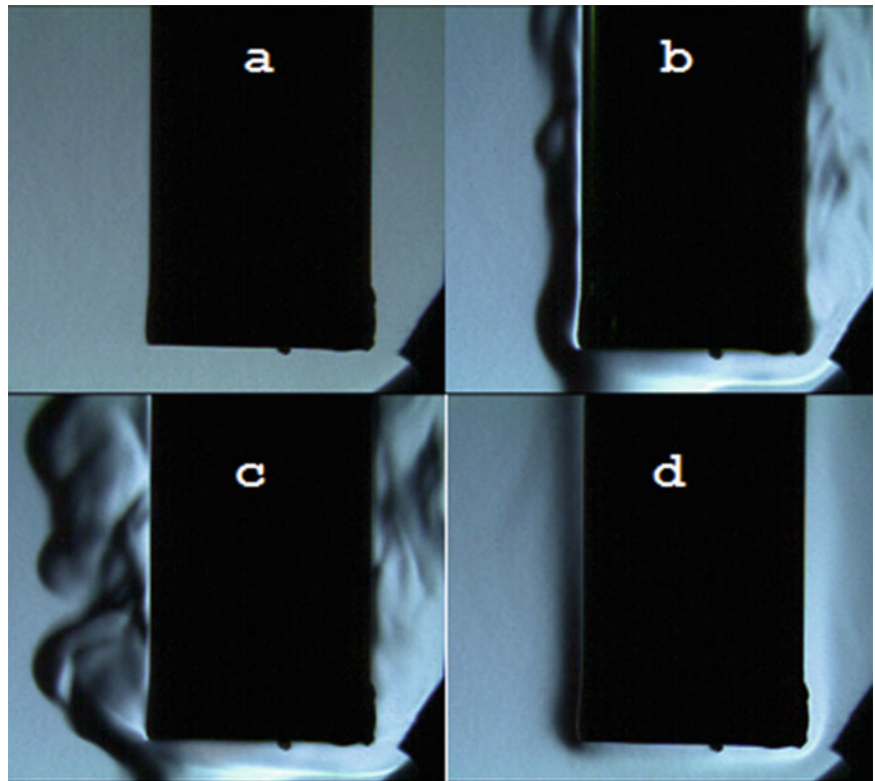
12.3 Experiment

In this research the Schlieren Z-type shown in Fig. 12.1 was used. The parts of the system and how it works will be explained below. A white light LED (Light emission diode) was used as a light source, using a pupil to get only a small part of the light due to its spherical form of propagating. This light beam is collimated by the mirror 1 and then the second mirror of the system concentrates it into the focal plane of the setup. Then the light beam expands to arrive at the image plane of the setup as shown in Fig. 12.3. In the focal plane a knife edge is located with the purpose to cut the non-deviated light rays and allowing its pass to form images in intensity scales from dark to bright. The intensity images have the information about the changes in x-direction of the refractive index of the test object. The Stirling engine was located in the middle of the Z-type Schlieren system, locating the cylindrical hot surface of the engine in the visualization area of the setup. The air-butane flame was used to heat the cylindrical hot surface of the Stirling engine. The image plane captures the gradients in intensities of the refractive index as explained before. The experimental setup has a 50 mm of focal length which allows forming the image at the image plane. The information was captured acquiring 52.4 frames per second (fps) at a spatial resolution of 480×752 pixels, using a CMOS sensor which saved it in an avi format video file. In this work three experiments were accomplished, in which were captured 1000 snapshots in each one of them. A reference image was taken before to start the experiments. In the process of the information the avi file was cut in consecutive images in .mat format using Matlab code. The images were processed to get the gradient of the refractive index of the object in form of intensities gradients. Then the density fields were obtained to finally obtain the temperature fields using (12.3)–(12.6).

12.4 Results

The results are shown in form of Schlieren images that represent the density gradients. In fact the Schlieren images of the convective hot gases allowed obtaining the temperature fields. First are presented the temperature gradients snapshots of the convective hot gases caused by the combustion in the flame. These Schlieren images are presented in gray scale intensities. Temperature fields obtained from the experimental Schlieren images processed in Matlab are shown in a scale of color intensities, so that going from room temperature to hot temperatures is equivalent to going from blue to red color. The images in these figures are shown in the xy-plane that represents the full field of the density gradients and temperatures. In Fig. 12.4 raw images directly taken from the Z-Schlieren setup are shown. In Fig. 12.4a corresponds to the reference images without

Fig. 12.4 Schlieren raw images directly obtained from the experiment, (a) reference image without flux, (b) and (c) forced convection heating the cylinder with the flame, and (d) natural convection cooling the cylinder at room temperature



test fluid, only with the atmospheric air at room conditions, Fig. 12.4b, c correspond to images when the cylinder is heating with the butane air mix flame, which represent the heat transfer in turbulent fluid flow. Figure 12.4d corresponds to convective heat transfer toward the atmosphere, without flame. As can be seen from Fig. 12.4b–d the Schlieren technique is a powerful optical test probe due to easy visualization and fast form to get information from the raw images.

Figure 12.5a, c show images during the flow heating of cylindrical surface with premixed air butane flame after processing the raw Schlieren images applying Matlab algorithms referred to the (12.3)–(12.6). The process of these figures in Matlab is $Im_{\text{fluid flux}} - Im_{\text{reference}}$. These figures show only the refractive gradients caused by the flame temperature [1]. This was used to remove the intrinsic noise from the Schlieren setup. Figure 12.5e shows the same process as in Fig. 12.5a, c but without flame, only the heat transferred by natural convection of the heated cylindrical surface was observed. Figure 12.5b, d, f show the temperature field images obtained after integrating linearly Fig. 12.5a, c, e, respectively. As can be seen the integration of the Schlieren images was accomplished in zones where the temperature gradients were well defined. Figure 12.5b, d, f show the qualitative behavior of the temperature. Figures 12.4 and 12.5 show how the heat is transferred to the cylindrical surface and from the cylindrical surface to the atmosphere.

In order to get more information about the temperature in quantitative manner, chromatic crayons were used as shown in Fig. 12.6. By using this procedure was possible to know the punctual temperature on the heated surface, and were estimated the starting and operating temperatures of the Stirling engine. The starting measured temperature of the engine was comprised between $T = 250$ and 300 °C, and the operating temperature reached $T = 600$ °C.

12.5 Conclusions

In this work were found interesting results about the temperature gradients and temperature distribution in a real Stirling engine. For this purpose the robust and full field Schlieren optical technique was used. Furthermore a punctual temperature was obtained using chromatic crayons in order to get detailed information about the temperature on the hot surface of a real Stirling engine. So with the use of the Schlieren technique and the chromatic crayons was possible to know more about how is the heat transfer in a real Stirling engine. The results of this research also showed that there is a lot of waste of heat during the work of a Stirling engine. In the future work, after to confirm these results it is possible to know using these techniques how to make more efficient the heat transfer in real Stirling engines.

Fig. 12.5 (a) and (c) are the Schlieren images in intensities of the heat transfer from the flame to cylindrical surface, subtracting the reference image. (e) Represents the cooling of the hot cylindrical surface by nature convection. (b), (d) and (f) show the temperature distribution of the temperature gradients

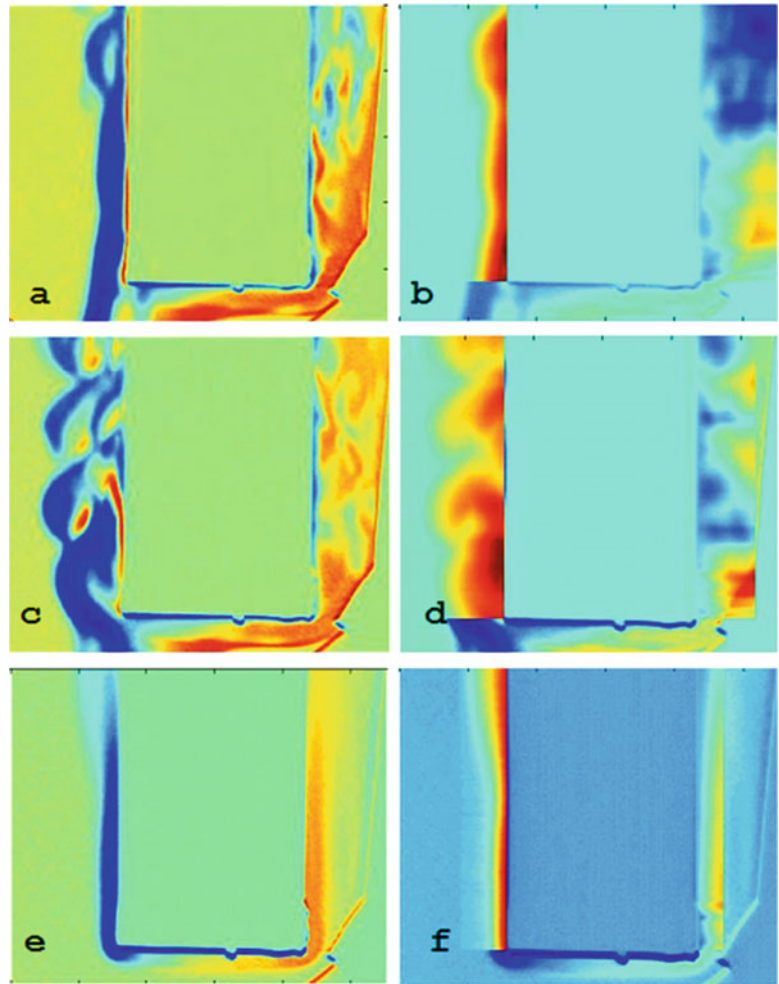
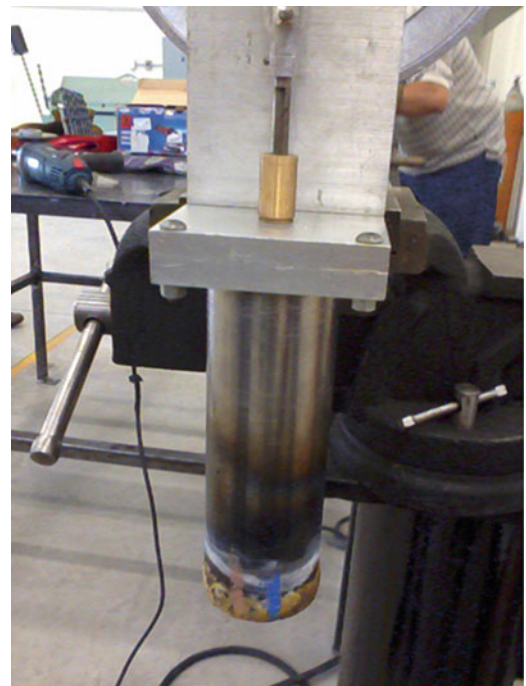


Fig. 12.6 Stirling engine cylindrical surface showing two crayon marks one for measure temperature of $T = 250\text{--}300\text{ }^{\circ}\text{C}$ and the other for $T = 600\text{ }^{\circ}\text{C}$ (blue color)



Acknowledgements Alvarez-Herrera C. and Moreno-Nieto A. R., want to thank the funding support of (PRODEP).

References

1. W. Merzkirch, *Flow Visualization*, 2nd edn. (Academic, Orlando, 1987)
2. T. Finkenstein, A.J. Organ, *Air Engines* (ASME, New York, 2001)
3. G.S. Settles, *Schlieren and Shadowgraph Techniques*, 1st edn. (Springer, Berlin, 2001)
4. R.J. Goldstein, *Fluid Mechanics Measurements*, 2nd edn. (Taylor and Francis, Philadelphia, 1996)
5. A.K. Agrawal, N.K. Butuk, S.R. Gollahalli, D. Griffin, Three-dimensional rainbow Schlieren tomography of a temperature field in gas flows. *Appl. Opt.* **37**, 479–485 (1998)
6. C. Alvarez-Herrera, D. Moreno-Hernández, B. Barrientos-García, Temperature measurement of an axisymmetric flame by using an Schlieren system. *J. Opt. A: Pure Appl. Opt.* **10**, 104014 (2008)
7. C. Alvarez-Herrera, D. Moreno-Hernández, B. Barrientos-García, J. Guerrero-Viramontes, Temperature measurement of air convection using a Schlieren system. *Opt. Laser Technol.* **41**, 233–240 (2009)
8. Y.A. Cengel, M.A. Boles, *Termodinámica*, 6ª Edición, MacGRAW-HILL/INTERAMERICANA EDITORES, S. A. DE C.V.(2009)

Chapter 13

On Axis Fringe Projection

Analía Sicardi-Segade, J.C. Estrada, Amalia Martínez-García, and Guillermo Garnica

Abstract The standard fringe projection technique requires a non-zero angle between projection and observation directions to have sensitivity in the z direction. In this work, a new method is presented where the angle between projection and observation directions is zero, but the system presents sensitivity due to divergent projection which changes the fringes frequency in each one of the normal planes to z-axis. The experimental results compared with the standard fringe projection technique are presented in this work to show the accuracy of the method proposed.

Keywords Fringe projection • On axis • 3D surface recover

13.1 Introduction

Optical measurement methods have the advantage of being highly sensitive, rapid, whole field and non-invasive, compared with other measurement techniques.

In recent years, the use of the fringe projection technique for generating three-dimensional (3D) surface information has become one of the most active research areas in optical metrology [1–8]. Some of the characteristics of the objects obtained by using optical metrology techniques are: refraction index, mechanical parameters or its topography. With these techniques the information from various objects or components can be obtained in a non-destructive and fast way. For this reason these techniques are widely used in industry, in automatic robotic vision, in medicine, in the protection of cultural heritage, security, navigation, object recognition, virtual reality, among many others [2–4].

Standard fringe projection systems use an off axis setup for doing profilometry [2, 3], but due to this configuration objects may present shadow areas where no fringe patterns are formed and, as a result, it would be impossible to obtain the elevation measure [9]. Many contributions to resolve the shadows problems have been reported. Hani et al. [9] proposed an image processing method using wavelet analysis for shadows detection. Bringier et al. [10] proposed a photo-metric stereo method to detect shadow and specularity. Feng et al. [5] proposed a method that predicts the appropriate exposure times based on the histogram distribution. Skydan et al. [11] proposed a method for shadows detection using a camera, two projectors and colored structured light. Hao et al., Harizanova et al. and Sasso et al. [12–14] have proposed methods based on the use of multiple projectors. Flores et al. [7] proposed a panoramic fringe projection method, but to have sensitivity in the system they incorporate a convex axicon. All these techniques are more complex because they use more than one projector, additional devices or need additional image data processing to solve the problem.

Standard fringe projection method uses a setup out of axis and the equation used to recover the shape is

$$z(x, y) = \frac{\phi(x, y)}{2\pi} \frac{p}{\tan \alpha + \tan \beta} \quad (13.1)$$

where $\phi(x, y)$ is the phase of the object, p is the pitch of the fringe pattern, α is the angle between the optical axis and the observer, and β is the angle between the optical axis and the projection direction [3]. It is easy to see that there is an indetermination in the equation when the system is on axis (i.e., $\alpha = 0$ and $\beta = 0$). However, if we could have an on axis fringe projection system, the problem with the shadows could be significantly reduced. In the following section, we show

A. Sicardi-Segade (✉) • J.C. Estrada • A. Martínez-García • G. Garnica
Centro de Investigaciones en Óptica A.C., Loma del Bosque 115, Col. Lomas del Campestre, León,
Guanajuato C.P. 37150, Mexico
e-mail: analiass@gmail.com; julio@cio.mx; amalia@cio.mx; garnica@cio.mx

how to recover the object profile using a projected fringe pattern by using an on axis projection system. A pin-hole camera model is used to obtain the fringe pattern modulation by means of divergent rays. A theoretical model will be shown and it will be supported by experimental results. Discussions and conclusions will be given at the end of this paper.

13.2 On Axis Fringe Pattern Model

Let us consider a 3D orthogonal coordinate system with a camera placed at the origin O and a pinhole camera model, for simplification purposes [15]. The z axis is pointed in the viewing direction of the camera and is referred to as the optical axis. The reference plane S_0 where the fringes are projected on is placed at a distance L_0 from the origin of the coordinate system, as shown in Fig. 13.1.

Without taking into account the background illumination, the equation for the fringe pattern on the reference plane S_0 can be written as follows:

$$I_0(x) = \cos(\omega_0 x) \quad (13.2)$$

where $\omega_0 = 2\pi f_0$ and f_0 is the frequency of the fringes pattern projected at the reference plane. Only the light ray coming from a point P positioned at the plane S_0 with coordinates (L_0, p) which passes through the hole at the origin of the camera coordinate system meets the image plane at point P_i [15]. If we move S_0 a distance z from the image plane, perpendicular to the optical axis, the plane would be located at position S_1 , and the point P would be shifted to position P' with coordinates (z, p) . Now, the light ray passing through the center of the system O towards point P' intersects the plane S_0 in P'' with coordinates $(L_0, p + \Delta p)$ corresponding to point P''_i at the image plane. The fringe pattern image I_1 can be written as

$$I_1(x) = \cos(\omega_1 x) \quad (13.3)$$

where $\omega_0 \neq \omega_1$ due to the fact that we are using divergent illumination. Now, we can obtain z by calculating the intersection of the ray OP'' with the straight line $P'P$. That is

$$\begin{cases} OP'' : x = \frac{p + \Delta p}{L_0} z \\ PP' : x = p \end{cases} \quad (13.4)$$

and solving for z , from the system equations we obtain

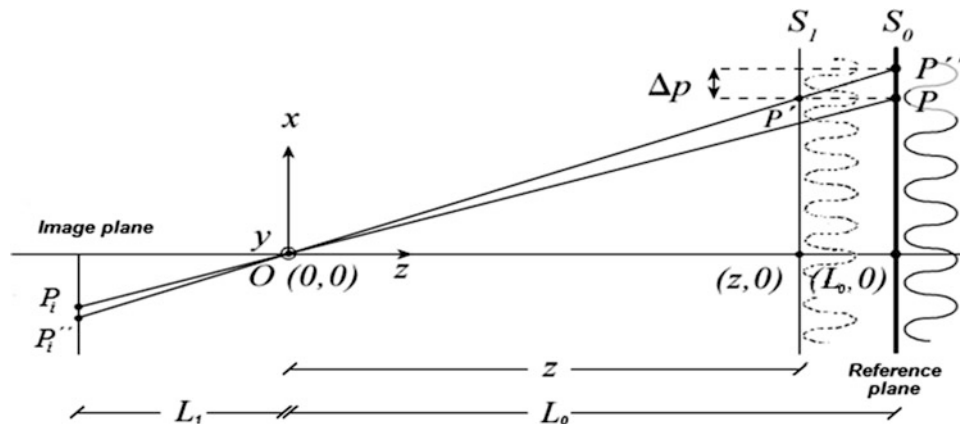


Fig. 13.1 Geometry of the model as seen from the y axis

$$z = \frac{pL_0}{p + \Delta p} \quad (13.5)$$

where all the parameters are known, except Δp . By using (13.2) and (13.3), Δp can be calculated. In order to do that, (13.3) can be rewritten as

$$I_1(x) = \cos(\omega_1) = \cos(\omega_0 x + \Delta\phi(x)) \quad (13.6)$$

where $\Delta\phi(x)$ is a shift in the x axis. On the other hand, if we shift the point x a distance Δp we have

$$I_0(x + \Delta p) = \cos(\omega_0 x + \omega_0 \Delta p) = \cos(\omega_0 x + \Delta\phi(x)), \quad (13.7)$$

and then, the following equality holds:

$$\Delta p = \frac{\Delta\phi(x)}{2\pi f_0} \quad (13.8)$$

Finally, substituting (13.8) into (13.5) we find the equation for z in terms of known parameters

$$z(x) = \frac{pL_0}{p + \frac{\Delta\phi(x)}{2\pi f_0}} \quad (13.9)$$

But, as we are interested in the height differences $h(x)$ measured from the reference plane, we get for a 2D system

$$h(x) = L_0 - z(x) = L_0 - \frac{pL_0}{p + \frac{\Delta\phi(x)}{2\pi f_0}} \quad (13.10)$$

Finally, the system equations for all the rows, $h(x, y)$, can be expressed as

$$h(x, y) = L_0 - z(x, y) = L_0 - \frac{pL_0}{p + \frac{\Delta\phi(x, y)}{2\pi f_0}} \quad (13.11)$$

Equation 13.11 allows to recover the 3D object profile for all x, y , except for points in the vertical line $x = 0$, because when $x = 0$, $\Delta\phi(x, y) = 0$ and there is an indetermination in the equation right second term. The latter can be clarified with the help of Fig. 13.2a that shows the reference plane perpendicular to the optical axis in 3D with a fringe pattern projected on it. If we place a new plane at distance $h(x, y)$ in front of the reference plane, we could see that the fringes that are in both sides of this plane would move laterally but the one that is in the optical axis would not. This effect is shown in Fig. 13.2b. This corresponds only to the fringe that is at the optical axis, and therefore, we cannot recover $h(x, y)$ at the optical axis. However, this can be solved by interpolating $h(x, y)$ for $x = 0$ once we have estimated their neighborhood, or the object can be placed in a position where it does not cross the optical axis. As long as the illumination be divergent and we have a fringe pattern reference, the mathematical model does not change and the proposed system would work well. Fringes may be vertical parallel, as shown in the performed experiments. They could also be horizontal parallel, and circular [16]. In this work, a parallel vertical fringe pattern was chosen in order to allow a better comparison with the standard fringe projection technique.

13.3 Experiment and Results

The setup used to verify the principle in which our method is based was a DELL multimedia projector with a resolution of 1200×800 , a Pixelink CCD camera with maximum resolution of 2048×1536 , a beam splitter 70:30 and a screen (the reference plane). The setup is presented in Fig. 13.3. Distance $L_0 + L_1$ was 85.50 cm. The camera and the projector must be

Fig. 13.2 (a) Diagram of the reference plane aligned with the optical axis in 3D, and (b) image captured with the camera showing the fringe shift when an additional plane of smaller height is placed in front of the reference plane

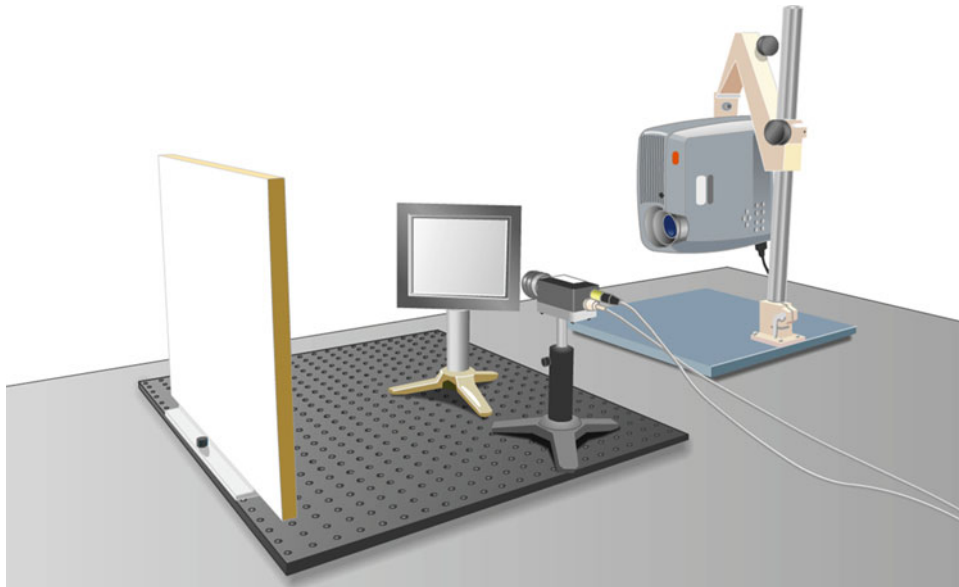
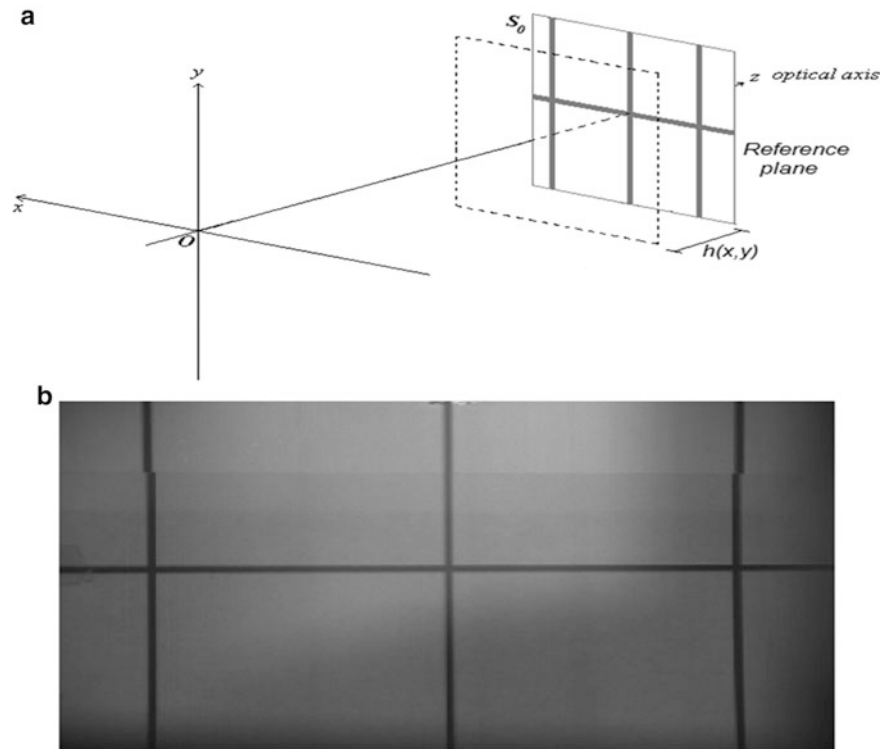


Fig. 13.3 Experimental setup

carefully aligned to achieve the on axis projection and viewing. Distance $L_0 + L_1$ is measured from the CCD camera to the beam splitter and from the beamsplitter to the reference plane. To calibrate the camera we have to estimate the parameters L_0 and L_1 from the camera to the reference plane. In order to do that, we projected a set of squares over the reference plane and measured their projected sides in centimeters. Then, we related them with their image sizes in pixels, according to the relationship between the 3D camera and the 2D image coordinates based on a pinhole camera model, whose equation is given by

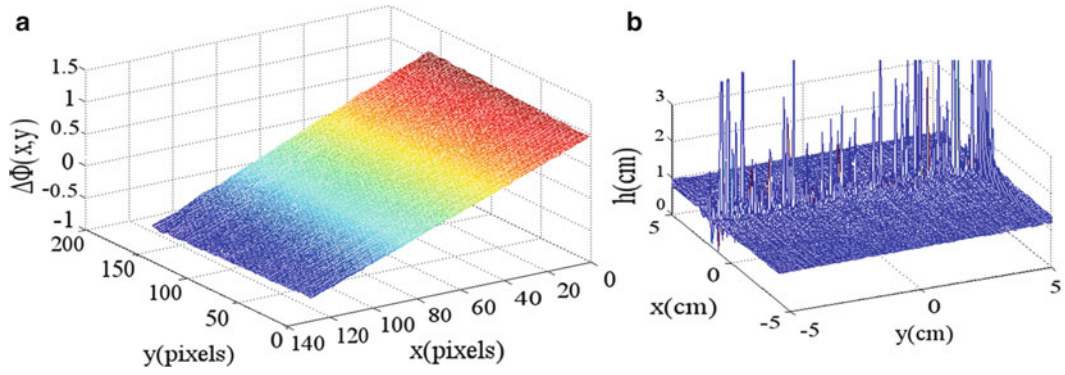
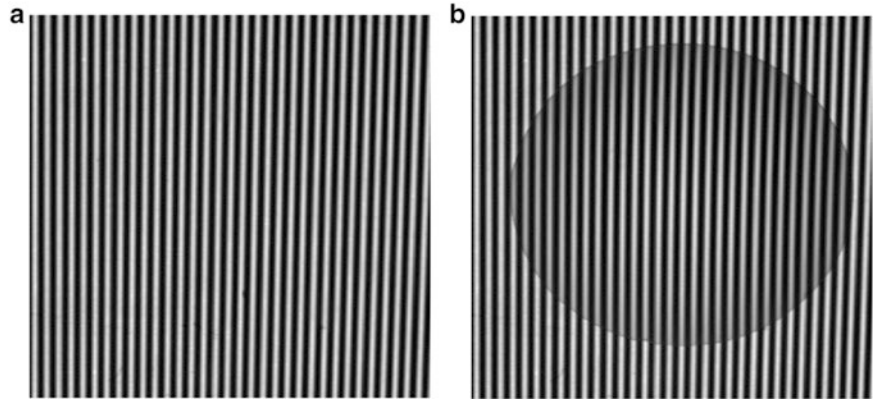


Fig. 13.4 Calculation of the phase difference $\Delta\phi(x,y)$ and $h(x,y)$; (a) $\Delta\phi(x,y)$ when we move the plane 1 cm to the front of the reference, and (b) height profile, $h(x,y)$, of the plane moved, showing the indetermined zone

Fig. 13.5 Projected fringe pattern: (a) reference, and (b) with the test object



$$\frac{p_0}{L_0} = \frac{p_1}{L_1} \quad (13.12)$$

where p_0 is the period distance of the fringe pattern in the reference plane and p_1 is the period distance of the fringe pattern mapped in the camera CCD (image plane) [15]. In this way, we found that $L_0 = 80.63\text{ cm}$ and $L_1 = 4.87\text{ cm}$. Just like in the standard fringe projection technique, the distance L_0 and L_1 changes between sets of images with the same parameters. The L_0 values reported are then the average of many measurements performed without changing the system parameters. The maximum variation of the distance L_0 calculated in this way was 0.67% with respect to the average value for the reported experiment. The first test we performed was to capture an image of the reference plane, to move the plane 1 cm to the front of the reference and to capture the image of the plane when $h(x,y) = 1\text{ cm}$. The phase difference was calculated and $h(x,y)$ was recovered by using (13.11). In Fig. 13.4 the phase difference and the calculated $h(x,y)$ are shown. Note that this phase difference is not wrapped. We can see in Fig. 13.4b that the plane recovered is in $h(x,y) = 1\text{ cm}$ but in $x = 0$ the values are indetermined.

After this, we used a test object to compare this method with the standard fringe projection and the CMM method that we used as a reference. The object was a portion of a sphere with a 4.7 cm diameter and 1.2 cm length. A fringe pattern was projected on the screen with the projector. Two images were recorded by the CCD, the first corresponds to the projected fringes over a reference plane, and the second one corresponds to the projected fringes over the target, as shown in Fig. 13.5. From Fig. 13.5 we can appreciate that the fringe pattern on the reference plane and over the object is not deformed, but fringes were displaced slightly over the test object. The processing of these images by the proposed method gives us the topography information. These images cannot be used to get the topography by using the conventional projected fringes technique. To recover the shape, a 6-step phase shifting method in both images was applied. Afterwards, the phases of both images were obtained, and finally both phases were subtracted and wrapped and $\Delta\phi(x,y)$ was obtained. In Fig. 13.6 the phase difference of the test object is shown. We can see that the object was placed out of the optical axis to avoid an indetermination in the (13.11). In Fig. 13.7a the shape of the test object is shown. The topography of the same object by projected fringes, using the same devices and a 6-step phase shifting method can be observed in Fig. 13.7b. Both profiles were centered in a new coordinate system $x-y$ for comparison purposes.

Fig. 13.6 Phase difference of the test object

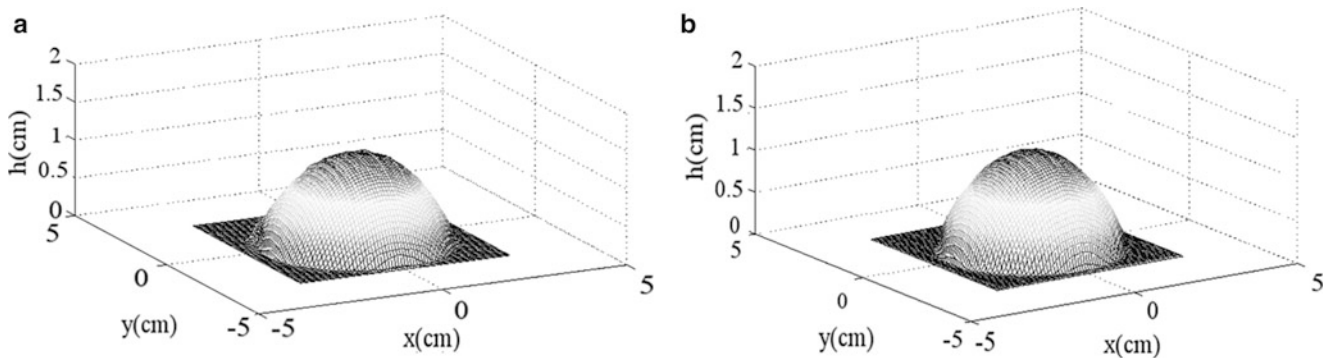
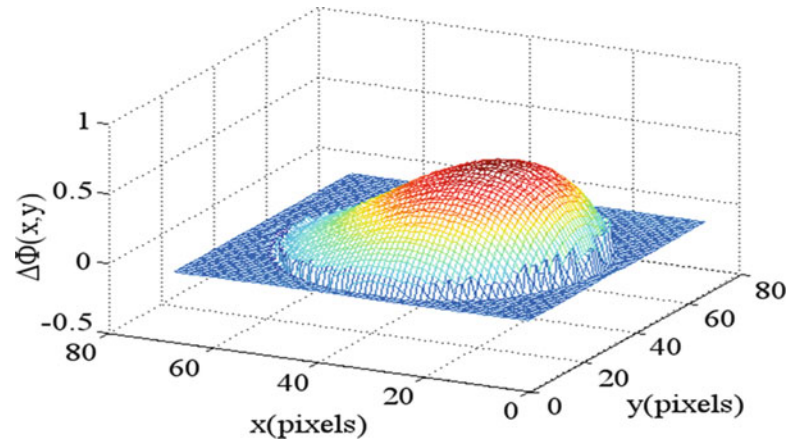


Fig. 13.7 (a) Shape of the test object recovered with our proposed method (on axis) (b) Shape of the test object recovered with standard fringe projection (off axis)

To analyze the results we compared the profile obtained by using on axis fringe projection and the profile obtained with the standard fringe projection with the one obtained from a CMM. Figure 13.8 shows a plane of the topography profiles by using on axis fringe projection, standard fringe projection and the profile obtained with the CMM in (a) $y = 0$ and (b) $x = 0$. A root-mean-square error (RMS) associated to the topography measurement was calculated with the equation [17]

$$RMS = \sqrt{\frac{1}{N} \sum_{i=1}^N (h(i) - \hat{h}(i))^2} \quad (13.13)$$

where $h(i)$ was the result obtained using standard fringe projection and using on axis fringe projection, and $\hat{h}(i)$ was the profile of the CMM that we used as a reference in both cases. The percentage with respect to the maximum height of the object was calculated. The results were: with standard fringe projection $RMS (\%) = 1.02$ and with on axis fringe projection $RMS (\%) = 1.16$.

In the Fig. 13.9a shows the phase difference obtained by applying on axis fringe projection of a test object consisting of a theater mask. And in the Fig. 13.9b shows the theater mask recovered using our proposed method. The errors observed in one edge of the recovered mask in Fig. 13.9b are due to the object was very close to the area where information cannot be recovered.

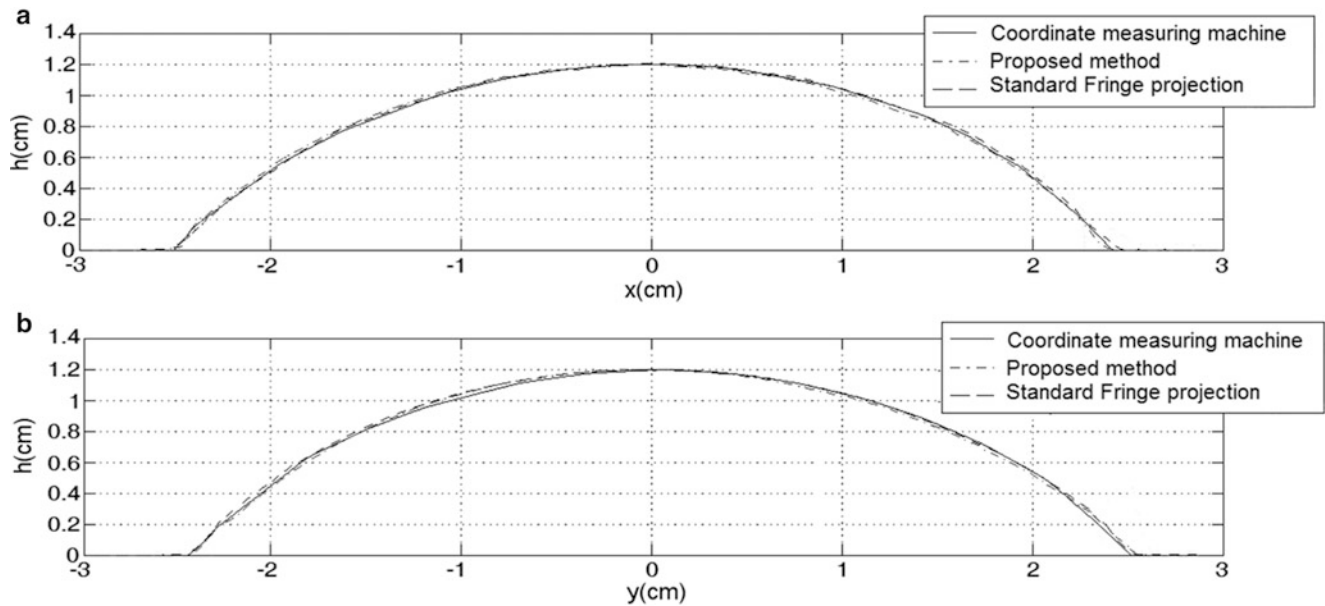


Fig. 13.8 Measurements obtained from the CMM (*continuous line*), fringe projection on axis (*dashed-point line*) and standard fringe projection (*dashed line*), in: (a) $y = 0$, and (b) $x = 0$

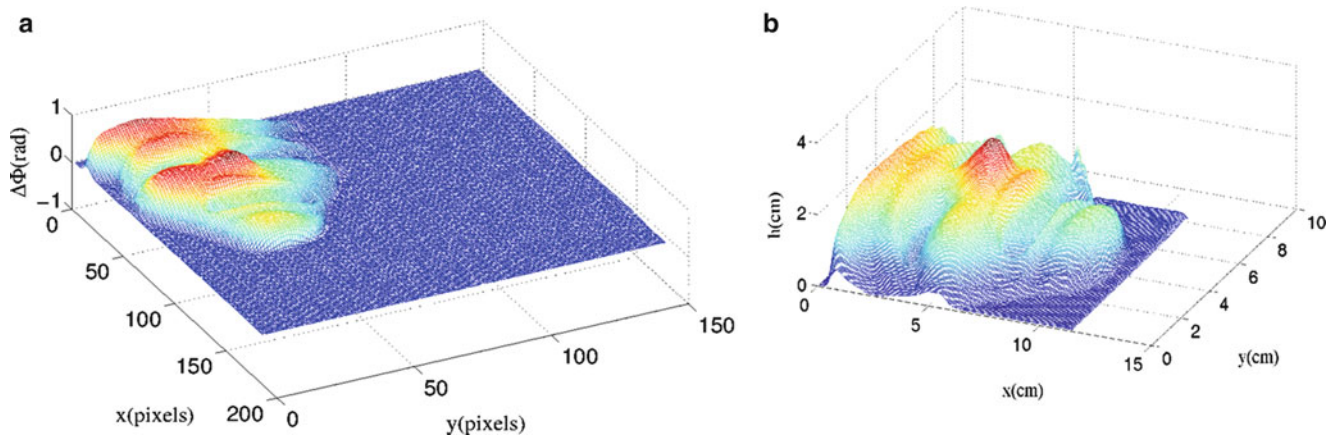


Fig. 13.9 (a) Phase difference of a theater mask and (b) the topography of a theater mask

13.4 Conclusions

In this work, we have presented a theoretical analysis supported by experimental results of a new method based on an on axis fringe projection setup. The theoretical analysis is used in standard fringe projection systems (off axis) does not work in this setup. Our results are in good agreement with those obtained with standard fringe projection and a coordinate measuring machine. Our method has the advantage that the problem of shading is reduced considerably due to the fact that the projected fringes and the observation position are on axis. In this setup, the phase difference is in the range between $(-\pi, \pi)$, therefore, the phase difference is not wrapped and we do not need a phase unwrapping processing in the $h(x,y)$ estimation, avoiding problems like the 2π phase ambiguity due to measurements of surfaces with height discontinuities greater than the period of the fringe pattern [18, 19]. The system only needs simple calibration to obtain good results. Even though the topography information at $x = 0$ is lost, it can be obtained by interpolation or, alternatively, the object can be placed at a position different than the optical axis and its topography can be then completely evaluated. As a projection system with divergent light is used, there will always be a phase difference and therefore it will be possible to recover the shape of the object by means of the proposed technique.

References

1. A. Sicardi-Segade, J.C. Estrada, A. Martínez-García, G. Garnica, On axis fringe projection: a new method for shape measurement. *Opt. Lasers Eng.* **69**, 29–34 (2015)
2. K.J. Gasvik, Moire methods. Triangulation, in *Optical Metrology*, 3rd edn. (Wiley, New York, 2002) [Chapter 7]
3. S.S. Gorthi, P. Rastogi, Fringe projection techniques: whither we are? *Opt. Lasers Eng.* **48**(2), 133–140 (2010)
4. F. Chen, G.M. Brown, M. Song, Overview of three-dimensional shape measurement using optical methods. *Opt. Eng.* **39**(1), 10–22 (2000)
5. S. Feng, Y. Zhang, Q. Chen, C. Zuo, R. Li, G. Shen, General solution for high dynamic range three-dimensional shape measurement using the fringe projection technique. *Opt. Lasers Eng.* **59**, 56–71 (2014)
6. J.M. Di Martino, A. Fernández, G.A. Ayubi, J.A. Ferrari, Differential 3D shape retrieval. *Opt. Lasers Eng.* **58**, 114–118 (2014)
7. V.H. Flores, L. Casaletto, K. Genovese, A. Martinez, A. Montes, J.A. Rayas, A panoramic fringe projection system. *Opt. Lasers Eng.* **58**, 80–84 (2014)
8. C.A. García-Isáis, N.A. Ochoa, One shot profilometry using a composite fringe pattern. *Opt. Lasers Eng.* **53**, 25–30 (2014)
9. A.F.M. Hani, A.A.Khoiruddin, N. Walter, I. Faye, Wavelet analysis for shadow detection in fringe projection profilometry, in *Proceedings of the IEEE Symposium on Industrial Electronics and Applications (ISIEA2012)*, Bandung, Indonesia, 23–26 September 2012
10. B. Bringier, A. Bony, M. Khoudeir, Specularity and shadow detection for the multi source photometric reconstruction of a textured surface. *J. Opt. Soc. Am. A Opt. Image Sci. Vis.* **29**(1), 11–21 (2012)
11. O.A. Skydan, M.J. Lalor, D.R. Burton, Technique for phase measurement and surface reconstruction by use of colored structured light. *Appl. Opt.* **41**(29), 6104–6117 (2002)
12. Y. Hao, Y. Zhao, D. Li, Shape measurement of objects with large discontinuities and surface isolations using complementary grating projection, in *Proceedings of SPIE*, vol. 3898 (1999), pp. 338–343
13. J. Harizanova, V. Sainov, Three-dimensional profilometry by symmetrical fringes projection technique. *Opt. Lasers Eng.* **44**(12), 1270–1282 (2006)
14. M. Sasso, G. Chiappini, G. Palmieri, D. Amodio, Superimposed fringe projection for three-dimensional shape acquisition by image analysis. *Appl. Opt.* **48**(13), 2410–2420 (2009)
15. B. Jähne, From objects to images, in *Practical Handbook on Image Processing for Scientific Application*. (Interdisciplinary Center for Scientific Computing University of Heidelberg, Heidelberg, Germany and Scripps Institution of Oceanography University of California, SanDiego, LaJolla, CA, 1997) [Chapter 1]
16. M. Servin, Synchronous phase-demodulation of concentric-rings Placido mires in corneal topography and wavefront aberrometry (theoretical considerations) Cornell University Library (2012), <http://arxiv.org/abs/1203.1886v2>
17. W.J. Dixon, F.J. Massey Jr., Introduction to measures of central value and dispersion, in *Introduction to Statistical Analysis*, International student edition. (Mc Graw-Hill Kogakusha, Tokyo, 1969), [Chapter 3]
18. Y.R. Huddart, J.D.R. Valera, N.J. Weston, A.J. Moore, Absolute phase measurement in fringe projection using multiple perspectives. *Opt. Express* **21**(18), 21119–21130 (2013)
19. Z. Wang, H. Du, H. Bi, Out-of-plane shape determination in generalized fringe projection profilometry. *Opt. Express* **14**(25), 12122–12133 (2006)

Chapter 14

Instrument for Recording Purkinje Images

I.U. Cosme-Cisneros, G.A. Escamilla-Ruiz, D. Flores-Montoya, G. Hernández-Gómez, and A. Gómez-Vieyra

Abstract Purkinje images are images generated by the reflection of light at different interfaces of the ocular reflective surfaces. The study of the Purkinje images is aimed to determine changes in the alignment of those surfaces. An optoelectronic system capable of generating and detecting Purkinje images in a patient is presented. A symmetric near-infrared illumination array is used to relate the position and orientation of the images obtained with misalignment in the optical axes of the eye. Besides, the images are processed to identify each of the Purkinje images using multi-thresholding.

Keywords Purkinje images • Image processing • Human cornea • Optical system • Infrared

14.1 Introduction

A compact instrument for recording images of ocular surfaces has been designed and used in living eyes of young people. It is based on recording Purkinje images. Also, we propose a new method for estimating the position of the Purkinje images in an optical human system. This is really important as we know, the position of the first and the fourth Purkinje are used as the features for calculating the Z gaze position in some publications [1].

Vision algorithms are commonly used to improve the accuracy in the measurement of the localization of Purkinje point in the image [2]. It is a common practice to consider each point has an Airy diffraction pattern [3] and in this way each centroid is located at the center of mass of the spot. One of the limitations in the estimation of the centroid has to do with the spatial resolution of the CCD and the quantization error [4]. The background noise is another limiting factor for the success of this process of detecting the spots. Thresholding is commonly used to reduce this problem [5]. In this paper we present a simple and rapid morphological algorithm for the detection of spots generated by Purkinje images.

Quality of vision in patients who have corneal refractive surgery depends upon the optimal centration of the procedures used. The center of the pupil is used as a reference point in some corneal ablation procedures. Because the human eye is not an aligned, rotationally symmetrical optical system, the question about the optimum location of the treatment's centration of the surgery on the cornea is still open and remains a topic for discussion. Intraocular lens misalignment is thought to play a negative role in the optical performance in eye that has an aspherical and multifocal optic [6–8]. There are several methods of measuring impact of intraocular lens misalignment in the clinical setting. The methods are more qualitative than quantitative and do not allow for high resolution of intraocular lens. In a real human eye fixed to a point, Purkinje images are typically misaligned. There are three possible causes for this misalignment to occur: a global eye rotation, lens decentration and lens tilt [9]. It is common to use the Purkinje images to measure the alignment of the optical human system.

The human optic system is a relatively simple optical instrument. It consists in two positive lenses, the cornea and the crystalline which project the world images onto the retina. The eye has the ability to form high-resolution images of large fields of view containing objects placed at different distances using transparent living tissues. In the Fig. 14.1 we can see this human optical system. The adult human eye has approximately 24 mm in diameter. The eye is covered by a resistant and flexible tissue called sclera.

I.U. Cosme-Cisneros • G.A. Escamilla-Ruiz • D. Flores-Montoya • G. Hernández-Gómez • A. Gómez-Vieyra (✉)
Laboratorio de Sistemas Complejos, Departamento de Ciencias Básicas, Universidad Autónoma Metropolitana,
Unidad Azcapotzalco, Av. San Pablo 180, 02200 México, D.F., Mexico
e-mail: agvte@correo.azc.uam.mx

Fig. 14.1 Optical human system

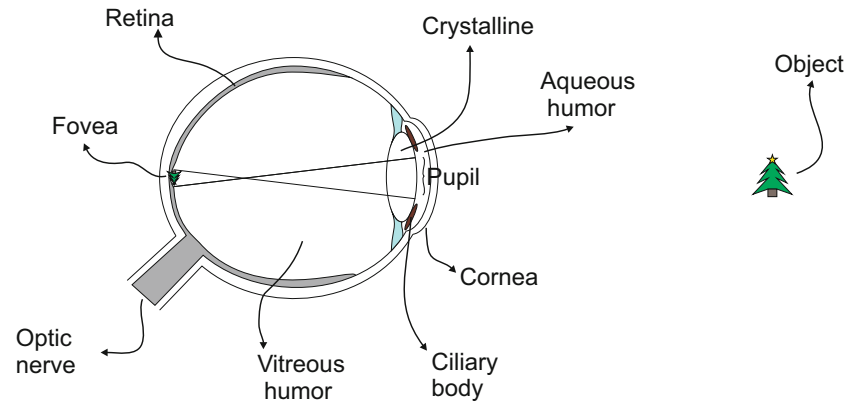
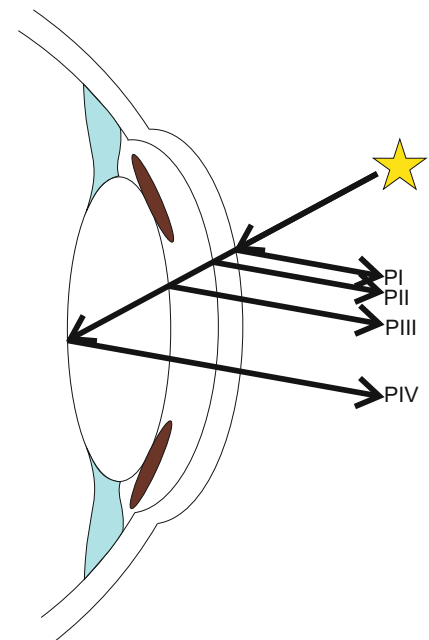


Fig. 14.2 Purkinje reflections from the anterior surface of eye



The cornea is a lens with fixed optical power, the crystalline lens is an active optical element. The crystalline changes its shape by modifying its optical power. This is the basis of the mechanism of accommodation that allows the eye to focus on objects placed at different distances. The cornea is approximately aspherical with an anterior radius of curvature of 7.8 mm, posterior radius of curvature of 6.5 mm and refractive index of 1.3771. The crystalline is a biconvex lens with radii of curvature of 10.2 and -6.0 mm for the anterior and posterior surfaces. The internal structure of the crystalline is layered which implies a non-homogeneous refractive index, higher in the centre than in the periphery and with a value of 1.42.

The Purkinje images are the virtual images formed by the light reflected on the cornea that is referred to the detector (view Fig. 14.2). The Purkinje images are classified in four cases in occurrence order. The first Purkinje image (PI) has the larger intensity that is an important feature to make a first eye detection. A second Purkinje (PII), formed by reflection from the rear surface of the cornea, is almost exactly coincident with the first Purkinje image. The light that is not reflected by the cornea passes through the aqueous humor to arrive to the crystalline of the eye. The third Purkinje image (PIII), a virtual image formed by light reflected from the front surface of the lens, is much larger and more diffuse. The fourth Purkinje image (PIV) is formed by light reflected from the rear surface of the crystalline.

In this paper we describe a system and method to produce and detect the first and fourth Purkinje images (PI and PIV) that is based on simple images process. The system is based in infrared LED illumination. The infrared LED illumination is used not only for illuminating the eye region but also for producing the dual Purkinje images (first and fourth Purkinje

images). The goal of this work is to determine the location of both references using a simple algorithm of image processing to determinate the automatic localization of the first and fourth Purkinje with a compact instrument.

14.2 Optical System to Make Purkinje Images

The instrument is based on the projection of infrared light on the cornea. In our case, we make a plate with five infrared LEDs to generate a pattern on the optical systems. This plate is shown in the Fig. 14.3, where we can see five spots where LEDs are positioned for illumination. Each spot is at the same distance ρ from the center of the plate and with a same θ .

In the Figs. 14.4 and 14.5a, b, we can see the complete instrument includes a camera Thorlabs model DCU224, a beam splitter (50:50), a lens of 60 mm and the plate of infrared LEDs. In the computer we record a set of images that we process to find the localization of the Purkinje images (PI and PIV). An example of the images that we obtain with this system is shown in the Fig. 14.5c.

The instrument registers images PI and PIV of the pupil. The infrared illumination LEDs have a dominant wavelength of 840 nm.

14.3 Methodology

First, we describe the generated models of Purkinje images based on human eye using infrared LED illumination. The positions of the first and fourth Purkinje images are in the center of the pupil but not in the center of the image. The first Purkinje images present the larger intensities and we can detect them using a simple image thresholding process. The pupil is

Fig. 14.3 Purkinje plate

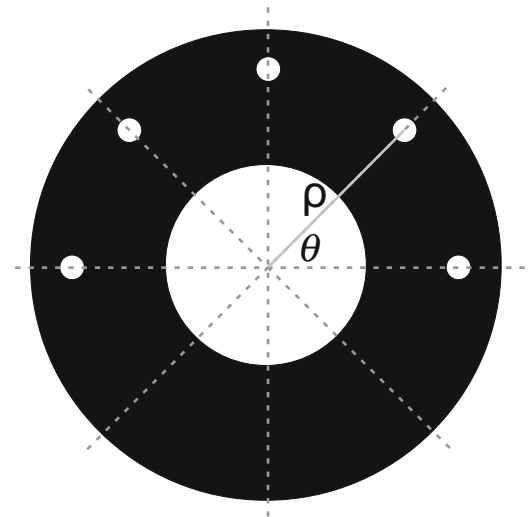
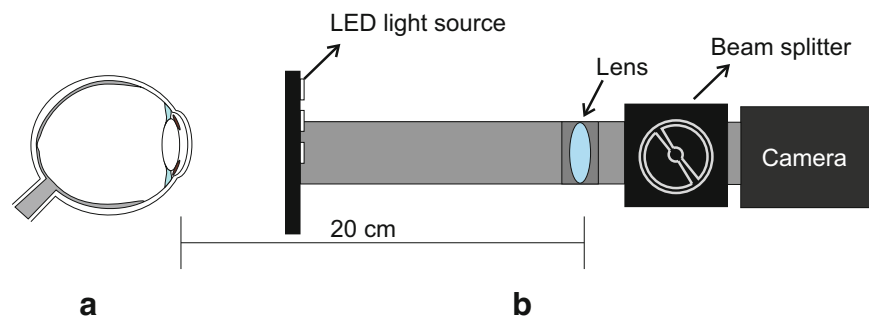


Fig. 14.4 Purkinje image system; (a) Optical human system, (b) Generator and detector of images



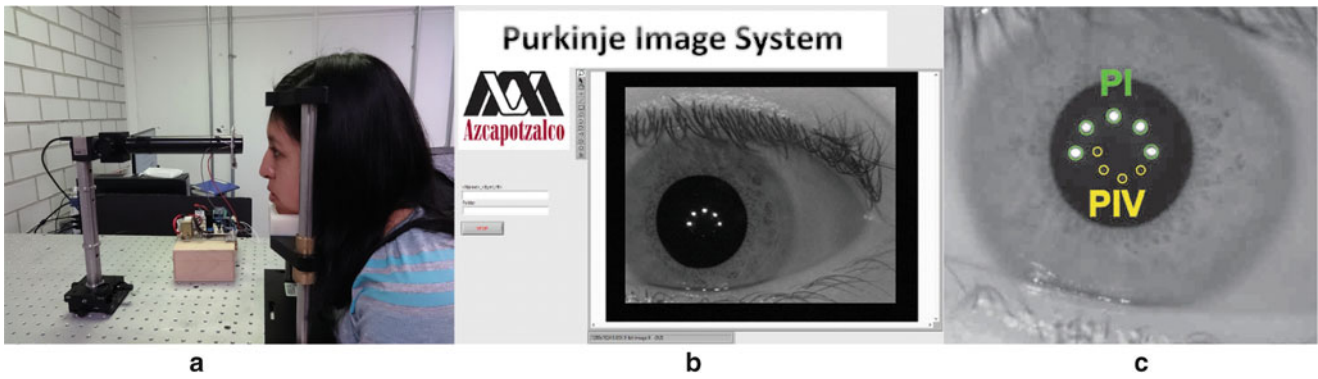


Fig. 14.5 Purkinje generation in the surface of the eye, (a) Optical system, (b) Acquisition software, (c) Purkinje images of the cornea

used to detect the fourth Purkinje image. Our method uses the first Purkinje images of point light sources to determine the localization of the fourth Purkinje images using basic image processing.

The algorithm generated in this work is a series of consecutive steps which allow us to create a localization map of Purkinje images. These steps can be described as follows:

1. Input data to the system. For proper system operation, the image includes the total number of reflections that correspond to the number of LEDs in the experimental arrangement.
2. Change color workspaces. Convert the acquired RGB images to gray color images.
3. Generation of maps of areas of interest, related to the I Purkinje images. Binarization is performed by automatic detection of a threshold value. A subroutine modifies the threshold value until a binarized image with a number of holes equal to the number of LEDs reflected on the pupil (PI).
4. Subimages. Once the area with the first Purkinje images (PI) is located, we generate subimages from the original image where the analysis will be focused. Since the fourth Purkinje images (PIV) are in a smaller area close to the PI, a subimage with PIV is generated.
5. Normalization of subimage intensities. Intensity normalization of the images is done to improve the contrast of the images.
6. Localization of PIV images. To achieve this, it is necessary to perform a second binarization process by thresholding, producing an identification map (coordinates matrix). The coordinates of each centroid are found using a suitable mask for each image. Thus we obtain a matrix of centroids for each of Purkinje image.
7. Coordinates calculation.

The reflections within the acquired image, correspond to the areas with high intensities and these are the zones used to locate the Purkinje images (see the Fig. 14.6).

14.4 Thresholding Process

A binarization function uses a threshold value (Fig. 14.7). See (14.1).

$$I_{U_i} = \begin{cases} 1 & I_i \geq U_i \\ 0 & I_i < U_i \end{cases} \quad (14.1)$$

14.5 Image Segmentation

The threshold value is calculated by Otsu method [10]. This process is carried out in order to generate segments using the number of spots in an the image. By increasing or decreasing that threshold value we can obtain a binarized image where the number of holes corresponds to the reflecting LEDs of the instrument. The segmentation method called FIF (Flood Index

Fig. 14.6 Area of interest within the image obtained by the instrument

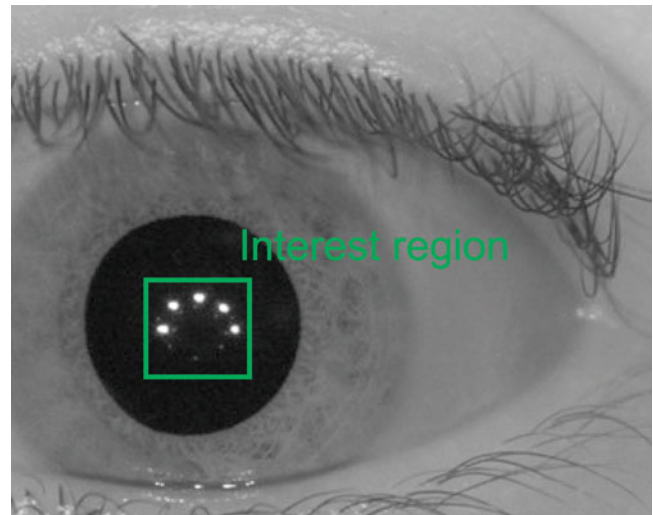


Fig. 14.7 Binarization of image based on a threshold value

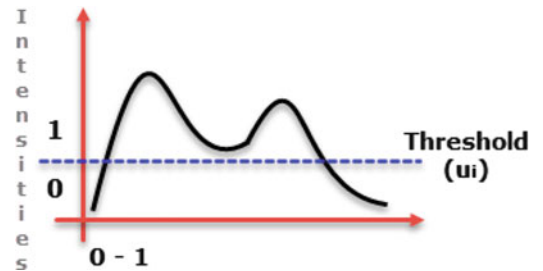


Fig. 14.8 (a) First binarized image. (b) Sub image based on max and min spots coordinates. (c) Sub image (b) double sized. (d) Sub image1. Interest region

Fill) is used to identify the number of holes within the image [11]. FIF sets a different label for each group of pixels (spots). Those labels are used to stop binarization and manage sub images. The binarized image allows the creation of sub images by using the coordinates of the recently located spots as maximum and minimum values for a preliminary sub image. All the information corresponding to the pupil serves to obtain a proper sub image to localize the PIV (see the Fig. 14.8).

Most of noise (irrelevant data) is eliminated from the sub image by setting null values to all elements whose distance from the center of the sub image is greater than a selected ratio as shown in Fig. 14.9.

The subimages are segmented again and a new sub image with the PIV is obtained. The binarization of this new subimage provides a binary image which contains the PIV spots.

Fig. 14.9 Noise reduction within the interest region

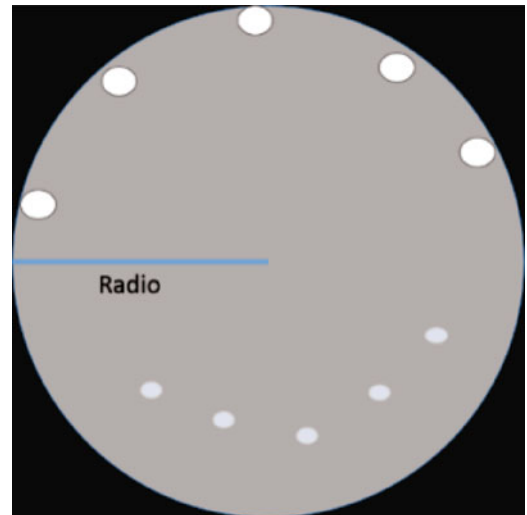
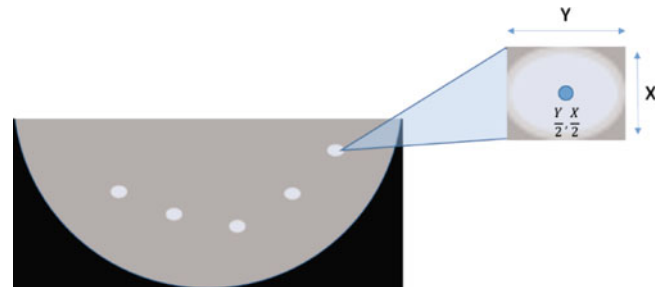


Fig. 14.10 Centroids calculation



14.6 Centroid Calculation

Following a centroid calculation of the spots is done. Figure 14.10 shows an example.

14.7 Results

Next figures show the results to obtain the centroids coordinates of the spots corresponding to Purkinje images IV within a pupil. In the Figs. 14.11 and 14.12, we can see the result of the thresholding process. We separate the PI images from the image.

In Fig. 14.13, the intensities of the PIV are plotted.

In Figs. 14.14 and 14.15, we can see the centroids of the PIV.

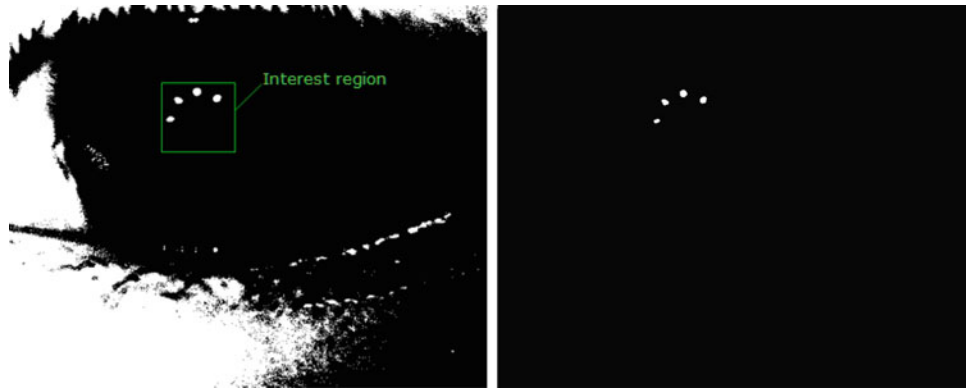


Fig. 14.11 Binarized image and interest region

Fig. 14.12 Sub image based on thresholding result and noise reduction

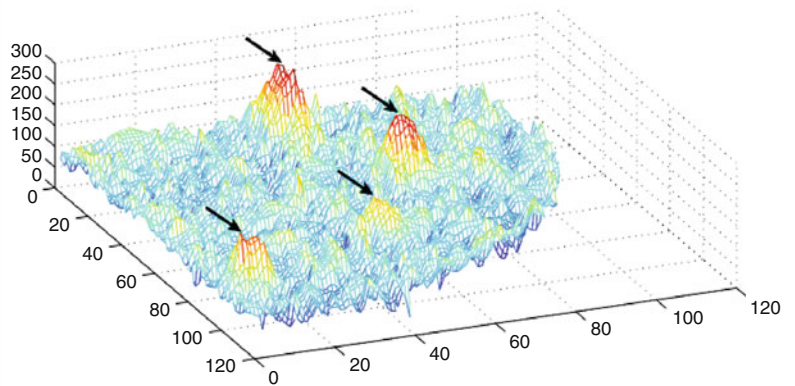
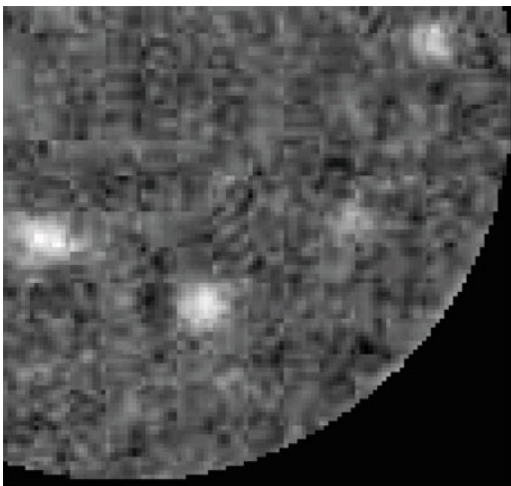
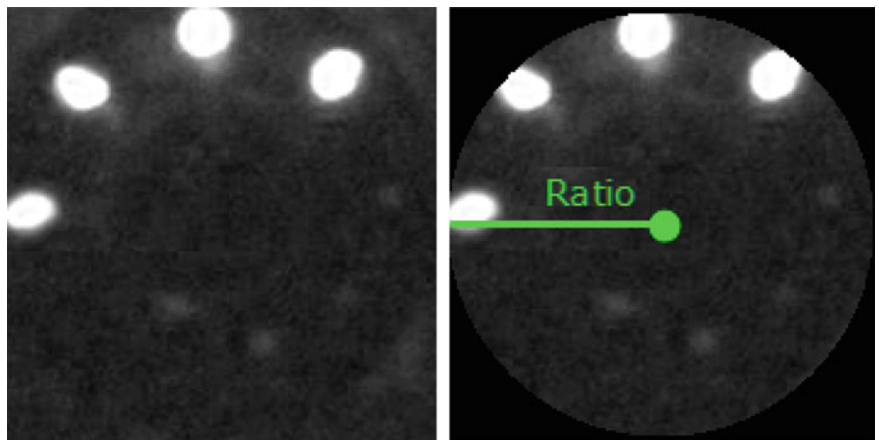


Fig. 14.13 Sub image with PIV and intensities chart. Spots whit highest values correspond to PIV

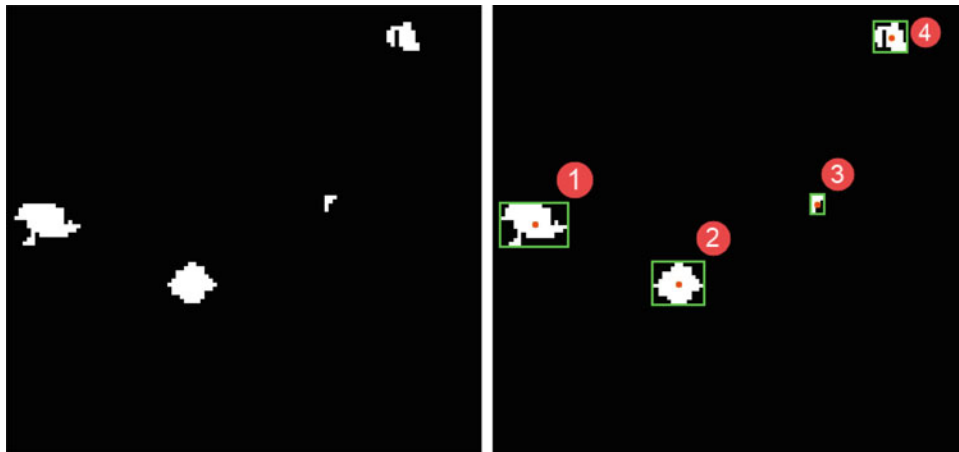


Fig. 14.14 Final binarization and centroid calculation

Fig. 14.15 PIV centroids of the original image



14.8 Conclusions

This paper presents the development of an optoelectronic instrument to acquire images of Purkinje. This is a low cost instrument that includes 940 nm LEDs and a Thorlabs CCD camera. The optical system incorporates an achromatic lens and a cube beamsplitter. In addition, an automatic algorithm identifies the first and fourth Purkinje images. The image is segmented by thresholding. The results are of young individuals with moderate refractive error.

References

1. J.W. Lee, C.W. Cho, K.Y. Shin, E.C. Lee, K.R. Park, 3D gaze tracking method using Purkinje images on eye optical model and pupil. *Opt. Lasers Eng.* **50**(5), 736–751 (2012)
2. J.C. Barry, U.M. Pongs, W. Hillen, Algorithm for Purkinje images I and IV and limbus centre localization. *Comput. Biol. Med.* **27**(6), 515–531 (1997)
3. Hecht, E, in *Optics* (Addison-Wesley, USA, 2002), pp. 467–475

4. B.M. Welsh, C.S. Gardner, Performance analysis of adaptive-optics systems using laser guide stars and sensors. *J. Opt. Soc. Am. A* **6**(12), 1913–1923 (1989)
5. J. Ares, J. Arines, Influence of thresholding on centroid statistics, in *19th Congress of the International Commission for Optics: Optics for the Quality of Life* (2003), pp. 180–181
6. P.A. Piers, E.J. Fernandez, S. Manzanera, S. Norrby, P. Artal, Adaptive optics simulation of intraocular lenses with modified spherical aberration. *Invest. Ophthalmol. Vis. Sci.* **45**(12), 4601–4610 (2004)
7. D.A. Atchison, Design of aspheric intraocular lenses. *Ophthalm. Physiol. Opt.* **11**(2), 137–146 (1991)
8. H.C. Yang, S.K. Chung, N.H. Baek, Decentration, tilt, and near vision of the Array multifocal intraocular lens. *J. Cataract Refract. Surg.* **26**(4), 586–589 (2000)
9. J. Tabernero, A. Benito, V. Nourrit, P. Artal, Instrument for measuring the misalignments of ocular surfaces. *Opt. Express* **14**(22), 10945–10956 (2006)
10. N. Otsu, A threshold selection method from gray-level histograms. *IEEE Trans. Syst. Man Cybern.* **9**(1), 62–66 (1979)
11. G. Hernández-Gómez, Z. Malacara-Hernández, D. Malacara-Hernández, A. Gómez-Vieyra, Hartmann and Hartmann-Shack spot identification and centroid evaluation by a new efficient segmentation and thresholding algorithm, in *8th Ibero American Optics Meeting/11th Latin American Meeting on Optics, Lasers, and Applications* (2013), p. 87855Y

Chapter 15

Ultrasonic Arc Maps and Its Potential Application in Non-destructive Testing

Fabio Tomás Moreno Ortiz, Antonio Hernández Zavala, Alejandro Gómez Hernández, and Noé Amir Rodríguez Olivares

Abstract The ultrasound is a widely extended technique in non-destructive testing (NDT). Some its advantages are: low cost, safety and simplicity to be implemented, environment friendly and reliability. The ultrasound probes are useful to detect gaps, corrosion, breakages, changes of density and impurities in materials. However, the C-Scan used to produce a 3D image is complex and requires the use of a special probe made of a transducers matrix and a powerful computer to run the image processing algorithm. The cross-talk, spurious echoes and the position uncertainty of the reflected point make it harder to locate in the space the true points. This work describes the ultrasonic arc maps (UAM) technique and proposes to use them in NDT. Originally, the UAM was developed in robotics, where it showed good features to locate the true reflected points using a simple pulse-echo transducer. The algorithms for data processing are fast, easier to program and could be embedded in a digital system like a microcontroller or a FPGA.

Keywords Non-destructive testing • Ultrasonic arc map • Single transducer • Angular resolution • Position uncertainty

15.1 Introduction

The fast development of ultrasonic systems due to technological advances allows us to count on fully computerized systems. In addition, they have the ability to manipulate the ultrasonic beam with special techniques as ultrasonic phased array. It is also possible to get accurate fault information with ultrasound diffraction information. Currently there are ultrasonic techniques based on impedances and resonances, which allow specific applications in the inspection of composite materials [1].

On robotics, the ultrasound is employed to detect and avoid obstacles. The most common type of sensor is the pulse-echo SONAR [2], because of its low cost and reliability. This type of sensor provides good distance measuring but has a wide positional uncertainty caused by the wave dispersion in the far zone [3, 4]. This uncertainty is commonly called angular resolution $\delta\beta$ or bearing [5] and defines the distance where it is not possible to distinguish two objects placed on the same distance and on different positions (Fig. 15.1). The wide of position uncertainty is determined by the divergence angle θ_0 of the beam spread and is inherent to all wave-based sensors. When a single pulse-echo transducer is used, the position uncertainty could be represented by a circular arc on the plane or by a spherical cap on the space.

According to ultrasound waves propagation, the ultrasonic inspection types can be classified into two: straight beam and angle beam. The straight beam (90°) by the pulse-echo technique works as transmitter and receiver, the signals transmission is perpendicular to the surface of the inspection part. The angle beam (45° , 60° and 70°) uses a wedge to emit the desired angle signals, the wedge allows inspections in areas that are not accessible by straight beam. A common use of angle beam inspection is in welding [6].

F.T. Moreno Ortiz (✉)

División de Tecnologías de Automatización e Información, Universidad Tecnológica de Querétaro, Querétaro, Mexico

Centro de Investigación en Ciencia Aplicada y Tecnología Avanzada Unidad Querétaro, Instituto Politécnico Nacional, Querétaro, Mexico

e-mail: famoreno@uteq.edu.mx

A. Hernández Zavala

Centro de Investigación en Ciencia Aplicada y Tecnología Avanzada Unidad Querétaro, Instituto Politécnico Nacional, Querétaro, Mexico

e-mail: anhernandez@ipn.mx

A. Gómez Hernández • N.A. Rodríguez Olivares

División de Tecnologías de Automatización e Información, Universidad Tecnológica de Querétaro, Querétaro, Mexico

e-mail: alejandro.gomez@uteq.edu.mx; noe.rodriguez@uteq.edu.mx

Fig. 15.1 Angular resolution.
The objects a and b cannot be distinguished

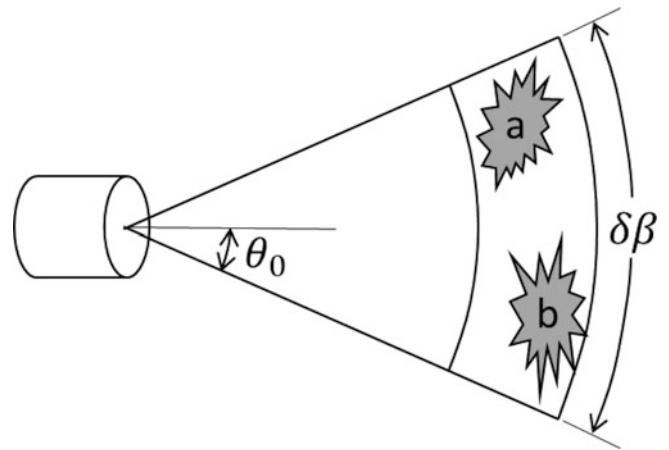
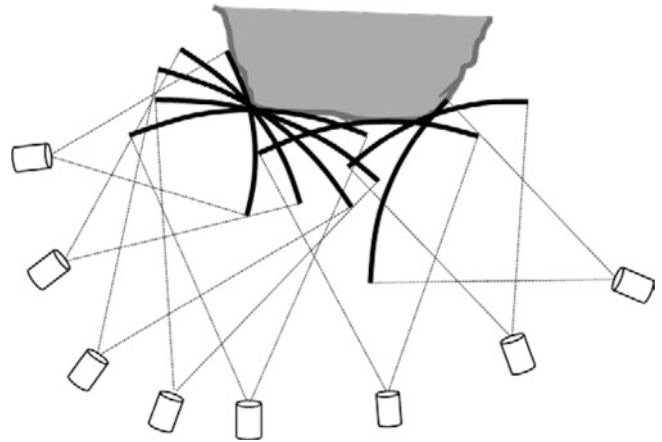


Fig. 15.2 Ultrasonic arc map



This paper is organized as follows: The second part describes the UAM and three representative techniques. The third part relates to our hypothesis and the potential application of UAM in NDT. Finally, in the fourth part we show the results of the experiment and our conclusions.

15.2 Ultrasonic Arc Maps

For robotics purposes, the angular uncertainty, the cross-talk and the specular reflection makes very hard to distinguish non-perpendicular planes, corners, edges, curves and thin objects. To solve this issue, some authors have proposed the Ultrasonic Arc Map (UAM). In these technique, the uncertainty is represented by a rasterized circular arc on a mesh map. Normally, a single pulse-echo transducer is employed to scan the surroundings and its position and orientation are indefinitely changing by the robot movements. The generated arcs reinforce the point where many of them are crossing (Fig. 15.2).

To find the “real points”, some UAM techniques only require the range provided by the SONAR, and the position and orientation of the SONAR provided by the navigation system. Three of those techniques are described next.

15.2.1 Spatial Voting and Threshold (VT)

This technique is described in [7]. To select the true points and discard the false echoes, each measured range is expanded to an uncertainty arc. Those arcs are rasterized and placed on the mesh map. Each pixel from an arc has a value of 1. When a specific pixel is crossed by several arcs, the value from each arc is added to the others (voting), then the pixel has a number of votes that corresponds to the number of arcs crossing on this point (Fig. 15.3). The pixels with a number of votes greater than the threshold are selected as the true points.

Fig. 15.3 Spatial voting, the *black dots* mark the place where several arcs are crossing

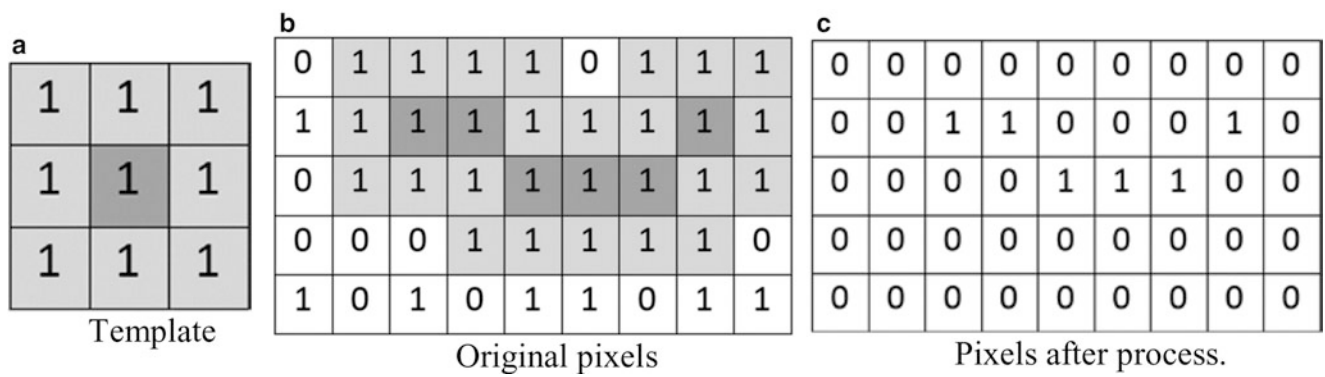
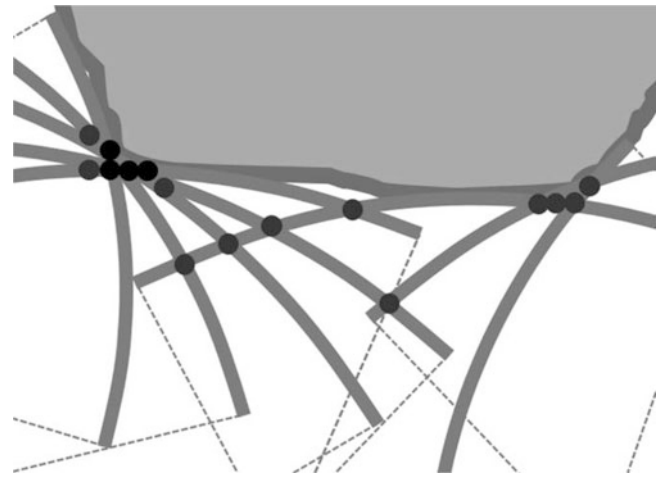


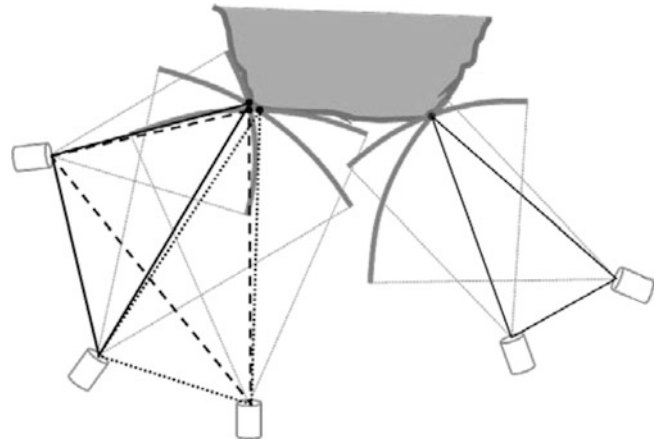
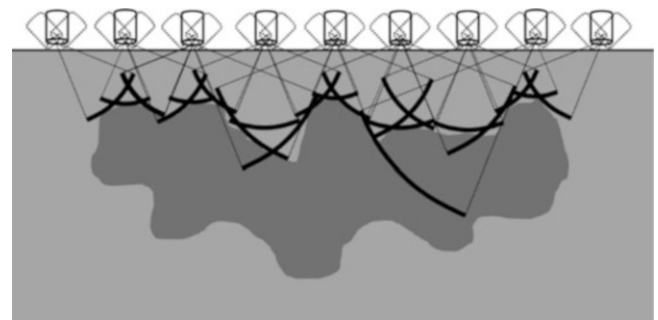
Fig. 15.4 Thinning operation. (a) Template, (b) original pixels, (c) pixels after process

15.2.2 Morphological Processing (MP)

In this technique, each pixel from the arc positioned on the mesh map has a value of 1. A morphological process is employed to discard false points. The thinning operation is applied as in [8]. The operation algorithm takes a central pixel marked by 1 and checks the surrounding pixels delimited by a template (Fig. 15.4a); if the number of neighbor pixels marked by 1 is larger than the thinning parameter, then the central pixel is considered as a true point and its value remains as 1 (Fig. 15.4b). The central pixel which has many neighbors with 0, it is not enough supported, its value is shifted to 0 (Fig. 15.4c).

15.2.3 Triangulation-Based Fusion (TBF)

This technique relies on triangulation of ranges measured from different transducer locations and was employed in [9] to extract the point position marks and achieve the mobile robot localization. The main idea is to locate the common reflected point through the triangle formed by the two transducer positions and the intersection between the uncertainty arcs (Fig. 15.5). To achieve this, first a range is taken from a start place. Then the transducer is moved to a new place located at a minimum distance and the next range is taken. If the measurement creates a crossing between arcs determined by triangulation, a hypothetical point is established to the cross point and is stored with a value of 2. After that, the transducer is moved again and the process is repeated. When a crossing does not take place, the hypothesis point is established at the middle of the uncertainty arc and the hypothesis value is initialized with 1. Each time that hypothesis point matches with another, its value is increased by 1. The hypothesis point who has a value less than a threshold value is discarded.

Fig. 15.5 Triangulation**Fig. 15.6** UAM at NDT

15.3 Potential Application at NDT

In basic inspection techniques, a significant portion of the signals information is obtained by the time difference of the maximums of the echoes. With that maxima, it is possible to know the approximate thicknesses for location of indications in a material; this technique is useful in lamination, corrosion, intermediate echoes, and uniform indications. If the indications have this morphology, it is possible to try to reconstruct the shaped of the defect by any reconstruction technique, such as ultrasonic arches (Fig. 15.6).

In NDT, the use of a single transducer or probe is the most extended technique to detect corrosion, gaps or breakages. The single probe is able to locate and estimate the size of a failure. To produce images about the shape of the failure is necessary the use of transducer arrays [10] and a complex computer processes to drive the array, process the signals and generate the image. Our hypothesis is that it is possible make an image of the failure employing the time of flight, the orientation and the position of a single transducer. The complex computing of the signal processing or the sequence for transducer arrays are avoided by using UAM techniques.

15.4 Experiment

Some issues to develop the method are the design of the wedge that enables rotate the transducer and the system to calculate the orientation and the position of the transducer. We propose the use of an inertial measurement unit (IMU) to estimate the orientation and position. To test the idea, we built a system composed by an IMU, a single transducer and a communication interface. The system was moved and rotated at the same time over a straight line to scan an edge. Using the range provided by the transducer and the orientation estimated by the IMU measures, we applied the VT technique (Fig. 15.7a) and obtained an image of the edge (Fig. 15.7b).

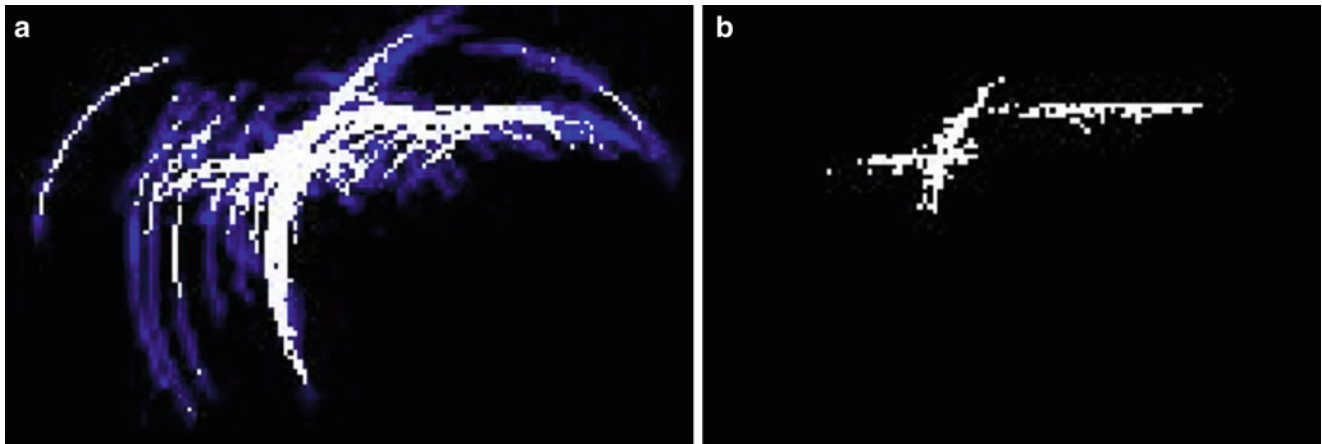


Fig. 15.7 Test of on an edge. (a) UAM, (b) pixels after VT technique

15.5 Conclusion

The results of the ultrasound test demonstrate that it is possible to make an image of a shape employing only the time of flight and the inertial measures and this encourages us to continue the research. Future work will be related to improving the accuracy on the estimation of the orientation and position through simultaneous localization and mapping (SLAM), extend the UAM techniques to three dimensions and redesign the wedge that enables the rotation.

Acknowledgments This work was supported in Mexico by the Instituto Politécnico Nacional (IPN), the Universidad Tecnológica de Querétaro (UTEQ) and the Consejo Nacional de Ciencia y Tecnología (CONACyT).

References

1. J. Sagrero Rivera, Manual Ultrasonido Industrial Nivel I, Centro de Ingeniería y Desarrollo Industrial, 2012
2. Y. Xiaole, G. Lichen, Time-delay estimation of ultrasonic echoes based on the physical model matching, in *8th IEEE International Conference on Automation Science and Engineering*, Seoul, 2012
3. A. Elfes, Sonar-based real-world mapping and navigation. *IEEE J. Robot. Autom.* **3**(3), 249–265 (1987)
4. J. Borenstein, Y. Koren, Histogrammic in-motion mapping for mobile robot obstacle avoidance. *IEEE Trans. Robot. Autom.* **7**(4), 535–539 (1991)
5. R.E. Hansen, Introduction to Sonar, Universitetet i Oslo, 26 Sep 2012. http://www.uio.no/studier/emner/matnat/ifi/INF-GEO4310/h12/undervisningsmateriale/sonar_introduction_2012_compressed.pdf. Accessed 26 Sept 2013
6. Olympus Corporation, Ultrasonic transducers technical notes, 2011
7. B. Barshan, Ultrasonic surface profile determination by spatial voting. *Electron. Lett.* **35**(25), 2232–2234 (1999)
8. D. Baskent, B. Barshan, Surface profile determination from multiple sonar data using morphological processing. *Int. J. Robot. Res.* **18**(8), 788–808 (1999)
9. O. Wijk, H.I. Christensen, Localization and navigation of a mobile robot using natural point landmarks extracted from sonar data. *Robot. Auton. Syst.* **31**(1–2), 31–42 (2000)
10. B.W. Drinkwater, P.D. Wilcox, Ultrasonic arrays for non-destructive evaluation: a review. *NDT & E Int.* **39**(7), 525–541 (2006)

Chapter 16

Phase-Shifting Generated by Wavelength Modulation by Means of Switching On-Off a Laser Diode

Uriel Rivera-Ortega and Joris Dirckx

Abstract It is well known that one of the features of a laser diode is its wavelength tunability which can be modulated with a variable injection current and/or temperature of its active region. For many industrial and scientific applications it is desirable that the laser gets stabilized. In this paper, on the contrary, the laser diode is turned on-off for a short period of time. The generated peak variations of voltage and temperature will cause a modulation of its wavelength. This modulation is used to add phase-shifts in an unbalanced Twyman-Green interferometer and by using Carré algorithm the phase of the resulting interference wave will be retrieved.

Keywords Wavelength modulation • Optoelectronics • Interferometry • Phase-shifting

16.1 Introduction

Phase-shifting interferometry (PSI) [1] is a technique widely used for precise optical testing. In PSI, the phase difference between the interfering beams is either changed in discrete steps or it is changed at a constant rate. The irradiance due to the interference of two waves for each point (x, y) can be expressed by

$$I_j(x, y) = a(x, y) + b(x, y) \cos [\phi_0(x, y) + \alpha_j], \quad (16.1)$$

where $a(x, y)$ is a bias intensity, $b(x, y)$ is a modulation intensity, $\phi_0(x, y)$ is the phase difference between the two interfering waves and α_j with $j = 0, 1, \dots, N - 1$ is the phase step generated to obtain N equations. In this way a set of N equations (interferograms) changed in phase are created; then a $N \times 3$ system is formed that can be solved when $N \geq 3$ [2, 3]. There are many well-known methods used to generate α_j for example: changing the optical path difference by displacing a mirror with a piezoelectric transducer [4, 5] or changing the refraction index by means of tilting a glass plate [6], by displacing a diffraction grating, by changing the polarization state and others [7, 8].

An alternative method to generate phase steps is by using the tunability of a laser diode (LD) [9–11], in which the wavelength of a single-mode laser can be changed ($\Delta\lambda$) by the variation of the injection current and/or the temperature of active region. It is possible to modulate the laser current by applying analog voltages to its input, producing a phase shift in the interferograms [12]. This characteristic of the LD has been used for instance in speckle shearing interferometer [13], distance measurements [14], surface contouring [15], digital phase measuring [16], among others.

It is known that vibrations, random noise, temperature fluctuations and air pressure can destabilize the frequency of a laser diode, which is directly related with its wavelength by $\lambda = c/\nu$, where λ is its wavelength, ν its frequency and c the velocity of light in vacuum. The destabilization is undesirable for practical applications, and some methods proposed to overcome this issue [14, 15].

The aim of this manuscript is to present a low-cost and easy to implement method suitable to generate phase-shifting under the scheme of an unbalanced Twyman-Green interferometer by turning on-off a laser diode used as its light source.

U. Rivera-Ortega (✉) • J. Dirckx
Laboratory of Biomedical Physics, University of Antwerpen, 171, Antwerpen, Belgium
e-mail: mecatronica00@hotmail.com

16.2 Methodology

A schematic diagram of the present proposal is shown in Fig. 16.1, in which for a normal incidence the corresponding path difference between the two arms of the interferometer is the distance d .

The respective phase difference is given by $\phi_0 = 2\pi nd/\lambda_0$, where n is the refractive index of the medium, and λ_0 is the operating wavelength of the light source. If the wavelength is changed from λ_0 to $\lambda_0 + \Delta\lambda$ by the modulation of the input voltage (ΔV), the corresponding phase-step variation can be approximated as

$$\Delta\phi \approx 2\pi nd \left(\frac{\Delta\lambda}{\lambda_0^2} \right). \quad (16.2)$$

It can be noted from the above equation that with a larger optical path difference (d) between the interfering beams, the voltage ΔV needed to modulate the wavelength $\Delta\lambda$ causing a $\Delta\phi$, will be proportionally less and vice versa. For this reason an unbalanced Twyman-Green interferometer setup was chosen. Then the phase-step corresponding to the j th sampled intensity is given by

$$\alpha_j \approx j2\pi nd \frac{\Delta\lambda}{\lambda_0^2}. \quad (16.3)$$

16.3 Experimental Setup

The light emitted by a laser diode (LD) with an operating wavelength λ_0 of 635 nm and 10.5 mW (Coherent model 31-0334-000) is expanded and filtered (SF) with a microscope objective (MO) and a pinhole (PH) respectively and collimated by means of lens L as shown in Fig. 16.2a.

A plane wavefront is used as the input of a Twyman-Green (TG) interferometer setup with fixed reflected mirrors M1 and M2 with an unbalanced optical path difference and a beam splitter (BS) with a polarizer (P) at its output to decrease the intensity of the interference pattern; with a CCD camera (FOculus FO442B) to record the output interferograms. The fringes

Fig. 16.1 Schematic diagram of the proposed setup

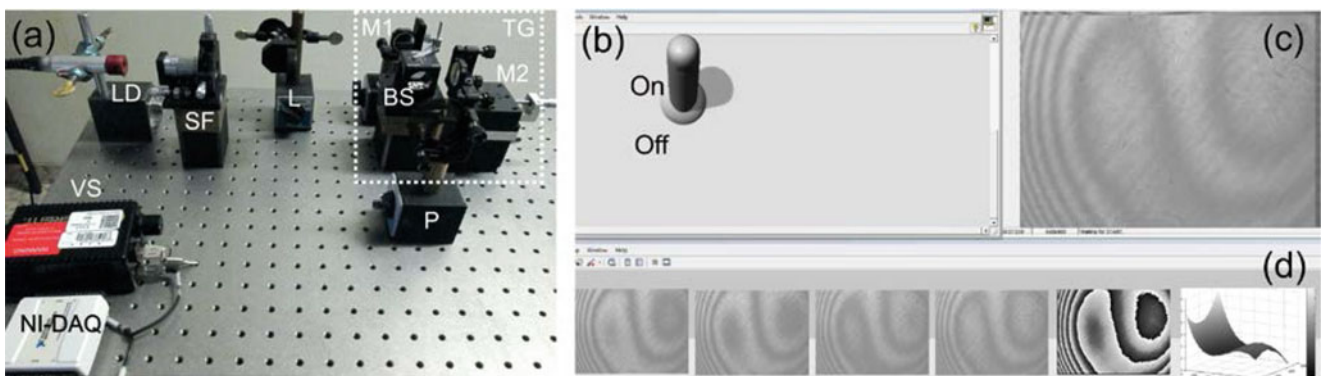
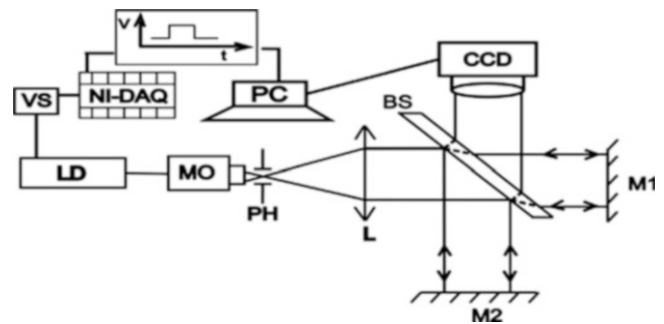


Fig. 16.2 (a) The experimental setup and (b–d) the user interface designed in LabView

of the interference pattern are obtained by tilting the reflected mirrors without the use of a phase object. The tunability of the wavelength is achieved by turning on-off the laser by means of a pulse voltage signal (0–2.3VDC) from a Data Acquisition Device (NI-USB6008) through an RCA input plug directly connected to the voltage source (VS) and to the laser.

The emulation of the on-off switching of the laser diode is done by means of a pulse voltage signal controlled with a vertical toggle switch in LabVIEW (Fig. 16.2b). The control of the CCD camera (Fig. 16.2c), the recordings of the phase-shifted interferograms and the calculation of the wrapped and unwrapped phase of the interfering waves are done via Matlab-scripts. Once the unwrapped phase has been calculated, M2 is manually tilted to get a different interferogram, then the laser is switched again to generate more phase-shifted interferograms from which the new unwrapped phase is calculated (Fig. 16.2d). Once the process is completed the laser is automatically switched off; repeating the whole process a few more times.

16.4 Phase Calculation

When the phase-shiftings have been achieved by any of the methods mentioned in Sect. 16.1, the 4-step Carré [17] algorithm has been used because it allows calculating the phase $\phi_0(x, y)$ from a set of four phase-shifted interferograms $I_{1\dots 4}(x, y)$ without explicitly knowing the value of the phase-shift among them.

$$\phi_0 = \arctan \left\{ \frac{\sqrt{[(I_1 - I_4) + (I_2 - I_3)][3(I_2 - I_3) - (I_1 - I_4)]}}{(I_2 + I_3) - (I_1 - I_4)} \right\}, \quad (16.4)$$

where α_j is unknown and needs to remain constant during every irradiance measurement. As this proposal uses the wavelength changes due to the instability of the laser diode, it is not possible to have a control of the generated phase-shift, however it will be demonstrated that the value of the phase-shift between interferograms still permits the calculation of the wrapped phase using (16.4).

It is well known that two important requirements for PSI are the conservation of the visibility of the fringes and a constant phase-step value between interferograms [3]. As it was mentioned, it is not possible in this setup to have control of the phase-shift between each consecutive interferogram; nevertheless the wrapped and unwrapped phase [18] has been successfully calculated.

Figure 16.3a shows in red the 8-bit grayscale value for a cross section along the x-direction passing through the center in the y-coordinate of each adjacent interferogram (resized to 480×480 pixels for evaluation purposes) indicating with a straight orange line the corresponding mean value as well as the visibility. In this figure, the estimated values of the phase difference between each pair of the four consecutive interferograms used for the wrapped phase calculation (16.4) are also

Fig. 16.3 (a) Visibility and (b) phase-step measurements from the four adjacent interferograms used for the phase calculation

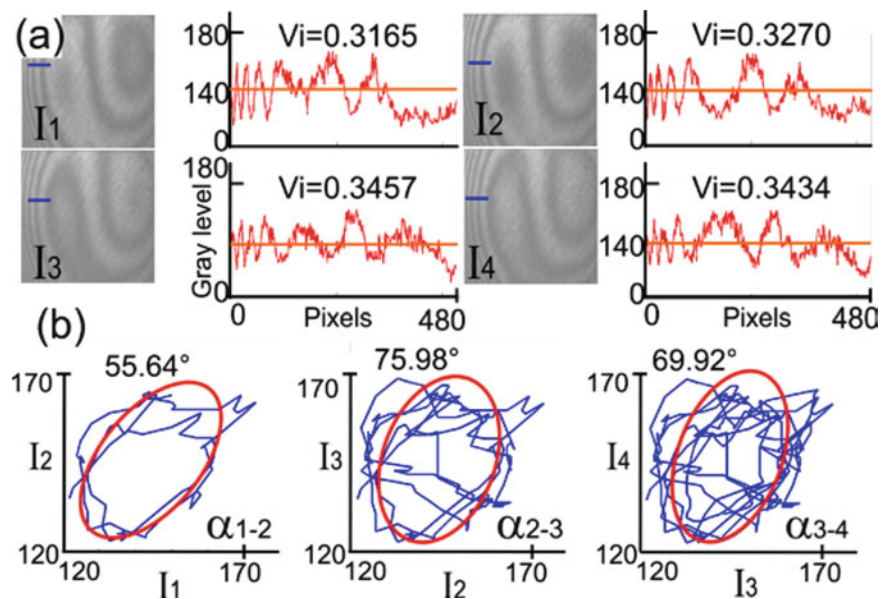
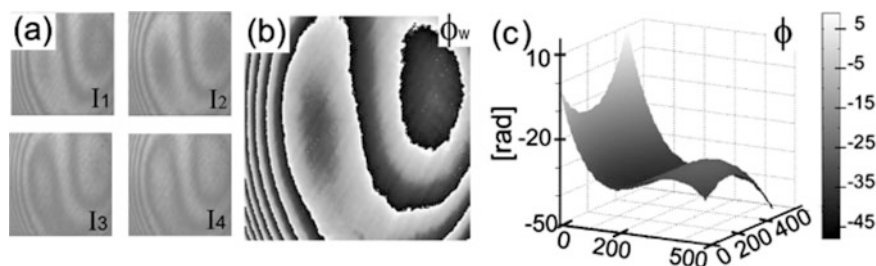


Fig. 16.4 (a) Four phase-shifted interferograms and the corresponding (b) wrapped and (c) unwrapped phase



indicated. This has been achieved by using the method introduced by Farrell [19], which utilizes Lissajous figures and their adjustment to intensity ellipses. In this proposal three pair of spatial intensity profile domain (I_1, I_2) , (I_2, I_3) , (I_3, I_4) were taken in order to obtain the Lissajous figures by plotting from each pair, one profile against the other. The resulting figure and its fitting ellipse is computed to calculate the phase differences α_{1-2} , α_{2-3} , α_{3-4} . Figure 16.3a shows the intensity domain (blue straight line) data from each interferogram used to form the experimental intensity ellipse (Fig. 16.3b, blue lines), while the ellipses plotted in red show the ellipses formed with the adjusting method.

It can be observed from the above figure that the visibility remains approximately constant but not the phase-shift between two adjacent interferograms as it was expected. The calculated wrapped and unwrapped phases corresponding to the four consecutive interferograms (Fig. 16.4a) are shown in Fig. 16.4b–c.

16.5 Conclusions

In this manuscript it has been presented a simple method for phase-shifting and phase retrieval with a laser diode under the scheme of an unbalanced Twyman-Green interferometer setup. Unlike the common stabilization requirements for industrial or researching applications, the phase-shifts generated by the frequency variations due to the on-off switching of the laser in a short period of time were used to calculate the phase difference of the interfering waves. In the present proposal the value of the phase-shift is not controlled or modified causing errors in the phase calculation by using Carré algorithm. However it could still be possible to obtain an accurate wavefront because techniques and algorithms have been developed for non-constant phase displacements [20], or to allow the estimation of the relative differences in the unknown phase-step [21]. A commercial laser diode and software have been used for the presented optical setup but a simple laser pointer manually switched can be perfectly used which could considerably reduce the cost of implementation, as well as by the simple optical arrangement.

Acknowledgement U. Rivera-Ortega appreciates the postdoctoral scholarship from Consejo Nacional de Ciencia y Tecnología (México) under grant 230729.

References

1. D. Malacara, *Optical Shop Testing* (Wiley, New York, 2007)
2. J. Schwider, Advanced evaluation techniques in interferometry, in *Progress in Optics*, vol. XXVIII, ed. by E. Wolf (Elsevier, Amsterdam, 1990), pp. 274–276
3. K. Creath, Phase-measurement interferometry techniques, in *Progress in Optics*, vol. XXVI, ed. by E. Wolf (Elsevier, Amsterdam, 1988), pp. 358–366
4. Y.Y. Cheng, J.C. Wyant, Phase shifter calibration in phase-shifting interferometry. *Appl. Opt.* **24**, 3049–3052 (1985)
5. J. Cheng-Chung, S. Yi-Lin, T. Chien-Jen, L. Yeuh-Yeong, C. Chun-Ming, Y. Chii-Rong, Determination of displacement with a piezoelectric transducer using phase-shift algorithms. *Opt. Rev.* **16**, 170–172 (2009)
6. Q.Z. Yang, B. Zhao, Principle of the moving mirror-pair interferometer and the tilt tolerance of the double moving mirror. *Appl. Opt.* **47**, 2486–2493 (2008)
7. T. Suzuki, R. Hioki, Translation of light frequency by a moving grating. *J. Opt. Soc. Am.* **57**, 1551 (1967)
8. T. Kiire, S. Nakadate, M. Shibuya, Phase-shifting interferometer based on changing the direction of the linear polarization orthogonally. *Appl. Opt.* **47**, 3784–3788 (2008)
9. Y. Ishii, R. Onodera, Laser-diode phase-shifting interferometer insensitive to the changes in laser power. *Proc. SPIE* **2544**, 173–176 (1995)
10. Y. Ishii, Phase measuring interferometry with a tunable semiconductor laser. *Proc. SPIE* **0813**, 7–8 (1987)
11. U. Rivera-Ortega, J. Dirckx, On-off laser diode control for phase retrieval in phase-shifting interferometry. *Appl. Opt.* **54**, 3576–3579 (2015)

12. T. Suzuki, T. Adachi, O. Sasaki, S. Choi, Phase-shifting laser diode interferometer using pulse modulation. *Appl. Opt.* **51**, 4109–4112 (2012)
13. J.-R. Huang, H.D. Ford, R.P. Tatam, Heterodyning of speckle shearing interferometers by laser diode wavelength modulation. *Meas. Sci. Technol.* **7**, 1721–1727 (1996)
14. A. Hafidi, P. Pfeifer, P. Meyrueis, Tunable laser diode for absolute distance measurement. *Proc. SPIE* **3479**, 339–344 (1998)
15. R.P. Tatam, J.C. Davies, C.H. Buckberry, J.D.C. Jones, Holographic surface contouring using wavelength modulation of laser diodes. *Opt. Laser Technol.* **22**, 317–321 (1990)
16. Y. Ishii, J. Chen, K. Murata, Digital phase-measuring interferometry with a tunable laser diode. *Opt. Lett.* **12**, 233–235 (1987)
17. Q. Kema, S. Fangjun, W. Xiaoping, Determination of the best phase step of the Carré algorithm in phase shifting interferometry. *Meas. Sci. Technol.* **11**, 1220–1223 (2000)
18. K. Itoh, Analysis of the phase unwrapping problem. *Appl. Opt.* **21**, 2470 (1982)
19. C.T. Farrell, M.A. Player, Phase-step insensitive algorithms for phase-shifting interferometry. *Meas. Sci. Technol.* **5**, 648 (1994)
20. A. Téllez-Quiñones, D. Malacara-Doblado, Inhomogeneous phase shifting: an algorithm for nonconstant phase displacements. *Appl. Opt.* **49**, 6224–6231 (2010)
21. H. Guo, M. Chen, Least-squares algorithm for phase-stepping interferometry with an unknown relative step. *Appl. Opt.* **44**, 4854–4859 (2005)

Chapter 17

Index of Refraction Measurements in Liquid Substances of Full Field Using Holographic Interferometry

Carlos Guerrero-Mendez, Tonatiuh Saucedo-Anaya, M. Araiza-Esquivel, Enrique De la Rosa, and Carlos Olvera-Olvera

Abstract We present a novel method based on Digital Holographic Interferometry to detect slight physical variations of refractive index with high sensitivity in liquid substances. The technique is grounded in the measurement of a phase difference between two reconstructed wavefields. The optical system was tested using a series of sodium chloride (NaCl) solutions to detect a variation in its physical property such as concentration. A first hologram records a wavefront coming from the light scattered by a common cylindrical glass container filled with certain NaCl solution. Later, a second hologram is recorded when the solution mentioned above slightly changes its concentration. The difference between the phase maps obtained from the correlation from the two holograms will provide information about a refractive index variation, which is directly related to a concentration change. The achieved results have proven to be more accurate and faster to get than with other techniques. The process requires just a few special optical elements and is able to measure the three-dimensional distribution of the refractive index of a sample. This method can be extended to identify adulteration in liquids, measure the variation in refractive index in gaseous flames, apart from analyzing and visualizing the mechanical properties of a liquid sample.

Keywords Digital holographic interferometry • Phase measurement • Refractive index • Phase difference • Non-destructive methods

17.1 Introduction

Physical properties of liquids such as concentration, weight, color and others are important parameters that can be used as an identification tool or “fingerprint” of some solutions [1, 2]. Likewise analysis of the variations of one or more of such parameters is important to some areas of science. For example, in medicine, the study of certain physiological fluids (like urine) is an important aspect that may indicate the state of health of the body [3]. Generally speaking, detailed analysis of any variations in parameters in a medical solution can mark the difference for a suitable treatment of a disease when necessary [4]. On the other hand, adulteration problems in many commercial substances have increased in the last days, and we require reliable and simple techniques to detect changes of the liquid properties that can help controlling adulteration of liquids [5].

Optical techniques are able to detect changes in concentration of liquid solutions through measurements of the unique optical parameter of a medium called refractive index [6, 7]. The typical optical technique to determine a refractive index utilizes the displacement of the angle of a beam refracted by a sample, and these methods use a prism [8–11], square [12, 13] and special containers [14]. Additionally, these methods are easy to implement and understand, and require few optical elements. However the refracted angle is difficult to measure, and ultimately you can only make a good estimation of the measured angle, which decreases the accuracy of measurements and we can only get the refractive index in the illuminated region [15].

Advanced optical techniques of full-field, non-destructive, non-contact, non-invasive nature with a metrology potential to detect a variety of physical parameters variation in fluids with high resolution and stability have been developed [16–18]. These are called Schlieren, Shadowgraph, Interferometry techniques, from which DHI arised [19].

C. Guerrero-Mendez (✉) • M. Araiza-Esquivel • E. De la Rosa • C. Olvera-Olvera
Doctorado en Ciencias de la Ingeniería, Facultad de Ingeniería Eléctrica, Universidad Autónoma de Zacatecas,
Av. Ramón López Velarde #801, Zacatecas C.P. 98000, Mexico
e-mail: capacti@gmail.com

T. Saucedo-Anaya
Unidad Académica de Física, Universidad Autónoma de Zacatecas, Calzada Solidaridad Esq. Con Paseo La Bufa S/N,
Zacatecas C.P. 98060, Mexico

Important works have established methods to measure the refractive index values using DHI [20], which may be related with the concentration of the liquid solution [21, 22]. However, these researches consider the thickness of the container as known.

In this work we present a simple, fast, full-field, non-destructive, high-precision technique to measure the refractive index of a liquid solution. The method can detect slight differences in concentration of liquid mixtures, through the relationship between concentration and refractive index. The method detects differences on the order of $\pm 0.007\%$ with the thickness of the mixture container unknown. The system was tested using sodium chloride solutions. The obtained results show consistence with data published in [23].

17.2 Principles and Experimental Setup

The experimental setup is shown in Fig. 17.1. A monochromatic light coming from He-Ne laser with a wavelength $\lambda = 543\text{ nm}$ and a maximum output power of 15 mW is divided into two beams by a Beam splitter BS1. The transmitted beam (called “an object beam”) impinges on a mirror M1 and is reflected towards the lenses L1, L2 and the diffuser D1, in such a way that it illuminates the common glass tube that contains the liquid sample S to be analyzed. Part of the light enters through a rectangular aperture A1 and is collected by a positive lens L3 that forms the image of the tube with the sample in the Charge-Coupled Device (CCD) sensor. The reflected beam (named “the reference beam”) travels through a single mode optical fiber SSMF1, and is sent into the cube beam splitter BS2 placed in front of the CCD in such a manner that it interferes with the “object beam” in the CCD sensor. As an initial step, a hologram (H1) is recorded coming from the first mixture sample (named s_1). The CCD is a mono color sensor with 1280×1024 pixels (1.3 MP). During the experiment the temperature was controlled at $20\text{ }^\circ\text{C}$. The wavefront scattered by the glass tube in this first state can be represented as a complex amplitude as $U_1(x, y) = u_1(x, y)\exp[i\varphi_1(x, y)]$, with $u_1(x, y)$ the real amplitude and $\varphi_1(x, y)$ the phase.

A second hologram (H2) is recorded when the solution in the tube is slightly modified in its concentration (creating the sample s_2). This second state or mixture in the glass is represented as $U_2(x, y) = u_2(x, y)\exp[i(\varphi_1(x, y) + \Delta\varphi(x, y))]$ or simply $U_2(x, y) = u_2(x, y)\exp[i\varphi_2(x, y)]$. The phase map from each hologram is calculated using the method of the Fourier-transform [24, 25]. Figure 17.2a shows the hologram of the common glass tube filled with a sample liquid. Fig. 17.2b shows one example of the Fourier-transform of an intensity distribution recorded with the arrangement shown in Fig. 17.1. We can filter out the central term and one of the images of the aperture and keep the other as shown in Fig. 17.2c.

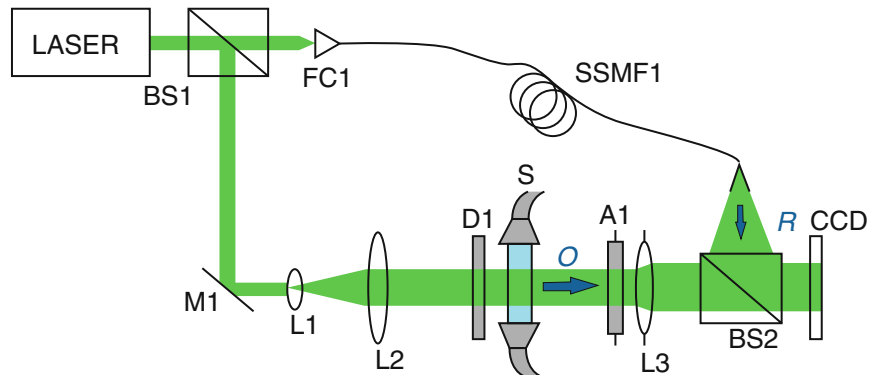
The phase of a wavefront is related to the optical path length δ via $\varphi = 2\pi\delta/\lambda$. This path length is linked with the morphology and physical properties of the transmitting medium as $\delta = nd$, where n is the index refraction and d as the thickness of the sample. According to cylinder geometry, the phase of a hologram can be described as:

$$\varphi = k[(d_i - d_o)*n_g + d_i*n_s],$$

where $k = 2\pi/\lambda$; d_i and d_o are the inner and outer diameters of the glass tube respectively; n_s and n_g are the known refractive indices of the mixture and the glass respectively. See Fig. 17.3.

To get a quantity value of the refractive index difference between any two liquid samples, called s_1 and s_2 , we use their phase terms to calculate a phase difference ($\Delta\varphi_{s_2-s_1} = \varphi_{s_2} - \varphi_{s_1}$) and generate a phase map described as:

Fig. 17.1 Experimental setup using the DHI. BS1, BS2 cube beam splitters, FC1 fiber collimator, M1 mirror, L1, L2, L3 lenses, SSMF1 single mode fiber, S sample liquid (glass tube), D1 diffuser, A1 aperture, O object beam, R reference beam



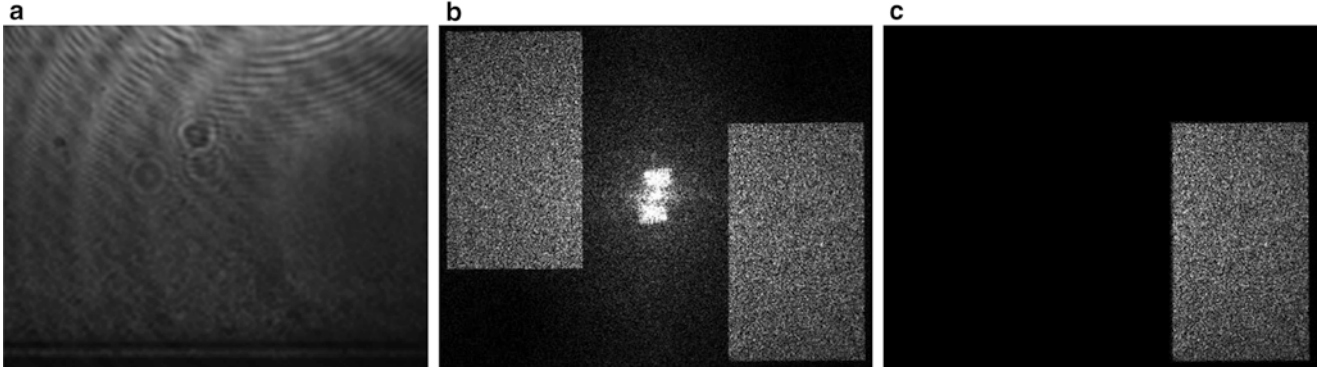
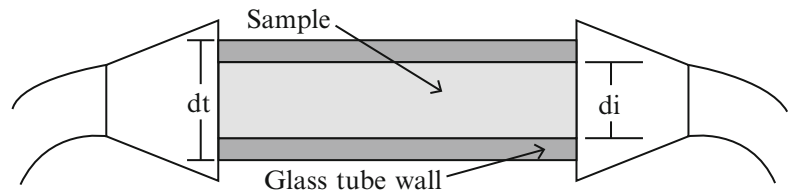


Fig. 17.2 A Fourier-transform method. (a) Digital hologram of the container; (b) separated Fourier spectra with the image of the aperture; and (c) single spectrum selected

Fig. 17.3 Shows the glass tube with the liquid sample. d_i inner diameter, d_r outer diameter



$$\Delta\varphi_{s_2-s_1} = kd_i(n_{s_2} - n_{s_1}), \quad (17.1)$$

Using (17.1) we can calculate a refractive index difference between aqueous substances, but given that in our optical system, the phase object or the tube used is an ordinary glass cylinder whose walls are optically imperfect and thickness measurements are unknown (d_i). To solve this, we use a liquid with known properties values; this can be a reference solution s_o to create an expression that eliminates the dependence on this parameter. We construct

$$d_i = \frac{\Delta\varphi_r}{\Delta n_r} k^{-1}, \quad (17.2)$$

where $\Delta\varphi_r = \varphi_{s_1} - \varphi_{s_0}$ is the phase difference obtained (called “of reference”) from the two known liquid substances and Δn_r is the index refraction difference of them.

Using (17.1) and (17.2) we can get the value of the refractive index difference between two substances as:

$$\Delta n_{2-1} = \frac{\Delta n_r}{\Delta\varphi_r} \Delta\varphi_{2-1}, \quad (17.3)$$

To get a refractive index value regarding our reference value, (17.3) changes as:

$$n_{s_2} = \frac{\Delta n_r}{\Delta\varphi_r} \Delta\varphi_{2-0} + n_{s_0}, \quad (17.4)$$

where $\Delta\varphi_{2-0} = \Delta\varphi_{2-1} + \Delta\varphi_{1-0}$.

17.3 Experimental Method and Results

In order to calculate and visualize an index refraction distribution in a liquid sample, we use three liquid substances, two of them have known values of index refraction and molarity (s_1 and s_0), and the last substance has a refractive index unknown (s_2). The optical system was tested using a series of solutions with a certain amount of sodium chloride (NaCl) to be

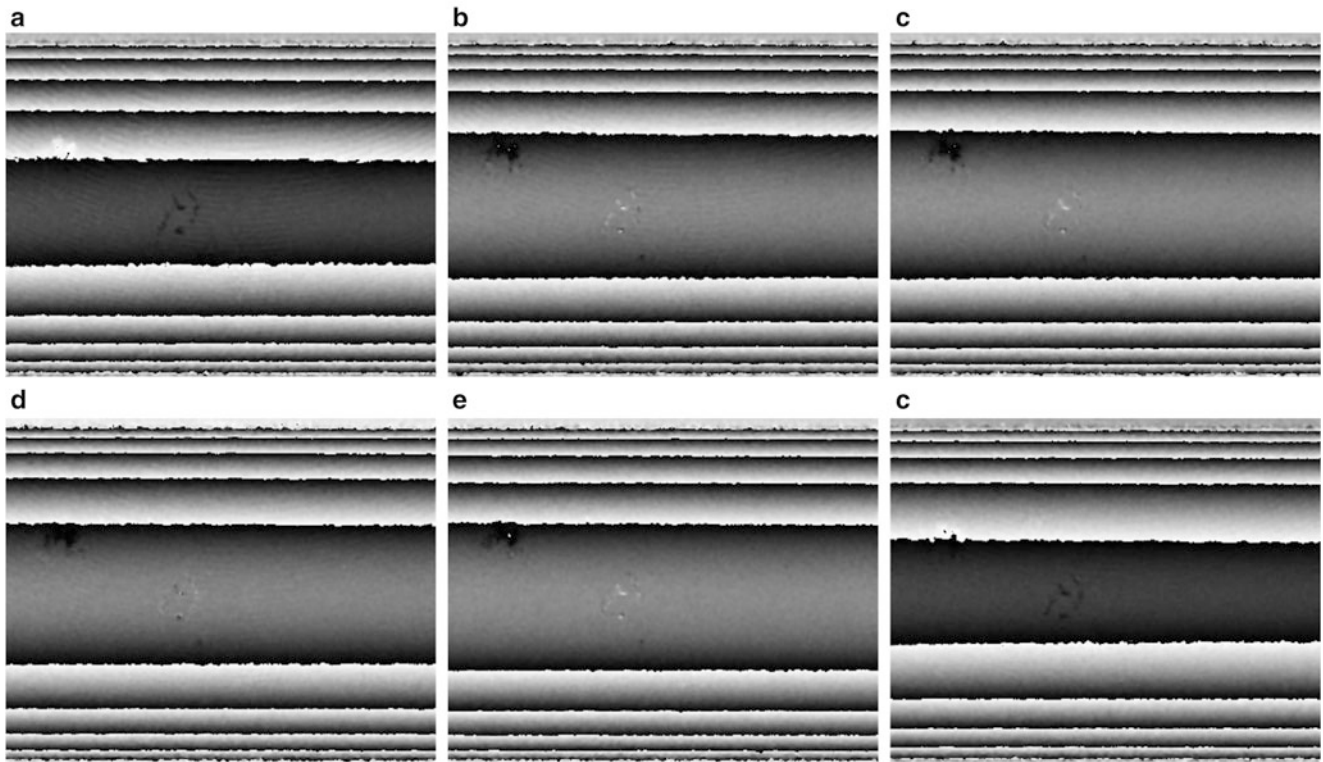


Fig. 17.4 Maps of wrapped phase difference. Samples: (a) $s_2 = 0.086$ mol and $s_1 =$ distilled water, (b) $s_2 = 0.172$ mol and $s_1 = 0.086$ mol, (c) $s_2 = 0.258$ mol and $s_1 = 0.172$ mol, (d) $s_2 = 0.344$ mol and $s_1 = 0.258$ mol, (e) $s_2 = 0.43$ mol and $s_1 = 0.344$ mol, (f) $s_2 = 0.516$ mol and $s_1 = 0.43$ mol

compared with the values found in [23]. A first hologram with the tube filled with distilled water is recorded and was used as s_0 in all our experiments. After that, a series of holograms are recorded with their corresponding saline solution (with 0.086, 0.172, 0.258, 0.344, 0.430, 0.516 mol). The phase reference was created using distilled water (s_0) and the solution with 0.086 mol (s_1). Then a series of phase difference maps are obtained from the correlation between the holograms calculated from the solution that works as the unknown liquid sample (i.e. s_2) and the next substance with a lower concentration (s_1). See Fig. 17.4.

The n_{s_0} value in (17.4) is the known value determined for the distilled water ($n_{s_0} = 1.3330$). If we use the n_{s_0} and the value from the correlation between solutions (i.e. in $\Delta\varphi_{2-0}$), it is very high and produces a wrapped phase map that has high frequencies (see Fig. 17.5). We will have to add more small values in (17.4). The small parts are unwrapped (see Fig. 17.6), in such a way that allows us to calculate the refractive index of s_2 .

Table 17.1 shows the deviation in the refractive indices measured by the method proposed and those found in [23] that are approximately $\pm 0.007\%$.

The method proposed using the DHI allows to visualize the distribution of the refractive index value of full-field and is linked with the different physical properties in the liquid sample. See Fig. 17.7. Figure 17.8 shows the comparison of the values obtained among those found in [23].

17.4 Conclusions

In this paper, we report a new method to detect with a high sensibility a possible variation on the physical properties of a liquid by the DHI. The process registers phase variations between wavefields scattered by full-field liquid samples. The method is inexpensive, noninvasive, fast and easy to develop in a laboratory. The technique can resolve extremely small changes in refractive index, on the order of 0.007% , that is, differences of ± 0.0001 of accuracy in comparison to the value of the refractive index reported in [23]. In addition to this, the method does not use a special device to hold the aqueous sample and neither is it necessary to know the inner diameter d_i and n_g , that refer to the thickness and the refractive index of

Fig. 17.5 Wrapped phase map that has high frequencies ($s_2 = 0.516$ mol and $s_0 =$ distilled water)

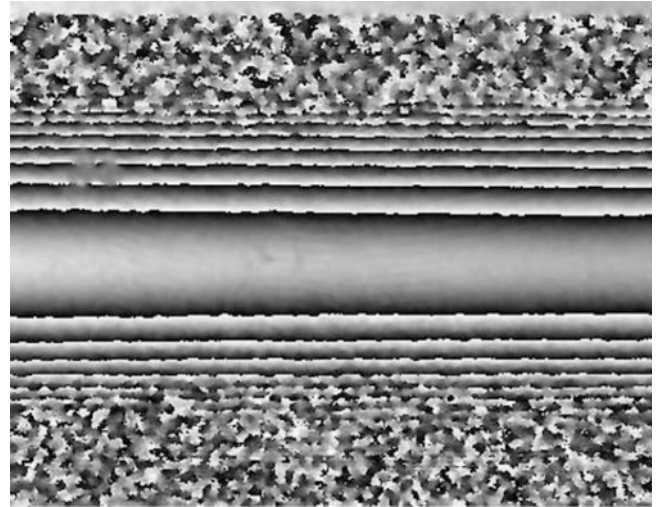


Fig. 17.6 Phase unwrapped ($s_2 = 0.0866$ mol and $s_1 =$ distilled water)

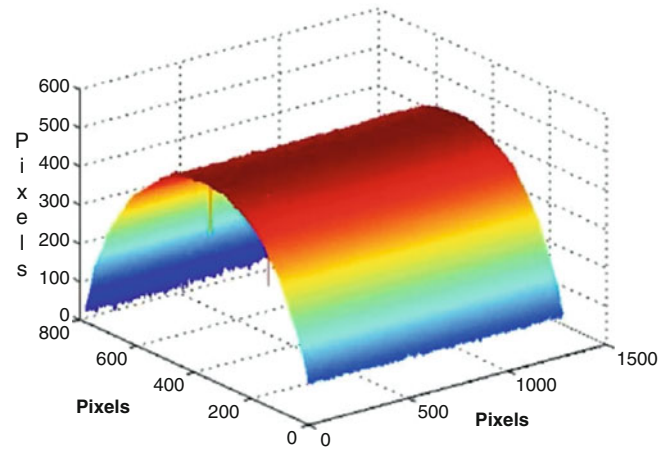


Table 17.1 Comparisons among refractive indices measured by the DHI and those found in [23]

Molarity	Index refraction in [23]	Index refraction (n_{s_2}) measured with DHI
0.086	1.3339	1.3339
0.172	1.3347	1.3348
0.258	1.3356	1.3357
0.344	1.3364	1.3365
0.430	1.3373	1.3374
0.516	1.3382	1.3383

the glass tube respectively, and are considered negligible values for another similar researches. The method can be extended to study a variety of applications requiring noncontact, real-time remote monitoring of liquid concentration and to identify liquid adulterations.

Fig. 17.7 Full-field index refraction distribution on the liquid sample with 0.516 mol

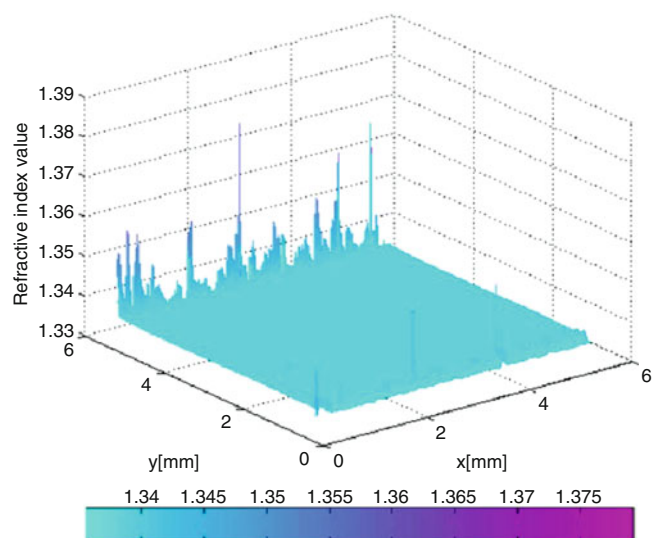
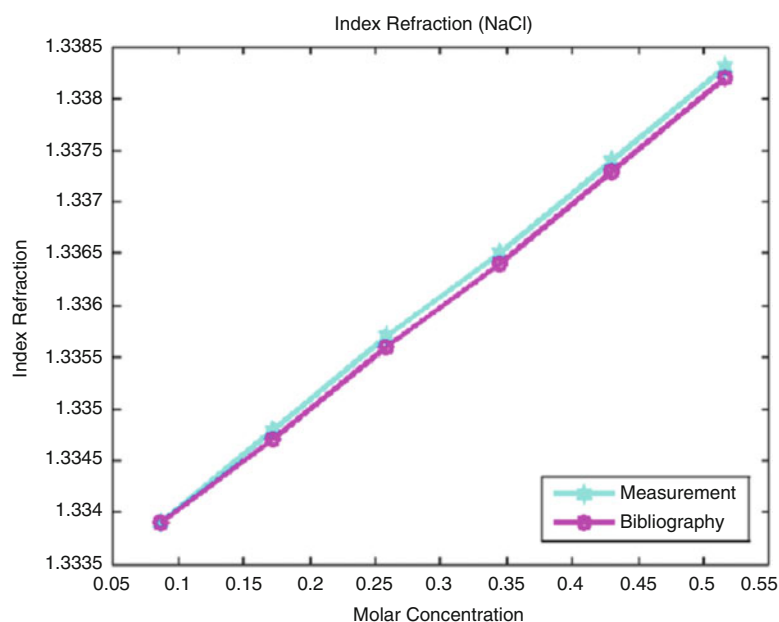


Fig. 17.8 Shows refractive indices calculated and those found in [23]



Acknowledgments The authors acknowledge Prof. S. Guel Sandoval for the useful suggestions and encouraging comments, for the suggestions on this paper. On the other hand, one of the authors (Carlos Guerrero-Mendez) acknowledges CONACYT (Mexico) for providing partial financial support for this work, and the helpful assistance of Sonia A. Saucedo for the technical support.

References

1. M. Cracolice, *Basics of Introductory Chemistry with Math Review* (Brooks/Cole, Belmont, 2006)
2. J.W. Moore, C.L. Stanitski, P.C. Jurs, *Principles of Chemistry: The Molecular Science* (Cengage Learning, Belmont, 2009)
3. R.W. Schrier, *Diseases of the Kidney and Urinary Tract*, vol. 1 (Lippincott Williams & Wilkins, Philadelphia, 2007)
4. A. Smit, A. O'Byrne, *Introduction to Bioregulatory Medicine* (Thieme, Stuttgart, 2011)
5. C.K. Kokate, A.P. Purohit, S.B. Gokhale, *Pharmacognosy*, 42nd edn. (Nirali Prakashan, Pune, 2006)
6. M. Satake, Y. Hayashi, Y. Mido, S.A. Iqbal, M.S. Sethi, *Colloidal and Surface Chemistry* (Discovery Publishing House, New Delhi, 2003)
7. G.V. Karas, *New Topics in Crystal Growth Research* (Nova, New York, 2006)

8. B.P. Chandra, S.C. Bhaiya, A simple, accurate alternative to the minimum deviation method of determining the refractive index of liquids. *Am. J. Phys.* **51**(160), 160–161 (1983)
9. B.W. Grange, W.H. Stevenson, R. Viskanta, Refractive index of liquid solutions at low temperatures: an accurate measurement. *Appl. Opt.* **15**(4), 858–859 (1976)
10. M.D. Edmiston, Measuring refractive indices. *Phys. Teach.* **24**(260), 160–163 (1986)
11. M.R. Shenoy, S. Roy, K. Thyagarajan, Simple prism coupling technique to measure the refractive index of a liquid and its variation with temperature. *Rev. Sci. Instrum.* **61**(3), 1010–1013 (1990)
12. J.P. Longtin, C.-H. Fan, Precision laser-based concentration and refractive index measurement of liquids. *Microscale Thermophys. Eng.* **2**, 261–272 (1998)
13. S. Nemoto, Measurement of the refractive index of liquid using laser beam displacement. *Appl. Opt.* **31**(31), 6690–6694 (1992)
14. E. Moreels, C. de Greef, R. Finsy, Laser light refractometer. *Appl. Opt.* **23**(17), 3010–3013 (1984)
15. S. Singh, Refractive index measurements and its applications. *Phys. Scr.* **65**, 167–180 (2002)
16. C.M. Vest, *Holographic Interferometry* (Wiley, New York, 1979)
17. J. Colombani, J. Bert, Holographic interferometry for the study of liquids. *J. Mol. Liq.* **134**, 8–14 (2007)
18. T. Kreis, *Handbook of Holographic Interferometry: Optical and Digital Methods* (Wiley, Weinheim, 2005)
19. R. Goldstein, *Fluid Mechanics Measurements* (CRC Press, New York, 1996)
20. M.M. Hossain, D.S. Mehta, C. Shakher, Refractive index determination: an application of lensless fourier digital holography. *Opt. Eng.* **45**(10), 1062031–1062037 (2006)
21. Y. Zhang, J. Zhao, J. Di, H. Jiang, Q. Wang, J. Wang, Y. Guo, D. Yin, Real-time monitoring of the solution concentration variation during the crystallization process of protein-lysozyme by using digital holographic interferometry. *Opt. Express* **20**, 18415–18421 (2012)
22. J. Zhao, Y. Zhang, H. Jiang, J. Di, Dynamic measurement for the solution concentration variation using digital holographic interferometry and discussion for the measuring accuracy, in *International Conference on Optics in Precision Engineering and Nanotechnology Proc. of SPIE*, vol. **8769**, 2013, pp. 87690D1–87690D18
23. W. Haynes, *Concentrative Properties of Aqueous Solutions: Density, Refractive Index, Freezing Point Depression, and Viscosity CRC Handbook of Chemistry and Physics*, 92nd edn. (CRC Press, Boca Raton, 2012)
24. M. Takeda, H. Ina, S. Kobayashi, Fourier-transform method of fringe-pattern analysis for computer-based topography and interferometry. *J. Opt. Soc. Am.* **72**(1), 156–160 (1982)
25. A.T. Saucedo, F. Mendoza Santoyo, M. De la Torre-Ibarra, G. Pedrini, W. Osten, Endoscopic pulsed digital holography for 3D measurements. *Opt. Express* **14**, 1468–1475 (2006)

Chapter 18

Geometrical Thickness Measurement of Thin Films by a Transmitted Gaussian Beam

Moisés Cywiak, Octavio Olvera-R, and Joel Cervantes-L

Abstract We describe a technique for measuring the local geometrical thickness of semi-transparent thin films by means of the diffractive properties of a transmitted Gaussian beam. In particular, we measure the semi-width of a beam transmitted through the sample with a homodyne technique especially devised for this purpose. We present analytical and experimental results with our technique.

Keywords Fourier optics and signal processing • Instrumentation, measurement, and metrology • Optical properties

18.1 Propagation of the Gaussian Beam

Measuring the thickness of a thin film, supported only by the border is a difficult task as the film vibrates continuously; thus, especial techniques have been designed for this purpose [1–13]. In this report we describe a technique based on the defocusing properties of a Gaussian beam which is accurate and has the advantage of been immune to piston-like vibration of the film.

The propagation of a Gaussian beam is well-known. A brief description follows.

In Fig. 18.1 the system is adjusted to focus the laser beam at the plane of observation with coordinates (ξ, η) in the absence of the sample, by means of a focusing lens placed on a coordinate plane (x_1, y_1) at a distance z_0 from the laser output. For simplicity the lens is considered very thin and the aperture is large enough to allow neglecting truncation of the beam. The plane of observation is adjusted at a distance z_T behind the lens to attain the best focusing conditions (minimum beam semi-width). We will refer to this plane as the best focusing plane. Once z_T has been fixed, the sample with geometrical thickness t is introduced transversally to the optical axis z in the optical path. It can be seen that,

$$z_T = z_1 + t + z_2, \quad (18.1)$$

where z_1 and z_2 are the distances depicted in Fig. 18.1 which can be chosen arbitrarily as it will be demonstrated below.

For illustrative purposes the width of the sample has been exaggerated in Fig. 18.1.

The propagation of the Gaussian beam throughout the system can be calculated by means of the Fresnel diffraction integral [14].

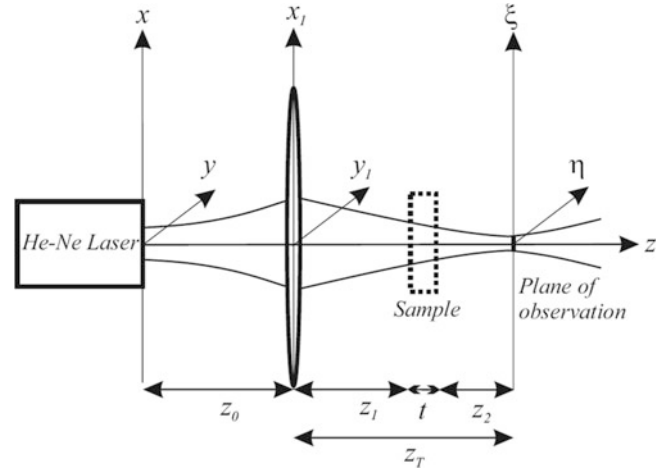
First, we consider a virtual sample, a slice with a refractive index equal to one and geometrical thickness t . For this condition we calculate the propagation from the laser up to the plane of observation and we plot the semi-width of the Gaussian beam as a function of distance z_T . These calculations allow characterizing all the parameters involved in the propagation of the beam.

The value of z_T in which the semi-width exhibits a minimum at the plane of observation will be referred as the best focusing distance and, as indicated, the corresponding transversal plane as the best focusing plane.

The calculations can be simplified by only characterizing the beam that emerges just after the lens. For this, we consider a circular amplitude distribution of the Gaussian just at the back surface of the lens as [15],

M. Cywiak (✉) • O. Olvera-R • J. Cervantes-L
Centro de Investigaciones en Óptica, A.C., León 37150, Guanajuato, Mexico
e-mail: moi@cio.mx

Fig. 18.1 Propagation of the Gaussian beam. z_T is set such that the plane (ξ, η) corresponds to the best focusing plane



$$\Psi_1(x_1, y_1) = A \exp\left(-\frac{x_1^2 + y_1^2}{r^2}\right) \exp[-i\beta(x_1^2 + y_1^2)]. \quad (18.2)$$

In (18.2) A is a complex constant term, r is the semi-width of the Gaussian beam and β is the corresponding coefficient of the convergent quadratic phase.

The field given by (18.2) is propagated up to the plane of observation. We obtain for the corresponding semi-width (r_A) at this plane [15],

$$r_A = \frac{\sqrt{\lambda^2 z_T^2 + r^4 (\beta \lambda z_T - \pi)^2}}{\pi r}. \quad (18.3)$$

We emphasize that (18.3) corresponds to the case of a virtual sample with a refractive index equal to one. r_A , r , β and λ are determined experimentally as it will be described in Sect. 18.4. In this manner we propose a value for z_T which matches with our experimental conditions and it is unique.

By maintaining z_T constant, we now repeat the same calculation substituting the virtual sample by a film with a refractive index n and geometrical thickness t . The semi-width r_B in this case is given as,

$$r_B = \frac{\sqrt{\lambda^2 (z_T - t + \frac{t}{n})^2 + r^4 (\beta \lambda [z_T - t + \frac{t}{n}] - \pi)^2}}{\pi r}. \quad (18.4)$$

In the next section we describe the technique for measuring the corresponding semi-widths.

18.2 Homodyne Detector

As described in [13], the homodyne detector uses a vibrating knife-edge as depicted in Fig. 18.2. The knife-edge is placed at the detection plane. For our purposes, the lens has a working distance of 1 cm allowing the placement of the sample. An attenuator (A) is included to avoid damaging the optical components due to excessive heating. A photo diode whose sensitive area is much larger than the spot size of the beam is positioned behind the knife-edge. The knife-edge is fixed to a flexure piezoelectric transducer (PZT) to vibrate in a plane transversal to the optical axis at a low frequency (f), in our case 10 Hz, with small amplitude (δ_0) of 500 nm. The PZT is also used to displace in plane the knife-edge and has high resolution of about 50 nm. A flexure type PZT is preferred as it exhibits low tilt of less than 5 μ rad.

The vibrating knife-edge allows determining the semi-width of the Gaussian beam in a homodyne way as follows. First, when the knife-edge is not vibrating, due to the photodiode large sensitive area, the power collected (P) can be written as,

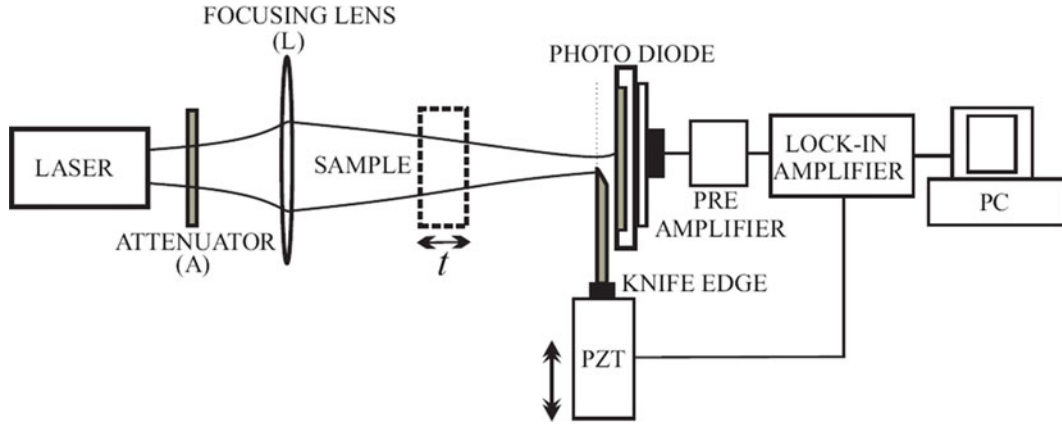


Fig. 18.2 Homodyne detector setup for measuring the semi-width and centroid of the transmitted Gaussian beam

$$P = A \int_{\alpha}^{\infty} \exp\left(-2\frac{x^2}{r_0^2}\right) dx. \quad (18.5)$$

In (18.5) A is a constant scale factor and the lower limit of the integral (α) represents the initial position of the knife-edge. r_0 is the semi-width of the beam at the plane of detection. Equation 18.5 indicates that the photodiode integrates the overall beam excluding the portion covered by the knife-edge.

Now, when the knife-edge is vibrating, the lower limit is written as,

$$\alpha = x_0 + \delta_0 \cos(2\pi ft), \quad (18.6)$$

where x_0 is a static position. By substituting (18.6) in (18.5) and by only preserving the linear term of a series expansion of the resulting equation, we obtain,

$$P_{\text{linear}}(x_0) = B \exp\left(-2\frac{x_0^2}{r_0^2}\right) \cos(2\pi ft), \quad (18.7)$$

where B is a constant. Only the first order term of the expansion has to be considered because the lock-in amplifier is tuned to the first harmonic. As a consequence, the signal detected by the lock-in results proportional to the intensity Gaussian profile evaluated at x_0 as indicated by (18.7).

To obtain the shape of the Gaussian beam with our homodyne detector it is necessary to displace the position of the knife-edge to different values of x_0 . In this way, the profile and width of the Gaussian beam are obtained with high accuracy at the plane of detection.

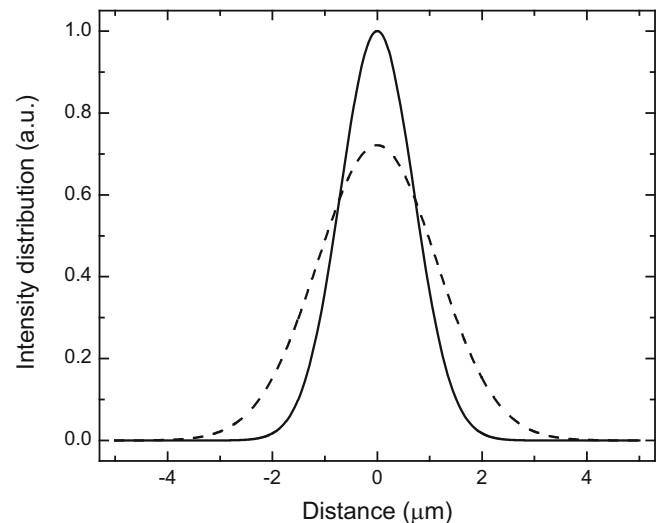
In the next section we provide experimental results.

18.3 Experimental Section

The working conditions in our measurements were: $\beta = 4.971 \times 10^8 \text{ m}^{-2}$, $r = 2.2 \text{ mm}$, $r_A = 1.4 \mu\text{m}$, $z_T = 1.0 \text{ cm}$, $\lambda = 0.632 \mu\text{m}$. Refractive film index = 1.7. With these parameters r_B can be determined. With the film sample present, $r_B = 8.77 \mu\text{m}$. Figure 18.3 depicts the experimental intensity distributions.

The acquisition time for each profile is approximately 1 min and is a consequence of the slow vibrating rate. The acquisition time can be diminished by increasing the frequency vibration of the knife-edge. For the moment being we are working in this direction.

Fig. 18.3 Intensity distributions recorded with the homodyne detector normalized with respect to the virtual sample (*continuous trace*). The *dashed trace* corresponds to the measurement with the sample film



18.4 Conclusions

A technique for measuring the geometrical thickness of a semi-transparent thin film by means of the diffractive properties of a transmitted Gaussian beam has been described and tested. The technique is based on measuring the semi-width of the transmitted beam. We demonstrated that the technique is immune to piston-like vibrations of the film and as it is not interferometric, it showed to be immune to external noise. The technique was applied in determining experimentally the geometrical thickness of a commercially available stretch film.

References

1. S. Kim, J. Na, M. Kim, B. Lee, Simultaneous measurement of refractive index and thickness by combining low-coherence interferometry and confocal optics. *Opt Express* **16**, 5516–5526 (2008)
2. M. Ohmi, H. Nishi, Y. Konishi, Y. Yamada, M. Haruna, High-speed simultaneous measurement of refractive index and thickness of transparent plates by low-coherence interferometry and confocal optics. *Meas. Sci. Technol.* **15**, 1531–1535 (2004)
3. H. Maruyama, S. Inoue, T. Mitsuyama, M. Ohmi, M. Haruna, Low-coherence interferometer system for the simultaneous measurement of refractive index and thickness. *Appl. Opt.* **41**, 1315–1322 (2002)
4. M. Haruna, M. Ohmi, T. Mitsuyama, H. Tajiri, H. Maruyama, M. Hashimoto, Simultaneous measurement of the phase and group indices and the thickness of transparent plates by low-coherence interferometry. *Opt. Lett.* **23**, 966–968 (1998)
5. T. Fukano, I. Yamaguchi, Simultaneous measurement of thicknesses and refractive indices of multiple layers by a low-coherence confocal interference microscope. *Opt. Lett.* **21**, 1942–1944 (1996)
6. T. Fukano, I. Yamaguchi, Separation of measurement of the refractive index and the geometrical thickness by use of a wavelength-scanning interferometer with a confocal microscope. *Appl. Opt.* **38**, 4065–4073 (1999)
7. F. Gao, H. Muhamedsalih, X. Jiang, Surface and thickness measurement of a transparent film using wavelength scanning interferometry. *Opt. Express* **20**, 21450–21456 (2012)
8. P. de Groot, Measurement of transparent plates with wavelength-tuned phase-shifting interferometry. *Appl. Opt.* **39**, 2658–2663 (2000)
9. K. Hibino, B. Oreb, P. Fairman, Wavelength-scanning interferometry of a transparent parallel plate with refractive-index dispersion. *Appl. Opt.* **42**, 3888–3895 (2003)
10. G. Coppola, P. De Natale, S. De Nicola, P. Ferraro, M. Gioffre, M. Iodice, Thickness measurement of thin transparent plates with a broad-band wavelength scanning interferometer. *IEEE Photon. Technol. Lett.* **16**(5) (2004)
11. Y. Kumar, S. Chatterjee, Simultaneous determination of refractive index and thickness of moderately thick plane-parallel transparent glass plates using cyclic path optical configuration setup and a lateral shearing interferometer. *Appl. Opt.* **51**, 3533–3537 (2012)
12. Y. Kumar, S. Chatterjee, Thickness measurement of transparent glass plates using a lateral shearing cyclic path optical configuration setup and polarization phase shifting interferometry. *Appl. Opt.* **49**, 6552–6557 (2010)
13. O. Olvera-R, M. Cywiak, J. Cervantes-L, A. Morales, Refractive index and geometrical thickness measurement of a transparent pellicle in air by Gaussian beam defocusing. *Appl. Opt.* **53**, 2267–2272 (2014)
14. M. Cywiak, J. Murakowski, G. Wade, Beam blocking method for optical characterization of surfaces. *Int. J. Imaging Syst. Technol.* **11**, 164–169 (2000)
15. M. Cywiak, A. Morales, J. Flores, M. Servín, Fresnel-Gaussian shape invariant for optical raytracing. *Opt. Express* **17**, 10564–10572 (2009)

Chapter 19

Topography and Color Study of an Object Using Fringe Projection and Colorimetry Techniques

Y. Yanet López D., Amalia Martínez-García, and Julián Gómez S.

Abstract Besides the topography of an object, color and texture are important parameters to study in some fields. In food industries, variations in color and volume of a piece of fruit are important in order to determine its condition. Using the fringe projection technique, the topography of an object is evaluated through time; hence the change of volume. Using colorimetric techniques, optical devices can be profiled and calibrated. The change of topography and color are measured every 3 days during two months in order to make comparisons with the previous measurements of volume and color. Thus, the condition of food or a piece of fruit can be evaluated as it evolves through time.

Keywords 3D reconstruction • Color topography • Colorimetry • Fringe projection • Color evaluation

19.1 Introduction

The structured light technique is useful to quantify both macro surfaces [1] and micro surfaces [2]. By using the Fourier transform, the phase of a fringe pattern is obtained from a single image. Using a phase shifting technique, the phase is obtained from a set of images. With the phase information and the sensitivity vector of the optical system, the value $z(x, y)$ at each object's point can be determined.

Because color is a subjective sensation and changes depending on the observer [3], it is necessary that all the optical devices involved in the experiment are correctly calibrated. There is equipment and software in the market that can be used to obtain the color profile of the devices and calibrate them following a pattern of standardized colors (CIE). In this case, the I1 Profiler de X-Rite and the Color Checker software are used. The described process is based in Colorimetry which deals with the study, measurement and quantification of colors.

19.2 Theory

19.2.1 Fringe Projection

Figure 19.1 shows the optical geometry where it is obtained the relationship to the height of the object under study. It projects a grating with parallel lines to the axis y . The z axis coincides with the direction of observation and the xy plane ($z = 0$) is a reference plane; i.e. the height is equal to 0 on this plane. The projected grating normal makes an angle θ with respect to the optical axis. The surface is then illuminated with an incoherent cosine grating and recorded by a CCD camera on the xy plane normal. In the case of collimated illumination, the mathematical relationship between the height of the object, the phase and the parameters of the experimental optical system is given by (19.1) [4]:

Y.Y.L. D. (✉) • A. Martínez-García
Centro de Investigaciones en Óptica, A.C., León 37150, Guanajuato, México
e-mail: yanetld@cio.mx; amalia@cio.mx

J.G. S.
Universidad DeLaSalle Bajío, León 37150, Guanajuato, México
e-mail: juangocero@hotmail.com

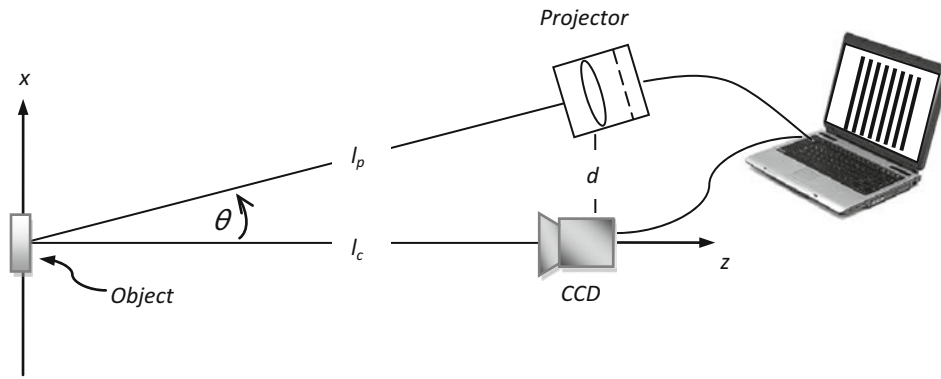


Fig. 19.1 Experimental setup for a fringe projection system

$$z = \frac{\varphi}{2\pi} \cdot \frac{p}{\tan \theta} \quad (19.1)$$

where the phase φ can be obtained with the phase shifting method or Fourier transform method [5], and p is the period of the grating projected onto the plane $z = 0$.

The intensity function of the interferogram, is given by (19.2):

$$I(x, y) = a(x, y) + b(x, y) \cos [\phi(x, y) + \Delta\phi] \quad (19.2)$$

where $a(x, y)$ describes the variations of the intensity background, $b(x, y)$ describes the amplitude of the fringes, $\phi(x, y)$ is the phase information and $\Delta\phi$ is an introduced phase shifting. Thus, at least three-steps are needed in order to obtain the phase information.

$$\tan \phi = -\frac{I_2 - I_4}{I_1 - I_3} \quad (19.3)$$

For a four-step phase shifting technique, the phase information is obtained with (19.3).

19.2.2 Colorimetry

The Colorimetry is the science that studies colors and characterizes them through numbers; once they are characterized, we can operate with them, as well as classify and reproduce them [3, 6].

A relationship can be established between the perceptual terms and the colorimetric terms. So, tone is the dominant wavelength, saturation is the excitation purity, and luminance is the clarity or brightness; thus one color can be characterized through three attributes (dominant wavelength, excitation purity and luminance) [7].

If light is achromatic (without color), it means that the only attribute present is its intensity, and a greyscale from black to white is defined. Two colors are metameres if they come from different stimuli (spectral distribution), but they are perceived as equal colors; however, two different colors will always come from different stimuli [3].

In order to do the profiling of optical devices (camera, projector, screen), a spectrophotometer is needed in order to measure the spectral distribution or response of the devices. For color measuring, the encoded spectral curve of CIE is used as a reference. The procedure consists of adding the stimulus of color response, to then normalize it to the response curve of the photo-receptor, which is sensitive to color. With the spectrophotometer the values of color for each device are measured and analysed, and then related with the standardized values. This way, the profiling and calibration is achieved.

19.3 Experimental Part

Before starting with the process to obtain the topography, it is necessary to calibrate the optical devices involved in the experiment.

Using the I1 Profiler X-Rite kit [8], the monitor where the images will be displayed is calibrated. The spectrophotometer is placed in the center of the screen while the different colors of the visible spectrum are projected in the screen. Thus, the measuring of the color values that the screen shows and the adjustment to the theoretical values that it has to show are done. Finally, the profile of the screen is created and saved. For profiling and calibrate the projector, the same procedure is followed.

To profile the camera, it is necessary to take a picture of a color patch (standardized by CIE) included in the kit of the I1 Profiler (Fig. 19.2). The picture is taken under the same conditions of light of the experiment and using the Color Checker Passport; the profile of the camera is analyzed by making comparisons between the picture taken and the correct colors. A profile for the camera is created, and using any image processing software, the profile can be loaded and applied to all the images taken.

It is important to apply the created profile to all the images taken in the process of fringe projection. Figure 19.3 shows the object sample with a non-calibrated color and the same object with the profile of the camera applied.

Using the experimental setup of Fig. 19.1, the cosine grating is projected over the surface and then captured by a color camera. In this case, a four-steps shifting is used, thus the phase shifting between each other is $\frac{\pi}{2}$. The profile of the camera has to be applied to all the captured interferograms, as can be observed in Fig. 19.4.



Fig. 19.2 Calibration process of optical devices

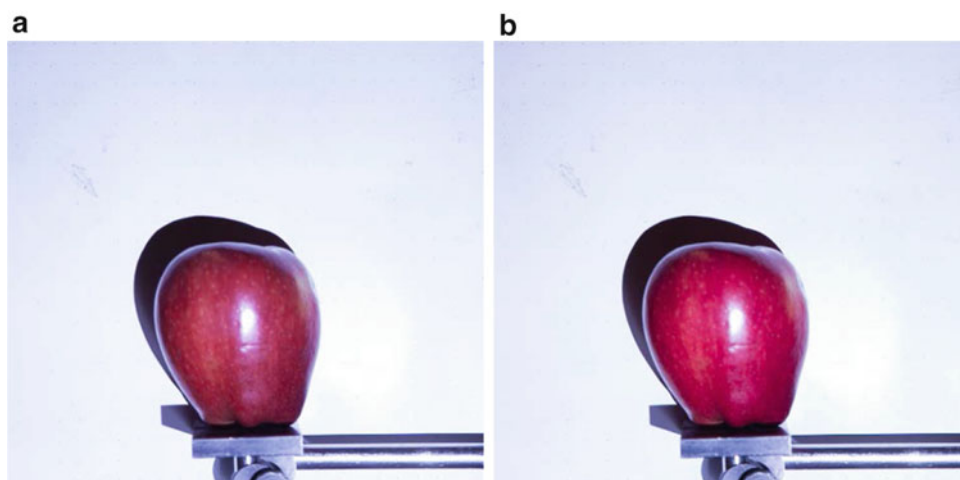


Fig. 19.3 (a) Image with non-calibrated color and (b) image with color calibration

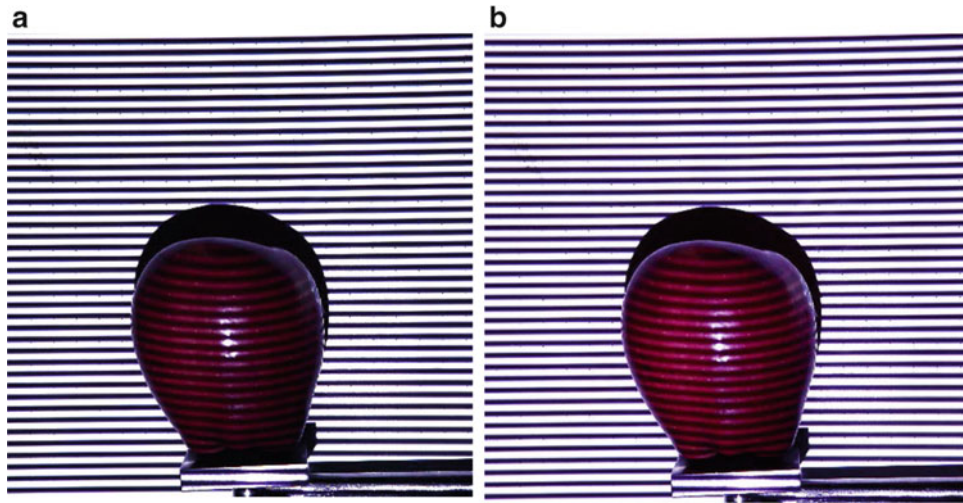
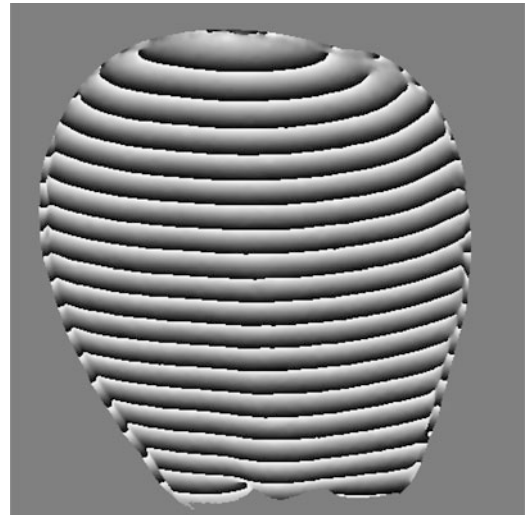


Fig. 19.4 (a) Projected fringe pattern with non-calibrated color and (b) projected fringe pattern with color calibration

Fig. 19.5 Wrapped phase of the object



Using the phase shifting technique and applying the (19.3), the phase of the projected fringe pattern is obtained, as can be observed in Fig. 19.5. Since this equation depends on a tangent function, the obtained phase information is wrapped. Using the path follower algorithm, the unwrapped phase information is obtained and shown in Fig. 19.6.

After the unwrapped phase is obtained for both reference and object, the topography is obtained by subtracting the phase information of the object and the phase information of the reference plane. In order to obtain the dimensions of the sample object, the (19.1) is used.

In this case, the parameters of the experimental setup are:

- $l_c = 91 \text{ cm}$ → *Distance from Reference Plane to CCD*
- $d = 17 \text{ cm}$ → *Distance from Projector to CCD*
- $\theta = 10.58^\circ$ → *Angle of illumination*

Using these parameters, the height Z is obtained. Finally, the color information is attached to the topography obtained with fringe projection technique, as can be observed in Fig. 19.7.

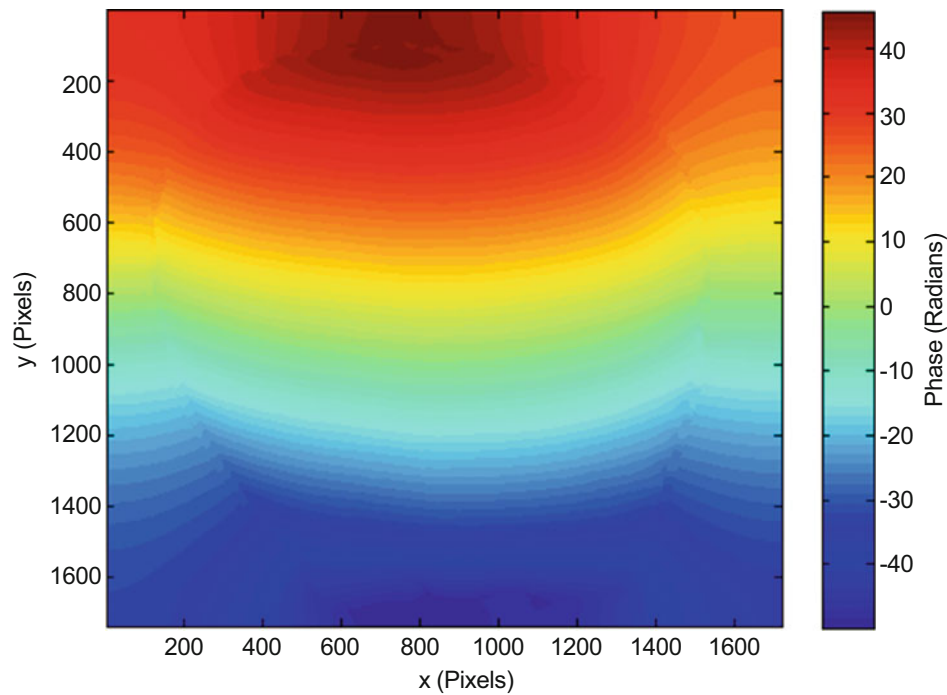
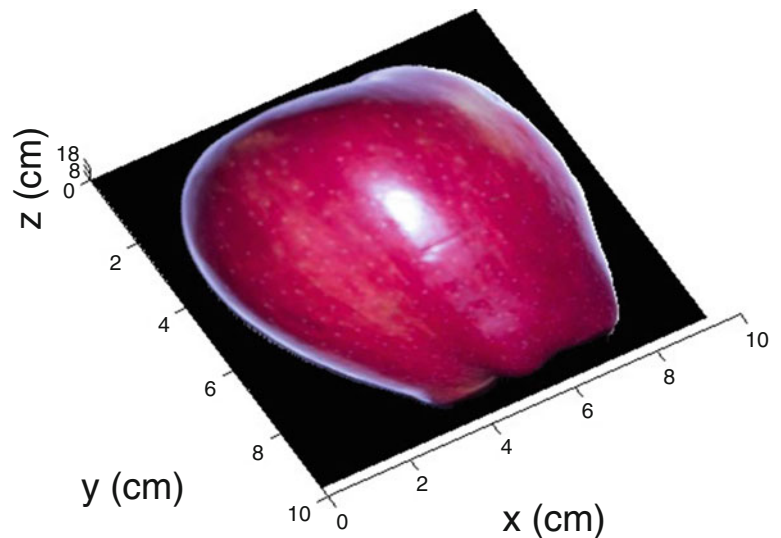


Fig. 19.6 Unwrapped phase map of the object

Fig. 19.7 Obtained topography of the object



For evaluating the change of topography and color in order to evaluate the object sample evolution through time, the measurements were made every 3 days. Fringe projection process has to be done under the same conditions of light and the fruit has to be stored under the same temperature along the duration of the study.

19.4 Results

One important parameter in order to determine the evolution of the quality of the fruit, is the color. A change of color can indicate if the fruit is getting mature or losing quality. So, a comparison of color is done in each measurement, as can be observed in Figs. 19.8 and 19.9.

The variations of color can be evaluated by comparing the histograms of every image as can be observed in Fig. 19.9.

Fig. 19.8 Variations of color between three measurements

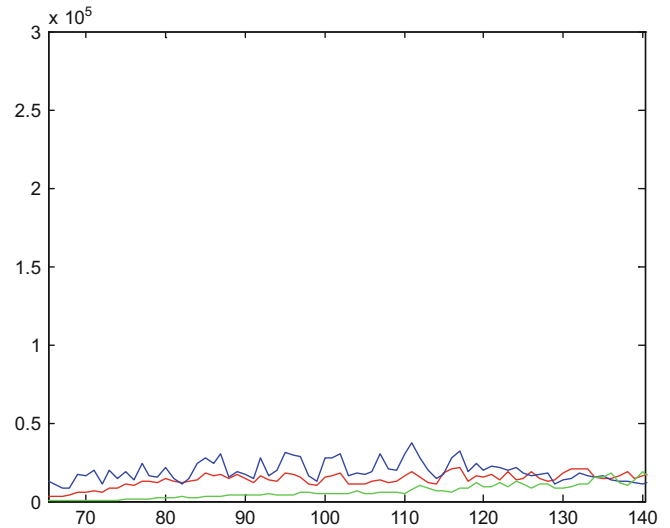
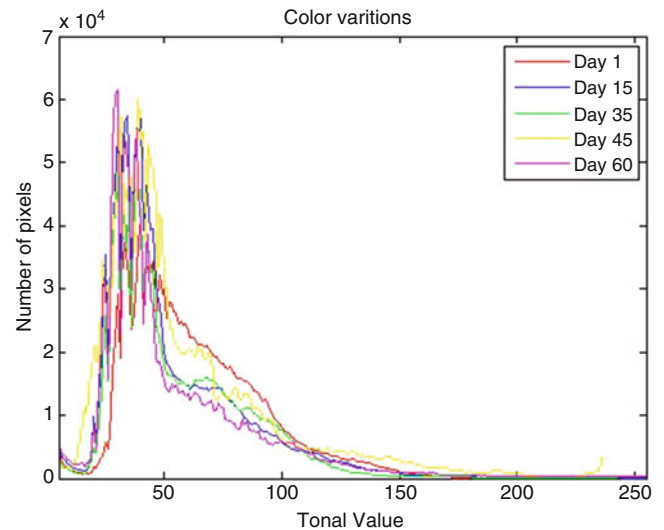


Fig. 19.9 Variations of color observed in five measurements



In order to obtain the change of volume, it is necessary to evaluate the object in 360° . This was made by taking different views of the object and evaluating the topography of each view (Fig. 19.10).

The topography of every view of the object was obtained by using the fringe projection technique mentioned before. In this case, topography of view 3 (Fig. 19.11) and topography of view 4 (Fig. 19.12) are shown.

To evaluate the change in volume, it is necessary to merge all the views together; this can be achieved by using the ICP algorithm (Iterative Closest Point). One of the views of the object will be used as the model, and the other view will be used as data (data will be adjusted to the model). It is important to consider that both model and data have a similarity in their profiles. The ICP algorithm will compare the error difference between the two sets of points (model and data), as can be observed in Fig. 19.13.

The ICP algorithm will compare every set of points until it finds the lowest difference that guarantees that both profiles have their best matches. The profile of the data will be transformed (displaced and rotated) in order to match it with the model, as can be observed in Fig. 19.14. This algorithm and the merging of all views is a future goal in order to continue this work.

To evaluate the change in topography, we can compare the difference between two profiles (two different measurements), as can be observed in Fig. 19.15. A loss of dimensions can indicate a minor volume, hence a loss of water into the fruit. In this figure, the profiles use a reference $y=4.50$ cm. For this purpose, measurements in days 1 and 30 are compared.

Fig. 19.10 Views of the object at different angles

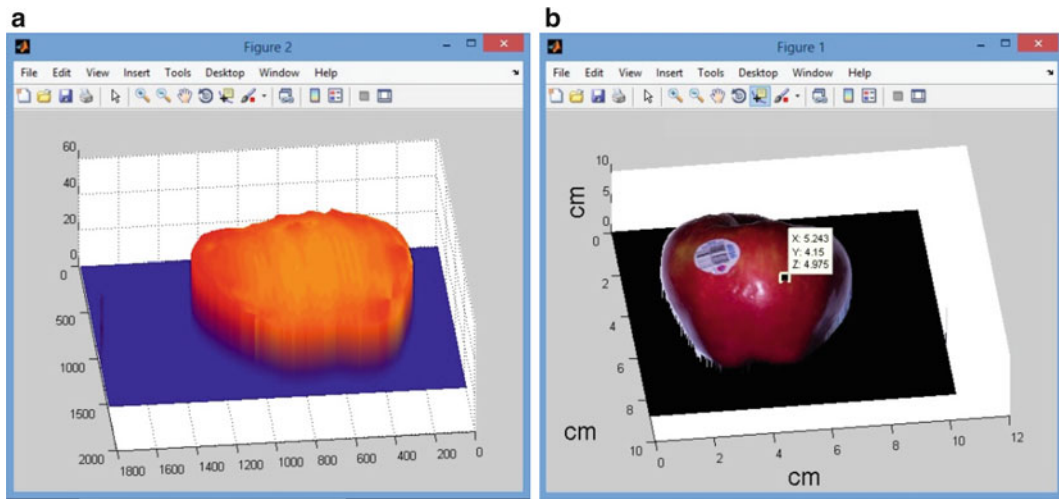


Fig. 19.11 (a) Topography of view 3 and (b) color and measurements of view 3

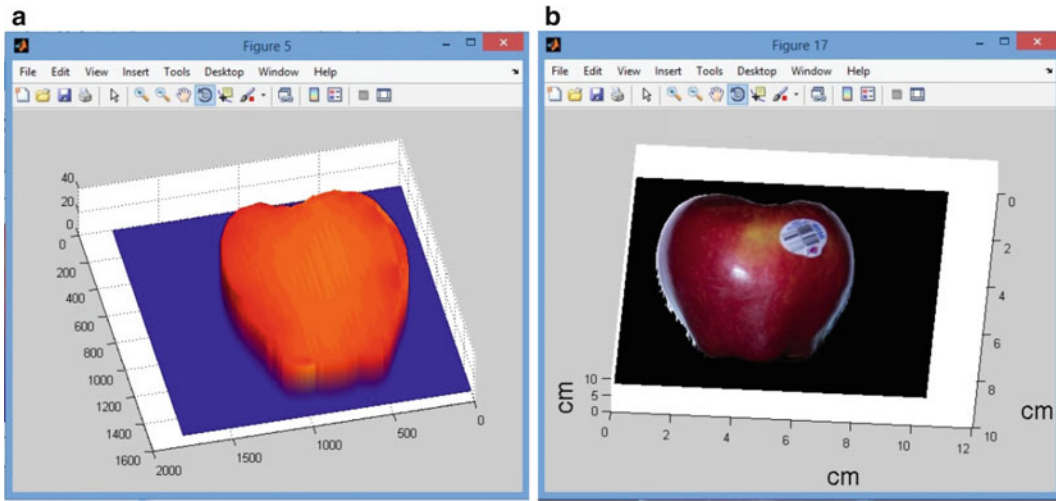


Fig. 19.12 (a) Topography of view 4 and (b) color and measurements of view 4

Fig. 19.13 Profile of model and data

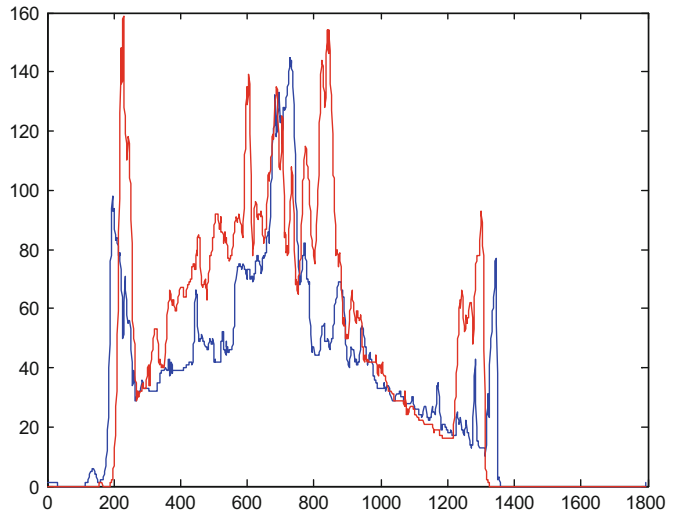


Fig. 19.14 ICP algorithm converged

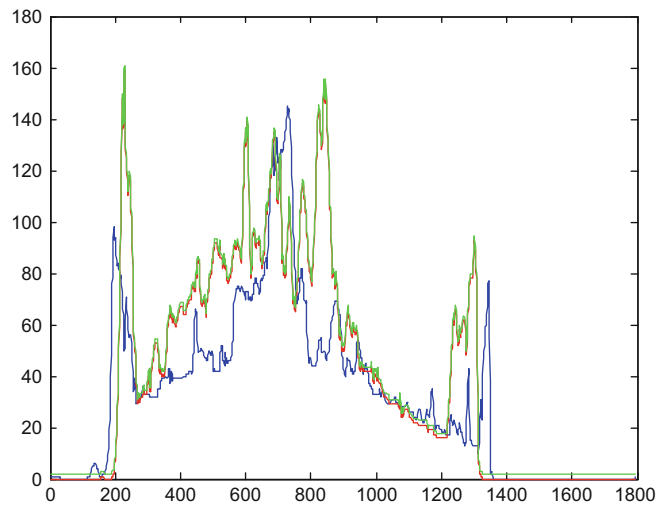


Fig. 19.15 Change of topography between two different measurements

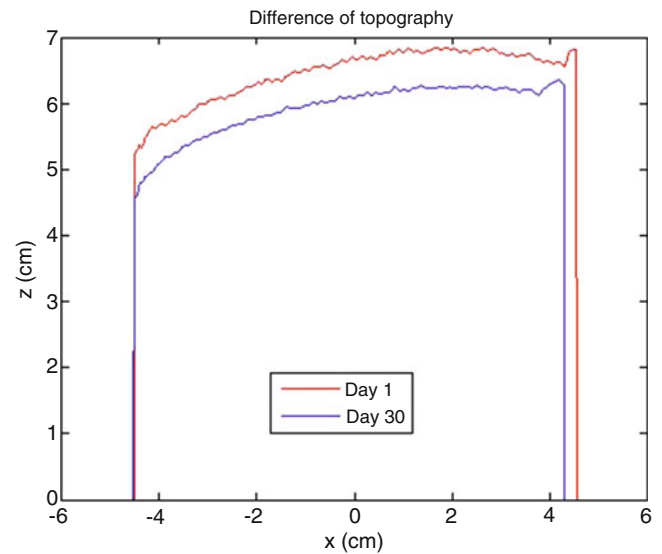
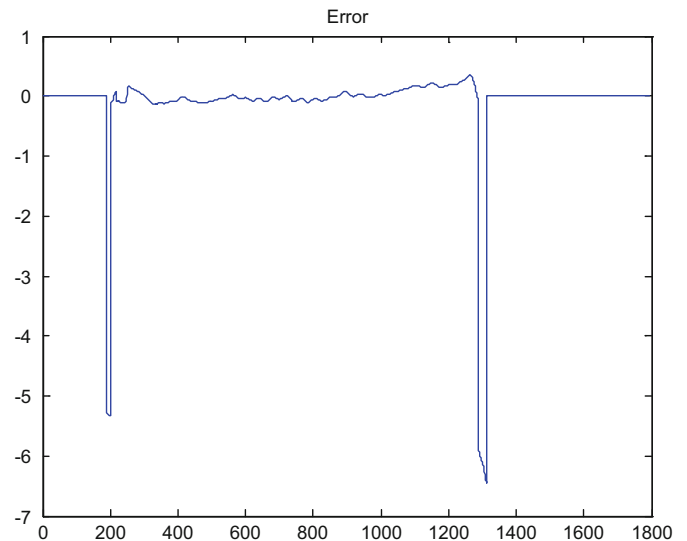


Fig. 19.16 Difference between each measurement



To have the exact difference between the measurements, the error has been calculated using two topographies; this is shown in Fig. 19.16. According to the calculations made, the maximum difference is 0.49 cm between each measurement.

19.5 Conclusions

The fringe projection method has proved to be very useful to evaluate the topography of objects. Combining this method with colorimetric techniques has been helpful to evaluate the change in topography and color of a piece of fruit. These parameters are very important in food industry in order to determine food condition and therefore its quality. The measurements were made as days went by, and were compared with the previous measurements of color and topography. The changes of topography and color indicate the change in the condition of fruit as it evolves through time, and hence, they can be used as a quality indicator.

Acknowledgments The authors wish to acknowledge the financial support for this research to the Consejo Nacional de Ciencia y Tecnología de México, CONACYT, under grant 180449.

References

1. A. Martínez, J.A. Rayas, H.J. Puga, K. Genovese, Iterative estimation of the topography measurement by fringe projection method with divergent illumination by considering the pitch variation along the x and z directions. *Opt. Lasers Eng.* **48**, 877–881 (2010)
2. J.A. Rayas, R. Rodríguez Vera, A. Martínez, in *Three-Dimensional Micro-Topography by Talbot-Projected Fringes*, ed. by E. Rosas, R. Cardoso, J.C. Bermudez, O. Barbosa García. 5th Symposium on Optics in Industry. Proceedings of SPIE, vol. 6046 (SPIE, Bellingham, 2006), pp. 60461 y-1–60461 y-6
3. D. Malacara, *Color Vision and Colorimetry: Theory and Applications*, 2nd edn. (SPIE Press, Bellingham, 2011)
4. K.J. Gasvik, *Moiré Methods. Triangulation in Optical Metrology*, 3rd edn. (Wiley, New York, 2002), pp. 173–190
5. D. Malacara, M. Servin, Z. Malacara, Phase shifting interferometry, in *Interferogram Analysis for Optical Testing* (Marcel Dekker, New York, 1998), pp. 247–278
6. G. Wyszecki, W. Stiles, *Color Science: Concepts and Methods Quantitative Data and Formulas* (Wiley, New York, 1967)
7. A.J. Woods, Compatibility of display products with stereoscopic display methods, in *International Display Manufacturing Conference*, Taiwan, February 2005
8. http://www.xrite.com/product_overview.aspx?ID=1397

Chapter 20

Temperature Measurement of a Synthetic Jet Produced by a Helmholtz Cavity

Alan D. Blanco M., Bernardino Barrientos G., Andrew J. Moore, and Carlos Mares C.

Abstract We present preliminary results of the measurement of temperature distribution fields of a synthetic jet produced by a Helmholtz resonant cavity when used for the cooling of an aluminum plate. The plate is set at 80 °C and background-oriented schlieren images are registered by a high speed camera at 2000 fps. The background consists of sinusoidal fringes printed on a transparent slide and it is back-illuminated by a matrix of 20 3-W white LEDs. A reference image is taken with no jet and a series of images are then recorded with the cavity working in the first resonance frequency, 125 Hz. The observation region corresponds to an area of $1 \times 10 \text{ cm}^2$. Results show an oscillatory behavior of the temperature distribution at the resonant frequency.

Keywords Ray deflection • Synthetic air jet • Background-oriented schlieren • Temperature measurement

20.1 Introduction

Fringe Deflection (FD) is a technique capable of measuring ray deflections (or equivalently, projected refractive index gradients [1]) in two mutually orthogonal directions. The deflections field can be integrated to obtain the spatial distribution of the projected refractive index, which may be related to density [2–4] and concentration variations [5], for example. In this technique, a synthetic background (a pattern of sinusoidal fringes uniformly distributed) is imaged by a camera. The object under analysis is placed between the background and the camera. Two images are captured, with and without object (reference image and displaced image, respectively). As the object is introduced, the spatial structures of the background are displaced according to the deflection of the corresponding bundle of rays that propagate through the object. Thus, it is possible the calculation of displacement fields by comparing the reference image and the displaced image.

Due to its simplicity, when compared with other schlieren methods, FD has been used recently successfully in several applications of fluid dynamics [2–5]. In the present work, synthetic or zero-net mass jets are studied. A synthetic jet is produced by successive ejection and suction of fluid across an orifice. The oscillatory flow is typically generated by a movable diaphragm forming part of a sealed cavity.

An unconfined synthetic jet flow [6, 7] may be characterized by two adimensional numbers: the dimensionless stroke length L_0/d_o and the Reynolds number $Re = U_0 d_o/\nu$, where $L_0 = \int_0^{T/2} U(t) dt$ (length that a slug of fluid travels away from the orifice during the ejection portion of a period T), $U(t)$ is the spatially averaged velocity at the exit plane of the orifice, d_o is the orifice hydraulic diameter, ν is the kinematic viscosity of the fluid, $U_0 = L_0/(T/2)$. Also, L_0/d_o is inversely proportional to the Strouhal number, since $L_0/d_o = 1/2(f d_o/U_0)^{-1}$, where $f = 1/T$, the driving frequency. When the diaphragm and the cavity are driven into resonance, the electrical power input is relatively low. This makes synthetic jets very efficient actuators for heat transfer, such as in thermal management of electronic devices.

A.D.B. M. (✉) • B.B. G. • C.M. C.

Centro de Investigaciones en Óptica A.C., Loma del Bosque 115, Col. Lomas del Campestre, León, Guanajuato, Mexico
e-mail: alan@cio.mx; bb@cio.mx

A.J. Moore

School of Engineering and Physical Sciences, Heriot-Watt University, Edinburgh EH14 4AS, UK
e-mail: a.moore@hw.ac.uk

© Springer International Publishing Switzerland 2017

A. Martínez-García et al. (eds.), *Emerging Challenges for Experimental Mechanics in Energy and Environmental Applications, Proceedings of the 5th International Symposium on Experimental Mechanics and 9th Symposium on Optics in Industry (ISEM-SOI), 2015*, Conference Proceedings of the Society for Experimental Mechanics Series, DOI 10.1007/978-3-319-28513-9_20

20.2.2 Fringe Deflection

Fringe deflection is well suited for the calculation of in-plane displacements such as those involved in deflection of rays [13]. In this case, the background synthetic image corresponds to a pattern with sinusoidal fringes. As displacements cannot be measured along the direction of the fringes, an additional crossed grating can be incorporated for sensitivity along two mutually perpendicular directions [14]. The displacements can be calculated as follows. Let the reference image be expressed by [15, 16]

$$I_1(x, y) = a(x, y) + b(x, y) \cos(2\pi f_0 x + \phi_{ref}), \quad (20.5)$$

where $a(x, y)$ is the background illumination, $b(x, y)$ the modulation term, f_0 a carrier frequency that allows us the use of the Fourier method for automatic phase calculation, and ϕ_{ref} is a phase term that accounts for perspective and aberration effects. Likewise, the displaced image is given by

$$I_2(x, y) = a(x, y) + b(x, y) \cos(2\pi f_0 x + \phi_{ref} + \Delta\phi), \quad (20.6)$$

with $\Delta\phi(x, y)$ being the phase resulting from deviations of the straight fringes, after introducing the object. The argument of (20.5) can be calculated by applying the Fourier method [17], so first we rewrite (20.6) as

$$I_1(x, y) = a(x, y) + \frac{1}{2}b(x, y) \exp(i2\pi f_0 x) \exp(i\phi_{ref}) + \frac{1}{2}b^*(x, y) \exp(-i2\pi f_0 x) \exp(-i\phi_{ref}), \quad (20.7)$$

After a Fourier transformation, we get

$$I_F(f_x, f_y) = A(f_x, f_y) + B(f_x - f_0, f_y) + B^*(-f_x - f_0, f_y), \quad (20.8)$$

where $A(f_x, f_y) = \mathfrak{F}\{a(x, y)\}$ and $B(f_x, f_y) = \mathfrak{F}\{\frac{1}{2}b(x, y) \exp(i2\pi f_0 x) \exp(i\phi_{ref})\}$.

Then a band-pass filter is applied to (20.8) to isolate one of its lobes (centered at the carrier frequency f_0),

$$I_{FP}(f_x, f_y) = B(f_x - f_0, f_y), \quad (20.9)$$

We take the inverse Fourier transform of (20.9),

$$\begin{aligned} \mathfrak{F}^{-1}\{B(f_x - f_0, f_y)\} &= \mathfrak{F}^{-1}\left\{\mathfrak{F}\left\{\frac{1}{2}b(x, y) \exp(i2\pi f_0 x) \exp(i\phi_{ref})\right\}_{f_x - f_0, f_y}\right\} \\ &= \frac{1}{2}b(x, y) \exp[i(2\pi f_0 x)] \exp(i\phi_{ref}) \\ &= R(x, y) + iM(x, y), \end{aligned} \quad (20.10)$$

where $R(x, y) = \frac{1}{2}b(x, y) \cos(2\pi f_0 x + \phi_{ref})$ and $M(x, y) = \frac{1}{2}b(x, y) \sin(2\pi f_0 x + \phi_{ref})$. Therefore, the reference argument can be obtained by $2\pi f_0 x + \phi_{ref} = \tan^{-1}\left[\frac{M(x, y)}{R(x, y)}\right]$. In a similar way the displaced argument $(2\pi f_0 x + \phi_{ref} + \Delta\phi)$ can be calculated; and the desired phase term can be finally obtained by subtracting the latter two arguments [18], $\Delta\phi = (2\pi f_0 x + \phi_{ref} + \Delta\phi) - (2\pi f_0 x + \phi_{ref})$. Displacements Δx are related to $\Delta\phi$ by

$$\Delta x = P \frac{\Delta\phi}{2\pi}, \quad (20.11)$$

where $P = 1/f_0$ corresponds to the period of the grating.

20.3 Experimental Results

The experimental setup consists of a Photron UX100 camera (1280×1024 pixels), a printed sheet with sinusoidal fringes, with 25 fringes per centimeter, which acts as the reference background, and an imaging Canon lens with focal distance of 300 mm (working at $f\#16$). The printed background is located at a distance $d' = 5170$ mm from the camera, and the synthetic air jet is placed at a distance $s = 600$ mm from the background. Both background and object plane are positioned within the depth of focus of the lens. Images are acquired at 2000 fps. A schematic diagram of the device for producing the synthetic air jet is shown in Fig. 20.2. The orifice diameter is 3 mm and its streamwise length is 6.31 mm.

The region of observation is 10×100 mm² for full images. However, the results are presented in smaller regions. A speaker driven by a sinusoidal signal generates the airflow. The background is illuminated by a 2×10 matrix of 3-W white LEDs. The background is printed on a transparent slide and placed over the surface of an acrylic sheet.

The Reynolds number and the adimensional stroke length of the synthetic air jet are set to 520 (which implies laminar flow) and 4.4 (which in turn accomplishes the condition for jet formation [19]), respectively. The driving frequency of the speaker matches the first resonance cavity frequency, 125 Hz. The heated surface (80°C) corresponds to the aluminum plate of a programmable temperature device (Model Echotherm IC30, Torrey Pines Scientific).

The reference object state relates to the convective plume produced by the plate surface at 80°C . A uniform temperature distribution along the plate surface is obtained, Fig. 20.3d. The displaced images are in turn registered with the speaker turned on. Figure 20.3a shows a typical FD image for the air jet.

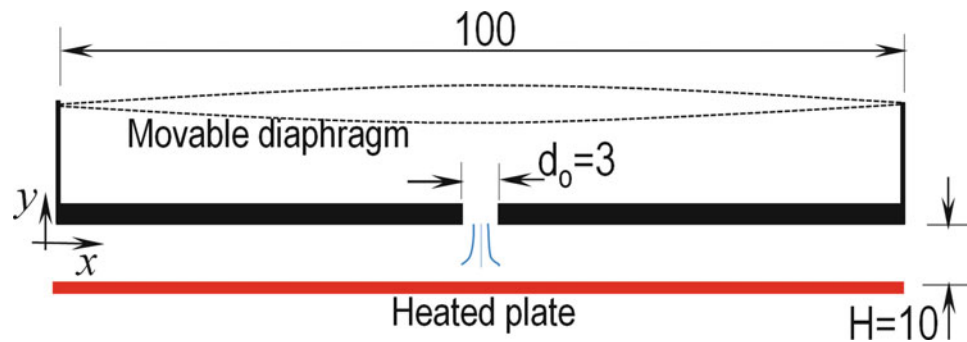


Fig. 20.2 Synthetic air jet generator. Dimensions are in mm

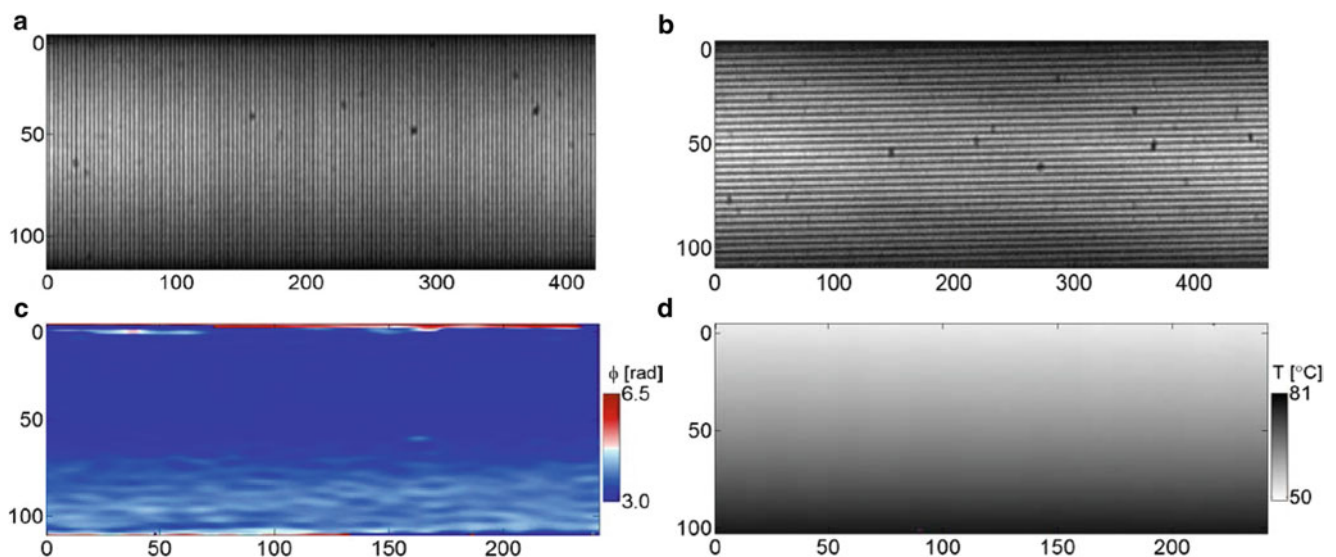


Fig. 20.3 Typical images of FD for (a) the synthetic air jet (the observation region is 10×36 mm²) and (b) the convective flow from the heated plate, with no jet. The corresponding phase map and temperature field of (b) are shown in (c) and (d), respectively

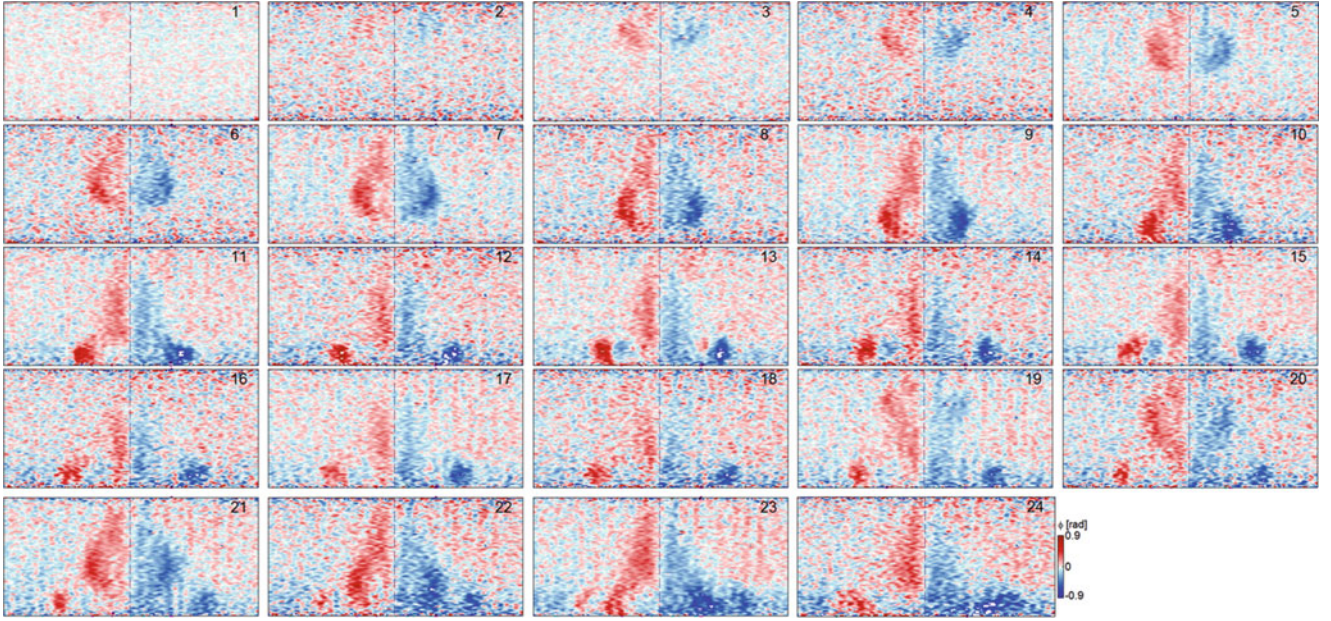


Fig. 20.4 Phase maps corresponding to a complete cycle of the resonator. The image size is 116×201 pix. The colormap denotes phase values in the range -0.9 to 0.9 rad

Fringe displacements are calculated by the Fourier method [17]. When the aluminum plate is heated, the resulting time-series displacement maps for one and a half cycles of the ensuing jet are shown in Fig. 20.4. One cycle of the system comprises 16 images. The first half of the sequence of images of a cycle starts with the forward movement of the diaphragm, which produces the ejection of air. At the 9th image from the onset of the ejection period, the synthetic jet reaches the heated plate and interacts with it. By considering these data, an approximated average speed of 3.3 m/s is calculated for the air jet. The ejected jet forms a vortex pair at the exit of the cavity. The vortices move downstream, and before reaching the hot plate, they lose their coherence (image 12) and become turbulent. In images 9–16, we can see that the jet interacts with the plate and at the same time air is drawn into the cavity. At the hot plate surface, we notice an enhanced mixing of the spatial structures arising from the breakdown of the vortex rings that impinge on the plate [19]. From image 17, a new cycle starts, and another jet is created. This jet interacts with the previous one and enhances the mixing process.

By considering the time series phase maps, it is noticed that for the first cycle after turning on the speaker, it takes nine images for the jet to reach the heated plate and only six for the second cycle. We think that this discrepancy stems from the fact that the first cycle corresponds to the moment at which the speaker is turned on and apparently the systems takes some time to respond. At later cycles, complete periodicity of the phenomenon is observed.

The jet dynamics can be optionally shown by the associated temperature fields. By considering that the variation of the index of refraction is axisymmetric and modeled as a Gaussian function of (y, z) , then (20.3) can be simplified to

$$\frac{\partial n}{\partial x} = \frac{n_0 \Delta x(x, y)}{s\ell}, \quad (20.12)$$

where ℓ is the equivalent width of the jet and is related to the diameter of the jet, d_j , as $\sqrt{\pi}d_j/2$. As pointed out in [20], the jet diameter may be modeled as a function of the streamwise length, y . This parameter is estimated by measuring the spanwise length of the jet for each instant. Then, maps of the change of the refractive index can be obtained by any integration method from the displacement distribution; here we have used the trapezoidal method along the x -direction [21]. When integration is performed, the initial values of the variation of refractive index (values for first column) are set to zero. Temperature values are obtained by (20.4). As it is noticed, the reference temperature at each point, T_0 , are needed. These can be known by measuring the temperature field resulting from comparing images without convective plume (heated plate turned off, ambient temperature of 20 °C) and with convective plume (heated plate set at 80 °C)—no synthetic jet for both images. For this latter case, we use a horizontal grating, and for the variation of the refractive index $\partial n/\partial y = n_0 \Delta y/(s\ell_P)$, where ℓ_P is the length of the heated plate along the observation direction, 12.5 cm. The integration process is done along the vertical

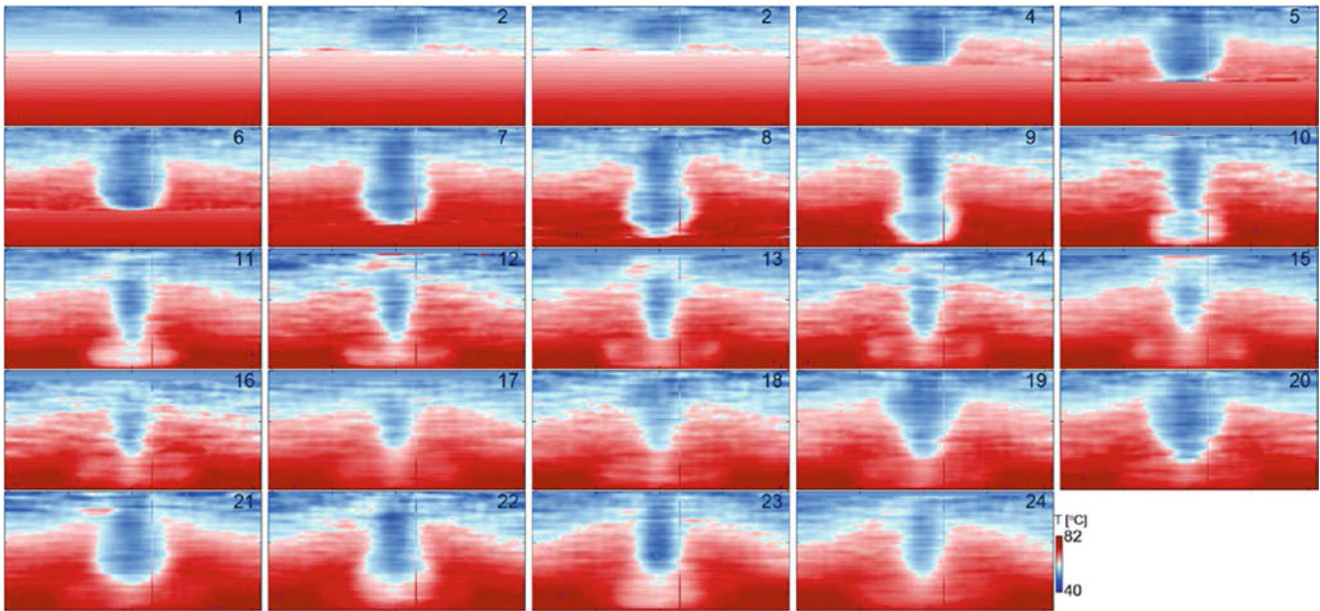


Fig. 20.5 Temperature distribution maps corresponding to Fig. 20.4

direction, where the values of temperature at the heated plate are assumed to be $80\text{ }^{\circ}\text{C}$ and the corresponding values for n_0 , 1.000186. A second value of temperature is necessary for the reference temperature distribution to be estimated; this value is measured by a thermocouple located at the bottom surface of the resonator cavity and is $52\text{ }^{\circ}\text{C}$. The corresponding phase map and temperature fields for this reference measurement are shown in Fig. 20.3c, d.

Considering the reference temperature measurement described above and the phase maps of Fig. 20.4, the resulting temperature maps of the synthetic jet are obtained and are given in Fig. 20.5. The generation of a synthetic jet in each cycle is clearly seen. The temperature image 1 shows the onset of the ejection of the jet, which is embedded in a varying temperature distribution which coincides with that shown in Fig. 20.3d. As is noticed, the synthetic jet transports air which is basically at the temperature observed at the exit of the cavity. As this cool air gets close to the heated plate it becomes warmer, image 9. After impinging with the plate (images 10–17), it is observed a further increase of the jet temperature. As mentioned previously, in image 17 a new ejection period begins and the new jet starts interacting with the debris of the previous jet. The results shown by the times series agrees with the expected phenomenon: the synthetic jet entrains cool air from ambient, impinges on the bottom heated plate surface and circulates the surrounding air back to the ambient.

Temperature values above $80\text{ }^{\circ}\text{C}$ arise from the content of noise in the raw images.

It is worth noting that the main difference of these results compared to those in [3, 20] is that in the present work, in order to enhance the visibility of the jet, no gas is injected in the cavity. This imposes severe restrictions on the optical layout, since the variations of refractive index are relatively small. Therefore, the background-to-object distance has to be as large as the depth of field allows it. Furthermore, to increase the spatial resolution, a small grating period is chosen. Then, to resolve such small periods, moderate values for the lens aperture are implied. This in turn affects the depth of field.

20.4 Conclusions

The FD technique has been applied to the measurement of temperature of a synthetic air jet when interacts with the thermal flow produced by a heated surface. The results show the ensuing of the synthetic air jet and the subsequent downstream motion, which occurs during about half the cycle of the driving frequency. In the other half of the period, the air jet interacts with the heated plate and draws away warmed air surrounding the plate.

Despite the region of interest was relatively small in the vertical direction, 1 cm, the results show that FD can be potentially used for the analysis of this type of devices.

References

1. B.S. Dalziel, G.O. Hughes, B.R. Sutherland, Whole-field density measurements by synthetic schlieren. *Exp. Fluids* **28**, 322–335 (2000)
2. H. Richard, M. Raffel, Principle and applications of the background oriented schlieren (BOS) method. *Meas. Sci. Technol.* **12**, 1576–1585 (2001)
3. J. Sznitman, T. Rosgen, Optical density visualization and reconstruction of negative buoyant vortex rings, in *12th International Symposium on Flow Visualization*, Göttingen, Germany, 10–14, 2006
4. G.E. Elsinga, B.W. Oudheusden, F. Scarano, D.W. Watt, Assessment and application of quantitative schlieren methods: calibrated color schlieren and background oriented schlieren. *Exp. Fluids* **36**, 309–325 (2004)
5. G.E.A. Meier, Computerized background-oriented schlieren. *Exp. Fluids* **33**, 181–187 (2002)
6. T. Persoons, T.S. O'Donovan, A pressure-based estimate of synthetic jet velocity. *Phys. Fluids* **19**(12), 128104-1 (2007)
7. A. McGuinn, T. Persoons, T.S. O'Donovan, P. Valiorgue, D.B. Murray, Heat transfer measurements of an impinging synthetic air jet with constant stroke length, in *5th European Thermal-Sciences Conference*, The Netherlands, 2008
8. H. Schardin, Toepler's schlieren method, basic principles for its use and quantitative evaluation, in *Selected Papers on Schlieren Optics*. SPIE Milestones Series, vol. MS61 (SPIE, Bellingham, 1992)
9. W. Hauf, U. Grugull, *Optical Methods in Heat Transfer* (Academic, New York, 1970), pp. 166–167
10. O.S. Jensen, J.P. Kunsch, T. Rosgen, Optical density and velocity measurements in cryogenic gas flows. *Exp. Fluids* **39**, 48–55 (2005)
11. C. Alvarez-Herrera, D. Moreno-Hernandez, B. Barrientos, Temperature measurement of an axisymmetric flame by using a schlieren system. *J. Opt. A Pure Appl. Opt.* **10**(10), 7 (2008). 104014
12. C. Alvarez-Herrera, D. Moreno, B. Barrientos, J.A. Guerrero Viramontes, Temperature measurement of air convection using a schlieren system. *Opt. Laser Technol.* **41**, 233–240 (2008)
13. P. Siegmann, P. Álvarez-Fernández, V.F. Díaz-Garrido, E.A. Patterson, A simultaneous in- and out-of-plane displacement measurement method. *Opt. Lett.* **36**(1), 10–12 (2011)
14. Z. Zhang, C.E. Towers, D.P. Towers, Time efficient color fringe projection system for 3D shape and color using optimum 3-frequency selection. *Opt. Express* **14**(14), 6444–6455 (2006)
15. D.W. Robinson, *Interferogram Analysis (Digital Fringe Pattern Measurements)* (IOP Publishing, Philadelphia, 1993)
16. K.J. Gasvik, *Optical Metrology*, 3rd edn. (Wiley, Sussex, 2003)
17. M. Takeda, H. Ina, S. Kobayashi, Fourier-transform method of fringe-pattern analysis for computer-based topography and interferometry. *J. Opt. Soc. Am.* **72**(1), 156–160 (1982)
18. B. Barrientos, M. Cywiak, W.K. Lee, P. Bryanston-Cross, Measurement of dynamic deformation using a superimposed grating. *Rev. Mex. Fis.* **50**, 12–18 (2004)
19. U. Ingard, On the theory and design of acoustic resonators. *J. Acoust. Soc. Am.* **25**(6), 1037–1061 (1953)
20. B.L. Smith, A. Glezer, The formation and evolution of synthetic jets. *Phys. Fluids* **10**(9), 2281–2297 (1998)
21. J. Davis, P. Rabinowitz, *Methods of Numerical Integration* (Academic, New York, 1984), pp. 51–52

Chapter 21

Gates' Interferometer as Fringe Projection System for Recovering 3D Shapes

J.A. Rayas, M. León-Rodríguez, Amalia Martínez-García, and R.R. Cordero

Abstract 3D shape recovery systems, based on structured light projection, allow recovering three-dimensional shape from complex opaque surfaces. Particularly, when a fringe pattern with sinusoidal profile is projected on a surface and algorithms for recovering optical phase are performed for its demodulation, sub-micrometer resolutions can be obtained. The resolution is closely related to the angle formed by the axis system of projection and the observation direction; other important parameters are the local gradient of the sinusoidal profile projected and the bit depth of the digital camera used to capture the deformed patterns. In this work, the projected sinusoidal fringe pattern is generated by a Gates' interferometer where an expanded and collimated laser beam is impinged onto a non-polarizing cube beam splitter (parallel to the splitter coating). Internal reflections and refractions of the laser beam passing through the cube generate the interference fringes that are projected over the test object. The Fast Fourier Transform, FFT, technique and a simple phase unwrapping method are used for demodulation of registered fringe patterns. Results of the three-dimensional surface of a coin that has a relief of about 150 μm with a theoretical axial resolution varying from 0.1 to 7 μm are presented.

Keywords 3D shape recovery • Interferometer • Fringe projection • Variable resolution

21.1 Introduction

The structured-light projection systems have become a powerful tool in the recovery of complex surface shapes of objects [1, 2]. It is common to find, in the literature, 3D contouring systems operating in real time with remarkable results thanks to multiple corrections implemented in the system or subsystems [3–5]. Digital retrieving of the topography of a real object can pursue various purposes such as biological, mechanicals and medical applications, among others [6–8]; its remote sensing (non-contact) implies a high level of confidence when the object in question is delicate.

In these systems it is possible to project different geometric patterns, straight lines, circles, dots, etc., using laser light or white light [2]. However, when sinusoidal fringe patterns are projected, you can apply digital interferogram analysis techniques, which allow recovering the 3D shape simultaneously for a large number of points (as many as the resolution of a modern digital camera) in a short lapse of time.

In this paper, we propose to apply a Gates' interferometer as a system of generation and projection of the sinusoidal fringe pattern. Except for the common path interferometers, the interferometric instability has complicated its implementation in fringe projection systems. However, the interferometer proposed in this paper simplifies the implementation and improves the stability for using in environments with little vibration control.

In Sect. 21.2, the fundamentals of fringe projection technique are presented, which is applied in the contouring of opaque objects of low relief. The proposed interferometer for generating and projecting fringes, its components and geometry, is addressed in Sect. 21.3. The experimental data and results are presented in Sect. 21.4; the methods used in the digital processing of interferograms are also presented. Finally, Sect. 21.5 presents the conclusions.

J.A. Rayas (✉) • R.R. Cordero
Universidad de Santiago de Chile, Ave. Bernardo O'Higgins 3363, Santiago, Chile
e-mail: juan.rayas@usach.cl

M. León-Rodríguez
Universidad de Santiago de Chile, Ave. Bernardo O'Higgins 3363, Santiago, Chile
Universidad Politécnica del Bicentenario, Carretera Silao—Romita Km. 2, Silao, Guanajuato, Mexico

A. Martínez-García
Centro de Investigaciones en Óptica, Loma del Bosque 115, León, Guanajuato, Mexico

21.2 Fringe Projection Technique

The fringe pattern projection technique regularly involves three components: the optical light projection system (white light or laser) itself, a system imaging (photographic or video camera) and obviously the test object. These three elements are arranged to form a right triangle. The optical axes of the projection system and vision system, pointing toward the center of the test object, form an angle θ . The projection is oblique and the observation direction is perpendicular to a virtual reference plane, as shown in Fig. 21.1a. The fringes are projected parallel to the y -axis.

As shown in Fig. 21.1b, recovering the height “ z ” involves a trigonometry problem. In the figure, the object under test is represented by dashed line while the solid line represents a reference plane of height $z = 0$. If a ray of light is sent from the projection system to the reference plane, the vision system will see its projection at point A. Secondly, when projecting this same light ray onto the tested object, the projection moves to point B. Since the vision system is monocular, the sensitivity to change in the axis “ z ” is negligible so it will be seen as if the projected point is shifted to point C. Each point “ x, y ” in the object can be scanned by the projected point or a vertical line in order to recover the 3D shape of the surface whose height is determined by:

$$z(x, y) = \frac{d(x, y)}{\tan(\theta)} \quad (21.1)$$

where d is the apparent lateral displacement of point (x, y) caused by its height “ z ”, and θ is the angle between projection and observation directions.

Under the same principle, but illuminating the whole area of interest of the target with a sinusoidal pattern, the fringe projection technique can determine the 3D shape (x, y, z) of the illuminated field with only one shot. The pattern observed by the camera meets the characteristics of an interferogram with lineal carrier frequency whose intensity distribution is given by:

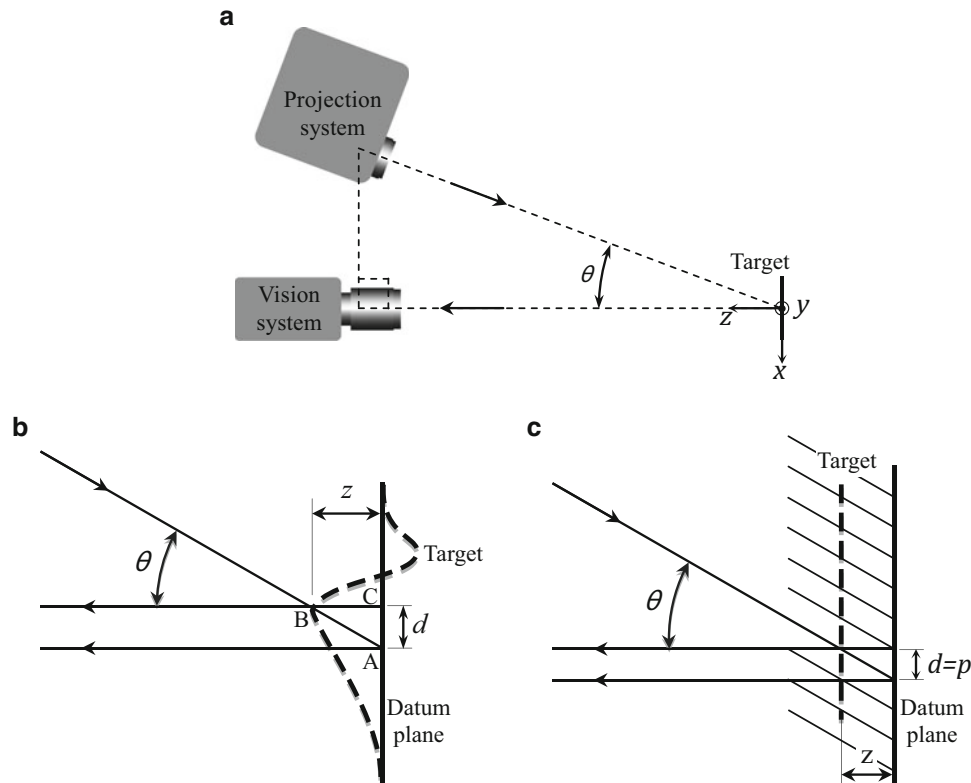


Fig. 21.1 Fringe projection system; (a) common configuration, (b) geometrical explanation for a point on the surface and (c) measurement ambiguity

$$I(x, y) = a(x, y) + b(x, y) \cos \left(x \frac{2\pi}{p} + \Delta\phi(x, y) \right) \quad (21.2)$$

where a is a bias value, b is the modulation amplitude, p is the projected period of the fringe pattern and ϕ is a phase value that is proportional to the local topography of the object under test. The intensity distribution for the reference plane is considered as the carrier signal which is constant for our particular case, and can be omitted ($\phi_0(x, y) = 0$). However, in cases where spherical projection is used, as in the case of digital video projectors, some corrections are necessary. [9] In order to extract (demodulate) the phase term of (21.2), corresponding to the test object ($\phi_1(x, y)$), methods of phase-shifting, which are widely described in the literature, can be implemented [10]. In any of these cases the topography shall be described by:

$$z(x, y) = \frac{\phi_1(x, y)}{2\pi} \frac{p}{\tan\theta} \quad (21.3)$$

It is noteworthy that the topography may not recover absolute values. As seen in Fig. 21.1c when the topography of the object causes a phase shift equal to a fringe pattern period, this will take the place of the neighboring fringes being impossible to determine their absolute height, only relative changes in height may be determined.

21.3 Experimental Set Up

The interferometric projection system used in this paper is based on the Gates' interferometer configuration [11] whose basic components are a laser and an unpolarized beam-splitter cube 50T-50R. This beam splitter is composed by two right angle prisms cemented together along their large faces; actually, on that interface, a thin film that generates the beam splitting (see Fig. 21.2a) on the face of one of the prisms is deposited.

As shown in Fig. 21.2b, the expanded and collimated laser beam is impinging on the edge of the splitter cube, parallel to the contact surface of the prisms, so that the two prisms are symmetrically illuminated. In order to differentiate the portion of the beam impinging on each prism, dashed and solid lines (ray traces) are drawn in the interferometric scheme. Following the path of the beams, represented by the dashed lines, it can be seen that after the first refraction, the beam is split into two (reflection and transmission), which are refracted again when leaving the cube. The same effect, but inverted, is seen in the rays represented by the solid lines, so that the output of each prism will carry an interference pattern whose frequency can be increased by rotating the beam-splitter cube.

By rotating the beam-splitter (angle α), the portion of the transmitted laser beam exits with the same angle as entered, while the reflected portion has an angle 2α , so that the distance between the resulting interfering fringes is given by [9]:

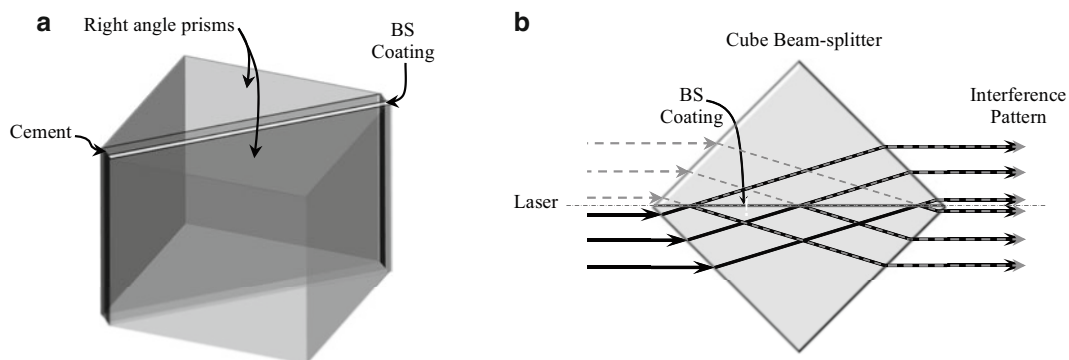
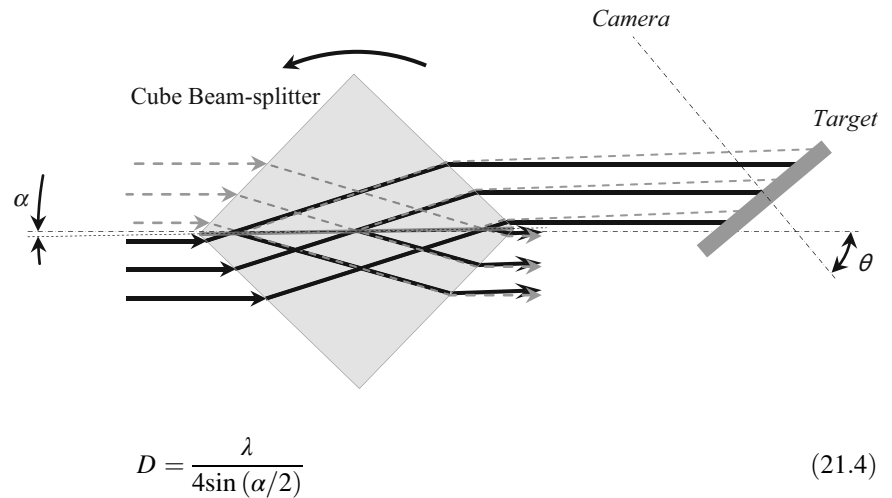


Fig. 21.2 Gates interferometer; (a) cube beam-splitter components and (b) amplitude-splitting interferometer

Fig. 21.3 Effect of the cube beam-splitter twist



where λ represents the wavelength of the laser used. Figure 21.3 shows a ray tracing for a cube rotation. As previously mentioned, the oblique illumination of the object under test produces the period observed by the vision system, $p = D / \cos \theta$.

This interferometric configuration does not allow us to shift the phase of a wavefront in order to apply the technique of phase-shifting in one shot [12]. Unlike this, the FFT technique, apart from recovering the phase, permits us to eliminate the carrier frequency corresponding to the phase; this process is widely known and it is described in the literature [13].

21.4 Results and Discussion

As observation system, a FireWire digital camera (CMOS sensor) is used, it has 1280×1024 pixels and 8-bit depth. The projection system uses a He–Ne laser of 12 mW and wavelength of 633 nm. An unpolarized beam-splitter cube of 1" is placed on a displacement stage with 6° of freedom for easy alignment. Similarly, the test object was positioned on a stage with three degrees of freedom corresponding to the rotation along each Cartesian axis. To ensure perpendicularity between the object plane and the camera sensor, a plane mirror was positioned in place of the object so that the camera could observe itself. The camera is attached to the rotating base of the object by an arm in order to avoid misalignment when setting an angle θ . A projection period of $125 \mu\text{m}$ is measured directly with the camera (previously calibrated); this period corresponds to an angle α of 0.27° . The angle θ was set to 58° as seen in the image of Fig. 21.4b of the experimental set up.

The object under test, shown in Fig. 21.4a, is a CLP\$100 (Chilean pesos) coin, it has the bust of a Mapuche Indian. This coin was covered with a coat of white paint in order to avoid specular reflections.

Figure 21.5 shows the results obtained for the area of the coin indicated in Fig. 21.4a; in Fig. 21.5a we show the resulting fringe pattern, the wrap phase is in Fig. 21.5b and the extracted topography in Fig. 21.5d. Applying the FFT technique to a pair of raw images, the phase shown in Fig. 21.5b is obtained; as can be seen, this phase is wrapped, so a simple unwrapping process is applied to obtain the result shown in Fig. 21.5c.

21.5 Conclusions

3D contouring results for a Chilean coin, using a Gates' interferometer as generator and projector of fringes, are presented. The stability of the common path interferometer makes it an ideal instrument for use in uncontrolled environments. Although Gates' interferometer is not a common path interferometer, it is as stable as one of these types. Its stability arises from the fact that both arms are part of the same solid cube beam-splitter. In particular, for the configuration used, the instrument resolution varies from 0.1 to $7 \mu\text{m}$, depending on the local gradient of the sinusoidal profile projected onto the object.

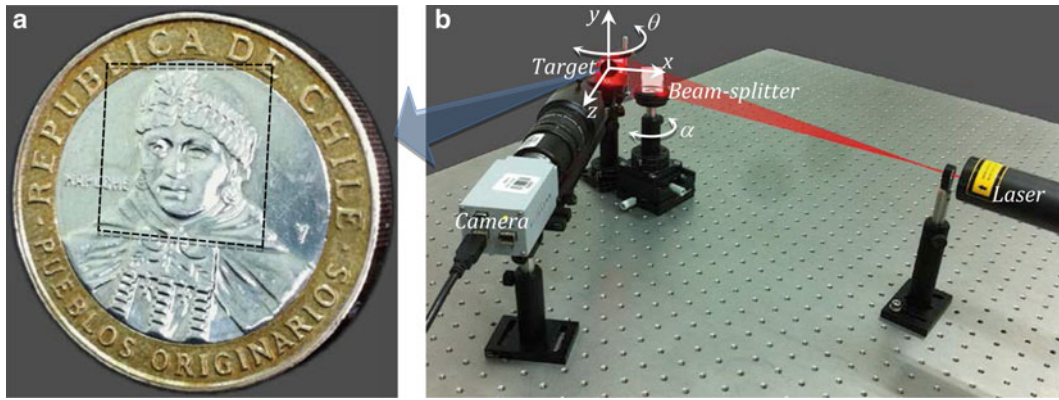


Fig. 21.4 (a) Object under test (Chilean coin) area of interest is indicated and (b) experimental set up

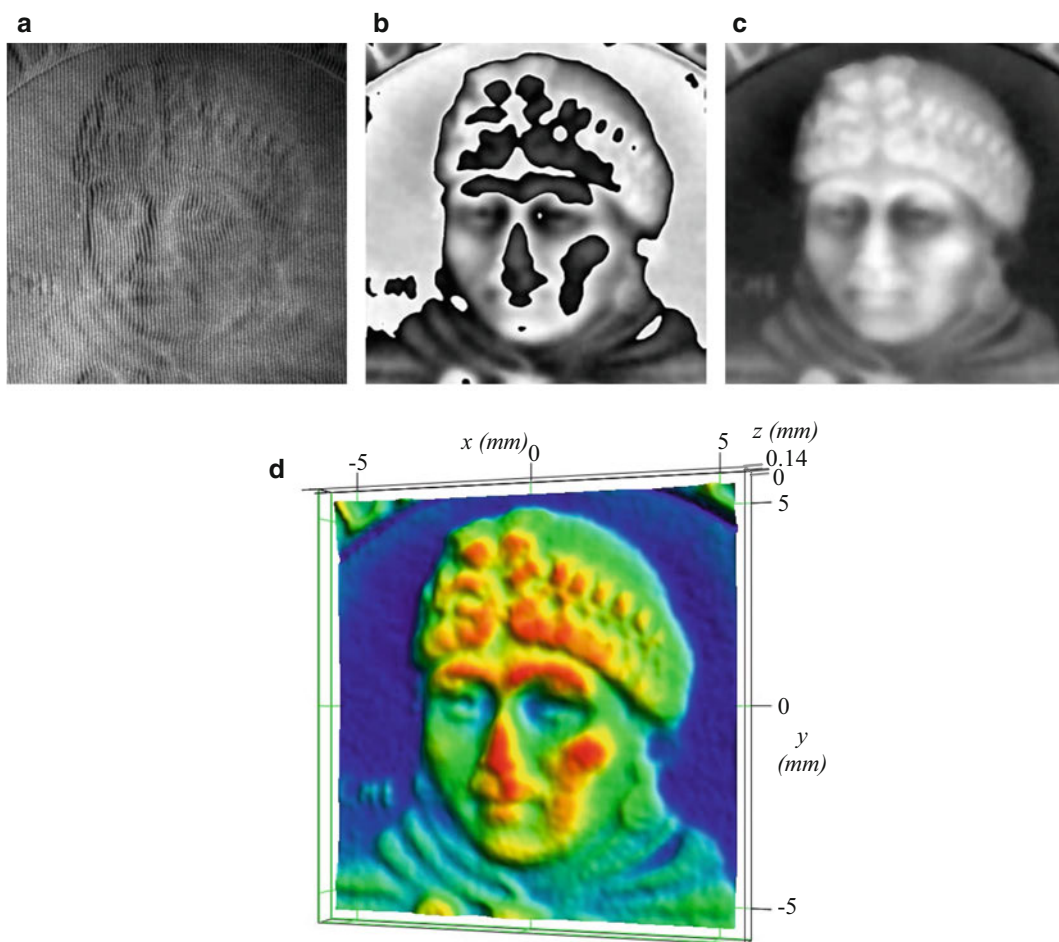


Fig. 21.5 Experimental results; (a) fringe pattern projected on the coin, (b) wrapped phase retrieved, (c) unwrapped phase, and (d) 3D surface counteracted

Acknowledgements The support of CONICYT-PCHA/Doctorado Nacional/2013- 63130065, FONDECYT (Preis 3140076, Preis 1140239 and Preis 1120764), FONDEF (Preis IT13I10034), CORFO (Preis 14BPC4-28651), USACH-DICYT ASOCIATIVO, SEP-PROMEP Preis 14146 F-38, and UTFSM- DGIP, is gratefully acknowledged.

References

1. S.S. Gorthi, P. Rastogi, Fringe projection techniques: whither we are? *Opt. Lasers Eng.* **48**(2), 133–140 (2010)
2. J. Salvi, S. Fernandez, T. Pribanic, X. Llado, A state of the art in structured light patterns for surface profilometry. *Pattern Recogn.* **43**(8), 2666–2680 (2010)
3. S. Zhang, Recent progresses on real-time 3D shape measurement using digital fringe projection techniques. *Opt. Lasers Eng.* **48**(2), 149–158 (2010)
4. A. Martínez, J.A. Rayas, H.J. Puga, K. Genovese, Iterative estimation of the topography measurement by fringe-projection method with divergent illumination by considering the pitch variation along the x and z directions. *Opt. Lasers Eng.* **48**, 877–881 (2010)
5. H. Miao, C. Quan, C.J. Tay, Y. Fu, Analysis of phase distortion in phase-shifted fringe projection. *Opt. Lasers Eng.* **45**, 318–325 (2007)
6. A. Martínez, J.A. Rayas, R.R. Cordero, D. Balieiro, F. Labbe, Leaf cuticle topography retrieved by using fringe projection. *Opt. Lasers Eng.* **50**, 231–235 (2012)
7. R.R. Cordero, A. Martínez, J.A. Rayas, F. Labbe, Necking progression in tensile specimens monitored in real-time by using fringe projection. *Opt. Lasers Eng.* **48**(12), 1285–1290 (2010)
8. G. Sansoni, M. Trebeschi, F. Docchio, State-of-the-art and applications of 3D imaging sensors in industry, cultural heritage, medicine, and criminal investigation. *Sensors* **9**(1), 568–601 (2009)
9. K.G. Gåsvik, *Optical Metrology* (Wiley, New York, 2003)
10. D. Malacara, M. Servín, Z. Malacara, *Interferogram Analysis for Optical Testing*, 2nd edn. (CRC Press, Hoboken, 2005)
11. Malacara D., *Optical Shop Testing*, 3rd ed. vol. 26, no. 7 (Wiley, Hoboken, 2007)
12. Z.H. Zhang, Review of single-shot 3D shape measurement by phase calculation-based fringe projection techniques. *Opt. Lasers Eng.* **50**(8), 1097–1106 (2012)
13. M. Takeda, H. Ina, H. Kobayashi, Fourier-transform method of fringe-pattern analysis for computer-based topography and interferometry. *J. Opt. Soc. Am.* **72**(1), 156 (1982)

Chapter 22

Development of an Automated Laser Induced Breakdown Spectroscopy System for Compositional Mapping of Surfaces

E. Ponce Flores, J.R. Domínguez Torres, R. Galindo Del Valle, and A.E. Villarreal

Abstract In this work it is described the integration of a system capable of performing automatically the compositional mapping of surfaces, by the method of laser induced breakdown spectroscopy. This system consists of a mobile mechanical base, a control system whose processing center is a development board Arduino Mega, which interacts with the user through a visual environment programmed in National Instruments LabVIEW and a piece of software for processing the spectrum obtained. Also, it describes the first experimental tests and shows preliminary results.

Keywords Arduino • LabView • LIBS • Spectrometry • Mapping • Automate • Visual interface

22.1 Introduction

Because all elements of the periodic table emit light in a characteristic manner when they receive energy, determining the resulting spectrum permit to identify different substances. As the excitation source, the laser-induced plasma spectroscopy (LIBS) [1] uses a high energy laser which allows the analysis of samples regardless of the state of aggregation [2, 3]. For the purposes of this article, tests were conducted only on solid state samples.

Through the use of the LIBS technique, it is possible to do compositional mapping surfaces, i.e., determining the distribution of components in different parts of a sample [4]. They used double laser pulses sources, an echelle spectrometer and an ICCD camera, in a cell that houses the interaction built for analyzing the distribution of chemical elements on the surface of samples obtained from different rocks.

In order to get a similar, Laser-induced breakdown spectroscopy (LIBS) more economical, modular and portable equipment, an automated system for the compositional mapping of surfaces was developed at “Centro de Investigación en Ciencia Aplicada y Tecnología Avanzada” (CICATA) Unit Altamira.

22.2 Experimental Development

The developed system consists of three main parts: the X–Y table to control the position of the sample, the control circuit that drives the motors and communicates with the PC, and a visual environment designed in Labview. In the visual environment the user has two options: make timely analysis using LIBS in the area of the table, selecting the location of the shot, or make shots matrices for surface mapping with the possibility to choose the mapping area, position and the number of shots. This eases the task of chemical analysis by LIBS, providing the option to control the trigger position with a resolution of 0.014 mm.

The test of the equipment capabilities was realized by a compositional mapping of a \$10 Mexican pesos coin, with a previously known composition, this in order to make a comparison with the results obtained by the LIBS equipment.

E.P. Flores (✉) • J.D. Torres • R.G. Del Valle
Facultad de Mecatronica, Universidad Tecnologica de Altamira, Blvd. de los Ríos Km. 3 + 100, Puerto Industrial Altamira,
89608, Altamira, Tamaulipas, Mexico
e-mail: ernestoponce92@gmail.com

A. Villarreal
Instituto Politécnico Nacional, Centro de Investigación en Ciencia Aplicada y Tecnología Avanzada, Unidad Altamira,
CICATA-IPN. Km. 14.5 Carretera Tampico-Puerto Industrial Altamira, Altamira, Tamaulipas, Mexico

22.3 Experimental Setup

The spectrometer used is an Ocean Optics model USB4000; the excitation source is an Nd:YAG laser with energy per pulse of 60–360 mJ and shots widths of about 100 μ s, each composed of a train of pulses of 8 ns duration. The emission wavelength was 1064 nm.

As the displacement system, it was used a displacing stage consisting of a pair of micrometric screws coupled to stepper motors NEMA 17" of 200 steps per revolution, allowing movement in two directions (Fig. 22.1). At the top of the picture it is observed the mobile base with the optical fiber, in the right part we can see the laser and in the bottom left there is a box that contains the control circuit along with its power supply. Finally, in the bottom right we find the laser power supply.

For the control system were used a development board Arduino Mega, a shield for CNC, and two drivers for stepper motors [5]. The circuit power is obtained from a ATX power supply.

An H bridge and a solid state relay were included to activate of the laser through the visual environment [6].

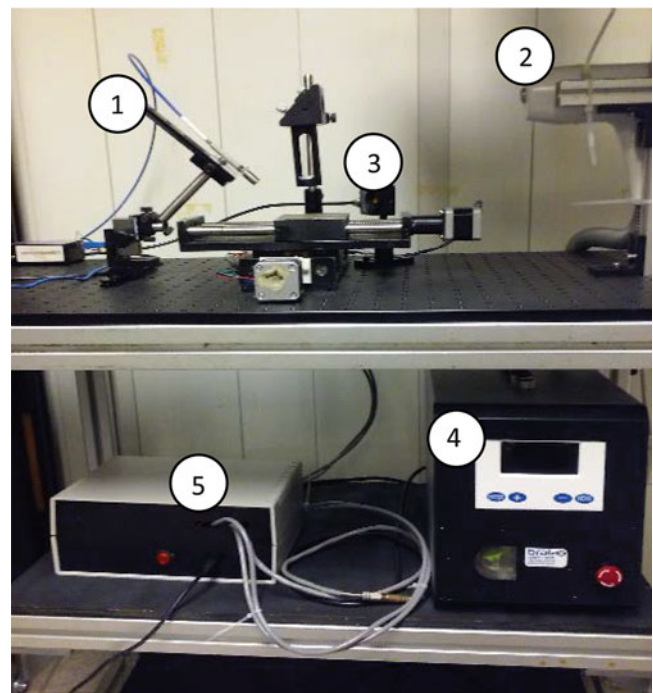
22.4 Visual Interface

The system is controlled by the user through a visual interface or environment designed in LabView (the software was chosen due to the integration it has with the Arduino microcontrollers). In it we find three different windows: positioning, mapping and configuration [7].

In the positioning window (Fig. 22.2), the user can move the sample to a specific coordinate and do a shot as a separate action. Measuring movement is in motor steps, they are transformed by the program in millimeters (0.015 mm per step). We can plot the position of the stage where shooting is done. Finally, in the bottom left we find the buttons of position, shot, and stop, which stops the program. It is also included is a view of the information as it is sent to the microcontroller through a USB-Serial port.

The next window corresponds to mapping (Fig. 22.3). Here you can see different sections with information from matrix mapping. In the configuration section we can select the start and end points of the mapping in the X–Y axes. Based on the selected points, the program performs the calculations for the possible numbers of rows and columns. Once all the settings are selected for the matrix, the conversions are done automatically to millimeters and dimensions of the area to be covered and the separation between shots are calculated.

Fig. 22.1 Diagram of the setup. (1) Spectrometer, (2) Laser, (3) Stage, (4) Power supply and power control, (5) Mapping system



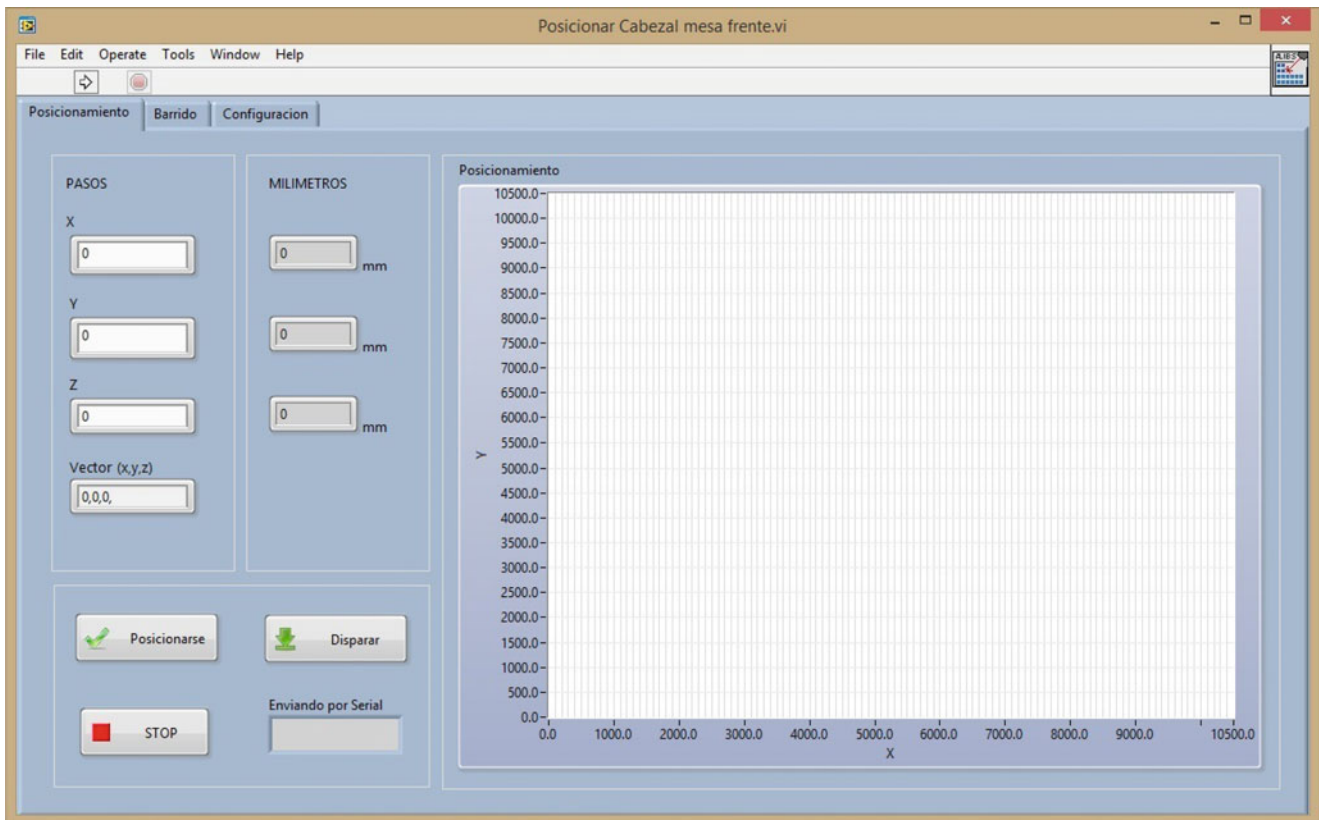


Fig. 22.2 Positioning window

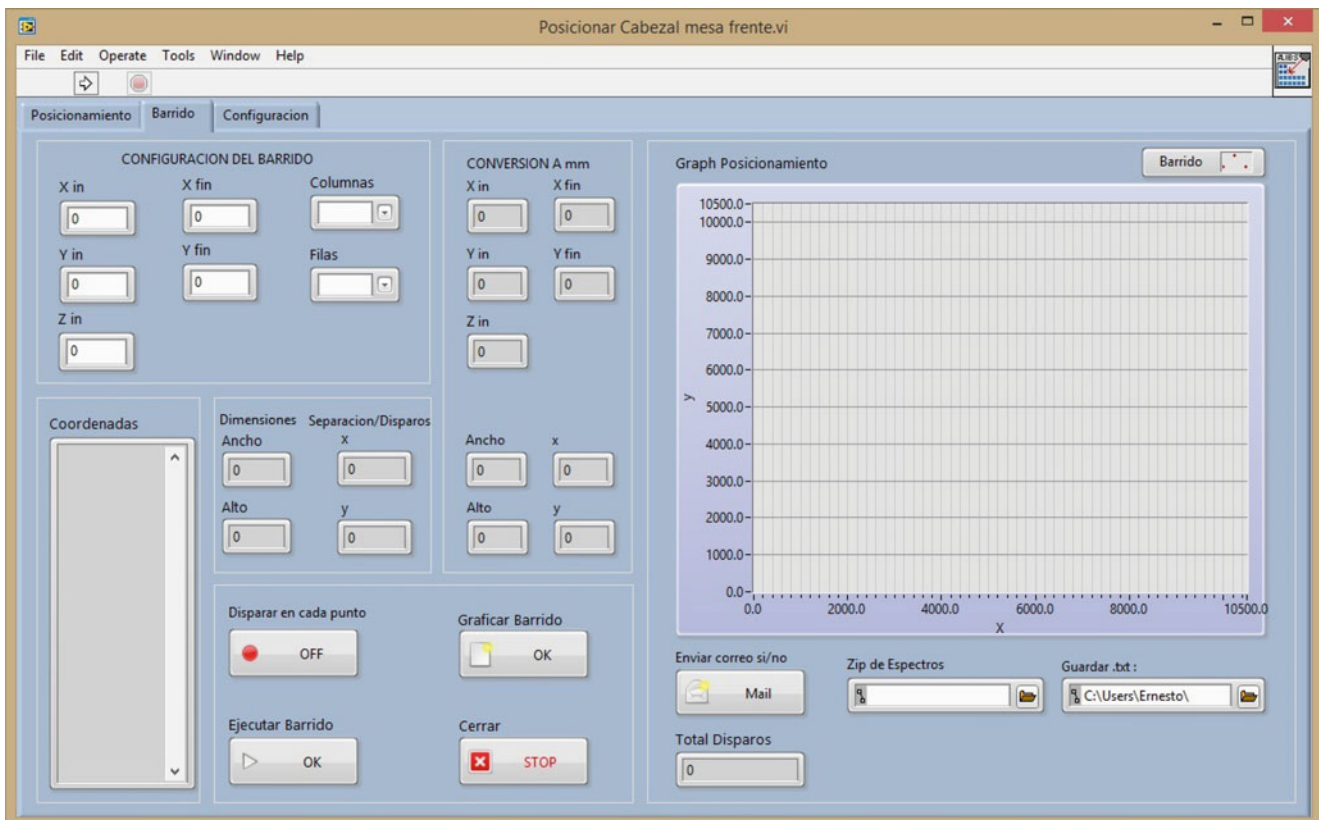


Fig. 22.3 Mapping window

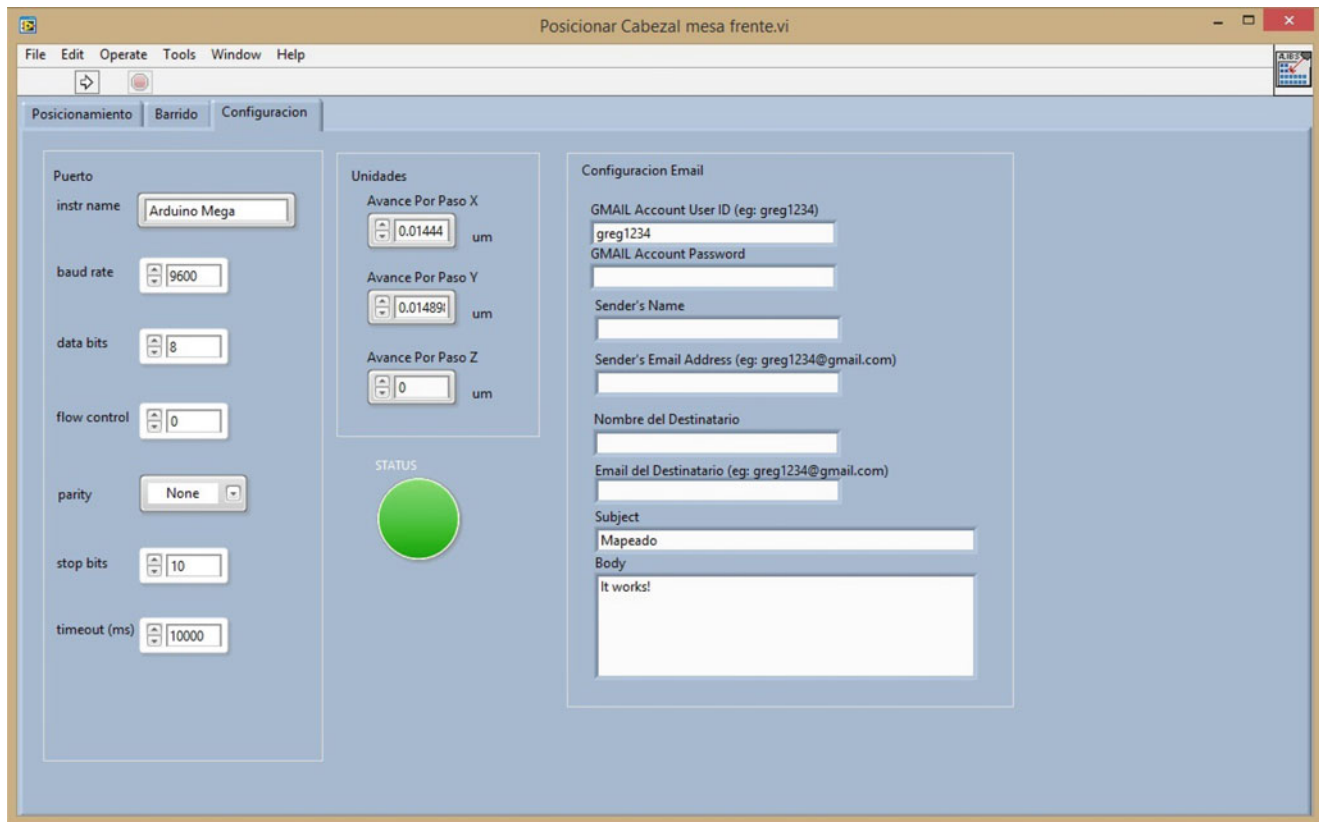


Fig. 22.4 Configuration window

As in the previous window, it contains a graph plotting the position of each shot that forms the matrix. In this case, the coordinates of each shot (in motor steps) are shown, information that is necessary for the phase of analysis of results. We can select the option of shots during mapping or execute the movement only, this can be used for testing purposes prior to analysis. The “graph button” shows in the graph the position of the shots and the “run” button starts the process. The “stop” button stops the program execution.

As an additional utility, it is offered the possibility to configure an email account to send the results upon completion of the process, so it is not necessary that the user is present all the time, especially in large mappings.

A third window contains the settings for the connection with the development board Arduino (Fig. 22.4), the user must select the COM port where it is connected your board and the Baud Rate. “Units” section can change the relationship between motor steps and millimeters, a default is the real relationship. All this can be changed to user convenience. Finally, the last section configures the emails from which you send and receive the results.

22.5 Analysis of the Spectra

The software used to obtain the spectrums is supplied by the company OceanView. During mapping, each of the results obtained during the shooting is saved in a .txt format within a user-selected folder to be read later.

For the analysis of the data collected, the LIBS Analyzer software is used, developed in CICATA Altamira [8]. In it you can make a number of adjustments, such as smoothing and baseline correction to improve spectrum and reduce the occurrence of noise. The smoothing filter that was used in the test analysis was the Savitzky—Golay. This software similarly allows detection of the peak intensities and selection of elements to be identified. With the coordinates of the shootings, it is possible to distinguish which part of the sample corresponds to each spectrum and thus plots a graph showing the distribution of its components.

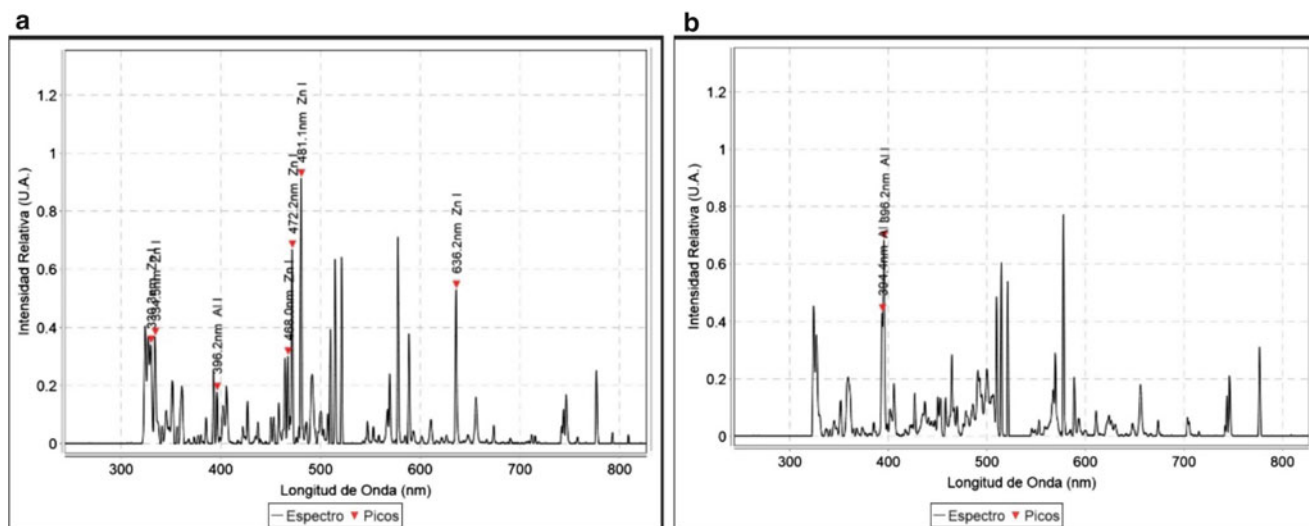


Fig. 22.5 (a) Coin central part spectrum, (b) coin external ring spectrum

22.6 Experimental Tests

As an example of the capabilities of the equipment, a mapping of 121 shots on a coin of 10 Mexican pesos was realized to compare the results obtained with the database of the Bank of Mexico [9], where you can find the exact composition of alloys that forms it.

The coin is formed by a central part composed of 65 % copper, 10 % nickel and 25 % zinc, and an external ring of 92 % copper, 6 % aluminum, and 2 % nickel. As shown, the difference between them is the presence of zinc and aluminum respectively. Because of this, the analysis focused on the search for the two elements to identify the part of the coin that corresponds to the spectrum obtained in each shot.

Mapping duration was approximately 6 min and covered an area of 583.56 mm²; spectrums were analyzed individually and based on the identified element it was prepared a graph showing the result obtained at each position. Four different patterns were found corresponding to the two parts of the coin (Fig. 22.5a, b), one to the shots that left the area of the sample and fell on the mobile stage, and one to the shots that fell off the X–Y table due to an error in calculating the position of the mapping.

As can be seen, the spectrum corresponding to the center of the coin shows numerous peaks associated with Zn, and only a peak associated with Al. The presence of Al peak may indicate their presence as minority element. In the second spectrum, of the wanted elements only Al was identified, element with a greater presence in the external ring.

Once the analysis was completed, the coordinates of the shooting were used to associate each position with the element found and produced the following graph (Fig. 22.6a, b).

Comparing the graph obtained (Fig. 22.6a) with the size of the coin (Fig. 22.6b), we show that the results correspond to the compositional distribution of the sample surface.

22.7 Conclusions

Currently the LIBS technique is mainly used in scientific laboratories and the equipment necessary for their use is scarce and very costly, and there are few automated systems on the market.

Hardware was developed which includes the implementation of scanning mechanisms, hardware power, coupling mechanisms of optic fiber and laser, among others. The control device was programmed and a user interface was designed. The performance of the equipment of CICATA Altamira, where it is already installed and running, has been adequate.

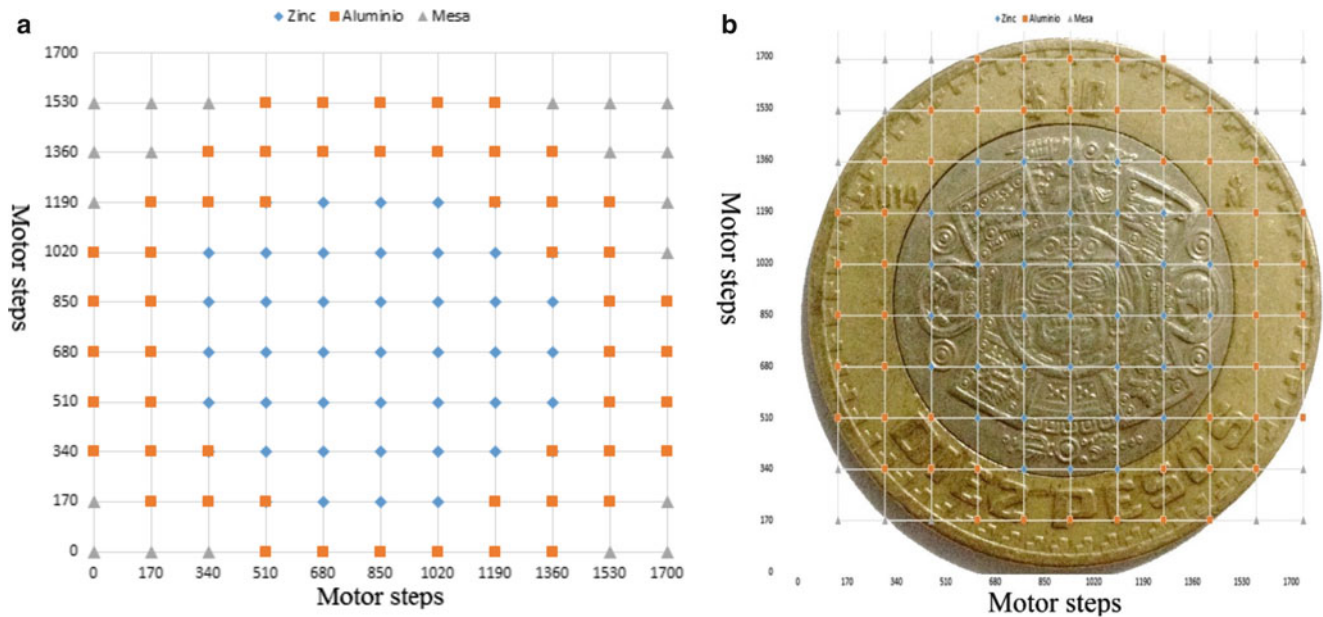


Fig. 22.6 (a) Elements found, (b) comparison with the coin

References

1. T. Flores, L. Ponce, M. Arronte, E. de Posada, Free-running and Q: switched LIBS measurements during the laser ablation of prickly pears spines. *Opt. Lasers Eng.* **47**(5), 578–583 (2009)
2. L. Moreira Osorio, L.V. Ponce Cabrera, M.A. Arronte García, T. Flores Reyes, I. Ravelo, Portable LIBS system for determining the composition of multilayer structures on objects of cultural value. *J. Phys.* (2011). Conference series, 274, 012093
3. L. Ponce, T. Flores, F. Alvira, G.M. Bilmes, M. Sosa, LIBS determination of toxic metals in fresh fish. *Appl. Optics* **V55**(N2), 254–258 (2016)
4. J. Novotný, K. Novotný, D. Prochazka, A. Hrdlic'ka, J. Kaiser, Two dimensional elemental mapping by laser-induced breakdown spectroscopy. *Spectrosc. Eur.* **26**(6), 6–10 (2014)
5. M. Banzi, *Getting Started with Arduino* (O'Reilly Media, New York, 2011)
6. D. Shetty, R.A. Kolk, *Mechatronics System Design: SI* (PWS, Boston, 2010)
7. M. Schmidt, *Arduino* (Pragmatic Bookshelf, Raleigh, 2011)
8. Pérez Báez, Zeferino, Desarrollo de software para el análisis de espectroscopia de ruptura inducido por láser (2015), <http://tesis.ipn.mx:8080/xmlui/handle/123456789/13457>
9. Banxico, Monedas de 10 pesos (2015), <http://www.banxico.org.mx/billetes-y-monedas/informacion-general/billetes-y-monedas-de-fabricacion-actual/billetes-y-monedas-de-fabricacion-actual/monedas/moneda-10-pesos.html>

Chapter 23

Artificial Visual System Used for Dental Fluorosis Discrimination

Miguel Mora-González, Evelia Martínez-Cano, Francisco J. Casillas-Rodríguez, Francisco G. Peña-Lecona, Carlos A. Reyes-García, Jesús Muñoz-Maciel, and H. Ulises Rodríguez-Marmolejo

Abstract A new technique for the estimation of the degree of fluorosis based on Dean Index and artificial vision system to improve the diagnostic of dental fluorosis is proposed. A group of 15 people diagnosed with dental fluorosis according with the Dean Index was studied. The images were digitally processed in order to discern and estimate the dental fluorosis using a discrimination algorithm based on one layer of Artificial Neural Networks and statistics criterion. A vision system and the implemented algorithm showed the ability to detect the different degrees of dental fluorosis in accordance with the diagnosis. Additionally, with this technique it was possible to identify the different affection degrees of fluorosis by dental piece. The inclusion of a vision system and an algorithm for the estimation of dental fluorosis in this technique contributes as an alternative tool for an objective diagnostic by specialists.

Keywords Dental fluorosis • Dean index • Standard deviation • Back-propagation • RGB

23.1 Introduction

Dental enamel is the most mineralized structure in human body. Approximately 85 % of dental enamel volume is occupied by highly organized hydroxyapatite crystals. Enamel mineralization is highly sensitive to free fluoride ions, which uniquely promotes the hydrolysis of acidic precursors such Dean Index (DI) as octacalcium phosphate and precipitation of fluoridated apatite crystals, which in turn leads to enamel hypomineralization [1, 2].

The process of hypomineralization of the enamel caused by the ingestion of fluoridated water, is known as dental fluorosis [3, 4]. A high incidence of dental fluorosis has been identified in the western-central region of Mexico, in states like Aguascalientes, Chihuahua, Durango, Guanajuato, Hidalgo, Jalisco, San Luis Potosí, etc. In particular, in the city of Lagos de Moreno, Jalisco [5], a very high incidence has also been identified [6].

The fluorosis degree varies in relation with the ingested quantity of fluoride and the duration of the consumption [7, 8]. Medical conditions can be observed like opaque white spots or colored spots, yellowish and brownish, and in critical cases the morphology of the teeth can also be modified. The relationship between the high concentration of fluoride in the ingested water and the fluoride effect in the enamel of the teeth was first reported in [9]. The Dean Index (DI) establishes the degree of dental fluorosis affection depending of fluoride exposure [10].

In an attempt to understand the mechanism of the dental fluorosis, as well as the microstructural defects to which this entails, techniques to determine the damage of the dental enamel, in extracted pieces, have been used too. Among these techniques we find: histological, histochemistry, scanning electron microscopy, microradiography, Raman spectroscopy, among others [11–15].

M. Mora-González (✉) • E. Martínez-Cano • F.J. Casillas-Rodríguez • F.G. Peña-Lecona • J. Muñoz-Maciel
Departamento de Ciencias Exactas y Tecnología, Centro Universitario de los Lagos, Universidad de Guadalajara,
Lagos de Moreno, Jalisco 47460, Mexico
e-mail: mmora@culagos.udg.mx

C.A. Reyes-García
Instituto Nacional de Astrofísica, Óptica y Electrónica. Luis Enrique Erro No. 1, Sta. Ma. Tonanzintla,
C.P. 72840 Puebla, Mexico

H.U. Rodríguez-Marmolejo
Departamento de Ciencias Exactas y Tecnología, Centro Universitario de los Lagos, Universidad de Guadalajara,
Lagos de Moreno, Jalisco 47460, Mexico

Instituto Tecnológico de Aguascalientes, Av. Adolfo López Mateos 1801, Fracc. Bona Gens,
Aguascalientes, Aguascalientes 20256, Mexico

Apart from DI, to determine qualitatively the dental fluorosis degree in a visual way or in a subjective appreciation of the variation of the color of teeth and esthetical aspects, it has been implemented other several scales: Thilstrup-Fejerskov Index, Teeth Surface Index Fluorosis, Fluorosis Risk Index, among others [16–18]. However, selection and acceptance of these indexes depends largely of the specialist capacity to distinguish the pigmentation changes produced in the enamel. It is well known that DI is one of the most currently utilized and is supported by the World Health Organization (WHO) due to its simplicity [19]. Some investigations have indicated limitations in the use of these indexes, since the diagnosis is based on the maximum damage localized in a place in the teeth and not on superficial quantification by dental piece (damage/mm²) [20, 21]. Some optical techniques have been reported to detect roughness and erosions in teeth enamel [22, 23]. In this work an alternative methodology, based on an artificial vision system and a Digital Image Processing (DIP) algorithm, for the quantification of the degree of fluorosis in a non-invasive way, is tested in tooth samples.

In the following sections, the proposed methodology to develop the artificial vision system algorithm is presented. Then, the experimental setup for capturing the teeth samples is explained. After that, the experimental results obtained through the proposed algorithm are shown and discussed. Finally the conclusions of the results are expressed.

23.2 Methodology

In the present study a group of 15 participants were selected as voluntaries of fluorosis patients. Its 15 experimental images were used by selecting the corresponding area of the dental plaque. Then a pixel to pixel exploration was performed and a statistical criterion was applied. Additionally, three control individuals was considered, each diagnosed by a dentist (using DI) as severe, moderate and mild, respectively, as shown in specialist diagnosis of Table 23.1. Some individuals diagnosed with any of the three degrees of fluorosis, volunteered to test our system. The participants were clinically evaluated in accordance with the ethical principles for medical research involving human subjects postulated in 1964 for the World Medical Association in its declaration of Helsinki [24].

The motivation to use DIP and Artificial Neural Network (ANN) as the methods for dental fluorosis discrimination came up from observing the characteristics brown spots from the fluorosis teeth expressed in DI. In order to discriminate the characteristics and diagnostic the fluorosis degree, the following digital processes need to be applied to teeth samples: experimental set-up for capturing images, algorithms to analyze the control and study cases images, evaluation to the study case images with a Back-Propagation ANN. Simultaneously to the experimental work, a group of specialists surveyed volunteers and issued their visual diagnostics. These processes are detailed below.

23.2.1 Experimental Setup

A dental image using a commercial digital camera (SONY DSC-F828) was obtained for each participant previously diagnosed by the dentist. In order to process each image, a quad processor PC (3 GHz and 8 GB of RAM) and Matlab[®] software were used. Before taking a photo, the participants were asked cleaning the tooth with cotton gauze in order to reduce the bright. The optical set-up used to capture the teeth images are shown in Fig. 23.1. Two ultra-bright white LEDs with a separation of 24 cm between them. These LEDs were used as light source to uniformly illuminate in direction to the object plane. To capture the images, a digital camera was placed in the z direction at a distance of 50 cm from the object plane. A size of 2.8 MB was obtained from each image, corresponding to a maximum resolution of 3264 × 2448 pixels for the option selected in the camera.

Table 23.1 Control parameters measurement and the diagnosis assigned by specialists according to DI

Control cases	Specialists diagnosis DI level	Measurement parameters in control images (in mm ²)		
		Severe	Moderate	Mild
1	Severe	14.78	39.67	0.14
2	Moderate	1.36	32.28	0.55
3	Mild	0.00	0.03	33.06

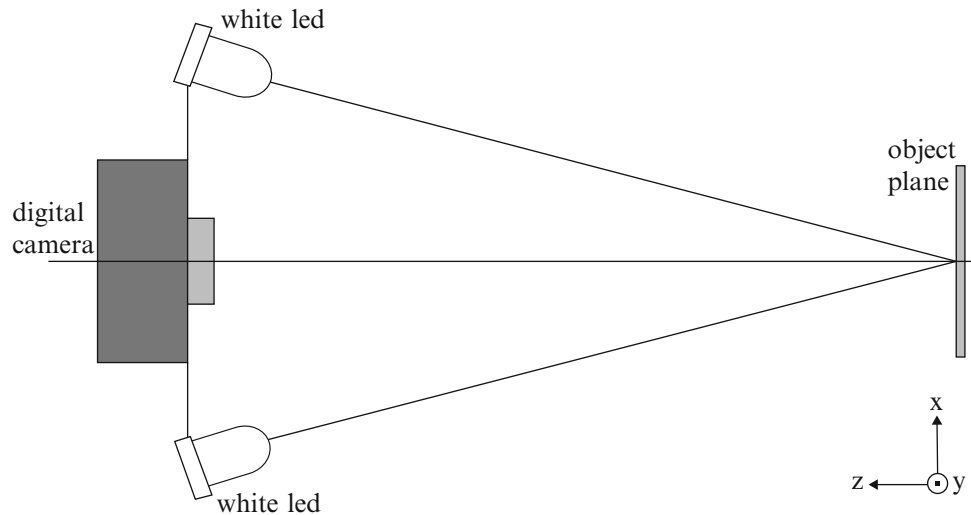


Fig. 23.1 Optical arrangement with LED illumination used to capture the teeth images

In order to obtain symmetrical controlled illumination conditions, only the illumination from the LEDs was used. A black mask with a squared aperture (13×7 cm real scale, or 1300×700 pixels in CCD plane, 1 pixel represents 0.01 mm^2) was positioned at the image plane to delimitate the area of analysis and minimize the additional information as reflections that would affect the images; also it was used to preserve the anonymity of the volunteers.

23.2.2 Control and Study Case of Fluorosis Image Algorithms

One procedure was used to find the control parameters, this was:

- Select the control images for the three DI fluorosis degrees (severe, moderate and mild).
- Select a control image area (25×25 pixels), for each one.
- RGB decomposition in selected zones.
- Find average μ of each color and fluorosis degree (in gsl):

$$\mu_{RS} = 71.72, \mu_{GS} = 40.33, \mu_{BS} = 37.77;$$

$$\mu_{RM} = 111.06, \mu_{GM} = 110.6, \mu_{BM} = 116.91;$$

$$\mu_{Rm} = 128, \mu_{Gm} = 123.96, \mu_{Bm} = 139.32.$$

With the subscripts S , M and m are the components severe, moderate and mild, respectively of the colors Red, Green and Blue.

- Find its standard deviations σ too:

$$\sigma_{RS} = 8.32, \sigma_{GS} = 7.46, \sigma_{BS} = 9.01;$$

$$\sigma_{RM} = 5.1, \sigma_{GM} = 6.86, \sigma_{BM} = 9.5;$$

$$\sigma_{Rm} = 4.24, \sigma_{Gm} = 4.83, \sigma_{Bm} = 5.26.$$

- Measurement the severe, moderate and mild zone for each control images.

As result of this procedure, nine parameters were found, as shown in measurement columns of Table 23.1. Another procedure was used to compare the control parameters with the study cases:

- Select Image to evaluate (15 cases).
- Select an image zone to evaluate, only teeth.
- RGB decomposition in selected zones.
- Compare the study case vs. control parameters:

$$\mu - \sigma \leq x_{i,j} \leq \mu + \sigma,$$

where $x_{i,j}$ is the study case element to evaluate and μ and σ are control images parameters determined in before algorithm.

- Determine pixel by pixel the fluorosis degree of each study case image.

23.2.3 ANN Analysis

A neural network is a system which contains some neurons interconnected. The type of neural network is defined by the arrangement of neurons and their connections. The ANN used in the experiment was a Back-Propagation, this has three inputs interconnected with five hidden layers and 100 neurons each one, and only one output. The internal characteristics of the ANN design were a 0.45 learning rate, 0.8 of momentum value and 0.001 of convergence error. This ANN where Artificial neural network (ANN)training with the nine parameters of the three control cases (see Table 23.1).

23.2.4 Visual Diagnosis

Clinical dental diagnostics of the participants was performed by specialists of the Jalisco's health sector. The dental fluorosis evaluation in permanent dentition based on the modified Dean index was done, this classifies the fluorosis with the maximum coloration presented in teeth to assign an affectation score [25]. The classification criteria considered for the study are as follows: in mild fluorosis degree, the white opaque areas in the enamel of the teeth are more extensive but involve as much as 50 % of the tooth; as the fluorosis degree is increasing to moderate degree, then all enamel surfaces of the teeth are affected, surfaces subject to attrition show marked wear, and brown stain is frequently a disfiguring feature; finally, severe degree is the maximum ID, in which all enamel surfaces are affected, hypoplasia is so marked that the general form of the tooth may be affected, brown stains are widespread, and teeth often present a corroded-like appearance.

23.3 Results

The results of 15 voluntaries scanned with the proposal statistical algorithm are shown in Table 23.2, where a resume of the frequency distributions of dental fluorosis in accordance with the DI diagnosed by the specialists is presented. In addition, the results of the back-propagation ANN are presented in the same table. 87 % of the results were in agreement between the specialists diagnosis and ANN, the only difference are the 7 and 9 study cases, the visual diagnosis its subjective and depends of several factors (illumination, teeth cleanliness and the most important judgment of the specialist opinion). Discrepancies are seen only in the 7 and 9 study cases, where a large difference between the moderate zones and the mild or severe zones can be observed in Table 23.2.

The proposed statistical algorithm provides information with respect to the affected area by different DI fluorosis degrees previously mentioned. The diagnosis of fluorosis is subjective because it depends only on the visual appreciation of a specialist, which is based on the highest degree of affectation observed, through the technical proposal, however it is possible to establish a criterion by zones and degrees of involvement in each patient.

Table 23.2 Proposed statistical algorithm and ANN results, as well as the diagnosis assigned by specialists according to DI

Study cases	Specialists diagnosis DI level	Measurement parameters (in mm ²)			ANN results
		Severe	Moderate	Mild	
1	Severe	14.48	16.11	0.32	Severe
2	Mild	0.46	10.08	1.39	Mild
3	Moderate	2.37	26.72	0.96	Moderate
4	Moderate	1.16	29.13	0.5	Moderate
5	Moderate	4.34	46.84	0.08	Moderate
6	Mild	0.83	11.37	0.26	Mild
7	Mild	1.14	25.29	0.81	Moderate
8	Severe	23.97	27.85	0.00	Severe
9	Severe	1.64	43.17	0.12	Moderate
10	Moderate	4.28	37.39	0.52	Moderate
11	Mild	5.45	23.29	1.57	Mild
12	Severe	15.02	46.63	0.05	Severe
13	Mild	0.00	1.77	7.62	Mild
14	Severe	41.71	7.76	0.00	Severe
15	Moderate	1.43	57.60	0.24	Moderate

The algorithm distinguishes between the identified regions as mild, moderate and severe. However, it should be mentioned that unlike the diagnosis made by specialists, the statistical algorithm also identified other affected areas and the ANN help in the diagnosis of the dental fluorosis. According to the data collected by the algorithm, Fig. 23.2 shows some images of the study cases results (1, 2, 4, 7 and 9 of Table 23.2), the areas affected by the dental fluorosis are highlighted in pseudocolor: red for severe, green for moderate and blue for mild. It can be seen that with this algorithm the assessment of affected areas is more objective, since it identifies areas affected by the different degrees of fluorosis.

However, within the diagnostic procedures currently used, all involve the visual and subjective criterion of the specialist to determine accurately the varying degrees of fluorosis. The proposed technique comes to be a reliable alternative tool for the diagnosis of fluorosis, since it is based on an artificial vision system that allows identifying the affected areas by means of an algorithm. Moreover, the system can be adapted to be used with any of the indexes until now accepted as a diagnostic tool.

23.4 Conclusions

A system for the measurement and diagnosis the degree of dental fluorosis based on statistical discrimination and back-propagation artificial neural network has been proposed. The capture of the images of dental plaques under controlled conditions and the assessment diagnosis based on an algorithm of discrimination for different degrees of fluorosis according to the DI, has been demonstrated.

The system proves to be easy in the implementation and in the interpretation. Furthermore, it is a fast processing and precise algorithm.

Finally, the results reported in this work suggest that the proposed system can be a useful tool and that it permits an objective diagnosis of dental fluorosis, and thus provides a more appropriate treatment to patients.

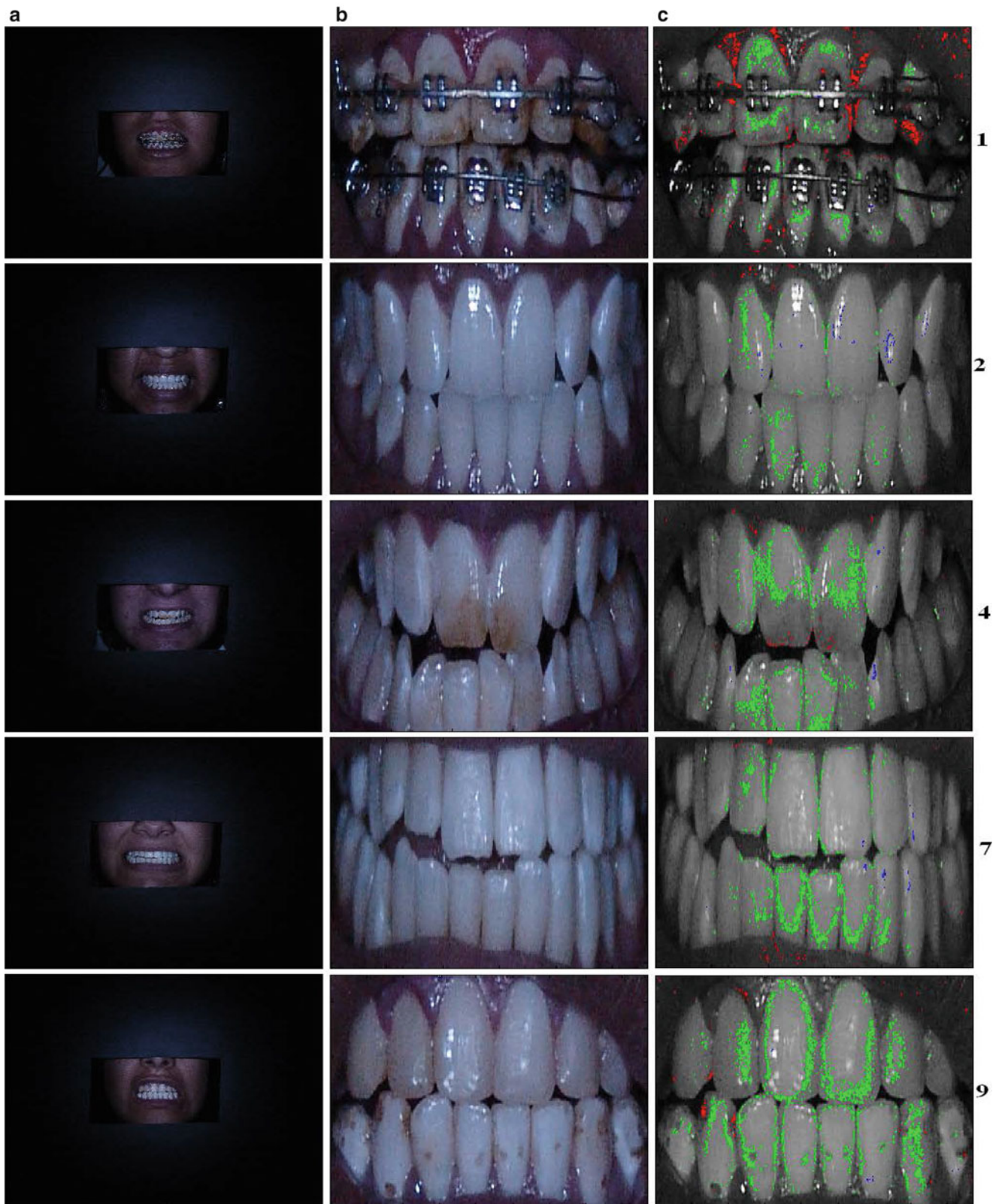


Fig. 23.2 Processed examples of 1, 3, 4, 7 and 9 fluorosis cases. (a) Experimental photographs; (b) zoom of teeth zones; and (c) pseudocolored processed of dental images

Acknowledgements The authors wish to thank the students of the *Centro Universitario de los Lagos* for their contribution to finishing of this work. The authors also wish to thank the administrative staff of the University for the facilities granted for the implementation of this work. The authors would like to thank too Ing. Hugo Reyes García for their contributions to the development of this work. Besides, the authors would like to express special thanks to the fluorosis voluntaries examined in this work.

References

1. J.P. Simmer, A.G. Fincham, Molecular mechanisms of dental enamel formation. *Crit. Rev. Oral Biol. Med.* **6**, 84–108 (1995)
2. T.A. Marshall, S.M. Levy, J.J. Warren, B. Broffitt, J.M. Eichenberger-Gilmore, P.J. Stumbo, Associations between intakes of fluoride from beverages during infancy and dental fluorosis of primary teeth. *J. Am. Coll. Nutr.* **23**, 108–116 (2004)
3. O. Fejerskov, M.J. Larsen, A. Richards, V. Baelum, Dental tissue effects of fluoride. *Adv. Dent. Res.* **8**, 15–31 (1994)
4. R. Hurtado, J. Gardea-Torresdey, Environmental evaluation of fluoride in drinking water at “Los Altos de Jalisco”, in the central Mexico region. *J. Toxicol. Environ. Health A* **67**, 1741–1753 (2004)
5. CIEPS Consultores, S.A. de C.V., Proyecto ejecutivo para rehabilitar y ampliar la red de agua potable y alcantarillado y Estudio geohidráulico de Lagos de Moreno, Jal., Comisión Nacional del Agua, México, 1991
6. V. Trejo, P. Bonilla, Exposición a fluoruros del agua potable en la ciudad de Aguascalientes, México. *Pan Am. J. Public Health* **10**, 108–113 (2001)
7. A. Richards, J. Kragstrup, K. Josephsen, O. Fejerskov, Dental fluorosis developed in post-secretory enamel. *J. Dent. Res.* **65**, 1406–1409 (1986)
8. P.R. Beltrán-Valladares, H. Cocom-Tun, J.F. Casanova-Rosado, A.A. Vallejos-Sánchez, C.E. Medina-Solís, G. Maupomé, Prevalencia de fluorosis dental y fuentes adicionales de exposición a fluoruro como factores de riesgo a fluorosis dental en escolares de Campeche México. *Rev. Invest. Clin.* **57**, 532–539 (2005)
9. G.V. Black, F. McKay, Mottled teeth and endemic developmental imperfection of the enamel heretofore unknown in the literature of dentistry. *Dent. Cosmos* **58**, 129–156 (1916)
10. H.T. Dean, Classification of mottled enamel diagnosis. *J. Am. Dent. Assoc.* **21**, 1421–1426 (1934)
11. E. Newbrun, F. Brudevold, Studies on the physical properties of fluorosed enamel—I: microradiographic studies. *Arch. Oral Biol.* **2**, 15–20 (1960)
12. H. Shinoda, H. Ogura, Scanning electron microscopical study of the fluorosis on enamel in rats. *Calcify Tissues Res.* **25**, 75–83 (1978)
13. A.K. Susheela, M. Bhatnagar, Fluoride toxicity: a biochemical and scanning electron microscopic study of enamel surface of rabbit teeth. *Arch. Toxicol.* **67**, 573–579 (1993)
14. N.J. Giambro, K. Prostack, P.K. Den-Besten, Characterization of fluorosed human enamel by color reflectance, ultrastructure and elemental composition. *Caries Res.* **29**, 251–257 (1995)
15. J.L. Gonzalez-Solís, E. Martínez-Cano, Y. Magaña-López, Early detection of dental fluorosis using Raman spectroscopy and principal component analysis. *Lasers Med. Sci* **30**(6), 1675–81 (2015)
16. H.S. Horowitz, W.S. Driscoll, R.J. Meyers, S.B. Heifetz, A. Kingman, A new method for assessing the prevalence of dental fluorosis the tooth surface index of fluorosis. *J. Am. Dent. Assoc.* **109**, 37–41 (1984)
17. D.G. Pendrys, The fluorosis risk index: a method for investigating risk factors. *J. Public Health Dent.* **50**, 291–298 (1990)
18. A. Kingman, Current techniques for measuring dental fluorosis: issues in data analysis. *Adv. Dent. Res.* **88**, 56–65 (1994)
19. P.E. Petersen, R.J. Baez, *Oral Health Surveys—Basic Methods*, 5th edn. (World Health Organization, Geneva, 2013)
20. B.W. Small, J.J. Murray, Enamel opacities: prevalence, classifications and a etiological considerations. *J. Dent.* **6**, 33–42 (1978)
21. J. Clarkson, Review of terminology, classifications, and indices of developmental defects of enamel. *Adv. Dent. Res.* **3**, 104–109 (1989)
22. H.A. Rahman, H.R.A. Rahim, H. Ahmad, M. Yasin, R. Apsari, S.W. Harun, Fiber optic displacement sensor for imaging of tooth surface roughness. *Measurement* **46**, 546–551 (2013)
23. B. Holme, L.H. Hove, A.B. Tveit, Using white light interferometry to measure etching of dental enamel. *Measurement* **38**, 137–147 (2005)
24. <http://www.wma.net/en/30publications/10policies/b3/index.html>
25. M. Sulieman, An overview of tooth discoloration: extrinsic, intrinsic and internalized stains. *Dent. Update* **32**, 463–471 (2005)

Chapter 24

Inspection of Laser Ablated Transparent Conductive Oxide Thin Films by a Multifunction Optical Measurement System

Chi-Hung Hwang, Ming-Hsing Shen, Shih-Feng Tseng, Wen-Tse Hsiao, I-Feng Cheng, and Wei-Chung Wang

Abstract In recent years, laser ablation method has been increasingly used in the touch panel industry. Touch panel devices are produced by applying laser ablation process on transparent conductive oxide (TCO) thin films coated on glass substrates. The pattern and the surface profile of the transparent conductive layer on glass substrates after laser ablation are crucial on the quality of the touch panel. Therefore, a self-assembled multifunction optical measurement system was employed to investigate the details of the surface of the test specimen of the TCO thin films after ablation. The system integrates both optical microscope and white-light scanning interferometer to inspect the specimen under the same field of view. The transparency of the test specimen was inspected by the optical microscope to examine the uniformity of the gray levels throughout the ablated region. The depth of the ablated thin films and whether the thin films are fully cut can be determined from the surface profile obtained from the white-light scanning interferometer. Based on the aforementioned experimental results, the self-assembled multifunction optical measurement system is full of potential to be used to determine the manufacturing parameters in laser ablation process.

Keywords Laser ablation • TCO thin films • Multifunction • Optical microscope • White-light scanning interferometer

24.1 Introduction

In recent years, transparent conductive oxide (TCO) thin films have been widely used in optoelectronic products [1]. For example, the circuit patterns on the substrate of a touch panel display were manufactured mostly by wet etching process. However, wet etching process is not suitable for customized production. Besides, chemical waste produced during the etching process may pollute the environment. Moreover, the isotropic etching characteristics may cause the problem of undercut inevitably. Hence, Transparent conductive oxide (TCO) thin films the environmental-friendly dry etching process which uses laser to ablate materials becomes more popular nowadays [2]. Transparent conductive oxide (TCO) thin films Laser ablation method is an anisotropic etching process so that it can avoid the problem of undercut. Specifically speaking, laser ablation method is suitable for producing a variety of different circuit patterns in a short period of time. Nevertheless, the laser ablation energy must be carefully controlled to avoid damaging the material strength and optical characteristics of the substrate [3]. Therefore it is important to examine the substrate after laser ablation process to determine the better manufacturing parameters.

White-light scanning interferometry (WLSI) White-light scanning interferometry (WLSI) has been used to measure the surface profile because it eliminates the ambiguity existing in monochromatic fringes [4, 5]. Leslie et al. [6] introduced a system for three-dimensional profilometry based scanning white-light techniques. Larkin [7] proposed a five-step phase-shifting algorithm (PSA) to determine the zero optical phase difference (ZOPD) positions. To achieve higher accuracy, Shen et al. [8] used higher steps PSAs in WLSI to measure the surface profile. In this paper, by integrating both optical microscope and WLSI system, a self-assembled multifunction optical measurement system was employed to investigate the details of the surface of the test specimen of the TCO thin films after ablation. The system helps inspect the transparency and the surface profile of the laser ablated substrates. Different patterns of TCO substrates were examined to define their quality.

C.-H. Hwang • S.-F. Tseng • W.-T. Hsiao
Instrument Technology Researcher Center, National Applied Research Laboratories, Hsinchu Science Park,
Hsinchu, Taiwan, Republic of China

M.-H. Shen • I.-F. Cheng (✉) • W.-C. Wang
Department of Power Mechanical Engineering, National Tsing Hua University, Kuang Fu Road, Hsinchu, Taiwan, Republic of China
e-mail: s9933222@gmail.com

24.2 Theory of White-Light Scanning Interferometry

White-light scanning interferometry uses broad-band white-light with short coherence length to produce interference. This interference will only occur when the optical path differences (OPDs) achieve the corresponding ZOPD position. The main merit of the WLSI is that the ambiguity of measurement rarely happens [8].

The light intensity function of a point on a specimen can be represented as

$$I(z) = I_B + I_B \gamma \exp \left[- \left(\frac{2\pi(z - z_0)}{\ell_c} \right)^2 \right] \cos \left[\frac{4\pi}{\lambda_0} (z - z_0) + \varphi_0 \right] \quad (24.1)$$

where I_B is the background intensity; γ is the fringe contrast; z is the position of the object along the optical axis; z_0 is the position along scanning direction where maximum value of the envelope of WLSI occurs; ℓ_c is the coherence length; λ_0 is the center wavelength; and φ_0 is the relative phase difference between the reference and object light beams. Equation 24.1 can also be re-written as

$$I(z) = I_B \{ 1 + \gamma g(z) \cos [\varphi(z)] \} \quad (24.2)$$

where $g(z) = \exp \left[- (2\pi(z - z_0)/\ell_c)^2 \right]$ is defined as the WLSI envelope signal function; and $\varphi(z) = \frac{4\pi}{\lambda_0} (z - z_0) + \varphi_0$. A typical WLSI signal and its associated envelope signal function are shown in Fig. 24.1.

To obtain the ZOPD position accurately, 11-step PSA was used to determine the phase value and peak value from the captured WLSI signal. By the 11-step PSA, 36 possible phase-determining functions (PDFs) were obtained and the selected PDF with minimum error is [8]

$$\phi(z) = \tan^{-1} \left[\frac{4(I_{-5} - I_{-3} + 3I_{-1} - 3I_1 + I_3 - I_5)}{5(I_{-4} - 2I_{-2} + 2I_0 - 2I_2 + I_4)} \right] \quad (24.3)$$

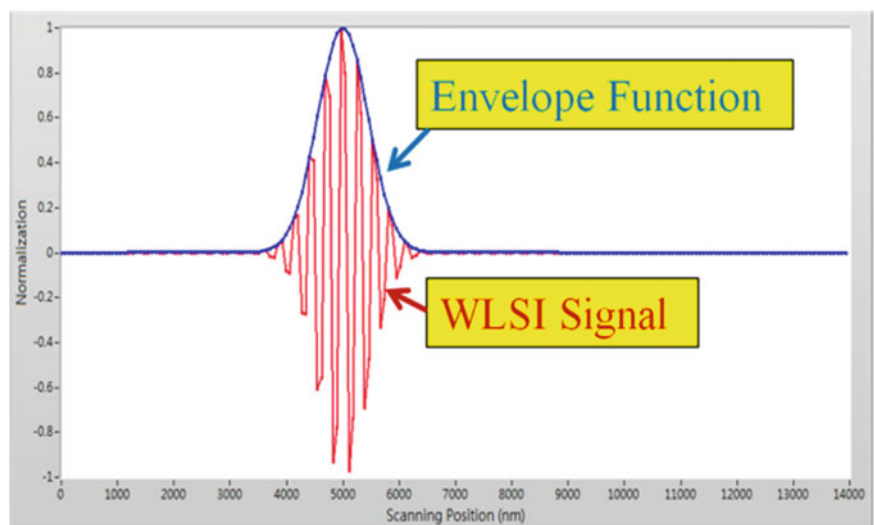
where I_0 represents the maximum recorded intensity; I_n and I_{-n} are respectively the recorded intensity with $n\lambda_0/2$ phase shift from " I_0 ".

Besides, due to the distortion, the recorded peak position z' of the WLSI signal can be modified into

$$z_0 = z' - \frac{\lambda_0}{4\pi} \phi(z') \quad (24.4)$$

By (24.3) and (24.4), the actual ZOPD position can be therefore determined.

Fig. 24.1 The simulated WLSI signal



24.3 Experimental System and Procedure

24.3.1 Structure of Experimental System

The self-assembled multifunction optical measurement system was built up to implement the WLSI theory on measuring the laser ablated TCO thin-film substrate. The system combines a typical Linnik WLSI system with an optical microscope as shown in Fig. 24.2. A halogen light was chosen as the light source and the light was transmitted through a set of achromatic lenses. The light beam was then divided by a beam splitter into objective and reference beams. The system uses the objective lens with $40\times$ magnification and 0.65 numerical aperture to get a detailed view of the test specimen. The light beam reflected from the test specimen interfered with the reference beam in front of the charge-coupled device (CCD) camera when the OPD is within the coherence length of the light source. By blocking the reference beam from the mirror, one can have the vision of optical microscope. In order to move the specimen in the vertical direction, the system was setup with a piezoelectric positioning stage.

24.3.2 Experimental Procedure

As shown in Fig. 24.3a–c, the test specimens were prepared by depositing different kinds of TCO thin films, such as Al doped ZnO (AZO), indium tin oxide (ITO) and Fluorine doped Tin Oxide (FTO) thin films, on the glass substrates respectively and were then etched by laser ablation process with diverse patterns. To examine the quality of the laser ablated TCO thin-film substrates, the specimen was placed under the multifunction optical measurement system. By using the optical microscope, the gray level variations between different regions were observed. In order to measure the surface profile of the test specimen, the substrate was observed under the Linnik WLSI system.

Fig. 24.2 The self-assembled multifunction optical measurement system

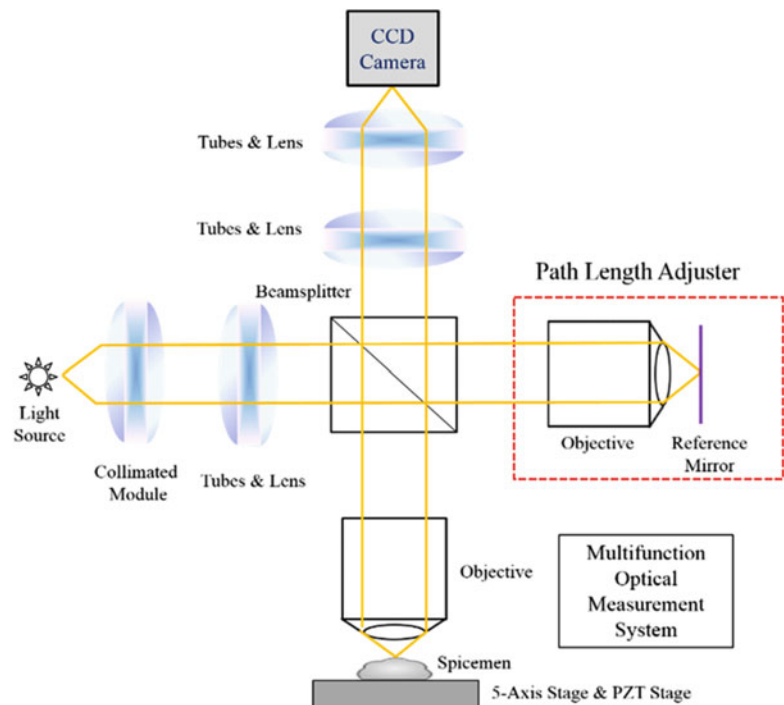
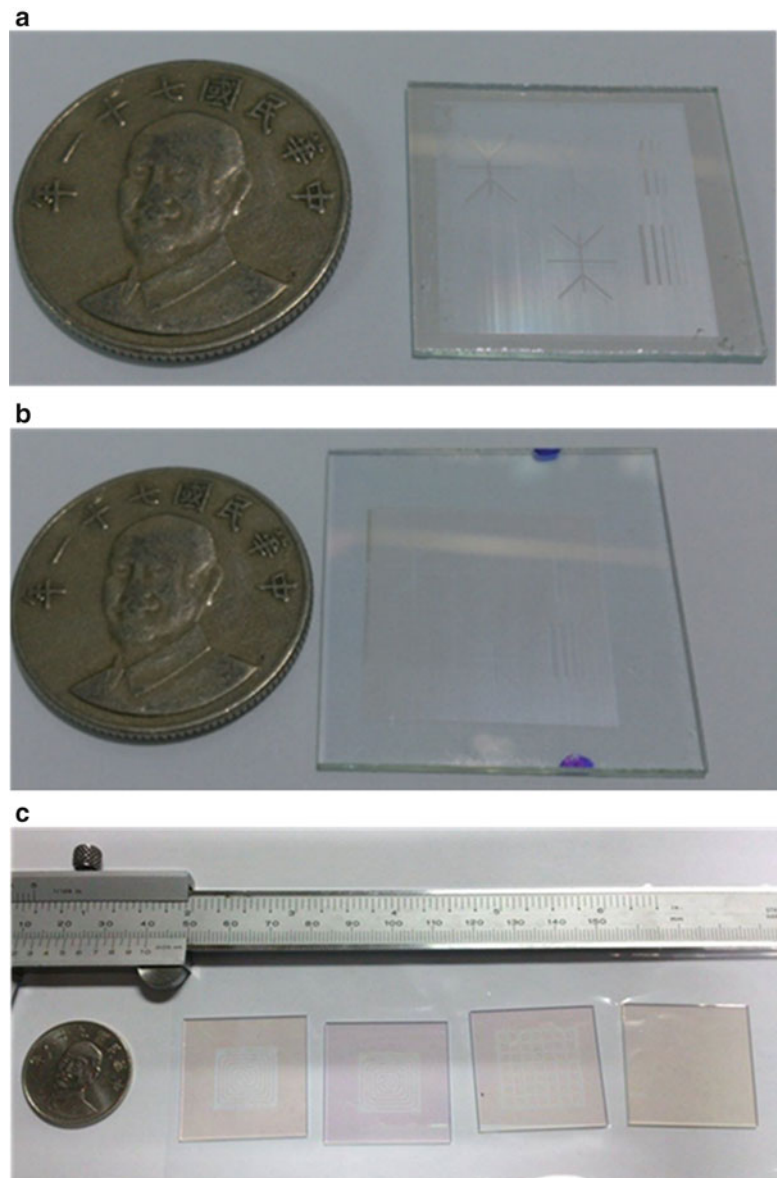


Fig. 24.3 TCO thin-film substrates. (a) AZO thin-film specimen. (b) ITO thin-film specimen. (c) FTO thin-film specimens



24.4 Results and Discussions

The surface profiles of the TCO thin-film substrates were observed under the self-assembled multifunction optical measurement system. The specimen shown in Fig. 24.3a is a 1.0 mm thick glass substrate deposited with 50 nm thick AZO thin films and was then etched by a UV laser. Figure 24.4a shows the microscopic image of the specimen under the examination of the optical microscope. Although the gray levels between the cut and uncut parts are different, the variation among each region is too small to differentiate. This kind of pattern is good when used on the touch panel devices since the large variation of transparency may cause problem on display quality. To be more detailed, the captured interferogram of WLSI system which gives the information of the surface profile is shown in Fig. 24.4b. By using the PSA, the depth of the whole region and the selected section AA' was calculated and shown in Fig. 24.5a, b respectively. With the data of the depth, the region of the films and substrate can be easily defined since the film thickness was already known. The glass substrate was said to be damaged when the ablated depth surpassed the thin-film thickness.

The specimen shown in Fig. 24.3b is a glass substrate deposited with ITO films of 40 nm thickness. The UV laser beam was used to ablate the films to manufacture special pattern on the surface. As shown in Fig. 24.6a, under the optical microscope, the gray levels in the ablated region varies more drastically than those of the AZO specimen. The interferogram shown in Fig. 24.6b shows that the ablated depths fluctuate apparently. Moreover, the three-dimensional surface profile of

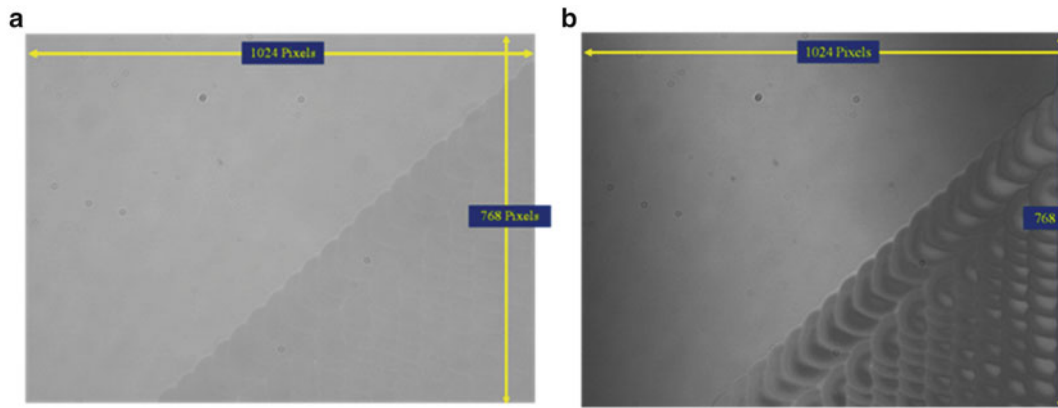


Fig. 24.4 Images of the AZO thin-film substrate. (a) Image under optical microscope. (b) Image under WLSI system

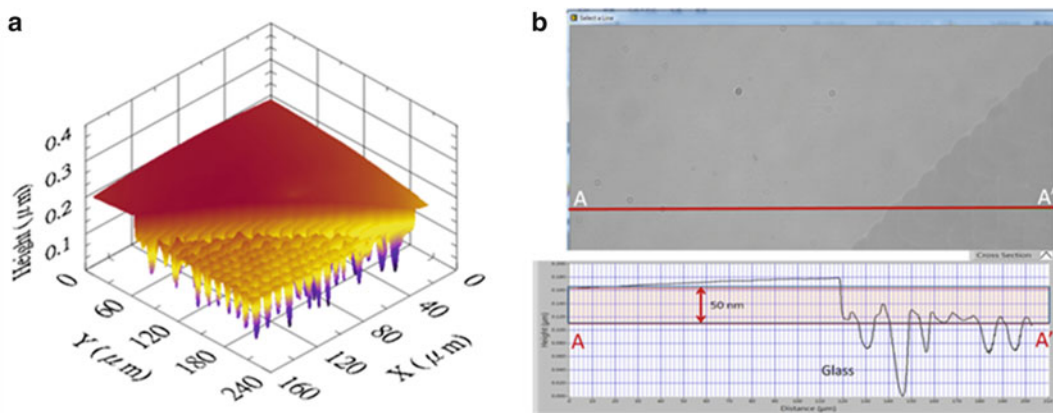


Fig. 24.5 Surface profiles of the AZO thin-film substrate. (a) Three-dimensional surface profile. (b) The surface height of the cross section AA'

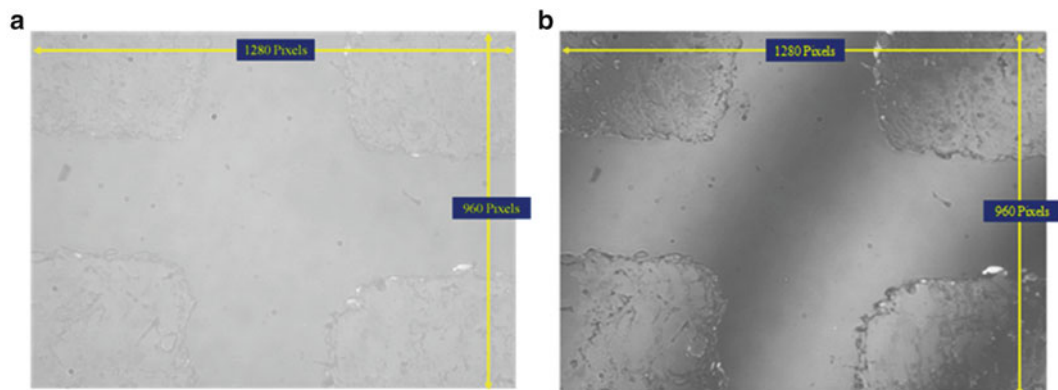


Fig. 24.6 Images of the ITO thin-film substrate. (a) Image under optical microscope. (b) Image under WLSI system

the ablated region shown in Fig. 24.7a is determined by using the PSA. The surface profile of an arbitrarily chosen section shown in Fig. 24.7b shows that the energy of the laser beam might be too strong so that the part of glass substrate was also ablated.

The specimen shown in Fig. 24.3c was prepared by depositing 320 nm FTO thin films on the glass substrate. The specimen was ablated by the UV laser beam with different manufacturing parameters. Figure 24.8a, b show the microscopic images under the optical microscope and WLSI system respectively. As shown in Fig. 24.9, the ablated tunnel is too deep so that some parts of the glass substrate were damaged. The bright dots in the tunnel shown in Fig. 24.8a might be the deep cut of the glass substrate, which may blur the image from the display of the touch panel.

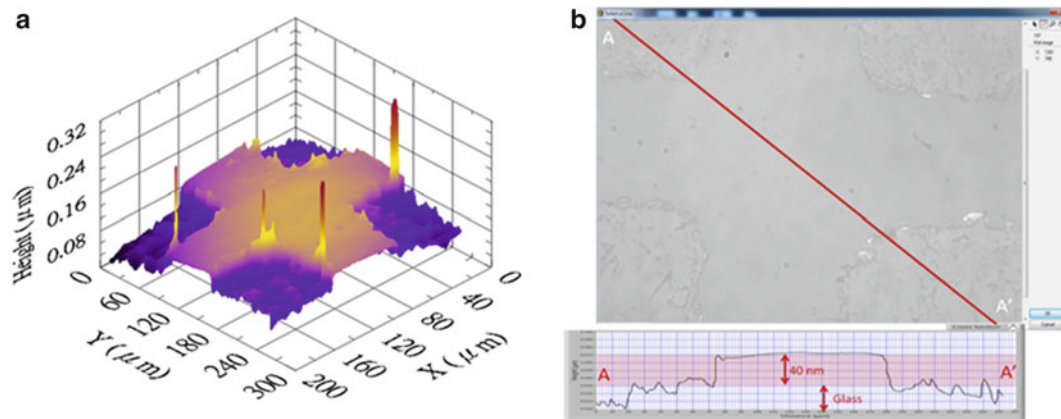


Fig. 24.7 Surface profiles of the ITO thin-film substrate. (a) Three-dimensional surface profile. (b) The profile of the cross section AA'

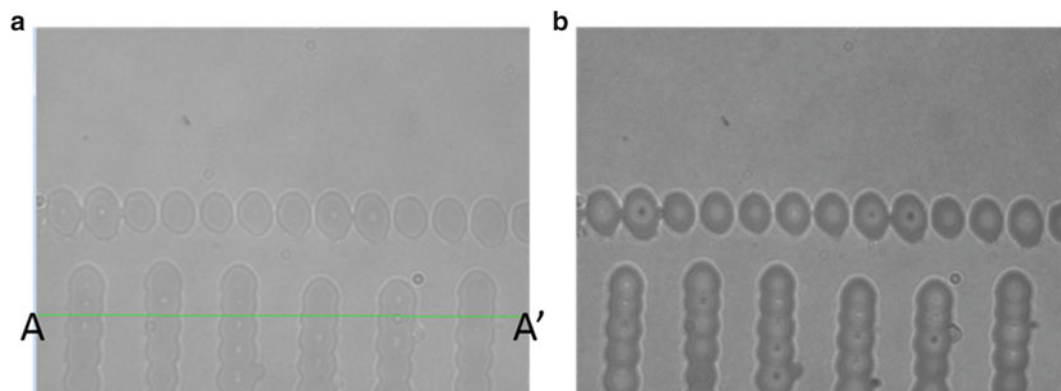


Fig. 24.8 Images of the FTO thin-film substrate. (a) Image under optical microscope. (b) Image under WLSI system

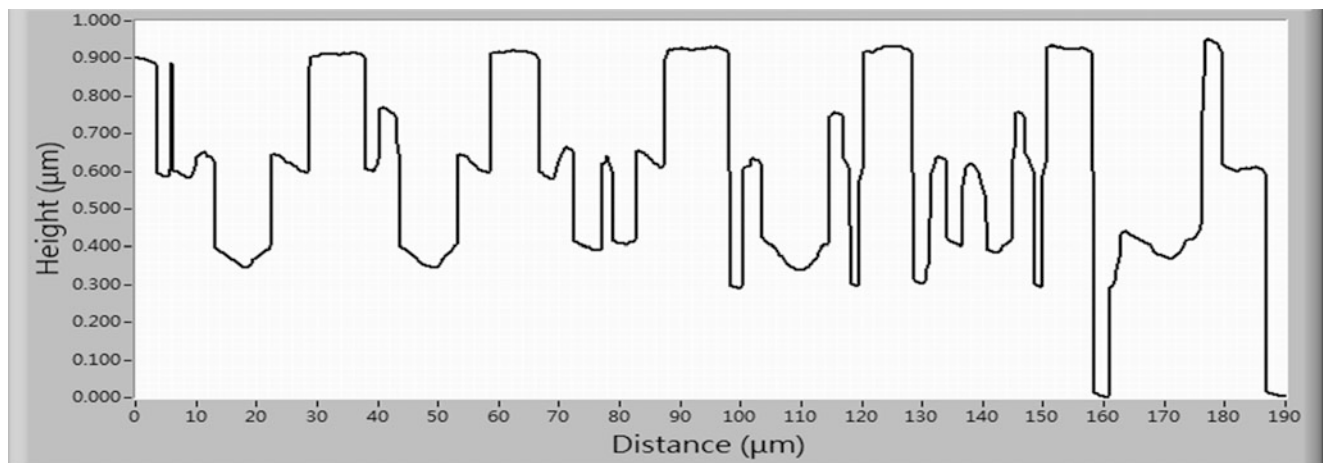


Fig. 24.9 The profile of the cross section AA' of FTO thin-film substrate

24.5 Conclusions

The quality of the ablated transparent conductive oxide (TCO) thin films TCO thin-film glass substrates were investigated by examining the image of the test specimen under the optical microscope and WLSI system. The transparency of the specimen was observed under the optical microscope, while the surface profile was determined by the WLSI system. Once the surface profile was known, the film layer and the glass layer can be defined clearly. By comparing the images captured from the two systems, it was found that the gray levels of the ablated region may be altered with the drastic fluctuation of the surface profile. Based on the results reported in this paper, the self-assembled multifunction optical measurement system is full of potential of helping the manufacturers modify their manufacturing parameters of the laser beam.

Acknowledgement This paper is partially supported by the Ministry of Science and Technology (Grant Nos. 102-2622-E-492-017-CC3 and 103-2221-E-492-017) of Taiwan, Republic of China and Hortech Co., Taiwan, Republic of China.

References

1. M. Tadatsugu, Transparent conducting oxide semiconductors for transparent electrodes. *Semicond. Sci. Technol.* **20**, 35–44 (2005)
2. S. Zoppel, H. Huber, G.A. Reider, Selective Ablation of thin Mo and TCO films with femtosecond laser pulses for structuring thin film solar cells. *Appl. Phys. A* **89**, 161–163 (2007)
3. M. Park, B.H. Chon, H.S. Kim, S.C. Jeoung, D. Kim, J.I. Lee, H.Y. Chu, H.R. Kim, Ultrafast laser ablation of indium Tin oxide thin films for organic light-emitting diode application. *Opt. Lasers Eng.* **44**, 138–146 (2006)
4. P.A. Flournoy, R.W. McClure, G. Wyntjes, White-light interferometric thickness gauge. *Appl. Opt.* **11**, 1907–1915 (1972)
5. J.C. Wyant, K. Creath, Advances in interferometric optical profiling. *Int. J. Mach. Tools Manuf.* **32**, 5–10 (1992)
6. L. Deck, P. de Groot, High-speed noncontact profiler based on scanning white-light interferometry. *Appl. Opt.* **33**, 7334–7338 (1994)
7. K.G. Larkin, Efficient nonlinear algorithm for envelope detection in white light interferometry. *J. Opt. Soc. Am. A* **13**, 832–843 (1996)
8. M.H. Shen, C.H. Hwang, W.C. Wang, Using higher steps phase-shifting algorithms and linear least-squares fitting in white-light scanning interferometry. *Opt. Lasers Eng.* **66**, 166–173 (2014)

Chapter 25

LIBS Technique for Identification of Crude Oils

F.G. Rendón, A.K. Frías, A.E. Villarreal, T. Flores, L. Ponce, and G. Vázquez-Bautista

Abstract LIBS technique for the identification of trace elements in oil samples from different sources using a compact LIBS system was used. In order to address the difficulties presented by the characteristics of the samples, two pretreatment stages, freezing and thermal treatment by ultrasound were performed. Obtained results are described and compared in both cases. It is demonstrated the potential of the technique to identify the origin of oil is by its composition.

Keywords LIBS • Crude oil • Nd: YAG • Multipulse

25.1 Introduction

The motivation for the detection of trace elements in crude oil is oil exploitation and its quality determination, if possible in-situ. Therefore, information on trace elements is increasingly important for the characterization of crude oil and to take corrective measures during production and its refinement [1].

Elemental analysis of a crude oil is performed to determine the presence and content of various elements such as C, H, O, S, N, Ni, V, Fe, etc. The first five elements are part of the matrix, while the others are considered impurities and their oil content is in the order of the traces [2].

Atomic absorption (AA) spectroscopy and plasma generated by inductive coupling (ICP-AES) are the most used techniques for the determination of trace elements. However, these methods have a number of drawbacks such as: use of expensive solvents, digestion processes, contamination with reactive, use of hazardous reagents, etc. [3].

LIBS is a technique of atomic emission spectroscopy firmly established for rapid determination of the elemental composition of matter represented in any state of aggregation [4]. This technique allows elemental analysis with a large number of advantages, among them the use of fiber optics and lenses, which allow to direct and collect radiation from places otherwise inaccessible; which makes it particularly attractive for the analysis of hazardous materials, at high temperatures, or for working in harsh environments. Furthermore, as the laser acts as sampling and excitation source, can be analyzed virtually all kinds of samples whether conductive or not, regardless of the state of aggregation in which they are. Additionally, the result is delivered quickly and in principle the equipment may have the necessary degree of portability required for in-situ analysis.

In recent years, the LIBS technique has been successfully used for the rapid analysis of multi-elemental contaminants in solid matrix [5]. LIBS can be useful for the analysis of liquid and solid samples in a variety of applications such as industrial materials analysis, prospecting and mining, environmental monitoring, national security measures, chemical and biological agents, forensics, pharmaceutical research and development [6–8].

LIBS has found utility in monitoring elementary processes and in field portable analyzers for in situ analysis of real samples traces, where accuracy and precision are not the primary requirement [9].

In the case of compositional analysis of crude oil, although previous reports can be found [10, 11], it is work done with expensive laser equipment and, moreover, spectra show an intense electronic background caused by sample conditions, that limits sensibility.

In this work, crude oil of Maya crude, Arabian and North Sea are analyzed by laser induced breakdown spectroscopy (LIBS) technique in order to identify trace elements accompanying hydrocarbons, depending on the region where they were extracted, as well as to determine the optimal experimental conditions for analysis of heavy metals in crude applying LIBS

F.G. Rendón • A.K. Frías • A.E. Villarreal (✉) • T. Flores • L. Ponce • G. Vázquez-Bautista
Centro de Investigación en Ciencia Aplicada y Tecnología Avanzada (CICATA) Unidad Altamira del Instituto Politécnico Nacional (IPN),
Carretera Tampico- Puerto Industrial Altamira Km. 14.5, C.P. 89600 Altamira, Tamaulipas, Mexico
e-mail: viva.aev@gmail.com

and to demonstrate the ability to quickly identify the source of crude for its elemental composition. To obtain best spectra in terms of well-defined spectral lines and a better electronic signal/noise ratio as well as to reduce “splashing” [12] due to the physical state of the samples, were proposed two treatments for each sample, the first was to freeze the sample, while the second was a heating by ultrasonic vibration.

25.2 Experimental Methodology

25.2.1 Samples Preparation

For this work representative samples of crude oil from three different regions: Arabian, Maya and North Sea, were taken. In order to improve the emission generated by each sample during the LIBS analysis; each sample was subjected to two types of pre-treatments, one was to frozen the sample during 12 h at $-4\text{ }^{\circ}\text{C}$ and the other was an ultrasonic heating treatment for a period of 10 h at $65\text{ }^{\circ}\text{C}$ in a Branson 1510 ultrasonic equipment.

25.2.2 Experimental Facility

The Fig. 25.1 shows the LIBS system uses an own manufacturing, Q:Switched Nd:YAG pulsed laser, emitting at wavelength of 1064 nm [13]. It is focused on the sample resulting in the formation of a plasma whose light is collected through a P600-1-SR Ocean Optics optical fiber, bringing it to the USB 4000 UV–VIS Ocean Optics spectrometer (wavelength range 200–900 nm and optical resolution of 0.35 nm). Finally, the information is transmitted to a PC where it is processed with the SpectraSuite software. The laser spot on the sample is 1 mm in diameter and its pulse energy is 360 mJ, measured by a PM300 Thorlabs energy meter. The working fluence is 57.29 J/cm^2 .

25.2.3 Spectral Lines Identification

The identification of spectral lines was carried out by the “LIBS Analyzer” software, developed in the laboratory of laser technology IPN-CICATA, Altamira, from the databases of the National Institute of Standards and Technology (NIST) [14] and the United States Army Research Laboratory [15] database. Also, it was compared with a proprietary database from the Laboratory of Laser Technology IPN-CICATA Altamira, which contains LIBS spectra obtained from high purity materials which composition is certified by suppliers as Kurt J. Lesker and Aldrich Chemistry. These are shown in Table 25.1.

Fig. 25.1 Diagram of experimental setup

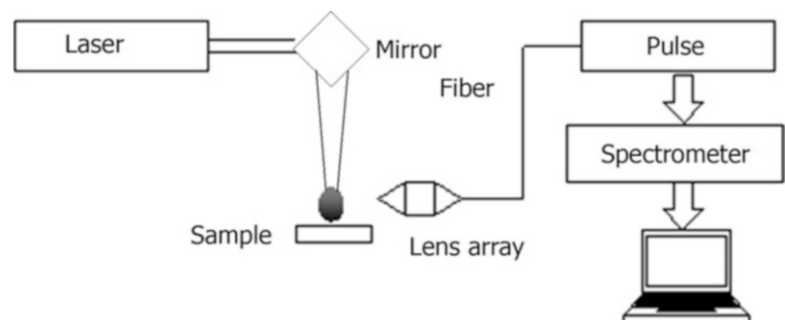
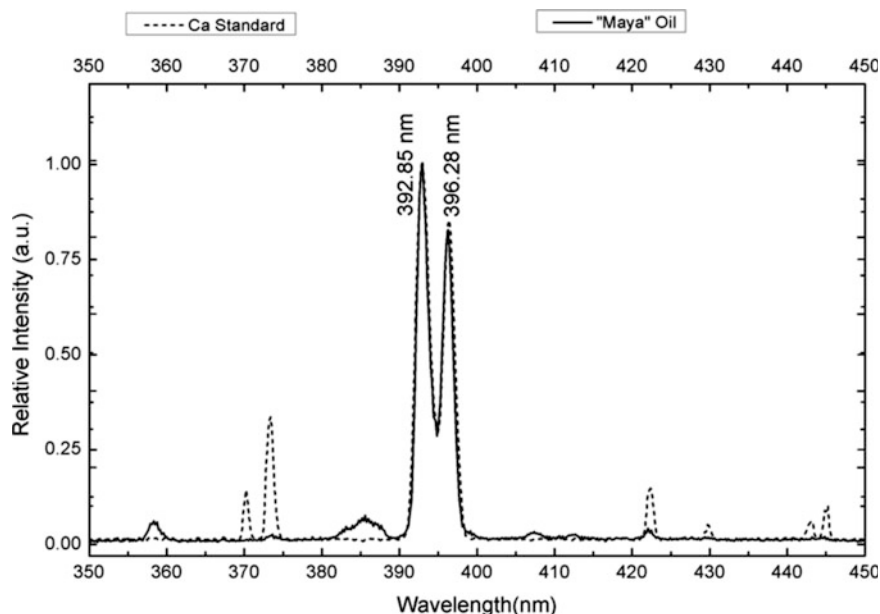


Table 25.1 Standard elements used for doing the LIBS library

Element	Purity (%)	Diameter (mm)
Calcium (Ca)	99	3
Copper (Cu)	99.999	19
Iron (Fe)	99.95	3
Magnesium (Mg)	99.95	2.5
Lead (Pb)	99.95	3
Titanium (Ti)	99.995	6

Fig. 25.2 Overlap of spectral lines

25.3 Results and Discussion

Ten spectra for both treatments (frozen and heated) for each of the samples of crude oil (Arabian, Maya and North Sea) were captured for LIBS analysis. In Fig. 25.2, spectra captured to the standard sample of Ca and Maya crude sample are shown. It is observed the coincidence of both spectra, particularly for more intense emission lines of Ca, in 392.85 nm and in 396.28 nm. Other Ca lines of lower intensity also appear in, although, they are obviously less distinguishable. Maya crude spectrum also presents additional lines which belong to other elements.

In the Fig. 25.3 LIBS spectra generated by both treatments are compared for Maya oil. It is observed that for heated oil, spectrum showed less background noise than in the frozen one, also emission lines such as that of Fe in 358.70 and 670.51 nm; and Ti in 703.88 nm that were not detected in the frozen oil are observed for the heated one.

The Fig. 25.4 shows the spectra obtained and identified in samples of Arabian oil, which confirm the previous trend, greater presence of electronic background for frozen treating than for the heated. In this case, all emission lines in the heated sample also appear in the frozen one.

The Fig. 25.5 shows the spectra obtained from North Sea crude with both treatments shown. It is noted that the emission lines in the heated sample similarly present reduced electronic noise. In this case, hydrogen lines 656.3 and 766.5 nm and 769.9 Potassium nm were being overlapped by background noise, as well as a line of V 385.6 absent from the frozen sample.

A list of the basic elements in the crude oil determined by other techniques are shown in Table 25.2 [2]. The elements that were detected by LIBS are marked with an "X".

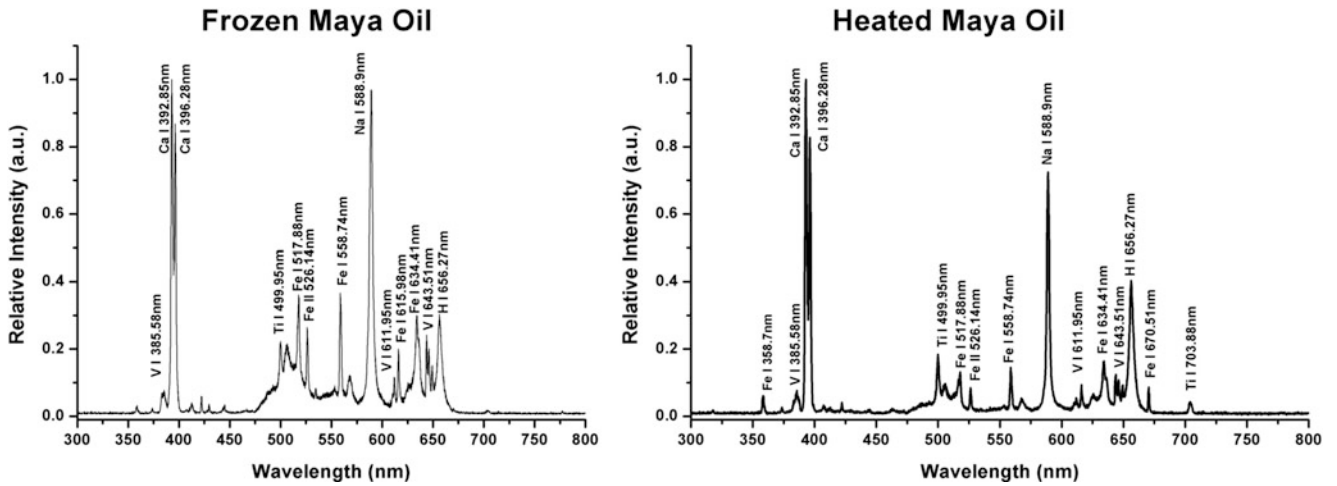


Fig. 25.3 Maya oil spectra

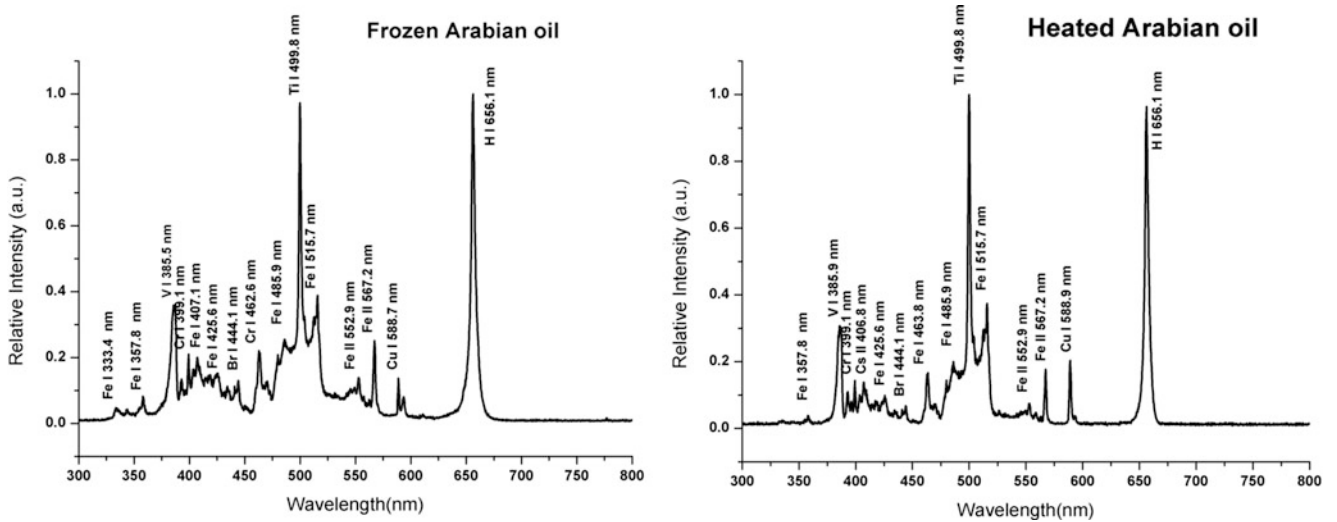


Fig. 25.4 Arabian oil spectra

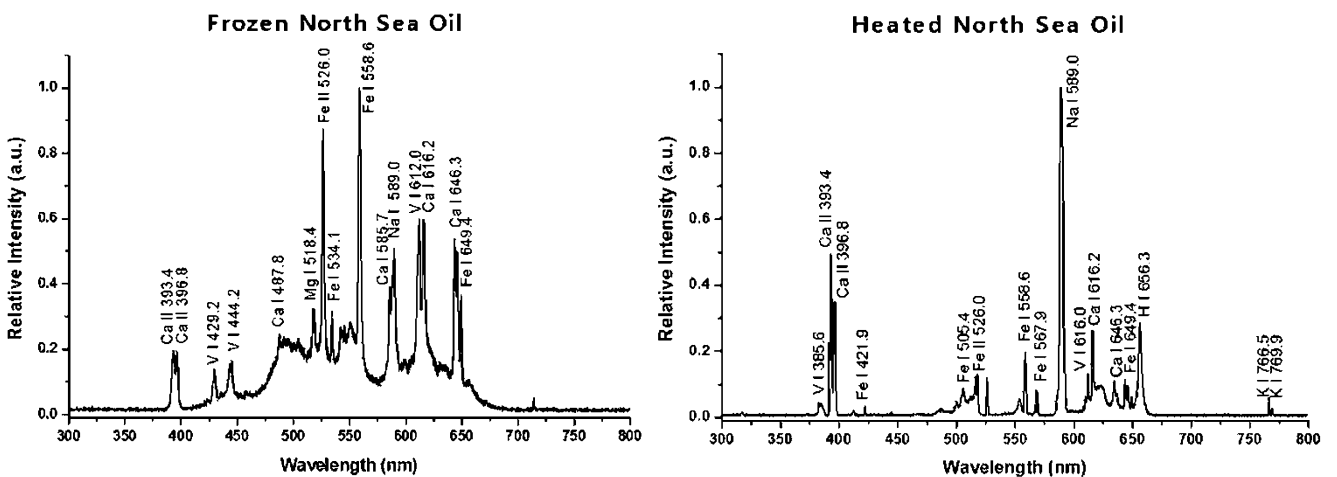


Fig. 25.5 North Sea oil spectra

Table 25.2 Elements present in each spectra

Sample	V	Na	Mg	Ni	Ca	Fe	S	P	K
Maya oil	x	x	–	–	x	x	–	–	–
Arabian oil	x	–	x	–	x	x	–	–	–
North Sea oil	x	x	–	–	x	x	–	–	x

25.4 Conclusions

Heating the oil samples before analyzing LIBS, allows obtaining spectra with less electronic background and to identify more spectral lines compared to frozen samples. This improvement, in the case of ultrasonic heating, is attributed to evaporation of the volatile light crude oils in the process. In particular, in the cases of North Sea and Maya oil, the heated sample showed higher spectral information, while in the case of Arabian oil the same characteristic information was observed.

Because of these two criteria, one might conclude that the method of ultrasonic heating helps the technique by reducing noise and favoring the presence of certain emission lines, however, if it is not needed the accuracy achieved by the first method, freezing provides good results as it reduces the effect of “splashing” that difficult to obtain spectra, one of the reasons which led us to seek treatment for the samples.

Finally a list with the detected element is presented, where we can see how certain elements could not be detected, but the causes can be many, since it could not be present in the samples as well as the emission lines are weak and cannot be captured by the spectrometer. Even so, due the portability and the simplicity of analysis, this method could have great potential for the oil industry.

Acknowledgement The authors thank CONACYT and COFAA-IPN for the financial support. This work was supported by project SIP-IPN 20150573.

References

1. A.S. Laxmiprasad, V.L.N. Sridhar Raja, S. Menon, A. Goswami, M.V.H. Rao, K.A. Lohar, An in situ laser induced breakdown spectroscopy (LIBS) for chandrayaan-2 rover: ablation kinetics and emissivity estimations. *Adv. Space Res.* **52**, 332–341 (2013)
2. R.C. Selley, S.A. Sonnenberg, Chapter 2 - The physical and chemical properties of petroleum, in *Elements of Petroleum Geology*, ed. by R.C.S.A. Sonnenberg, 3rd edn. (Academic, Boston, 2015), pp. 13–39
3. R.S. Amais, C.D.B. Amaral, L.L. Fialho, D. Schiavo, J.A. Nóbrega, Determination of P, S and Si in biodiesel, diesel and lubricating oil using ICP-MS/MS. *Anal. Methods* **6**, 4516–4520 (2014)
4. L.J. Radziemski, From LASER to LIBS, the path of technology development. *Spectrochim. Acta B At. Spectrosc.* **57**, 1109–1113 (2002)
5. D.A. Cremers, L.J. Radziemski, *Handbook of Laser-Induced Breakdown Spectroscopy*, 2nd edn. (Wiley, Chichester, 2014)
6. T. Flores, L. Ponce, M. Arronte, E. de Posada, Free-running and Q:Switched LIBS measurements during the laser ablation of Prickle Pears spines. *Optics and Lasers in Engineering*, **47**, 578–583 (2009)
7. C. Pasquini, J. Cortez, L.M.C. Silva, F.B. Gonzaga, Laser induced breakdown spectroscopy. *J. Braz. Chem. Soc.* **18**, 463–512 (2007)
8. R.S. Harmon, J. Remus, N.J. McMillan, C. McManus, L. Collins, J.L. Gottfried Jr. et al., LIBS analysis of geomaterials: geochemical fingerprinting for the rapid analysis and discrimination of minerals. *Appl. Geochem.* **24**, 1125–1141 (2009)
9. A.K. Rai, V.N. Rai, F.Y. Yueh, J.P. Singh, *Trends in Applied Spectroscopy*, vol. 4 (Research Trends, Trivandrum, 2002), p. 165
10. M.A. Gondal, T. Hussain, Z.H. Yamani, Optimization of the LIBS parameters for detection of trace metals in petroleum products. *Energy Sources, Part A* **30**, 441–451 (2008)
11. M. Gondal, T. Hussain, Z. Yamani, M. Baig, Detection of heavy metals in Arabian crude oil residue using laser induced breakdown spectroscopy. *Talanta* **69**, 1072–1078 (2006)
12. J.P. Singh, S.N. Thakur, *Laser-Induced Breakdown Spectroscopy* (Elsevier Science, Amsterdam, 2007)
13. L. Moreira Osorio, L.V. Ponce Cabrera, M.A. Arronte García, T. Flores Reyes, I. Ravelo, Portable LIBS system for determining the composition of multilayer structures on objects of cultural value. *Journal of Physics: Conference Series*, **274**, 012093 (2011)
14. U. S. D. o. Commerce, National Institute of Standards and Technology (2010), <http://www.nist.gov/>
15. U. S. Army, United States Army Research Laboratory (ARL) (2010), <http://www.arl.army.mil/www/default.cfm?page = 250>

Chapter 26

3D Displacement Distribution Measurement Using Sampling Moire Method with Multiple Cameras

Daiki Tomita, Yorinobu Murata, and Motoharu Fujigaki

Abstract A sampling moire method is useful to measure deformations of a large structure such as a building and a bridge. The sampling moire method can analyze 3D displacement using two cameras. The sensitivity of the displacement measurement for the z -direction is lower than the displacement measurement in the x - and the y -directions in this method because the cameras are placed near the direction of the z -axis against the object in general. However, the measurement noise level can be decreased with increasing the number of cameras. In this paper, the principle and the calibration method to measure 3D displacement using the sampling moire method with multiple cameras are shown. As the application, 3D displacement distribution measurement of a cantilever using the sampling moire method with multiple cameras is performed. The accuracy of the 3D displacement measured with using three cameras is compared to the displacement of the cantilever.

Keywords Digital image processing • Health monitoring of large structures • Sampling moire method • 3D displacement distribution measurement • Multiple cameras

26.1 Introduction

Large structures require the development of a non-contact deformation measurement method [1]. The deformation measurement can be applied to predict landslides and for health monitoring of large structures, such as bridges, steel towers, or tall buildings.

The phase analysis method of a grating is a useful method to accurately measure deformation. It is better to measure deformation from a single image in the case of a moving object or a vibrating object. A spatial fringe analysis method using a sampling technique to analyze the phase distribution of moire images produced from one-shot grating images on a computer was proposed by Arai et al. [2, 3]. This method was applied to the phase analysis of 2D grating images. The authors called this method a sampling moire method. This method was applied to deformation and strain measurements [4–6]. The accuracy of the phase difference analysis is in the range of $1/100$ – $1/1000$ of the grating pitch. The accuracy of this method is higher than a digital image correlation method [7, 8] due to the phase of the grating pattern, which is analyzed using a phase-shifting method. The phase-shifting method can be performed by generating phase-shifted moire images on a computer via a one-shot grating image. The analysis speed is faster than a Fourier transform method [9] or the digital image correlation method [7, 8].

In reality, structures, such as steel towers, or tall buildings are displaced in three directions. 3D displacement measurement is necessary to evaluate the safety of the structures. As the 3D displacement measurement, several methods using a digital image correlation method are proposed [10–12]. Authors also proposed a 3D displacement measurement method using the sampling moire method [13]. The sampling moire method can analyze 3D displacement using two cameras. However, the sensitivity of the displacement measurement for the z -direction is lower than the displacement measurement in

D. Tomita (✉)
Graduate School of Systems Engineering, Wakayama University, Wakayama, Japan
e-mail: tomita.daiki.0070@g.wakayama-u.jp

Y. Murata
Faculty of Systems Engineering, Wakayama University, Wakayama, Japan
e-mail: murata@sys.wakayama-u.ac.jp

M. Fujigaki
Graduate School of Engineering, University of Fukui, Fukui, Japan
e-mail: fujigaki@u-fukui.ac.jp

the x - and the y -directions in this method because the cameras are placed near the direction of the z -axis against the object in general. It is necessary that the noise level of the displacement measurement for the z -direction is decreased. One of easy methods to decreasing noise is an averaging method of the time series results obtained with the same condition. This method is, however, not suited for the dynamic measurement. Another method to decreasing noise is an averaging method of the results obtained with the multiple cameras.

In this paper, the principle and the calibration method to measure 3D displacement using the sampling moire method with multiple cameras are shown. As the application, 3D displacement distribution measurement of a cantilever using the sampling moire method with multiple cameras is performed. The accuracy of the 3D displacement measured with using three cameras is compared to the displacement of the cantilever.

26.2 Principle

26.2.1 Sampling Moire Method

The sampling moire method can analyze the phase distribution of a grating image. Figure 26.1 shows the scheme of a special fringe analysis method. The phase analysis algorithm of a sampling method for 2D grating is the same as this method. Figure 26.1a shows the brightness distribution of an original grating pattern on the specimen. Figure 26.1b shows the grating image taken by a digital camera. Figure 26.1c shows the sampling process. First, a starting sampling point is determined, and the original grating image is sampled at intervals. A length of sampling pixels does not fulfill the definition of sampling theorem. In Fig. 26.1c, the pitch of the grating pattern image is 5 pixels. In this case, the length of the sampling pixels is 4 pixels. Next, the starting sampling point is changed, and a sample is taken again. This process is repeated for the same numbers of times as the sampling pitch. Figure 26.1d shows the linear interpolation process for four sampling pattern images. Figure 26.1e shows an initial phase of the linear interpolation process, which can be analyzed in the phase shift moire method.

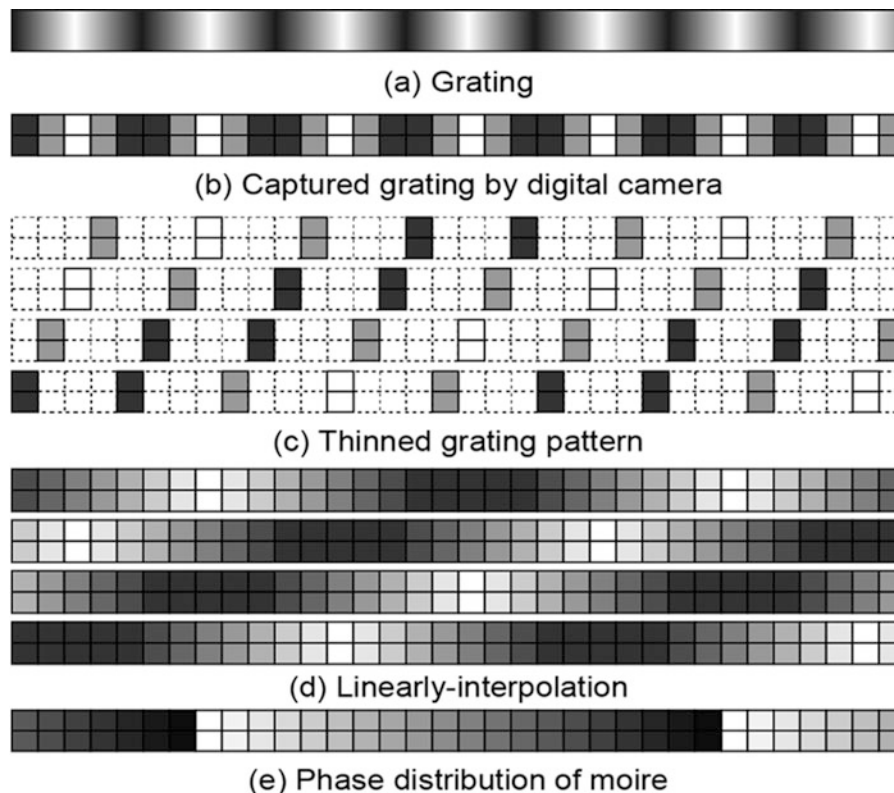


Fig. 26.1 Special fringe analysis method

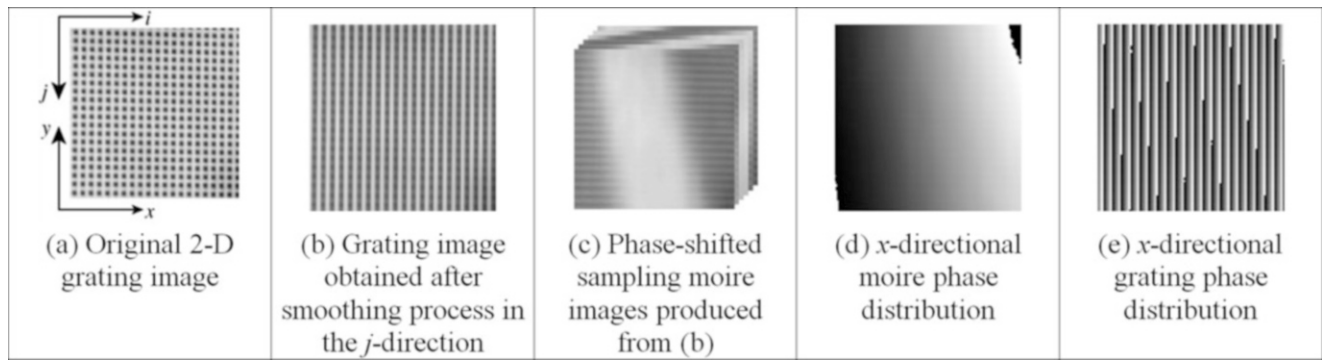


Fig. 26.2 Sampling moire method for x -directional analysis. (a) Original 2-D grating image. (b) Grating image obtained after smoothing process in the j -direction. (c) Phase-shifted sampling moire images produced from (b). (d) x -directional moire phase distribution. (e) x -directional grating phase distribution

Fig. 26.3 Illustration of 3D displacement measurement with two cameras

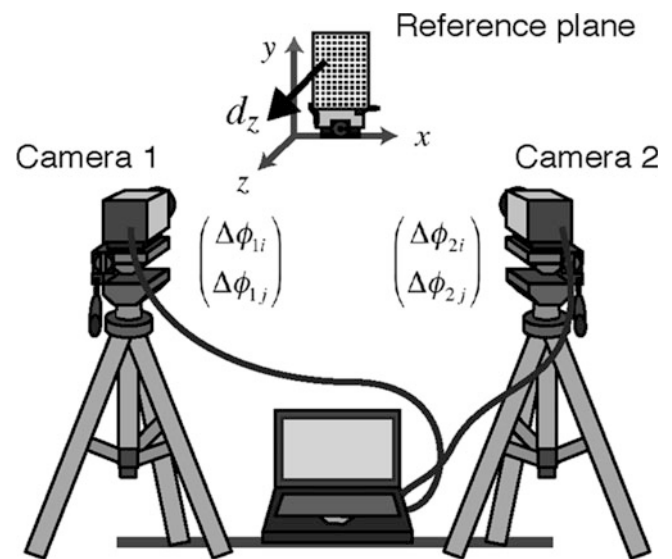


Figure 26.2 shows an x -directional phase analyzed by the sampling moire method. In this study, a 2D grating pattern pasted on an object is analyzed. Figure 26.2a shows the 2D grating pattern image captured by a digital camera. Figure 26.2b shows a grating image obtained after smoothing process in the y -direction. By this process, x -dimensional phase distribution can be analyzed because the 2-D grating is converted into the pattern image as one-dimensional grating pattern image. Figure 26.2c shows phase-shifted sampling moire images produced from Fig. 26.2b. Figure 26.2d shows the phase distribution for x -direction produced from Fig. 26.2c by phase-shifting method. Figure 26.1e shows a grating phase for the x -direction obtained from Fig. 26.1d with subtracting the phase of grating of the reference sampling pitch. Next, a moire phase distribution θ_m , a reference phase distribution θ_r , and a phase distribution of grid pattern θ_g can be calculated from (26.1):

$$\theta_g(i, j) = \theta_r(i, j) - \theta_m(i, j) \quad (26.1)$$

In the same process, the y -dimensional phase distribution can be obtained.

26.2.2 3D Displacement Measurement Method with Multiple Cameras

Structures are displaced in three directions. Therefore, 3D displacement measurement is necessary to evaluate the safety of the structures.

Figure 26.3 shows an illustration of 3D displacement measurement with two cameras. More than three phase differences are necessary to calculate three directional displacements. The sampling moire method can analyze 2D phases from a camera

image. Therefore, the 3D displacement measurement is calculated from four phases analyzed from two images with two cameras when $N \geq 2$. Here, the 3D displacement measurement method using the sampling moire method with N cameras is shown.

The 3D displacement with N cameras is calculated from (26.2):

$$\begin{pmatrix} d_x \\ d_y \\ d_z \end{pmatrix} = \mathbf{A} \begin{pmatrix} \Delta\phi_{1i} \\ \Delta\phi_{1j} \\ \Delta\phi_{2i} \\ \Delta\phi_{2j} \\ \vdots \\ \Delta\phi_{Ni} \\ \Delta\phi_{Nj} \end{pmatrix} \quad (26.2)$$

where d_x , d_y and d_z are the displacement for the x -, y - and z -directions, $\Delta\phi_{ni}$ and $\Delta\phi_{nj}$ are the phase differences for the i - and j -directions, and \mathbf{A} is the transformation matrix.

The matrix \mathbf{A} must be decided to calculate the 3D displacement. The pseudo-inverse matrix \mathbf{S} of the matrix \mathbf{A} is defined as (26.3):

$$\mathbf{S} = \begin{pmatrix} e_{1ix} & e_{1iy} & e_{1iz} \\ e_{1jx} & e_{1jy} & e_{1jz} \\ e_{2ix} & e_{2iy} & e_{2iz} \\ e_{2jx} & e_{2jy} & e_{2jz} \\ \vdots & \vdots & \vdots \\ e_{Nix} & e_{Niy} & e_{Niz} \\ e_{Njx} & e_{Njy} & e_{Njz} \end{pmatrix} \quad (26.3)$$

Equation 26.2 can be rewritten as (26.4):

$$\begin{pmatrix} \Delta\phi_{1i} \\ \Delta\phi_{1j} \\ \Delta\phi_{2i} \\ \Delta\phi_{2j} \\ \vdots \\ \Delta\phi_{Ni} \\ \Delta\phi_{Nj} \end{pmatrix} = \mathbf{S} \begin{pmatrix} d_x \\ d_y \\ d_z \end{pmatrix} \quad (26.4)$$

When d_x , d_y and d_z are defined as (26.5):

$$\begin{pmatrix} d_x \\ d_y \\ d_z \end{pmatrix} = \begin{pmatrix} p_x \\ 0 \\ 0 \end{pmatrix} \quad (26.5)$$

where p_x is the pitch of the 2D grating for the x -direction, the phase difference is expressed as (26.6):

$$\Delta\phi_{ni} = 2\pi (n = 1, 2, \dots, N) \quad (26.6)$$

By substituting (26.5) for (26.4), e_{nix} is expressed as (26.7):

$$e_{nix} = 2\pi/p_x (n = 1, 2, \dots, N) \quad (26.7)$$

Similarly, when d_x , d_y and d_z are defined as (26.8):

$$\begin{pmatrix} d_x \\ d_y \\ d_z \end{pmatrix} = \begin{pmatrix} 0 \\ p_y \\ 0 \end{pmatrix} \quad (26.8)$$

e_{niy} is expressed as (26.9):

$$e_{niy} = 2\pi/p_y (n = 1, 2, \dots, N) \quad (26.9)$$

It is impossible to calculate e_{niz} and e_{njz} from the pitch of the 2D grating. However, when the 2D grating is displaced a known value in the z -direction, it is possible to calculate e_{niz} and e_{njz} from the phase difference and the displacement of the 2D grating as (26.10) and (26.11):

$$e_{niz} = \Delta\phi_{ni}/d_z (n = 1, 2, \dots, N) \quad (26.10)$$

$$e_{njz} = \Delta\phi_{nj}/d_z (n = 1, 2, \dots, N) \quad (26.11)$$

Therefore, all of the parameters of S can be calculated.

A is calculated from the inverse matrix of S . Therefore, the 3D displacement is calculated from the phase differences obtained by each camera using (26.2).

26.3 Experiment of 3D Displacement Distribution Measurement with a Cantilever

An application of the 3D displacement measurement method on a cantilever is demonstrated. Figure 26.4a shows a photograph of the cantilever. The length of the cantilever is 215 mm. A micro meter is installed 203 mm away from the left side of the cantilever. The pitch of the 2D grating is 5.00 mm for the x -direction and 4.98 mm for the y -direction. A moving stage is installed under the cantilever for calibration. Figure 26.4b, c shows a photograph and an illustration of an experimental composition. The distance between the moving stage and cameras is 2.3 m. The distance between the cameras is 920 mm. Figure 26.5 shows the captured images from the cameras. The exposure time of all cameras is 15 ms. The output image size is set as 512×512 pixels.

The results of calibration are shown. The phase differences of the three cameras when the 2D grating is displaced 1.98 mm in the z -direction are shown in Table 26.1. d_z is the displacement of the moving stage in the z -direction. $\Delta\phi_i$ and $\Delta\phi_j$ are the averages of the phase differences in the i - and j -directions in Area A in Fig. 26.6 of 100 captured images, respectively. The size of Area A is 330×11 pixels.

Therefore and A are calculated from the phase differences and expressed as (26.12):

$$A = \begin{pmatrix} 0.26 & -0.01 & 0.27 & -0.01 & 0.27 & 0.01 \\ 0.01 & 0.27 & -0.01 & 0.27 & 0.00 & 0.26 \\ 1.07 & 0.61 & -1.10 & 0.62 & 0.03 & -1.22 \end{pmatrix} \quad (26.12)$$

Equation 26.12 shows the transformation matrix using the three cameras.

First, the results of the 3D displacement measurement when the micro meter of the cantilever is displaced from 0 to 1 mm are shown. The phase differences of the 3D displacement measurement are shown on Point P in Fig. 26.6. Figure 26.7a shows the results of the 3D displacement measurement. Figure 26.7b shows the differences between the measured 3D displacement and the displacement of the cantilever. In the x - and y -directions, the averages of the differences are 0.02 mm and 0.01 mm, and the standard deviations of the differences are 0.011 mm and 0.009 mm, respectively. The differences is 1/310 and 1/359 of the grating pitch. In the z -direction, the averages and the standard deviation of the differences are -0.06 mm and 0.042 mm, respectively. The differences is 1/84 of the grating pitch.

Next, the results of the 3D displacement distribution measurement when the micro meter of the cantilever is displaced 0.99 mm are shown. The phase differences of the 3D displacement distribution measurement are shown in Line L in Fig. 26.6. Figure 26.8a shows the results of the 3D displacement distribution measurement. Figure 26.8b shows the differences between the measured 3D displacement and the displacement of the cantilever. In the z -direction, the average of the difference is 0.01 mm from 8 to 103 mm of the position of the cantilever. On the other hand, the average of the difference is -0.02 mm from 108 to 203 mm of the position of the cantilever.

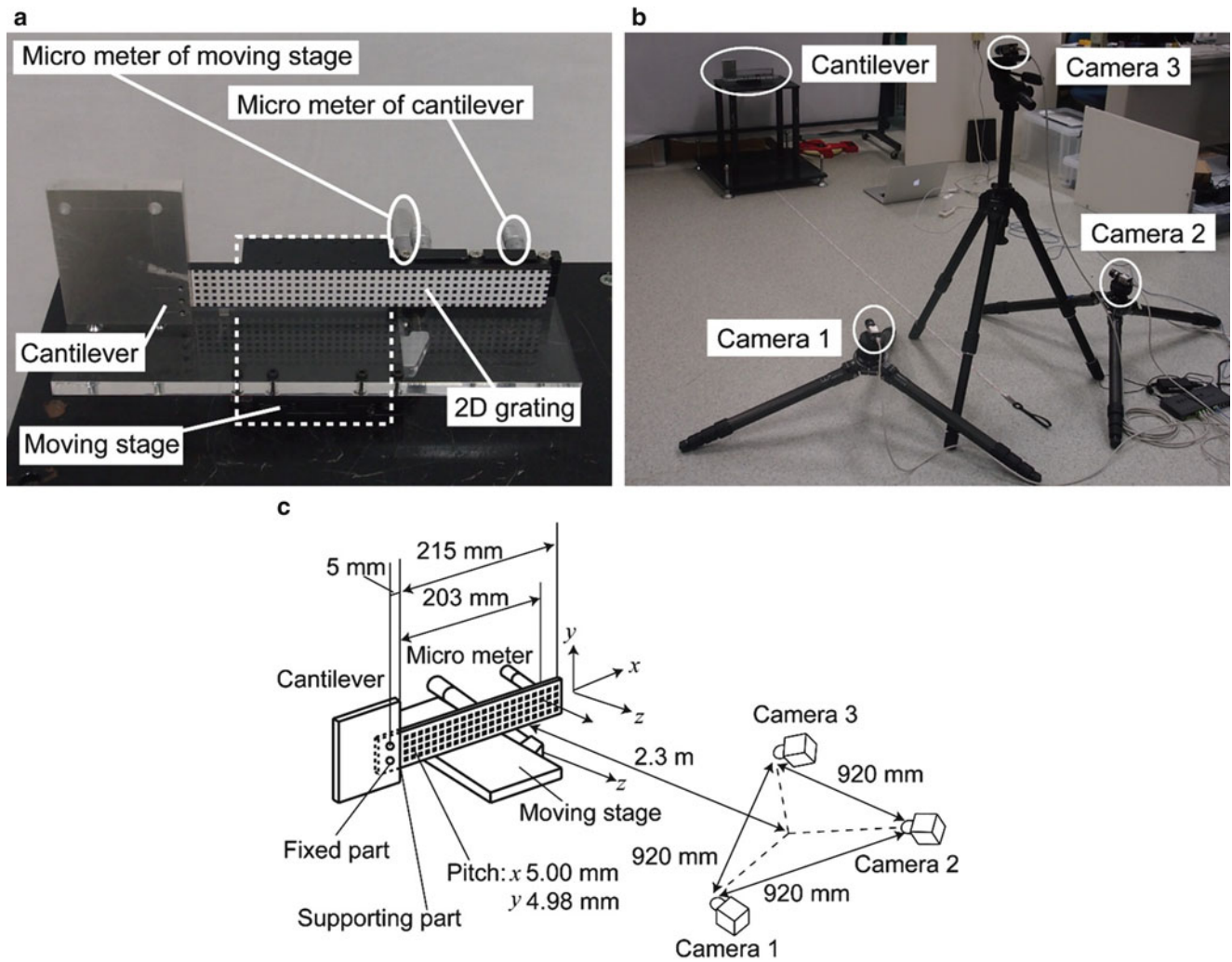


Fig. 26.4 3D displacement measurement of cantilever. (a) Photograph of cantilever. (b) Photograph of experimental composition. (c) Illustration of experimental composition

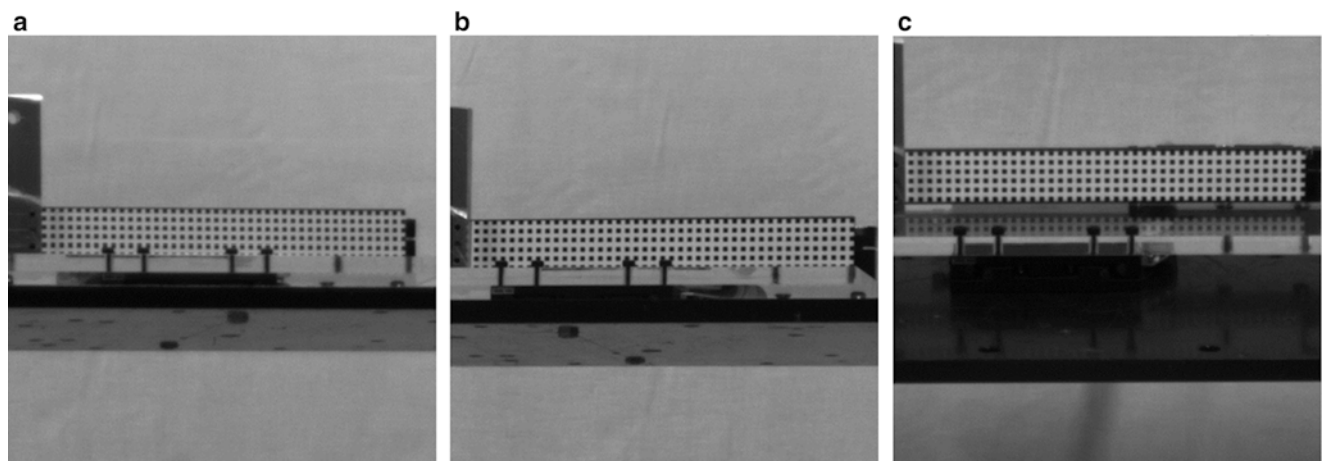
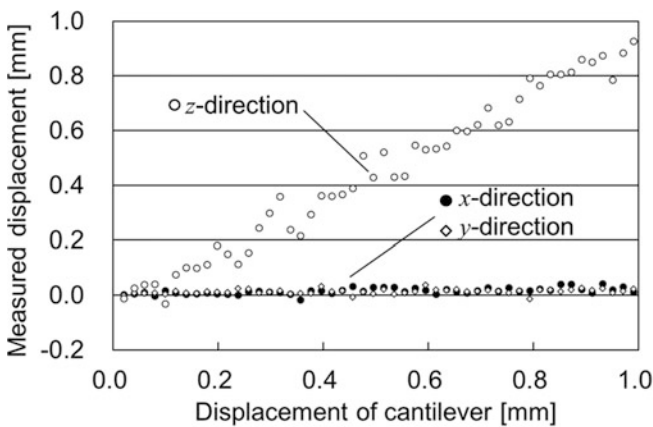
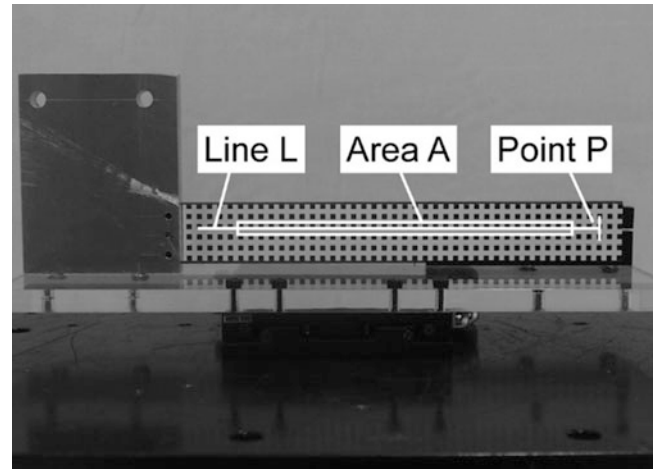


Fig. 26.5 Captured images from three cameras. (a) Camera 1, (b) Camera 2, (c) Camera 3

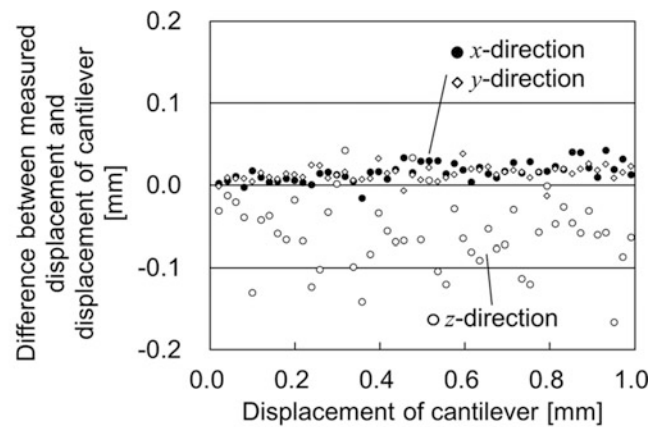
Table 26.1 Phase difference of reference plane ($d_z = 1.98$ mm)

Phase difference $\Delta\phi$ (rad)					
Camera 1		Camera 2		Camera 3	
$\Delta\phi_{1i}$	$\Delta\phi_{1j}$	$\Delta\phi_{2i}$	$\Delta\phi_{2j}$	$\Delta\phi_{3i}$	$\Delta\phi_{3j}$
0.48	0.25	-0.45	0.25	0.03	-0.54

Fig. 26.6 Position of used data

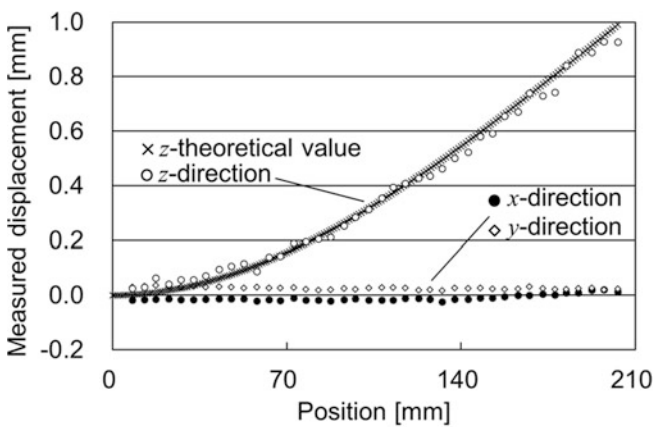


(a) Measured 3D displacement

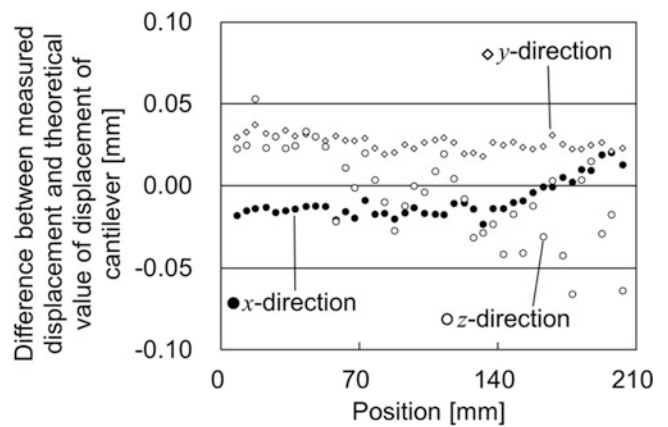


(b) Differences

Fig. 26.7 Results of 3D displacement measurement (from 0 to 1 mm). (a) Measured 3D displacement, (b) Differences



(a) Measured 3D displacement



(b) Differences

Fig. 26.8 Results of 3D displacement distribution measurement. (a) Measured 3D displacement. (b) Differences

26.4 Conclusions

In this paper, the principle and the calibration method to measure 3D displacement using the sampling moire method with multiple cameras were shown. The evaluation was performed with comparing the experimental results to measure 3D displacement distribution measurement with three cameras and the displacement of the cantilever. As the results, it was confirmed that the 3D displacement distribution was measured with highly accuracy.

It is expected that 3D displacement measurement using the sampling moire method with multiple cameras can be applied to predict of a landslides and for health monitoring of large structures, such as bridges, steel towers, or tall buildings.

Acknowledgement This work was supported by NEDO.

References

1. H. Matsuda, Y. Ito, Construction management and maintenance of infrastructures by optical measurement method (in Japanese). *J. JSEM* **11-3**, 161–170 (2011)
2. Y. Arai, T. Kurata, Improvement of spatial fringe analysis method using sampling technique on pixel of CCD (in Japanese). *Jpn. J. Opt.* **24-9**, 581–586 (1995)
3. Y. Arai, S. Yokozeki, K. Shiraki, T. Yamada, High precision two-dimensional spatial fringe analysis method. *J. Mod. Opt.* **44-4**, 739–751 (1997)
4. R. Hanada, M. Miyazawa, M. Fujigaki, K. Simo, Y. Morimoto, A sampling moire method to measure the dynamic shape and strain of rotating tires. *Tire Sci. Technol.* **41-3**, 214–225 (2013)
5. K. Shimo, M. Fujigaki, A. Masaya, Y. Morimoto, Development of dynamic shape and strain measurement system by sampling moire method, in *ICEM2009, Proceedings of SPIE*, vol. 7522 (2009)
6. S. Ri, M. Fujigaki, Y. Morimoto, Sampling moire method for accurate small deformation distribution measurement. *Exp. Mech.* **50-4**, 501–508 (2010)
7. S. Yoneyama, A. Kitagawa, K. Kitamura, H. Kikuta, In-plane displacement measurement using digital image correlation with lens distortion correction. *JSME Int. J. Ser. A* **49-3**, 458–467 (2006)
8. C.H. Chiang, M.H. Shin, W. Chen, C.P. Yu, Displacement measurements of highway bridges using digital image correlation methods, in *Proceedings of SPIE*, vol. 8321 (2011)
9. M. Takeda, H. Ina, S. Kobayashi, Fourier-transform method of fringe-pattern analysis for computer-based topography and interferometry. *Opt. Soc. Am.* **72-1**, 156–160 (1982)
10. A. Piekarczyk, M. Malesa, M. Kujawinska, K. Malowany, Application of hybrid FEM-DIC method for assessment of low cost building structures. *Exp. Mech.* **52-9**, 1297–1311 (2012)
11. H. Schreier, J.J. Orteu, M.A. Sutton, *Image correlation for shape. Motion and deformation measurements* (Springer, New York, 2009), pp. 175–208
12. F. Chen, X. Chen, X. Xie, X. Feng, L. Yang, Full-field 3D measurement using multi-camera digital image correlation system. *Opt. Lasers Eng.* **51-9**, 1044–1052 (2013)
13. M. Nakabo, T. Hara, M. Fujigaki, T. Tajiri T, Development of small displacement measurement method in sub-millimeter resolution by long distances (in Japanese), in *Proceedings of JSNDI Fall Conference 2011* (2011), pp. 219–222

Chapter 27

Automatic Generation of Codes for Routine of CNC Machining Based on Three-Dimensional Information Obtained by Fringe Projection

S. Bustos, C. Aguilera, and Amalia Martínez-García

Abstract The use of machining systems by Computer Numerical Control (CNC) has notable advantages in the area of industrial production compared with traditional techniques. This facilitates a significant decrease of time, higher precision and optimization of operation parameters. The control of sequences in these systems is based on codes that define the parameters to produce the machining of a determined piece. However, the generation of these codes presents two major challenges, first, know the tridimensional information of the piece to produce, and second, define the sequence by CNC machining. In this work, the fringe projection technique is used to obtain three-dimensional information from an object and based on this information, automatically generate programming codes for the machining routine of a three-axial CNC milling machine. The results are compared to apply the fringe projection technic to recover three-dimensional shape of an object based on Least Squares Algorithm, using information from three to eight images.

Keywords Fringe projection • Least squares algorithm • CNC • Image processing • Reverse engineering

27.1 Introduction

A crucial step that across all area of “Automation Engineering” is the acquisition of signals with relevant information for a process or system determinate. This input signals are the base for the execution of control activity, making decision, security procedures, resources optimization and any operation focused on giving autonomy to a system. This is how they have developed diverse class of sensors ant technics for measuring and analysis of varied physical quantities. More and better applications can be made, as well more and better information are taken.

For this reason the acquisition of three-dimensional shape of objects and environments has become in a relevant matter, through deep measurement, made by technics classified in two groups: contact technics and no-contact technics. In the first group can be mentionated the CMM systems (Coordinate Measurement Machine) and touch-robots [1], in the second group are deep measurement technics based on principles such as focus variation [2], stereo-disparity [3, 4], triangulation [5], time of fly [6] or structured light projection [7].

The use of three dimensional information of the objects to generate digital models and make applications based on these is known as inverse engineering, mainly used on industrial manufacturing [8, 9], has been relevant in the medicine field, for example for made prosthesis [10, 11], or in architecture, for the conservation of pieces with heritage value [12, 13]. For that, has been developed works where the points cloud obtained by the techniques mentioned before are used to generate CAD models [9], or manipulate directly this data to define works of manufacturing by subtraction or addition of material [13].

In this work, the fringe projection Computer numerical control (CNC) technique is used for obtain the three dimensional shape of an object whose results, representing as an image in grayscale, is analyzed through image process algorithms to generate G-codes, that define a sequence of CNC milling machine, manufacturing a reply of the object. In the Sect. 27.2 of this paper, the theoretical bases of the technique described, the least-squares algorithm and unwrapping phase process are described; in the Sect. 27.3 the system developed is presented; then, the results in the Sect. 27.4 and finally the comments and conclusions in the Sect. 27.5.

S. Bustos (✉) • C. Aguilera
Universidad del Biobío, Concepción, Chile
e-mail: sambusto@egresados.ubiobio.cl; cristhia@ubiobio.cl

A. Martínez-García
Centro de Investigaciones en Óptica, León, Mexico
e-mail: amalia@cio.mx

27.2 Fringe Projection Theory

A technique for obtain three-dimensional information of an objects, is the fringe projection technique which consists in project on an object a fringe pattern formed by lights lines that vary its intensity in sinusoidal form, and analyze the images with the deformation of the fringes on the objects. In the Fig. 27.1 the layout with the components of the system are represented.

Considering the capture image as a matrix of intensity light $I(x,y)$, this is defined by the equation:

$$I(x,y) = a(x,y) + b(x,y) \cos [\phi(x,y)] \quad (27.1)$$

Where a is the average of intensity, b is the intensity amplitude of the fringes and ϕ is the phase that contain the information of the deformation of the fringes on the surface of the object, then, the deep z of the figure is defined by the equation:

$$z(x,y) = \frac{\phi(x,y)}{2\pi f \cdot \tan \alpha} \quad (27.2)$$

Being ϕ the variable that must be determined, The Phase Shifting method is used, that consist in to induce a variation in the argument of coseno, shifting the fringes of the projected pattern, and capturing a set of images for generate an equation system. Whose solutions is find the phase value for every point x, y of the scene.

27.2.1 Least Squares Algorithm

Three unknown values in the (27.1), should be taken at least three images to obtain an equations system for find the ϕ value, however, the lot of images can be extended for obtain better results, based on the Least-Squares algorithm [14], where the intensity matrix can be definite by:

$$I_i = \alpha_0 + \alpha_1 \cdot \cos(\Delta\phi_i) - \alpha_2 \cdot \text{sen}(\Delta\phi_i) \quad (27.3)$$

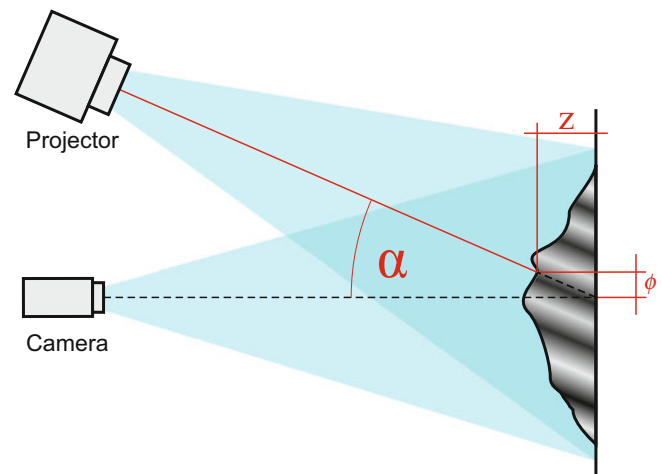
Where:

$$\alpha_0 = a \quad (27.4)$$

$$\alpha_1 = b \cdot \cos(\phi) \quad (27.5)$$

$$\alpha_2 = -b \cdot \text{sen}(\phi) \quad (27.6)$$

Fig. 27.1 Layout of components for fringe projection system



Applying the Least Squares method, the result is defined by the matrix equation:

$$\begin{bmatrix} \alpha_0 \\ \alpha_1 \\ \alpha_2 \end{bmatrix} = A^{-1}(\Delta\phi_i)B(x, y, \Delta\phi_i) \quad (27.7)$$

Where the matrices are defined by:

$$A(\Delta\phi_i) = \begin{bmatrix} N & \sum \cos(\Delta\phi_i) & \sum \text{sen}(\Delta\phi_i) \\ \sum \cos(\Delta\phi_i) & \sum \cos^2(\Delta\phi_i) & \sum \cos(\Delta\phi_i)\text{sen}(\Delta\phi_i) \\ \sum \text{sen}(\Delta\phi_i) & \sum \cos(\Delta\phi_i)\text{sen}(\Delta\phi_i) & \sum \text{sen}^2(\Delta\phi_i) \end{bmatrix} \quad (27.8)$$

And:

$$B(x, y, \Delta\phi_i) = \begin{bmatrix} \sum I_i \\ \sum I_i \cos(\Delta\phi_i) \\ \sum I_i \text{sen}(\Delta\phi_i) \end{bmatrix} \quad (27.9)$$

Every summation is defined from 1 to N. The matrix $A(\Delta\phi_i)$ depends only of the phase-shift values arbitrary defined. The matrix B is composed by the weighted summations of every intensity pattern taken. This results are obtained the values of α_0 , α_1 and α_2 . The phase ϕ is calculated using the (27.5) and (27.6) and is:

$$\phi(x, y) = \arctan \left[\frac{-\alpha_2}{\alpha_1} \right] \quad (27.10)$$

This result has the relevance that to be valid for a quantity N of images, better than or equal to three, with different phase shifts $\Delta\phi_i$ that must not to be equally spaced, however, if this are defined by:

$$\Delta\phi_i = i2\pi/N; \quad i = 1, 2, \dots, N \quad (27.11)$$

Then, the function to found the phase ϕ is finally:

$$\phi(x, y) = \arctan \left[\frac{-\sum_{i=1}^N I_i \text{sen}(\Delta\phi_i)}{\sum_{i=1}^N I_i \cos(\Delta\phi_i)} \right] \quad (27.12)$$

27.2.2 Unwrapping Phase

Having the ϕ value from the (27.12), is necessary to solve the mathematic limitation that the range of the function arctangent is between $-\pi/2$ and $\pi/2$. Although is possible, through mathematics analysis, extend this range from 0 to 2π , the result is still between limited values, appearing discontinuities every time that the value come over the limits of the range, phenomenon that is called wrapping. To solve it, a proceeding is applied to eliminate the discontinuities of the results, this proceeding is called phase unwrapping.

A basic algorithm of phase unwrapping presented by K. Itoh [15] consist in evaluate the difference between the values of every pixel in the image with its neighbor pixel, adding or resting a multiple of 2π every time that this difference overcome a threshold value, determining that appear a discontinuity in the phase. The result of this algorithm is a matrix with the phase unwrapped, that is to say, without discontinuities.

The process of calculate the phase is used to analyze only the reference surface as well the object on the reference surface alone. The final result is the subtraction between both calculations.

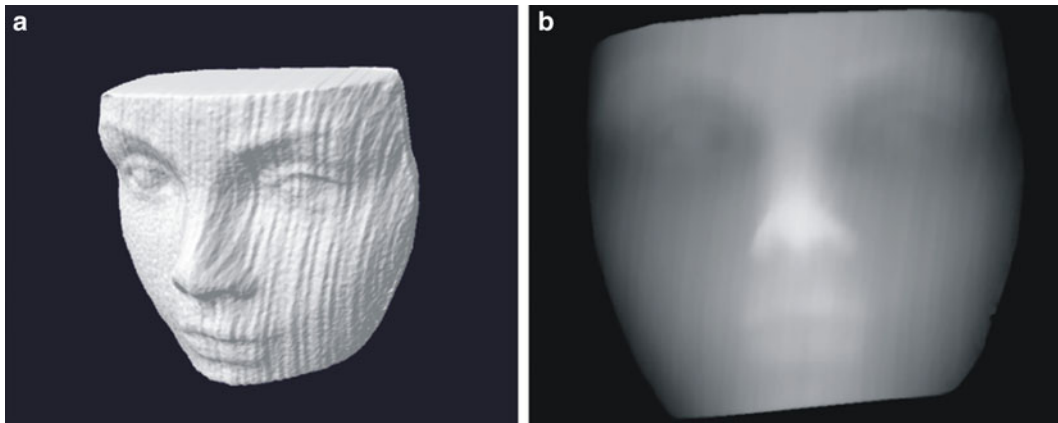


Fig. 27.2 (a) 3D visualization of the object, (b) grayscale image associated to the deep of the object

27.3 System Developed

This work consist in an application that, through the fringe projection technique generate a three dimensional model of an object, for the purpose of generate programming codes to CNC milling machine. To do this, it is developed one software with three principal modules: Projection and Capture Module, Process Module, and Programming Module.

In the Projection and Capture Module, the parameters that determine the features of the fringe pattern and the capture process are entered that is, the quantity of fringes of the pattern, orientation, the quantity of images to capture, or if it is analyzing the object or the reference. Then, the pattern is projected, shifted, and capturing the corresponding images.

In the Process Module, the phase calculating and unwrapping is executed, with the images of the reference well as the images with the object, and the subtraction of both. Then, this result is represented as a 3D model and as grayscale image, where the deep of the objects is associated with the intensity of white, represented in the Fig. 27.2.

In the Programming Module, the process to generate the sequence of instructions is developed, for a CNC milling machine manufacture a figure replicating the shape of the analyzed object. This system is developed to work for a three axis CNC milling machine, implying that the programed movements are controlled assigning values on the axis X, Y and Z.

The machining routine has two main stages, the first is a fast roughing, where the material is subtracted as much as possible, without details in the finished; the second, is a fine roughing, where the material is subtracted in lesser amounts, slower, and generally with a smaller tool, defining the details with more precision.

Through the application, firstly the parameters needed to execute the machining are ingressed, means the dimension of the unprocessed material, tool diameter and cutting depth of the fast and fine roughing. Once these parameters are defined, the software calculates the tool movements.

For generate the fast roughing routine, the grayscale image associated to the “unwrapping phase” result represented in the Fig. 27.2b is used. Applying a threshold on this image in different levels, as shown in the Fig. 27.3, for every case the points where the tool should get down, move and get up are determined depending of the limits of white regions.

To define the fine roughing routine, the thresholding on the grayscale image shown in the Fig. 27.2b is used again, but in this case, a Canny Edge Detector is applied on every image, as shown in the Fig. 27.4.

Following the detected contour, series of points are determinated to define the coordinates of the movements of the tool. Repeating this process to every image, finally the shape of the object is manufacturing on the material.

27.4 Results

As it is described, the system offers the possibility of recover the three dimensional shape of the object based on the Least Square Algorithm, using three or more images, specifically in this case, a set from three to eight images may be used. For evaluating the performance of the 3D scan, Eid et al. propose a procedure that analyze the difference between the virtual model resulting and the real object [16], aligning the point clouds by the comparison of siluettes, and then comparing it. In this case, the evaluation is realized between the result of analysis of an object with hemispherical geometry, and a semi

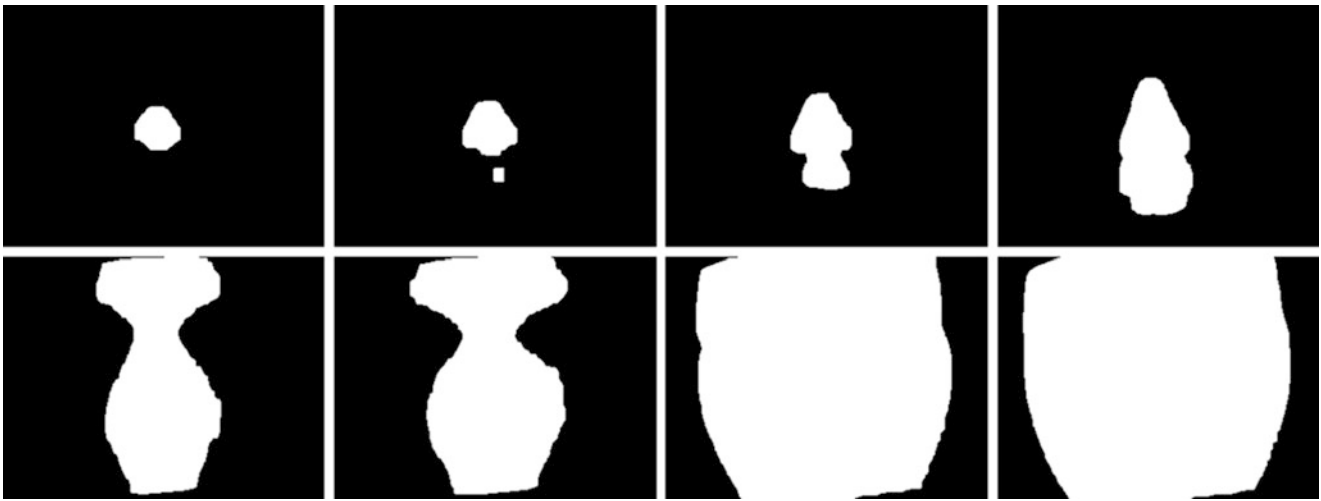


Fig. 27.3 Results of threshold on the grayscale image in different levels

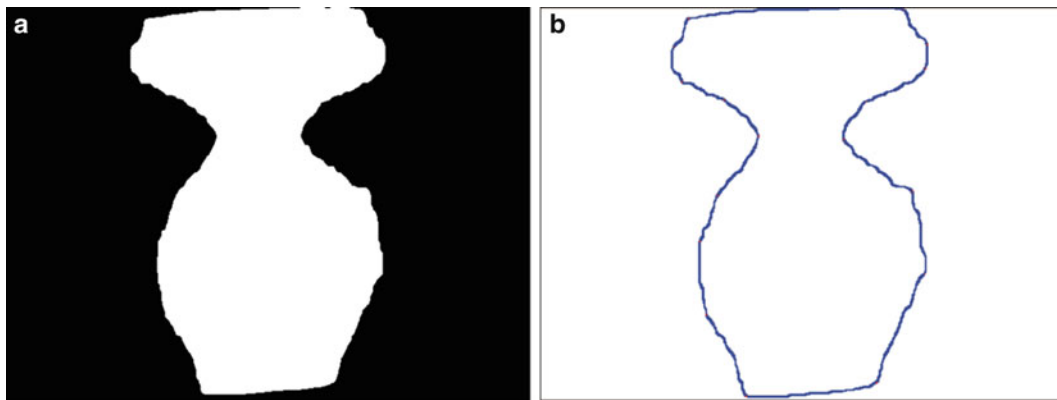


Fig. 27.4 (a) Threshold applied on the grayscale image, (b) Canny edge detector applied on the thresholded image

sphere modeled mathematically, represented by images associated to data matrix. The process of 3D shape recovery is repeated with a set from three to eight images.

Furthermore, to analytically evaluating the results, the indicator E is defined by the average of the absolute differences between both data matrix, measured in millimeters, represented by the equation:

$$E = \sum_{i=1}^I \sum_{j=1}^J \frac{|I_{i,j} - S_{i,j}|}{I \cdot J} \quad (27.13)$$

Where S is the matrix with the values of the semi-sphere resulting and I is the matrix with the values of the semi-sphere modeled. The error matrix, results of the absolute difference between both data matrix represented by surface plots are presented in the Fig. 27.5, the results of the indicator E are presented in the Table 27.1.

The results of the sequence instructions generated are defined as a G-code, which is interpreted for any CNC system. In this case, is executed on a CNC control software, showing the simulation of the fast and fine roughing process in the Fig. 27.6.

Table 27.1 Performance indicator E for N number of images

N	3	4	5	6	7	8
E (mm)	6.61	4.35	3.33	2.88	2.70	2.70

Fig. 27.5 Surface plots of error matrix using N images
(a) N = 3, (b) N = 4,
(c) N = 5, (d) N = 6,
(e) N = 7, (f) N = 8

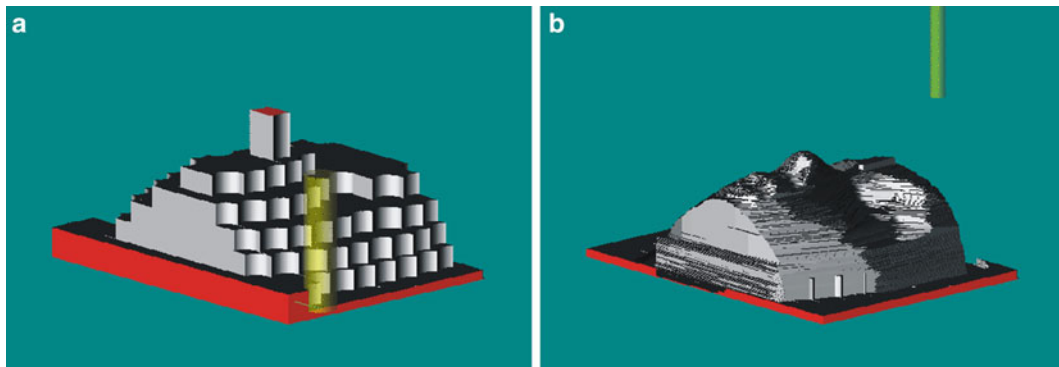
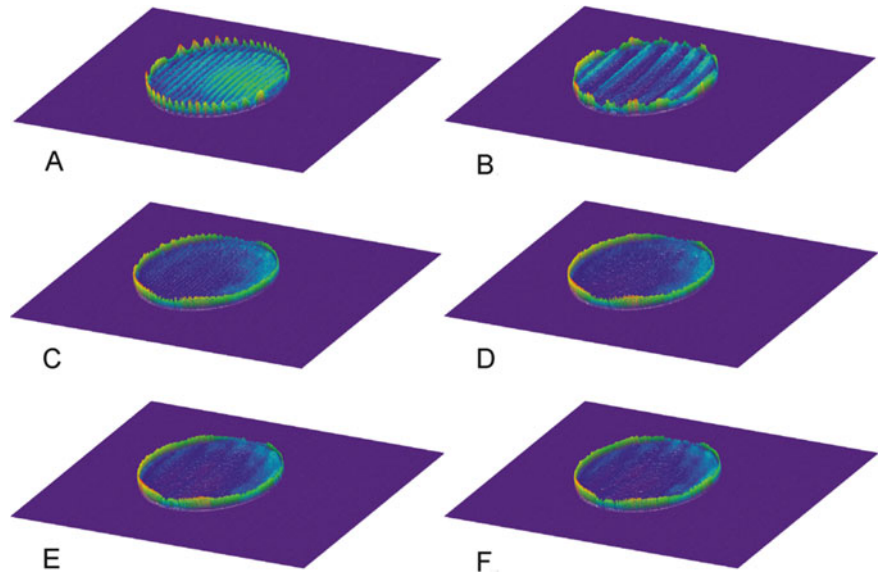


Fig. 27.6 Screen view of CNC control software: (a) simulation of fast roughing, (b) simulation of fine roughing

27.5 Comments and Conclusions

Based on the developed work, it can be noted the relevance of the integration of Fringe Projection technique as a way for assist programming works in industrial manufacturing, in this case the programming of G-codes to drive the movements of a CNC milling machine system. The advantage is related principally with the reduction of time, on the one hand in the design of a three dimensional model of an object, and on the other hand in the programming work of the sequence of movements to reproduce it by machining, cases that, when is trying of complex shapes, maybe use a lot of time.

Furthermore, it is emphasized the use of image process algorithms to comply the targets of the project, which is not an area where these have the principal focus, but these are useful tools to face challenges in engineering.

The system limitation is related to the conditions that affect the deep measuring system, for example, the obtention of information from only one view, obstruction phenomenon, shadows, brightness or not controlled light in the scene. These problems can be solved based on works in this line of research, extending the abilities of the application.

As future work, it could be used five axis CNC milling machine for the purpose of avoid staggered results in finishing the machined shape, and manufacturing of objects analyzed from more than one view.

According to the comparison of results to use different number of images in the Least Squares algorithm, these are clearly improved by increasing the images, however, this produces a slower process by the image capturing and processing.

Acknowledgement This work was done in two stages, the first in the Centro de Investigaciones en Óptica, México, under the supervision of Guillermo Garnica, J. Ascención Guerrero and Francisco Cuevas; and the second stage in the CIM Laboratory of the Universidad del Bío-bío, Chile, under the supervision of Luis Vera.

References

1. S. Lemes, M. Cabaravidic, N. Zaimovic-Uzunovic, *Robotic Manipulation in Dimensional Measurement*, XXIV International Conference on Information, Communication and Automation Technologies (ICAT), IEEE (2013)
2. G.-B. Kim, A novel depth-from-hybrid-focus method for surface morphology with depth discontinuity. *Int. J. Adv. Manuf. Technol.* **46**, 267–274 (2010)
3. S. Zhang, C. Wang, S.C. Chan, A new high resolution depth map estimation system using stereo vision and kinect depth sensing. *J. Signal Process Syst.* **79**, 19–31 (2013)
4. S.-J. Huang, F.-R. Ying, Stereo vision system for moving object detecting and locating based on CMOS image sensor and DSP chip. *Pattern Anal. Appl.* **15**, 189–202 (2012)
5. D.Y. Chang, Y.M. Chang, A freeform surface modeling system based on laser scan data for reverse engineering. *Int. J. Adv. Manuf. Technol.* **20**, 9–19 (2002)
6. Y. Cui, S. Schuon, D. Stricker, C. Theobalt, Algorithms for 3D shape scanning with a depth camera. *IEEE Trans. Pattern Anal. Mach. Intell.* **35**, 1039–1050 (2013)
7. R. Orghidan, J. Salvi, M. Gordan, C. Florea, J. Battle, Structured light self-calibration with vanishing points. *Mach. Vis. Appl.* **25**, 489–500 (2014)
8. Y. Zhao, J. Zhao, L. Zhang, L. Qi, *Development of a Robotic 3D scanning for Reverse Engineering of Freeform*, International Conference on Advanced Computer Theory and Engineering, IEEE (2008)
9. D. Zhang, J. Liang, C. Guo, X. Zhang, *Digital Photogrammetry Applying to Reverse Engineering*, Symposium on Photonics and Optoelectronic, IEEE (2010)
10. X. Chen, J. Sun, J. Xi, Y. Xiong, J. Qiu, X. Gu, *Development of a 3D Optical Measurement System based on Fringe Projection for Facial Prosthesis*, Instrumentation and Measurement Technology Conference, IEEE (2011)
11. R. Racasan, D. Popescu, C. Neamtu, M. Dragomir, *Integrating the Concept of Reverse Engineering in Medical Applications*, Automation Quality and Testing Robotics, IEEE (2010)
12. A. Manferdini, M. Russo, *Multi-scalar 3D Digitalization of Cultural Heritage Using a Low-Cost Integrated Approach*, Digital Heritage International Congress, IEEE (2013)
13. G. Santana, A. Alitany, L. Gimenez, E. Redondo, *Development of a Method for Direct Conversion of a Photogrammetric Point Cloud, to Points of Head's Movement of a CNC Milling Machine*, Information Systems and Technologies, IEEE (2014)
14. D. Malacara, *Optical Shop Testing*, 3rd edn. (Wiley, New York, 2007). Cap. 14
15. K. Itoh, Analysis of the phase unwrapping algorithm. *Appl. Opt.* **21**(14), 2470 (1982)
16. A. Eid, A. Farag, A Unified Frameworks for Performance Evaluation of 3-D Reconstruction Techniques, IEEE Computer Society Conference on Computer Vision and Pattern Recognition Workshop (2004)

Chapter 28

Automatic Generation of Movement Sequences to Robotic Arm Based on Three-Dimensional Data Obtained Through Fringe Projection Technique

S. Bustos, C. Aguilera, and Amalia Martínez-García

Abstract The use of robotic manipulators is a subject that has become relevant in the process of automation in different branches of industrial manufacturing. Today is possible to make routines works with robotic manipulator in dangerous conditions for human operators, providing flexibility in production lines, doing multiple types of tasks and executing actions with precision and quickly. All operations of a robotic arm is controlled by a computer system that controls the mechanism positions. Since the work of these machines is to manipulate tools or pieces, it is necessary to have tridimensional information of the environment or manipulated elements. In this work, the fringe projection technique is used to obtain three-dimensional shape of an object, and based on this information to generate the trajectories of the manipulator for the painting of complex objects through paint spraying. The obtained results have been successful, generating simulated trajectories for the painting of pieces with good quality and short times compared with times using traditional methods to program sequences.

Keywords Fringe projection • Least squares algorithm • Robotic arm • Industrial manufacturing • Painting

28.1 Introduction

A crucial step that across all area of Automation Engineering is the acquisition of signals with relevant information for a process or system determinate. Robotic arm This input signals are the base for the execution of control activity, making decision, security procedures, resources optimization and any operation focused on giving autonomy to a system. This is how they have developed diverse class of sensors ant technics for measuring and analysis of varied physical quantities. More and better applications can be made, as well more and better information are taken.

For this reason the acquisition of three-dimensional shape of objects and environments has become in a relevant matter, through deep measurement, made by technics classified in two groups: contact technics and no-contact technics. In the first group can be mentionate the CMM systems (Coordinate Measurement Machine) and touch-robots [1], in the second group are deep measurement technics based on principles such as focus variation [2], stereo-disparity [3, 4], triangulation [5], time of fly [6] or structured light projection [7].

Between the applications of deep measurement to assist the control of industrial robots can be mentioned the work developed by Alenyà et al. [8], controlling the manipulation of a robotic arm based on environment perception, evaluating the use of a ToF (Time of Fly) and RGBD (Red Green Blue Deep) cameras. In the work made by Skotheim et al. [9] the triangulation technique is used for localized objects in a flexible system of industrial assembled operate by robotic arm. On other hand, for the inverse case, it's means, the use of robotic arms to assist deep measurement process, can be mentioned the works developed by Y. Zhao et al. [10] and R. Franke et al. [11] using a robotic arm to control a deep measurement system based on triangulation technique and deep measurement system based on structured light technique respectively.

The focus of this work seek to generate automatically programs for the control of movements of a robotic arm simulating a painting routine of an object, based on the acquisition and processing of images to obtain longitude measurements of the

S. Bustos (✉) • C. Aguilera
Universidad del Biobío, Concepción, Chile
e-mail: sambusto@egresados.ubiobio.cl; cristhia@ubiobio.cl

A. Martínez-García
Centro de Investigaciones en Óptica, León, Mexico
e-mail: amalia@cio.mx

object in three dimensions, specifically based on fringe projection, that belong to structured light projection technique. In the Sect. 28.2 of this work is described the theory of fringe projection, least-squares algorithm and unwrapping phase process; in the Sect. 28.3 the system developed is presented; followed of the results in the Sect. 28.4 and finally the comments and conclusions in the Sect. 28.5.

28.2 Fringe Projection Theory

A technique for obtain three-dimensional information of an object, it is the fringe projection technique [12], which consists in project on surface a fringe pattern formed by light lines that vary its intensity in sinusoidal shape, and analyze the images with the deformation of the fringes on the objects. In the Fig. 28.1 the layout with the components of the system are represented.

Considering the captured image as a matrix of intensity light $I(x,y)$, this is defined by the equation:

$$I(x,y) = a(x,y) + b(x,y) \cos [\phi(x,y)] \quad (28.1)$$

Where a is the average of intensity, b is the intensity amplitude of the fringes and ϕ is the phase that contain the information of the deformation of the fringes on the surface of the object, then, the height z is given by the equation:

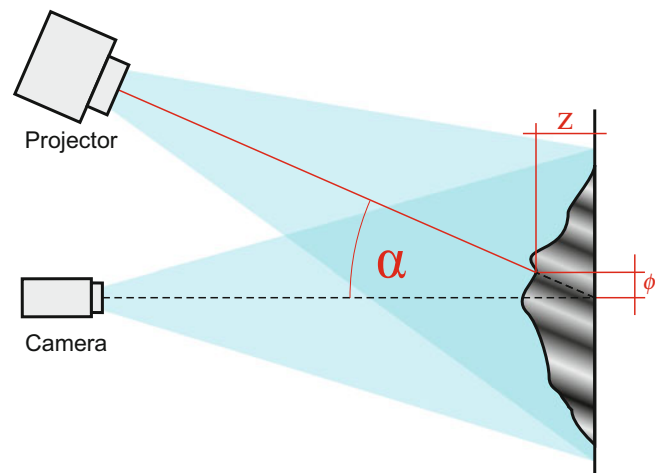
$$z(x,y) = \frac{\phi(x,y)}{2\pi f \cdot \tan \alpha} \quad (28.2)$$

Being ϕ the variable that must be evaluated. The Phase Shifting method is used, that consists in to induce a variation in the argument of coseno, shifting the fringes of the projected pattern, and capturing a set of images for generate an equations system. Whose solution is find the phase value for every point (x, y) of the scene.

28.2.1 Least Squares Algorithm

Three unknown values in the equation (28.1) implies that should be taken at least three images to obtain an equations system to find the ϕ value, however, more images can be considered to obtain better results, based on the Least-Squares algorithm, where the intensity matrix can be defined by:

Fig. 28.1 Layout of components for fringe projection system



$$I_i = \alpha_0 + \alpha_1 \cdot \cos(\Delta\phi_i) - \alpha_2 \cdot \text{sen}(\Delta\phi_i) \quad (28.3)$$

Where:

$$\alpha_0 = a \quad (28.4)$$

$$\alpha_1 = b \cdot \cos(\phi) \quad (28.5)$$

$$\alpha_2 = -b \cdot \text{sen}(\phi) \quad (28.6)$$

Applying the Least Squares method, the result is defined by the matrix equation:

$$\begin{bmatrix} \alpha_0 \\ \alpha_1 \\ \alpha_2 \end{bmatrix} = A^{-1}(\Delta\phi_i)B(x, y, \Delta\phi_i) \quad (28.7)$$

Where the matrices are defined by:

$$A(\Delta\phi_i) = \begin{bmatrix} \sum_{i=1}^N \cos(\Delta\phi_i) & \sum_{i=1}^N \cos^2(\Delta\phi_i) & \sum_{i=1}^N \cos(\Delta\phi_i)\text{sen}(\Delta\phi_i) \\ \sum_{i=1}^N \text{sen}(\Delta\phi_i) & \sum_{i=1}^N \cos(\Delta\phi_i)\text{sen}(\Delta\phi_i) & \sum_{i=1}^N \text{sen}^2(\Delta\phi_i) \end{bmatrix} \quad (28.8)$$

And:

$$B(x, y, \Delta\phi_i) = \begin{bmatrix} \sum I_i \\ \sum I_i \cos(\Delta\phi_i) \\ \sum I_i \text{sen}(\Delta\phi_i) \end{bmatrix} \quad (28.9)$$

Every summation is defined from 1 to N. The matrix $A(\Delta\phi_i)$ depends only of the phase-shift values arbitrary defined. The matrix B is composed by the weighted summations of every intensity pattern taken. These results are obtained α_0 , α_1 and α_2 . The phase ϕ is calculated using the (28.5) and (28.6) and is given by:

$$\phi(x, y) = \arctan\left[\frac{-\alpha_2}{\alpha_1}\right] \quad (28.10)$$

This result has the relevance that to be valid for a quantity N of images, better than or equal to three, with different phase shifts $\Delta\phi_i$ that must not to be equally spaced, however, if this are defined by:

$$\Delta\phi_i = i2\pi/N; \quad i = 1, 2, \dots, N \quad (28.11)$$

Then, the function to found the phase ϕ is finally:

$$\phi(x, y) = \arctan\left[\frac{-\sum_{i=1}^N I_i \text{sen}(\Delta\phi_i)}{\sum_{i=1}^N I_i \cos(\Delta\phi_i)}\right] \quad (28.12)$$

28.2.2 Unwrapping Phase

Having the ϕ value from the (28.12), it is necessary solve the mathematic limitation that the range of the function arctangent is between $-\pi/2$ and $\pi/2$. Although is possible, through mathematics analysis, extend this range from 0 to 2π , the result is still between limited values, appearing discontinuities every time that the value come over the limits of the range, phenomenon that is called wrapping. To solve it, a proceeding is applied to eliminate the discontinuities of the results, this proceeding is called phase unwrapping.

A basic algorithm of phase unwrapping presented by K. Itoh [13] consists in evaluate the difference between the values of every pixel in the image with its neighbor pixel, adding or resting a multiple of 2π every time that this difference overcome a threshold value, determining that appear a discontinuity in the phase. The result of this algorithm is a matrix with the phase unwrapped, that is to say, without discontinuities.

The process of calculate the phase is used to analyze only the reference surface as well the object on the reference surface alone. The final result is the subtraction between both calculations.

28.3 System Developed

The fringe projection technique is used to generate a tridimensional model of an object, with the goal of use it to program a sequence of movements of a robotic arm. For that, it is developed one software with three principal modules: Projection and Capture Module, Process Module, and Programming Module.

In the Projection and Capture Module, the parameters that determine the features of the fringe pattern and the capture process are entered, that is, the quantity of fringes of the pattern, orientation, the quantity of images to capture, and if is analyzing the object or the reference. Then, the pattern is projected, and shifted, capturing the corresponding images.

In the Process Module, the phase calculating and unwrapping is executed, with the images of the reference well as the images with the object, and the subtraction of both. Then, this result is represented as a 3D model and as grayscale image, where the deep of the objects is associated with the intensity of white, represented in the Fig. 28.2.

In the Programming Module, the sequence of movements to a robotic arm is determined, with the goal of to round to the analyzed object, simulating its spray painting. The robotic arm used in this project is a KUKA robot, model KR-6, facilitated by the CIO “*Centro de Investigaciones en Óptica*” and its programmation is based on language with similar syntax to C. This language offer the capabilities of configure velocities, accelerations, coordinate reference and movements points, assigning angles values for its six articulations (direct cinematic) or assigning three coordinate values X, Y, and Z determining the position of final element, and other three values named A, B, and C determining its angles of orientation (inverse cinematic).

Based on the image represented in the Fig. 28.2b, a lot of points considered as relevant are chosen, for that, using it as reference the robotic arm can surround the object. Once defined these points, the program offers the option to put them in order, the movements of the robotic arm are executed in a sequence that sweep the points from left to right, starting for the points situated in the top of the image. In the Fig. 28.3 is represented the selection and putting in order of the reference points.

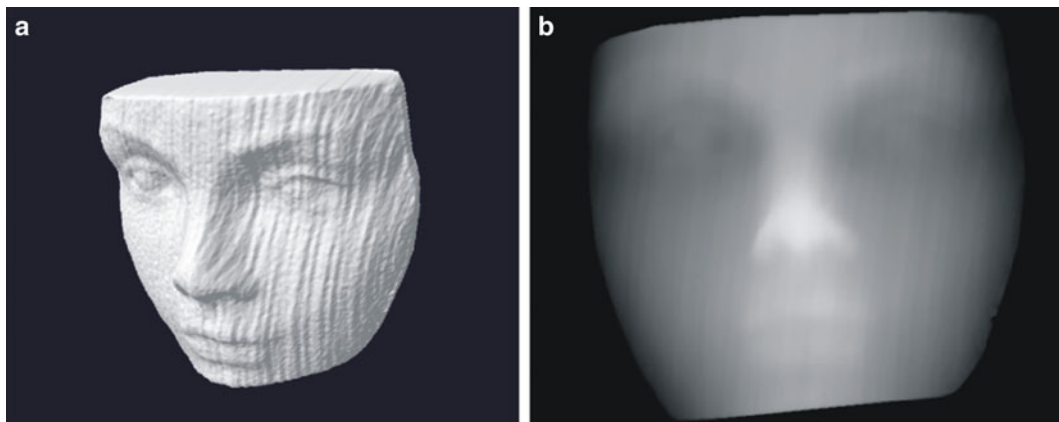


Fig. 28.2 (a) 3D visualization of the object. (b) grayscale image associated to the deep of the object

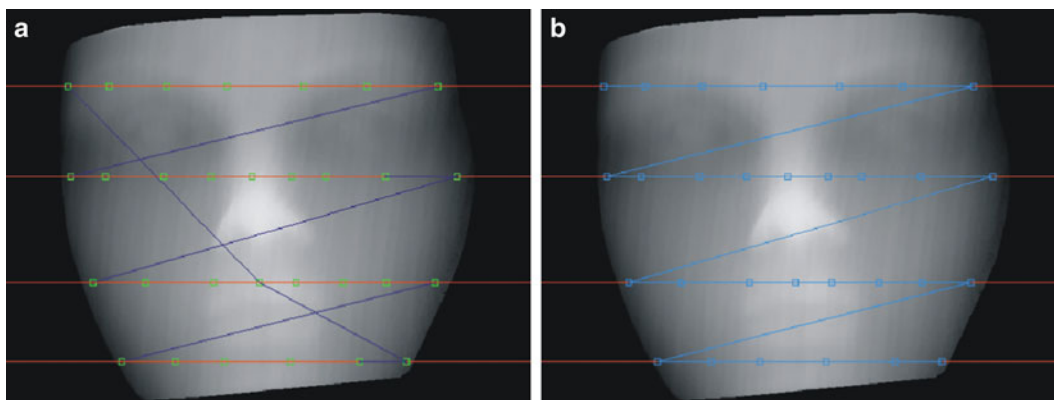
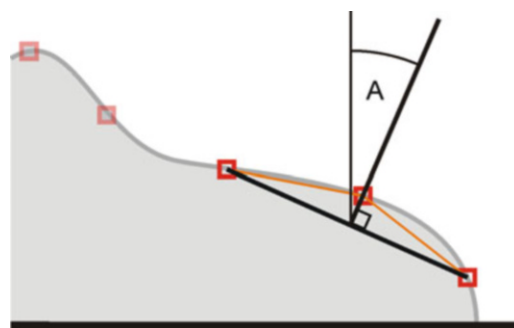


Fig. 28.3 (a) Image with selected points, represented by *green squares*. (b) Image with ordered points represented by *blue squares*

Fig. 28.4 Scheme to determine the orientation of the robot arm



Defined the order of every point, the code for the movements of the robot is generated, assigning the coordinates of every point selected, relating the horizontal position of the pixel in the image with the X variable of the robot, the vertical position of the pixel with the Y variable, and the intensity of white, associated to the deep of the object, with the Z variable. In addition, as the orientation of the robot manipulator must be perpendicular to the surface of the object, for every point are defined the parameters based on the position of their adjacent reference points. In the Fig. 28.4 is presented a transversal view of the object, schematizing how is determined the orientation of the effector through the angle A, formed between the normal to the object base, and the normal to the line formed for the link of the points adjacents to analyze the point.

Iterating this process for every reference point, all the sequence of instructions of movements for the robotic arm is generated.

28.4 Results

Once generates the sequence of instructions, this is interpreted by the control software of robotic arm, following a trajectory that round the shape of the object. In the sequence of images in the Fig. 28.5 is presented a succession of movements of the robot, corresponding to a conjunct of points along of one horizontal sweep, it is means, the elevation of the effector, that is to say, the value on the Y axis is constant, varying only the position along of the space work, corresponding to the movement on the X axis, the deep of the position, corresponding to the movement on the Z axis, and the angles of orientation.

28.5 Comments and Conclusions

Based on this work can be emphasized the relevance of the use of the technique of fringe projection as a way for assist programming works in industrial manufacturing, in this case, the use of a robotic arm for simulate the movements of a painting-routine of a free shape piece. The relevance is associated with the programming time reduction, where the common



Fig. 28.5 Sequence of movements based on three-dimensional information

way to generate the routine of movement consists in lead manually the effector around to the object, and saving the coordinates of the reference points.

Secondly, flexibility to the system is given, generating sequences to round free shape objects, case that through common programming technique is limited, and cause only is worth to do in cases where serial production is made, where the routine must be repeated more than once. Furthermore, using a robotic arm, is widely feasible associate to the effectors other kind of work, depending of the tool that is handled.

The limitations are given by the conditions that affect the deep measuring system, for example, the obtention of information from only one view, obstruction phenomenon, shadows, brightness or not controlled light in the scene. These problems can be solved based on works in this line of research, extending the capabilities of the application.

It can be considered as future work improve the autonomy of the system, avoiding the user intervention to define the references points of the movements of robotic arm, programming in automatic and optimal way the path to follow by the effector.

Acknowledgements This work was done in two stages, the first in the Centro de Investigaciones en Óptica, México, under the supervision of Guillermo Garnica, J. Ascención Guerrero and Francisco Cuevas; and the second stage in the CIM Laboratory of the Universidad del Bío-bío, Chile, under the supervision of Luis Vera.

References

1. S. Lemes, M. Cabaravdic, N. Zaimovic-Uzunovic, *Robotic Manipulation in Dimensional Measurement*, XXIV International Conference on Information, Communication and Automation Technologies (ICAT), IEEE (2013)
2. G.-B. Kim, A novel depth-from-hybrid-focus method for surface morphology with depth discontinuity. *Int. J. Adv. Manuf. Technol.* **46**, 267–274 (2010)

3. S. Zhang, C. Wang, S.C. Chan, A new high resolution depth map estimation system using stereo vision and kinect depth sensing. *J. Signal Process Syst.* **79**, 19–31 (2013)
4. S.-J. Huang, F.-R. Ying, Stereo vision system for moving object detecting and locating based on CMOS image sensor and DSP chip. *Pattern Anal. Appl.* **15**, 189–202 (2012)
5. D.Y. Chang, Y.M. Chang, A freeform surface modeling system based on laser scan data for reverse engineering. *Int. J. Adv. Manuf. Technol.* **20**, 9–19 (2002)
6. Y. Cui, S. Schuon, D. Stricker, C. Theobalt, Algorithms for 3D shape scanning with a depth camera. *IEEE Trans. Pattern Anal. Mach. Intell.* **35**, 1039–1050 (2013)
7. R. Orghidan, J. Salvi, M. Gordan, C. Florea, J. Batlle, Structured light self-calibration with vanishing points. *Mach. Vis. Appl.* **25**, 489–500 (2014)
8. G. Alenyà, S. Foix, C. Torras, Using ToF and RGBD cameras for 3D robot perception and manipulation in human environments. *Intell. Serv. Robot.* **7**, 211–220 (2014)
9. O. Skotheim, M. Lind, P. Ystgaard, S. Fjerdigen, *A Flexible 3D Object Localization System for Industrial Part Handling*, International Conference on Intelligence Robots and Systems, IEEE (2012)
10. Y. Zhao, J. Zhao, L. Zhang, L. Qi, *Development of a Robotic 3D scanning for Reverse Engineering of Freeform*, International Conference on Advanced Computer Theory and Engineering, IEEE (2008)
11. R. Franke, T. Bertram, M. Schulte, C. Kopylow, *Development of a High Accuracy Automatic Measurement System Utilizing an Industrial Robot and a Fringe Projection System*, International Conference on Technologies for Practical Robot Applications, IEEE (2009)
12. D. Malacara, *Optical Shop Testing*, 3rd edn. (Wiley, New York, 2007). Cap. 14
13. K. Itoh, Analysis of the phase unwrapping algorithm. *Appl. Opt.* **21**(14), 2470 (1982)

Chapter 29

Application of Optomecatronics Load Cell for Measuring Work Force and Efforts in Industrial Machinery

A.A. Camacho and F.J. Martínez-Serrano

Abstract We have been working on different stages of a project and the last one was remote monitoring. Now part of a sensor application will be reviewed on a machine that can exert loads in an industrial scale. Some results obtained by this system are shown. The principle on which this research is based is the fact that any load applied to a soil or column will scroll causing deformation, with reference to a point on an unloaded ítem, which is the absolute reference. Optomecatronics loading lets us determine how different points deform; for example in a column a pair of optical sensors (transmitter and receiver) send signals to a DAQ NI and they are read in LABVIEW VI. They received data are written in a database for analysis. The complete design system is applied to measuring force and stress in industrial machinery.

Keywords Load cell • Strain effect • Data adquisition system • Sensors • Instrumentation

29.1 Introduction

Preventive service or corrective maintenance, metrological testing, standardization and calibration of scales, balances and standard weights, it is the background considered for this project. So it should be noted that one of three stages that precedes this proposal is called “Optomechatronic load cell validation according the american standards” [1–2] where there have been improvements to the mechanical and electronic design in the another proposals. A device whose operating principle is different from the commercial was developed to present the result with basic metrological characteristics: resolution, repeatability etc. required by the applicable standard of ASTM E74-06 (American Society for Testing Materials). This standard sets out the practical calibration of measuring instruments of power, and in which we have relied to confirm the applicability of the measuring device. So far we have worked on developing applications load cell with static forces, that is, which remain unchanged at magnitude or direction. The adjustments and improvements to the mechanical design by changing the operating principle of buckling column simple bending beam is performed. It should be emphasized however that the most interesting applications are those in which the load changes over time, specially when dealing with machinery where its elements are in motion. In the case of varying loads cam concept it included making changes to data acquisition system with electronic components better response to change of the physical variable to be measured (the effect of force, the deformation is equivalent to direct displacement—amplitude), the device dimensions are reduced, and the linearity increases in the input–output relationship, to obtain reliable measurements of the optomecatronics load cell.

The proposed system has the versatility to be applied in different areas of knowledge such as: construction, medicine, industry, education etc. This type of system is based on the principle of operation of so-called SCADA Systems that are widely used in industry for control, monitoring and data acquisition industrial processes. Companies that are members of standardization committees are dictating trends in the field of information technology in general for the development of these systems. In fact already in experimental physics laboratories in control of auxiliary systems such as cooling, ventilation, electricity distribution, etc.

A.A. Camacho (✉) • F.J. Martínez-Serrano
Department of Electromechanical Engineering, La Salle University, Leon, Guanajuato, Mexico
e-mail: acamacho@delasalle.edu.mx; javiermartinez53@gmail.com

29.2 Description

For the presented study take into account a so-called industrial machinery “INDUSTRIAL PANTOGRAPH computer controlled (CNC)”. For this first, it begins with the most basic definition of pantograph, which is a link mechanism based on the properties of parallelograms; this instrument has rods connected so that they can move with respect to a fixed point (pivot). It allows you to copy a figure or play to a different level. To achieve different scale drawings the distance between the articulation points (kneecaps) while preserving the condition of parallelism between the rods, two by two ranges.

There are also 3D pantographs, born of computer development with that drawn in the plane, objects can be reproduced by volume; although these instruments could also be considered as an “around” more capable of reproduction, with which you can play, for example a human head, scale, taking information from a digital database from a metric analysis with a scout team infographic (scanner). This technique is often used for modeling objects or parts; making models of automobiles, architectural designs, custom promotional items, etc.

The need to produce objects or parts in series, in such a way that lead to mass production followed the rules and own design specifications, has led to the development of machine tools that meet this function by enabling the manufacture of countless numbers of parts or copies of an original model, however suitable automation and control production lines introduced the concept of robotics, because through these mechanisms integrated applications developed in previous systems, best results are obtained. Thus the pantograph as machine tool works in industrial applications such as cutting material as is the case with oxyfuel, water, plasma, laser providing solutions to one of the main needs of the manufacturing process.

29.3 Experimental Part

Industry metal processing is an area where many of the processes have stagnated technologically, because of the complexity and ways you can get the steel, it is difficult to standardize or automate processes. However Plasma Automation Group S.A. de CV, a company 100 % Mexican dedicated for 20 years to improve and innovate processes metal mechanical industry. This is reflected in the creation of the first 100 % Mexican pantograph devised by the partners of the company, Eng. Ernesto Sandoval Rocha and Eng. Omar Sandoval. Currently in Mexico there are 200 pantographs placed throughout the Mexican republic, with the integration of the best technologies such as plasma cutting, water jet, laser and flame cutting.

Thanks to the growth of the company over the years the business has diversified into other areas, such as high precision machining CNC, welding and qualified Pailer, custom designs machinery, automation and robotic cutting systems.

In Fig. 29.1 shows the image of the different pantographs that are implemented in the company Plasma Automation Group.

Then the isometric view of the frame in which the sensors are placed to locate on the bridge numerical control pantograph is presented in Fig. 29.2.

Figure 29.3 shows blocks diagrams of the data acquisition system that consists in supply source, optics sensor, voltage amplifier, microcontroller and exhibition [3–18].

In the Fig. 29.4 shows several results to obtained when the sensor is located in a test to monitor soil characteristics.



Fig. 29.1 Illustration of different working models Plasma Automation Group

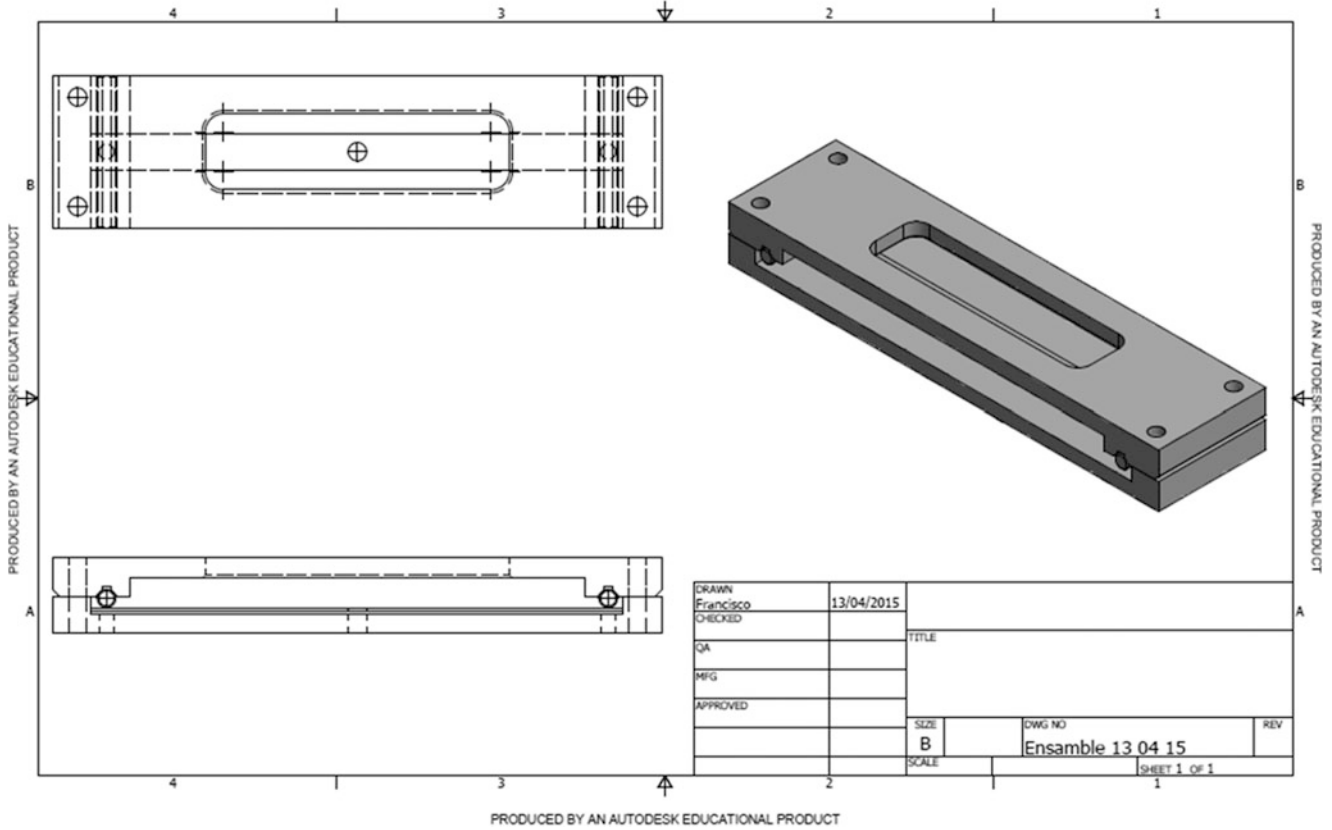


Fig. 29.2 Isometric view of the mount where optical sensors will be placed for measurement



Fig. 29.3 Blocks diagram of the data acquisition system

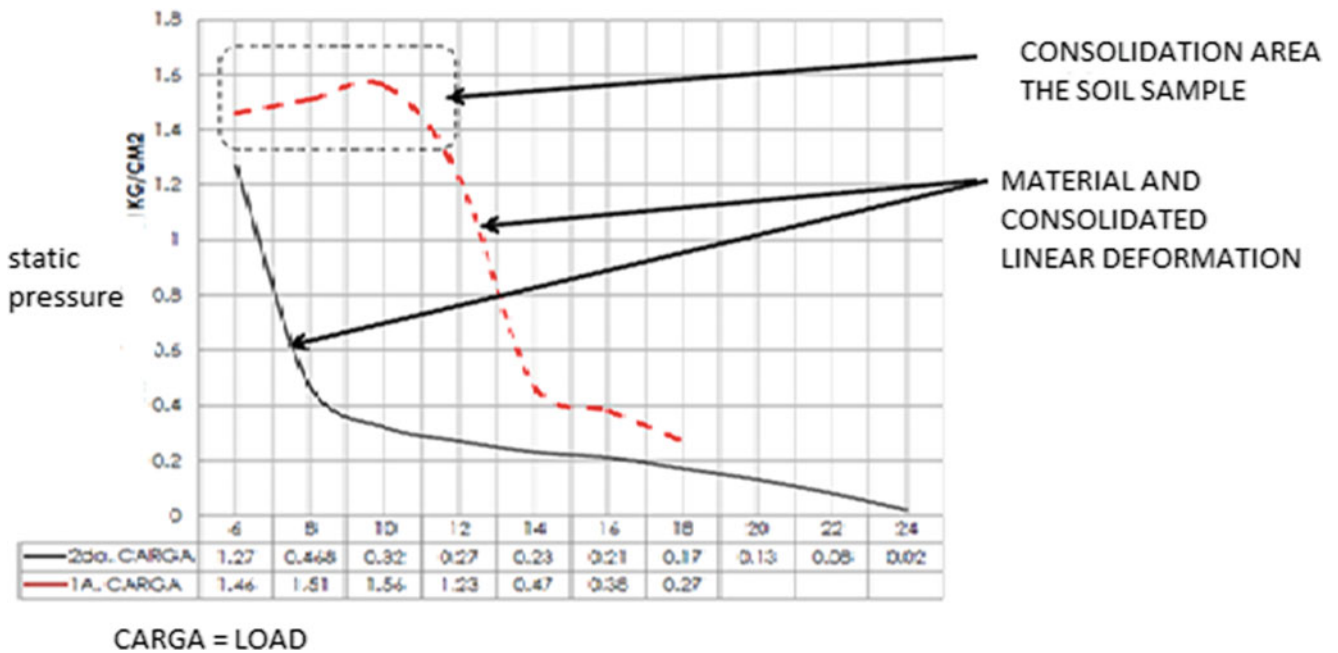


Fig. 29.4 Graph showing the stress distribution in soil mass to permanent loads

29.4 Conclusions

In developing this paper we have integrated different stages of the control system such as: sensor, signal conditioning and monitoring noteworthy that the installation and connection of sensors and monitoring of signals depending on the selection of the industrial machinery to study which depends on external factors such as the availability of use for testing.

Acknowledgements We want to thank Eng. Ernesto Sandoval and Omar Sandoval for the facilities for testing of machinery manufactured in their companies. We especially want to thank the University of La Salle by supporting this project.

References

1. F.J. Martínez Serrano, A.A. Camacho Pérez, Optomechatronic load cell validation according the american standards, in *Proceedings of SPIE*, vol. 7499 (2009), p. 74990Q-1
2. W. Bolton, Mecatrónica, *Sistemas de Control Electrónico en Ingeniería Mecánica y Eléctrica*, 2da. ed, Alfaomega, 5ta. Reimpresión (2010)
3. www.Datasheet PHOTOTRANSISTOR
4. www.Datasheet 18F4550 8-Bit CMOS FLASH Microcontrollers PIC MCU FLASH 16KX16 Microship. 8 BITS to 48 MHz
5. [www.Datasheet](http://www.datasheet.com) MSP430 TEXAS INSTRUMENTS
6. A. Daneels, W. Salter, in *What is SCADA? International Conference on Accelerator and Large Experimental Physics Control Systems* (CERN, Trieste, Italy, 1999), p. 5
7. R.P. Areny, *Sensores y Acondicionadores de señal* (Marcombo, S.A., Barcelona, 2004)
8. K. Dembowski, *Gran Libro de Hardware*, 2nd ed. (Marcombo, S.A., Barcelona, 2003)
9. HEAPG (s.f.), Store HEAPG. Recovered 21 June 2012, de <http://store.heapg.com>
10. InfoPLC (s.f.), 3 razones por las cuales los software scada tradicionales irán en declive
11. <http://www.infopl.net/documentacion/10-hmi-scada/996-3-razones-por-las-cuales-los-software-scada-tradicionales-iran-en-declive-InfoPLC>. (s.f.), Sobre Nosotros. Recovered 23 July 2012, de InfoPLC
12. <http://www.infopl.net/sobre-nosotros> Lantronix (s.f.), Store Lantronix. Recovered 21 June 2012, de <http://store.lantronix.com>
13. Microsoft (s.f.), Clases Win32. Recovered 21 June 2012, de MSDN: [http://msdn.microsoft.com/en-us/library/windows/desktop/aa394084\(v=vs.85\).aspx](http://msdn.microsoft.com/en-us/library/windows/desktop/aa394084(v=vs.85).aspx)
14. Texas Instruments, *FindAppUART.cpp*. (EEUU, Dallas, TX, 2012)
15. Texas Instruments, *MSP430x'xx Family User's Guide* (EEUU, Dallas, TX, 2012)
16. Texas Instruments, *MSP4302x53, MSP430G2x13 Mixed Signal Microcontroller* (EEUU, Dallas, TX, 2011)
17. UM Control y Adquisición (s.f.), UMControl y Adquisición—Revision 248. Recovered 8 October 2012
18. <http://subversion.assembla.com/svn/UMControl y Adquisición/Desarrollo/documentos/Celda%20de%20carga%20-%20Principio.pdf>

Chapter 30

ASE Noise Attenuation for Signal at 1548.4 nm Through a Sagnac Interferometer Using High-Birefringence Fiber Which Is Subjected to Temperature Changes

Manuel May-Alarcón, Héctor H. Cerecedo-Núñez, Aarón Flores-Gil, Miguel A. García-González, Francisco Méndez-Martínez, Marco A. Rodríguez-Blanco, and Víctor Golikov

Abstract This paper reports the construction of an experimental setup to attenuate the ASE (Amplified Spontaneous Emission) noise around 1548.4 nm. A Sagnac Interferometer (SI) which uses high-birefringence fiber (Hi-Bi fiber) at 8, 22 and 110 cm is used as band pass filter for attenuating the ASE noise. Temperature variations are made to tune in the filter SI. A test signal containing noise ASE is taken from an erbium-doped optical fiber and a fiber Bragg grating (FBG), therefore the 1548.4 nm signal surrounded for ASE is obtained. This test signal is introduced into the SI filter and the transmitted power of the interferometer is measured, the transmitted signal of SI has periodic variations with maximums and minimums, the SI is tuned in with temperature to bring the maximum transmitted power at the same wavelength of the signal 1548.4 nm. We found experimentally that is possible to attenuate the ASE noise contribution around 1548.4 nm by comparing the input test signal versus the output signal at the output port of SI. In addition, we found the displacement of the transmittance with respect to temperature ($\Delta\lambda/\Delta T$) and the period of the transmitted power ($\Delta\lambda$).

Keywords Fiber Bragg Grating • Sagnac Interferometer • High-Birefringence Fiber • Amplified Spontaneous Emission • Erbium Doped Fiber

30.1 Introduction

All-fiber systems have many applications, specifically, a Sagnac all-fiber interferometer can be used as a band pass filter [1, 2]. This type of filters have several advantages, low insertion losses, small size, high performance and these not need periodic readjustments, such as other optical bulk filters. ASE noise was produced by spontaneous emission, which has been amplified by stimulated emission in a gain medium [3]. There are a lot of reported information about ASE noise elimination techniques [4], however, in this paper, we present the attenuation of ASE noise, by filtering a signal of interest at 1548.4 nm, which is generated by an Erbium Doped Fiber Amplifier (EDFA) and a Fiber Bragg Grating (FBG) at the same wavelength, 1548.4 nm [5].

About ASE noise attenuation in fiber, there are some examples, such as the uses of tuning filter, Bragg grating and long period gratings, which flat the gain in an EDFA [6, 7]. In the case of the use of LPG, usually they have only one attenuation pick around 1550 nm, and cannot reduce significantly the noise. Here it is necessary a special spectral profile with many LPG picks. However, one disadvantage of that is that LPG's are sensitive and unstable.

In other hand, also there are some techniques to build all fiber Sagnac filters. Here, this device provides a periodic transmitting with wavelength, birefringence and fiber length dependence. Changing the fiber length [8], it is possible to use as a band pass filter and, such as their temperature sensitivity [9], it is possible to think in a tuning band pass filter. In this work, we present experimental results about the implementation of a tuning Sagnac Interferometer Sagnac interferometer (SI) with the final purpose of reduce the ASE noise of the signal probe, produced by an EDFA.

M. May-Alarcón (✉) • A. Flores-Gil • M.A. García-González • F. Méndez-Martínez • M.A. Rodríguez-Blanco • V. Golikov
Department of Electronic Engineering, Universidad Autónoma del Carmen, Carmen, Campeche 24153, Mexico
e-mail: mmay@pampano.unacar.mx; aflores@pampano.unacar.mx; mike_9007@hotmail.com; fmendez@pampano.unacar.mx;
mrodriguez@hotmail.com; vgolikov@pampano.unacar.mx

H.H. Cerecedo-Núñez
Faculty of Physics, Universidad Veracruzana, Xalapa, Veracruz 91090, Mexico
e-mail: hcerecedo@uv.mx

30.2 Experimental Setup

In order to reduce the ASE noise of the signal probe at 1548.4 nm, our experimental setup is formed by three parts: (1) one EDFA, (2) an all fiber interface to monitor the reflected power, and (3) a Sagnac Interferometer (SI) as a filter, see Fig. 30.1. The EDFA, part 1 of the system, is pumped with a diode laser at 980 nm (Qphotonics QFBGLD980-250), a WDM (WD202A), 1.6 m of Erbium doped fiber (Er30-4/125) and a FBG (Broptics 1550 nm); all this together produce the ASE noise signal from 1500 to 1600 nm. The all-fiber interface, part 2, is inserted between the EDFA and the SI, it is built with a 90/10 fiber coupler (10202A-90), and we used one arm of this coupler to monitor the reflected output, see Fig. 30.1. The SI, the parte 3, has the function of a selective filter, which is tuned in by temperature. It is built with a coupler 50/50 (10202A-50) and a Hi-Bi fiber (HB1550Z) into the loop. The relative phase difference between the counter propagating beams determines whether an input beam is reflected or transmitted by the SI. We tested different lengths of Hi-Bi fibers (8, 22 and 110 cm). To tune the signal here, we apply thermal changes in the Hi-Bi fiber. To monitor the output signals we used an optical spectrum analyzer (YOKOGAWA, AQ7360C, with 0.02 nm of resolution), this output signal is the transmitted power of the system.

30.3 Methodology

Initially, we generate a test signal with ASE noise in our system by pumping the EDFA with a semiconductor laser working at 980 nm and pump power of 58 mW. This test signal propagates in all the system, interface, and the SI, see Fig. 30.1. When this signal comes into the SI through port 1, it pass through the Hi-Bi fiber in clockwise and counterclockwise, and then, is reflected in port 1 or transmitted in the port 2. In this moment, to tune a maximum or minimum of intensity, we introduce

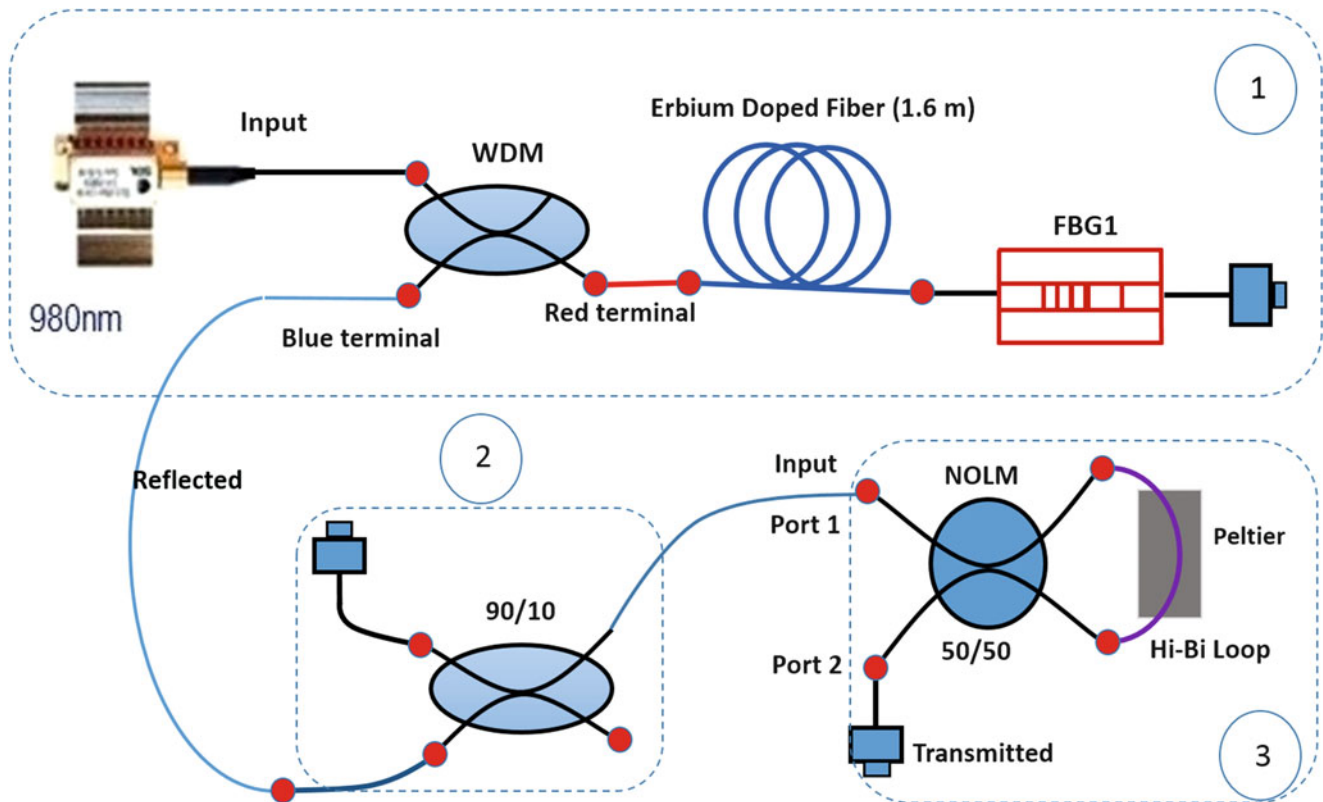


Fig. 30.1 Experimental setup to ASE noise attenuation of a test signal, (1) EDFA, (2) the interface and (3) the Sagnac Interferometer

temperature changes to the Hi-Bi loop, we done it with a Peltier cell (TEC1-12706-12 V), from room temperature to 50 °C. After, the optical signal continues in reflection to the interface and EDFA stages. The final signal, the transmitted signal therefore is monitored in the port 2 in stage 3.

The main mathematical relations are as follow, the transmitted signal periods ($\Delta\lambda$) were $\lambda_1 > \lambda_2$, is:

$$\Delta\lambda = \lambda_{1T1} - \lambda_{2T2} \quad (30.1)$$

and the transmitted signal period with respect to temperature changes is:

$$\frac{\Delta\lambda}{\Delta T} = \frac{\lambda_{1T1} - \lambda_{2T2}}{T1 - T2} \quad (30.2)$$

where λ_{1T1} is the wavelength at the minimum of the transmitted power, at room temperature ($T_A=T1$), and λ_{2T2} is the wavelength at the minimum of the transmitted power, but at raised temperature ($T2$), by the Peltier cell.

30.4 Results and Analysis

We get out several results testing fiber lengths of 8 cm, 22 cm and 110 cm of birefringence fiber. Figures 30.2, 30.3, 30.4 show the spectral difference in the test signal, the transmitted and reflected spectrum when we used 8 cm Hi-Bi fiber, at room temperature, 34 °C and 48 °C, respectively.

The first results are about the spectrum shapes. The input ASE noise test signal is not modulated in comparison with the transmitted and reflected signals. Modulation is due to the presence of the SI. Our next results are that the three signals have the same wavelength of operation at 1548.4 nm, which is the expected behavior because the SI is a pass band filter. Then, considering temperature changes, in Fig. 30.2, at room temperature, all spectrums are arbitrary. The transmitted and reflected spectrums are lower than the test signal. Now, following the maximum wavelength signal, and heating the Hi-Bi fiber in the loop (Fig. 30.3) at 34 °C, we observed changes in the reflected and transmitted maximum signal wavelength at 1548.4nm; transmitted signal is tuned closer at a maximum of modulation, and reflected signal is closer to a minimum. Increasing the temperature until 48 °C we obtain the opposite as shown in Fig. 30.4.

Fig. 30.2 This figure shows the test, reflected and transmitted signals. The Hi-Bi fiber length is 8 cm and the temperature is 28.5 °C

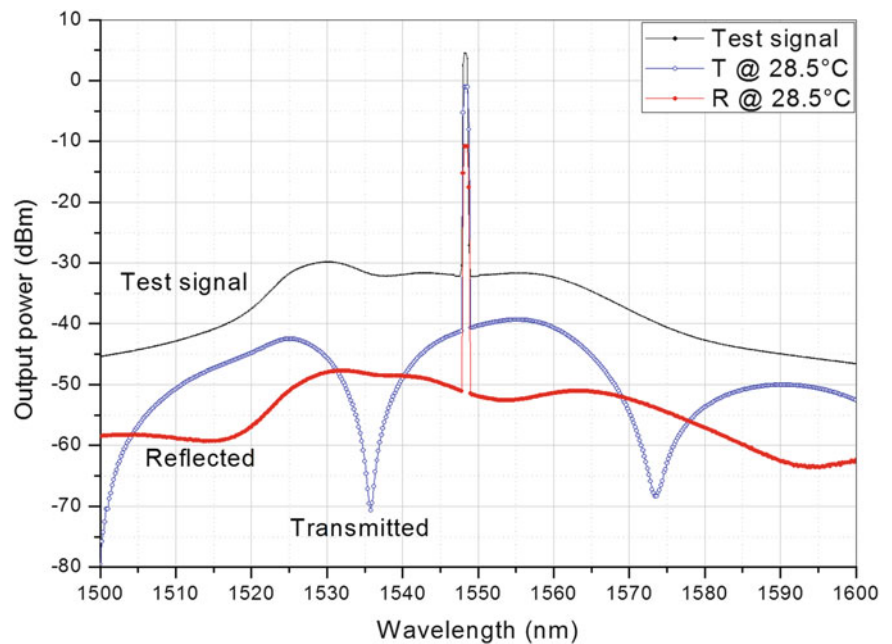


Fig. 30.3 This figure shows the transmitted and the reflected signals when the SI has the maximum transmitted power and the minimum reflected power at 1548.4 nm. The Hi-Bi fiber length is 8 cm and the temperature is 34 °C

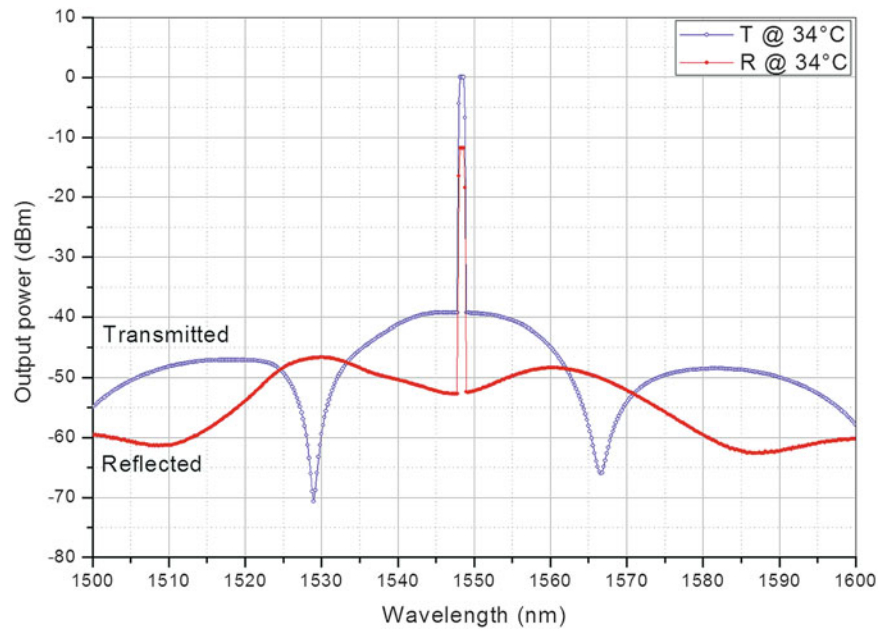
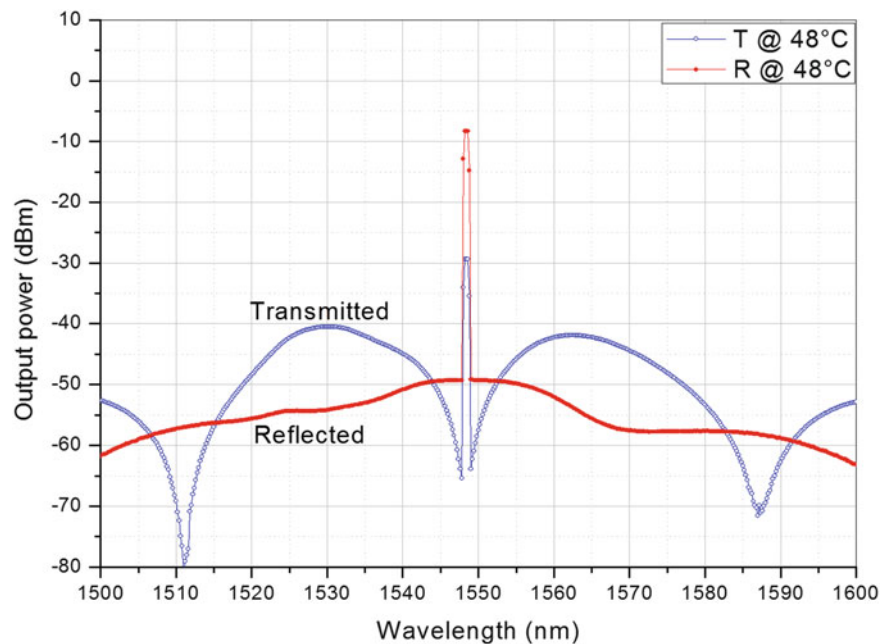


Fig. 30.4 This figure shows the transmitted and the reflected power when the SI has the maximum reflected power and the minimum transmitted power at 1548.4 nm. The system is the opposite than the Fig. 30.3. The Hi-Bi fiber length is 8 cm and the temperature is 48 °C



Results of the second experiment are shown in Figs. 30.5 and 30.6, here, the Hi-Bi fiber loop was 22 cm, at room temperature and at 37.5 °C, respectively. Observations were similar to the previous described, however periods of transmitted and reflected signals are increased. Here the average separation between minimums of transmission is $\Delta\lambda = 27.6$ nm and these minimums are centered 1500.6 nm, 1527.2 nm, 1554.6 nm and 1583.2 nm respectively. An additional result is that minimums of transmission shifts to shorter wavelengths at $\Delta\lambda_1/\Delta T = -1.3$ nm/°C, just with this Hi-Bi fiber length. The last result here is that the test signal wavelength is the same in all cases while its output power changes with the transmitted power changes.

Results for the third experiment are shown in Fig. 30.7, here the Hi-Bi fiber was 110 cm length. We observed clearly in Fig. 30.7 the increase in signals modulation. We can observe that when we have a maximum of transmitted power then we have a minimum of reflected power.

Fig. 30.5 This figure shows the test, reflected and transmitted signals. The Hi-Bi fiber length is 22 cm and the temperature is 28.5 °C

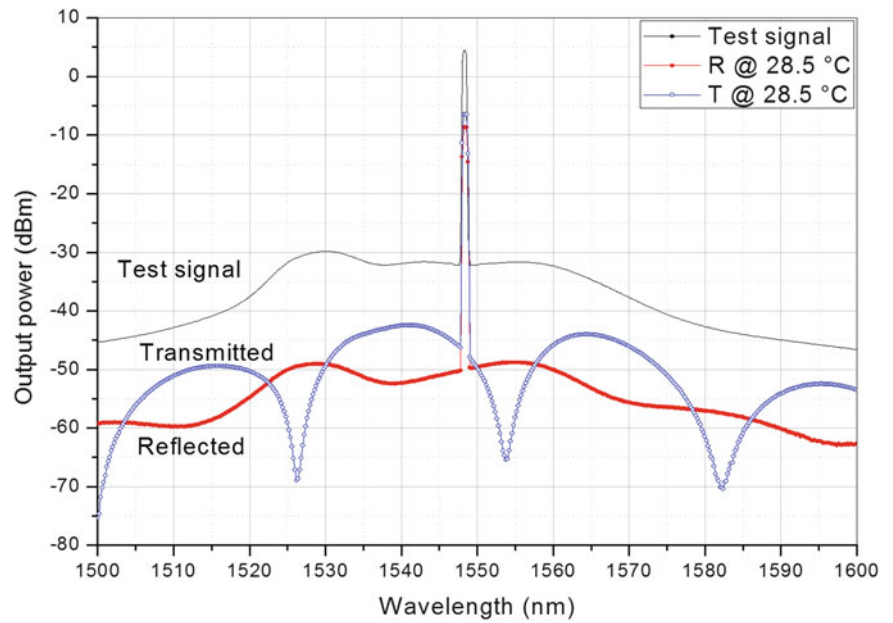
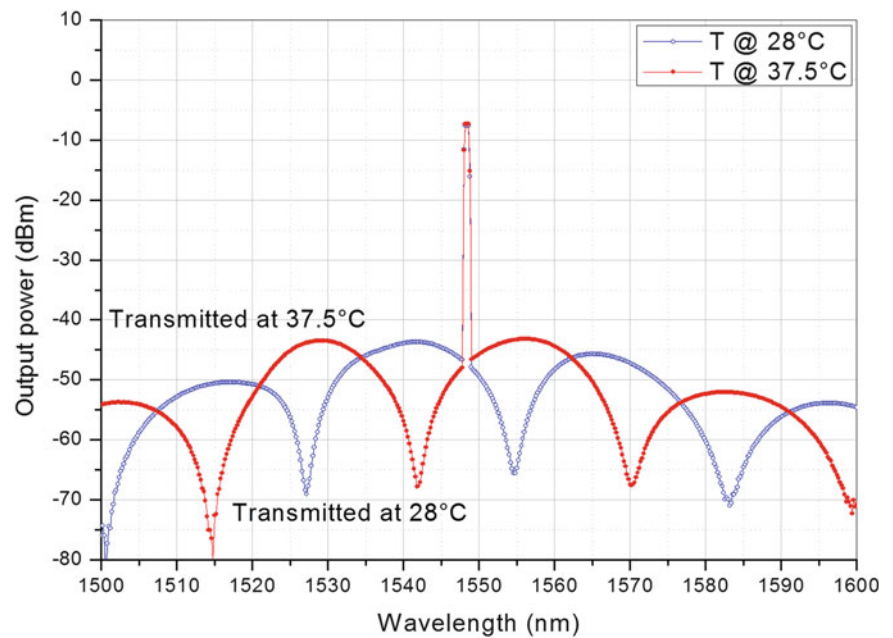


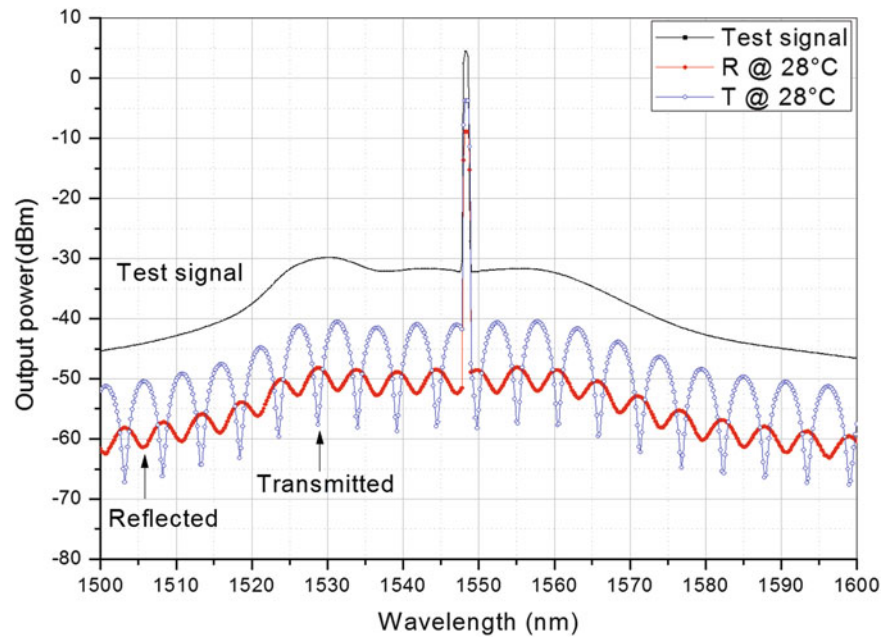
Fig. 30.6 This figure shows the transmitted power for two temperatures (28.5 °C and 37.5 °C) and the same Hi-Bi fiber length of 22 cm



30.5 Conclusions

We research an experimental implementation of a Hi-Bi SI filter, tuned thermally. We considered different loop lengths. We prove it in an ASE signal from an EDFA. According to our results, we found that it is possible to reduce the ASE noise with our proposal. We also obtained the average separation between minimums of transmission of the three lengths loops 8 cm, 22 cm and 110 cm, $\Delta\lambda = 27.6$ nm, 36.8 nm and 5.0 nm, respectively. Finally we report the change of that minimums of transmission with respect to temperature to be $\Delta\lambda_1/\Delta T = -1.3$ nm/°C, -1.4 nm/°C and -1.35 nm/°C, respectively too.

Fig. 30.7 This figure shows the test, reflected and transmitted signals. The Hi-Bi fiber length is 110 cm and the temperature is 28 °C



References

1. D. Monzón, A.N. Starodumov, L.A. Zenteno, A. Boyain, E. de la Rosa, Interferómetro de Sagnac con selectividad espectral. *Rev. Mex. Fís.* **43** (6), 972–980 (1997)
2. A. González-García, O. Pottiez, R. Grajales-Coutiño, Estudio experimental de un láser sintonizable en longitud de onda usando un filtro de Sagnac con selectividad espectral mediante cambios de temperatura. *Rev. Mex. Fís.* **56**(4), 275–280 (2010)
3. D. Kouznetsov, J.F. Bisson, K. Takaichi, K. Ueda, Single-mode solid-state laser with short wide unstable cavity. *J. Opt. Soc. Am. B* **22**, 1605–1619 (2005)
4. A. Flores-Rosas, E.A. Kuzin, B. Ibarra-Escamilla, M. Bello-Jiménez, Eliminación de ruido de ASE en una fibra dopada con erbio empleando un filtro basado en el interferómetro de Sagnac con fibra de Hi-Bi en el lazo. *Rev. Mex. Fís.* **54**(2), 130–134 (2008)
5. M. May Alarcón, M.A. García González, W.A. Silva, L. de la Cruz, D. Tentori, M.A. Rodríguez Blanco, J.G. Pacheco, A. Flores Gil, Caracterización de los parámetros de rejillas de Bragg de fibra óptica usando el espectro de emisión espontánea en la región de 1550 nm de una fibra dopada con erbio bombeada con 980 nm. XIII Congreso Nacional de Ingeniería Eléctrica y Electrónica del Mayab, Abril 2013, ISSN: 1665-0271, pp. 1042–1051
6. B.O. Guan, A.P. Zhang, H.Y. Tam, L.W. Chan, C.L. Choy, X.M. Tao, Step-changed long-period fiber grating. *IEEE Photon. Technol. Lett.* **14** (5), 657–659 (2002)
7. J.R. Qian, H.F. Chen, Gaim flattening fiber filters using phase-shifted long period fiber gratings. *Electron. Lett.* **34**, 1132–1133 (1998)
8. X. Fang, H. Ji, C.T. Allen, K. Demarest, L. Pelz, A compound high-order polarization-independent birefringence filter using Sagnac interferometers. *IEEE Photon. Technol. Lett.* **9**(4), 458–460 (1997)
9. A.N. Starodumov, L.A. Zenteno, D. Monzon, A.R. Boyain, All-fiber polarization-independent narrow band wavelength-division multiplexer. *Elsevier* **138**, 31–34 (1997)

Chapter 31

Single-Shot Phase Shifting Interferometry for Microscopic Measurements of Non-Birefringent Transmissive Phase Samples

V.H. Flores Muñoz, B. López Ortiz, N.I. Toto-Arellano, Amalia Martínez-García, and G. Rodríguez-Zurita

Abstract Its well known that there is a variety of techniques to obtain n-phase shifts in one shot, and most of them use diffractive elements, holographic ones or pixelated phase masks attached to a CCD camera, among others, to generate from 4 to 9 interferograms simultaneously; nevertheless, some of the components utilized in this arrangements are still expensive, and in order to reduce the cost of operations, we developed an alternative system that does not use diffractive elements, in this research we present a simultaneous phase-shifting interferometer based on polarizing coupled interferometers, this device can be measured the optical phase of non-birefringent microscopic phase samples, generating four interferograms in single capture of the ccd camera with relative phase shifts of $\pi/2$. In order to present the capabilities of the system, the results obtained for the phase measurement of Red Blood Cells (RBC) and non-birefringent transparent samples are presented.

Keywords Phase shifting • Interferometry • Polarization • Phase object • Shearography

31.1 Introduction

It is known that in lateral shearing interferometry, two mutually displaced versions of the same wavefront are able to interfere. The resulting interference pattern consists of fringes of equal wavefront slope with respect to the shear (shearograms), this permits to obtain the directional derivative of the wavefront directly, which can be lateral or radial by applying the convenient. The technique presents the advantage of being free of non-linear shifting as the ones found in a piezoelectric; another advantage is that the system is immune to vibrations because the reference wavefront and the object wavefront are in common path. Also, the shearing interferometer is insensitive to temperature and air vibrations, due to the fact that the diffractive elements are not used in the optical system. Errors caused by difference in amplitude or modulation and errors generated by the diffraction orders upon the interference patterns are not present in our arrangement as they are in other systems [1–7]. In the following sections we show the patterns generated by the system which have relative phase shifts of $\pi/2$, in this way, we only use two interferograms avoiding the use of phase shifts. In order to process the optical phase we utilized the Vargas-Quiroga method which uses a Regularized Optical Flow (ROF) algorithm Regularized Optical Flow (ROF) algorithm [8] which will allow us to analyze static and dynamic phase objects. As mentioned before, the principal advantages of this system, compared with others previously published [2–4, 7], are that the system doesn't need a temporal phase shift to obtain the phase and it eliminates the use of diffractive and polarizing elements at the output of the interferometer.

V.H. Flores Muñoz (✉)

Departamento de Ingeniería Robótica, Universidad Politécnica del Bicentenario, C.P. 36283 Silao, Guanajuato, Mexico
e-mail: vfloresm@upbicentenario.edu.mx

B. López Ortiz • N.I. Toto-Arellano

Universidad Tecnológica de Tulancingo, C.P. 43642 Tulancingo, Hidalgo, Mexico
e-mail: beleloort@gmail.com; noel.toto@utec-tgo.edu.mx

A. Martínez-García

Centro de Investigaciones en Óptica A.C., C.P. 37150 León, Guanajuato, Mexico

G. Rodríguez-Zurita

Benemerita Universidad Autónoma de Puebla, C.P. 72000 Puebla, Puebla, Mexico

31.2 Phase Processing Algorithm

The optical phase is calculated by the Vargas-Quiroga method described in [8], which requires a constant phase shift between the interferograms that can vary between the values of 0 and 2π ; the algorithm does not require the value of the shift due to the configuration of the proposed system.

The interference patterns generated for the optical device a relative $\pi/2$ phase shift between them are represented as:

$$\begin{aligned} I_1(x, y) &= A_0 + A_1 \cos [\phi(x, y)] \\ I_2(x, y) &= A_0 - A_1 \sin [\phi(x, y)] \end{aligned} \quad (31.1)$$

where A_0 represents background illumination, A_1 is the contrast term, and $\phi(x, y)$ is the term of the optical phase. We used an algorithm that allows us to obtain the wrapped phase using both interferograms: first, it obtains the direction of the fringes using a regularized optical flow method to obtain the sign of the phase; then, it applies a spiral phase transform to calculate the optical phase. Our system, along with this method, allows us to perform the analysis of static and dynamic samples. The 2π ambiguity can be retrieved by means of a phase unwrapping process, so the optical unwrapped phase can be obtained. In order to remove the background phase, the phase retrieval procedure should include a reference phase measured beforehand [9, 10], which is calculated without the target object.

31.3 Experimental Setup

We know that a polarizing phase shifting Cyclic Shear Interferometer (CSI) can generate a shearogram with circular polarization of opposite rotations after passing a quarter wave retarder Q ; if we use this shearogram as an input in a non-polarizing beam splitter, this component will only create a replica of the interference pattern, in this way, one interferogram is transmitted and the other one is reflected; as a result, we obtain two interference patterns. The experimental setup for microscopic samples using parallel interferograms is shown in Fig. 31.1, it can be seen that the experimental set-up consists of a CSI and a polarizing beam splitter. At the entrance of the CSI the H-P system generates a 45° polarized beam. At the output of the CSI, a quarter-wave plate Q converts one of the two interfering beams into a right-handed circularly polarized beam and the second one into a left-handed circularly polarized beam [4].

Considering the $NPBS$ and the polarizer-array (covering each one of interferograms) as a polarizing device, where the polarizing array consists of two polarizers with their crossed polarizations at a $\pi/4$ angle to each other (P_0 and P_{45}). If the shearogram has the described polarization properties when it enters the non-polarized beam splitter $NPBS$ and according to the polarization phase shifting principles [1–4], the two parallel interferograms resulting have a relative phase shift of $\pi/2$. As a result, we are able to obtain the necessary two $\pi/2$ -phase shifted interferograms in only one stage. Figure 31.2 shows representative results obtained with the proposed system. In Fig. 31.2a the reference patterns generated by the reference's wavefront. Figure 31.2b shows the same wave front with a Red Blood Cells. The experimental results for all cases shown the phase changes.

31.4 Experimental Results

The parallel interferograms were acquired by a 3.0 Megapixel CMOS sensor (color camera) with 2048×1536 pixels (pixel size, $3.2 \times 3.2 \mu\text{m}$). The laser beam is expanded to a diameter of 10 mm, the microscope objective used has a magnification $M = 40\times$ and numerical aperture $NA = 0.6$. The CCD camera is adjusted to capture the images of two interference patterns simultaneously; each pattern was filtered using a conventional low-pass filter to remove sharp edges and details. One of the advantages of the system is that diffractive elements are not included to generate the two patterns. Consequently, it is not necessary to make corrections in fringe modulation.

Figure 31.3 show the experimental results obtained static inorganic samples. Figure 31.3a presents the experimental result for an acetate sheet with an average thickness of about 0.1 mm, which has obstructed half of the wavefront, as it can be seen in the patterns, an arbitrary deformation in the z direction was originated and the change in the fringes can be noticed by the border of the acetate. Figure 31.3b shows the experimental results obtained collocating 3 microparticles (with a mean

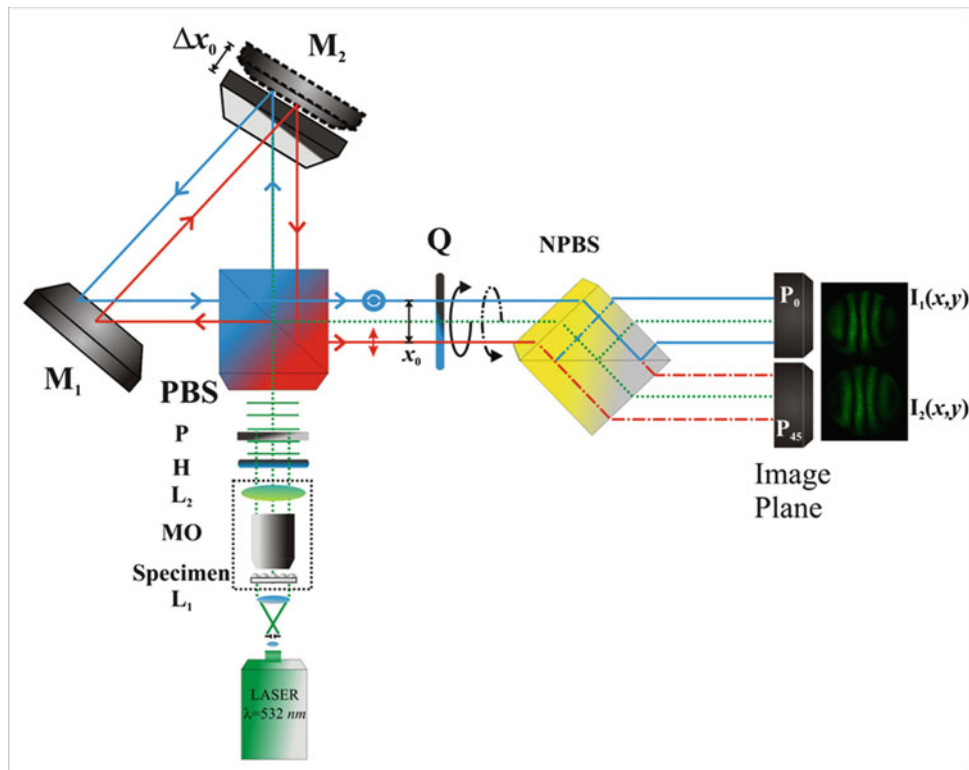


Fig. 31.1 Experimental set-up. L_i : lenses. MO: Microscope objective. H: Half Wave Plate. P: polarizer filters. Mi: Mirrors. Δx_0 : Adjustment of mirrors. x_0 : beam separation. x_1 : shearograms separation. Q: Quarter Wave Plate. $I_i(x,y)$: Interference patterns

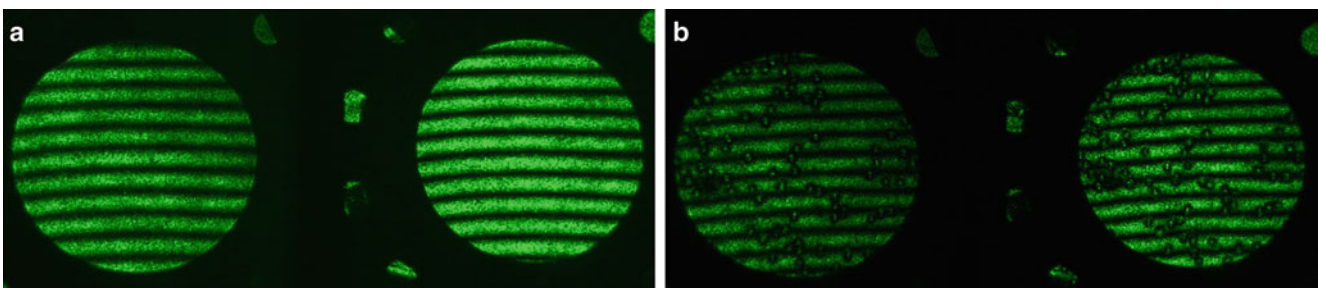


Fig. 31.2 Preliminary results: (a) Reference spherical wavefront (b) Red Blood Cells

diameter of 0.5 mm) on a microscope slide, the deformation of the surface can be clearly seen in shearograms. For every sample we present the two patterns obtained in one shot and the slope associated to the derivative of the phase.

Figure 31.4 shows the results obtained from a sample of Red Blood Cells (RBC) collocated on a microscope slide; in this case we utilized a CSI operating in the non-shearing mode. In the presented results the sample phase is represented in terms of the optical path difference (OPD) in units of the wavelength of the utilized light source. Figure 31.4a presents the phase reconstruction of the group of RBC, Fig. 31.4b shows the OPD for a two transversal sections of RBC. By observing one blood cell, it can be noticed that the OPD and it allows us to calculate the mean thickness as $OPD/\Delta n = 2.28 \mu\text{m}$ [11–13].

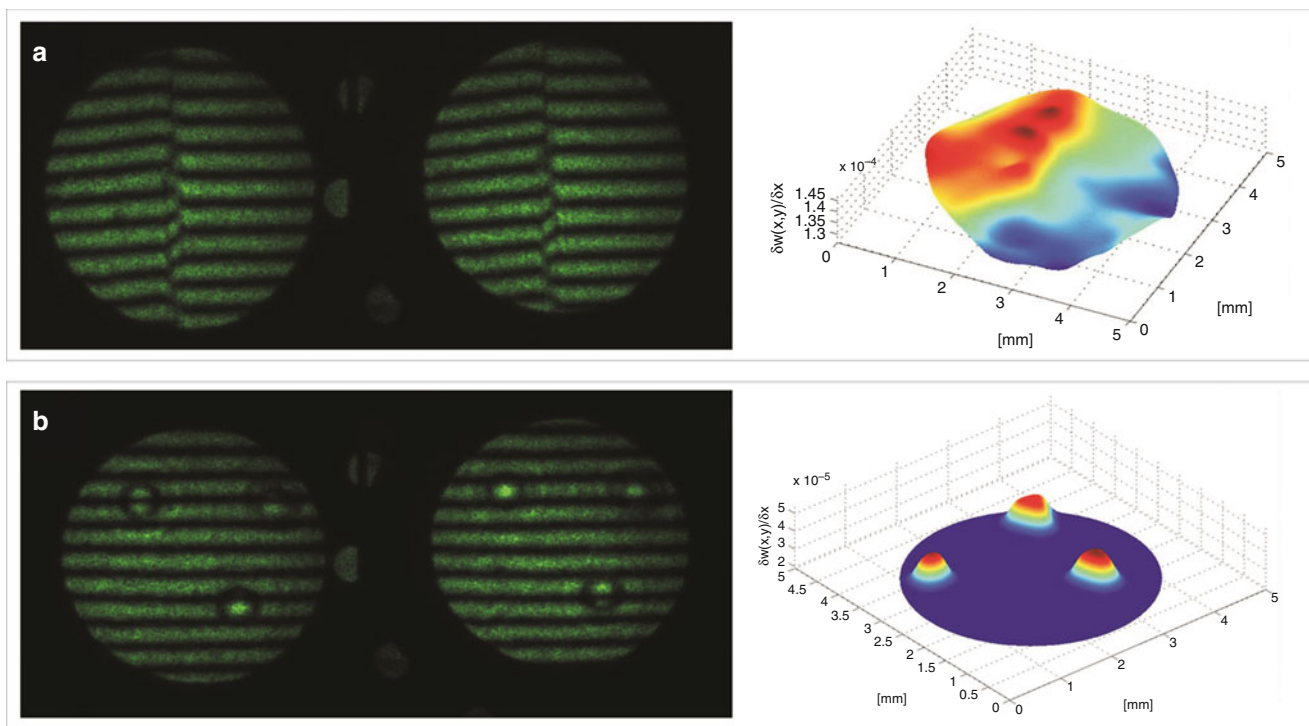


Fig. 31.3 Inorganic Samples. Experimental results of: (a) Edge of an acetate sheet, (b) Transparent microparticles

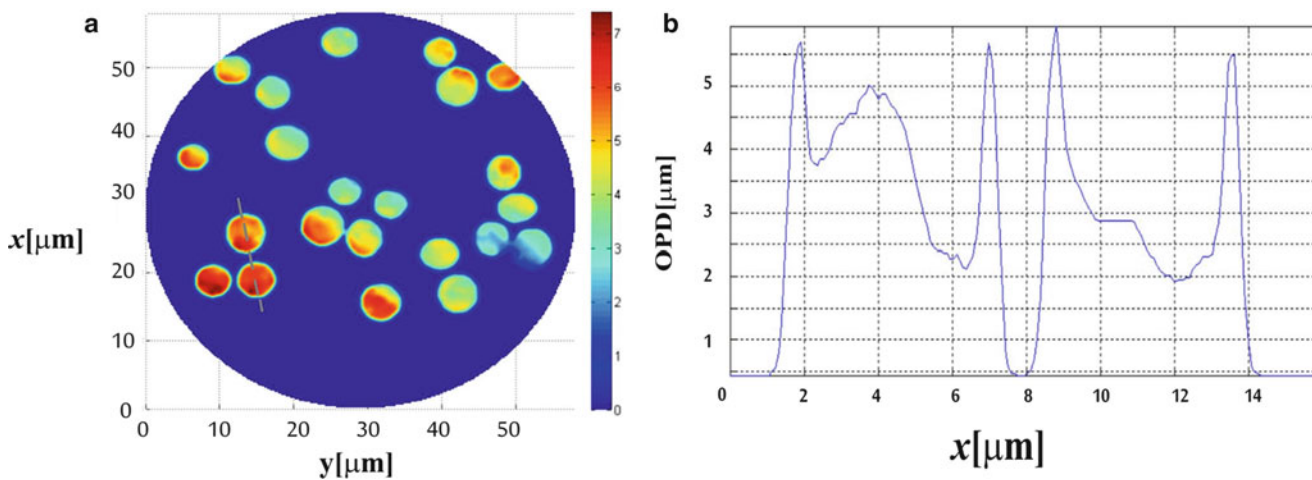


Fig. 31.4 Phase changes introduced by RBC smeared on a microscope slide. (a) OPD. (b) Transversal section of two RBC

31.5 Final Remarks

In this research, we proposed a configuration for the analysis of biomedical samples (RBC) based on a parallel shearing interferometry system. The system is considerably simpler than other proposals, due to the use of few optical elements, showing a suitable alternative to implement in an environment outside laboratory. In the present case, as phase shifting is achieved through polarization means, the proposed method is not suitable for birefringent transparent samples. For further applications, this system can be developed to perform parallel four-step phase shifting interferometry or real time applications.

Acknowledgments This research was supported by the Technological University of Tulancingo, according to *The Initiative* for the creation of the *First Optics and Photonics Engineering* undergraduate program in Mexico. Author V. H. Flores Muñoz is grateful to CONACYT for the scholarship provided (Grant. 224506) and Programa para el Desarrollo Profesional Docente (PRODEP) for grant UPBIC-PTC-022. Author N.-I. Toto-Arellano expresses sincere appreciation to Luisa, Miguel and Damian for the support provided. Authors thank M. A. Ruiz for his contribution in proofreading the manuscript.

References

1. M.N. Morris, J. Millerd, N. Brock, J. Hayes, B. Saif, Dynamic phase-shifting electronic speckle pattern interferometer, in *Proceedings of SPIE*, vol. 5869, (2005), p. 58691B-1
2. J.E. Millerd, J.C. Wyant, Simultaneous phase-shifting Fizeau interferometer, U.S. Patent 7,057,738 B2 (2006)
3. B. Lopez-Ortiz, N.-I. Toto-Arellano, V. H. Flores Muñoz, A. Matínez García, L. García Lechuga J.-A. Martínez Dominguez, Phase profile analysis of transparent objects through the use of a two windows interferometer based on a one beam splitter configuration, *Optik*, 125, 7227–7230 (2014)
4. J.E. Millerd, N. Brock, J. Hayes, M. North-Morris, M. Novak, J. Wyant, Pixelated phase-mask dynamic interferometer. *Proc. SPIE* **5531**, 304–314 (2004)
5. B. Barrientos-García, A.J. Moore, C. Pérez-López, L. Wang, T. Tschudi, Transient deformation measurement with electronic speckle pattern interferometry by use of a holographic optical element for spatial phase stepping. *Appl. Opt.* **38**(28), 5944–5947 (1999)
6. B. Barrientos-García, A.J. Moore, C. Pérez-López, L. Wang, T. Tschudi, Spatial phase-stepped interferometry using a holographic optical element. *Opt. Eng.* **38**(12), 2069–2074 (1999)
7. J.C. Wyant, Dynamic interferometry. *Opt. Photon. News* **14**(4), 36–41 (2003)
8. J. Vargas, J. Quiroga, C.O.S. Sorzano, J.C. Estrada, J.M. Carazo, Two-step interferometry by a regularized optical flow algorithm. *Opt. Lett.* **36**(17), 3485–3487 (2011)
9. N.I. Toto-Arellano, G. Rodriguez-Zurita, C. Meneses-Fabian, J.F. Vázquez-Castillo, A single-shot phase-shifting radial-shearing interferometer. *J. Opt. A: Pure Appl. Opt.* **11**(4), 045704 (2009)
10. P. Gao, B. Yao, J. Min, R. Guo, J. Zheng, T. Ye, I. Harder, V. Nercissian, K. Mantel, Parallel two-step phase-shifting point-diffraction interferometry for microscopy based on a pair of cube beamsplitters. *Opt. Express* **19**(3), 1930–1935 (2011)
11. I. Shock, A. Barbul, P. Girshovitz, U. Nevo, R. Korenstein, N.T. Shakeda, Optical phase nanoscopy in red blood cells using low-coherence spectroscopy. *J. Biomed. Opt.* **17**(10), 101509 (2012)
12. H. Pham, H. Ding, N. Sobh, M. Do, S. Patel, G. Popescu, Off-axis quantitative phase imaging processing using CUDA: toward real-time applications. *Biomed. Opt. Express* **2**(7), 1781–1793 (2011)
13. V. Mico, Z. Zalevsky, J. García, Common-path phase-shifting digital holographic microscopy: a way to quantitative phase imaging and superresolution. *Opt. Commun.* **281**(17), 4273–4281 (2008)

Chapter 32

Design of a Customized Myoelectric Hand Prosthesis

A.A. Silva-Moreno and E. Lucas Torres

Abstract Hand amputation is typically the result of a traumatic injury and/or disease related complications. The loss of a hand has a profound physical and psychological impact on the amputee. A high quality prosthesis can be facilitative in restoring an amputee's body image. Traditional methods of manufacturing prostheses are time consuming and often lack the anatomical features to ensure the comfort of the user. The emergence of modern print manufacturing techniques can ensure a higher quality product with increased anatomical accuracy. In this study, we designed a print manufacturing process for myoelectric hand prosthetic. The process commenced with the use of a 3D scanner to obtain an anatomically accurate image of the non-amputated hand, of which a mirror image of the amputated hand was then generated. The resulting data was then transferred to a 3D printer. Individual fingers of the hand were print manufactured from a pliable material as separate components for the purpose of emphasizing the movement of the phalanges. By applying the above print manufacturing method we are confident that the customized prosthesis would contain the majority of the bodily features of the non-amputated hand. In turn, this method could also be applied for the construction of prostheses for other body limbs.

Keywords Prosthetic hand • Upper-limb amputation • 3D printer • 3D scanner • Electromyography

32.1 Introduction

The causes of hand amputation are typically the result of disease related complications or traumatic injury. Traditional prosthetic manufacturing methods are time consuming and labor intensive, often resulting in an inferior product. The emergence of modern computer based 3D scanners, design software and laser printers allow prosthesis manufactures to construct a higher quality artificial limb which is anatomically coordinated to the amputee. There have been prior studies conduct on the design of a prosthetic hand based on a biomechanical modeling of a natural hand [1].

Human muscles generate an electrical signal which is measured in microvolts, in the form of electromyography (EMG). EMG signals can then be collected through electrodes to analyze: local activity level, neuromuscular disease, motor-control disorders, as well as, a method for developing control signals for prosthetic devices. Surface electrodes recordings are limited to superficial muscles and are influenced by the subcutaneous depth of the tissue and the unique tissue traits of the patient. The advantage of surface electrodes is that they are non-invasive, so placing them is simple and painless. In our study, we implemented a modern 3D foot scanner and a 3D printer for the manufacturing of a myoelectric hand prosthesis. The prosthesis was controlled with the aid of surface electromyography (EMG) signals.

A.A. Silva-Moreno (✉)
Department of Biomechanics, CIATEC, A.C., Omega 201, Industrial Delta, Leon, Guanajuato, Mexico
e-mail: asilva@ciatec.mx

E.L. Torres
Mechatronics Engineering, Ibero-American University, Leon, Guanajuato, Mexico
e-mail: kicologo@gmail.com

32.2 Methodology

The following methodology was applied: first, a digital 3D image of the non-amputated hand was taken as shown in Fig. 32.1. In this case, the scanner implemented was a 3D foot scanner (model IFU-H-I-01, Laboratory-ware Co. Ltd.). The resulting dimensional data was then computed using Meshmixer (open-source) software to remove any irregularities generated by the scanning process.

The mirror image prosthetic is constructed to have similar characteristics as the non-amputated hand. Natural mobility is further facilitated by the inclusion of additional apertures for the artificial flexible joints and tendons of the fingers as shown in Fig. 32.2, which was printed manufactured from non-pliable materials, and later joined to the flexible materials as part of the assembly process. The joints of the individual fingers were designed using an open-source software called Flexy-Hand, which is available for download without cost and then can be subsequently printed using PLAFlexible material as shown in Fig. 32.3. To act as a tendon for facilitating flexion at metacarpophalangeal, proximal interphalangeal, and distal interphalangeal joints, a cable was attached to the distal phalanx [2].

Then the model file is exported and prepared for 3D printing with the assistance of Microsoft Model Repair software. We used the Repetier Host software to control the 3D printer. The parameters for the layout of the layers were then further adjusted with Slic3r code generator. The impression was then made with a 3D printer (i3 prusa model) as shown in Fig. 32.4. The parameters included: Layer height 0.3 mm, first-layer height: 0.3 mm, perimeters: 4, solid-layers top: 4, bottom 4, fill was made at different percentages ranging from 10 to 20 % combine infill every layer, loop minimum: 2, skirt-height 1 layers, filament diameter 1.75, extruder first layer 210, other layers 200, bed first layer 115, other layers 110, filament diameter 1.75 mm, extruder first layer 210, other layers 200, bed first layer 115, other layers 110.

The duration of the printing process for the palm of the hand took an average time between 4 and 6 hrs. Next the printing of the flexible articulations (Fig. 32.4c) were made with the following parameters: layer height 0.3 mm, first layer height 0.3 mm, perimeters 2, solid layers top 2, bottom 2, fill density 0 %, combine infill every 1 layers, loops minimum 0, skirt height 0, diameter 1.75, first layer 175, other layers 167, bed first layer 80, other layers 70.

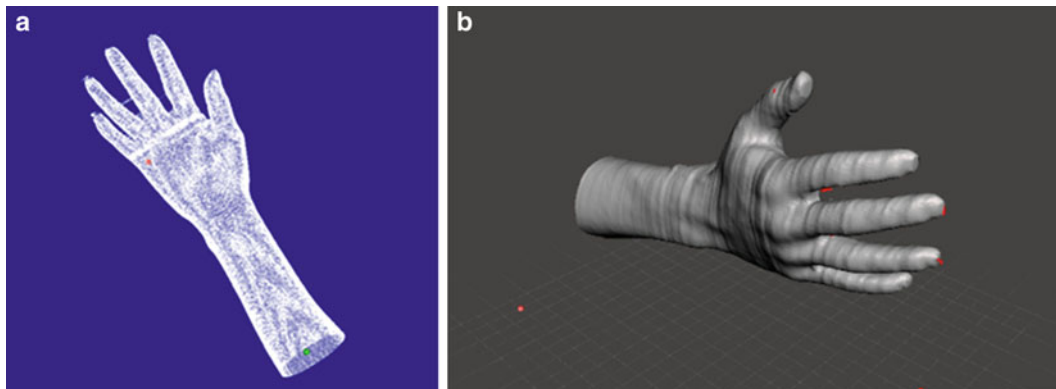


Fig. 32.1 Scanned hand (a) point clouds (b) with imperfections

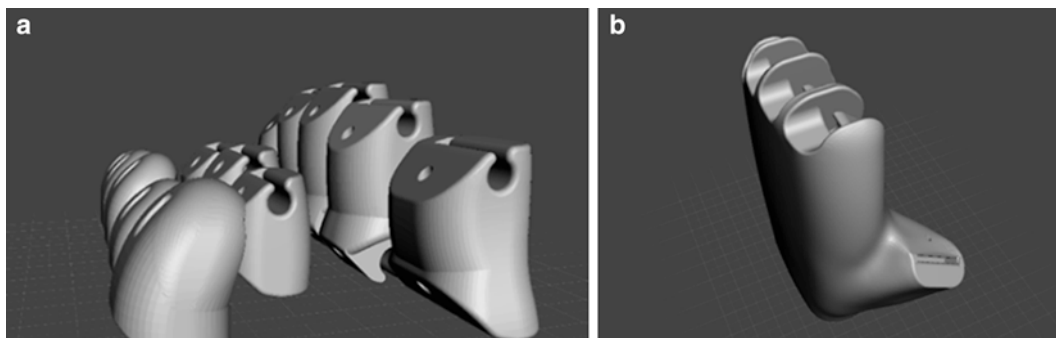


Fig. 32.2 Hand flawless, sectioned with apertures for joints (a) Fingers. (b) Palm

Fig. 32.3 Flexible hinges for printing on flexible material

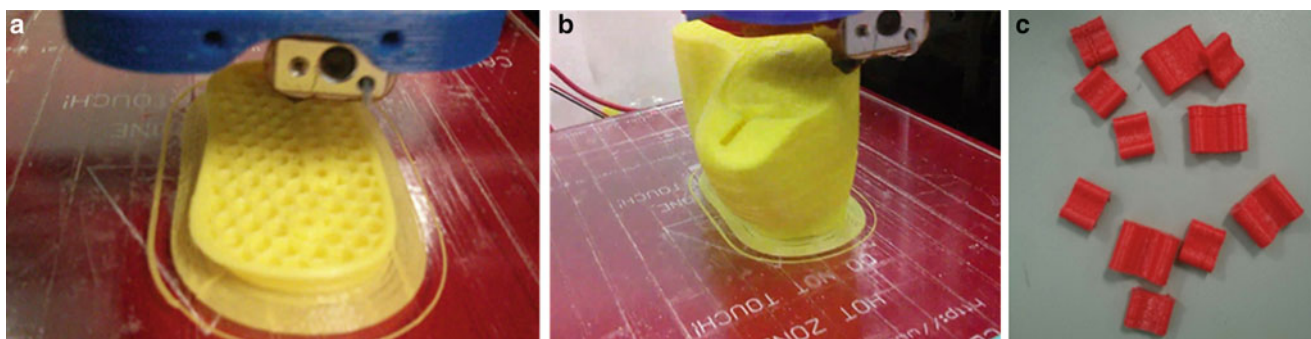
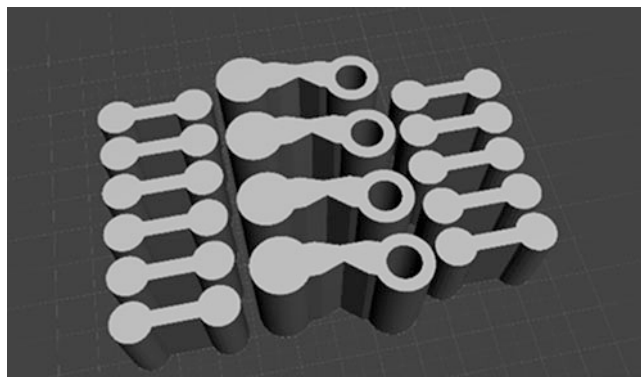


Fig. 32.4 3D printing in ABS (a) 20 % Density (b) Hand palm (c) flexible joints

Fig. 32.5 3D printed hand assembled



Once all the pieces have been printed, the joints were assembled by pressure, with plastic wires inserted through passages in the palm of the hand to function as tendons, which will be powered electronically to mimic the movement of the fingers as shown in Fig. 32.5.

The control signals for the patient's prosthetic were generated by a surface analysis of the electromyography (EMG). The EMG signals were acquired by attaching non-invasive silver/silver chloride surface electrodes. These type of electrodes provide adequate signal to noise ratio and are electrically consistent [3]. The EMG signals are subject to noise distortion, so signal processing techniques were implemented to eliminate the noise distortion [4]. We used an instrumental amplifier to increase the generated EMG signal approximately 74 times since the amplifier is not very sensitive to external noise. The amplified signal was then filtered from mixer noises. The signal was conditioned to be in the range of 0–5 V. The analog signal was connected to a micro-controller and the output signal of the microprocessor was connected to the 5 servomotors

responsible for moving the individual digits of the hand prosthesis. Each servomotors were connected to the cable of each finger to trigger a displacement signal at the distal phalanges, causing the fingers to flexion, when the servomotors cease displacement signal the cable tension is ceased thereby permitting the digits extention to form an open hand, with the cable tension producing a prehensile force. The cable consists of stretch resistant polyethylene fiber that offers adequate tensile strength. The customized prosthetic had several positive properties, including being light-weight and flexible. In order to identify an optimal weight which coincides with positive performance, we experimented with different print densities. The ideal print density was identified as 10 %.

32.3 Discussion

Based on a mirror image of the complete non-amputated hand a prosthetic was generated. The fingers remain extended until the cable is retracted by the servomotor, as part of the retraction function which enables the flexible joint phalanges restrict finger movement. The prosthesis allows for flexion as transferred by the cable attached to the distal phalanx of each finger. The thumb provides power grip, thereby, allowing the user to manipulate objects and providing for more realistic finger movements. The use of a latex surgical glove as a cover of the prosthetic hand improved appearance and gripping capacity.

The benefits of using this method for the print manufacturing of a prosthetic include: the development a non-invasive anatomical design, a data image which can be transferred by internet, a print manufacturing processes which implements a typical 3D printer and printing material, which can be manipulated by a standard computer including the software, which is inexpensive and accessible.

As shown in Fig. 32.6 the prosthetic has been shown to grasp large and small objects of a variety of shapes (Fig. 32.6a, b). The thumb can be alternatively positioned to grasp different objects (Fig. 32.7a, b). Also can be positioned inward and outward to grasp smaller objects (Fig. 32.8).

The individual digits separately extend, so no return tendon cables or springs are required. Pliable tendons offer adaptive gripping mechanism for irregular objects, of which all the digits are powered by a single motor, for this prosthetic. In order to improve the appearance of the prosthetic an external glove or skin form can be used [5]. Since this prototype has not being tested by persons with amputation, long-term durability and maintenance requirements are presently unknown. This prosthetic is very basic, for controlling multiples degrees of freedom movements, however it will be important to implement a pattern recognition method [6]. One of the main areas for revision includes the improvement of the socket design. In addition, an actuation method which is self-mechanized in a similar manner to the natural biomechanical method would be a significant improvement [7]. One of the challenges is to develop a self-powered actuation capabilities comparable to biological systems [8].

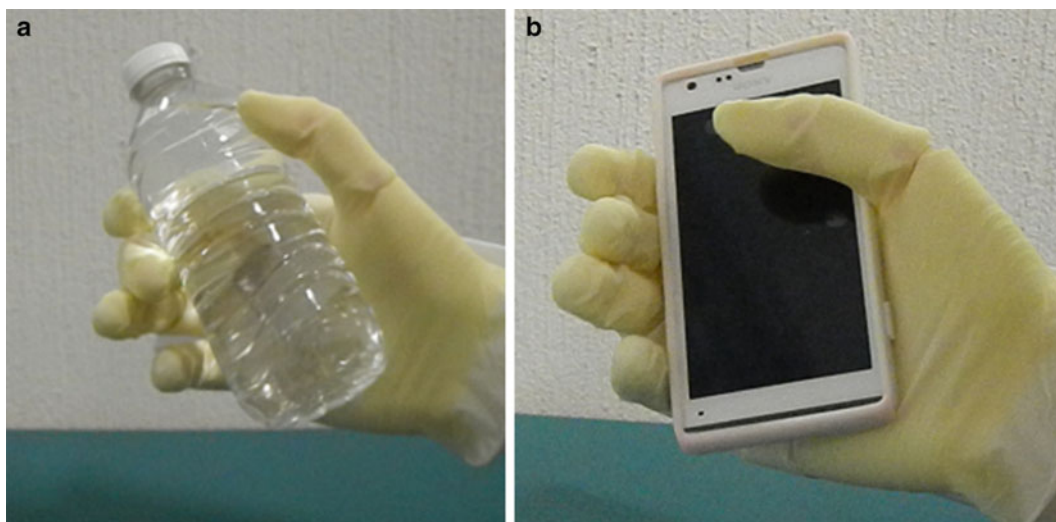


Fig. 32.6 The prosthetics can grasp objects of various shapes and sizes (a) Bottle of water (b) Cell phone

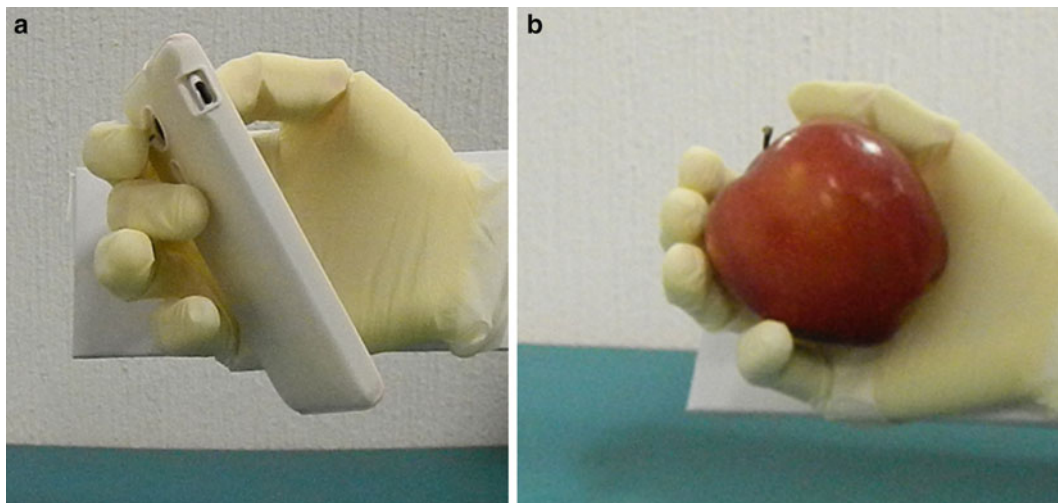


Fig. 32.7 The thumb positioned to grasp different objects (a) Cell phone (b) Apple

Fig. 32.8 The thumb positioned to grasp thin objects



32.4 Conclusions

Designing a prosthetic with the implementation of three-dimensional technology will result in a higher-quality prosthetic with a reduced manufacturing time. Further research is required to determine the optimal printable material. In addition, further research is needed to optimize the socket shape where the prosthetic connects to the amputation site. The printable prosthetic is an affordable option due to the simplicity of the required manufacturing equipment and software, and should be considered a viable option for development of a customized artificial limb.

Acknowledgements The authors would like to express their appreciation for the support from the State Council of Science and Technology (CONCYTEG) and CIATEC, A. C. for their partial support as well as, the Biomechanics Laboratory team. We would also like to thank Joel M. Anderson, M.B.A for his language and topic consultation.

References

1. S.W. O'Driscoll et al., The relationship between wrist position, grasp size, and grip strength. *J. Hand Surg.* **17**(1), 169–177 (1992)
2. R. Doshi, C. Yeh, M. LeBlanc, The design and development of a gloveless endoskeletal prosthetic hand. *J. Rehabil. Res. Dev.* **35**(4), 388–395 (1998)
3. X. Navarro, T.B. Krueger, N. Lago, S. Micera, T. Stieglitz, P. Dario, A critical review of interfaces with the peripheral nervous system for the control of neuroprostheses and hybrid bionic systems. *J. Peripher. Nerv. Syst.* **10**(3), 229–258 (2005)
4. R.H. Chowdhury, M.B. Reaz, M.A. Ali, A.A. Bakar, K. Chellappan, T.G. Chang, Surface electromyography signal processing and classification techniques. *Sensors* **13**(9), 12431–12466 (2013)
5. S. Bilotto, Upper extremity cosmetic gloves. *Clin. Prosthet. Orthot.* **10**, 87–89 (1986)
6. E. Scheme, K. Englehart, Electromyogram pattern recognition for control of powered upper-limb prostheses: state of the art and challenges for clinical use. *J. Rehabil. Res. Dev.* **48**(6), 643–659 (2011)
7. Z. Shuxian, Z. Wanhua, L. Bingheng, 3D reconstruction of the structure of a residual limb for customizing the design of a prosthetic socket. *Med. Eng. Phys.* **27**(1), 67–74 (2005)
8. F. Sup, A. Bohara, M. Goldfarb, Design and control of a powered transfemoral prosthesis. *Int. J. Rob. Res.* **27**(2), 263–273 (2008)

Chapter 33

Finite Element Static Analysis Simulation for a Grain Dispenser Mechanism

J.E. Valtierra, A.A. Silva, B.L. Vargas, and E.A. Ruelas

Abstract The objective of this study was to identify a material for a transfer system used in the packaging of gains for human consumption which is in compliance with the regulations established by Federal Commission for Protection Against Health Risks (COFEPRIS) of México.

A static material analysis was performed testing different materials to determine the optimal plastic material for connecting the grain dispenser hopper mechanism to the bagging system. SolidWorks, a computer aided engineering software was implemented for finite-element analysis testing, testing the strength, displacement and safety of four Mexican food industry COFEPRIS compliant materials. The study revealed that the most suitable material for the connection mechanism is Polyamide commercially known as “Nylon” because of the material’s high-rigidity, low-friction and positive dimensional stability.

Keywords Finite element model • Static analysis • Grain dispenser • SolidWorks • Materials

33.1 Introduction

Various materials such as: wood, stainless steel, ceramics, glass, etc., have been used in the manufacturing of equipment and utensils used in food processing. Properties such as: durability, ease of cleaning, resistance to wear, safety, cost and having antimicrobial properties are considerations when determining an optimal material [1]. Currently, stainless steel is one of the most commonly implemented materials which encompasses those characteristics [2]. With the evolution of material science, the use of plastics is becoming more prevalent as a low-cost, durable and light-weight alternative to stainless-steel.

The advantages of modern food industry plastics is that they are principally inert to corrosion resistant to acids and detergents, as well as, having low thermal and electrical conductivity characteristics. The characteristics of plastics vary according to the material’s composition and manufacturing method. In the food industry the use of plastics is primarily based on the material’s capacity for temperature resistance. Plastics which tolerate temperature variations are found within a category referred to as: “thermoplastics” and include: polyethylene (PE), polypropylene (PP), polyamide (Nylon), polyethylene terephthalate (PET). A suitable material for the food industry must conform to certain criteria as shown in Table 33.1 [2].

The design and development of grain dispenser is principally based on granular flow. A *granular medium* is a set of particles (grains) with similar characteristics, whose dynamics is governed by the laws of classical mechanics [3]. Depending on the conditions the granular medium, the grain can behave as solid, a liquid or a gas, but the resemblance is never exact [4]. As a liquid, the granular medium will take form of the container. As a solid, the medium can take multiple forms, including the capacity flow through a pipe as if the medium were a liquid. When the density concentration of the grains is low and the medium has a high-kinetic energy level, the granular media can be likened to a gas [4], though there are significant differences in the dynamics of both because a granular gasses are dissipative. Therefore, some authors believe that there is a new state of matter [5]. The industrial process of the granular material can trigger blockages due to their capacity to form arches, as specially structured particles become bonded [5]. So the design and development of grain dispenser must take in account granular flow and the particular medium’s accompanying properties.

J.E. Valtierra (✉) • B.L. Vargas • E.A. Ruelas

Department of Industrial Engineering, ITESI, Instituto Tecnológico Superior de Irapuato, Irapuato, Guanajuato, Mexico
e-mail: jovaltierra@itesi.edu.mx; bevargas@itesi.edu.mx; edruelas@itesi.edu.mx

A.A. Silva

Department of Biomechanics, CIATEC, A.C. Centro de Innovación Aplicada en Tecnologías Competitivas A.C., León, Guanajuato, Mexico
e-mail: asilva@ciatec.mx

33.2 Methodology

In our study, we evaluated packaging process of one company whose process commenced with the filling of the hopper, followed by the granular medium being gravity fed to the bagging machine which volumetrically determines the weight. In Fig. 33.1, the storage hopper shown has a capacity of 4 t. Figure 33.1, (A) shows the hopper, (B) the discharge tube from the hopper, (C) the cone of the bagging machine, (D) the bagging machine, (E) a bean grain bag. The identified problem of our evaluation was that the weight of the filled bags was inconsistent. The variation in the weight of the filled bags was due to the pressure of the granular flow from the hopper into the components of the bagging machine. This resulting complication required frequent weight adjustments to be manually made by the operator. Another complication was the 15 min filling time for the hopper which was required for every production hour. Figure 33.2, shows a XR weight control chart of samples every 4 min of five 500 g bags during a 1 h period, showing that the process yielded inconsistent results, as the upper and lower control limits were 498.6 and 494.91, respectively. As observed, there is an identified trend. In sample #5 the weight decreased, which subsequently was identified by the operator and manually adjusted after the sample #7, and then again after sample #12 when the weight decreased. If the operator does not compensate by manual adjustment the arithmetic mean of the filled bags will continue to decrease over a prolonged period.

A dispenser design was developed (Fig. 33.3) to reduce the output pressure variation which in turn affects the weight of the full bags. Key characteristics of the food industry thermoplastic materials should include the following [2]: stress-cracking resistance, fatigue-resistance, as well as, having a low-friction coefficient.

The dosing test design included a 15 cm diameter polyvinyl chloride test control tube prior to the final manufacturing in order to confirm its functionality. See Fig. 33.4. The granular medium flow behavior was observed for rice, peas and beans at the discharge site of the grain dispenser.

The designed dosing test occurred in the production area, where we studied the process control weight of the full bags. The XR control chart for each bag of 900 g during a 1-h period as is shown in Fig. 33.5, with the upper and lower control limits of: 903.643 and 899.397, showing a controlled process. By implementing the reconfigured grain dispenser tube during the process consistency in weight control of the bags was achieved, therefore, reducing the number of manual adjustments to the bagging machine. As a result a 50 % reduction in the weight variation was achieved regardless of the quantity of grain

Table 33.1 Characteristics of materials

Does not transmit	• Toxic substances
Does not modify	• Odors • Flavors
That is resistant	• Wear • Impact • To rust • To corrosion

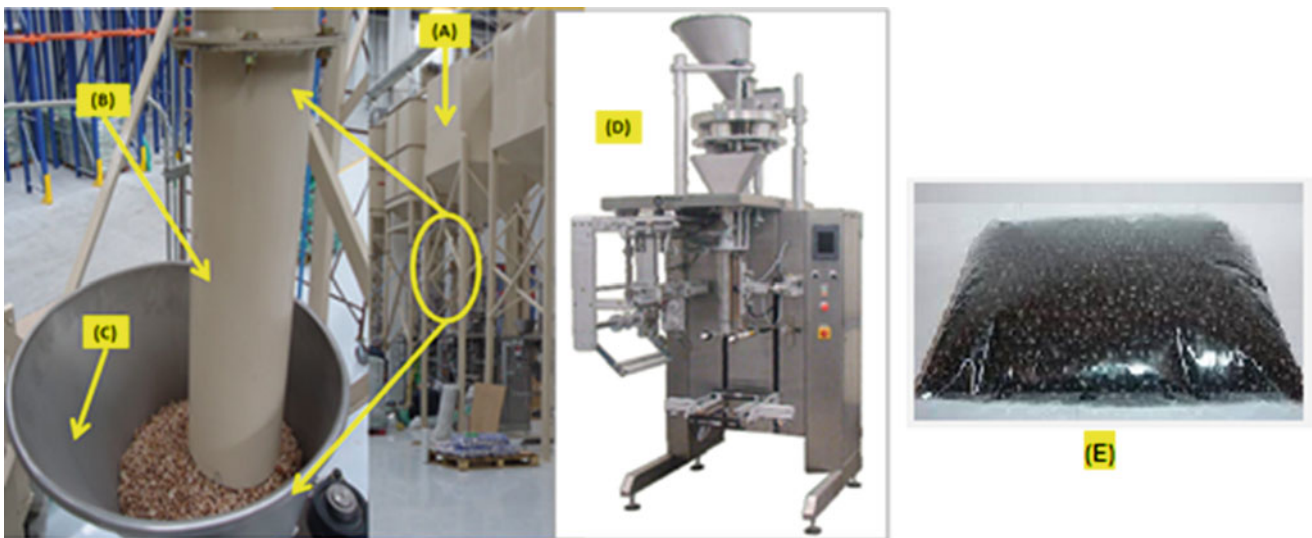


Fig. 33.1 (A) Hopper, (B) Outlet Tube, (C) Cone, (D) Bagging Machine, (E) Bag

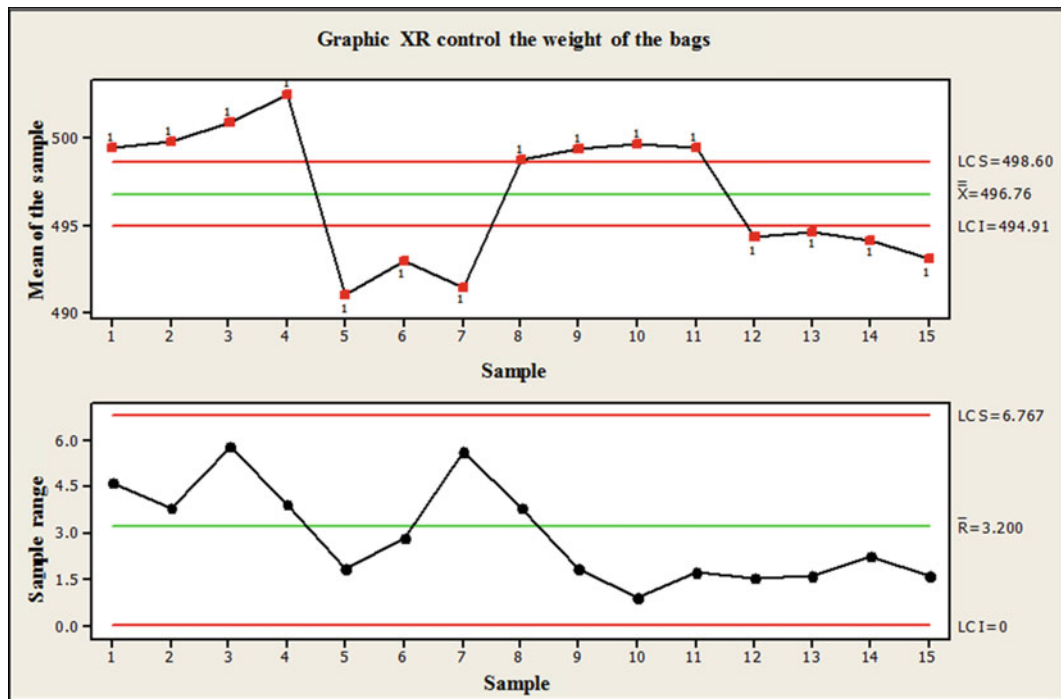
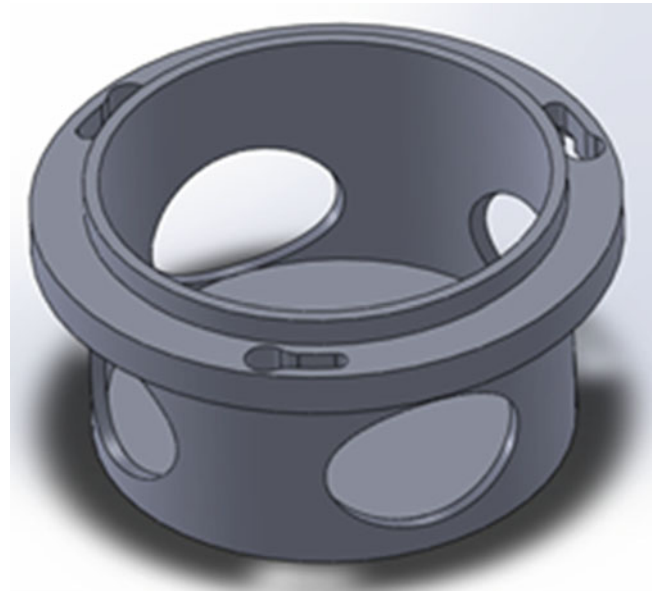


Fig. 33.2 Graphic XR control the weight of the bags

Fig. 33.3 Model of grain dispenser



held in the hopper. In addition, the waiting time for refilling the hopper was reduced, resulting in an overall increase in production. Though the implementation of the reconfigured grain dispenser tube, stopping the production process to refill the hopper was no longer required, as the dosing into the bagging machine remains consistent, regardless of the quantity of granular medium in the hopper.

The reconfigured dispenser was evaluated, using a finite element analysis of four different materials: PET, Nylon, acetal copolymer and PE HD of which these materials share similar features and physical properties, as show in Table 33.2 [1].

Materials testing is an essential factor of mechanical engineering, especially when those materials are expected to perform under arduous conditions. Therefore, a stress-analysis is critical in establishing a statistical level of reliability. Finite-element-method (FEM) is the preferred method for testing mechanical simulations. Modern software systems use



Fig. 33.4 Pilot Testing dispenser, rice (a), chickpea (b) and beans (c)

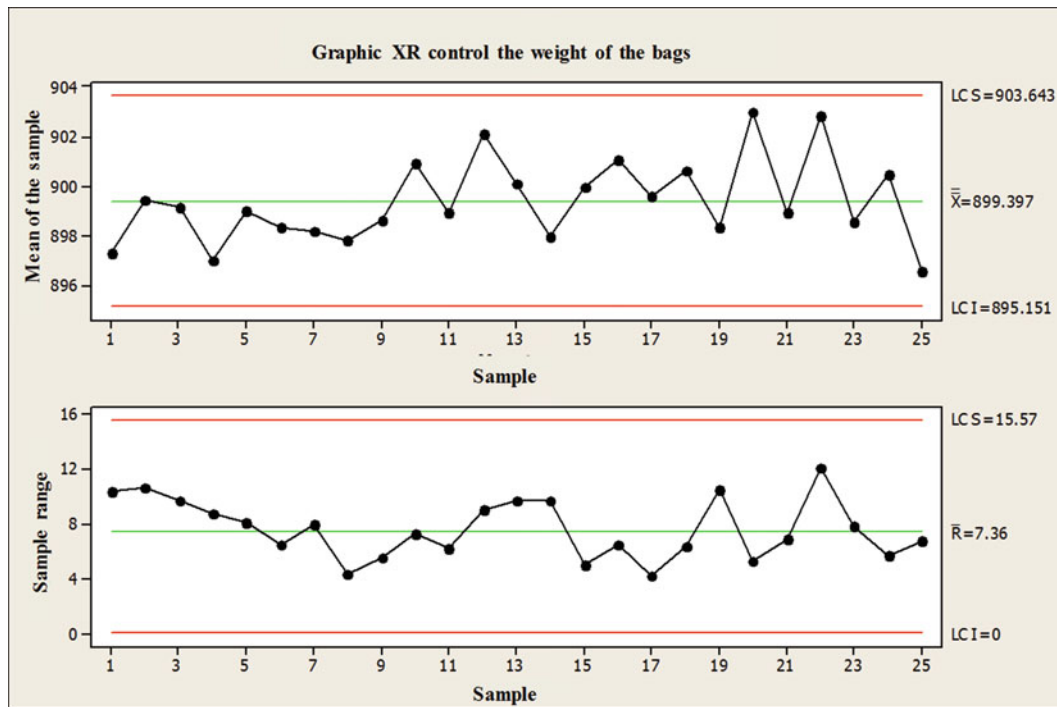


Fig. 33.5 Graphic XR control the weight of the bags

Table 33.2 Characteristics of materials

Materials	Characteristics
Polyamides Nylon 6	High flexibility, resistance to oils, grease, corrosive resistance and resistance to low temperatures
Acetal copolymer	High stiffness and strength, impermeability for wet environments and resistance to chemicals
Polyethylene terephthalate (PET)	Excellent chemical and corrosion resistance, high mechanical strength, does not absorb moisture and impact resistance
Polyethylene (PE HD)	Excellent chemical and corrosion resistance, high mechanical strength, does not absorb moisture and impact resistance

Note: Some of these plastics can be damaged by solvents

FEM analysis for solving mathematically complex and time consuming operations. The basic idea of the FEM is simple, as it requires a split solution to a finite number of sub-area-elements. This model of FEM analysis requires the creation of finite-elements. The density of the elements fundamentally alters the quality of the results and amount of computer memory consumed to complete the analysis. FEM is commonly implemented for solving problems of elasticity, dynamics, liquids flow and gases, etc. [6, 7].

For our evaluation we implemented SolidWorks simulation software which enables the analysis to include structural properties such as: stress, displacement, natural frequency, etc. In addition, SolidWorks software also provides a motion analysis, used in the investigation of moving assemblies (effects of forces, springs, damper and friction). The SolidWorks analysis combines elements of kinetic studies and bonds-in-motion calculation. Restrictions of the movement, the material properties, physical properties and the contact-parts are also included in the calculation of the kinematic solutions [8, 9].

33.3 Results

In the finite-element computer simulation, a static-analysis of the identified thermoplastics was conducted. Stress, displacement and deformations were calculated, as well as, the safety factor (also commonly referred to as *failure criterion*) with SolidWorks software [10]. Part of the analysis included calculating the pressure of the dosing grains. The subsequent calculations determined that the base of the dispenser must withstand a pressure of approximately 20310.2 Pa, according to (33.1). The calculations were based on the height of the discharge pipe and the density of the grain medium, with the assumption that the dispenser does not have discharge apertures. This then requires the optimal mechanism to be able to support the weight of the 2.5 m grain discharge tube. The density of the beans was 0.847 kg/L. Beans were selected because they are representative of the heaviest grain medium to be implemented within the system.

$$p = \frac{F}{A} = \frac{36.4 \text{ kg} * 9.81 \left[\frac{m}{s^2} \right]}{0.0176 \left[m^2 \right]} = 20310.2 \left[\frac{N}{m^2} \right] \quad (33.1)$$

In which the variables mean:

p = pressure (N/m²)

F = strength (kg/m/s²)

A = Total contact area (m²)

The value 9.81 is the gravitational constant.

The physical properties of the materials used to make the static analysis of the dispenser are shown in Table 33.3.

The finite element analysis was performed by applying a pressure of 20310.2 Pa. At this pressure, we found the breaking strength of the PET material is 2963653.3 N/m², as shown in Fig. 33.6.1a. The maximum stress according to the Von Mises criterion [10, 11] develops at the base of the dispenser.

In Fig. 33.6.2b, as observed the region of greatest displacement is located in the center-base of the dispenser with respect to URES criterion [10, 11].

The breaking strength of the acetal copolymer was calculated as 3008573.3 N/m² (Fig. 33.6.1c). The region of greatest displacement is located in the center-base of the dispenser with respect to URES criterion (Fig. 33.6.2d). The result of the Nylon 6 was 3020292.8 N/m². In Fig. 33.6.1e, and in Fig. 33.6.2f we can observe the greatest displacement also occurs in the center of the base of the dispenser as identified by URES criterion. The tension of PE HD was calculated as 2.936,857.0 N/m². See Fig. 33.6.1g. The area of greatest displacement can be observed in Fig. 33.6.2h.

Table 33.3 Mechanical properties of chosen material

Properties	PET	Acetal copolymer	Nylon 6	PE HD	Units
Elastic modulus	2960000000	2900000000	8300000000	1070000000	N/m ²
Poisson's ratio	0.37	0.3	0.28	0.4101	N/D
Shear modulus			3200000000	377200000	N/m ²
Mass density	1420	1410	1400	952	Kg/m ³
Tensile strength	57300000	40700000	142559000	22100000	N/m ²
Compressive strength	92900000				N/m ²
Yield strength		63000000	139043000		N/m ²
Thermal expansion coefficient			3e-005		/K
Thermal conductivity	0.261		0.53	0.461	W/(m-K)
Specific heat	1140		1500	1796	J/(kg-K)
Hardening factor					N/D

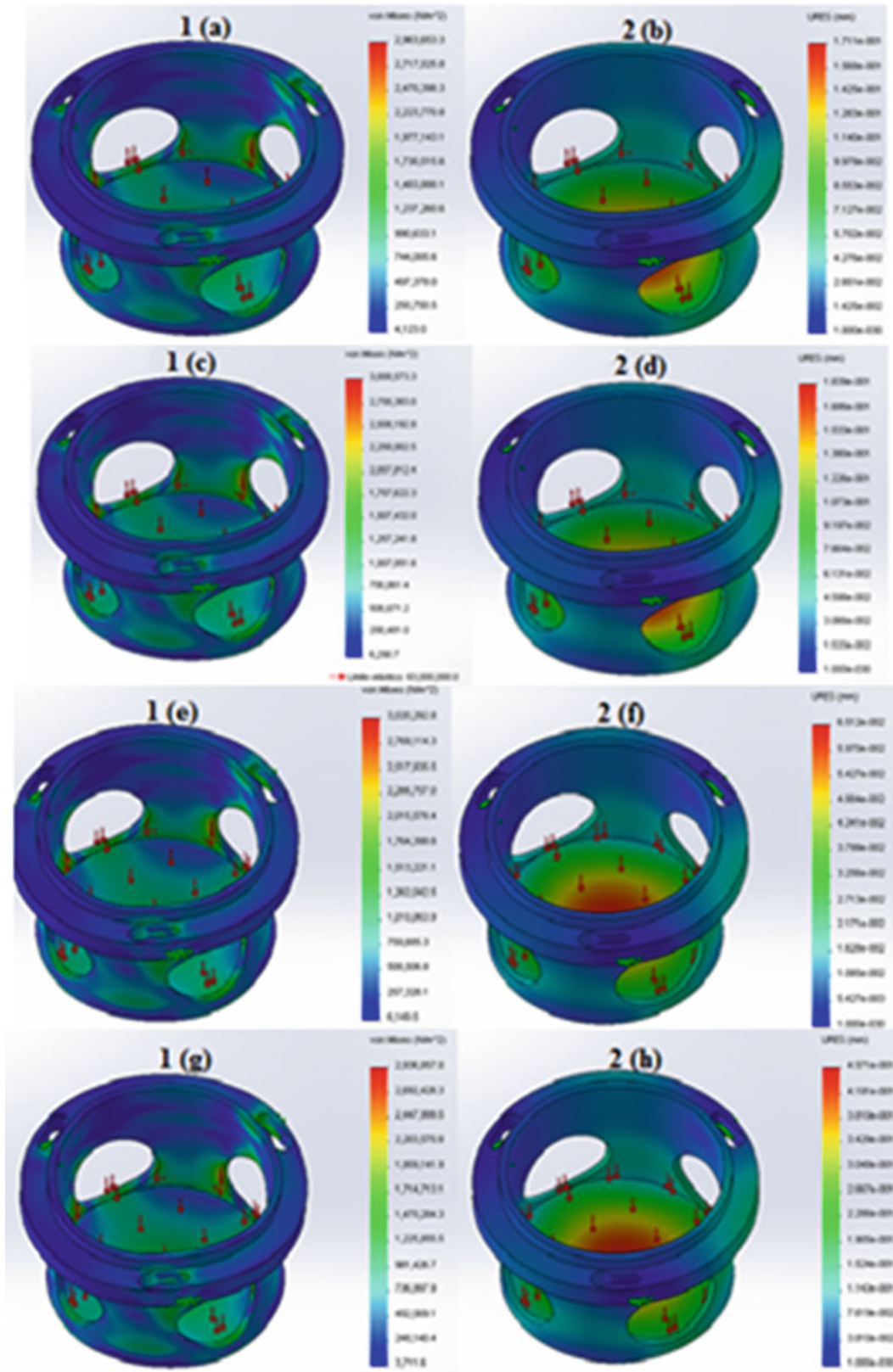


Fig. 33.6 (1) Stress Analysis, (2) Displacement, (1a, 2b) PET, (1c, 2d) Acetal copolymer, (1e, 2f) Nylon, (1g, 2h) PE HD

Table 33.4 Results of the analysis of test materials

Analysis	Stress Von misses (N/m ²)	Displacement URES (mm)	Unit deformations ESTRN	Safety factor FDS
PET	2,963,653.3	1.711e-001	8.248e-004	18.88
Acetal copolymer	3,008,573.3	1.839e-001	8.384e-004	20.94
Nylon 6	3,020,292.8	6.512e-002	2.922e-004	46.04
PE HD	2.936,857.0	4.771e-001	2.280e-003	–

In conjunction stress-analysis, displacement, deformation and safety-factor were also analyzed, with the results are shown in Table 33.4. In Table 33.4, it is observed that the results of PET and acetal copolymer materials were similar, with the PE HD material being superior to the previous two, though nylon 6 demonstrated even higher level of performance. The selected material to manufacture the dispenser was Nylon 6 because of the material's durability and strength, both of which are critical features when used under load and impact in moderate temperatures [11, 12].

33.4 Conclusions

In this study, a static analysis was performed using finite-elements to identify an optimal material and configuration for a grain dispenser which is conjoined to the output of a storage hopper. SolidWorks software was implemented for the analysis of stress, displacement, strain, and the safety factor of four different materials. The materials analyzed are authorized for use in the food industry based on the standards established by regulating agencies including: COFEPRIS (Mexico), the FDA, and the USDA international. Our research revealed that the optimal material for the dispenser was the Nylon 6 because of the material's high impact and fatigue resistance, while also having durability and resistance capacity under low temperature conditions. Our simulation revealed that Nylon 6 has higher tensile and flexural strength. In addition, Nylon 6's elasticity permits for shock absorption and vibration by having an elevated softening point which is resistant to the environment changes.

Acknowledgements We appreciated the support of CIATEC, A.C. and ITESI Irapuato Guanajuato. The authors would also like to thank Joel M. Anderson, M.B.A., for the language editing of this article.

References

1. A.W. Chin, *Polymers for Innovative Food Packaging* (Faculty of Worcester Polytechnic Institute, Worcester, 2010)
2. A.L. Andrady, M.A. Neal, Applications and societal benefits of plastics. *Philos. Trans. R. Soc. Lond. B Biol. Sci.* **364**(1526), 1977–1984 (2009). doi:10.1098/rstb.2008.0304
3. H.M. Jaeger, R.N. Sindey, R. Nagel, Physics of the granular state. *Science* **255**, 1523 (1992)
4. H.M. Jaeger, R.N. Sindey, R.P. Behringer, Granular solids, liquids, and gases. *Rev. Mod. Phys.* **68**, 1259–1273 (1996)
5. B. Zuriguel, Flujo y Atascos de un medio granular en la descarga de silos Departamento de Física y Matemáticas aplicadas. Facultad de Ciencia, Universidad de Navarra, Pamplona, España, 2005
6. V. Ivančo, K. Kubín, K. Kostolný, *Finite Element Method* (Elfa, Košice, 1994)
7. R. Flores, A. Martínez, J. Samá, *The finite elements of impact loads for the determination of tensions and deformations in a beam of an agricultural trailer*. *RCTA*. **18**, 21-27, ISSN: 1010-2760 (2009)
8. M. Vrbka, M. Vaverka, *Finite Element Method Contribution* (Institute of Machine Engineering, Brno, 2010)
9. SolidWorks Corporation, *SolidWorks Fundamentals* (2013). http://help.solidworks.com/2013/English/SolidWorks/sldworks/c_solidworks_fundamentals_overview.htm
10. help.solidworks.com/2011/spanish/SolidWorks/cosmosxpresshelp/AllContent/SolidWorks/NonCore/SimulationXpress/t_How_to_Assess_the_Safety_of_your_Design.html
11. K. Chang, *Product Performance Evaluation Using CAD/CAE*, 1st edn. (Academic Press, Burlington, 2013)
12. Dassault Systemes SolidWorks Corp, *Proyecto de análisis y diseño de SAE con el software SolidWorks* (2013). http://www.solidworks.com/sw/docs/edu_sae_instructor_2013_esp.pdf

Chapter 34

Controlling Bounce of Vacuum Circuit Breakers' Contacts

Masao Narita, Naoki Yaegashi, Minoru Kobayashi, and Shigeru Inaba

Abstract In the process of closing three-phase vacuum circuit breakers (VCBs), the collisions between the contacts in the vacuum interrupters cause the contacts to bounce. Consequently, repetition of make-and-break of the electrical circuit happens. If the duration of this phenomenon exceeds a certain time length, the surfaces of the contacts are damaged by the heat of the arcs between the contacts. This causes deterioration of the intrinsic functions of the VCB.

The paper presents an experimental process to investigate this phenomenon using a 10 kV 40 kA VCB as an example. Since disconnection of the contacts in the closing process occurs when the magnitude of the reaction forces between the contacts falls below a certain level, we examined the following process to predict the bounce phenomenon. First, the time functions of the contacts' collision forces were estimated using the frequency response functions of the structural system and the response vibrations of the structure measured in the closing process. Second, the reaction force functions between contacts were estimated using the frequency response functions and the collision forces. Next, the bounce duration was derived by evaluating these reaction forces. Finally, we investigated a method to decrease the duration.

Keywords Vacuum circuit breaker • Collision • Bounce • Frequency response function • Coupling analysis

34.1 Introduction

In the power generation, transmission and distribution fields, gas circuit breakers in medium-voltage systems have been replaced by vacuum circuit breakers (VCBs). This is mainly because SF₆, the most potent greenhouse gas, and the particular substances specified by RoHS must be excluded from new products to reduce environment load.

On the other hand, VCBs introduced an emerging issue. Concerning the three-phase alternating current VCB, if the bounce occurs in the closing process, the arc breaks out between the contacts. As a result, the surfaces of the contacts are damaged and the VCB functions deteriorate. Therefore, the bounce duration must be controlled. An overview of a typical VCB is shown in Fig. 34.1. In general, a three-phase VCB consists of three vacuum interrupters and an actuating mechanism. A vacuum interrupter and its related parts are shown in Fig. 34.2. A vacuum interrupter is configured by a pair of contacts, one of which is standing still and the other is movable. The bounce of a movable contact results from the collision forces of the contacts in the VCB closing process [1].

The paper investigates the bounce phenomenon of VCB contacts. Assuming that the VCB structure is a linear system after the contacts have touched in the closing process, the reaction forces between them are calculated as frequency functions and transformed to time functions. Comparing the magnitude of the forces with a certain threshold level, we estimated the moments when the detaching will probably occur. When the VCB is in a closed state, a particular level of static contact force is required to ensure the electrical current between the contacts. Despite this, immediately after the closing operation, transient vibration due to the collision of the mutual contacts occurs in the VCB structure and the vibration component of contact force is superimposed on the former static contact force. In this situation, if there is a moment when the contact force becomes less than a threshold level, the electrical disconnection happens. If we can estimate the time functions of the reaction forces between contacts, we can predict the bouncing phenomena.

M. Narita (✉) • N. Yaegashi

Mitsubishi Electric Corporation, Advanced Technology R and D Center, 8-1-1 Tsukaguchi-Honmachi, Amagasaki City, Hyogo 661-8861, Japan
e-mail: Narita.Masao@bc.MitsubishiElectric.co.jp

M. Kobayashi • S. Inaba

Mitsubishi Electric Corporation, Power Distribution Systems Center, 8 Horaicho, Marugame City, Kagawa 763-8516, Japan

Fig. 34.1 A vacuum interrupter and its related parts

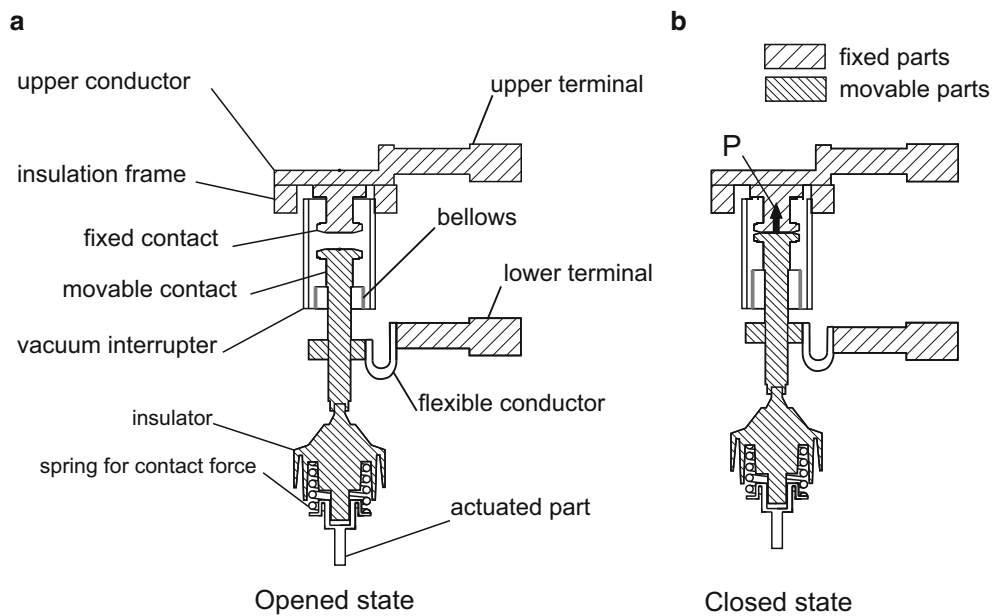
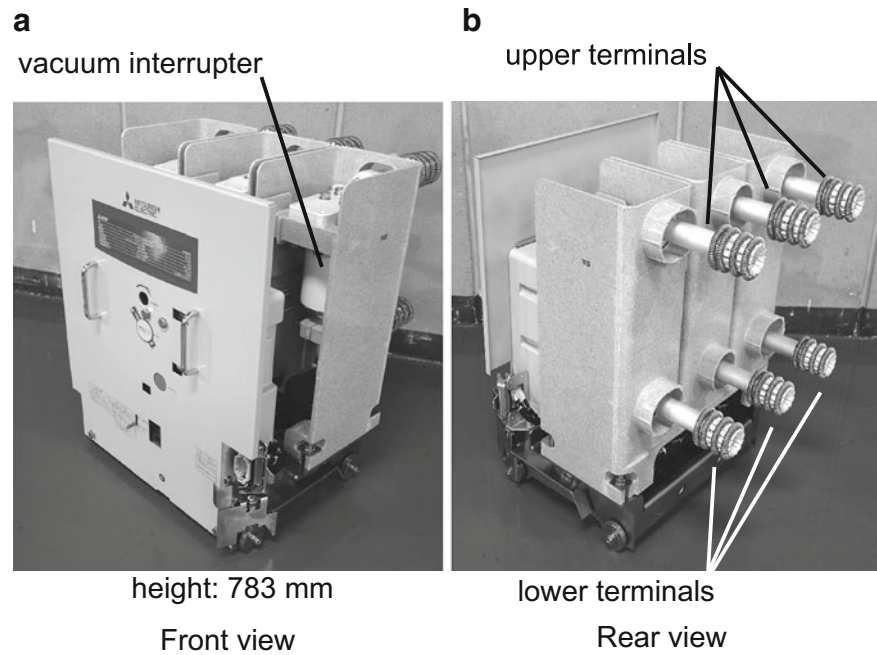


Fig. 34.2 A vacuum interrupter and its related parts

In many past studies about the motion of VCB contacts, the structural system was treated as a time-variant one. Consequently, a time integration technique was generally used to analyze the motion. However, this approach was not suitable to handle the multiple collision phenomena in a three-phase VCB because the bounce of a certain phase depended on the vibration responses caused by the collisions that occurred in the other phases. For this reason, we used a linear response analysis in this study. Under a condition where the VCB was in a closed state, we considered a time-invariant structural system in which a linear relationship was established among the collision forces, the response forces between the contacts and the response displacements on the VCB structure. Consequently, we used linear modal analysis for this study [2].

34.2 Theory

34.2.1 Estimation of Collision Forces

A simplified VCB structural model in closed state is shown in Fig. 34.3. In Fig. 34.3a, the external exciting forces $f_k^{(1)}$, $f_k^{(2)}$, \dots , $f_k^{(n)}$, $n = 3$, which were caused by collisions, were loaded on the n degrees-of-freedom on the structure for discrete time $k = 0, 1, 2, \dots, N - 1$. As a result, response displacements $d_k^{(1)}$, $d_k^{(2)}$, \dots , $d_k^{(m)}$ on m degrees-of-freedom and response reaction forces between contacts $r_k^{(1)}$, $r_k^{(2)}$, \dots , $r_k^{(n)}$ on n degrees-of-freedom were generated (Fig. 34.3b).

Our objective is to predict $r_k^{(1)}$, $r_k^{(2)}$, \dots , $r_k^{(n)}$. For this, first, $f_k^{(1)}$, $f_k^{(2)}$, \dots , $f_k^{(n)}$ are estimated from $d_k^{(1)}$, $d_k^{(2)}$, \dots , $d_k^{(m)}$ and second, $r_k^{(1)}$, $r_k^{(2)}$, \dots , $r_k^{(n)}$ are estimated from $f_k^{(1)}$, $f_k^{(2)}$, \dots , $f_k^{(n)}$.

Let $F_k^{(1)}$, $F_k^{(2)}$, \dots , $F_k^{(n)}$ and $D_k^{(1)}$, $D_k^{(2)}$, \dots , $D_k^{(m)}$ be the Fourier transforms of $f_k^{(1)}$, $f_k^{(2)}$, \dots , $f_k^{(n)}$ and $d_k^{(1)}$, $d_k^{(2)}$, \dots , $d_k^{(m)}$ respectively. Let \mathbf{F}_k and \mathbf{D}_k be column vectors:

$$\mathbf{F}_k = [F_k^{(1)} F_k^{(2)} \dots F_k^{(n)}]^T \quad (34.1)$$

$$\mathbf{D}_k = [D_k^{(1)} D_k^{(2)} \dots D_k^{(m)}]^T, \quad (34.2)$$

where T denotes a transposition without a conjugate transformation. Let \mathbf{H}_k be an $m \times n$ frequency response function (FRF) matrix between input \mathbf{F}_k and output \mathbf{D}_k in the closed state of the VCB. The relationship among \mathbf{H}_k , \mathbf{F}_k , and \mathbf{D}_k is expressed as follows:

$$\mathbf{H}_k \mathbf{F}_k - \mathbf{D}_k = 0. \quad (34.3)$$

Assume that measurement noise is contained in \mathbf{D}_k . Hence, $\hat{\mathbf{F}}_k$, which minimizes $\|\mathbf{H}_k \hat{\mathbf{F}}_k - \mathbf{D}_k\|^2$ and $\|\hat{\mathbf{F}}_k\|^2$, is given as follows:

$$\hat{\mathbf{F}}_k = \mathbf{H}_k^+ \mathbf{D}_k, \quad (34.4)$$

where matrix \mathbf{H}_k^+ denotes the Moore-Penrose generalized inverse matrix of \mathbf{H}_k .

To obtain \mathbf{H}_k , a structural coupling analysis, which is called impedance method, is applied [3]. One reason for this is that the structural system's full FRF matrix cannot be obtained directly by testing because it is impossible to measure accelerations on the contact points in VCB closed state. In addition, $r_k^{(1)}$, $r_k^{(2)}$, \dots , $r_k^{(n)}$ are able to be obtained only by

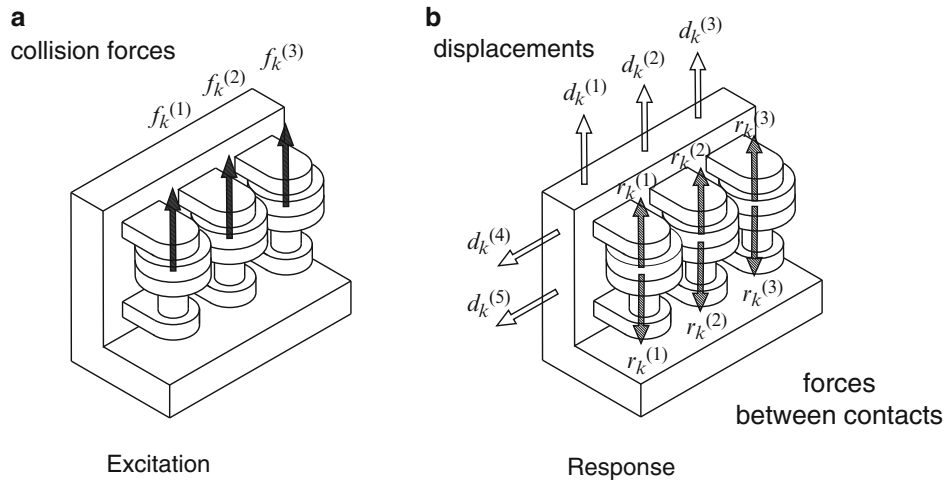


Fig. 34.3 Simplified VCB structural model in closed state

the structural coupling analysis. For this, the complete VCB structure is divided into fixed and movable portions. The former includes fixed contacts, upper terminals, lower terminals, and an actuating mechanism. The latter includes the movable contacts and the insulators. The FRFs are estimated for each portion separately by testing. Then they are coupled analytically to obtain the total FRF matrix and reaction forces between contacts. For this analysis, we used an improved coupling technique proposed by Jetmundsen et al. [4].

34.2.2 Estimation of Reaction Forces Between Contacts

$R_k^{(1)}, R_k^{(2)}, \dots, R_k^{(n)}$ denote the Fourier transforms of $r_k^{(1)}, r_k^{(2)}, \dots, r_k^{(n)}$. These are expressed by column vector \mathbf{R}_k as follows:

$$\mathbf{R}_k = \left[R_k^{(1)} R_k^{(2)} \dots R_k^{(n)} \right]^T. \quad (34.5)$$

Because displacements of the fixed contacts equal to those of the movable contacts in closed state, the following equation is derived.

$$\mathbf{H}_{Fk}(\mathbf{F}_k + \mathbf{R}_k) + \mathbf{H}_{Ck}\mathbf{R}_k = 0, \quad (34.6)$$

where \mathbf{H}_{Fk} and \mathbf{H}_{Ck} are $n \times n$ FRF matrix about the fixed contacts and movable ones respectively. Let \mathbf{G}_k be an $n \times n$ FRF matrix from \mathbf{F}_k to \mathbf{R}_k . The relationship among \mathbf{R}_k , \mathbf{F}_k , and \mathbf{G}_k is expressed as follows:

$$\mathbf{R}_k = \mathbf{G}_k \mathbf{F}_k. \quad (34.7)$$

\mathbf{G}_k can be derived from (34.6) and (34.7) as follows:

$$\mathbf{G}_k = -(\mathbf{H}_{Fk} + \mathbf{H}_{Ck})^{-1} \mathbf{H}_{Fk}. \quad (34.8)$$

Let $\widehat{\mathbf{R}}_k$ be the estimate of \mathbf{R}_k , and we obtained the following equation from (34.4) and (34.7):

$$\widehat{\mathbf{R}}_k = \mathbf{G}_k \mathbf{H}_k^+ \mathbf{D}_k. \quad (34.9)$$

Equation 34.9 is calculated for $k = 0, 1, 2, \dots, N - 1$ frequency by frequency. Then $r_k^{(1)}, r_k^{(2)}, \dots, r_k^{(n)}$ are given by the inverse Fourier transform of \mathbf{R}_k .

34.2.3 Control of Bounce Occurrence

In the actual assembly process of VCB in the factory, we adjusted the opening distance between the contacts to shorten the bounce duration. The method described below gives an analytical basis for this adjustment operation and eliminates the time loss caused by trial and error.

By varying the opening distance between the contacts, the relative delays are changed among $F_k^{(1)}, F_k^{(2)}, \dots, F_k^{(n)}$. This implies changing $R_k^{(1)}, R_k^{(2)}, \dots, R_k^{(n)}$ and results in various duration bounce times.

The delay of a time function can be expressed by a convolution calculation of a delayed unit impulse function in the time domain. In the frequency domain, this is done by multiplication of the Fourier transform of the time function. The Fourier transform of time function x_k for time $k = 0, 1, 2, \dots, N - 1$ is given as follows:

$$X_k = \sum_{n=0}^{N-1} x_n e^{-i2\pi kn/N} \quad (34.10)$$

Therefore, the discrete Fourier transform of the following unit impulse function

$$\left. \begin{aligned} x_k &= 0 & k &= 0, 1, \dots, j-1 \\ x_k &= 1 & k &= j \\ x_k &= 0 & k &= j+1, \dots, N-1 \end{aligned} \right\} \quad (34.11)$$

is expressed as follows:

$$X_n(j) = e^{-i2\pi kj/N}. \quad (34.12)$$

Based on delays 0 , j_2 , and j_3 for the first, second, and third phases, $R_k^{(1)}$, $R_k^{(2)}$, and $R_k^{(3)}$ are given as follows:

$$\begin{bmatrix} R_k^{(1)} \\ R_k^{(2)} \\ R_k^{(3)} \end{bmatrix} = \mathbf{G}_k \begin{bmatrix} X_k(0) & 0 & 0 \\ 0 & X_k(j_2) & 0 \\ 0 & 0 & X_k(j_3) \end{bmatrix} \mathbf{H}_k^+ \mathbf{D}_k. \quad (34.13)$$

Time functions $r_k^{(1)}$, $r_k^{(2)}$, and $r_k^{(3)}$ are obtained by the inverse Fourier transform of frequency functions $R_k^{(1)}$, $R_k^{(2)}$, and $R_k^{(3)}$, respectively.

34.3 Experiments

We conducted two kinds of experiments. The first one was common modal testing, and the second obtained accelerations and strains in the VCB closing process.

In these experiments, modified 'bare vacuum interrupters' were installed in the test specimen. The outer ceramic cylinder of the vacuum interrupter was replaced by four steel bars. Three vacuum interrupters of this configuration were installed in the test VCB. Figure 34.4 shows a VCB with these vacuum interrupters.

Table 34.1 shows the instruments used for our measurements.

Fig. 34.4 Test VCB with bare vacuum interrupters

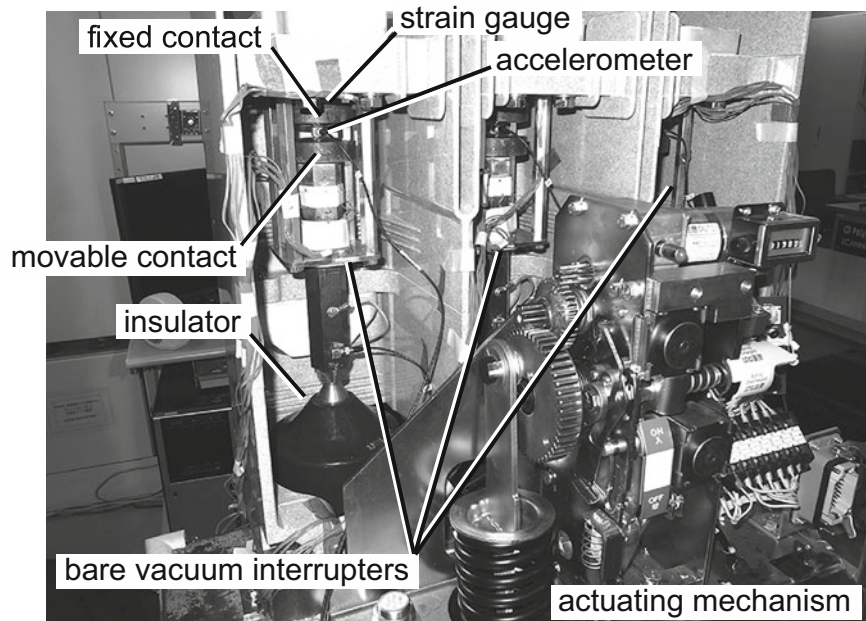
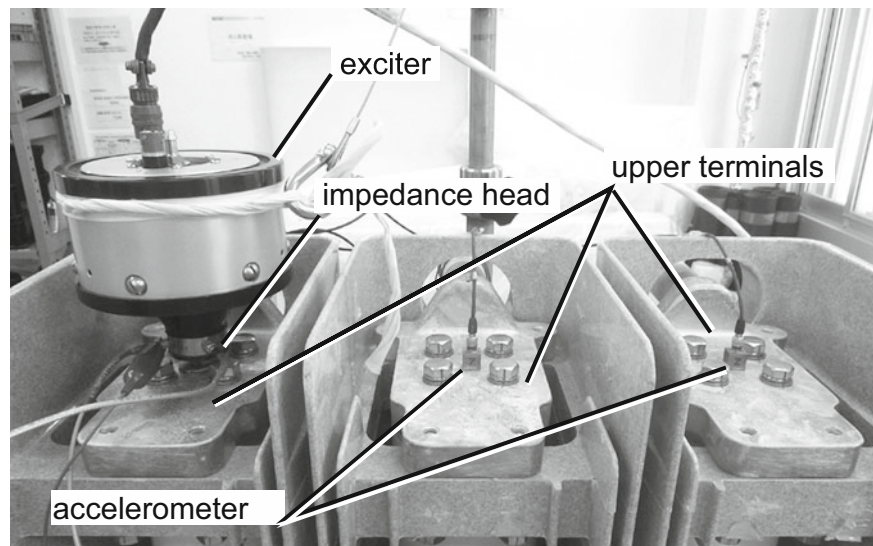


Table 34.1 Measuring instruments

Instrument	Type	Manufacturer
Accelerometer	4520	B&K
Accelerometer	356B20	PCB
Accelerometer	352B01	PCB
Strain gauge	KFG-03	Kyowa
Strain amplifier	DPM-713	Kyowa
Impulse hammer	086C03	PCB
Exciter with impedance head	F4/F7	Willcoxon
Signal analyzer	3560C	B&K
Signal analyzer	Test. Lab	Siemens

Fig. 34.5 An example of modal testing configuration using random excitation



34.3.1 Modal Testing

We used burst random excitations by an electromagnetic exciter with an impedance head and impulse excitations by an impact hammer with a load cell to obtain the system input forces and accelerometers to obtain the system output responses. From these measured signals, the FRFs of the structural system were estimated [2]. An example of the modal testing configuration is shown in Fig. 34.5.

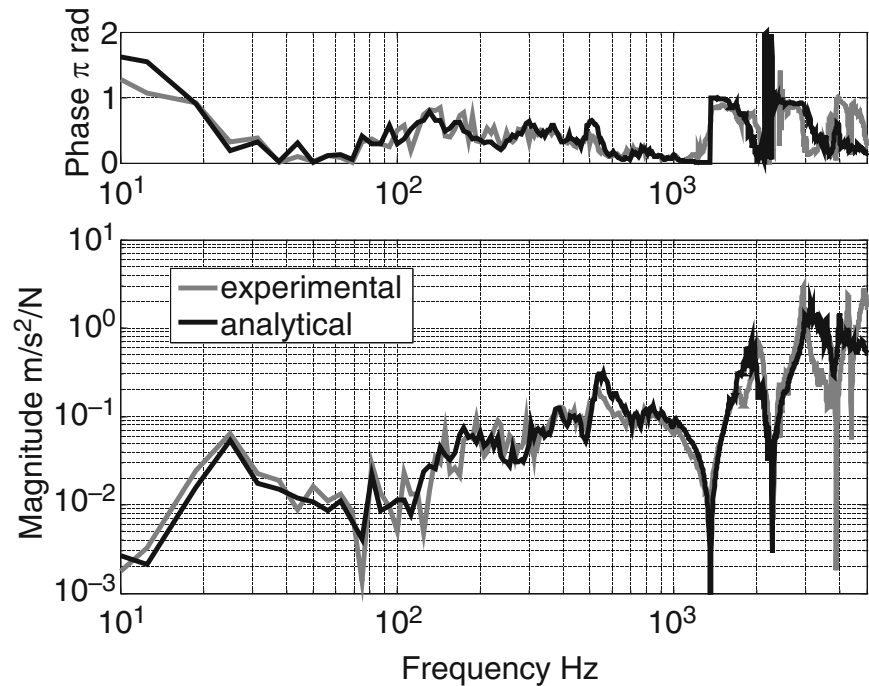
These tests were done under the opened state. This is because the only method that can obtain reaction forces between contacts was coupling analysis as mentioned in the former section. The full FRF matrix was synthesized from the modal parameters obtained for a column vector of the matrix.

34.3.2 Accelerations and Forces in VCB Closing Process

The accelerations of the structure and the strains of the column of the fixed contacts were measured by the VCB closing process. The time functions of the make-and-break signals of the respective phases were simultaneously obtained as conduction between the contacts.

Strain gauges were put on the opposing sides of the cylindrical columns of the contacts. These pairs of strain signals were added to cancel the bending strains. As a result, the strains of the axial direction of the columns were extracted.

Fig. 34.6 Comparison of FRFs obtained by coupling analysis and experimentally



34.4 Discussion

34.4.1 Validity of FRF From Coupling Analysis

FRF matrices \mathbf{H}_k and \mathbf{G}_k were obtained by coupling analysis based on the FRFs of the fixed and the movable portions. First, to demonstrate the efficiency of coupling analysis to obtain the system's FRF, our experimental results are presented.

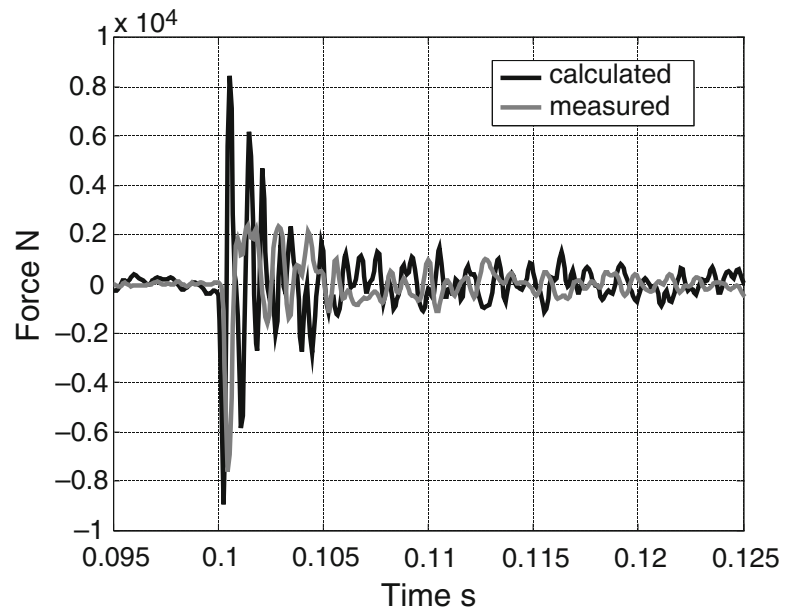
Figure 34.6 compares an FRF obtained by coupling analysis with one that was estimated experimentally. Both excitation and response points were degrees-of-freedom P shown in Fig. 34.2b. According to Fig. 34.6, the FRF obtained by coupling analysis coincided with the one that was estimated experimentally. The validity of coupling analysis was confirmed.

34.4.2 Prediction of Reaction Forces Between Contacts

The collision forces were calculated using (34.4). Based on these forces, the forces between the contacts were derived by (34.9). Figure 34.7 compares the contact force of the second phase of the VCB calculated in this way with the corresponding contact force measured using strain gauges. To these signals, Butterworth 50–2000 Hz band-pass filter was applied because FRF estimation errors were contained in frequencies lower than 50 Hz.

From Fig. 34.7, although the two did not fully coincide, we judged them as similar. It follows that the bounce's time function can be predicted based on the vibration measurement in the VCB's closing process when its FRF matrices are known.

Fig. 34.7 Forces between contacts



34.5 Conclusions

We investigated the bounce phenomenon concerning the contacts of vacuum circuit breakers. In this study, we assumed a time-invariant system and applied a modal analysis technique. First, a procedure to estimate the reaction forces between the contacts was shown. Next, a method that gives an analytical basis for an adjustment operation in a factory was described. We achieved modal testing and transient vibration measurement and the following results:

1. We experimentally confirmed our procedure's validity to obtain a structural system model that was necessary to analyze the reaction forces between the contacts by comparing the mutual frequency response functions obtained by coupling analysis and measurements.
2. The time function of the reaction force between the contacts, which was obtained analytically, coincides with the force measured using strain gauges. This verified that the reaction forces were calculated correctly by the proposed method.

We conclude that our proposed procedures can contribute to understand the bounce phenomenon of vacuum circuit breakers.

A remaining issue is that we must improve the accuracy to estimate the frequency response functions experimentally because they greatly affect the prediction of the forces between the contacts.

References

1. T. Koizumi, N. Tsujiuchi, Y. Hiratoko, M. Narita, Optimum design for dynamic characteristics of vacuum circuit breaker. *Trans. Jpn Soc. Mech. Eng. C* **62**(596), 1347–1353 (1996)
2. D.J. Ewins, *Modal Testing: Theory, Practice and Application*, 2nd edn. (Research Studies Press, England, 2000)
3. N.M.M. Maia, J.M.M. Silva, J. He, N.A.J. Lieven, R.M. Lin, G.W. Skingle, W. To, A.P.V. Urgueira, in *Theoretical and Experimental Modal Analysis* (Research Studies Press, England, 1998), pp. 265–302
4. B. Jetmundsen, R.L. Bielawa, W.G. Flannelly, Generalized frequency domain substructure synthesis. *J. Am. Helicopter Soc.* **33**, 55–64 (1988)

Chapter 35

Experimental and Numerical Investigation of Effects of Fiber Orientation of Wood Stiffness

Tzu-Yu Kuo and Wei-Chung Wang

Abstract Wood is one of the most useful and important natural materials with diverse applications in civil, architectural and constructional engineering. The stiffness of the wood depends on the fiber orientation, distribution of knot and percentage of latewood, etc. Japanese cedar (*Cryptomeria japonica*) was used to prepare the tensile test specimen in this paper to investigate the effects of fiber orientation on wood stiffness. Before performing the tensile test, surface image of the test specimen was captured and the image was analyzed by least squares method and digital image processing software of MATLAB to obtain the fiber orientation. Based on the obtained fiber orientation, finite element method (FEM) software package ANSYS was employed to calculate the strain distribution of the test specimen. Three-dimensional digital image correlation (3D-DIC) method was also used to verify the FEM results. The DIC software, VIC-3D, was used to analyze the surface deformation of the test specimen under tension. Strain distribution differences between the earlywood and latewood were investigated. With the integration of the digital image analysis technique, FEM and 3D-DIC method, the effective stiffness of the wood can be predicted and the reliability and safety of wood construction can be ensured.

Keywords Wood stiffness • Fiber orientation • Digital image correlation (DIC) • Finite element method (FEM) • Japanese cedar

35.1 Introduction

Wood has been an important construction material in the history since Stone Age [1]. Due to international advocacy for energy efficiency and reduction, wood gets attention again. Wood is a composite material in natural world [2], and the fiber directions of annual ring differ from environment conditions and wind directions [3]. Moreover, there are some factors effect wood mechanical features such as specific gravity, knots, and slope of grain [4]. During the process of tree growth, the width of the annual ring is different with the growth environment, soil density, and sunshine. Some studies applied micro-tensile and microscope to test Young's modulus and Poisson's ratio [5] of latewood (LW) and earlywood (EW) as well as fracture behavior [6–8]. Cramer et al. [9] applied broadband viscoelastic spectroscopy (BVS) device to obtain Young's modulus of ""3D-DIC method LW and EW by slender beam specimens of LW and EW. Moreover, Pereira et al. [10] used 3D-DIC method to measure full-field strain on radial cross-section and calculate effective modulus of elasticity of LW and EW. Besides, Lin et al. [11] applied ultrasonic tomographic technique to detect the defects of the trunk. Therefore, how to analyze wood structure stiffness precisely, insure quality, and increase the safety of wood structure has become a critical issue.

35.2 Digital Image Processing

Digital image processing is an efficient tool to determine profile and detect defects of wood surface. By using the histogram charts, Pham et al. [12, 13] determined wood defects and Daniel et al. [14] measured percentage of carbon fiber, epoxy and void of the polymer composite [14]. Computed Tomography (CT) was used to measure dimensions of knots and defects in tree stem [15–18]. In order to know wood fiber orientation, a laser dot was projected to the wood surface and the dot shape was changed from circular to elliptical due to tracheid cell orientation, called tracheid effect [19]. Therefore, digital image processing technique was used to calculate major-axis direction of the ellipse to analyze wood fiber orientations [19–23].

T.-Y. Kuo (✉) • W.-C. Wang

Department of Power Mechanical Engineering, National Tsing Hua University, Hsinchu, Taiwan, Republic of China
e-mail: asmit.com@msa.hinet.net

In this paper, digital image processing software of MATLAB was applied to measure wood fiber orientation by the surface image of wood specimen. During the process of determining fiber orientation, image had to be filtered because of too much unnecessary information such as noise. The first step of image processing was to change color image to gray level image. Second, linear filter was used to smooth images. Third, histogram equalization was conducted to enhance image contrast and make edge lines of fiber clear. And then edge detection method was employed to find the fiber edge. Finally, the least squares method was used to measure the angle of fiber orientation.

35.3 Materials and Experimental Procedure

Japanese cedar (*Cryptomeria japonica*) produced in Hsinchu, northern Taiwan was adopted as the specimen material. In order to meet experiment requirements, the cross section of the wood log should be in circular shape and almost nil defects can be found on the wood surface. The dimensions of the tensile test specimens used in this paper follows the CNS 450 O2001 [24] standard. The wood log was cut into pieces of wood boards and air-dried for more than 1 year before experiments. All tensile specimens were placed in a room with temperature controlled at 25 °C and relative humidity was set between 50 and 60 % for more than 1 week. Therefore, the moisture of wood specimens would be maintained between 10 and 12 %.

The test specimen with irregular fiber orientation is shown in Fig. 35.1. The front view is longitudinal-radial (LR) section, the side view is radial-tangential (RT) section, and the top view is longitudinal-tangential (LT) section. The DIC software, VIC-3D, was used to analyze the surface deformation of the LT section of the test specimen under tension. As shown in Fig. 35.1, to prevent the grip effect affects the results of strain observation during the tensile test, the area of interest (AOI) should be sufficiently away from the grip edges of the specimen. The dimensions of the AOI zone is 100 mm × 25 mm.

Experimental apparatus of the wood specimen with irregular fiber orientation under tensile test is shown in Fig. 35.2. The wood specimen was placed on the tensile fixture and tensile load was measured by the load cells. Two LED light sources were placed on both sides of the two cameras. The image was captured from the complementary metal-oxide-semiconductor (CMOS) cameras (Basler ACA2500-14gm) with one shutter per second. In the test, to increase the surface characteristics, spraying black speckle pattern was necessary. A tensile test machine, Hungta HT-2402, of capacity 50 kN was used. The speed of tensile test was set at 1 mm/min and data was recorded every per second.

Stiffness and percentage of EW and LW were obtained from the image processing and 3D-DIC results of the tensile test. Effective stiffness of the wood specimen was then calculated by the rule of mixture.

35.4 Finite Element Method

In this paper, the finite element method (FEM) software package ANSYS was employed to calculate the strain distribution of the test specimen. A computer with Intel i7 3930 CPU, 32 Gb of memory, and Windows 7 enterprise edition was used. The solid model was built based on dimensions of the specimen of 100 mm × 25 mm × 3 mm.

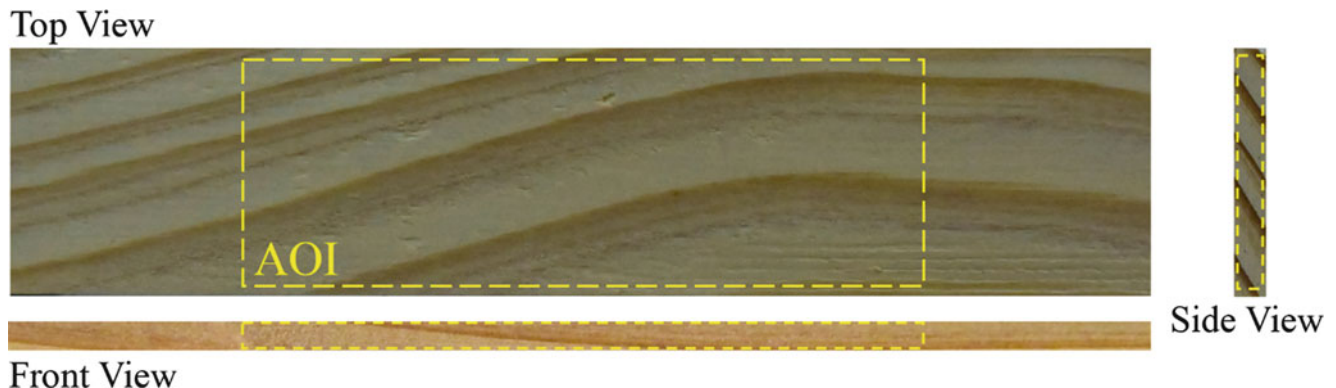


Fig. 35.1 The specimen image with irregular fiber orientation

Eight-node solid element with three degrees of freedom called Solid 185 was used in the FEM model. In order to rebuild FEM model of the wood structure, coordinates of original angle of the solid element should be replaced by current angle of fiber orientation obtained from the digital image processing technique.

35.5 Results and Discussions

In the tensile test, 3D-DIC method was used to measure the surface strain of wood specimens with irregular fiber orientation. Surface strain distributions of the longitudinal and tangential directions are shown in Figs. 35.3 and 35.4, respectively. In both Figs. 35.3 and 35.4, no visible strain appears before the application of tensile loading. It was found that critical load

Fig. 35.2 Experimental apparatus of wood specimen under tensile load

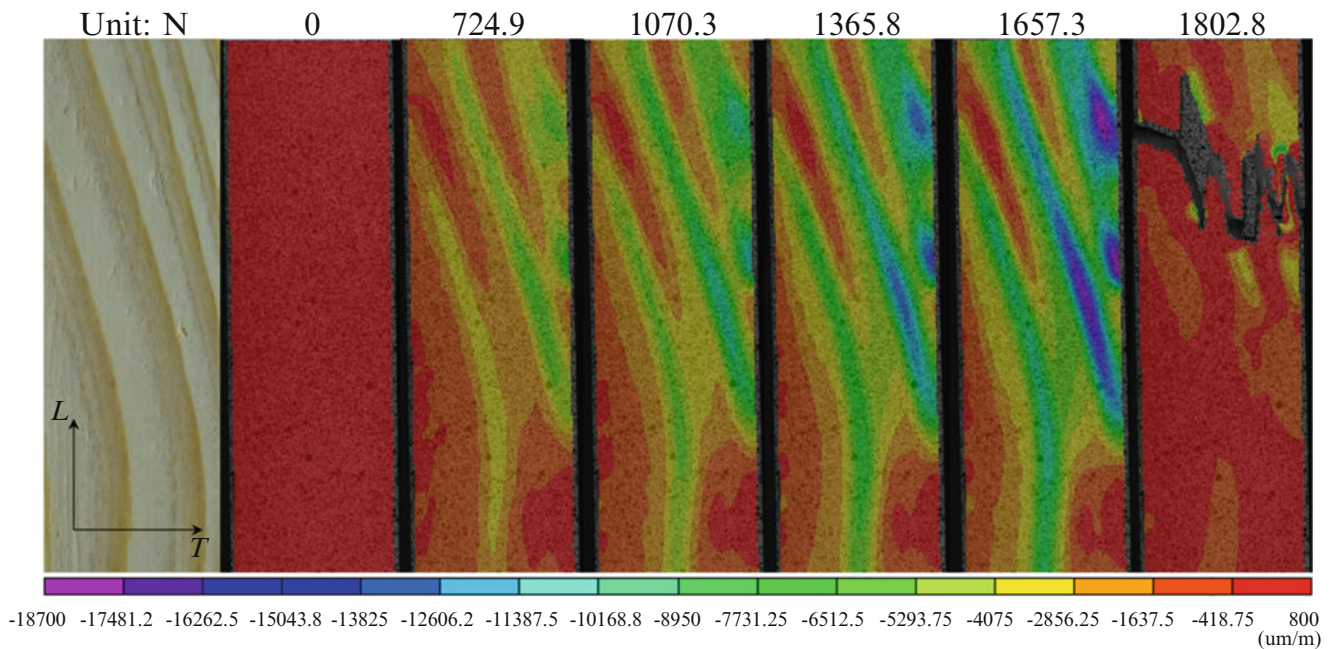
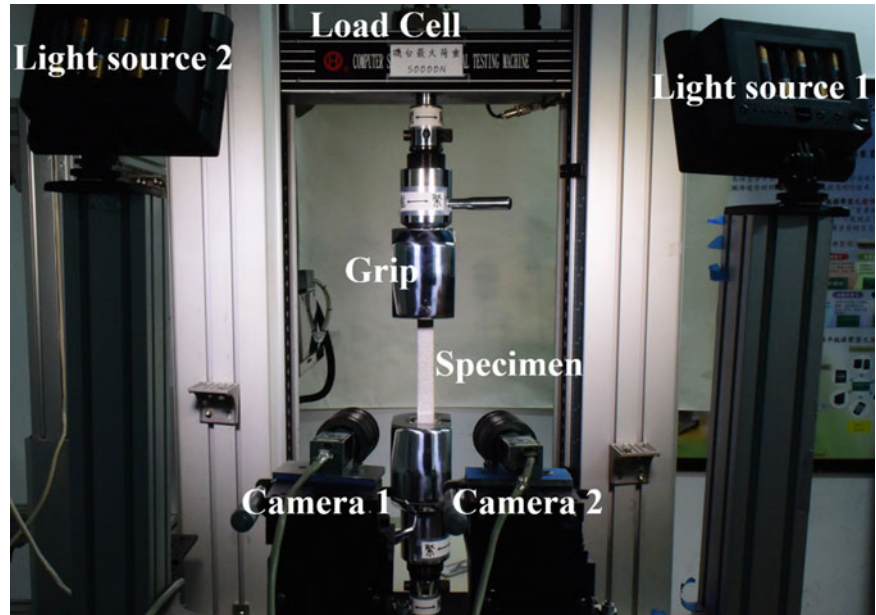


Fig. 35.3 3D-DIC results of surface strain with tangential direction under tensile loads

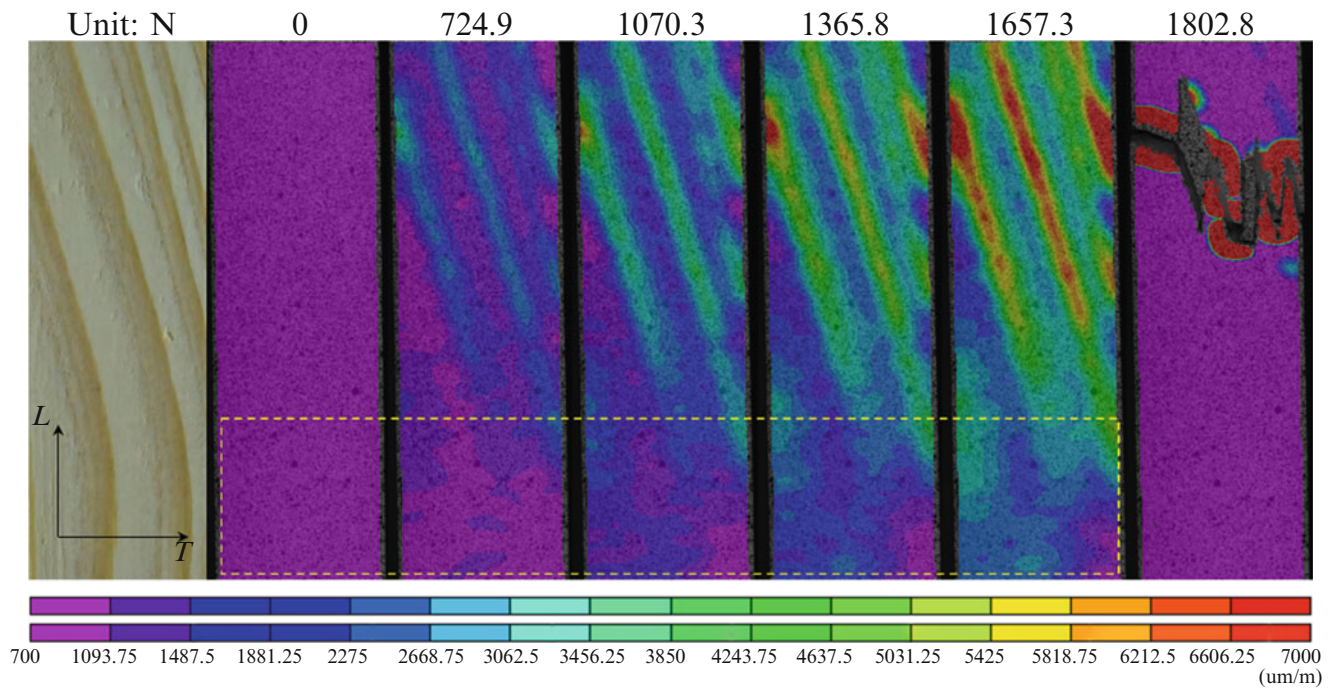


Fig. 35.4 3D-DIC results of surface strain with longitudinal direction under tensile loads

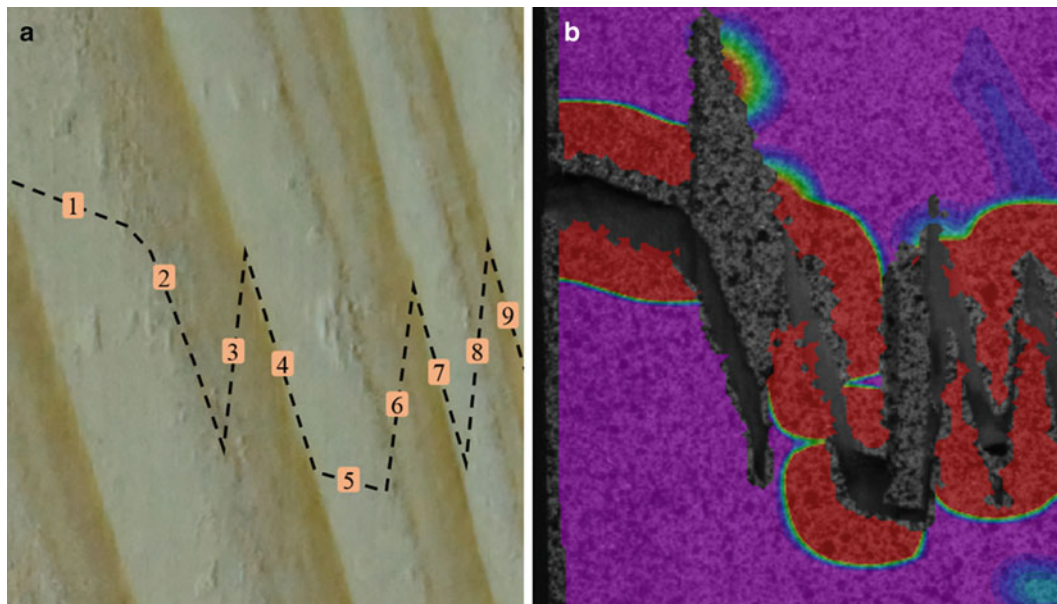


Fig. 35.5 Disruptive behavior of the wood specimen. (a) Tendency of the disruptive behavior (*dotted lines*) superimposed on the specimen image with irregular fiber orientation. (b) Disruptive behavior displays in the 3D-DIC results

happened under 1657.3 N, and finally the specimen cracks under 1802.8 N. Since the stiffness of LW is different from that of EW, lower and higher strains can be observed in LW and EW, respectively.

As shown in the yellow dotted area of Fig. 35.4, relatively small strains were obtained for fiber orientation nearly parallel to the longitudinal axis. In other words, the part of specimen in the yellow dotted area has higher stiffness. In comparison, relatively higher strains occur in the zone of fiber orientation inclined to the longitudinal axis. As depicted in Fig. 35.5, the specimen failure occurs in the zone of irregular fiber direction. It is interesting to see that the disruption of the wood starts from and across the EW (dotted line 1) and significantly propagates along the interface between the LW and EW (dotted

lines 2, 4, 7 and 9) with intermediate deviation across the LW (dotted line 3) and EW (dotted line 5) as well as both EW and LW (dotted line 8). Apparently, the variation of fiber orientation affects the stiffness of the wood plate structures. Further investigation of the disruptive behavior of the wood specimen is still undergoing.

After digital image processing, the results of edge line are shown in Fig. 35.6. The least squares method was used to calculate the angle of fiber orientation. Also, the edge lines of AOI were meshed into sub-images. To verify the results of the angle of fiber orientation, the MATLAB results were substituted into FEM software ANSYS to simulate strain behaviors of wood plates under tensile load.

Figure 35.7 shows the strain distributions obtained by 3D-DIC and ANSYS under 1657.3 N. It is obvious that the tendency of the strain variation of the two results is similar. However, higher magnitude of variation of strain is shown in the 3D-DIC results than that in the ANSYS results. This is not unexpected since the material properties of EW and LW used in



Fig. 35.6 Digital image processing results of edge line of wood specimen surfaces

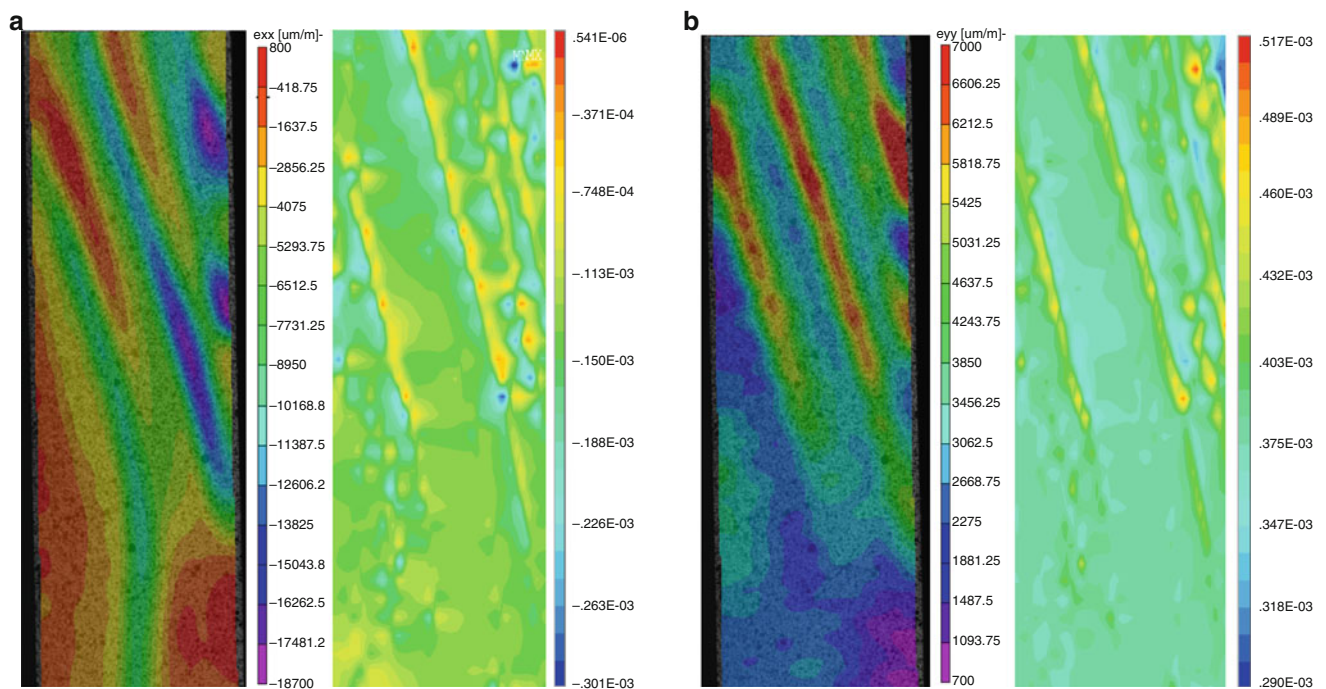


Fig. 35.7 Comparison of 3D-DIC and ANSYS results under tensile load. (a) Strain result with tangential direction (b) Strain result with longitudinal direction

ANSYS are obtained by the rule of mixture, i.e. by estimation. Even so, ANSYS results do help explain the variation fashion of the 3D-DIC results. Thus, the information of the angle of fiber orientation obtained from the digital image processing technique has proved to be useful for ANSYS.

35.6 Conclusions

In this paper, digital image processing technique was adopted to measure wood fiber orientation by the surface image of wood specimen with the use of the least squares method. The angles of fiber orientation thus obtained were substituted into the FEM software ANSYS to simulate strain behaviors of wood plates under tensile load.

Based on the 3D-DIC results, relatively lower strain can be found when the fiber orientation is approximately parallel to the longitudinal axis, i.e. where the higher stiffness exists. It was found that the variation of fiber orientation does affect the stiffness of the wood plates. Further investigation of the disruptive behavior is needed. Moreover, with the use of the effective stiffness, the tendency of the 3D-DIC results can be correctly calculated from the ANSYS results. Therefore, the proposed method presented in this paper has great potential to predict the reliability and safety of wood construction.

References

1. I.M. Daniel, O. Ishai, *Engineering Mechanics of Composite Materials* (Oxford University Press, New York, 1994)
2. F.L. Matthews, R.D. Rawlings, *Composite Materials: Engineering and Science* (CRC Press, Boca Raton, 1999)
3. C. Mattheck, H. Kubler, *Wood—The Internal Optimization of Trees* (Springer, Berlin, 1997)
4. Forest Products Laboratory, *Wood Handbook—Wood as an Engineering Material*, Centennial ed., USDA, U.S.A. (2010)
5. F. Farruggia, P. Perre, Microscopic tensile tests in the transverse plane of earlywood and latewood parts of spruce. *Wood Sci. Technol.* **34**, 65–82 (2000)
6. J. Bodner, M.G. Schlag, G. Grull, Fracture initiation and progress in wood specimens stressed in tension—part I. Clear wood specimens stressed parallel to the grain. *Holzforschung* **51**, 179–184 (1997)
7. J. Bodner, M.G. Schlag, G. Grull, Fracture initiation and progress in wood specimens stressed in tension—Part II. Compression wood specimens stressed parallel to the grain. *Holzforschung* **51**, 571–576 (1997)
8. J. Bodner, M.G. Schlag, G. Grull, Fracture initiation and progress in wood specimens stressed in tension—part III. Clear wood specimens with various slopes of grain. *Holzforschung* **52**, 95–101 (1998)
9. S. Cramer, D. Kretschmann, R. Lakes, T. Schmidt, Earlywood and latewood elastic properties in loblolly pine. *Holzforschung* **59**, 531–538 (2005)
10. J. Pereira, J. Xavier, J. Morais, J. Lousada, F. Pierron, On the evaluation of elastic properties of P. Pinaster at the growth ring scale. *Mecanica Exp.* **20**, 51–58 (2012)
11. C.J. Lin, Y.C. Kao, T.T. Lin, M.J. Tsai, S.Y. Wang, L.D. Lin, Y.N. Wang, M.H. Chan, Application of an ultrasonic tomographic technique for detecting defects in standing trees. *Int. Biodeterior. Biodegrad.* **62**, 434–441 (2008)
12. D.T. Pham, R.J. Alcock, Automatic detection of defects on birch wood boards. *Proc. Inst. Mech. Eng. J. Process Mech. Eng.* **210**, 45–52 (1996)
13. D.T. Pham; R.J. Alcock, segmentation of birch wood board images, in *Proceedings IWISP '96* (Manchester, UK, 1996), pp. 637–640
14. I.M. Daniel, O. Ishai, *Engineering Mechanics of Composite Materials*, 2nd edn. (Oxford University Press, New York, 2006)
15. L. Breinig, F. Brüchert, R. Baumgartner, U.H. Sauter, Measurement of knot width in CT images of Norway spruce (*Picea abies* [L.] Karst.)—evaluating the accuracy of an image analysis method. *Comput. Electron. Agric.* **85**, 149–156 (2012)
16. H. Boukadida, F. Longuetaud, F. Colin, C. Freyburger, T. Constant, J.M. Leban, F. Mothe, Pith extract: a robust algorithm for pith detection in computer tomography images of wood—application to 125 logs from 17 tree species. *Comput. Electron. Agric.* **85**, 90–98 (2012)
17. A. Krähenbühl, B. Kerautret, I. Debled-Rennesson, F. Longuetaud, F. Mothe, Knot detection in X-Ray CT images of wood. *Adv. Vis. Comput. II LNCS* **7432**, 209–218 (2012)
18. Q. Wei, S.Y. Zhang, Y.H. Chui, B. Leblon, Reconstruction of 3D images of internal Log characteristics by means of successive 2D Log computed tomography images. *Holzforschung* **63**, 575–580 (2009)
19. J. Nystrom, Automatic measurement of fiber orientation in softwoods by using the tracheid effect. *Comput. Electron. Agric.* **41**, 91–99 (2003)
20. J. Zhou, J. Shen, Ellipse detection and phase demodulation for wood grain orientation measurement based on the tracheid effect. *Opt. Lasers Eng.* **39**, 73–89 (2003)
21. M. Hu, M. Johansson, A. Olsson, B. Enquist, Comparison of local variation of modulus of elasticity determined on basis of scanned fiber angles and full strain field measurements, in *The 18th International Nondestructive Testing and Evaluation of Wood Symposium*, Madison, 2013
22. A. Olsson, J. Oscarsson, E. Serrano, B. Kallsner, M. Johansson, B. Enquist, Prediction of Timber Bending Strength and In-member Cross-sectional Stiffness Variation on the Basis of Local Wood Fiber orientation. *Eur. J. Wood Prod.* **71**, 319–333 (2013)
23. M. Hu, M. Johansson, A. Olsson, J. Oscarsson, B. Enquist, Local variation of modulus of elasticity in timber determined on the basis of non-contact deformation measurement and scanned fiber orientation. *Eur. J. Wood Prod.* **73**, 17–27 (2015)
24. CNS 450 O2001, Wood-sampling methods and general requirements for physical and mechanical tests (2013)

Chapter 36

Auto-Calibration and Micro-Flow Injection Procedure Based on Automated Hydrodynamic System for Spectrophotometric Determination of Cobalt

R.M. Camarillo E., J.A. Padilla M., J.A. García M., C.A. Ocón D., Ch. Reyes C., J.M. Camarillo E., and R. Rodríguez R.

Abstract The development of analytical system has been focused on two aspects, first in the design of large versatile and robust equipment where operation is performed in a controlled laboratory. The second aspect developed in parallel, is focused on miniaturization and automation of analytical systems that can be used in the place where the sample is taken and generate results in real time. In this work, an automated hydrodynamic system was implemented with miniaturized actuators to provide a micro-flow injection and auto-calibration. The micro-flow injection procedure was operated exploited the multicommutation technique for handling solutions. The auto-calibration was operated by a virtual instrument allowing the response control process in real time. Automated micro-flow injection was developed to perform calibration. The auto-calibration process, the precision and accuracy of the hydrodynamic system was evaluated by spectrophotometric determination of cobalt concentration. A linear response was observed from 0.1 to 3.0 mg L⁻¹. The result was validated with a commercial instrument.

Keywords Analytical system • Hydrodynamic flow system • Auto-calibration • Spectrophotometric • Cobalt determination

36.1 Introduction

There is a need for chemical information to perform monitoring and control of chemical processes by determining the chemical concentration, this drives to the development of *in situ* instrumentation systems, with high selectivity and sensitivity, preferably autonomous, capable of being applied to more than one type of sample, that allows for simple modification and adaptation of the analytical method, enabling *on-line* and *real-time* measurements [1]. In the last decades, refined methods and techniques of analysis had been developed because they have been becoming necessary for more analytical information of increasingly lower concentrations, greater efficiency, accuracy and precision in measurements, in a shorter period of time and a at lower cost and with minimum human intervention [2–6]. The trend has resulted in the development of new analytical instrumentation systems, based in different strategies for integrating the steps of the analytical process. Microanalyzers based on flow injection system, generally use larges equipment which results in larges systems that limit portability. Recent developments have been towards to instrumentation, automation of analytical processes for continuous information to perform analysis *in situ*, *on-line* and *real-time*, focused on the philosophy of green chemistry and the wireless communications [1, 7, 8].

According to the industrial purification process of the ZnO product, it is currently performed in the electrolytic process for obtaining zinc, there is a need for chemical information to perform monitoring and control of chemical process, determining the concentration of metals such as cobalt, copper and cadmium. Nowadays this monitoring is achieved frequently off-line [9]. The flow injection analysis FIA, generally is used in order to determine these elements in an industrial process [10].

Analyzers based on flow injection systems, generally use large equipment, resulting in large systems limiting its portability. Several alternatives have been reported for the management of fluids as hybrid systems, incorporating injection of solutions by microsyringes, microburettes and micropumps to drive switching solutions [11–15]. An investigation about

R.M. Camarillo E. (✉) • C.A. Ocón D. • C. Reyes C. • J.M. Camarillo E. • R. Rodríguez R.
Instituto Tecnológico de la Laguna, Blvd. Revolución and Calz. Cuahtémoc, S/N, Torreón, Coahuila 27000, Mexico
e-mail: rosycamarillo01@hotmail.com

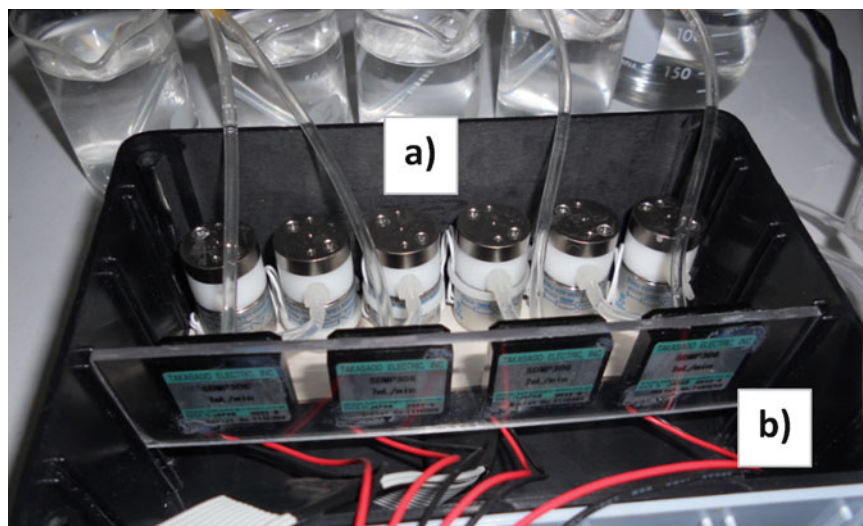
J.A. Padilla M. • J.A. García M.
Instituto Tecnológico de Celaya, Av. Antonio García Cubas and Av. Tecnológico, Celaya, Guanajuato 38010, Mexico

the pulsed flows was presented [16]. Currently, in the industry for the determination of trace heavy metals are used colorimetric methods involving nitric acid, acetates and citrates raising them to temperatures above 80 °C [17, 18]. According to these methods, the analytical process to cobalt measurement has been simplified, miniaturized and automated. In this work an auto-calibration and microflow injection procedure for spectrophotometric determination of cobalt at 525 nm was developed. An automated hydrodynamic system [19] based on miniaturized actuators and multicommutation techniques, for *in situ*, *on-line* and real-time applications were used. The procedure can be reprogrammed and reconfigured to implement any other method of analysis to determine others analytes as copper (560–650 nm) and cadmium (477–566 nm) in the industrial process. A microfluidic device fabricated in LTCC Low Temperature Co-fired Ceramics (LTCC) (Low Temperature Co-fired Ceramics) was used to operate as an autonomous node wireless communication [20]. Energy management system based on a rechargeable lithium ion battery was implemented. The details of the proposed procedure are discussed.

36.2 Hydrodynamic System

Usually, the operation of analytical systems is performed in controlled laboratory environments and uses large volumes of reagents and samples. The hydrodynamic flow system miniaturization, would allow independence to these laboratories to perform portable and *in situ* analysis where the sample is taken, as well as the incorporating an *on-line* process to generate *real-time* results. Miniaturization, also offers certain advantages such as reduced reagent consumption, the reduction in waste generation and increase the number of analysis per day [21]. The hydrodynamic system is based on piezoelectric micro-pumps (Takasago Electric, Inc., Nagoya, Japan), with dimensions of 25 mm × 25 mm × 4.8 mm. The micro-pumps flow rate is controlled by drive voltage and frequency, so this may be implemented an electronic control. The injection flow system was implemented using 2-way solenoid NC micro-valves (161 T010, NResearch, NJ, USA) in a single line. The operation of each micro-valve was based on multicommutation techniques to generate a flow network in which all the steps, involved in the analytical process, could be implemented independently [22]. Basically, the injection process was based by programming of the sequences times to facilitate the automation. With this approach is possible to generated fixed and constant volumes. In order to provide a major versatility and robustness to miniaturized hydrodynamic flow system, was integrated a collector with six micro-valves, each one interconnected to a micro-pump. Therefore, the automated hydrodynamic system has the capability to manage 6 configurable solutions at different flow rate and injection volume. The hydrodynamic flow system shows in Fig. 36.1.

Fig. 36.1 Automated hydrodynamic system; (a): micro-valves, (b): micro-pumps



36.3 Electronic Control and Wireless Communication

The electronic control was designed based on the PIC18F4550 (Microchip Technology Inc., Chandler, USA) for data acquisition signal processing and control of the hydrodynamic flow system, RGB optical detection system, power management and the wireless communication between the microanalyzer and personal computer (PC). Electronic components SMD Surface mounted devices (SMD) (surface mounted devices) were selected to reduce the dimensions of the PCB Printed circuit board (PCB) (printed circuit board) according to microanalyzer dimension $53 \times 53 \text{ mm}^2$. Each micro-pump was connected with a driver control. The automation process (auto-calibration and sample analysis) was configured and controlled using a virtual instrument program. The microcontroller acquires the signal generated by the photodetector and sends it to the PC by Bluetooth in *real-time*. Wireless communication between devices and electronic control module was implemented by Bluetooth LM-058 (LM Technologies, London, UK). The modules are RS232 serial port adapters to v2.1 Bluetooth transmission links, in order to eliminate the cabling generally used for data acquisition module. Its dimension was $35 \times 65 \times 16 \text{ mm}$ and a 5 cm antenna was integrated to link devices range up to 100 m and 3 Mbs transmission speed. To verify correct Tx/Rx (transmission/reception) operation, it integrates three LED power indicators, data transmission and Bluetooth link. As an option to the portability and to operate as a wireless sensor node, the microanalyzer included an energy management system based on a rechargeable lithium ion battery (VSO-F550H Amstron, USA) of 7.2 Vdc and 2.2 Amp/h. In order to minimize noise, an electric regulator network was implemented in the control module. The regulators were 3.3 V and 5 V to maintain the independent supply to different devices avoiding voltages fluctuations to obtain a correct measurement.

36.4 Reagents and Microanalyzer

All solutions were prepared with analytical grade chemicals and de-ionized water. The baseline solution was prepared with 0.5 mol L^{-1} sodium citrate 2 mol L^{-1} sodium acetate solutions and NRSalt at 2.6 mM as reagent. A 0.25 mol L^{-1} sulfuric acid (H_2SO_4) as a carrier solution was prepared in order to decompose complex of cobalt. Working solutions were prepared by dilution of a 1000 mg L^{-1} cobalt stock in a final volume of 50 mL in water. All reagents were Sigma Aldrich (Sigma Aldrich Química, Toluca, México).

For procedure evaluation, was used a microanalyzer manufactured by LTCC technology [23]. This integrates a three-dimensional serpentine micromixer type L [24], with 4 inputs and 1 output for fluids. The sample cell with an optical path of 25 mm storing volume of $100 \mu\text{L}$ was placed after mixing. The optical system were implemented with a RGB LED module integrating a Full color surface mount LED lamp AAA-505103 (Kingbright Co., CA, USA.) and detection module integrating a light converter programmable frequency TCS3200 (Texas Advanced Optoelectronic Solution TAOS, Texas, USA). Connectors for the inlet and outlet solutions were made of titanium (MAFSA, Inc., Torreon, Mex.) with outer diameter $\text{DO} = 1.5 \text{ mm}$. The microanalyzer total area was $53 \times 53 \times 3 \text{ mm}$. The hydraulic connections used were based on silicone tubes $\text{DI} = 1.5 \text{ mm}$ (NRResearch, NJ, USA).

36.5 Procedure

36.5.1 Cobalt Spectrophotometric Measurement

The fundamental principle of molecular absorption spectrophotometry also called colorimetry is based on the measurement of radiation absorbed by a sample: absorbance (A); according to the relationship between the radiation leaving the sample: transmittance (T) and radiation light source before entering the sample. The absorbance was calculated by the (36.1) [25]

$$A = \log \frac{S_a - S_d}{S_r - S_d} \quad (36.1)$$

Where S_a is the analytical signal, S_r is the reference signal and S_d is the dark signal (signal intensity obtained with the LED turned off). According to the method for determination of cobalt [19], the microanalyzer was evaluated by colorimetric detection based on the reaction of cobalt with nitroso-R-salt. This reaction generates a colored cobalt sample. H_2SO_4

allowing decomposition of the substance formed enabling quantification of Co, it is seen when there is a decrease in the target signal. The microflow injection procedure was developed to cover auto-calibration analysis of cobalt within a range of 0.1–3 ppm. To avoid interference signal acquisition, the microanalyzer was placed inside a black box.

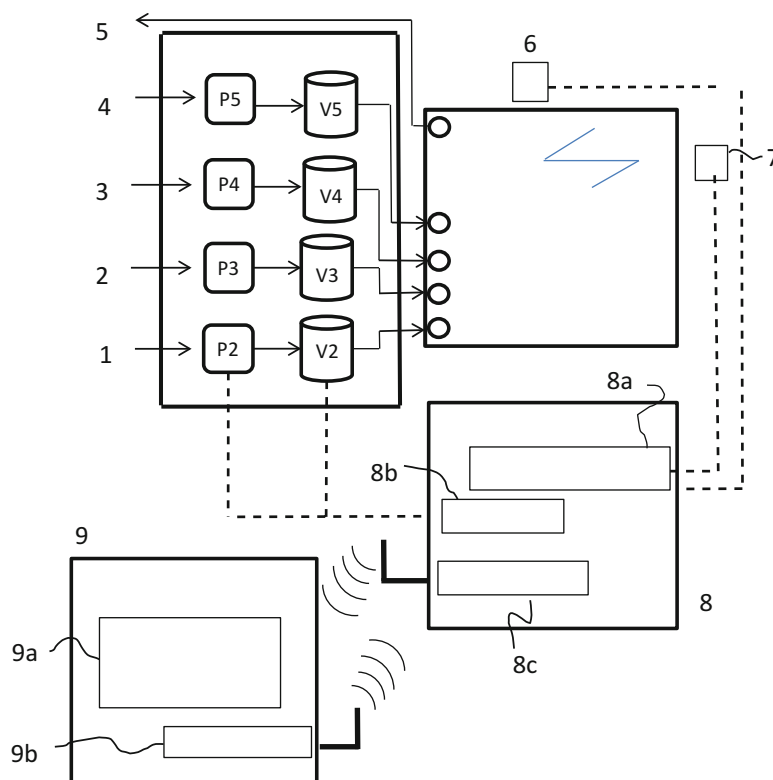
36.5.2 Auto-Calibration Process

The auto-calibration procedure establish specific conditions to define the relationship between the microanalyzer response developed and the analyte concentration, which leads to define the operating range wherein the microanalyzer can perform measurements to determine the concentration of cobalt in a real sample. For auto-calibration was developed an automated process for the injection of three reagents and a standard solution of cobalt. The injection volume of reagents and standard solutions are programmed based on operating times of on/off valves. The carrier solution composed of sulfuric acid, the standard solution and the reagent RNSalt are injected at a flow rate of 1.5 mL min^{-1} , the buffer solution comprises a mixture of sodium acetate and sodium citrate are injected at a flow rate of 3 mL min^{-1} . For the evaluation of auto-calibration and microflow injection procedure the experimental setup of Fig. 36.2 was implemented. The auto-calibration procedure begins with the development of baseline BL circulated by first mixing between the buffer and reagent throughout the analysis process. Later was injected the carrier solution to mix with the reagent and buffer. This mixture is considered the reference signal S_r for analytical measurement of absorbance. To inject the standard solution (as sample) is necessary to stop the flow of carrier solution (H_2SO_4) allowing just buffer, reagent and sample flows. When the cobalt standard solution contacts with NRSalt, coloration as a result of the reaction occurs. This physical phenomenon is measured and represents the response or reaction of the analyte concentration (Co) that appeared in the process. This is considered as the analytic signal S_a to calculate the absorbance. The insertion sequence of solutions based on time is shown in Fig. 36.3, operating times of the 4 valves configured are observed, where t_1 displays time on and t_2 time off are applied to each of the valves.

• Baseline

For the generation of the analytic base line, the injection buffer solutions (sodium acetate + sodium citrate) and reagent (RNS) are activated micro-valves V3 and V4 respectively. Through multi-commutation, the micro-valves operate *on-time* t_1 and *off-time* t_2 . The minimum time for filling the micro-channels occurs at time t_0 . After t_0 the carrier (H_2SO_4) is

Fig. 36.2 Block diagram for experimental set-up: 1–4 are inlet solution and 5 waste, 6 Detector RGB, 7 RGB LED, 8 Electronic Module: 8a Detector and LED RGB control, 8b Microactuators control, 8c Wireless communication, 9 Computer: 9a Virtual instrument, 9b Wireless communication, P2-P5 Micropumps, V2-V5 Microvalves [19]



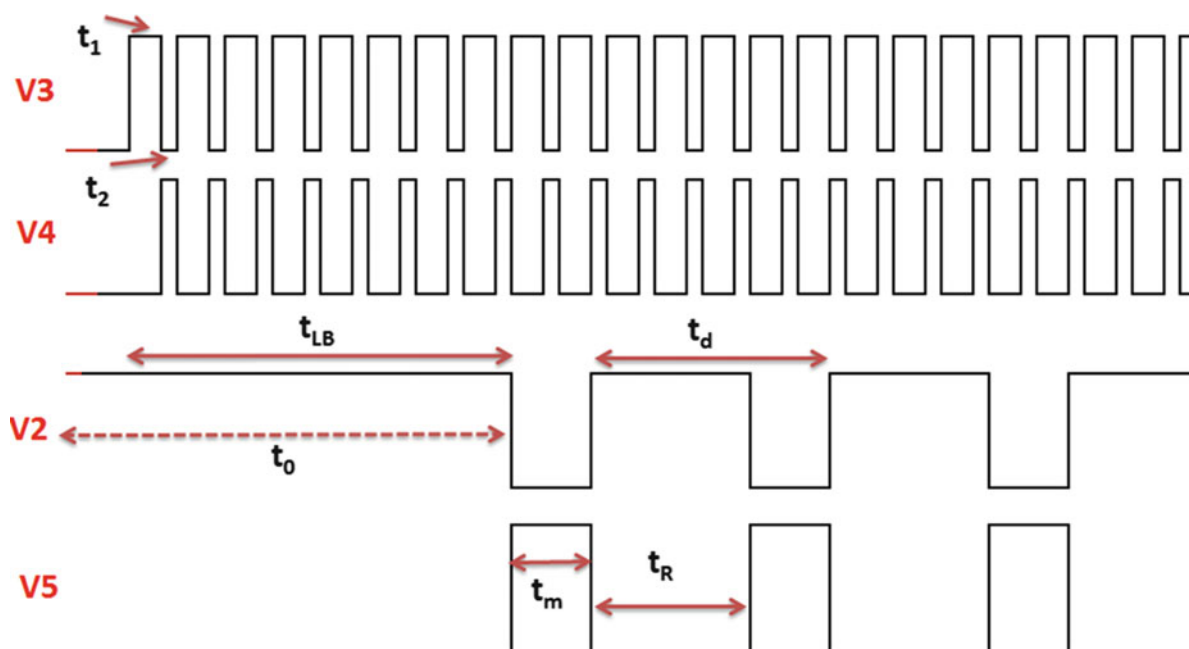


Fig. 36.3 Micro-valves operation times diagram by multi-commutation. V3: injection time of buffer solution; V4: injection time of R-NSalt; V2: injection time of H₂SO₄ and V5: injection time of Co sample

allowed to flow by activating valve V2, mixing it with the reagent and buffer. This mixture forms the baseline solution, the activated time of V2, V3 and V4 valves corresponds to t_{LB} time necessary for stability of the baseline. This mixture flows to the detection cell and S_r signal is obtained.

- **Standard solution injection**

For the injection of the sample solution (cobalt standard solution), it is necessary to stop the flow of carrier solution. With this observation, V2 and V5 are operated by commutation. In this case, the operation cycle is set to V5 with $t_1 = tm$ and V2 with $t_2 = tm$, where tm is the sample injection time. This mixture flows to the detection cell and S_a signal is obtained. To validate the repeatability and reproducibility of the auto-calibration measurements performed at least in triplicate, allowing a recovery time of the baseline between samples corresponding to a t_R time. To make an acceptable auto-calibration microanalyzer, should be performed recalibration at least 3 points or standard solutions at different concentrations.

- **Cleaning micro-channel**

After the calibration and S_a and S_r signals were obtained to calculate the absorbance, bi-distilled water is allowed to flow in all ports, micro-actuators, connections, as well as the internal channels of the microfluidic platform so any residue or material formed by the chemical reaction that could result in obstructions and damage to microactuators. This is done at least for a time t_0 until a minute.

36.5.3 Automation Process

To perform automated calibration, a virtual instrument was implemented. The design of this virtual instrument consists in two control windows. In one of these, the *Configuration Window*, the hydrodynamic parameters were set and also the optical detection system was configured. In the *Automation Window*, the parameters of the auto-calibration like the sample volume (tm), the injection operation in triplicate, recovery time (t_R), and response monitoring in *real-time* were set. This automation window allows the storage of data sending them to a file for later analysis.

36.6 Results

36.6.1 Precision and Accuracy of Automated Hydrodynamic System

To the auto-calibration process, the precision and accuracy of the hydrodynamic system was evaluated. Experimental precision was considered as the repeatability and stability of the pumped and injection by the microactuators performance. The repeatability was based on successive flow rate measurements as volume per minute of distilled water. Different values of frequencies between 1 and 5 Hz were selected. The hydrodynamic equation that describes the linear relationship between frequency and flow rate was $FR = 0.2146 [\text{Hz}] + 0.4318$; $r^2 = 0.9992$. Lowest flow rate was found at $650 \mu\text{L min}^{-1}$ (RSD = 1.78 % (n = 5; 95 % confidence)). For 1.5 mL min^{-1} flow rate was found (RSD = 1.55 % (n = 5; 95 % confidence)). Response stability was proved for the continuous flow for 5 min. A constant flow rate was developed of each frequency confirming the suitability and precision of the automatic control of hydrodynamic system for auto-calibration process.

36.6.2 Analytical Results

The initial analysis was performed in triplicate with a standard solution of cobalt to validate sensitivity sensor response. After that, auto-calibration is performed by automated injection for each concentration patterns acquiring triplicate values S_a and S_r in each analysis. Since the acquisition of these experimental data is possible to determine the absorbance. Once stored data can be processed and absorbance calculations according to Equation 1, defining the correlation between the cobalt concentration and the absorbance finding the operability range microanalyzer. In the metallurgical industry, the cobalt measuring is in the range of 0.01–2.8 ppm. According to this operating range, the microanalyzer auto-calibration was performed. After each measurement, the detector was calibrated using a baseline BL as reference. A linear response was observed. The microanalyzer equation that describes the linear relationship between concentration (Co) and absorbance (A) is $A = 0.0521[\text{Co}] + 1.6757$; $R^2 = 0.9919$. The calibration curve shows in Fig. 36.4.

For a concentration of 0.75 mg mL^{-1} , the RSD obtained was 0.000808 % (n = 4; 95 % confidence). The reproducibility of this method was determined by comparison of slopes of the calibration curves during the course of 5 days. There were no significant differences between calibration curves with 95 % confidence. The consumption of reagents was estimated as 1.11 mg of RNSalt, 20.75 μg of H_2SO_4 , 32.43 mg of citrate sodium and 36.57 mg of acetate sodium per determination. The hydrodynamic system with miniaturized actuators was integrated for fluid management and reagent

Fig. 36.4 Calibration curve

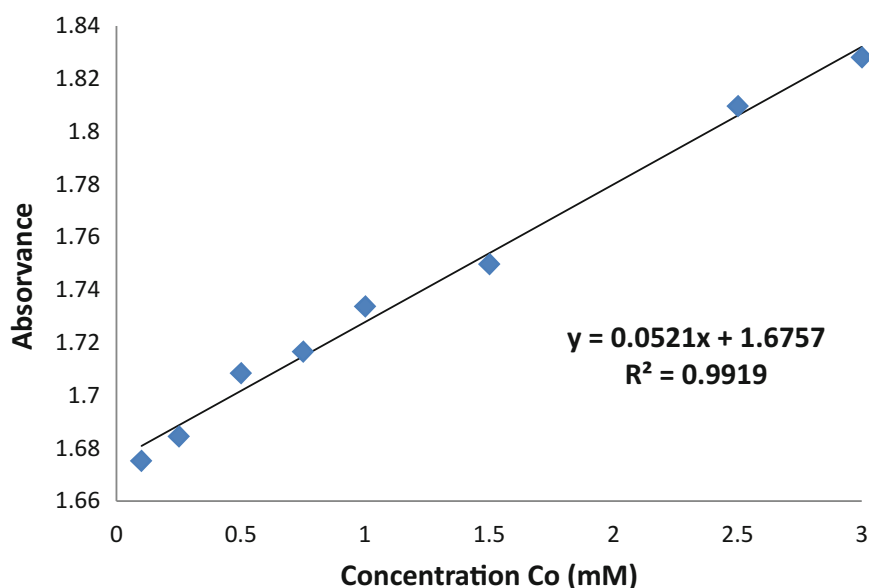


Table 36.1 Comparative consumer values of reagents and waste

System	H ₂ SO ₄	Buffer ^a	RN Salt	Co	One calibration point	Total calibration (waste)
Peristaltic pump and 6 way valve	750 μ L	3 mL	1.5 mL	250 μ L	5 mL	40 mL
Hydrodynamic system with auto-calibration and microflow injection procedure	83 μ L	222 μ L	111 μ L	250 μ L	666 μ L	5.3 mL

^aBUFFER: sodium citrate + sodium acetate

Table 36.2 Power consumption

Device	Operation	Power consumption
Micropump driver [26]	Stand by	40 mW
	Operation	240 mW
Micropump [27]	Maximum flow	18 mW
	Minimum flow	71 mW
Valve [28]	Off	10 mW
	On	1 W
Control system	Operation	603 mW
Bluetooth module [29]	Rx	5 mW
	Tx	100 mW μ s ⁻¹

consumption was reduced significantly as well as the generation of waste. The amounts of reagents injecting automation were controlled by the microflow injection process delivered only the necessary volume. The internal microfluidic structure had a total volume of 600 μ L through their channels by integrating the flow system calibration, the reagent consumption was reduced at 7.5 times compared to the use of peristaltic pump and 6-way valve. This new procedure is oriented toward philosophy of green chemistry. The comparative values of consumption and chemical waste can be seen in Table 36.1.

36.6.3 Electrical Result

The current required for the system in operation was 750–800 mA and standby was 183 mA. The Battery supplies 2.2 A-h. The dissolution pattern injection process is done in 30 s. Therefore the microanalyzer can perform 352 samples to operate with battery. With a speed of 2 measurements per hour, the microanalyzer can work 7 days. To extend and to supply the necessary current for a longer time, it is possible to adapt another battery in parallel with the existing battery. This result shows that the microanalyzer could be a step towards the development of portable analytical systems for monitoring *online*, *on-site* and in *real-time*.

36.7 Conclusion

Cobalt ion analysis was based on R-N-Salt reaction. To the flow of solution composed to a buffer solution and a chelating agent for masking metal ions, other than cobalt ions was added a coloring reagent for cobalt and mixed continuously into the microfluidic LTCC device. R-N-Salt reagent was added for decomposing other complexes of metals than cobalt. A sample volume was added, a highly coloured compound was obtained and finally the mixing was passed through an optical detector where by spectrophotometric the cobalt concentration is determined. Cobalt concentration was determined based on the method for measuring concentrations of cobalt in the electrolytic process for obtaining zinc by Hayashibe Y. The auto-calibration process aims to develop specific actions to define the relationship between the response of microanalyzer developed and analyte concentration (Co), based on standard solutions allowing to defining the operating range in which the microanalyzer can measure the concentration of cobalt in a real samples. To perform the auto-calibration a microflow injection procedure was developed.

An auto-calibration microflow injection procedure was developed using an automated hydrodynamic system and a microanalyzer LTCC. Their logic program is simple, if the flow rate is known and constant, the volume of insertion of the solutions can be controlled by the operation time of microactuators. The automated injection sequence was operated exploiting the multicommutation technique for solutions handling. In this work multicommutation was configured by wireless to prepare dilutions from a stock solution. The autonomous calibration was made with cobalt standard solutions in range from 0.1–3 ppm concentrations.

The implemented system and the microflow injection procedure shows the adaptability compared with other methods as FIA, the flexibility of the procedure is that easily to modification of its parameters. This characteristic allows the sample analysis to be performed in optimum experimental conditions in order to use other colorimetric determination. The autocalibration procedure, reduced sample and reagent volumes and its low power consumption result in an autonomous portable system for *in situ* and *in-line* monitoring of environmental variables and for the control of industrial processes. The result of this application could lead to advances in the development of wireless microanalyzer networks.

References

1. E.R. Camarillo, R.R. Rodriguez, Microanalyzer with optical detection and wireless communications. *Sensors Actuators A Phys.* **199**, 181–186 (2013)
2. J. Ruzicka, G. Marshall, Sequential injection: a new concept for chemical sensors, process analysis and laboratory assays. *Anal. Chim. Acta* **237**, 329–343 (1990)
3. B. Reis, M. Giné, E. Zagatto, J. Lima, R. Lapa, Multicommutation in flow analysis. Part 1. Binary sampling: concepts, instrumentation and spectrophotometric determination of iron in plant digests. *Anal. Chim. Acta* **293**, 129–138 (1994)
4. V. Cerda, J.M. Estela, R. Forteza, A. Cladera, E. Becerra, P. Altamira et al., Flow techniques in water analysis. *Talanta* **50**(4), 695–705 (1999)
5. J. Ruzicka, Lab on-valve: microflow analyzer based on sequential and bead injection. *Analyst* **125**, 1053–1060 (2000)
6. R. Lapa, J. Lima, B. Reis, J. Santos, E. Zagatto, *Anal. Chim. Acta* **466**, 125–132 (2002)
7. Z.M. Da Rocha, C.C. Martinez, A.C. Seabre, R.M. Gongora, C.J. Alonso, Compact and autonomous multiwavelength microanalyzer for in-line and in situ colorimetric determinations. *Lab Chip* **12**, 109–117 (2012)
8. X. Xiao, T. Zhu, L. Qi, L. Moga, X. Zhang, MS-BWME: A wireless real-time monitoring system for brine well mining equipment. *Sensors* **14** (10), 19877–19896 (2014)
9. A.M. Bond, 200 years of practical electroanalytical chemistry: past, present and future directions illustrated by reference to the on-line, on-stream and off-line determination of trace metals in zinc plant electrolyte by voltammetric and potentiometric techniques. *Anal. Chim. Acta* **400**, 333–379 (1999)
10. Y. Izadmanesh, J. Ghasemi, A rapid, automated gradient flow injection-spectrophotometric technique for study of metal complexation reactions. *Talanta* **128**, 511–517 (2014)
11. T.E. Rodenas, F.R.P. Rocha, F.R. Boaventura, R.A. Morales, M. Guadia, Evaluation of a multicommutated flow system for photometric environmental measurements. *J. Autom. Methods Manage. Chem.* **2006**, 1–9 (2006). ID 20384
12. N. Ibañez, J. Alonso, C. Martinez, F. Valdes, Green tape ceramics new technological approach for integrating electronic and fluidics in microsystems. *Trends Anal. Chem.* **7**(1), 24–33 (2008)
13. A. Fonceca, I.M. Raymundo, J.R. Rohwedder, L.O. Ferreira, Construction and evaluation of a flow injection micro-analyzer based on urethane-acrylate resin. *Anal. Chim. Acta* **603**, 159–166 (2007)
14. S. Silva, R.P. Rocha, A flow injection procedure based in solenoid micro-pump for spectrophotometric determination of free glycerol in biodiesel. *Talanta* **83**, 559–564 (2010)
15. R.M. Camarillo, J. Alonso, Development of a hydrodynamic system for miniaturized system flow analysis. *Rev. Mex. Ing. Quim.* **11**(2), 299–307 (2012)
16. P. Gonzalez, M. Knochen, M.K. Sasaki, E. Zagatto, Pulsed flows in flow analysis: potentialities, limitations and applications. *Talanta* **143**, 419–430 (2015)
17. Y. Hayashibe et al., Method for measuring impurity concentration and removing impurities from electrolytic solution for electrowinning of zinc. USA Patente US005178771A, 12 Jan 1993
18. B. Purachat, S. Liawruangrath, P. Sooksamitti, S. Rattanaphani, D. Buddhasukh, Univariate and simple optimization for the flow-injection spectrophotometric determination of copper using nitroso-R salt as a complexing agent. *Anal. Sci. JSAC* **17**, 443–447 (2001)
19. E.R.M. Camarillo, Sistema automatizado de analisis con comunicacion inalambrica utilizando tecnologia de ceramicas verdes de cocimiento conjunto a bajas temperaturas para mediciones espectrofotometricas in situ y on-line de variables ambientales e industriales. MEX Patente en tramite Mx/a/2013/013751, 25 Noviembre 2013
20. I. Akyildiz, V.M. Can, *Wireless Sensor Networks* (Wiley, Torquay, 2010)
21. D. Reyes, D. Iossidis, P. Aroux, A. Manz, Micrototal analysis system. 1. Introduction, theory and technology. *Anal. Chem* **7**(12), 2623–2636 (2002)
22. F. Rocha, B. Reis, E. Zagatto, Multicommutation in flow analysis: concepts, applications, potentialities. *Anal. Chim. Acta* **466**, 125–132 (2002)
23. R. Camarillo, J. García, Automated microanalyzer with auto-calibration and wireless control for in situ and on-line applications. *Analytical Instrumentation*, 1a edn. (Studium Press LLC, New Delhi, 2015)
24. N.T. Nguyen, S.T. Wereley, *Fundamentals and Applications of Microfluidics*, 2nd edn. (Artech House, Boston, 2006)

25. A. Fonceca, J. Raymundo, M. Ivo, A multichannel photometer based on an array of light emitting diode for use in multivariate calibration. *Anal. Chim. Acta* **522**, 223–229 (2004)
26. Data Sheet Takasago, Piezoelectric Micropump Driver Board MPD-200A
27. Data Sheet Takasago, Piezoelectric Micropump SDMP306
28. Data Sheet NResearch, Microvalves 161T010 2 way NC
29. Data Sheet LM Technologies, LM 058 RS232 to Bluetooth adapter

Chapter 37

Mathematical Model to Predict the Stress Concentration Factor on a Notched Flat Bar in Axial Tension

F.J. Ortega-Herrera, A. Lozano-Luna, J.P. Razón-González, J.M. García-Guzmán, and F. Figueroa-Godoy

Abstract This paper presents the development of a polynomial equation of second degree which allows to predict the value of the stress concentration factor on a flat bar with two notches under to axial load for different ratios r/L (notch radio/distance between notches) y W/L (bar width/distance between notches). To obtain the mentioned equation, one hundred simulations are carried out on finite element software to determine maximum stress on the bar and then the stress concentration factor is calculated. A regression analysis using the least square method is applied to fit the data to a quadratic polynomial equation which depends on the ratios r/L y W/L . The equation obtained presents a correlation value $R^2 = 0.98$, thus this equation represents reliably the obtained data. The results estimated by the proposed equation for stress concentration factor are compared with the results presented by other authors; a good matching among these approaches is obtained.

Keywords Stress • Concentration • Factor • Bar • Tension

37.1 Nomenclature

The nomenclature used in this study is shown in Table 37.1.

37.2 Introduction

The estimation of stress concentration factors is a difficult task for engineers when dealing with the design of an element that has sharp geometrical changes, such as holes and wedges, among others. It is important to minimize the stress concentration because strains can produce material plasticity by themselves; they can lead to fragile material fracture. If there are repeated loads, they can speed up the fatigue process and accelerate the material chemical corrosion. The stress intensity factors at sharp vertices are found as a result of the limit transition from rounded vertices by using the relation between the stress intensity factors and stress concentration factors at the sharp and rounded tips of a V-shaped notch [1]. According to Neuber's formula, the stress concentration factor of periodic notches can be evaluated by considering a single notch characterized by the same shape but a reduced depth [2]. In [3], notch stress intensity factors of a number of flat plates with periodic sharp V-notches under a remote applied normal stress are calculated. The averaged value of the strain-energy density over a well-defined volume is used to assess the static strength of U-notched specimens under mixed mode loading (I + II). The volume is centered considering the maximum principal stress present on the notch edge, by rigidly rotating the crescent-shaped volume already used in the literature to analyze U- and V-shaped notches under mode I loading [4].

In the presence of sharp (zero radius) V-shaped notches, the notch stress intensity factors (N-SIFs) quantify the intensities of the asymptotic linear elastic stress distributions [5]. In [6] an exact, closed-form relationship correlating the generalized stress intensity factors of classic notches (parabolic, semi-elliptic and hyperbolic), characterized by an exact mathematical profile, and pointed V-notches is obtained by using in combination the analytical expressions already available in the literature and some new equations developed in the present contribution. The theoretical stress concentration factor depends on the length of the member and on other standard geometric parameters; these factors can reach significantly larger values

F.J. Ortega-Herrera (✉) • A. Lozano-Luna • J.P. Razón-González • J.M. García-Guzmán • F. Figueroa-Godoy
Electromechanical Engineering Department, Instituto Tecnológico Superior de Irapuato,
Carr. Irapuato-Silao km 12.5, Irapuato, Gto 36821, Mexico
e-mail: frortega@itesi.edu.mx; alozano@itesi.edu.mx; jurazon@itesi.edu.mx; migarcia@itesi.edu.mx; fernando.figueroa@itesi.edu.mx

Table 37.1 Nomenclature

Symbol	Definition	Symbol	Definition
A	Cross-sectional area of the plate	r	Notch radius
\mathbf{B}	Deformation matrix	R^2	Correlation coefficient
F	Force applied to the workpiece	W	Width of plate
$H_{1,2}$	Weight coefficients of Gaussian quadrature	x	Global coordinate of the element
J	Jacobian	y	Global coordinate of the element
\mathbf{K}^e	Stiffness matrix	$z_{1,2}$	Ratio W/L r/L
K_r	Stress concentration factor	η	Local coordinate of the element
L	Distance between notches	ξ	Local coordinate of the element
N	Shape function Matrix	σ_{max}	Maximum stress
$N_{1..8}$	Shape function of node 1..8	σ_t	Theoretical stress

than the corresponding existing ones for long plates [7]. It was found that predicted results of the step by step finite element method have generally good correlation with experimental results [8]. The largest discrepancy from reality is the fact that the model solutions are obtained using a linear material model [9]. The stress concentration factors in cross bores have been investigated using the finite element method [10]. It is shown that significantly larger stress concentrations appear for shorter members, the transition length concept defining the threshold between long cylinders and short cylinders [11].

The maximum stress in a bolt as well as the stress concentration factors in a bolt head fillet increase with an increase in bolt circle diameter for a given outer flange dimension [12]. The effective stress intensity factors results are found to be profoundly influenced by the Bauschinger Effect, condition for the multiply-eroded pressurized cylinder [13]. The stress distribution in bolt-nut connectors is studied using an axisymmetric finite element model [14]. Stress concentration factors have been determined for large hole to small hole diameter ratios (D/d) of 10–50 for two holes in an infinitely wide tension-loaded panel. Finite element analysis was used to model the system of two holes in a plate that approximates the infinitely wide and large case [15]. The results of scattering of elastic waves and dynamic stress in semi-infinite plates are different from those in infinite plates [16]. The maximum stress locations for bending and tension loading are approximately the same, but can differ significantly from the maximum torsional stress location. In those cases, sharp surface gradients can cause the maximum equivalent notch stress under combined bending/axial and torsional loading to be overestimated when computed based on the maximum stress concentration factors for each load component [17].

2D optimal notch shapes can be successfully used to generate near optimal 3D surface notches with partial through thickness penetration [18]. In [19], a numerical approach for the stress concentration of periodic collinear holes in an infinite plate in tension is presented. In many engineering problems involving multiphysical solid–fluid interactions, there is a broad interest to couple stress concentration relationships with thermodynamics, fluid dynamics, or even diffusion equations in order to gain understanding on stress-driven interactions at solid–fluid interfaces [20]. In [21] using the ratio of the radius of curvature of the stress concentrating feature to the minimum thickness as the only fitting variable, generalized equations for both the bending and tension stress concentration factors were obtained for two generalized models, the conic model and the elliptic-arc-fillet model, through fitting the finite element results. In a flat plate with two holes loaded on its edges the stress concentration interaction depends on the distance to size relationship between them [22]. [23] Presents a study which examines the stress concentration on a flat plate with constant thickness subjected to stress at its edges; the results obtained by the finite element method and experimental techniques do not show significant differences.

The normal stresses increase in absolute value with the hole size for all orthotropic materials [24]. The tensions that arise around the circular hole of an orthotropic plate when is subjected to hydrostatic stresses in a plane, are strongly affected by the material elastic characteristics of the used plate [25]. Theoretical factor of stress concentration for orthotropic materials is influenced significantly by the type of load applied, as well as by parameters known as the relative size of the hole [26]. Stress concentration factor in composite materials depends on the geometry of the piece. Besides, the stress concentration factor value is not sufficient, by itself alone, in the failure prediction of laminated materials [27, 28]. Discusses the stress concentration that generates a small rectangular hole with rounded edges on an orthotropic plate, noting that higher stress concentration factors are in the main axis, which is at an angle of 67.5° with the x axis.

It is said that it is difficult to establish parameters of behavior in orthotropic materials [29], but there is a strong influence among the relations of the elastic constant and stress concentration factors. In [30], they examine the stress concentration on an infinite length plate with two holes of equal radius, using finite element software, by varying the distance between the holes centers and the diameter. In [31] they do a numerical evaluation of the stress distribution produced by the effect of different load conditions, analyzing a plate for internal attachment of fractures in distal radius; their results show a stress concentration in regions adjacent to the plate holes and in the screws located at the edges of the fixing plate. In general, the

maximum stress concentration for plate of finite width with central hole under static axial load always occurs on the hole periphery [32]; also, it is established that the stress concentration factor is maximum at the end of the hole (perpendicular to the load). Moreover, the stress concentration on flat plates with circular, triangular and rectangular holes, studying the variation of the stress concentration due to the holes geometry change, is discussed in [33]. In [34], a second-degree polynomial equation is developed to analyze the stress concentration factor in a flat bar with fillets subject to axial load.

In relation with the above context, here it is developed a second degree polynomial equation to calculate the stress concentration factor on a flat bar with notches; the bar is subjected to axial tensile load. The equation is developed using the finite element software ANSYS® and use the least squares method.

37.3 Method

This section outlines the use of the Finite Elements Method (FEM) in our proposal. The paper presents the study of stress concentrators on flat bars with notches under axial loading. To analyze this study case, a square element is used with intermediate nodes, therefore it presents the finite elements equations that govern the study of a square element. Then, we present the implementation of finite elements with the help of ANSYS®. To perform the analysis in ANSYS®, which is later presented, a square of 8-node elements is used. Figure 37.1 shows a diagram of a square 8-node element.

Equations (37.1)–(37.3) are the shape functions for the corners of quadrilateral shown in Figure 37.1 as a function of the local coordinates (ξ, η), ξ_j and η_j are the coordinates of each node.

$$N_j = \frac{1}{4}(1 + \xi_j\xi)(1 + \eta_j\eta)(\xi_j\xi + \eta_j\eta - 1), \quad j = 1, 2, 3, 4. \tag{37.1}$$

$$N_j = \frac{1}{2}(1 - \xi^2)(1 + \eta_j\eta) \quad j = 5, 7. \tag{37.2}$$

$$N_j = \frac{1}{2}(1 + \xi_j\xi)(1 - \eta^2) \quad j = 6, 8. \tag{37.3}$$

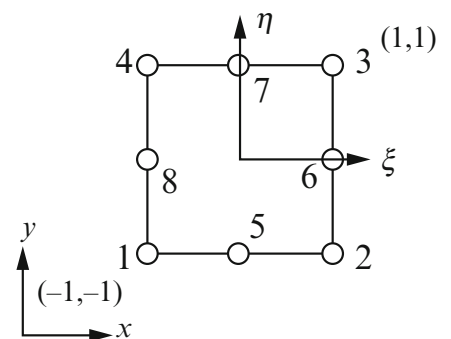
Equations (37.4)–(37.9) are the derivatives for shape function (37.1)–(37.3) with respect to the local coordinates

$$\frac{\partial N_j}{\partial \xi} = \frac{1}{4}\xi_j(1 + \eta_j\eta)(2\xi_j\xi + \eta_j\eta) \quad j = 1, 2, 3, 4. \tag{37.4}$$

$$\frac{\partial N_j}{\partial \eta} = \frac{1}{4}\eta_j(1 + \xi_j\xi)(\xi_j\xi + 2\eta_j\eta) \quad j = 1, 2, 3, 4. \tag{37.5}$$

$$\frac{\partial N_j}{\partial \xi} = -\xi(1 + \eta_j\eta) \quad j = 5, 7. \tag{37.6}$$

Fig. 37.1 8-node quadrilateral element



$$\frac{\partial N_j}{\partial \eta} = \frac{1}{2} \eta_j (1 - \xi^2) \quad j = 5, 7. \quad (37.7)$$

$$\frac{\partial N_j}{\partial \xi} = \frac{1}{2} \xi_j (1 - \eta^2) \quad j = 6, 8. \quad (37.8)$$

$$\frac{\partial N_j}{\partial \eta} = -\eta (1 + \xi_j \xi) \quad j = 6, 8. \quad (37.9)$$

The partial derivatives of the global coordinates in terms of the local coordinates are shown in (37.10)–(37.13).

$$\frac{\partial x}{\partial \xi} = \frac{\partial N_1}{\partial \xi} x_1 + \frac{\partial N_2}{\partial \xi} x_2 + \frac{\partial N_3}{\partial \xi} x_3 + \frac{\partial N_4}{\partial \xi} x_4 + \frac{\partial N_5}{\partial \xi} x_5 + \frac{\partial N_6}{\partial \xi} x_6 + \frac{\partial N_7}{\partial \xi} x_7 + \frac{\partial N_8}{\partial \xi} x_8 \quad (37.10)$$

$$\frac{\partial x}{\partial \eta} = \frac{\partial N_1}{\partial \eta} x_1 + \frac{\partial N_2}{\partial \eta} x_2 + \frac{\partial N_3}{\partial \eta} x_3 + \frac{\partial N_4}{\partial \eta} x_4 + \frac{\partial N_5}{\partial \eta} x_5 + \frac{\partial N_6}{\partial \eta} x_6 + \frac{\partial N_7}{\partial \eta} x_7 + \frac{\partial N_8}{\partial \eta} x_8 \quad (37.11)$$

$$\frac{\partial y}{\partial \xi} = \frac{\partial N_1}{\partial \xi} y_1 + \frac{\partial N_2}{\partial \xi} y_2 + \frac{\partial N_3}{\partial \xi} y_3 + \frac{\partial N_4}{\partial \xi} y_4 + \frac{\partial N_5}{\partial \xi} y_5 + \frac{\partial N_6}{\partial \xi} y_6 + \frac{\partial N_7}{\partial \xi} y_7 + \frac{\partial N_8}{\partial \xi} y_8 \quad (37.12)$$

$$\frac{\partial y}{\partial \eta} = \frac{\partial N_1}{\partial \eta} y_1 + \frac{\partial N_2}{\partial \eta} y_2 + \frac{\partial N_3}{\partial \eta} y_3 + \frac{\partial N_4}{\partial \eta} y_4 + \frac{\partial N_5}{\partial \eta} y_5 + \frac{\partial N_6}{\partial \eta} y_6 + \frac{\partial N_7}{\partial \eta} y_7 + \frac{\partial N_8}{\partial \eta} y_8 \quad (37.13)$$

The partial derivatives of shape function with respect to the global coordinates are shown in (37.14) and (37.15).

$$\frac{\partial N_{1...8}}{\partial x} = \frac{1}{|J|} \left(\frac{\partial y}{\partial \eta} \frac{\partial N_{1...8}}{\partial \xi} - \frac{\partial y}{\partial \xi} \frac{\partial N_{1...8}}{\partial \eta} \right) \quad (37.14)$$

$$\frac{\partial N_{1...8}}{\partial y} = \frac{1}{|J|} \left(-\frac{\partial x}{\partial \eta} \frac{\partial N_{1...8}}{\partial \xi} + \frac{\partial x}{\partial \xi} \frac{\partial N_{1...8}}{\partial \eta} \right) \quad (37.15)$$

J is defined by (37.16) as follows

$$|J| = \frac{\partial x}{\partial \xi} \frac{\partial y}{\partial \eta} - \frac{\partial x}{\partial \eta} \frac{\partial y}{\partial \xi} \quad (37.16)$$

Deformation matrix is defined by (37.17), while the shape function matrix is defined by (37.18).

$$B = \begin{bmatrix} \frac{\partial N_1}{\partial x} & 0 & \frac{\partial N_2}{\partial x} & 0 & \frac{\partial N_3}{\partial x} & 0 & \frac{\partial N_4}{\partial x} & 0 & \frac{\partial N_5}{\partial x} & 0 & \frac{\partial N_6}{\partial x} & 0 & \frac{\partial N_7}{\partial x} & 0 & \frac{\partial N_8}{\partial x} & 0 \\ 0 & \frac{\partial N_1}{\partial y} & 0 & \frac{\partial N_2}{\partial y} & 0 & \frac{\partial N_3}{\partial y} & 0 & \frac{\partial N_4}{\partial y} & 0 & \frac{\partial N_5}{\partial y} & 0 & \frac{\partial N_6}{\partial y} & 0 & \frac{\partial N_7}{\partial y} & 0 & \frac{\partial N_8}{\partial y} \\ \frac{\partial N_1}{\partial y} & \frac{\partial N_1}{\partial x} & \frac{\partial N_2}{\partial y} & \frac{\partial N_2}{\partial x} & \frac{\partial N_3}{\partial y} & \frac{\partial N_3}{\partial x} & \frac{\partial N_4}{\partial y} & \frac{\partial N_4}{\partial x} & \frac{\partial N_5}{\partial y} & \frac{\partial N_5}{\partial x} & \frac{\partial N_6}{\partial y} & \frac{\partial N_6}{\partial x} & \frac{\partial N_7}{\partial y} & \frac{\partial N_7}{\partial x} & \frac{\partial N_8}{\partial y} & \frac{\partial N_8}{\partial x} \end{bmatrix} \quad (37.17)$$

$$N = \begin{bmatrix} N_1 & 0 & N_2 & 0 & N_3 & 0 & N_4 & 0 & N_5 & 0 & N_6 & 0 & N_7 & 0 & N_8 & 0 \\ 0 & N_1 & 0 & N_2 & 0 & N_3 & 0 & N_4 & 0 & N_5 & 0 & N_6 & 0 & N_7 & 0 & N_8 \end{bmatrix} \quad (37.18)$$

To determine the stiffness matrix, the Gauss-Legendre quadrature is used. The stiffness matrix of each element is defined by (37.19).

$$K^e = K_{11}^e + K_{12}^e + K_{21}^e + K_{22}^e \tag{37.19}$$

where

$$K_{11}^e = tH_1^2 J(\xi_1, \eta_1) B^T(\xi_1, \eta_1) DB(\xi_1, \eta_1) \tag{37.20}$$

$$K_{12}^e = tH_1 H_2 J(\xi_1, \eta_2) B^T(\xi_1, \eta_2) DB(\xi_1, \eta_2) \tag{37.21}$$

$$K_{21}^e = tH_2 H_1 J(\xi_2, \eta_1) B^T(\xi_2, \eta_1) DB(\xi_2, \eta_1) \tag{37.22}$$

$$K_{22}^e = tH_2^2 J(\xi_2, \eta_2) B^T(\xi_2, \eta_2) DB(\xi_2, \eta_2) \tag{37.23}$$

37.4 Development

To perform the simulations by ANSYS®, steel with a modulus of elasticity of 210 GPa and a Poisson ratio of 0.28 is used. Figure 37.2 presents the flat bar with the notches analyzed. This bar has the following characteristics: for $W/L = 3$, W is 0.9 m, 3 m long, 0.1 m thick, r variable. For $W/L = 1.50$, r is 0.05 m and assumed as constant, thickness of 0.1 m, W is variable and the length is approximately three times the width. For cases $W/L = 1.20$ and $W/L = 1.10$, r is constant and equal to 0.1 m, thickness of 0.1 m, W is variable and the length is approximately three times W . The axial tension, denoted by P , is 100 kN and assumed as constant (Fig. 37.3).

For σ_{max} and K_t , a total of one hundred tests are performed, the simulations are distributed as follows: 22 simulations for the case $W/L = 3$, 24 simulations for the case $W/L = 1.50$, 26 simulations for the case $W/L = 1.20$, 28 simulations for the case $W/L = 1.10$. The stress concentration factor is obtained by (37.24).

$$K_t = \frac{\sigma_{max}}{\sigma_t} \tag{37.24}$$

The method of least squares is applied to fit data obtained from (37.16) and the simulations by ANSYS®, to a polynomial equation of second degree. The polynomial equation form is given in (37.25).

$$K_T = b_0 + b_1 z_1 + b_2 z_2 + b_3 z_1^2 + b_4 z_2^2 + b_5 z_1 z_2 \tag{37.25}$$

where, z_1 and z_2 are defined by (37.26) and (37.27).

$$z_1 = \frac{W}{L} \tag{37.26}$$

Fig. 37.2 Rectangular flat bar with notches in axial tension

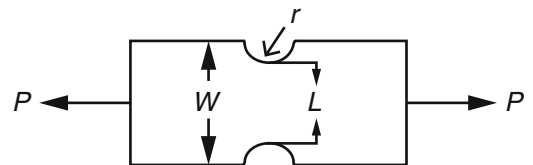


Fig. 37.3 Flat bar with notches in ANSYS®



$$z_2 = \frac{r}{L} \tag{37.27}$$

In (37.25) the coefficients $b_{0..5}$ are determined using the least squares method; the method generates the matrix system presented in (37.28).

$$\begin{bmatrix}
 n & \sum_{i=1}^n z_{1i} & \sum_{i=1}^n z_{2i} & \sum_{i=1}^n z_{1i}^2 & \sum_{i=1}^n z_{2i}^2 & \sum_{i=1}^n z_{1i}z_{2i} \\
 \sum_{i=1}^n z_{1i} & \sum_{i=1}^n z_{1i}^2 & \sum_{i=1}^n z_{1i}z_{2i} & \sum_{i=1}^n z_{1i}^3 & \sum_{i=1}^n z_{1i}z_{2i}^2 & \sum_{i=1}^n z_{1i}^2z_{2i} \\
 \sum_{i=1}^n z_{2i} & \sum_{i=1}^n z_{1i}z_{2i} & \sum_{i=1}^n z_{2i}^2 & \sum_{i=1}^n z_{1i}^2z_{2i} & \sum_{i=1}^n z_{2i}^3 & \sum_{i=1}^n z_{1i}z_{2i}^2 \\
 \sum_{i=1}^n z_{1i}^2 & \sum_{i=1}^n z_{1i}^3 & \sum_{i=1}^n z_{1i}^2z_{2i} & \sum_{i=1}^n z_{1i}^4 & \sum_{i=1}^n z_{1i}^2z_{2i}^2 & \sum_{i=1}^n z_{1i}^3z_{2i} \\
 \sum_{i=1}^n z_{2i}^2 & \sum_{i=1}^n z_{1i}z_{2i}^2 & \sum_{i=1}^n z_{2i}^3 & \sum_{i=1}^n z_{1i}^2z_{2i}^2 & \sum_{i=1}^n z_{2i}^4 & \sum_{i=1}^n z_{1i}z_{2i}^3 \\
 \sum_{i=1}^n z_{1i}z_{2i} & \sum_{i=1}^n z_{1i}^2z_{2i} & \sum_{i=1}^n z_{1i}z_{2i}^2 & \sum_{i=1}^n z_{1i}^3z_{2i} & \sum_{i=1}^n z_{1i}z_{2i}^3 & \sum_{i=1}^n z_{1i}^2z_{2i}^2
 \end{bmatrix}
 \begin{bmatrix}
 b_0 \\
 b_1 \\
 b_2 \\
 b_3 \\
 b_4 \\
 b_5
 \end{bmatrix}
 =
 \begin{bmatrix}
 \sum_{i=1}^n K_{ti} \\
 \sum_{i=1}^n z_{1i}K_{ti} \\
 \sum_{i=1}^n z_{2i}K_{ti} \\
 \sum_{i=1}^n z_{1i}^2K_{ti} \\
 \sum_{i=1}^n z_{2i}^2K_{ti} \\
 \sum_{i=1}^n z_{1i}z_{2i}K_{ti}
 \end{bmatrix} \tag{37.28}$$

37.5 Results

Figure 37.4 illustrates the behavior of K_t as a function of r/L ratio and the y-axis represents K_t , the plot lines represent the ratio W/L , for particular cases in which W/L is equal to 3, 1.5, 1.2 and 1.1.

A multiple regression is applied by the method of least squares to the hundred K_t values obtained using ANSYS[®] and (37.24). As mentioned to perform the regression is proposed (37.25), which is a second grade polynomial equation; this is shown in (37.25). To find the value of the coefficients $b_{0..5}$ in (37.25), the matrix system presented in (37.28) is solved, resulting in the following values.

$$b_0 = 2.1183 \quad b_1 = 1.8627 \quad b_2 = -13.5512 \quad b_3 = -0.3569 \quad b_4 = 26.3503 \quad b_5 = -0.9342$$

Substituting the values of $b_{0..5}$ and (37.26) and (37.27) into (37.25)–(37.29) is obtained.

Fig. 37.4 Stress concentration factor K_t of a flat bar with notches in axial tension

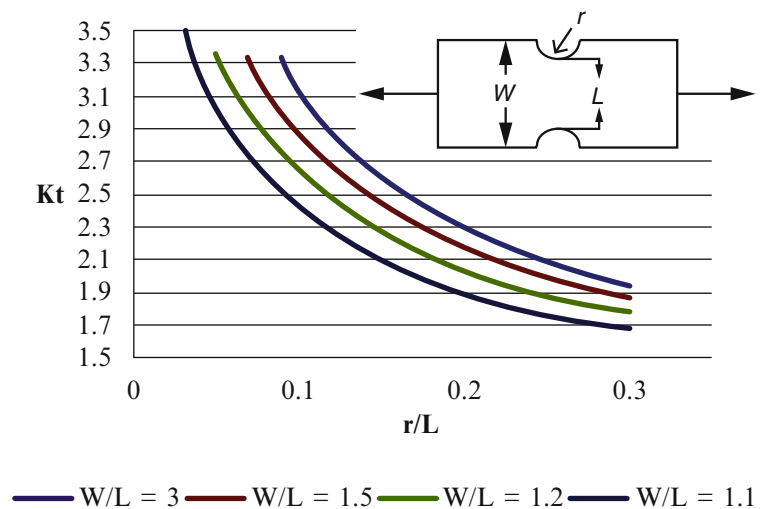


Table 37.2 Comparison with other authors

r/L	Equation (37.29)	Norton [35]	Shigley [36]	r/L	Equation (37.29)	Norton [35]	Shigley [36]
$W/L = 1.05$				$W/L = 1.5$			
0.10	2.49	1.90	1.90	0.10	2.88	2.63	2.60
0.15	2.09	1.72	1.75	0.15	2.46	2.27	2.25
0.20	1.82	1.61	1.65	0.20	2.17	2.04	2.00
0.25	1.69	1.52	1.55	0.25	2.02	1.88	1.90
0.30	1.69	1.45	1.45	0.30	1.99	1.76	1.75
$W/L = 1.1$				$W/L = 2$			
0.10	2.54	2.16	2.10	0.10	3.13	2.76	–
0.15	2.14	1.92	1.90	0.15	2.69	2.36	–
0.20	1.87	1.76	1.75	0.20	2.38	2.11	–
0.25	1.74	1.64	1.65	0.25	2.20	1.93	–
0.30	1.73	1.56	1.60	0.30	2.16	1.80	–
$W/L = 1.2$				$W/L = 3$			
0.10	2.63	2.37	2.40	0.10	3.12	2.85	2.80
0.15	2.23	2.09	2.10	0.15	2.63	2.42	2.40
0.20	1.96	1.90	1.90	0.20	2.28	2.15	2.15
0.25	1.82	1.78	1.75	0.25	2.05	1.96	2.00
0.30	1.81	1.68	1.70	0.30	1.96	1.82	1.85

$$K_T = 2.1183 + 1.8627 \left(\frac{W}{L}\right) - 13.5512 \left(\frac{r}{L}\right) - 0.3569 \left(\frac{W}{L}\right) + 26.3503 \left(\frac{r}{L}\right)^2 - 0.9342 \left(\frac{W}{L}\right) \left(\frac{r}{L}\right) \quad (37.29)$$

Equation (37.29) determines the stress concentration factor based on the relationship W/L and r/L . Equation (37.29) has a value of $R^2 = 0.98$ that strongly fits the data.

Table 37.2 presents a comparison of the obtained results using (37.29) with the results presented by Norton [35] and Shigley [36]. The values obtained by (37.29) are slightly higher than reference [35] and [36]. This implies that (37.29) yields values of stress concentration factor which are more conservative than by approaches of [35] and [36].

37.6 Conclusions

The proposed second-degree polynomial equation presents a very good correlation to the values of stress concentration factor obtained by both ANSYS[®] and (37.24), since the retrieved correlation coefficient is $R^2 = 0.9$. Comparing the obtained results for different r/L and W/L ratios calculated by (37.29) and those obtained by other authors, we can say that the approach is good since they don't present a wide variation in the value of the stress concentration factor. The application of the second-degree polynomial equation that predicts the value of the stress concentration factor causes more conservative designs. The application of the proposed equation in this work offers the advantage that a single equation can predict the value of the stress concentration factor for a wide variety of r/L y W/L ratios.

References

1. M.P. Savruk, A. Kazberuk, G. Tarasyuk, Stress concentration near holes in the elastic plane subjected to Antiplane deformation. *Mater. Sci.* **48** (4), 415–426 (2013)
2. R. Afshar, F. Berto, Stress concentration factors of periodic notches determined from the strain energy density. *Theor. Appl. Fract. Mech.* **56** (3), 127–139 (2011)
3. P. Lazzarin, R. Afshar, F. Berto, Notch stress intensity factors of flat plates with periodic sharp notches by using the strain energy density. *Theor. Appl. Fract. Mech.* **60**(1), 38–50 (2012)
4. K. Taghizadeha, F. Bertob, E. Baratia, Local strain energy density applied to martensitic steel plates weakened by U-notches under mixed mode loading. *Theor. Appl. Fract. Mech.* **59**(1), 21–28 (2012)

5. P. Lazzarin, S. Filippi, A generalized stress intensity factor to be applied to rounded V-shaped notches. *Int. J. Solids Struct.* **43**(1), 2461–2478 (2006)
6. M. Zappalorto, F. Berto, L.P. Paolo, Practical expressions for the notch stress concentration factors of round bars under torsion. *Int. J. Fatigue* **33**(1), 382–395 (2011)
7. N. Troyani, C. Gomes, G. Sterlacci, Theoretical stress concentration factors for short rectangular plates with centered circular holes. *J. Mech. Des.* **124**(4), 126–128 (2002)
8. Y. Yamashita, M. Shinozaki, Y. Ueda, K. Sakano, Fatigue crack growth life prediction for surface crack located in stress concentration part based on the three-dimensional finite element method. *J. Eng. Gas Turbines Power* **226**(1), 160–166 (2004)
9. T.F. Lehnhoff, B.A. Bunyard, Bolt thread and head fillet stress concentration factors. *J. Press. Vessel. Technol.* **122**(2), 180–185 (2000)
10. R.D. Dixon, D.T. Peters, J.G.M. Keltjens, Stress concentration factors of cross-bores in thick walled cylinders and blocks. *J. Press. Vessel. Technol.* **126**(2), 184–187 (2004)
11. N. Troyani, N. Jaimes, G. Sterlacci, C.J. Gomes, Stress concentration effects in short cylindrical vessels with holes subjected to tension: a complete account. *J. Press. Vessel. Technol.* **127**(1), 184–189 (2005)
12. G. Srinivasan, T.F. Lehnhoff, Bolt head fillet stress concentration factors in cylindrical pressure vessels. *J. Press. Vessel. Technol.* **123**(3), 381–386 (2001)
13. Q. Ma, C. Levy, M. Perl, The impact of the Bauschinger effect on stress concentrations and stress intensity factors for eroded Autofretted thick cylindrical pressure vessels. *J. Press. Vessel. Technol.* **134**(2), 021204 (2012)
14. S. Venkatesan, G.L. Kinzel, Reduction of stress concentration in bolt-nut connectors. *J. Mech. Des.* **128**(1), 1337–1342 (2006)
15. C.S. Sloan, M.D. Cowell, T.F. Lehnhoff, The effect of a large hole on the stress concentration factor of a satellite hole in a tension field. *J. Press. Vessel. Technol.* **121**(3), 252–256 (1999)
16. X. Fang, C. Hu, W. Huang, Dynamic stress concentration of a circular cutout buried in semi-infinite plates subjected to flexural waves. *J. Appl. Mech.* **74**(1), 382–387 (2007)
17. R. Rolovic, S.M. Tipton, J.R. Sorem Jr., Multiaxial stress concentration in filleted shafts. *J. Mech. Des.* **123**(2), 300–303 (2000)
18. R. Wescott, B. Semple, M. Heller, Stress analysis of near optimal surface notches in 3D plates. *J. Mech. Des.* **127**(6), 1173–1183 (2004)
19. C. Miao, Y. Wei, X. Yan, Stress concentration of periodic collinear square holes in an infinite plate in tension. *J. Press. Vessel. Technol.* **137**(5), 0512011–0512018 (2015)
20. H.E. Medina, R. Pidaparti, B. Hinderliter, Celebrating the 100th anniversary of Inglis result: from a single notch to random surface stress concentration solutions. *Appl. Mech. Rev.* **67**(1), 0108021–0108029 (2014)
21. G. Chen, J. Wang, X. Liu, Generalized equations for estimating stress concentration factors of various notch flexure hinges. *J. Mech. Des.* **136**(3), 0310091–0310098 (2014)
22. H.A. Monroy, L.A. Godoy, Un sistema computacional para la simulación de interacción de defectos estructurales. *Mecánica Computacional* **25**(1), 1–9 (2006)
23. F. Roldan, U. Bastidas, Estudio experimental y por análisis de elementos finitos del factor de concentrador de esfuerzo producido por un agujero en una placa plana. *Dyna* **69**(137), 1–5 (2002)
24. S. Maíz, R.E. Rossi, P.A.A. Laura, D.V. Bambill, Efectos de la ortotropía sobre el factor de concentración de tensiones: extensión del problema de kirsch. *Mecánica Computacional* **23**(1), 673–692 (2004)
25. D.V. Bambill, A. Susca, P.A.A. Laura, S. Maíz, Concentración de tensiones en placa ortótropa sometida a esfuerzo biaxial. *Mecánica Computacional* **24**(1), 2675–2694 (2005)
26. J.L. Méndez, J.I. Torres, Concentración de esfuerzo en una placa de material ortotrópico con una abertura elíptica, Congreso Iberoamericano de metalurgia y materiales, Habana Cuba (2006)
27. P.N. Domínguez, R.D. Santos, S.I. Robles, N.F. Ortega, Concentración de tensiones en piezas de materiales compuestos. *Mecánica Computacional* **25**(1), 537–548 (2006)
28. A. Susca, D.V. Bambill, P.A.A. Laura, R.E. Rossi, Factor de concentración de tensiones en el entorno de un orificio rectangular presente en una placa ortótropa. *Mecánica Computacional* **25**(1), 411–427 (2006)
29. A. Susca, D.V. Bambill, C.A. Rossit, Análisis de la concentración de tensiones en placas ortótropas con orificio circular sometidas simultáneamente a cargas normales y tangenciales. *Mecánica Computacional* **26**(1), 386–405 (2007)
30. M. Peñaranda, J.B. Pedroza, J.I. Méndez, Determinación del factor teórico de concentración de esfuerzo de una placa infinita con doble agujero, 8º Congreso Iberoamericano de Ingeniería Mecánica, Cusco Perú (2007)
31. A. Osorio, D. Rodríguez, B. Gámez, D. Ojeda, Análisis numérico de una placa para fijación de fracturas de radio distal utilizando el método de elementos finitos. *Rev. Ingeniería UC* **17**(1), 28–36 (2010)
32. S. Nagpal, S. Sanyal, N.K. Jain, Analysis and mitigation of stress concentration factor of a rectangular isotropic and orthotropic plate with central circular hole subjected to in-plane static loading by design optimization. *Int. J. Innov. Res. Sci. Eng. Technol.* **2**(6), 2903–2913 (2013)
33. K.M. Mohan, S. Rajest, H. Yogesh, B.R. Yeshaswini, Study on the effect of stress concentration on cutout orientation of plates with various cutouts and bluntness. *Int. J. Mod. Eng. Res.* **3**(3), 1295–1303 (2013)
34. F.J. Ortega Herrera, J.M. García Guzmán, J.P. Razón González, G. Tapia Tinoco, A. Lozano Luna, Análisis de esfuerzos en una placa plana con filetes, 3er Congreso Internacional Multi e Interdisciplinario de Ingeniería, Instituto Tecnológico Superior de Cintalapa (2014)
35. R.L. Norton, *Machine Design an Integral Approach* (Pearson, Upper Saddle River, 2006)
36. J.E. Shigley, C.R. Mischke, *Diseño en Ingeniería Mecánica* (McGraw-Hill, México, 2004)

Chapter 38

Mechanical Implementation of Kinematic Synergy for Multi-Point Grasping

M.A. Trejo Letechipia, J.A. Cortes Ramírez, and H. Aguayo Téllez

Abstract This article presents the virtual experimentation of the dynamics for diverse multipoint grasping mechanisms, similar to the anthropometric mechanism of a human hand, using a multibody dynamic simulator. These simulations will allow us to evaluate diverse mechanisms, for selecting the one with the best performance; that is the one that has the greater energy efficiency while presenting the most equal distribution of the force along the contact points.

The result tests the implementation of a grasping mechanism, and a support mechanism that allows a kinematic synergy between all the links of the mechanism, providing an immediate adaptation to the object shapes held by a force distribution along the contact points, increasing the stability of the supported object.

As another result, the mechanism also allows the transmission of force in a unidirectional way by means of a mechanical arrange in the support mechanism, which in turn allows undetermined interlocking resulting in greater energy efficiency because during this period there is no energy consumption by the actuator.

Keywords Grasping • Prosthetic hand kinematics • Kinematic synergy

38.1 Introduction

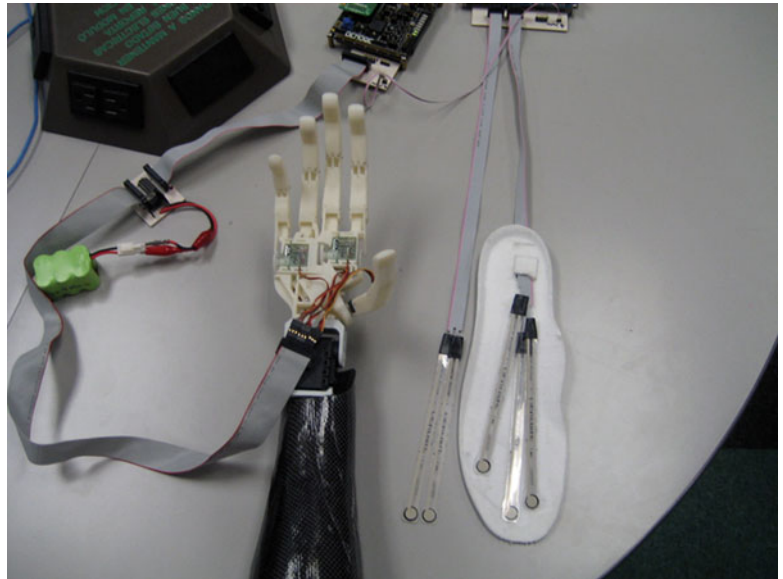
One of the main problems of modern biomedical engineering consists of designing a prosthetic hand capable of performing its natural function, taking into account several issues such as size, weight, number of control signals, mechanical properties, shape and efficiency. In the following work two previous developments will be retaken. These developments were based on the hand movements but original results were far from promising from a functional point of view because of the limited pressuring force provided by the mechanism, manufacturing complexities, and a too large quantity of motors, which implied an also greater quantity of signals than those provided by conventional prosthesis control systems [1]. Therefore, for this new development, the mechanism design will be based on the gripping function instead, used for holding objects of arbitrary geometries in their respective positions coordinating the movement of different points actuating simultaneously.

First developments [2]. This system consists of a prosthetic hand provided with six degrees of freedom (DOF) with two additional DOFs for the wrist. Control system is a pair of soles which include and input device similar to a computer keyboard (see Fig. 38.1), which manipulate the movements of a hand through six control channels. Likewise, voice signals are used to implement additional default functions, such as hand opening and closing. Control algorithm was design in LabVIEW.

Second development [3]. For this development, a control system using myoelectric signals was introduced. This system obtained signals from voluntary muscular contractions. Electronically, an embedded system was developed, and the use of a computer was no longer required, increasing the device portability. Ergonomic and organic design was drawn using surfaces. The hand also features independent movement in each finger. Finally, mechanical power increase was achieved by replacing the original plastic gears for ones made of metal (Fig. 38.2).

Problem statement. From these developments it was realized that the goal of replicating natural hand movements was not going to be feasible in the short term. In this sense, a scheme was redesigned in a way such that the hand functions take precedence and the mentioned DOFs act in a coordinated manner. That is to say, it is intended that by holding an arbitrary-shaped object, the system will be capable to adapt immediately by distributing the force equitably in more possible contact points through merely mechanical phenomena.

M.A.T. Letechipia (✉) • J.A.C. Ramírez • H.A. Téllez
ITESM Campus Monterrey, Av. Eugenio Garza Sada 2501, Monterrey, Nuevo León C.P. 64849, Mexico
e-mail: A01061265@itesm.mx

Fig. 38.1 First development**Fig. 38.2** Second development

38.2 Development Objectives

In summary, the proposal is focused in a mechanical array in form of a clamp that allows the suspension of multiple bodies with arbitrary geometries, which aims to increase energy consumption efficiency, strengthening the mechanism and simplifying the control algorithm without affecting functionality.

With the goal of increasing energy consumption efficiency, the mechanism must be fastened to prevent the opening of the clamp and giving it a chance to close when an eventual collision happens.

Meanwhile, the mechanism can be strengthened in a way such that the transmission gears are protected by means of a cam-follower mechanism that assures that the maximum couple is that produced by the gear motor.

Finally, to simplify the control algorithm without affecting functionality, a cam-follower mechanism will be used. This mechanism will have a rotational axis that will be shared with other two similar cams but with differing profiles, producing a coordinating movement involving all fingers.

38.3 Proposed Mechanism

Introduction. This new development has the goal of being implemented in a patient and for this reason it is intended to reduce the number of components to a minimum, keeping the functionality of the hand, increasing its energy efficiency, and strengthening the mechanism. Because of this, it is decided to reduce the number of motors to just one without scarifying finger coordination, performing different tasks such as total hand opening, closing, index finger pointing and the only movement of the index finger that could be used for pressing buttons and touching objects with accuracy. Simultaneously, energy efficiency can be improved if a unidirectional mechanism is employed, allowing clamp fastening during larger, indeterminate periods of time, which results in a reduced energy consumption.

Detailed Description

- A cam is used because it is a mechanism that works in a unidirectional way; that is, the cam can move the follower but not the other way around. It is worth noting that there are other unidirectional configurations containing gears but as they have teeth, these mechanisms are more susceptible to larger stress concentrations, especially because the contact surface is smaller.
- In two-position cams, where their highest and lowest are apart by 180° , there are two paths from highest to lowest: 0° to 180° , and 0 to -180° .
- The cam presents a cyclic movement with no critical positions, this means that it has no abrupt ends or singularity points.

Taking into account that the cam-follower mechanism rotates around an axis, this can be easily shared with two other cam-follower mechanisms such that all three spin at the same time. Nonetheless, each of the cams has different profiles causing that the followers describe unique displacements that simulate their coordinated movement in a hand (Fig. 38.3).

38.4 Movement Dynamics

More information about the kinematics of the previously described hand mechanism can be found if implemented on a dynamics simulation software such as ADAMS. In the following figure, the 3D path displacement of each of the fingers is drawn (Fig. 38.4).

Fig. 38.3 Detailed description of the mechanism

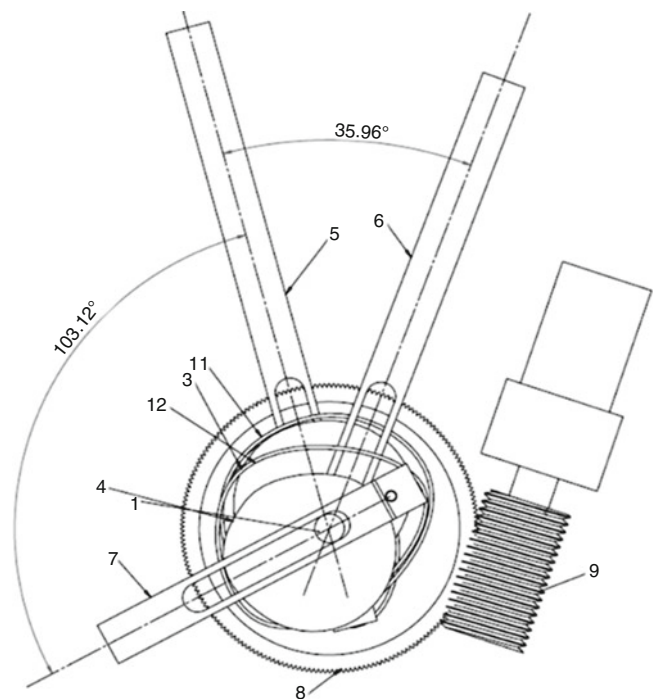
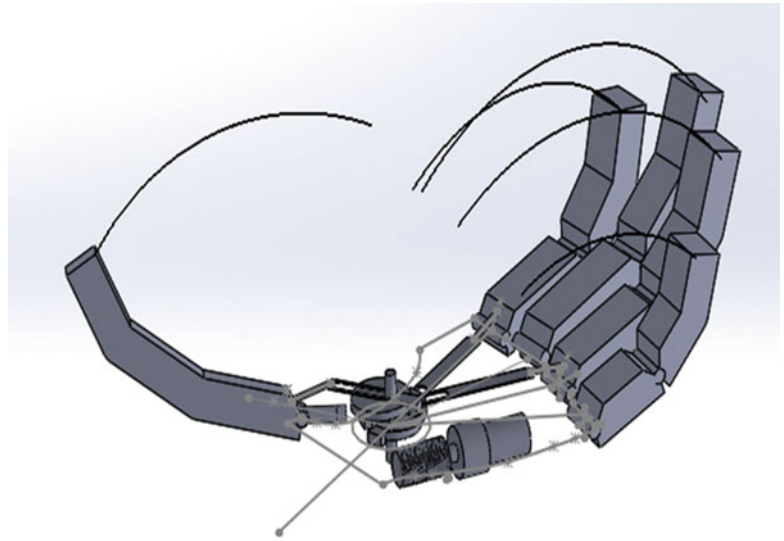


Fig. 38.4 Finger displacement paths, as simulated by ADAMS



The graphs resulting from the study show the rotation in degrees of each of the fingers in function of the cam rotation also in degrees. The red line shows a 0° position for the cam which corresponds to the hand in its most open configuration (Fig. 38.5).

From the graphs, similar behaviors in the -180° -to- 0° path for each of the fingers can be appreciated. In the 0° -to- 180° , some differences can be detected. This is a faithful reflex of the diverse trajectories that can be designed and simulated for each finger, using just one actuator. Table 38.1 shows vital information about each of the fundamental configurations.

Furthermore, this mechanism design has a very powerful characteristic because when the hand is subject to a collision, this closes right away. This is due to the one-way nature of the cam-follower mechanism, which is accomplished with the follower moving away from a sure collision against the cam and the opposing movement of an elastic spring, i.e. a rubber band (Fig. 38.6).

It is worth noting that the hand consists of just one motor, and in consequence the maximum mechanical power of a finger will be the same as the one registered in the hand. In contrast, a 5-motor hand proposed in the previous developments will have 1/5 of the mechanical power in the fingers from the maximum registered in the hand.

Performing an ADAMS simulation, a kinematics and kinetics analysis can be made before an idea is materialized, because it can be especially helpful in finding potential problematic areas. In conclusion, a single-motor hand idea is checked, taking into account the fastening which is used for energy saving. Furthermore, the simulation concludes that the mechanism is strong and the pieces are easy to manufacture (Fig. 38.7).

The graphical results from the ADAMS simulation, restricted to a 90° rotation of the fingers, are shown in the following picture.

38.5 Kinetics Study

The motor selected for the simulation tests is the D33S16M251001 model, manufactured by Stock Drive Products. This motor also includes a gear motor made of planetary gears, which helps to maximize the torque.

The following Figure shows the mechanism configuration, which includes a worm gear and a straight gear as the crown. This configuration is used to increase the torsional couple and change in 90° the rotation direction. It also is unidirectional, because the worm gear rotation will cause the crown to rotate and not the other way around (Fig. 38.8).

The rotation speed of the crown coupled with the cam is 11.53 rpm, with a torque of 177 N-mm. The worm gear is double-throated and the crown has 60 teeth.

The picture shown in Figure 38.9 will be helpful to describe the rest of the simulation procedure. The blue arrow show the 177 N-mm constant-value torque applied to the crown. The red arrow indicates a constant rotation for the cylinder located 85 mm from the axis, having the red line as its axis of rotation. Meanwhile, the solid representing the finger is moved by the

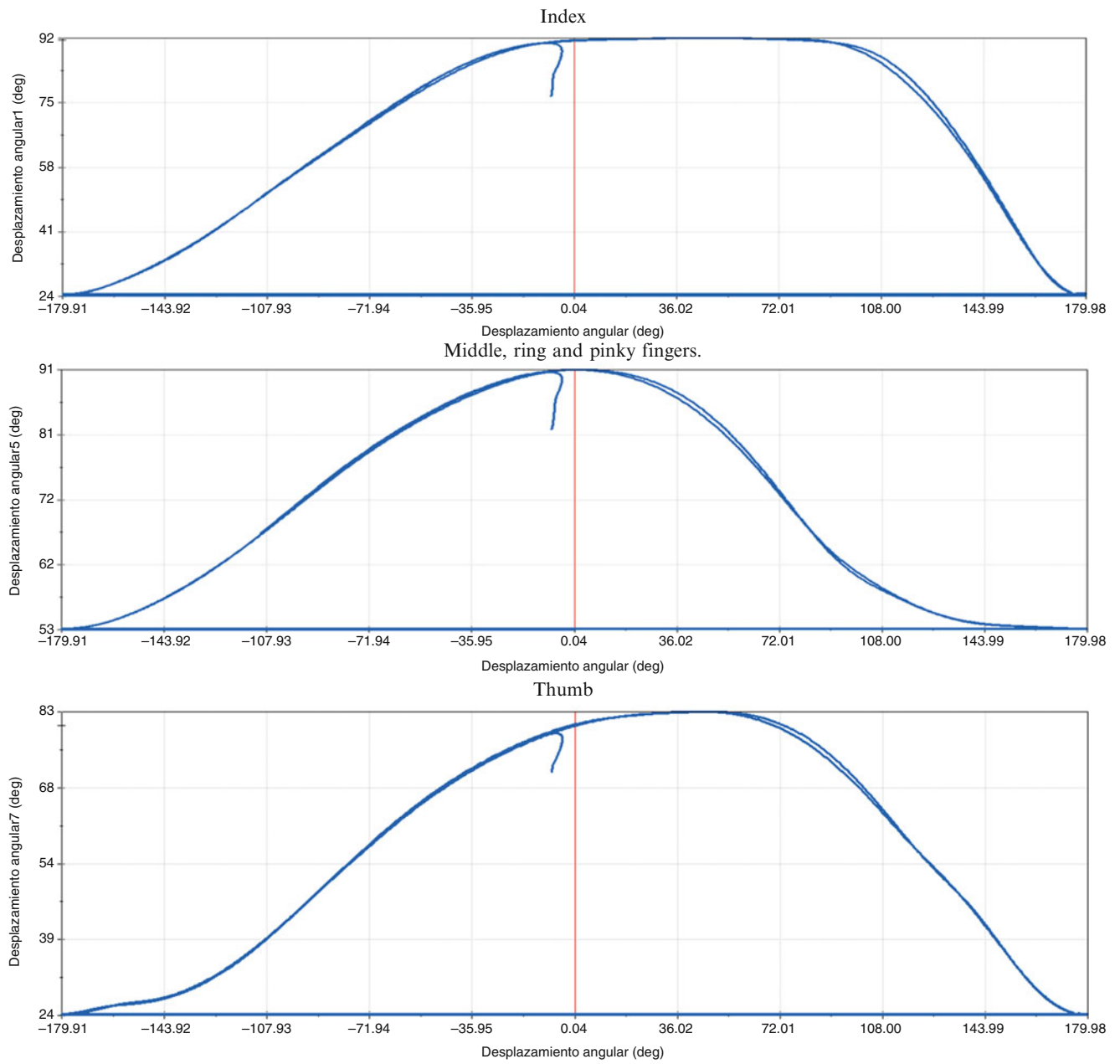


Fig. 38.5 Particular finger positions obtained from the ADAMS dynamic analysis

Table 38.1 Hand position

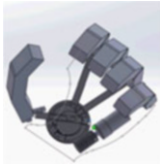
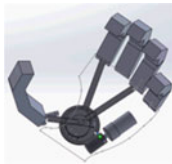
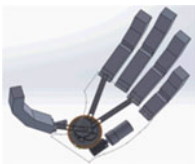

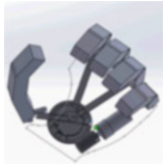
					
Hand position					
Cam rotation	-180°	-90°	0°	90°	180°

Fig. 38.6 Collision mechanism

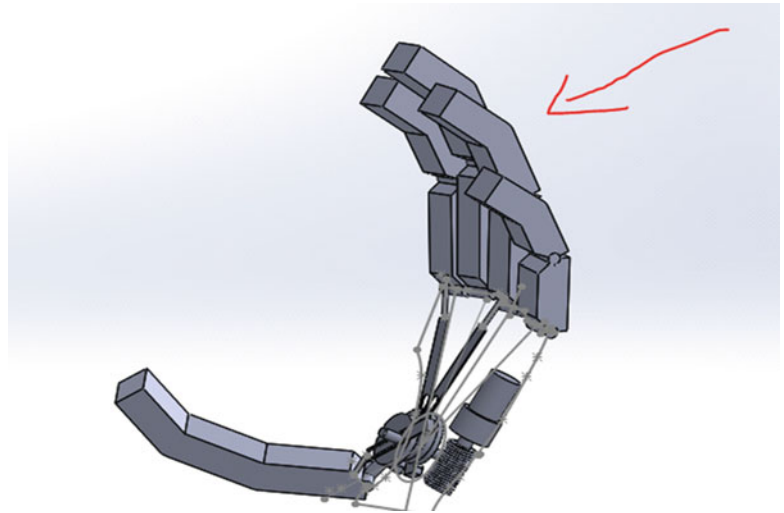


Fig. 38.7 Mobility check using ADAMS simulation software

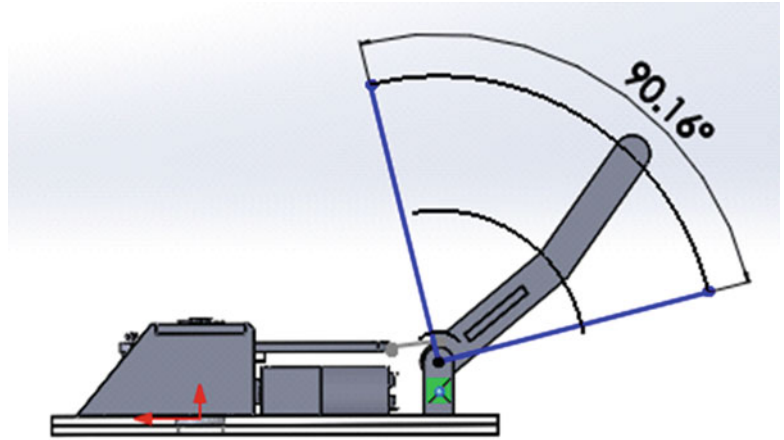
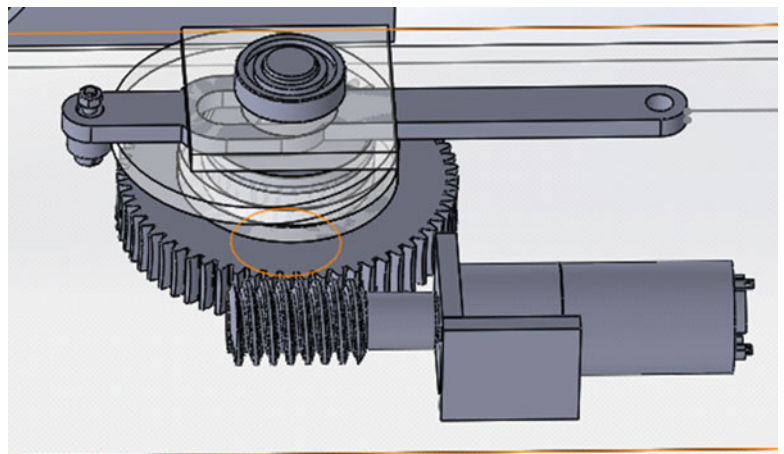
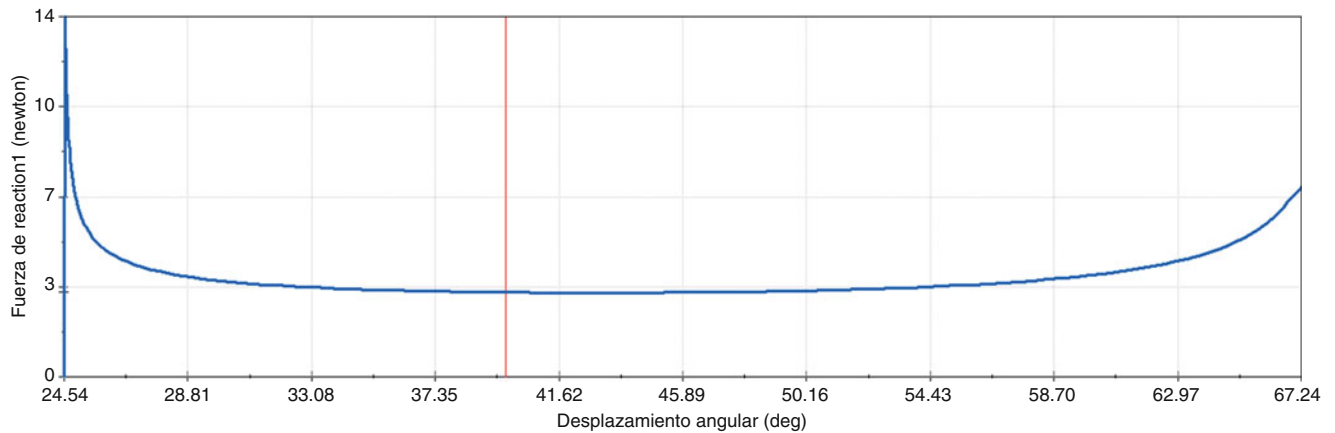
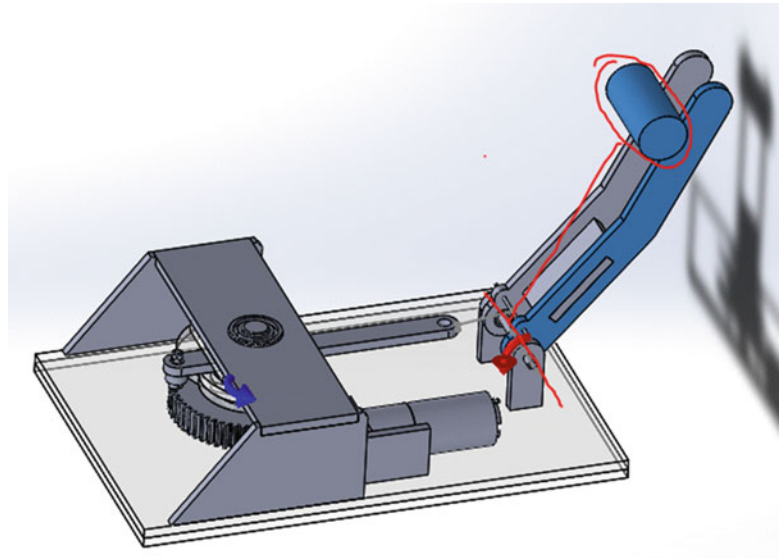


Fig. 38.8 Mechanism configuration used for the kinetic study



inverse follower, which in turn is moved by the cam joined to the crown gear. Taking into account these two behaviors, the collision force between these two aforementioned solids can be measured, by computing the pressure force registered by the finger (Fig. 38.10).

Fig 38.9 Experimental model**Fig. 38.10** Graph measuring collision force

The graph shows that the force caused by the contact pressure applied in a point located 85 mm from the rotation axis of a finger varies in function of the angular position of the same finger. In first place, this variation is due to the cam shape and also to the variation of the lever arm projected from the axis of rotation around which the finger moves. From the graphs it is determined that this point contact force, has a value that sticks around 3 and 7 N. Benchmarking these results with those from other commercial hands [4] it is found that the applied force is quite low and it is concluded that another motor will be needed in order to apply a larger force.

However, it is useful to remark that the benefits provided by this kinematic configuration (see Fig 38.11). For instance, once that an object is pressed, the mechanism one-way configuration allows that the clamp stops in a previously determined position without requiring addition energy from the motor. Another conclusion that can be extracted is that the fastener does not exert a direct force in the gear train but in the cam, which is a stronger component. For example, a supermarket plastic bag can be held up from its handle before being lift without requiring further force; once it is lift, the plastic bag will exert more force from the handle but in this moment the hand will be blocked and will remained closed until it reaches its destination, all of this with no additional energy consumption from the motor.

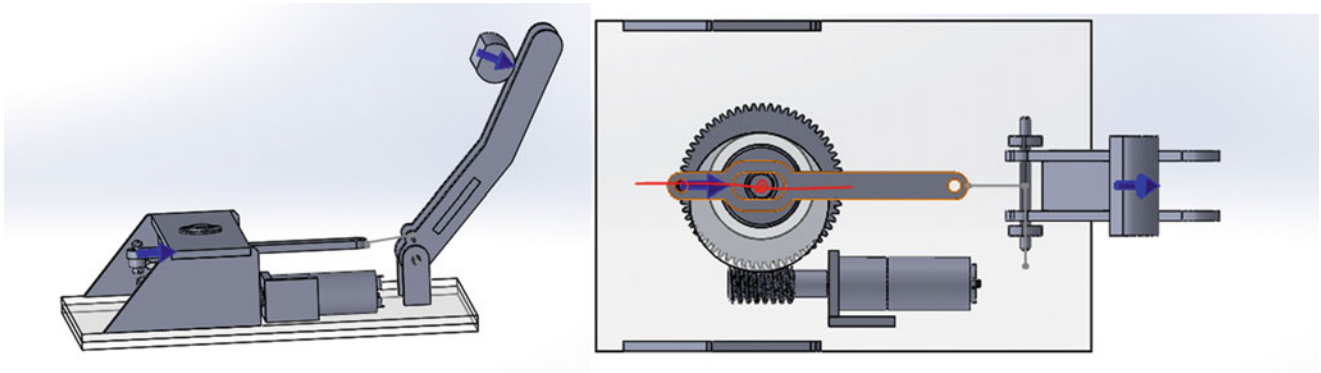


Fig. 38.11 Experimental model

38.6 Conclusions and Further Work

As this work is a first sketch to demonstrate the mechanical principles governing the natural hand movements, it is important to know how it performs, by kinematic simulations; these preceding its manufacture because they help to detect in an anticipated fashion all the required input forces, and in turn the selected motor.

These simulations also identify force distributions along the mechanism. Finally, these results also determine whether the design of the mechanism meets the required specifications before its manufacture.

From this simulation, several areas of opportunity were detected and will be used to drive future research. First of all, it will be necessary to proceed with the manufacture of the proposed model and perform experimental tests which will serve as a comparison basis for further studies. It also will be possible to know the manufacturing capabilities of the research group.

References

1. P. Parker, R. Merletti, *Electromyography* (Wiley, Hoboken, 2004)
2. M.A. Trejo, National instruments (2010 May 14), <https://decibel.ni.com/content/docs/DOC-11305>
3. M. Trejo, Design and construction of a prototype of a hand prosthesis, Thesis work, Instituto Tecnológico de Estudios Superiores de Monterrey, Campus Monterrey, 2013
4. J. Belter, A. Dollar, Performance characteristics of anthropomorphic prosthetic hands, in *International Conference on Rehabilitation Robotics*, Zurich, 2011

Chapter 39

Cascaded Ultra-Low Reflective Fiber Points for Distributed Sensing

Rodolfo Martinez Manuel and H.E. Sutherland

Abstract Distributed fiber sensors based on the frequency domain analysis of Rayleigh backscattered light are well established. They exhibit very good performance in both sensitivity and spatial resolution, but their application can be limited due to their cost and the complexity of the analysis. In this work we present a system based on coherent optical frequency domain reflectometry, used in Rayleigh distributed sensors, implemented with more readily available components and simplified analysis. A sensing fiber is prepared by printing uniformly spaced, ultra-low reflectivity fiber Bragg gratings of the same Bragg wavelength. When tuneable source light is introduced to the fiber the reflections from the gratings interfere with the reflection from the tip of the fiber. The gratings' reflectivity varies randomly which produces a frequency domain trace that shares some of the properties of a Rayleigh spectral trace, but is significantly stronger. This removes the need for specialized detection equipment. These Bragg gratings act as reflectors and not as sensors per se. Use of a reference interferometer and signal processing algorithms make it possible to replace a high precision linearly tuneable laser with a standard tuneable laser as optical source.

Keywords Ultra-low reflectors • Optical frequency domain analysis • Tunable laser source • Linear error correction • Distributed temperature sensing

39.1 Introduction

The advantages of using fibre optic cable for tasks like sensing are well known, and include immunity to electromagnetic interference, lightweight and compact size, high sensitivity and low propagating losses. Distributed sensing, especially of temperature, can be accomplished in several ways, most notably with OTD Optical time domain reflectometry (OTDR) (optical time domain reflectometry) using the Raman Stokes and Anti-Stokes ratio, or by measuring the frequency shift of the Brillouin spectrum. These methods have a limit on spatial resolution of 0.1–1 m, which is imposed by working in the time domain. However it is possible to attain spatial resolutions in the order of millimetres by working in the frequency domain [1]. In that case the limitation on spatial resolution is no longer determined by the rise time of the system but by the smallest sample size required to get an accurate spectral profile, and the optical frequency range of the light source. One of the most successful applications of OFD Optical frequency domain reflectometry (OFDR) (optical frequency domain reflectometry) is in the detection and analysis of Rayleigh backscatter using SWI Swept-wavelength interferometry (SWI) (swept-wavelength interferometry) as demonstrated by S. T. Kreger et al. [2]. This however relies on detecting a signal of -103 dB or smaller and typically involves a tuning range between 2.5 and 40 nm [3]. Other applications include multiple reflecting sensors placed on a fibre and interrogated by OFDR [4]. This last named instance results in a quasi-distributed sensing system that implements fibre Bragg gratings as sensors to detect changes in the measurand. All OFDR systems rely on the linearity of the tuneable source for good performance and this problem has typically found one of three solutions: improve the hardware and redesign the optical source, use an auxiliary interferometer to measure the instantaneous tuning rate of the source and then resample the measurement data, or use an auxiliary interferometer to trigger the acquisition of the signal [5]. Of these the first solution increases the cost of the system, it requires significant research and development resources to implement, and the last solution requires additional hardware for synchronisation and a specially designed layout of the transmission lines to compensate for

R. Martinez Manuel (✉)

Centro de Investigaciones en Óptica, A.C. Photonics, Prol. Constitución 607, Fracc. Reserva Loma Bonita, Aguascalientes 20200, Mexico
e-mail: rodolfom@cio.mx

H.E. Sutherland

Department of Electrical and Electronic Engineering, University of Johannesburg, Johannesburg, Gauteng, South Africa
e-mail: redpandaliza@gmail.com

© Springer International Publishing Switzerland 2017

A. Martínez-García et al. (eds.), *Emerging Challenges for Experimental Mechanics in Energy and Environmental Applications, Proceedings of the 5th International Symposium on Experimental Mechanics and 9th Symposium on Optics in Industry (ISEM-SOI), 2015*, Conference Proceedings of the Society for Experimental Mechanics Series, DOI 10.1007/978-3-319-28513-9_39

281

small delays in transmitting the electrical signals [5]. Post-acquisition processing however requires neither additional hardware nor expensive development of an improved optical source.

In this work we present a system which uses the principle of swept-wavelength interferometry with Rayleigh backscatter light, but which can be implemented with much more basic equipment. This is accomplished by slight modification of the optical fibre, and signal conditioning algorithms that improve the data before analysis is performed.

39.2 Experimental Setup

The sensing system consists of two optical fiber interferometers, one for sensing and one as a reference for signal conditioning, connected as shown in Fig. 39.1. The optical power is split 80/20 with the bulk going to the sensing arm and the remainder used to generate the reference signal. The measurement signal is generated by the interference between the reflection from the cleaved tip of the sensing arm in air, and the reflections from each of the ultra-low reflectors along the sensing section of the fiber. This signal is transferred by a circulator directly to detector 1. The reference interferometer is a standard Michelson fiber interferometer with the tips cleaved and left in air. An important design feature of the reference interferometer is the FBG printed very close to one of the tips, which assists in the phase tracking. The computer sends a signal to the tuneable optical source to initiate tuning, and at the same time sends a time delayed signal to the acquisition hardware to capture the output from the detector. The system does not rely on synchronisation hardware or software to acquire the signal but relies on post-acquisition signal processing to condition the signal before analysis. In this way it reduces the cost and complexity of the resources required to install the system. The only requirement is that the reference and measurement signals be acquired simultaneously on a per sample basis, which allows the reference signal to be used to perform corrections on the measurement signal.

In Fig. 39.2, the placement of the sensing section's reflectors is shown, with the tip on the left hand side to correspond with the DC position of the frequency spectrum, shown in Fig. 39.3 just below. The reflection at the end of the spectrum is produced by the connector, where the sensing arm is connected to the circulator.

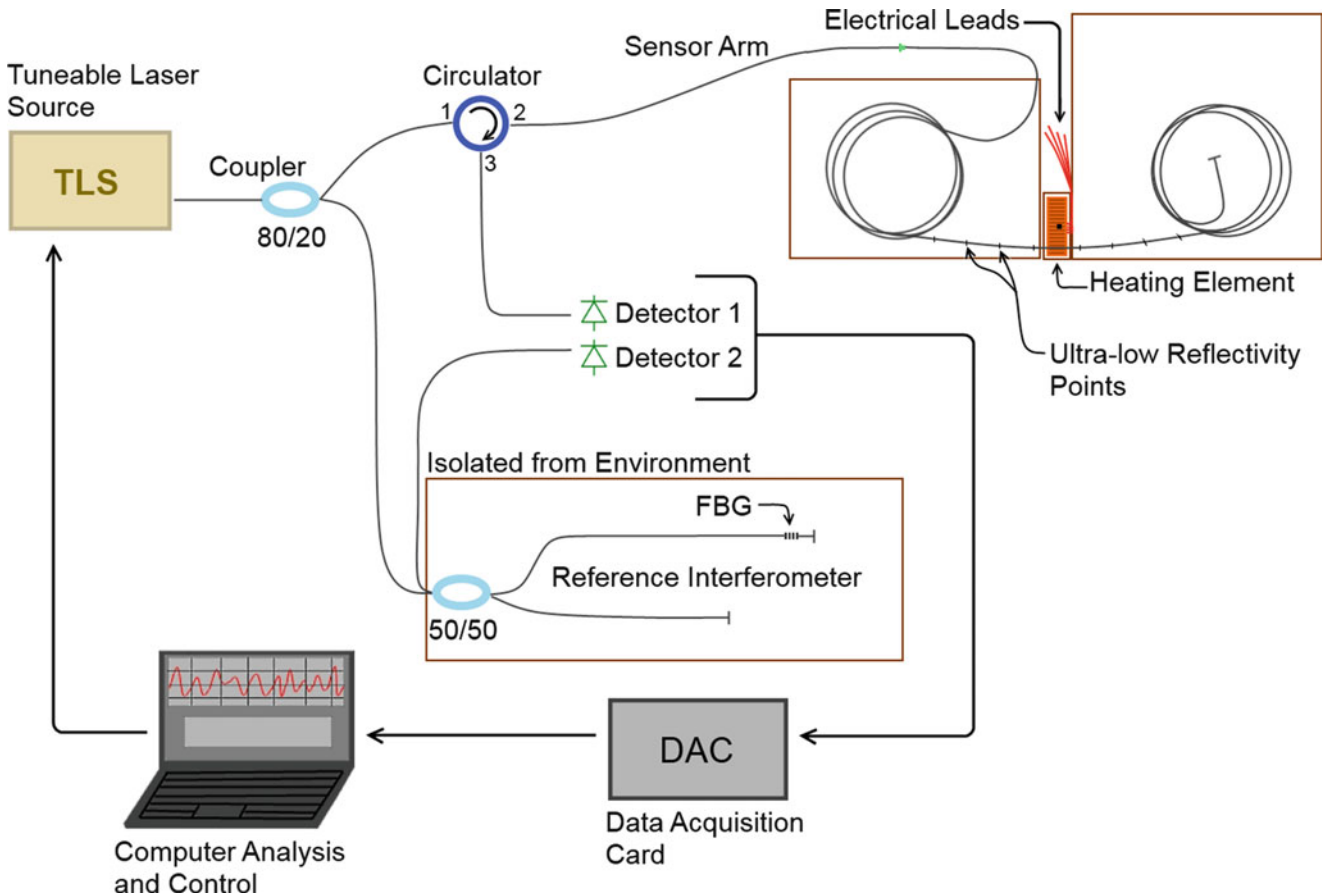


Fig. 39.1 Layout of the sensing system

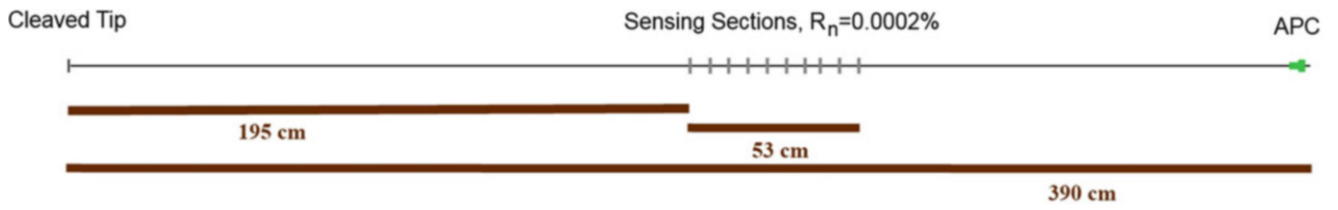


Fig. 39.2 Detail of the sensing section design

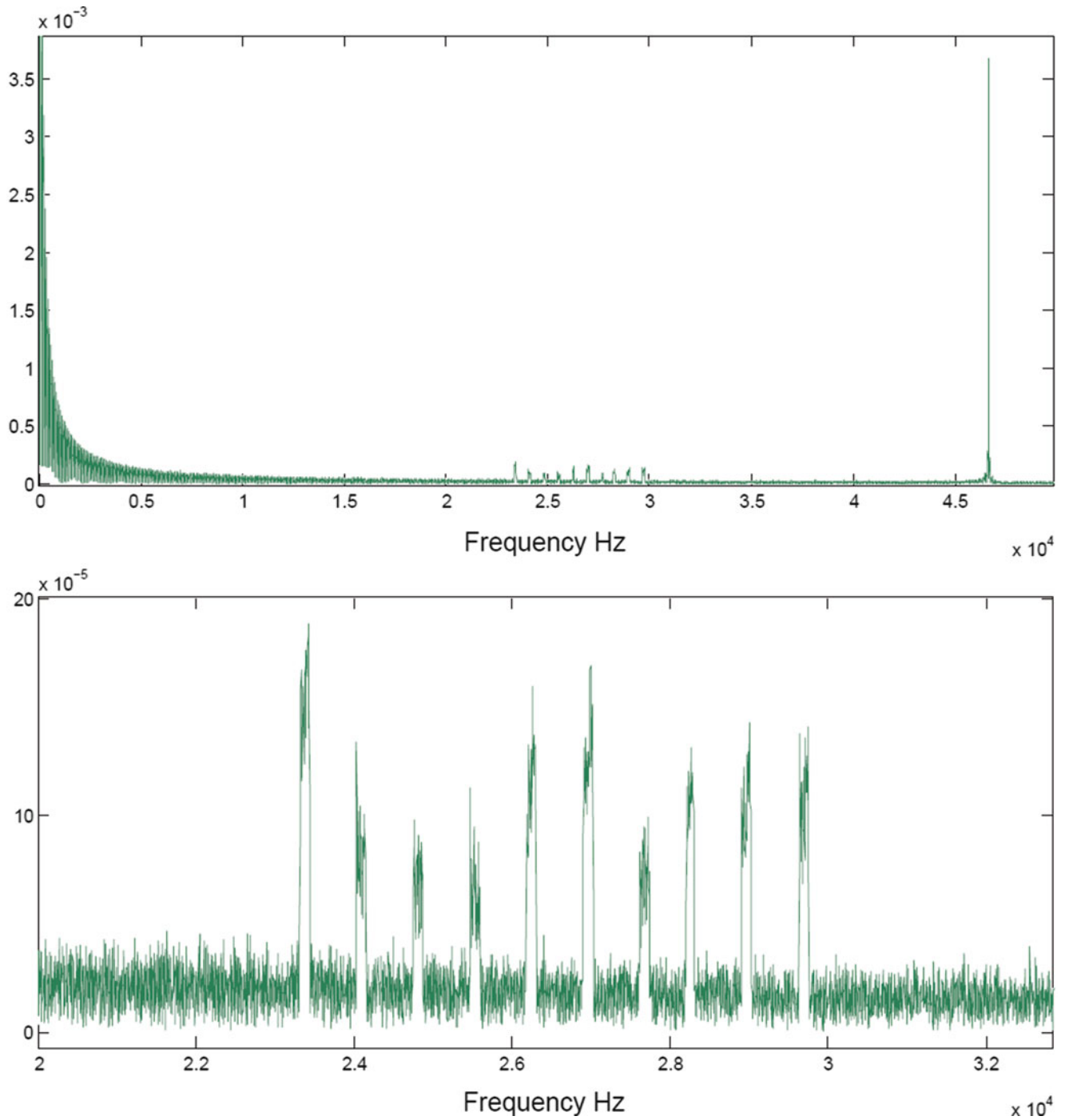


Fig. 39.3 The real spectrum of the signal from the sensing arm (top), and detail of the reflectors (bottom)

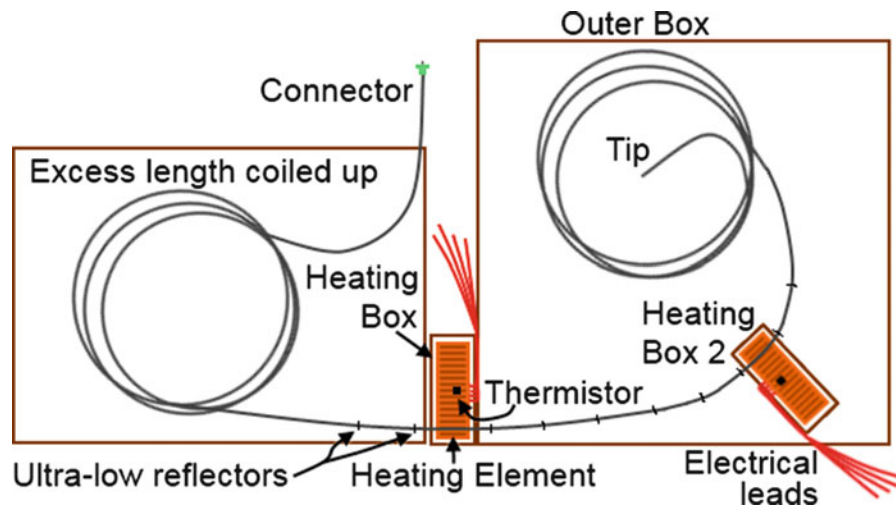


Fig. 39.4 Setup of the sensing arm for two point temperature sensing

Since the sensing section runs along the fiber it can be placed in various physical patterns, for example a grid, which can be used for surface mapping of temperature or strain. In order to engineer the simplest output signal two things were taken into consideration with the manufacture of the sensing arm: the reflectivity of the point reflectors, and the distance from the tip of the fiber to the start of the sensing section. Firstly the reflectors were chosen to have ultra-low reflectivity in the order of 0.0002 % per reflector because this places all second order reflections well outside the range of detectable power for the system. Secondly the distance from the tip of the fiber was chosen to be more than the total length of the sensing section, to separate the signal in the frequency domain from any first order interference between the reflectors. Printing the FBGs at the same wavelength reduces the range over which the optical source needs to sweep to about 0.5 nm, and ensures that the same signal conditioning is performed on all of the reflected signals.

An additional feature of the design of this system is that the reference interferometer has a fiber Bragg grating (FBG) of a wavelength slightly removed from the sensing reflectors printed close to the tip of one of the arms. This produces a low frequency signal superimposed on the reference signal to enable phase locking the signals once acquired.

The system was tested by changing the temperature independently at two sections of the sensing arm, in a setup as shown in Fig. 39.4. Two heating elements each with a thermistor in the centre were placed in small isolating boxes. The rest of the fiber was placed in larger boxes to isolate them from disturbances in the general environment. FBGs used for the ultra-low reflectors are not being used as point sensors in the conventional manner of FBGs; they act only as reflection points to generate a stronger signal to interfere with the reflection from the tip. The resulting signal carries information in its phase about the condition of the fibre between adjacent reflectors. This is what makes this sensor truly continuously distributed, albeit in a discrete manner, as opposed to quasi-distributed with several point sensors.

39.3 Processing of the Sensor Signal

Before the signal can be analysed it undergoes a conditioning process that enables the use of relatively basic equipment to perform tasks that generally require a high degree of precision. The raw data is sampled uniformly in time, but since the optical source does not tune linearly with respect to time the data needs to be resampled before a Fast Fourier Transform algorithm can be applied to it. Having a sinusoid signal from a Michelson interferometer with a fixed relationship between the phase of the signal and the optical frequency of the tuneable source; first interpolation is performed on both signals to increase the accuracy with which the indices (in the time domain) of the maxima and minima of the reference signal can be determined. Then these indices are used as a grid to resample the measurement signal in such a way that the samples are equally spaced with respect to optical frequency. This has the effect of changing the data to resemble data obtained from a highly linearly scanning source. This has the benefit of narrowing the signal's bandwidth and increasing the amplitude in the frequency domain, which leads to increased accuracy of phase measurements.

After the signal has been linearised the placement of the acquisition window needs to be zeroed with respect to optical frequency to ensure that the initial phase is always the same. Cross-correlation is used to compare the reference signal to a

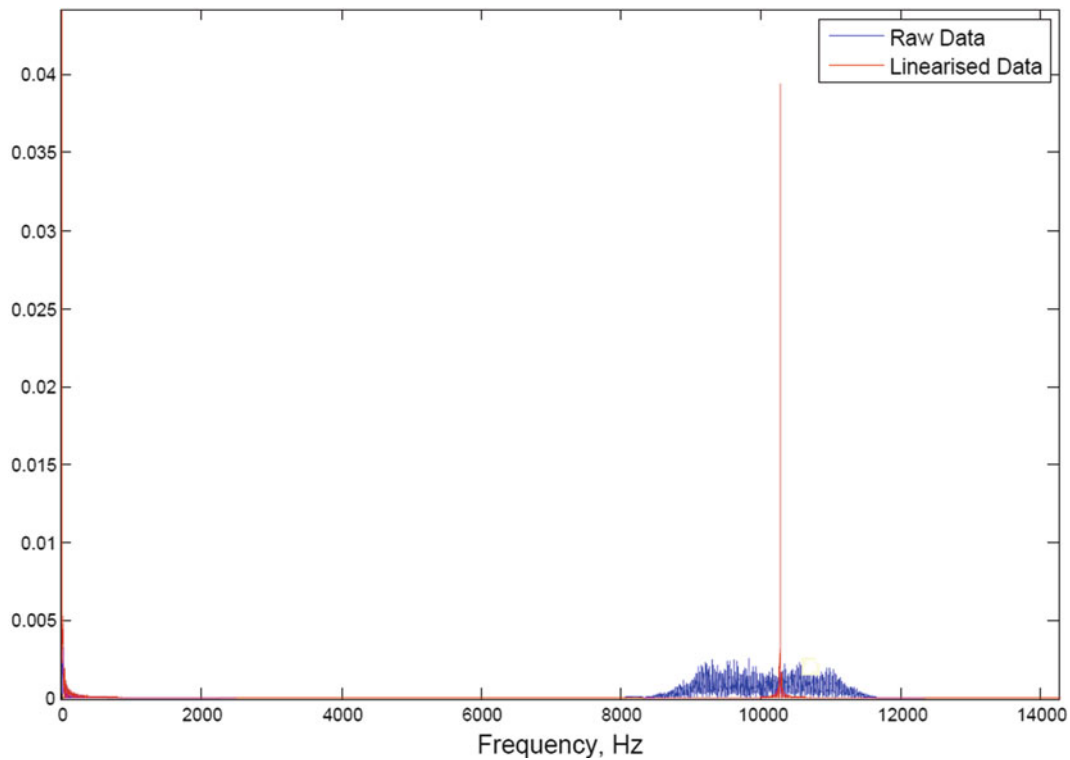


Fig. 39.5 An illustration of the effectiveness of the linearization algorithm

baseline signal in order to shift the acquisition window into the correct position. The uniquely identifiable envelope shape produced by the FBG in the reference interferometer ensures that the same optical wavelength is used to start the signal at every time (Fig. 39.5).

Once the signal has been conditioned it can be analysed to measure a change in the measurand, using the established technique for optical frequency domain analysis. A Fast Fourier Transform (FFT) is taken of the measurement signal, and it is multiplied with the complex conjugate of the FFT of a measurement signal obtained under calibration conditions. This gives the change in phase of the signal relative to the signal under calibration conditions, which in turn can be converted to a quantitative change in the measurand.

39.4 Experimental Results

Initially a single point was used to calibrate the system and test the phase response to a change in temperature, and then the two point experiment was performed.

From Fig. 39.6 it can be seen that the phase increases linearly with temperature, regardless of the increments of temperature change. This indicates that the sensor can accurately measure changes in temperature relative to the calibration temperature. The first data point in the plot is non-zero because of the heating properties of the elements that were used when driven with a low voltage.

In Fig. 39.7, we show a comparison between the temperature as measured by the optical sensing system and the two thermistors placed on the heating elements as two sections were independently heated and then allowed to cool down again.

Concerning the difference in slope between the heating and cooling stages for this experiment it is important to note that the temperature that was measured by the thermistors was not measured at exactly the same location as the fibre measurement. It is therefore possible that the edges of the small heating boxes cooled faster than the centre, and that the fiber was in fact at a lower temperature than the thermistors.

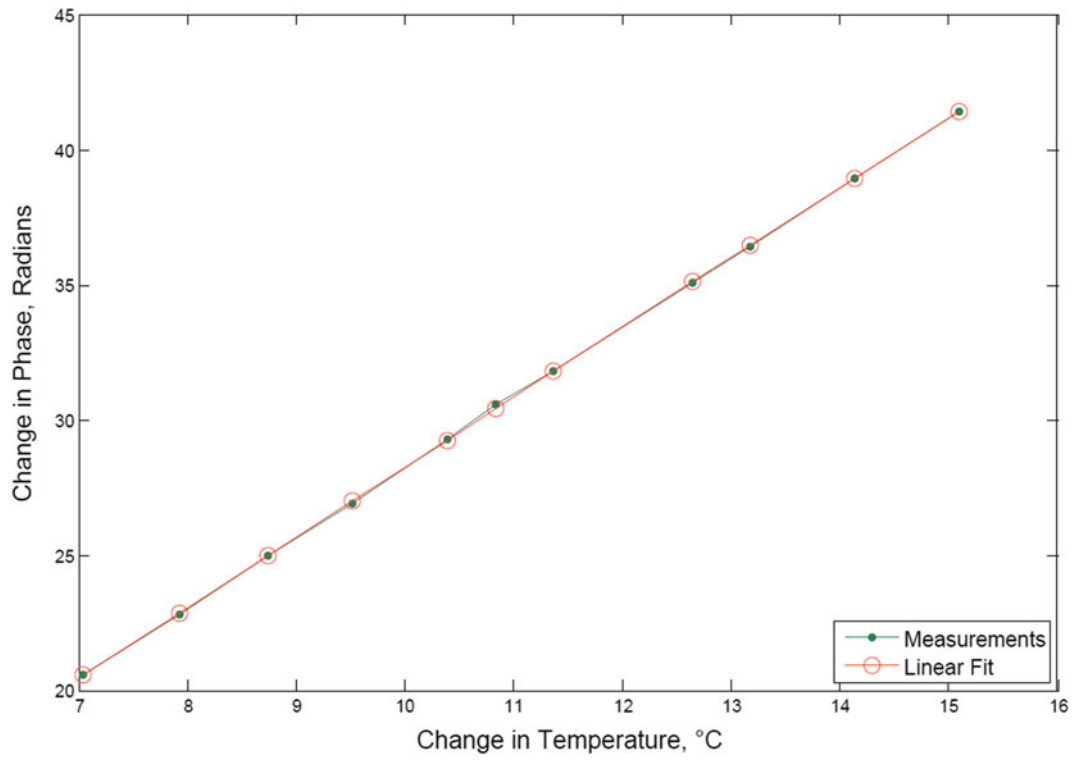


Fig. 39.6 Change in phase as temperature is increased, at one location

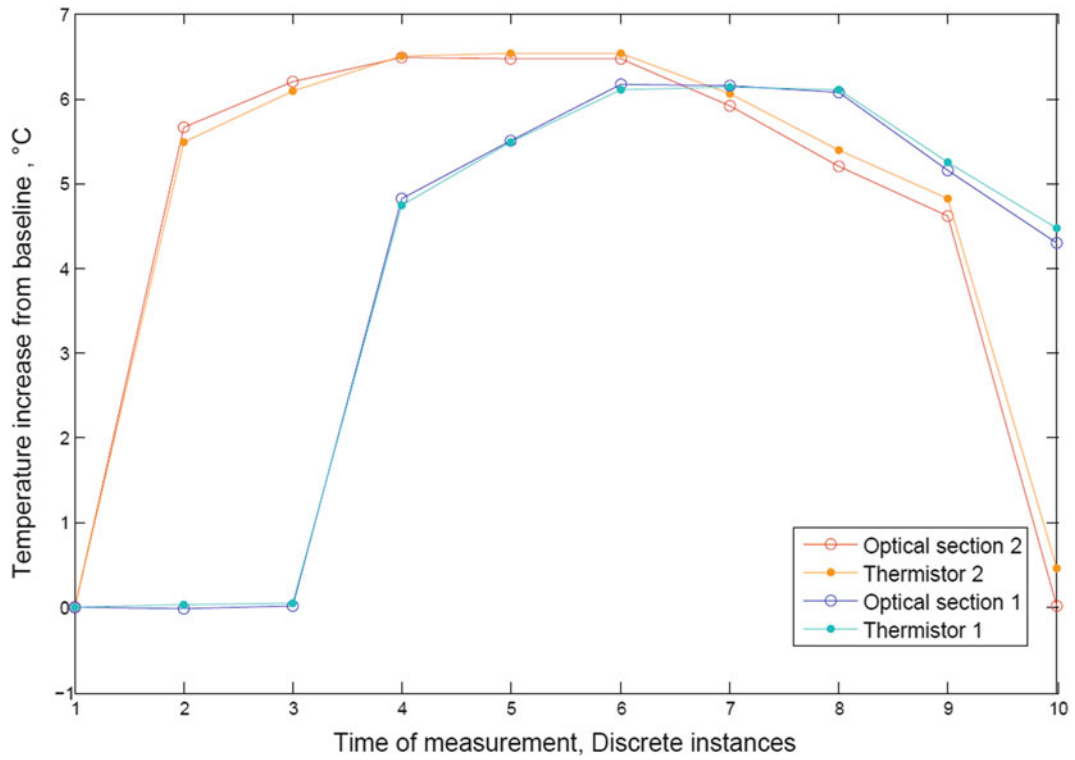


Fig. 39.7 Temperature changing with time at two points independently

39.5 Conclusion

A fully distributed sensing system has been developed that uses the principle of optical frequency domain analysis and implements it in a much simplified form, using cheaper more readily available resources. Implementation of the cascaded ultra-low reflective points has enabled the use of standard detectors and has reduced the scanning range requirement to 0.5 nm. It has also reduced the complexity of the analysis required by eliminating second order interference between the reflective points. The signal conditioning algorithms along with the reference FBG on the reference interferometer have done away with the requirements of highly linear tuning and high precision synchronisation systems.

References

1. X. Bao, L. Chen, Recent progress in distributed fiber optic sensors. *Sensors* **12**, 8601–8639 (2012)
2. S.T. Kreger, D.K. Gifford, M.E. Froggatt, B.J. Soller, M.S. Wolfe, High resolution distributed strain or temperature measurements in single- and multi-mode fiber using swept-wavelength interferometry, *Optical Fiber Sensors*, p. ThE42 (2006)
3. B. Soller, D. Gifford, M. Wolfe, M. Froggatt, High resolution optical frequency domain reflectometry for characterization of components and assemblies. *Opt. Express* **13**(2), 666–674 (2005)
4. K. Yüksel, V. Moeyaert, P. Mégret, M. Wuilpart, Complete analysis of multireflection and spectral-shadowing crosstalks in a quasi-distributed fiber sensor interrogated by OFDR. *IEEE Sensors J.* **12**(5), 988–995 (2012)
5. E.D. Moore, R.R. McLeod, Correction of sampling errors due to laser tuning rate fluctuations in swept-wavelength interferometry. *Opt. Express* **16**(17), 13139–13149 (2008)

Chapter 40

Object Surface Representation Via NURBS and Genetic Algorithms with SBX

J. Apolinar Muñoz Rodríguez and Francisco Calos Mejia Alanís

Abstract A technique to represent object surface via NURBS and genetic algorithms is presented. In this technique, the surface is generated based on control points. Then, the control points and the weights are optimized via genetic algorithms to find the NURBS, which represents the object surface. The genetic algorithm is constructed through an objective function, which is deduced from the NURBS surface. This objective function is minimized by using the simulated binary crossover. The proposed genetic algorithm improves accuracy and speed of the NURBS surface representation. The contribution of the proposed method is elucidated by an evaluation based on model accuracy and speed of traditional genetic NURBS surface representation.

Keywords NURBS surface representation • Genetic algorithms • Simulated binary crossover

40.1 Introduction

The standard method used to represent free-form object surface is the non-uniform rational B-splines (NURBS) [1]. This method performs the surface representation by means of gradients methods. However, several times the gradient is trapped in local minima, which is far away from the true global optimum [2]. To alleviate these limitations, NURBS performs surface representation via genetic algorithms (GA) [3]. These algorithms make an exploration in all research space to avoid trapping in local minima via mutation operator. Usually, the GA minimizes the distance between NURBS surface and the target surface to obtain the surface representation. In this field, several algorithms such as particle swarm [4], crossover operator [5], simulated annealing [6], simulated evolution [7] and ant colony [8] have been implemented to perform NURBS representation. The above genetic algorithms provide a smooth NURBS surface. Therefore, some object surface points are not interpolated by the NURBS surface. Additionally, the research space is not deduced via NURBS. Therefore, the algorithms consume long time to achieve the convergence.

To improve the accuracy and the speed of the NURBS representation via genetic algorithms, a GA is implemented via simulated binary crossover algorithm (SBX) [9]. The objective function and the research space of this GA are deduced by means of the NURBS surface. Thus, the convergence is achieved in a small number of iterations. The objective function is minimized via SBX to produce the optimal NURBS, which passes by all object points. Thus, a contribution is achieved in the field of NURBS for free-form representation. This advancement is elucidated by an evaluation based on the accuracy and speed of the traditional GA.

40.2 Basic Theory

The standard method to represent free-form surface is the NURBS [9]. This method constructs a particular object shape by means of control points. A rectangular NURBS surface is described by means of the next expression

J.A.M. Rodríguez (✉) • F.C.M. Alanís
Centro de Investigaciones en Óptica, A.C., León, GTO C.P. 37150, Mexico
e-mail: munoza@foton.cio.mx

$$S(u, v) = \frac{\sum_{i=0}^n \sum_{j=0}^m N_i^p(u) N_j^q(v) w_{i,j} P_{i,j}}{\sum_{i=0}^n \sum_{j=0}^m N_i^p(u) N_j^q(v) w_{i,j}}. \quad (40.1)$$

In this equation, $w_{i,j}$ are the corresponding weights of control points $P_{i,j}$, and $N_i^p(u)$, $N_j^q(v)$ are the B-splines basis function of order p and q , respectively [10]. These B-splines basis functions are defined over the vectors $\{u_0, u_1, u_2, \dots, u_{n+p}\}$ and $\{v_0, v_1, v_2, \dots, v_{m+q}\}$ in the u and v directions, respectively. Thus, the B-splines basis function are defined by the next expression

$$N_i^p(u) = \frac{u - u_i}{u_{i+p-1} - u_i} N_i^{p-1}(u) + \frac{u_{i+p} - u}{u_{i+p} - u_{i+1}} N_{i+1}^{p-1}(u), \quad N_i^1(u) = \begin{cases} 1 & u_i \leq u \leq u_{i+1} \\ 0 & \text{otherwise} \end{cases} \quad (40.2)$$

Now, surface representation is performed by optimizing the weights and control points to find the NURBS that passes through by all object points. To do so, a GA implemented based on an objective function, which is deduced via NURBS surface and object points $h_{i,j}$ by means of the next equation

$$F_{objective} = \sum_{i=0}^n \sum_{j=0}^m [h_{i,j} - S(u_i, v_j)]^2. \quad (40.3)$$

For this objective function, $s(u_i, v_j)$ is the surface computed via (40.1) by using chromosomes of the term $w_{i,j} P_{i,j}$. The operator SBX minimizes the objective function (40.3) to obtain the optimal weights and control points. To carry it out, the initial population is created by taking a random value from the search space. Thus, the first parents ($\mathcal{P}_{1,k}$, $\mathcal{P}_{2,k}$) and ($\mathcal{P}_{3,k}$, $\mathcal{P}_{4,k}$) are generated where k -index is the generation number. Also, the parents produce two children $\mathcal{C}_{1,k}$ and $\mathcal{C}_{2,k}$ via recombination based on probability distribution β , which is described by mean of the next expression

$$\beta = \begin{cases} (2\alpha)^{1/(\gamma+1)} & \text{if } \alpha < 0.5 \\ \frac{1}{[2(1-\alpha)]^{1/(\gamma+1)}} & \text{if } \alpha \geq 0.5 \end{cases} \quad (40.4)$$

For this equation, the spread factor α is a random value in the interval between 0 and 1. The γ value is a non-negative real number that characterizes the distribution of the children in relation to their parents. Thus, each pair of parents reproduces two children by means of the next expressions

$$\mathcal{C}_{1,k} = 0.5[(\mathcal{P}_{1,k} + \mathcal{P}_{2,k}) - \beta|\mathcal{P}_{2,k} - \mathcal{P}_{1,k}|], \quad (40.5)$$

$$\mathcal{C}_{2,k} = 0.5[(\mathcal{P}_{1,k} + \mathcal{P}_{2,k}) + \beta|\mathcal{P}_{2,k} - \mathcal{P}_{1,k}|], \quad (40.6)$$

Based on these equations, the recombination is carried out by replacing the chromosomes of the worst parents by the chromosomes of the best sons to create the new generation. The recombination procedure is repeated until to find the weights and control points that minimize the objective function (40.3). These chromosomes are replaced in the NURBS (40.1) to obtain the surface that represent the free-form object. These NURBS surface pass through by all object points in fast manner. With this procedure, the NURBS surface representation via GA with SBX has been completed.

40.3 Surface Representation via NURBS and GA

The free-form representation is carried out based on the objects points $h_{i,j}$, which are shown in Fig. 40.1 via symbol “o”. From these points, the knot vector defined by $\{u_0 = 0, u_1 = 0, u_2 = 0, u_3 = 1, u_4 = 2, u_5 = 3, u_6 = 4, u_7 = 4, u_8 = 4\}$ in u -direction and $\{v_0 = 0, v_1 = 0, v_2 = 0, v_3 = 1, v_4 = 2, v_5 = 3, v_6 = 4, v_7 = 4, v_8 = 4\}$ in v -direction. From these knots vectors, the B-splines basis functions are determined. Then, the optimal control points $w_{i,j} P_{i,j}$ are determined via GA to

Fig. 40.1 NURBS surface representation via GA with SBX

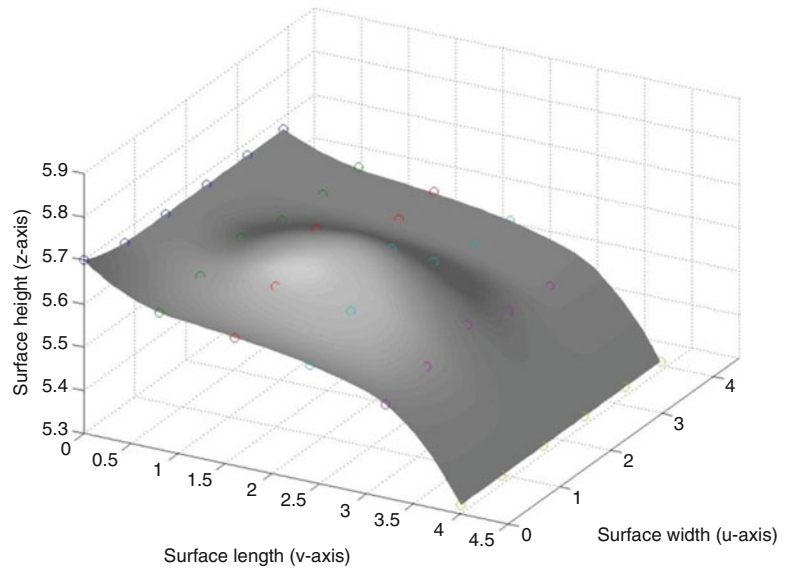


Table 40.1 Control points created by the GA with SBX for the first generation

Chromosome	Min	Max	$P_{1,1}$	$P_{2,1}$	$P_{3,1}$	$P_{4,1}$	$C_{1,1}$	$C_{2,1}$	$C_{3,1}$	$C_{4,1}$
$w_{00} P_{00}$	5.602	5.797	5.689	5.682	5.720	5.767	5.683	5.688	5.727	5.760
$w_{01} P_{01}$	5.616	5.682	5.657	5.675	5.634	5.651	5.659	5.672	5.637	5.648
$w_{02} P_{02}$	5.497	5.623	5.597	5.505	5.522	5.523	5.519	5.582	5.522	5.523
$w_{10} P_{10}$	5.632	5.671	5.668	5.646	5.632	5.658	5.649	5.664	5.636	5.654
$w_{11} P_{11}$	5.607	5.632	5.625	5.627	5.625	5.628	5.626	5.627	5.626	5.627
$w_{12} P_{12}$	5.497	5.678	5.529	5.499	5.578	5.501	5.504	5.524	5.513	5.565
$w_{20} P_{20}$	5.632	5.680	5.651	5.639	5.677	5.665	5.641	5.649	5.667	5.675
$w_{21} P_{21}$	5.557	5.681	5.673	5.582	5.615	5.604	5.597	5.659	5.606	5.613
$w_{22} P_{22}$	5.542	5.878	5.850	5.609	5.682	5.821	5.647	5.811	5.705	5.799
<i>Fitness</i>			0.034	0.099	0.034	0.046	0.061	0.021	0.025	0.020

represent the object surface. To do so, the GA determines the research space by means of the initial NURBS, which is computed by using $w_{i,j} = 1, P_{i,j} = h_{i,j}$. This surface provides the first limit of the research space. If the surface passes over the object point, then the term control point $w_{i,j} P_{i,j} = h_{i,j}$ is the maximum of the research space. The other hand, if the surface passes under the object point, then the control point $w_{i,j} P_{i,j} = h_{i,j}$ is a minimum. Then second limit value is determined based on the distance $d_{i,j} = h_{i,j} - hm$, where hm is the mean of object points. Thus, the second limit is given by the expression $w_{i,j} P_{i,j} = h_{i,j} + Ad_{i,j}$. Where $P_{i,j} = h_{i,j}$ and $w_{i,j} = (h_{i,j} + Ad_{i,j})/h_{i,j}$ and $A = 2$ for a rectangular segment of 3×3 points. The second limit provides a maximum when the initial NURBS is a minimum or a minimum when the initial NURBS is a maximum.

Then, the GA generates the initial population of chromosomes of control points $w_{i,j} P_{i,j}$ based on rectangular segments of 3×3 points. The data of the first generation are shown in Table 40.1, where the chromosomes of the control points are indicated in the first column. The minimum and maximum value of each chromosome $w_{i,j} P_{i,j}$ are indicated in second and third column, respectively. The first parents ($\mathcal{P}_{1,1}, \mathcal{P}_{2,1}$), ($\mathcal{P}_{3,1}, \mathcal{P}_{4,1}$) are created by taking a random value from the research space. These parents are indicated in fourth to seventh column, respectively. Then, chromosomes of parents ($\mathcal{P}_{1,1}, \mathcal{P}_{2,1}$) are substituted in (40.5) and (40.6) to generate the children $\mathcal{C}_{1,1}$ and $\mathcal{C}_{2,1}$. Also, the parents $\mathcal{P}_{3,1}, \mathcal{P}_{4,1}$, are substituted in (40.5) and (40.6) to generate the children $\mathcal{C}_{3,1}$ and $\mathcal{C}_{4,1}$. The first children are shown in 8–11 column, respectively. Then, the fitness of each parent is computed via (40.3) based on the object points $h_{0,0}, h_{0,1}, h_{0,2}, \dots, h_{2,2}$. To carry it out, the chromosomes control points $w_{i,j} P_{i,j}$ of each parent are substituted in (40.1) to compute the surfaces $S(u_0, v_0), S(u_0, v_1), S(u_0, v_2), \dots, S(u_2, v_2)$. Thus, the fitness of each parent is obtained and it is indicated in tenth row of Table 40.1. With this procedure, the population of the first generation has been completed.

The second generation is constructed by using the best children and the best parents of the first generation. Thus, $\mathcal{P}_{1,1}$ is selected from $(\mathcal{P}_{1,1}, \mathcal{P}_{2,1})$ and $\mathcal{P}_{3,1}$ is selected from the pair $(\mathcal{P}_{3,1}, \mathcal{P}_{4,1})$. Also, $\mathcal{C}_{2,1}$ and $\mathcal{C}_{4,1}$ are selected to be parents of second generation. Thus, the parents of the second generation are defined by $\mathcal{P}_{1,2} = \mathcal{P}_{1,1}$, $\mathcal{P}_{2,2} = \mathcal{C}_{2,1}$, $\mathcal{P}_{3,2} = \mathcal{P}_{3,1}$ and $\mathcal{P}_{4,2} = \mathcal{C}_{4,1}$. Then, the parents $(\mathcal{P}_{1,2}, \mathcal{P}_{2,2})$ are substituted in (40.5) and (40.6) to create the children $\mathcal{C}_{1,2}$ and $\mathcal{C}_{2,2}$. In the same manner, the parents $\mathcal{P}_{3,2}, \mathcal{P}_{4,2}$, are substituted in (40.5) and (40.6) to create the children $\mathcal{C}_{3,2}$ and $\mathcal{C}_{4,2}$. Again, the objective function of each parent is computed via (40.3) to select the parents of the next generation. The procedure that creates the second generation is repeated until to find the parents that minimize the objective function (40.5).

The chromosomes of the last generation are the optimal control points, which construct the NURBS surface that that represent an object segment. These chromosomes corresponds to the control points $\{w_{0,0}P_{0,0}, w_{0,1}P_{0,2}, w_{0,2}P_{0,2}, \dots, w_{2,2}P_{2,2}\}$, which produce an object rectangular surface. The procedure to obtain these control points is repeated to obtain the segments $\{w_{0,3}P_{0,3}, w_{0,4}P_{0,4}, w_{0,5}P_{0,5}, \dots, w_{2,5}P_{2,5}\}, \dots, \{w_{3,3}P_{3,3}, w_{3,4}P_{3,4}, w_{3,5}P_{3,5}, \dots, w_{5,5}P_{5,5}\}$. Then, the NURBS is computed in the intervals $u_i \leq u \leq u_{i+1}$, $v_j \leq v \leq v_{j+1}$ to obtain the surface shown in Fig. 40.1. The accuracy provided by NURBS via GA whit SBX is a $rms = 0.000121$ mm. This result leads to obtain a relative rms (%) = 0.002 %, which is calculated based on the mean $hm = 5.6511$ mm.

40.4 Experimental Results of Object Representation via NURBS Based on GA

To perform the free form representation, the object points are retrieved based on the vision system shown in Fig. 40.2a. This setup provides the object coordinates $(x, y, h_{i,j})$ via laser line scanning [11]. In this setup, the x -axis and y -axis are located in u -direction and v -direction, respectively. The object surface $h_{i,j}$ is in z -axis, which is perpendicular to plane (x, y) .

The free-form representation is performed for the dummy face eye shown in Fig. 40.2a. To carry it out, the slider moves the laser line in x -axis to scann the eye. During the scanning, a set of images is captured by the CCD camera. From these images, the vision system determines the object coordinates $(x, y, h_{i,j})$ via the line position [11]. Based on these points, the initial NURBS surface is constructed via (40.1). To carry it out, the B-splines $N_i^3(u)$ and $N_j^3(v)$ are determined based on the knot vectors in u -direction and v -direction. These basis function are substituted in (40.1) to obtain the initial NURBS. Then, the initial NURBS is fitted to the eye surface points via GA with SBX. To carry it out, the GA determines the first limit of the space research from the initial NURBS. Then, the second limit is computed by the term $w_{i,j}P_{i,j} = h_{i,j}Ad_{i,j}$ based on segments of 3×3 points. Then, the GA generates the first parents of chromosomes $w_{i,j}P_{i,j}$ by taking a random value from the research space. Then, each pair of parents creates the first children by means of (40.5) and (40.6). Then, the fitness of the parents and children is computed via (40.3) to select the parents of the second generation. This procedure is repeated until find the control points that minimize of the objective function. Thus, the control points $\{w_{0,0} P_{0,0}, w_{0,1} P_{0,2}, w_{0,2} P_{0,2}, \dots, w_{2,2} P_{2,2}\}$ have been obtained. The same procedure is repeated until to obtain de control points $\{w_{0,3} P_{0,3}, w_{0,4} P_{0,4}, w_{0,5} P_{0,5}, \dots,$

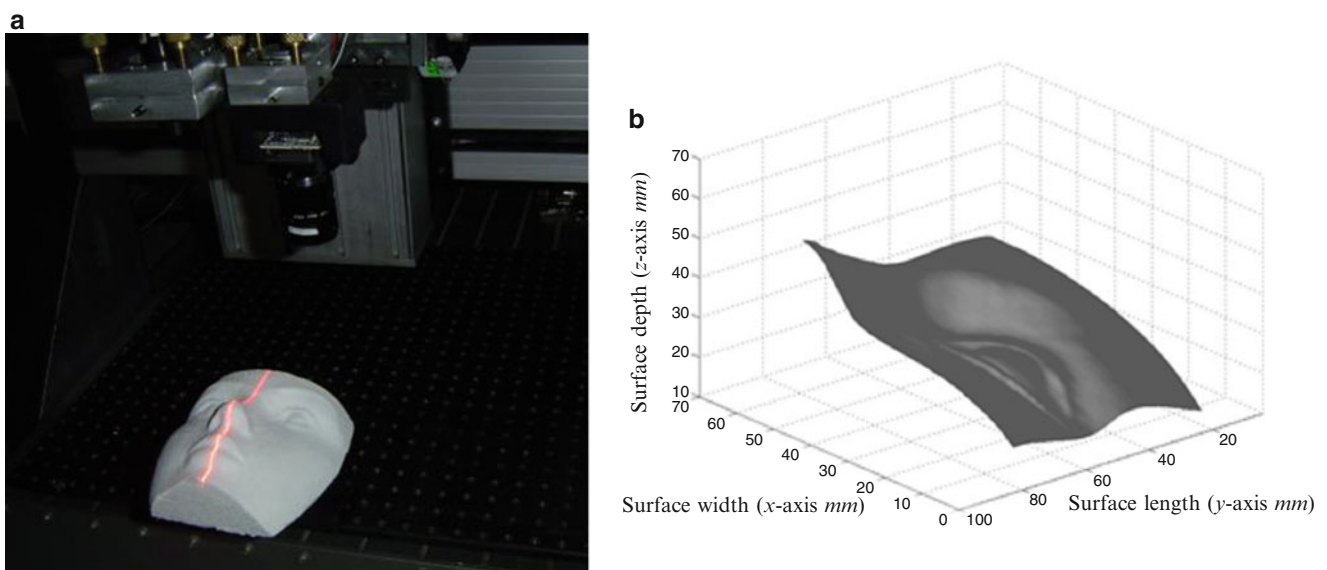


Fig. 40.2 (a) Vision system to retrieve surface points (b) Eye surface provided by NURBS based on GA with SBX

$w_{2,5} P_{2,5}\}, \dots, \{w_{m-2,n-2} P_{m-2,n-2}, w_{m-2,n-1} P_{m-2,n-1}, w_{m-2,n} P_{m-2,n}, \dots, w_{m,n} P_{m,n}\}$. Then, the NURBS is computed in each interval $u_i \leq u \leq u_{i+1}, v_j \leq v \leq v_{j+1}$ to obtain the dummy face eye shown in Fig.40.2b. The scale of this figure is in mm. The accuracy provide by the NURBS fitting is determined via *rms* by means of the next expression

$$rms = \sqrt{\frac{1}{m*n} \sum_{i=0}^n \sum_{j=0}^m [h_{i,j} - s(u_i, v_j)]^2}, \quad (40.7)$$

Thus, the model represents the dummy face with an accuracy of an $rms = 0.000432$ mm. Therefore, the relative error of the surface model is an $rms(\%) = 0.000183 \%$, which is calculated by the $rms(\%) = rms \times 100/hm$ based on $hm = 23.52$ mm.

The accuracy and speed of NURBS surface depend on the terms $w_{i,j} P_{i,j}$, which are computed via GA. Therefore, the GA provides the accuracy and speed of the NURBS fitting. Typically, the traditional GA does not define the research space by means of the NURBS. This leads to consume long time to achieve a convergence with an error over 0.01 % in NURBS surface fitting [4, 12]. Stead of, the proposed GA determines the research space based on NURBS. This leads achieve the NURBS fitting with an accuracy minor than 0.000185 % in short time. The NURBS fitting accuracy is related directly with the minimization of the objective function (40.3). In the proposed technique, the GA produces a low error in the first generation. Therefore, the GA converges to the minimum in less than 40 generations. The advancement of the proposed method is corroborated by the accuracy of the traditional GA such as particle swarm [13] and simulated annealing [14], ant colony [8]. The accuracy of these methods is an error over 0.01, which leads to an error over 0.2 % for NURBS surface fitting. The traditional methods achieve the convergence by using over one hundred iterations. These data corroborate that the proposed GA improves the NURBS fitting via GA. Thus the contribution of the GA with SBX in NURBS fitting has been elucidated.

40.5 Conclusions

A technique of NURBS surface representation based on GA with SBX been presented. In this technique, our algorithm determines the weights and control points based on a research space, which is defined by the NURBS surface. Thus, the NURBS surface fitting is achieved with high accuracy in short time. The described technique here provides a valuable tool for object modeling, industrial inspection and the reverse engineering. This technique enhances the accuracy of traditional GA because research interval is known. Therefore, this technique is performed in good manner.

References

1. D. Brujic, I. Ainsworth, M. Ristic, Fast and accurate NURBS fitting for reverse engineering. *Int. J. Adv. Manuf. Technol.* **54**, 691–700 (2011)
2. T. Mengistu, W. Ghaly, Aerodynamic optimization of turbomachinery blades using evolutionary methods and ANN-based surrogate models. *Optim. Eng.* **9**, 239–255 (2008)
3. A. Galvez, A. Iglesias, J. Puig-Pey, Iterative two-step genetic-algorithm-based method for efficient polynomial B-spline surface reconstruction. *Inf. Sci.* **182**, 56–76 (2012)
4. A. Gálvez, A. Iglesias, Particle swarm optimization for non-uniform rational B-spline surface reconstruction from clouds of 3D data points. *Inf. Sci.* **192**, 174–192 (2012)
5. M.M. Hassan, Optimization of stay cables in cable-stayed bridges using finite element, genetic algorithm, and B-spline combined technique. *Eng. Struct.* **49**, 643–654 (2013)
6. M. Sarfraz, M. Riyazuddin, M.H. Baig, Capturing planar shapes by approximating their outlines. *J. Comput. Appl. Math.* **189**, 494–512 (2006)
7. M. Sarfraz, Computer-aided reverse engineering using simulated evolution on NURBS. *Virtual Phys. Prototyp.* **1**(4), 243–257 (2006)
8. R. Xiao, J. Shang, H. Liu, NURBS fitting optimization based on ant colony algorithm. *Adv. Mater. Res.* **549**, 988–992 (2012)
9. J.A. Muñoz-Rodríguez, R. Rodríguez-Vera, Shape detection using light line and Bezier approximation network. *Imaging Sci. J.* **55**, 29–39 (2007)
10. N.E. Leal, O. Ortega Lobo, J. William Branch, Improving NURBS surface sharp feature representation. *Int. J. Comput. Intell. Res.* **3**(2), 131–138 (2007)
11. S. Shojaei, N. Valizadeh, M. Arjomand, Isogeometric structural shape optimization using particle swarm algorithm. *Int. J. Optim. Civil Eng.* **4**, 633–645 (2011)
12. M.C. Tsai, C.W. Cheng, M.Y. Cheng, A real-time NURBS surface interpolator for precision three-axis CNC machining. *Int. J. Mach. Tools Manuf.* **43**, 1217–1227 (2003)
13. S.M. Hu, Y.F. Li, T. Ju, X. Zhu, Modifying the shape of NURBS surfaces with geometric constraints. *Comput. Aided Des.* **33**, 903–912 (2001)
14. T. Elmidany, A. Elkeran, A. Galal, M. Elkhateeb, NURBS surface reconstruction using rational B-spline neural networks. *J. Constr. Eng. Technol.* **1**(1), 34–38 (2011)

Chapter 41

Photo-Oxidation of Polystyrene Film Irradiated with UV-B

C.G. Hernández, R. González, J.J. Soto, and I. Rosales

Abstract Polystyrene films were exposed to UV-B radiation during 2, 5, 7, 9 and 13 days, whose effects were evaluated by infrared spectroscopy, IR, with attenuated total reflectance, ATR. The infrared spectra of the films exposed to the UV-B radiation presented an increase in the absorbance in different bands and regions, like, the band at $2847\text{--}2975\text{ cm}^{-1}$, CH vibration, the region from the $3050\text{--}3150\text{ cm}^{-1}$, CH of the aromatic ring; this increasing in absorbance indicates that the polystyrene films are undergoing an oxidation reaction due to UV-B radiation; in the same way, the band at 1452 cm^{-1} , CH_2 group, presents an increase in absorbance; while, the bands of 700 and 760 cm^{-1} , aromatic ring, show a decrease. Therefore, using UV-B irradiation it is possible to change the molecular structures of polystyrene films.

Keywords Polystyrene films • UV-B radiation • Infrared spectroscopy • Oxidation • Molecular structures

41.1 Introduction

Plastics are materials formed of molecules of large length, although there are natural plastics such as cellulose and the rubber, the vast majority of these materials are synthetic. Some of the properties of plastics is that they have zero electrical conductivity, low thermal conductivity, high mechanical strength, low cost of production, and additionally to this, are ease of molded and alloyed with other materials [1, 2]. Actually, these make plastics one of the most used materials in daily life, coupled with its difficult disintegration and the accumulation in the environment which represents a recurring problem in soils and in oceans [3, 4].

Alternative methodologies are used to prevent the accumulation of these materials, for example, the use of natural polymers, called this way because they are derived from enzymatic processes of living beings (cellulose, chitin, inulin) [5–7] and the modification of the molecular structure of the polymers by means of the addition of oxidative agents, getting plastics oxodegradables. The above technique has the disadvantage that the oxidative agents are heavy metals that are added to plastic to accelerate its degradation, but they still remain in the environment causing pollution in ground-water [8, 9]. This suggests the need to develop alternative methods to prevent the accumulation of these plastic materials in the environment.

In this work, the effects of UV-B radiation on the molecular structures of polystyrene films at different exposure time, 2, 5, 7, 9 and 13 days, was characterized by infrared spectroscopy IR, with attenuated total reflectance ATR.

C.G. Hernández (✉)

Doctorado en Ciencias de la Ingeniería Eléctrica, Instituto Tecnológico de Aguascalientes, Aguascalientes, Mexico
e-mail: tecelectrigo@live.com.mx

R. González, Ph.D.

Department of Chemistry, Instituto Tecnológico de Aguascalientes, Aguascalientes, Mexico
e-mail: rgmota73@yahoo.com.mx

J.J. Soto, Ph.D. • I. Rosales, Ph.D.

Department of electric-electronic, Instituto Tecnológico de Aguascalientes, Aguascalientes, Mexico
e-mail: j2sb@yahoo.com; ilianaroca@yahoo.com

41.2 Theory

Polystyrene is a linear, amorphous and thermoplastic polymer belonging to the family of the styrene polymers, is transparent, has great ease to take color, is clear and its manufacture is very simple; all these advantages make this material quite demanded in the industrial world [10]. Also, it has many remarkable mechanical properties such as its lightness, water resistance, thermal insulation, acoustic and electric conductivity, optimal dimensional stability, toughness and rigidity and it is considered a perennial material; but all these properties of polystyrene are eroded when it is exposed to solar radiation, because it becomes yellow and cracked [11].

The glass transition of this polymer is around 80 °C and its melting point at 240 °C; then, this polymer has thermal characteristics similar to other crystalline plastics. Its optical properties, color and transparency are excellent and its high refractive index of 1.6 makes it very required in the optical industry to manufacture plastic optical components [10]. The total production of polystyrene exceeded 320 million tons in 2012, therefore it is one of the most polluting plastics in the world; also, it has been for several years a low-cost resin, so that its use at the global level is increasing [12–14].

The integration of the plastic to the environment is a problem that affects the entire population, because of some plastics last more than 100 years to return to nature, so that, there is a high rate of pollution in soils and oceans. This is because these polymers have strong structural chains and the microorganisms are not able to metabolize this structure. Beatriz Posada Bustamante, mentions that there are different ways to degrade a plastic material, and emphasizes the effect of the solar radiation on the material [13–16]. Thus, UV-B radiation can be used on them, once the plastic container is peeled off, to decrease its time of reintegration in the environment.

41.3 Materials and Methods

41.3.1 Material

Commercial polystyrene films of 1.57×1.97 in., with a thickness of 0.0197 in. were used.

41.3.2 Exposure to UV-B Radiation

The films of polystyrene were exposed to UV-B radiation for a period of time from 0 to 13 days, at a distance of 1.97 in between the sample and the radiation source used is a UV-B BYTEK lamp model Ultraviolet Multiprom Eraser, in a 320–280 nm range emission.

41.3.3 Spectroscopy IR

The effects of UV-B radiation in the films of polystyrene were characterized using an iS10 infrared spectrophotometer from Thermo Nicolet, with ATR, Germanium mirror and a Potassium bromide beam splitter.

41.4 Results

In Fig. 41.1, the infrared spectra of unirradiated polystyrene is shown: stretching vibrations of the carbon-hydrogen bonds (CH) at $2847\text{--}2975\text{ cm}^{-1}$ and axial deformation of the CH of aromatic ring at $3000\text{--}3068\text{ cm}^{-1}$; the band at $1590\text{--}1625\text{ cm}^{-1}$, axial deformation of the group C=C of the aromatic ring; the region at $1440\text{--}1490\text{ cm}^{-1}$, angular deformation of the CH₂ group; and the region at $699\text{--}730\text{ cm}^{-1}$, deformation angle of the CH groups in the aromatic ring [19–21].

Fig. 41.1 Infrared spectrum of unirradiated polystyrene film

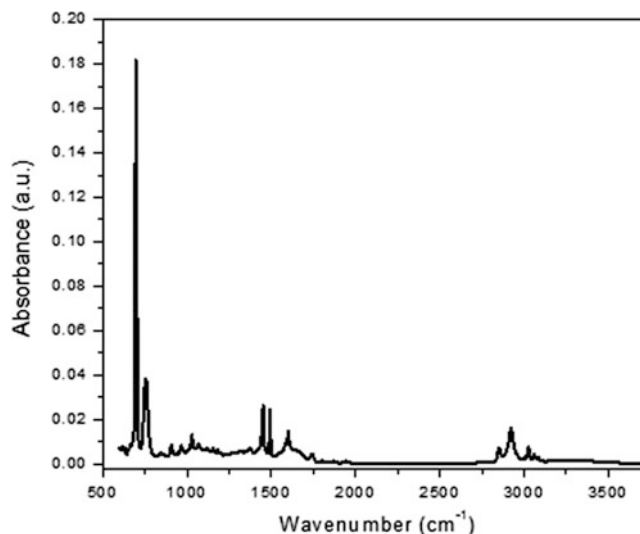
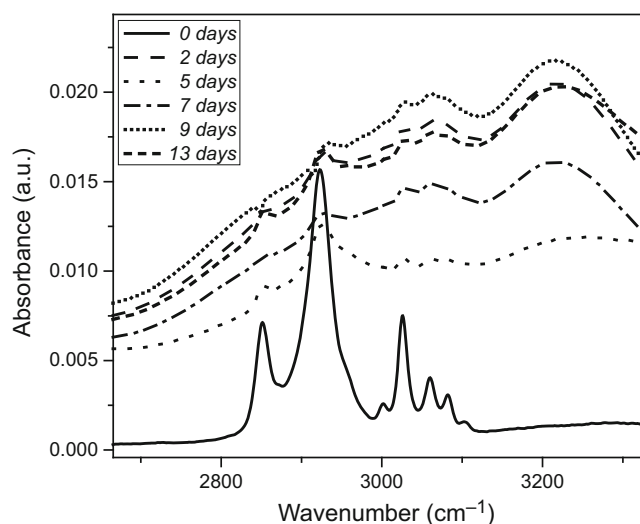


Fig. 41.2 IR absorption region of the CH group, 2800–3100 cm⁻¹, of polystyrene films exposed to UV-B radiation from 0 to 13 days



In Fig. 41.2, the infrared absorption region at 3000–3068 cm⁻¹, axial deformation of the CH bond of the aromatic ring [17], of polystyrene films from 0 to 13 days of exposure to UV-B radiation is shown. Since the beginning of the exposition to UV-B, it can be observed the increase in absorbance and a widen of the band throughout this region; also, it is obtained a constant increasing in absorbance for the post days of irradiation; this is due to the photo-oxidation of polystyrene films [22].

The region corresponding to the hydroxyl group (OH), 3100–3600 cm⁻¹, is shown in Fig. 41.3. The increase and widen of this IR absorption band, could be attributed to formation of hydroperoxides group (OOH), due to the thermo-oxidation of the polystyrene; the peaks at 3060 cm⁻¹ and 3220 cm⁻¹, confirm the presence of this group [20].

In Fig. 41.4, the infrared absorption region at 1600–1800 cm⁻¹, stretching vibration of the carbonyl functional group (C=O), of polystyrene films from 0 to 13 days of exposure to UV-B radiation is shown. In the first 2 days, there is an increase in absorbance throughout this region, this due to the onset of the photo-oxidation; from 7 to 13 days of exposure to UV-B radiation, the photo-oxidation of the aromatic ring is evidenced, this is because of the conjugated dienes absorb the electromagnetic radiation, whose absorbed energy is transferred to the main chain causing the polymeric chains undergo changes at structural molecular level [18] and consequently the IR absorption bands increase and widen. During the process of photo-oxidation, intermediate reaction products are formed, as hydroperoxides (OOH), that evolve to other products, like aliphatics ketones, 1720 cm⁻¹, whose absorbance increases with the increase of exposure time to UV-B [19].

Fig. 41.3 IR absorption region of the hydroxyl group, $3100\text{--}3600\text{ cm}^{-1}$, of polystyrene films exposed to UV-B radiation from 0 to 13 days

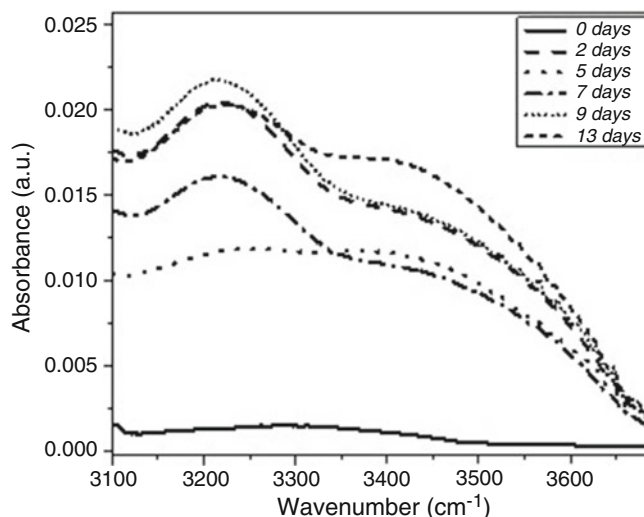
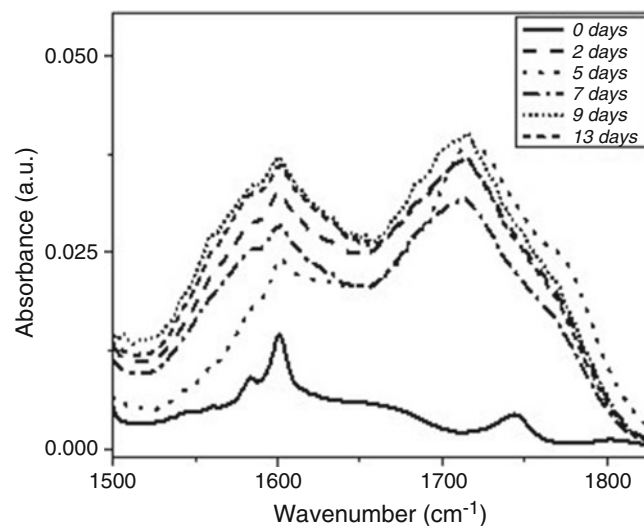


Fig. 41.4 IR absorption region of the carbonyl group, $1600\text{--}1800\text{ cm}^{-1}$, of polystyrene films exposed to UV-B radiation from 0 to 13 days



41.5 Conclusions

The exposure of polystyrene films to UV-B radiation, caused the polymeric chains undergo changes at structural molecular level, which are evident by the formation of carbonyl and hydroxyl groups, which are considered as the main products of the photo-oxidation of this polymer.

So, when polystyrene films are exposed to the UV-B radiation in presence of environmental oxygen, they undergo molecular structural changes; the double bonds present in the phenolic ring of polystyrene help to accelerate the photo-oxidation reaction, this is because of the conjugated dienes absorb the ultraviolet radiation, whose absorbed energy is transferred to the C-H bonds causing its rupture, condition required for oxidation reaction. Therefore, when the polystyrene films are exposed to UV-B radiation, the process of integration to the environment is accelerated. The increase in absorbance and widening of the IR absorption bands of the hydroxyl and carbonyl group in the polystyrene films, are caused the formation of different products due to photo-oxidation, such as aliphatic ketones, esters, anhydrides and the carbonyl and hydroxyl groups; formed due to the exposure time of polystyrene films to UV-B radiation.

References

1. R. Seymour, Additives for polymers, in *Introduction to Polymer* (McGraw-Hill Book Company, New York, 1971) pp. 268–271
2. Y. Orhan, J. Hrenovic, H. Buyukgungor, Biodegradation of plastic compost bags under controlled soil conditions. *Acta. Chim. Slov.* **51**, 579–588 (2004)
3. G.J.L. Griffin, *Chemistry and Technology of Biodegradable Polymers* (Blackie, Glasgow, 1999)
4. A. Karaduman, Pyrolysis of polystyrene plastic wastes with some. *J. Energy Sources* **24**, 667–674 (2002)
5. S.A. Sell, P.S. Wolfe, G. Koyal, J.M. McCool, I. Rodriguez, The use of natural polymers in tissue engineering: a focus on Electrospun extracellular matrix analogues. *Polymers* **2**, 522–553 (2010)
6. J.M. Danga, K.W. Leongb, Natural polymers for gene delivery and tissue engineering. *Gene Deliv. Tissue Eng.* **58**(4), 487–499 (2009)
7. P.B. Malafaya, G.A. Silva, R.L. Reis, Natural–origin polymers as carriers and scaffolds for biomolecules and cell delivery in tissue engineering applications. *Adv. Drug. Deliv. Rev.* **59**, 207–233 (2007)
8. O. Yashchuka, F.S. Portillo, B. Hermida, Degradation of polyethylene film samples containing oxodegradable. *Proc. Mater. Sci.* **1**, 439–445 (2012)
9. T.F.M. Ojeda, D. Emilene, M.M.C. Forte, R.J.S. Jacques, F.'t.M. Bento, F.'v.A.O. Camargo, Abiotic and biotic degradation of oxo-biodegradable polyethylenes. *Polym. Degrad. Stab.* **94**, 965–970 (2009)
10. F.W. Billmeyer, Polymers, in *Textbook of polyer science*, (Reverté., 1984), pp. 409–411
11. A. Andrady, S. Hamid, X. Hu, A. Torikai, Effects of increased solar ultraviolet radiation on materials. *Photochem. Photobiol. B Biol.* **46**, 96–103 (1998)
12. V. Sohrab, A.A. Yousefi, The use of polystyrene in lightweight brick. *Iran. Polym. J.* **12**, 323–329 (2003)
13. H. Hutchinson, S. Malcolm, J.P. Johann, Production of polystyrene beads. US Patent US 2566567 A, 14 May 1946
14. N. Komatsuzaki, M. Tsubone, B. Machida, Continuous process for the production of polystyrene foamed articles. US Patent US4426065 A, 27 Dec 1980
15. F. Gugumus, Re-evaluation of the stabilization mechanisms of various light stabilizer classes. *Polym. Degrad. Stab.* **39**, 117–135 (1993)
16. A.L. Andrady, Wavelength sensitivity in polymer photodegradation. *Polym. Anal. Polym. Phys.* **128**, 47–94 (1997)
17. B. Mailhot, J.L. Gardette, Polystyrene photooxidation. I. Identification of the IR-absorbing photoproducts formed at short and long wavelengths. *Macromolecules* **25**(16), 4119–4126 (1992)
18. D. Zhang, S.M. Dougal, M.S. Yeganeh, Effects of UV irradiation and plasma treatment on a polystyrene surface studied by IR-visible sum frequency generation spectroscopy. *Langmuir* **10**(16), 4528–4532 (2000)
19. E. Jabbari, A. Nicholas, Use of ATR-FTIR to study interdiffusion in polystyrene and poly (vinyl methyl ether). *Macromolecules* **26**(9), 2175–2186 (1993)
20. A.L. Andrady, Ultraviolet radiation and polymers, in *Physical Properties of Polymers Handbook*, ed. by J.E. Mark (Springer, New York, 2007), pp. 857–866
21. C.G. Levins, A. Nathan, S. Daly, Ultraviolet radiation absorbing polymers. US Patent 20140004060 A1, 2 Jan 2014
22. G. Laurent, G. Jean-Luc, Photooxidation mechanism of styrene–isoprene copolymer: evolution of the profile of oxidation according to the composition. *Polymer* **41**, 1669–1678 (2000)

Chapter 42

Dynamic Analysis of Trawl Doors Applied in Bottom Trawls to Catch Shrimp

S. Sarmiento-Nafaté, J. Enríquez-Zárte, J. Villalobos-Toledo, and C. Pineda-García

Abstract This work deals with the dynamic analysis of a new design of trawl doors. The model is constrained to steady towing conditions with velocity constant, flat seabed and gear symmetry. The Ordinary Differential Equations (ODE) of the system includes the effects of the warp and the ropes in terms of external forces. In the mathematical model the influences of the hydrodynamic forces over the trawl doors are considered. This paper is mainly focus in show preliminary results of the mathematical model of a new design of trawl doors used to catch shrimp in the Mexican littoral by bottom trawls system. This result will be used in the future to validate the numerical model of the system with experimental results using a prototype of trawl doors designed in the laboratory of the institute.

Keywords Trawl doors • Bottom trawls • Mathematical model • Hydrodynamic force • Dynamic analysis

42.1 Introduction

The trawl gears are complex systems that consider the presence of different external forces, acting directly on its operation. This system is integrated by coupled components as are: net, sweeps trawl doors or otterboards, warps and others [1, 2]. In the literature is possible to find information in relation with every one of these modules of trawl fishing gears. In this paper we are interested in bottom trawl systems, focusing in the analysis and performance of the trawl doors. Generally the design of trawl doors dependent of the some factors as the conditions of the sand in the bottom of the sea. The parameters of design consider the stability and equilibrium and the good contact with the seabed along the whole length of the keel, even the resistance of the overall structure when it struck with very hard rocks [3, 4]. In this case, the minimum force friction by contact of the shoe of the trawl doors with the seabed is a desirable condition. The stability of the trawl doors is influenced for the action of the hydrodynamic forces in the section of the structure known as wing. This hydrodynamic force is a component of resistance that is associated to the viscous friction over the trawl doors in the section of the wings. The trawl doors is a very complex system, that consider in their design the action of the components of the forces acting in the mechanical structure. In this case, is necessary known each coefficient in terms of the parameters as are: towing speed, angles of the ropes (headrope and footrope) and the warp in the trawl doors. These parameters can be obtained using a mathematical model of a structure designed to scale considering the real parameters of design even the flow conditions, represented by the theorem of similitude (Buckingham's Theorem) [5, 6].

The main purpose of the trawl doors is to keep open the input section of the net in the trawl gear system [5, 6]. The trawl doors are important components in the bottom trawl system, because its contribution in the overall resistance becomes a 25 % for flat rectangular trawl doors. The design of trawl doors with hydrodynamics shapes are performed for reduce the resistance in overall system, maintaining and even increasing the lift force significantly [7]. The technological innovation in the mechanical design for trawl doors in terms of efficiency, consists in reduce the effect of the lift and resistance forces R_L and R_D respectively, in terms of the lift and resistance coefficients C_L and C_D respectively. In this case, if the response of the lift force is greater than the resistance force then the performance of the trawl doors must be higher [5, 6].

S. Sarmiento-Nafaté • J. Villalobos-Toledo • C. Pineda-García

Instituto Nacional de Pesca INAPESCA-CRIPSC, Prolongación Ote. Playa Abierta S/N, Col. Miramar, Salina Cruz, Oaxaca C.P. 70680, Mexico

J. Enríquez-Zárte (✉)

Investigador Cátedras CONACyT, Avenida Insurgentes Sur No. 1582, Col. Crédito Constructor, Benito Juárez, México, D.F C.P. 03940, Mexico

e-mail: jenriquezza@conacyt.mx

42.2 Description of the Trawl Door “INAZTECA”

The mechanical structure is composed of two sheets with double curvature warped, allowing the acceleration of the downstream flow (Venturi). These sheets or plates are linked and stiffen together by two locking structures upper and lower. The previous subsystem is coupled to the main structure through one axis. The main structure consists in fixing frame, whose underside is a shoe or skate designed for allow the longitudinal sliding of trawl door. The angular width between the two sheets or plates is achieved by using a platen of articulated positioning that allows to change the parameter of the angle (see Fig. 42.1).

The dimension and category of materials of each of the components of the overall mechanical structure is presented below in the following tables (Tables 42.1, 42.2 and 42.3).

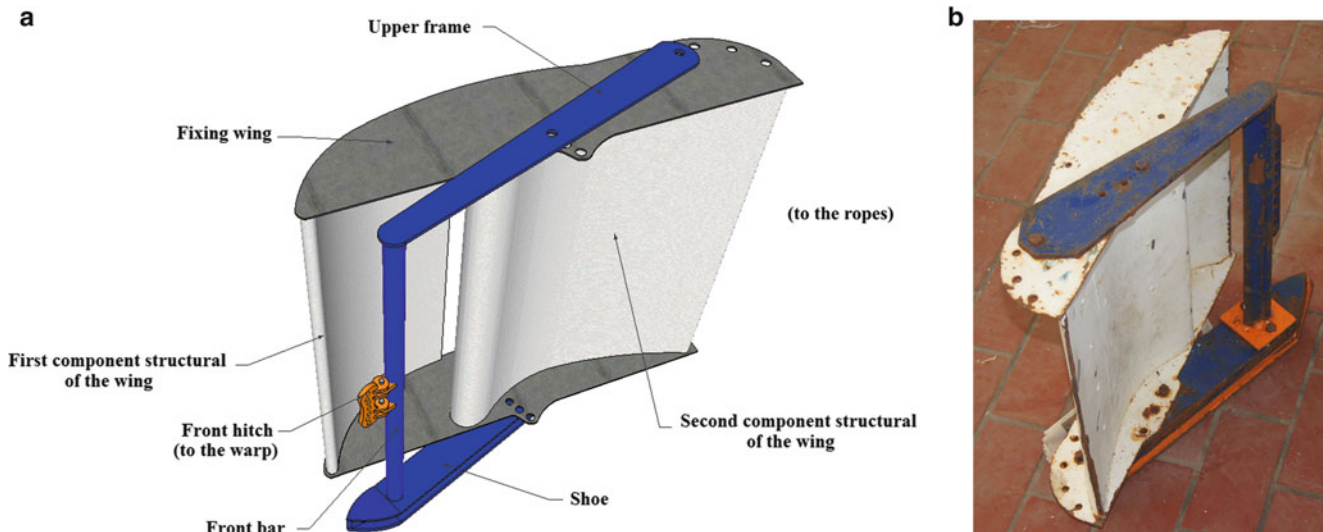


Fig. 42.1 Trawl door “INAZTECA”: (a) Mechanical design, (b) Experimental scale-prototype

Table 42.1 Dimension of the frame parts (Steel A36)

Part	High (mm)	Length (mm)	Thick (mm)	Weight (kg)
Front frame	254	711	19	26.5
Front frame	254	229	19	8.6
Front frame	1041	203	19	31.1
Upper frame	203	1676	19	50.0
Platen	254	1676	50	166.6
Front triangle			50	12.6
Bolt	2051		25	8.0
Total				303.4

Table 42.2 Dimension of the wing parts (Aluminum H14 alloy 3003)

Part	High (mm)	Length (mm)	Thick (mm)	Weight (kg)
Plates	978	823	5	10.4
Plates	978	823	5	10.4
Plates	978	823	8	17.3
Plates	978	823	8	17.3
First attachment structure	49	588	8	0.6
Second attachment structure	76	1295	8	2.1
First attachment structure	49	588	8	0.6
Second attachment structure	76	1295	8	2.1
Total				60.8

Table 42.3 Dimension of opening arm (carbon steel)

Part	High (mm)	Length (mm)	Thick (mm)	Weight (kg)
Opening arm	101	889	25	6.2
Total				6.2

In this paper we are interested in obtain the mathematical model of the trawl door “INAZTECA”, for which we consider the mechanical design of the trawl door. In order to reduce complexity in the analysis of the system, we assume that the wing surface of the trawl door is one piece and the effect of Venturi is not considered in the modeled.

42.3 Mathematical Model

42.3.1 Analysis of Forces on the Trawl Door

The bottom trawl in the real gear is a complex system (see Fig. 42.2), which is disturbed by external factors like the irregular forms of the seabed and others as the waves or water currents and the wind forces; these are factors that time-dependent and both are stochastic system. These external conditions influence in the towing speed of the vessel reflecting in energy consumption.

In order to simplify the analysis of the system, we assume the following constraints focus in the dynamic of the trawl doors: towing velocity is considered constant and the effect of the friction of the base (shoe) of the trawl doors with the seabed is negligible as well as the effect of the normal force and finally neither is considered the issue of pitch and heel angle.

The free body diagram of the trawl door connects warp and ropes (headrope and footrope) of trawl, as show in Fig. 42.3.

In terms of D’Alembert principal, dynamic equations of trawl door considering the forces from the free body diagram can be written as follows:

$$\vec{W} + \vec{T} + \vec{F} + \vec{B} + \vec{F}_{b1} + \vec{F}_{b2} + \vec{F}_{Friction} + \vec{N} = 0 \quad (42.1)$$

where \vec{W} is the weight of trawl door; \vec{T} is the tension of warp; \vec{B} is inertial force of the trawl door; \vec{F} is the force applied on trawl door by the fluid; \vec{F}_{b1} and \vec{F}_{b2} are the forces generated by the ropes (headrope and footrope) of trawl, respectively. $\vec{F}_{Friction}$ is friction force with the seabed and \vec{N} is the normal force in the trawl door. In this case for reduce the complexity of the system; consider the analysis of the trawl door as the end node of warp. The coordinate system of warp is analyzed through an inertial coordinate system $O_T^{i,j,k}$ and local coordinate system $P^{n,t,b}$, as show in Fig. 42.4. Both coordinate systems can be related by rotations trough Euler angles, as shown in Fig. 42.4 [10].

The forces applied on trawl door are described as follows:

$$\begin{aligned} \vec{W} &= (m_d - \rho V_d)g\vec{k} \\ &= (m_d - \rho V_d)g \cdot (\sin \phi_N \vec{t} + \cos \phi_N \vec{n}) \end{aligned} \quad (42.2)$$

where m_d is the mass of trawl door; V_d is the volume of trawl door; ρ is the fluid density and g is stands for the gravity acceleration.

$$\vec{T} = -T_N \vec{t} \quad (42.3)$$

where T_N is the tension of warp’s end point.

The force applied on trawl door by the fluid is evaluated considering the lift and resistance force R_L and R_D respectively, as follows:

$$R_L = \frac{1}{2} \cdot \rho S C_L V^2$$

Fig. 42.2 Classic bottom trawl system [8, 9]

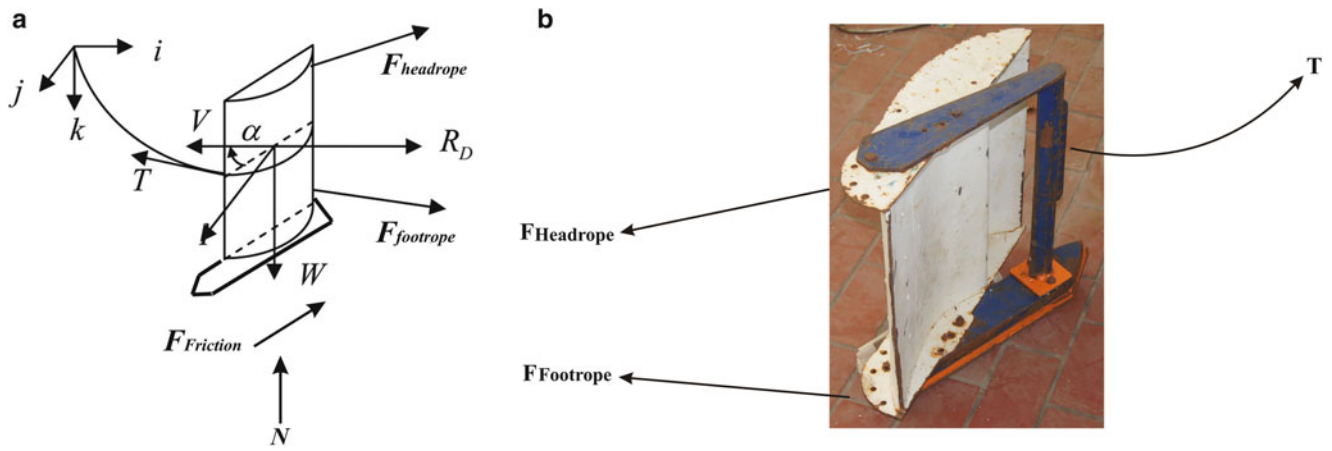
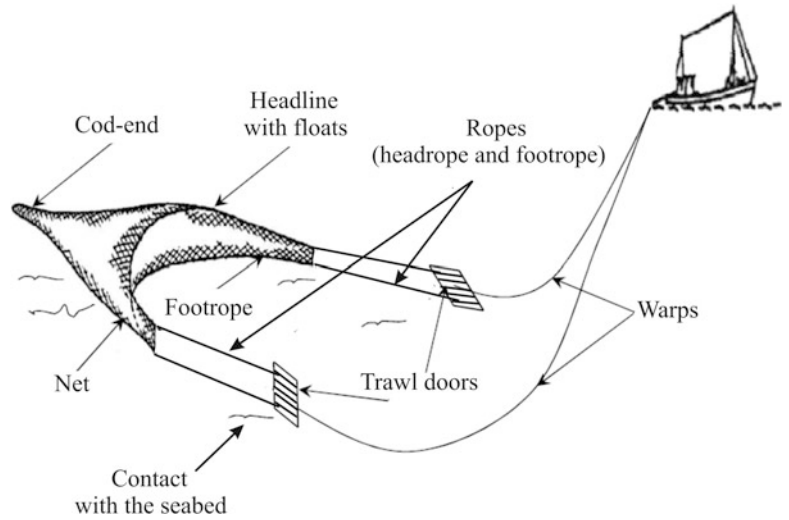
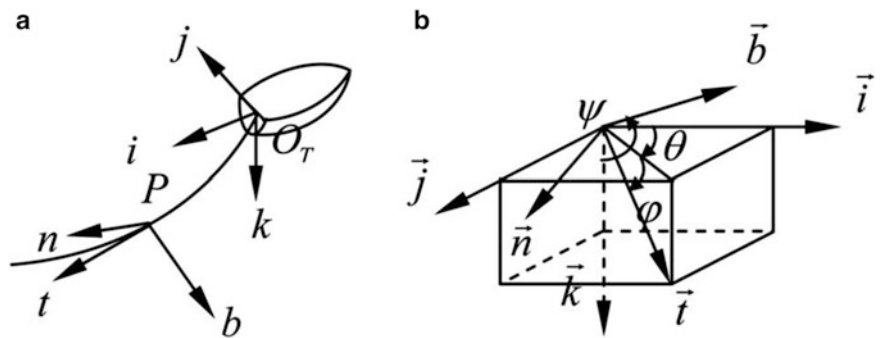


Fig. 42.3 Diagram of forces in the trawl door: (a) Analytical scheme [10], (b) Experimental scale-prototype

Fig. 42.4 (a) Coordinate system of warp, (b) Configuration of Euler angles

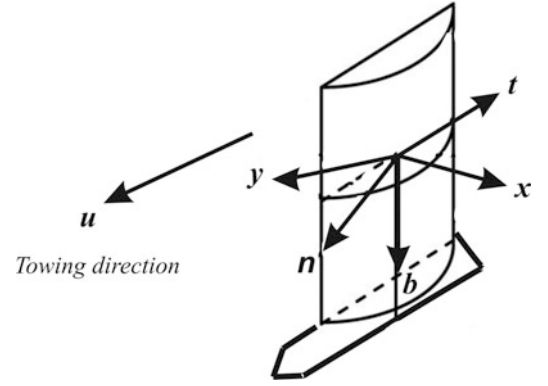


$$R_D = \frac{1}{2} \cdot \rho S C_D V^2 \tag{42.4}$$

where ρ is the fluid density; S is side area of trawl door; V is current speed C_L ; and C_D are lift and resistance coefficients respectively.

For simplification of the analysis, the fluid force of trawl door can be calculated as follows:

Fig. 42.5 The coordinate system X and the Cartesian frame of reference P



$$R_L = \frac{1}{2} \rho S C_L \sqrt{u_t^2 + u_n^2} (u_t \vec{i} - u_n \vec{j})$$

$$R_D = \frac{1}{2} \rho S C_D [u_t |u_t| \vec{t} + u_n |u_n| \vec{n} + u_b |u_b| \vec{b}] \quad (42.5)$$

considering the towed at speed u .

$$\vec{B} = -(m + \Delta m) (\dot{v}_t \vec{t} + \dot{v}_n \vec{n} + \dot{v}_b \vec{b}) \quad (42.6)$$

where Δm is added mass of trawl door; v is lateral velocities and m is mass of vessel.

The forces of the ropes (headrope and footrope) of trawl \vec{F}_{b1} , \vec{F}_{b2} , respectively and force R_L can be described in warp local coordinate system, as follows:

$$\vec{F}_{b1} + \vec{F}_{b2} + \vec{R}_L = Q_t \vec{t} + Q_n \vec{n} + Q_b \vec{b}. \quad (42.7)$$

where $Q_{t,n,b}$ is the torque of the ship in terms of propeller. An alternative form to obtain a simple dynamic model of the force of the ropes (headrope and footrope), is considering the ropes as a mechanical elements like springs with stiffnesses (K_{b1} , K_{b2}) [11, 12]. Finally in this paper to reduce the complexity of the model, we consider valueless the friction force $\vec{F}_{Friction} = 0$.

42.3.2 Matrix Form of the Mechanical Structure

The objective of the trawl doors is to spread the gear horizontally and, simultaneously, to keep it in contact with the seabed. In common, a trawl door has six degrees of freedom which must be balanced under the steady towing assumption. In order to obtain the equilibrium equations (forces and moments), we can move the orthonormal local frame of reference $P = \{t, n, b\}$ and attached to the trawl door and having the origin located at the center of the pressure (see Fig. 42.5) [10].

The coordinate system P and the Cartesian frame of reference X are related by $X = A \cdot P$ or $P = A^{-1} \cdot X$ or $P = A^T \cdot X$. In general, A results from composing a rotation of heel angle φ along the x axis, a rotation of pitch angle θ along the y axis, and a rotation of yaw angle ψ (angle of attack) along the z axis.

In this case we are interesting in the analysis of effect in the angle of attack (ψ), and it reduce the transformation matrix to a single rotation, considering the angle of heel and pitch valueless, i.e., $\beta = 0$ and $\alpha = 0$, respectively.

$$A = \begin{bmatrix} \cos \psi & -\sin \psi & 0 \\ \sin \psi & \cos \psi & 0 \\ 0 & 0 & 1 \end{bmatrix} \quad (42.8)$$

The matrix representation of the mass force of the trawl door due to weight (\mathbf{W}) along the vertical direction is described as follows:

$$(\mathbf{W})_X = \begin{bmatrix} 0 \\ 0 \\ (m_d - \rho V_d)g \end{bmatrix} \quad (42.9)$$

The matrix representation of the hydrodynamic force (\mathbf{F}) of the trawl door consist in the forces applied by the fluid that depend of the towing speed squared, angle of attack, and trawl door design. These hydrodynamic forces are evaluated experimentally in terms of the resistance or drag and lift coefficients as follows:

$$(\mathbf{F})_X = \frac{1}{2} \rho S |\mathbf{u}|^2 \begin{bmatrix} C_D(\psi) \\ C_L(\psi) \\ 0 \end{bmatrix} \quad (42.10)$$

An efficient design aims to maximize the ratio C_L/C_D while keeping the trawl door stable.

The matrix representation of the inertial force (\mathbf{B}) of the trawl door due to mass (Δm) along the horizontal direction is described as follows:

$$(\mathbf{B})_X = \begin{bmatrix} -(\Delta m)\dot{v} \\ 0 \\ 0 \end{bmatrix} \quad (42.11)$$

The matrix representation of the warp tension (\mathbf{T}) at the trawl door is described as follows:

$$(\mathbf{T})_X = -T_N \begin{bmatrix} \cos \psi_w \cos \theta_w \\ \sin \psi_w \cos \theta_w \\ \sin \theta_w \end{bmatrix} \quad (42.12)$$

where ψ_w and θ_w are the yaw and pitch angles of the warp at the trawl door bracket, considering $\{\psi_w, \theta_w\} > 0$.

Particularly the typical practice to catch shrimp in the Mexican littoral consist in connect straight the trawl doors with the trawl through the ropes (headrope and footrope) (see Fig. 42.6). The commercial shrimp trawl is designed with a twin backstop to join the ropes (headrope and footrope) from the trawl door to the trawl (see Fig. 42.6).

For the complete analysis of the forces generate by the ropes (headrope and footrope), is necessary consider the action of the angle yaw or angle of attack (ψ) of the wing in the trawl door (see Fig. 42.7).

Now, it is possible obtain the matrix representation of the forces generated by the ropes (headrope and footrope) of trawl \vec{F}_{b1} and \vec{F}_{b2} at the first configuration (Fig. 42.5a), as follows:

$$\begin{aligned} F_{b1} &= F_{b1} \begin{bmatrix} \cos \psi_b \cos \theta_{b1} \\ \sin \psi_b \cos \theta_{b1} \\ \sin \theta_{b1} \end{bmatrix} \\ F_{b2} &= F_{b2} \begin{bmatrix} \cos \psi_b \cos \theta_{b2} \\ \sin \psi_b \cos \theta_{b2} \\ \sin \theta_{b2} \end{bmatrix} \end{aligned} \quad (42.13)$$

In the second configuration (Fig. 42.5b), the matrix representation of the forces generated by the ropes (headrope and footrope) is the similar equation (42.13); in this case, we consider a twin backstop attachment into the model, and the forces \vec{F}_{b1} and \vec{F}_{b2} are described in the following equation:

$$(\mathbf{F}_{bT})_X = (F_{b1} + F_{b2})_X \quad (42.14)$$

In this paper, we consider the lengths of chains or ropes (headrope and footrope) in both configurations, are equals after and

Fig. 42.6 Configuration of ropes with the trawl to catch shrimp: (a) Classic of Mexican littoral, (b) Commercial

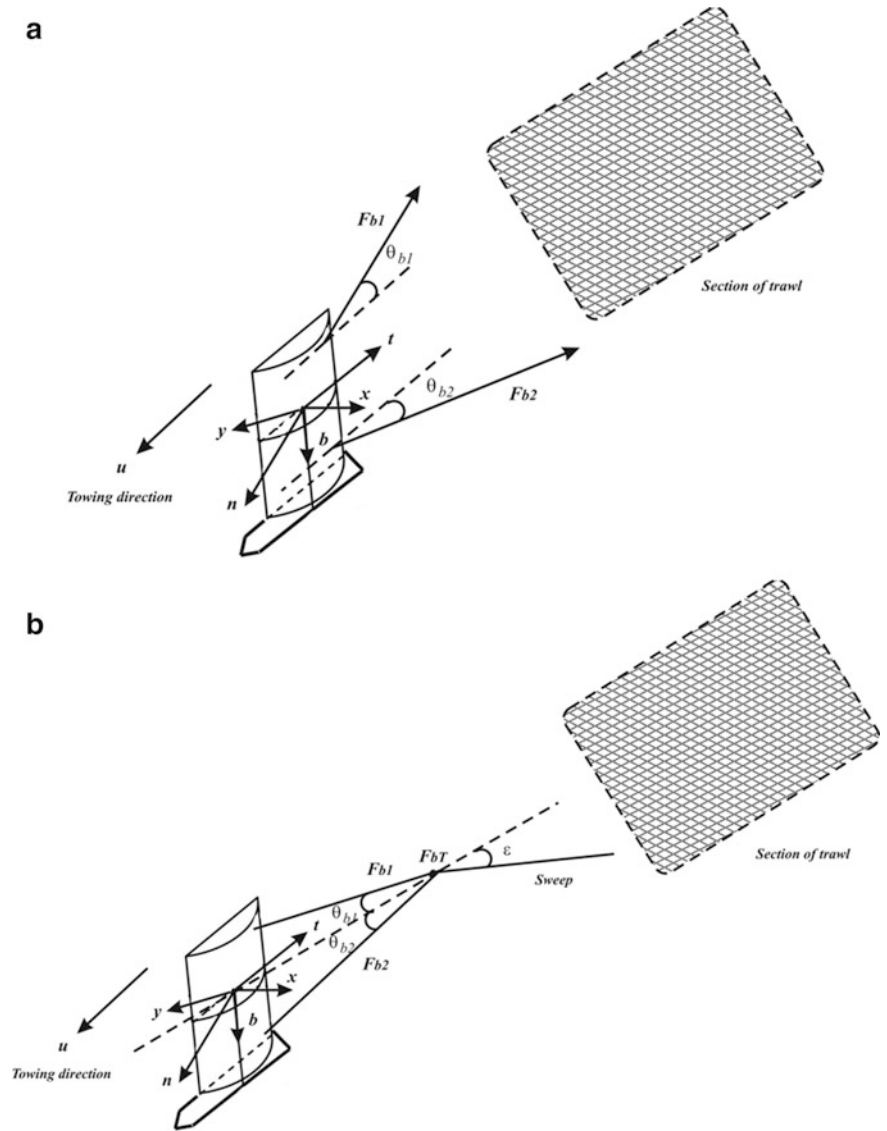


Fig. 42.7 Analysis of angle of attack (ψ), with respect to the wrap and the backstop

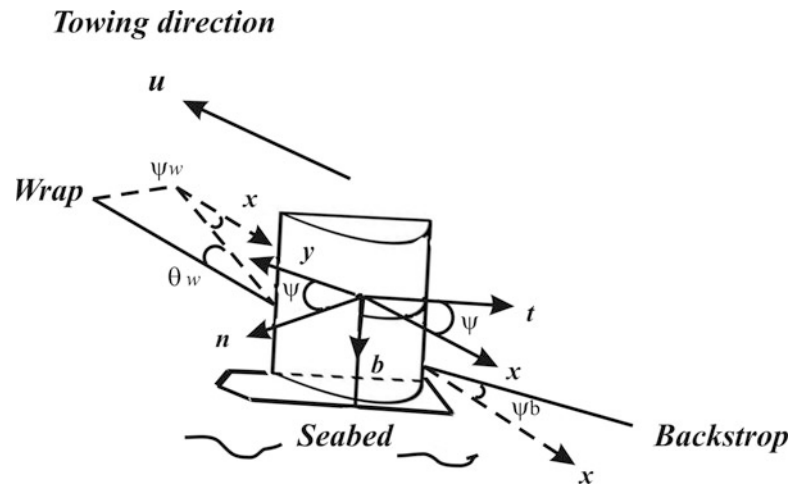
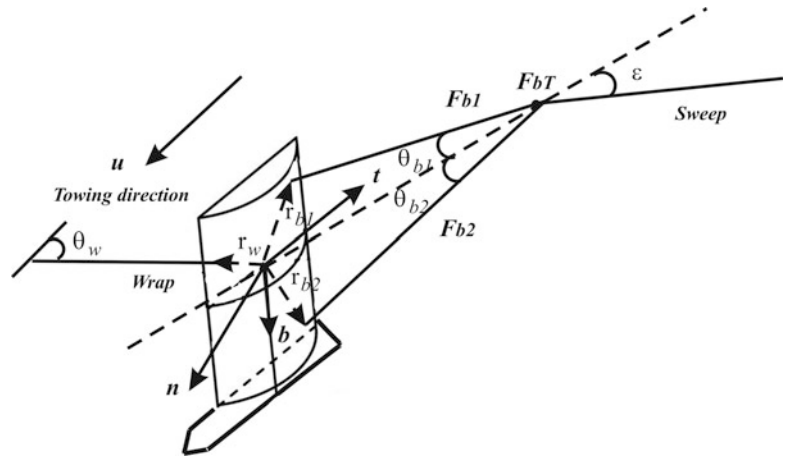


Fig. 42.8 Balance moment of the trawl door using the reference system P



before of the twin backstop, and have a pitch angle θ_b . In order to close the balance of forces it is necessary to add an additional constrain for F_{b1} and F_{b2} at the backstop attachment point:

$$\begin{aligned} (F_{b1} + F_{b2}) \cos \theta_b &= F_{bT} \cos \epsilon \\ (F_{b1} - F_{b2}) \sin \theta_b &= F_{bT} \sin \epsilon \end{aligned} \quad (42.15)$$

Finally the balance forces at the trawl door are obtained by combining (42.9)–(42.15) and imposing equilibrium. In addition the analysis of balance of moments is necessary to the equilibrium hypothesis [1, 2]. This is calculated with the reference of the system P (i.e. the center of pressure). Considering the constraint of zero heel (φ) neither moments is produce by the weight force. In consequence, we limit the balance of moments to the pairs applied by the warp and the ropes (headrope and footrope) (see Fig. 42.8).

The warp moment (M_w) is calculated using the subsequent expression $(r_w)_P = (t_w, n_w, b_w)^T$, that represent the position vector of the warp bracket in the P frame of reference. Considering the transformation matrix (42.8), we obtain that:

$$(r_w)_X = A \cdot (r_w)_P \quad (42.16)$$

Resulting that the moment applied by the warp is described as:

$$M_w = A \cdot (r_w)_P \times T, \text{ with } T \text{ given by (42.12)} \quad (42.17)$$

The ropes moment (M_b) is calculated using the subsequent expression $(r_{b1})_P = (t_{r_{b1}}, n_{r_{b1}}, b_{r_{b1}})^T$ and $(r_{b2})_P = (t_{r_{b2}}, n_{r_{b2}}, b_{r_{b2}})^T$ are the position vector of the ropes (headrope and footrope) attachments in the P frame of reference. We obtain the following equation:

$$\begin{aligned} (r_{b1})_X &= A \cdot (r_{b1})_P \\ (r_{b2})_X &= A \cdot (r_{b2})_P \end{aligned} \quad (42.18)$$

Resulting that the moment applied by the ropes is described as:

$$M_b = (r_{b1} + r_{b2}) \times F_{bT}, \text{ with } F_{bT} \text{ given by (42.14)} \quad (42.19)$$

In order, imposing equilibrium, (x) and (z) components in the system are:

$$\begin{aligned} ((M_w)_x + (M_b)_x) &= 0 \\ ((M_w)_z + (M_b)_z) &= 0 \end{aligned} \quad (42.20)$$

The overall system is constituted through of six non-linear equations for the six unknowns: trawl door angle of attack (ψ), warp tension and yaw angle at trawl door attachment (T and ψ_w), tensions at the ropes (headrope and footrope) (F_{b1} and F_{b2}), and ϵ angle.

The previous results are used to model the forces involved in the dynamic of the system, considering a simplified model of the trawl door “INAZTECA”. The system of equations obtained will be used for the dynamic equations of the structure and validate the behavior of the angle of attack (ψ) of the wings in the trawl door. Recently, hydrodynamic tests were performed at the trawl door “INAZTECA” in a flume tank test, evaluate their performance in terms of the lift and resistance forces C_L and C_D respectively. These experimental results are will be used to compare the numerical system response simulated in the platform of Matlab© and Simulink© software through the dynamic equations presented in this article and thereby validate the mathematical model presented.

42.4 Conclusions

The simplified mathematical model of the trawl doors “INAZTECA” is presented, considering the analysis of forces and moments acting in the dynamic of the system. In this previous work, the matrix representation of the equations are obtained in order to be used for the Ordinary Differential Equations to analyze their dynamic behavior by numerical simulations in Matlab© and Simulink© software. Finally, we consider some constraints in the analysis in order to reduce complexity of the mathematical model in the structure. Further work is being conducted to compare the experimental results. Future work related to the development of a mathematical model that considers the effect Venturi by the hydrodynamic forces in the trawl doors.

Acknowledgements This work is conducted with financial support from the Instituto Nacional de Pesca (INAPESCA), Project “Evaluar el Comportamiento Hidrodinámico del Prototipo de Portón “INAZTECA” en Tamaños a Escala y Estándar, Mediante el Análisis Numérico y Pruebas de Campo. INAPESCA-SC-CS-AD/006/2015” (México).

References

1. A. Folch, J. Prat, J. Antonijuan, A simplified model for bottom trawl fishing gears. Universitat Politècnica de Catalunya. Departament de Matemàtica Aplicada IV; Universitat Politècnica de Catalunya. SARTI—Sistemes d’adquisició Remota i Tractament de la Informació, 2007. <http://hdl.handle.net/2117/1014>
2. J. Prat, J. Antonijuan, A. Folch, A. Sala, A. Lucchetti, F. Sardà, A. Manuel, A simplified model of the interaction of the trawl warps, the otterboards and netting drag. *Fish. Res.* **94**(2008), 109–117 (2008)
3. J. Main, G. I. Sangster, A study of bottom trawling gear on both sand and hard ground (Scottish fisheries research report), Dept. of Agriculture and Fisheries for Scotland (1979)
4. Dominique Marichal, Benoît Vincent, Study of the manoeuvrability and security of a trawl gear, Hydroelas 2006 + Ergomare, 2006. <http://archimer.ifremer.fr/doc/2006/acte-4612.pdf>
5. Freiria Jorge, Ensayo de Portones para Redes de Arrastre “INAZTECA” (Informe final portones “INAZTECA”), Facultad de Ingeniería, Universidad de la República [UDERLAR], Uruguay (2012)
6. Jorge Freiria, Modelo Geométrico y Dinámico para Aparejos de Pesca de Arrastre, XXII Congreso Panamericano de Ingeniería Naval—COPINAVAL (Asociación Argentina de Ingeniería Naval, Buenos Aires, 2011)
7. M.P. Remesan, Otter Boards and Other Sheer Devices, in Winter School manual on “Advances in Harvest Technology” organized by CIFT at Cochin 20 Nov–19 Dec 2002, pp. 328–342
8. de la Prada Amelia I, *, Priour Daniel, The effect of the bottom boundary layer on trawl behaviour, *Ocean Engineering* June 2015, vol 101 (2015), pp. 142–151
9. de la Prada Amelia, González Manuel, Modeling and Simulation of Bottom Trawl Gears, *Multibody Dynamics 2011*, Ecomas Thematic Conference ed. by J.C. Samin, P. Fiset (Brussels), 4–7 July 2011
10. Xiao-Feng Sun, YongYin, He-Long Shen, Xin-Yu Zhang, Mathematical modeling method of trawler equipped with CPP, *Modelling and Computation in Engineering—Taylor & Francis Group, London. Proceedings of the International Conference on Modelling and Computation in Engineering, CMCE 2010*, Hong Kong, 6–7 Nov 2010, pp. 73–78
11. Ana Ivanovic, D. Neilson Richard, Chibisi Chima-Okereke, Modelling of the interaction between trawl gear components and the seabed—overview, *Fishing gear-seabed interaction DEMAT ’09*, pp. 21–31 (2009)
12. A. Ivanovic, D.N. Richard, F.G. O’Neill, Modelling the physical impact of trawl components on the seabed and comparison with sea trials. *Ocean Eng.* **38**(2011), 925–933 (2011)

Chapter 43

Simulator of an Adaptive Optics System Using Matlab

Marco A. Betanzos-Torres, Juan Castillo-Mixcóatl, Severino Muñoz-Aguirre, and Georgina Beltrán-Pérez

Abstract This article describes a program developed in Matlab that simulates an Adaptive Optics system, which allows observing a graphically simulated wavefront to understand the main concepts of an Adaptive Optics system and the constraints that have to be presented in classical control algorithms. The program is based on: (a) Simulation of a wavefront Shack-Hartmann sensor as a detection system and the wavefront reconstruction using Zernike polynomials from the slopes of the wavefront and (b) Simulation of a deformable mirror as the wavefront correction. This was characterized using the so called influence functions and Zernike polynomials. The voltage vector needed for the deformation that adopts the correction mirror wavefront was also calculated. Our results were corroborated graphically by the reconstruction of the wavefront and the deformation of the deformable mirror.

Keywords Adaptive Optics • Shack-Hartmann • Deformable mirror • Algorithm • Simulation

43.1 Introduction

For several decades, various Adaptive optics (AO) system devices have been developed for reconstruction and wavefront (WF) correction [1]. In the context of ophthalmic applications, Smirnov in early sixties proposed a method for measuring ocular aberrations, and suggested the possibility of correction [2]. Would not be until the nineties when the first static corrections of higher order aberrations were performed on the human eye [3, 4]. The dynamic characteristics of ocular aberrations require a correction in real time [5]. This leads to the creation of new control algorithms when using these devices. However, commonly the development of such systems involves understanding of different concepts in different areas, from optics to electronics both theoretical concepts and their practical implementation. These systems of Adaptive Optics (AO) can be divided in three major blocks: wavefront detection system, control algorithm and correction system [6]. The wavefront detection method is through the use of a Shack-Hartmann sensor (SH) in order to have control signals for the actuators of the deformable mirror (DM) from the measured data of an image, and then to rebuild the WF. There are devices to measure the WF, for instance [7] a static microlens array is substituted on a Shack Hartmann sensor by an LCD. On the other hand to perform the wavefront correction, the most used devices are mirrors with discrete actuators, segmented, of membrane, and bimorph or in other cases an LCD. The algorithm used for the control block was proportional where the main objective of the AO system usually is to determine the C parameter that adjusts the number of functions of the reconstruction matrix [8, 9]. When these issues are addressed first, it is not easy to establish the relationship between the WF and the responses of SH and the operation of the DM. Not to mention how dark it can be to understand how they are constructed. Therefore, in this paper a simulation of an AO system was developed to provide theoretical understanding of the use of the most important devices of this system. In particular, emphasis on SH and the DM was made. To archive, various programs were developed in Matlab environment for visualizing the reconstructed WF, well as the deformation that adopts the DM. The purpose of this simulation is to simplify the concepts of the matrices of influence functions and the use of Zernike polynomials to represent the WF. This article is divided in: Materials and Methods sections, where the concepts of AO system are presented as well as the strategy used to emulate the SH and DM, also it explains the parameters needed in both cases; the Results section presents graphs from the different programs developed for the simulation of this system and finally Conclusions summarizes the relevant aspects of this work.

M.A. Betanzos-Torres (✉) • J. Castillo-Mixcóatl • S. Muñoz-Aguirre • G. Beltrán-Pérez
Facultad de Ciencias Físico Matemáticas, Benemérita Universidad Autónoma de Puebla, Avenida San Claudio y 18 Sur,
Colonia San Manuel, Edificio 111A-109B, Puebla-Puebla, Mexico
e-mail: marcotronixs@gmail.com

43.2 Materials and Methods

Fig. 43.1a shows the elements of a classic AO system in closed loop. The elements enclosed in a circle are the ones to be simulated: (1) Input wavefront, whose dimensions can be selected by the user, (2) Wavefront of SH sensor, where it is possible to change the number of lenses, (3) Deformable membrane mirror, in this case with 36 actuators and finally (4) The distorted WF to be simulated as the input of the system. In Fig. 43.1b the operation principle of a SH sensor is shown.

43.2.1 Shack-Hartmann Sensor

Generally a WF is measured using an SH sensor, as is shown in Fig. 43.1b. However this device essentially measures the slopes of the incident wavefront on its lenses. Therefore, this paper proposes to simulate the SH sensor through a computer program called `Gradiente_xy()`. This program basically requires an area representing the wavefront to be evaluated, the distribution of the lenses (`xy_offset`, `xy_step`), the radius and the total number of lenses (`radius`, `lenses_Num`). The program evaluates the spatial derivatives in x and y using a numerical approximation of the second order derivative. Then the lens operation is simulated by the average of the derivatives on the circular regions resulting in the lens radius, with centers at coordinates determined by `xy_step` and `xy_offset` as is shown in Fig. 43.2. From this figure, two slope matrices are generated, in x and y . Following from the slopes, you want to rebuild the wavefront using the Zernike polynomials. To achieve that, the implemented program is based on generating the equations of Zernike polynomials [10]. These equations allow to obtain analytically Zernike polynomials and their derivatives. By obtaining those derivatives from modes (polynomials) the reconstruction matrix Z can be obtained, which can be expressed as equation [11].

$$C = Z^{-1}S_{xy} \quad (43.1)$$

where S_{xy} is a vector with information of the wavefront slopes, obtained by the SH sensor, $S_{xy} = (s_{1x}, s_{2x} \dots, s_{nx}, s_{1y}, s_{2y} \dots, s_{ny})^T$, with $2 \text{ lenses_Num} \times 1$ items. Z is the matrix of reconstruction which $2 \text{ lenses_Num} \times m$ elements, where m is the number of Zernike polynomials (modes) to be used for the reconstruction of the wavefront. Finally C is a vector with all the coefficients $C = (C_1, C_2 \dots, C_m)^T$, determining the weight of each polynomial in the wavefront under construction. The AO

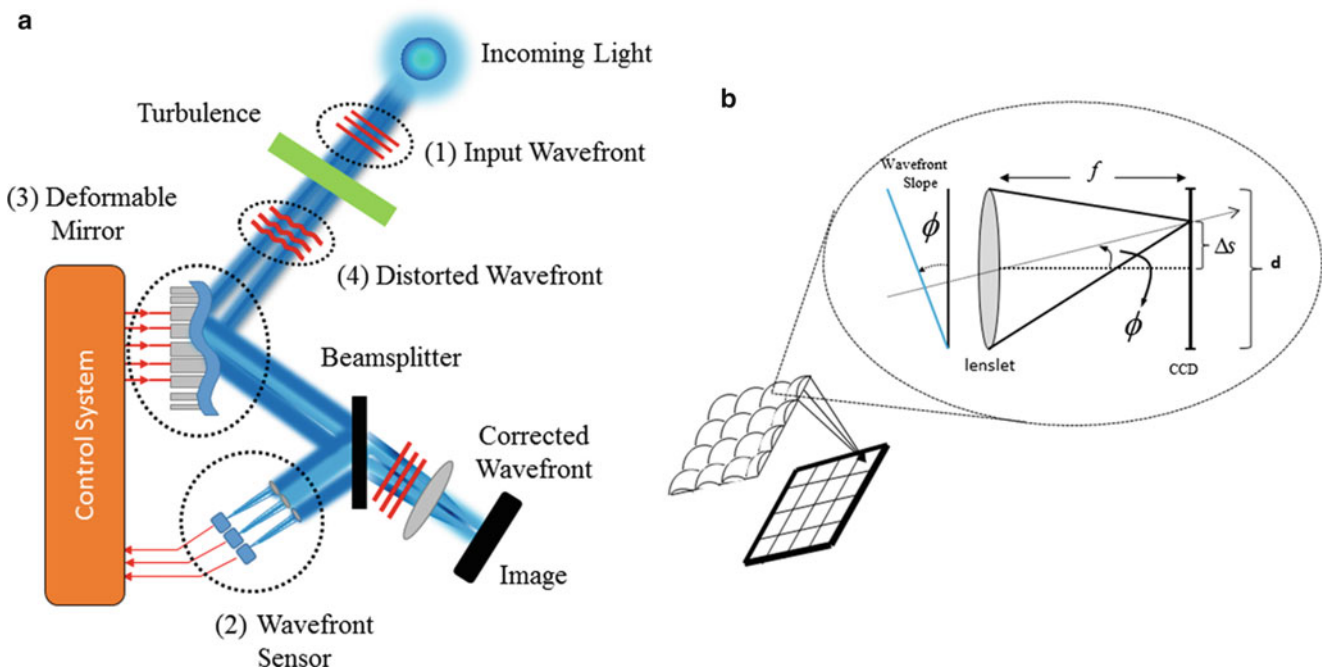


Fig. 43.1 (a) Adaptive Optics system with a closed loop and the various elements that comprise it. (b) Operation principle of an SH sensor, essentially this sensor measures the slopes of the WF under testing

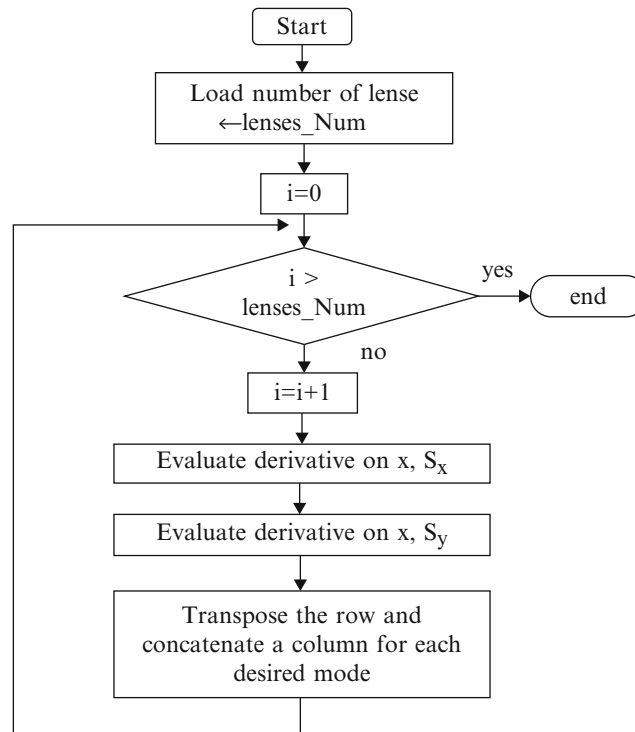


Fig. 43.2 Parameters for emulation SH by `Gradiente_xy()`

system objective usually is to find the C parameter that sets the number of functions of the matrix reconstruction to the appropriate values of the number of modes selected for reconstruction, this means that it has a system of n equations with m unknowns what makes Z not a square matrix and therefore in order to solve the system a method called pseudoinverse matrix was used [12, 13]. Each column of the matrix reconstruction Z consists of the derivatives (in x and y) modes expressed by the Zernike polynomials. The Fig. 43.3 shows the flowchart for the construction of the Z matrix.

43.2.2 Deformable Mirror (DM)

In order to model the response of the surface of the deformable mirror, a linear combination of surface deformation due to the action of a single actuator when the rest remains at a fixed voltage, was used. This response is known as the influence function (IF), see Fig. 43.4. A deformation of the mirror can be represented mathematically by a linear combination of the influence functions of all the actuators. Therefore to calculate Deformable (DM) the matrix (A) of the influence function, the program called `Influence_Matrix_DM()` was developed. This Adaptive optics (AO) system: Deformable (DM): requires the following parameters: *Resolution*, which determines the number of pixels, *Gaussian_width* is the width of the Gaussian function used as IF for the actuator, *xy_in* and *xy_end* are the simulation interval, *xy_offset_DM* and *xy_step_DM* determines the position of the actuators and *Actuator_Num* is the number of actuators. Within this program, it was used the program called `Gradiente_xy()`, which has already been explained above.

For DM simulation, we used the modal method [11] and the function was implemented by `Generate_Surface_DM()` which requires the following parameters: size of the surface (*xy_in*, *xy_end*), pixel resolution (*Resolution*), separation of actuators (*xy_step_DM*), width of the influence function (*Gaussian_width*), and the values of voltage actuators (V). This program performs the linear superposition of the influence functions of each actuator present in the DM. The magnitude of each IF was determined by the values of voltages and is described by (43.2).

$$V = A^{-1}ZC \quad (43.2)$$

where V is the vector $V = (V_1, V_2, \dots, V_n)^T$, with all the associated voltages for the DM to adopt the desired surface, with dimensions of $n \times 1$, where n is the number of actuators used to emulate the DM, A is the matrix of IF, with dimensions

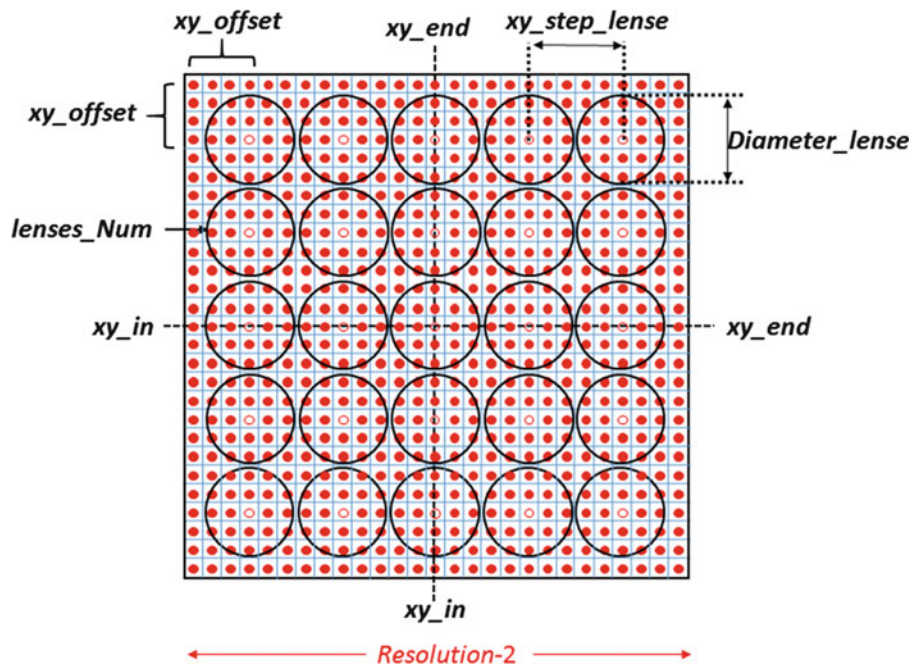


Fig. 43.3 Diagram for obtaining Z reconstruction matrix

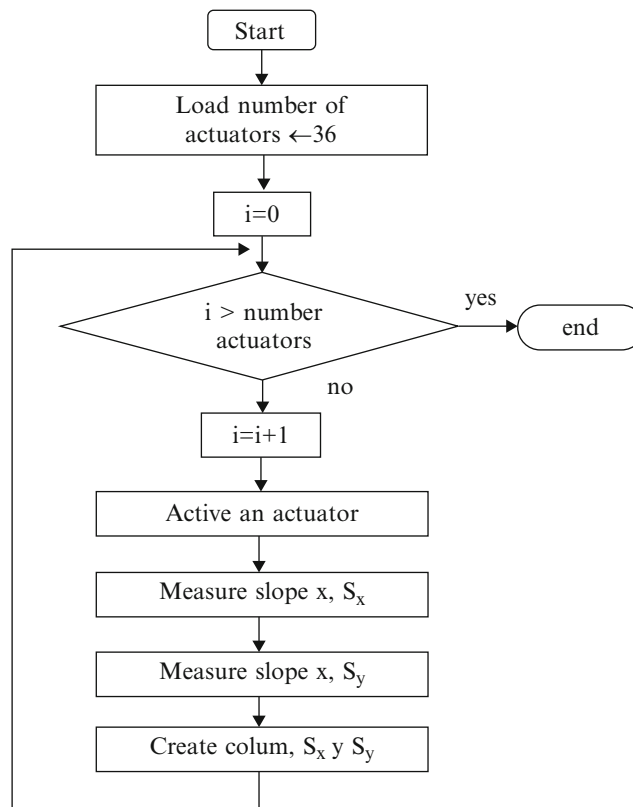


Fig. 43.4 Influence function for an actuator located in the center of the DM simulated

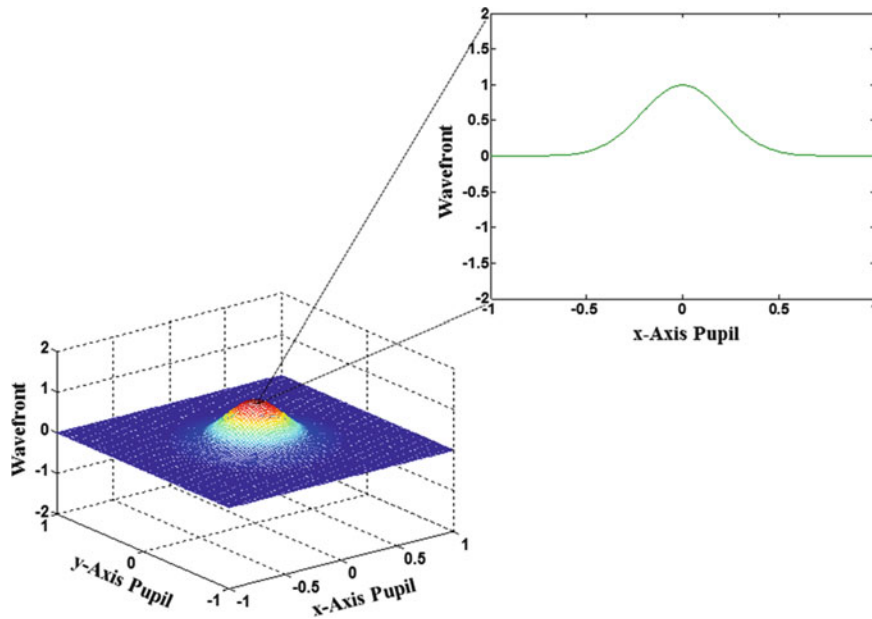


Fig. 43.5 Diagram for obtaining the influence function matrix

$2lenses_Num \times n, Z$ is the reconstruction matrix, and C is the coefficient estimated in the wavefront reconstruction. Since the dimensions of A are $2lenses_Num \times n$, again the pseudoinverse matrix method was used to evaluate the inverse. The pseudocode for evaluating the influence function matrix is presented in the Fig. 43.5.

43.3 Results

In order to validate the performance of the program developed, it was performed the following process: (1) It was generated a surface that models the wavefront by a linear combination of four Zernike polynomials, through the program called *Wavefront()*, with dimensions xy_in, xy_end from -1 to 1 respectively, and a resolution of 72 pixels. (2) The program that models the SH sensor for the derivatives in x y y was employed. (3) With information from the derivatives obtained in (1) and the reconstruction matrix, the coefficients of the Zernike polynomials were calculated. Fig. 43.7a shows a wavefront formed by $WF = 3Z1 + 2Z3 - 4Z6 + 1.7Z9$, and in Fig. 43.8a the coefficients calculated by our programs show the contribution of each Zernike polynomial, which practically are the same of the WF input. In the Fig. 43.6 shows the flowchart, which simulates a wavefront, obtaining: derivative, the influence function matrix, and finally, the deformation of the DM surface.

To verify the performance, different levels of white noise were added to the WF. Below we show the results for various cases. As may be seen in Fig. 43.7b the minimum addition of white noise, 2RMS, to WF do not strongly affect to the obtained Zernike coefficients, see Fig. 43.8b. However clearly appears small contributions of coefficients that were not present originally in the WF. In Fig. 43.7c, d by increasing noise level to 3 and 4 RMS, respectively, it can be seen the same effect and significant contributions from many others modes. It is clear that the coefficients that most contribute are those that were used to create WF input, see Fig. 43.8c, d.

As can be seen, in the presence of noise less than 4 RMS the calculation of the Zernike coefficients was quite successful.

Once the C coefficients were calculated, they were used to modify the surface of the DM to correct the wavefront. This was performed through (43.2), based on a linear combination of IF and thus simulate the deformation of the DM. Fig. 43.9a shows the surface obtained in the DM with the voltages calculated from (43.2) and from the C parameter in Fig. 43.7a. The surfaces on the DM with different noise levels are shown on Fig. 43.7b–e. As it can be seen, the DM surface has an acceptable similarity with the WF input, even with high noise levels from last simulations.

It is necessary to analyze the similarities between the WF and the surface at the DM to determine quantitatively the performance of the programs developed. This type of analysis will be performed in the near future. However qualitatively it can be said that these programs give a general idea of how the devices operate in a real AO system, which can be very useful for those professionals who wish to have a deeper understanding of this type of optical systems.

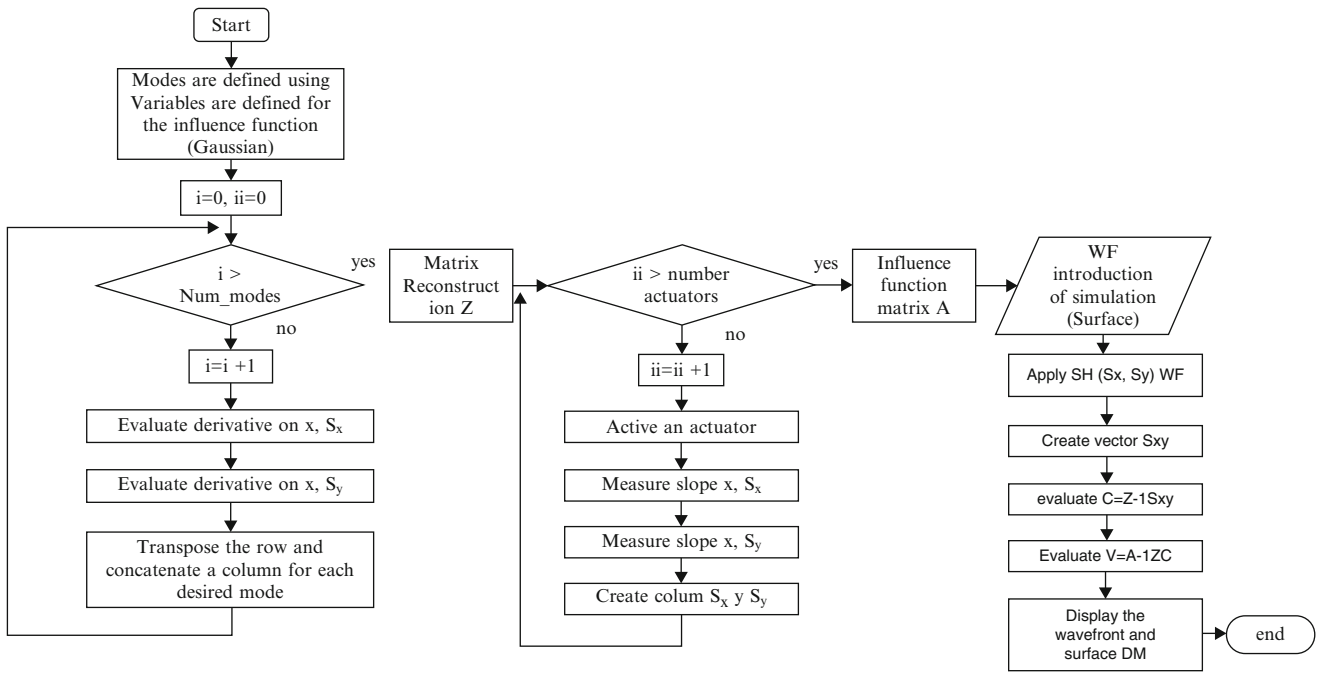


Fig. 43.6 Algorithm simulation AO System

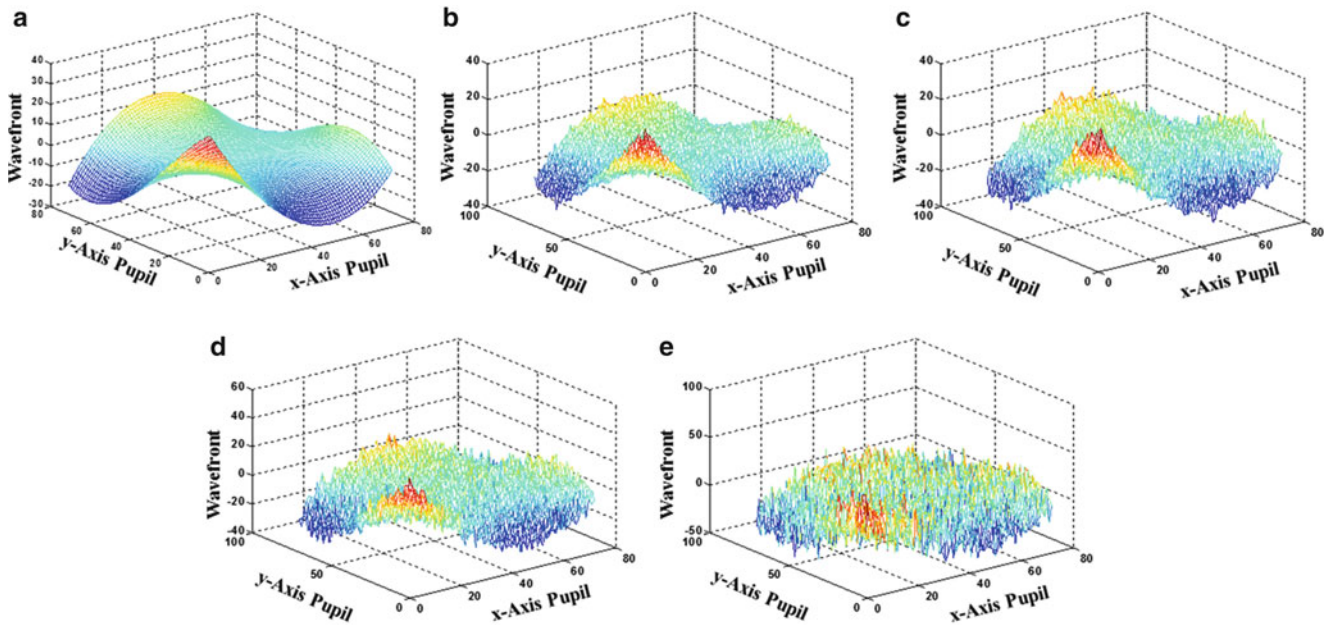


Fig. 43.7 In (a) Wavefront formed by $WF = 3Z1 + 2Z3 - 4Z6 + 1.7Z9$. Wavefront with a noise level of (b) 2RMS, (c) 3RMS, (d) 4RMS, (e) 10RMS

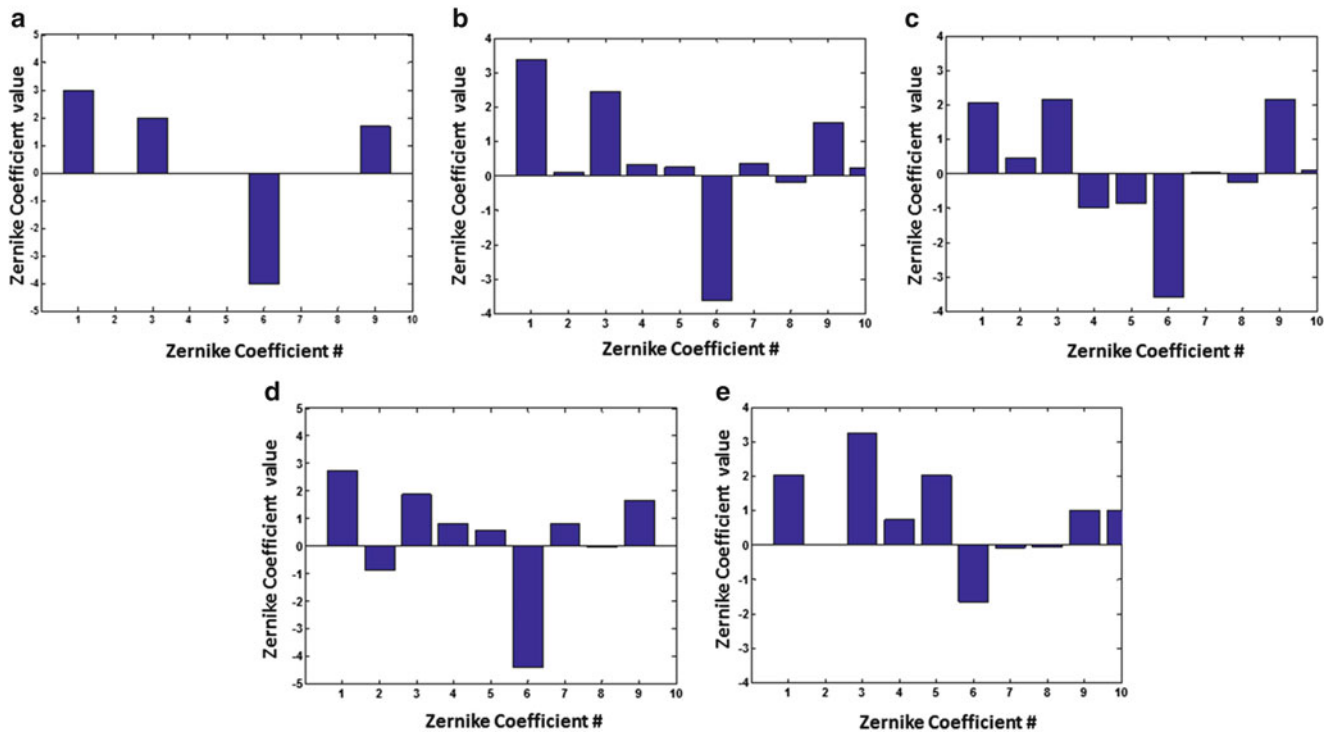


Fig. 43.8 Calculated Zernike polynomials coefficients from $WF = 3Z1 + 2Z3 - 4Z6 + 1.7Z9$, (a) without noise level, (b) with 2RMS noise, (c) 3 RMS noise, (d) 4 RMS noise and (e) 10 RMS noise

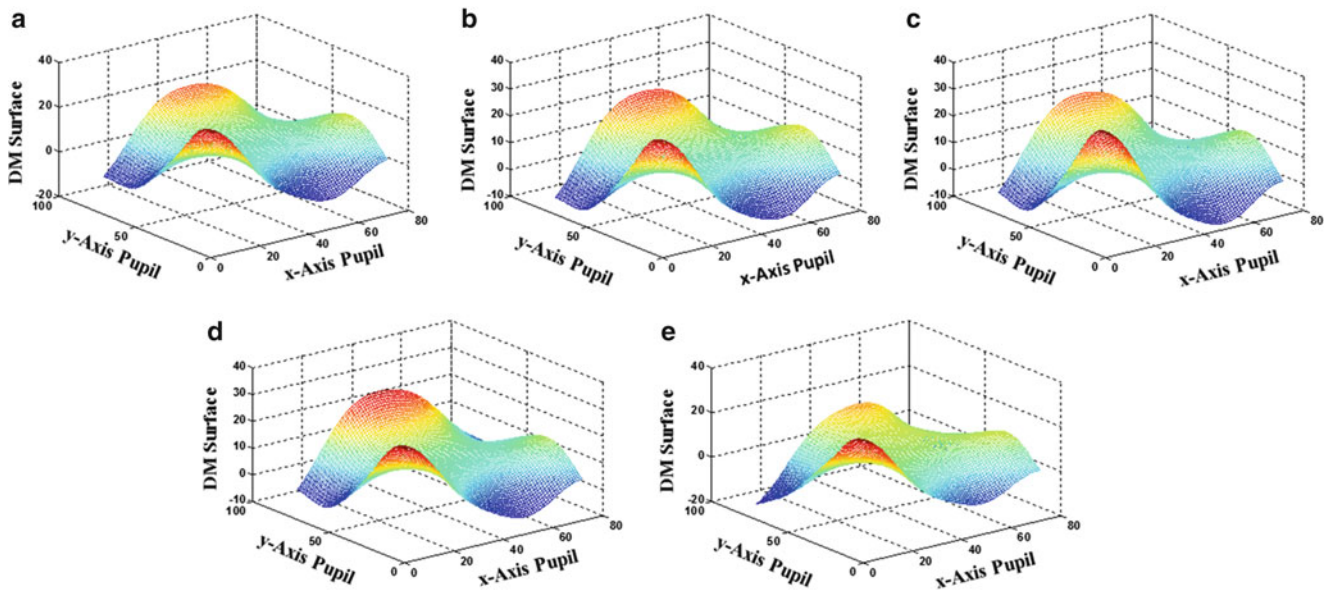


Fig. 43.9 DM Surface since the coefficients C on (a) The wavefront formed by $WF = 3Z1 + 2Z3 - 4Z6 + 1.7Z9$, and with a level noise of (b) 2RMS, (c) 3RMS, (d) 4RMS, (e) 10RMS

43.4 Conclusions

This research work was focused on the numerical determination of the key matrix for the evaluation of the wavefront and the deformation in the DM. A simulation was presented for an adaptive optics system. This allowed to understand its theoretical performance which can facilitate effective management of this system.

It has been proposed programs in Matlab, which allow to change the dimensions and resolution of the simulated WF as well as the collection of discrete simulation derived for the SH sensor, and the creation of the matrix of Z reconstruction and influence function matrix A .

Based on the simulation presented, important aspects were found using the reconstruction modal method of a wavefront, which it seems to be not affected by high levels of noise, at least in our simulations. We are currently working with the development of a Kalman filter, which could allow us to have a better estimation of the Zernike coefficients in the presence of noise in the system.

References

1. W.B. Bridges, P.T. Brunner, S.P. Lazzara, T.A. Nussmeier, T.R. O'Meara, J.A. Sanguinet, W.P. Brown Jr., Coherent optical adaptive optics techniques. *App. Opt.* **13**, 291 (1974)
2. M.S. Smirnov, Measurement of the wave aberration in the human eye. *Biophysics* **6**, 776 (1961)
3. J. Liang, D.R. Williams, D.T. Miller, Supernormal vision and high-resolution retinal imaging through adaptive optics. *J. Opt. Soc. Am. A* **14**, 2884 (1997)
4. F. Vargas-Martin, P. Prieto, P. Artal, Correction of the aberrations in the human eye with liquid crystal spatial light modulators: limits to the performance. *J. Opt. Soc. Am. A* **15**, 2 (1998)
5. H.J. Hofer, P. Artal, B. Singer, J.L. Aragón, D.R. Williams, Dynamics of the eye's wave aberration. *J. Opt. Soc. Am. A* **18**, 497 (2001)
6. Wenhan Jiang, Huagui Li, Hartmann-Shack wavefront sensing and wavefront control algorithm, in SPIE vol 127, Institute of Optics and Electronics (1990)
7. L. Seifert, J. Liesener, H.J. Tiziani, The adaptive Shack-Hartmann sensor. *Opt. Commun.* **216**(4–6), 313–319 (2003)
8. Y.-T. Lui, J. Steve Gibson, Adaptive control in adaptive optics for directed-energy systems. *Opt. Eng.* **46**(4), 046601 (2007)
9. B.L. Ellerbroek, L. Charles Van, R.J. Plemmons, N.P. Pitsianis, Optimizing closed-load adaptive-optics performance with use of multiple control bandwidths. *J. Opt. Soc. Am. A* **11**(11), 2871–2886 (1994)
10. J. Schwiegerling, Scaling Zernike expansion coefficients to different pupil size. *J. Opt. Soc. Am.* **19**(10), 1937–1945 (2002)
11. J. Porter, H.M. Queener, J.E. Lin, K. Thorn, A. Awwal, *Adaptive Optics for Vision Science: Principles, Practices, Design, and Applications* (Wiley, Hoboken, 2006)
12. A. Bjerhammar, Application of calculus of matrices to method of least squares with special reference to geodetic calculations. *Trans. Roy. Inst. Tech. Stockholm* **49**, 86 (1951)
13. R. Penrose, A generalized inverse for matrices. *Proc. Camb. Philol. Soc.* **51**, 406–413 (1955)

Chapter 44

Design, Development and Validation of an Artificial Muscle Biomechanical Rig (AMBR) for Finite Element Model Validation

A. Kriechbaumer, M.P. Trejo Ramírez, U. Mittag, M. Itskov, J.M. López Ramírez, and J. Rittweger

Abstract In modern physiological research the focus has advanced from the mechanostat theory to the functional muscle-bone-unit, investigating the relationship between muscle and bone. A recent study yielded *in vivo* data on the deformation of the human tibia and an inverse FE algorithm, which was developed to calculate the muscle forces triggering these deformations. In this context an Artificial Muscles Biomechanical Rig (AMBR) was developed, in order to validate the methods used and obtain further data on the relationship of muscle forces and bone deformations. With AMBR the biomechanical behavior of the human tibia can be simulated, comparable to the FE simulation. It is a custom-made mechanical platform including pneumatic actuators combined with a control system to simulate the lower leg muscles. The specimen tested is a biomechanical replica of the tibia. For validation and verification with AMBR, tests focused on the accuracy and repeatability of data acquisition of the specimen deformation during force application by using a motion capture system. The rig was able to serve its purpose by validating the inverse FE algorithm. Its further applications might comprise of profounder studies on various mechanical effects of muscles on bones and create new biomechanical insights for prevention and rehabilitation.

Keywords Bone deformation • Muscle force • Biomechanics • Inverse FE • Simulation

44.1 Introduction

The interaction between muscles and bones, as forces and solid bodies, is the basic mechanism of human locomotion. But this system in itself is not as constant as generally assumed. As one shapes the other, bone, as a living organ, is cycling through a permanent process of adaptation. It has been shown that the forces acting on it are one of the factors governing these activities and even give bone its shape [1, 2]. Nevertheless, this principle is far from being fully understood. The interaction between muscles and bones becomes especially important, when the balance gets disturbed [3], as can be seen for example in astronauts. The lack of gravity and therefore the altered and reduced usage of the legs shifts the equilibrium to an increased bone resorption and thus to an increased loss of muscle and bone mass in the abdomen [4–6]. The same principles apply for bed-ridden patients [7, 8], but in comparison to astronauts [9, 10], it can be prevented via an adequate training [11], the same is not valid for astronauts [10, 11]. In order to develop better countermeasures it is essential, to get a proper understanding on the relationship between muscles forces acting on the bone and the resulting bone deformation necessary to keep the adaptation in balance, both being difficult to measure [12, 13].

One of the scarce possibilities to investigate muscle activity is Electromyography (EMG), but only with certain limitations. On the one hand, EMG produces reasonable results only on surface muscles. On the other hand, the measurements do not directly express the forces, but only the action potential, which then requires an extensive and disputable conversion [14]. Another possibility which has found its way into the methodology of bone physiology is provided by computer aided modeling (CAM). Programs like OpenSim provide a tool for an inverse kinematic

A. Kriechbaumer (✉) • U. Mittag • J. Rittweger

Department of Space Physiology, Institute of Aerospace Medicine, German Aerospace Center (DLR), Linder Höhe, Cologne, Germany
e-mail: Andreas.Kriechbaumer@dlr.de

M.P.T. Ramírez • J.M.L. Ramírez

Instituto Tecnológico y de Estudios Superiores de Monterrey, Campus León. Eugenio Garza Sada s/n, León, Mexico
e-mail: manuela.paulina.trejo@itesm.mx

M. Itskov

Department of Continuum Mechanics, RWTH Aachen University, Kackertstraße 9, Aachen, Germany

(IK) calculation. Starting from a known kinematic sequence and mass distribution the muscle forces needed in order to achieve this movement are determined [15]. Yet, the quality of the results suffers from the great amount of abstractions and assumptions needed and from the fact, that the bones are considered to be rigid bodies.

Yang et al. were able to measure the deformation of the Tibia *in vivo* during various activities using a motion capture system (MoCap) [16]. Based on that data a software was developed, utilizing the finite element method (FEM), in order to determine the missing information on the acting muscle forces. Computer tomography (CT) and magnetic resonance imaging (MRI) scans provide the information to reconstruct the tibia geometry, material properties, and muscle alignment. Subsequently, the forces corresponding to the recorded deformation are calculated by utilizing an inverse optimization. However, the database on deformation is limited and the inverse algorithm incorporates, by nature, several assumptions. To overcome these gaps, we decided to conduct further experiments and build a special biomechanical test rig. The purpose of this apparatus is to validate the FE model and corresponding software thereby advancing our basic understanding of the relationship between muscle forces and bone deformation by allowing us to investigate them under controlled mechanical conditions. In this paper we present the development, construction and evaluation of the Artificial Muscle Biomechanical Rig (AMBR).

44.2 Design and Development

44.2.1 Requirements

The two main tasks to be met by the AMBR were:

- Verification of the inverse FE software program
- Generating data complementary to the already obtained

Subsequently, the rig needs to fulfill certain criteria. First and foremost all the mechanical variables (e.g. force magnitude and direction, friction losses, bone deformation, etc.) need to be quantifiable. A second constraint is the comparability to the biological model of the human lower leg. The materials employed and activities simulated must be as close to reality as feasible. On the other hand, it must be possible to accommodate and represent the elements incorporated in the FE model to fulfill the demands of the first main task. The last requirement emerges from the second main task. In order to investigate a system as complex as the human leg, the rig needs to be adaptable according to the focus of each study.

44.2.2 Mechanical Layout

Following the requirements, the general concept for this iteration of the rig is to study a single tibia specimen without joints or any soft ligaments subject to four simulated muscle forces applied via a pulley system.

A main framework made of ITEM profiles fixed to a baseplate provides a platform for the mechanical attachments (A). The structure is designed to keep its deformation due to the applied forces to an absolute minimum in order to avoid undesirable side effects (e.g. changes in the force vector orientations, specimen movement), but still to allow for an easy interchange of the single components or subsystems. Two vertical struts provide the means for attaching safety ropes to prevent the specimen, in case of structural failure, from harming other components. Centered in the frame and fixed onto the base is a force plate measuring ground reaction forces (B). It is an AMTI model OR6-6-2000 coupled with a Gen5 signal conditioner that uses a six-channel strain gage amplifier and is designed for the use in research and clinical studies investigating balance, gait and sports performance. This plate provides the bearing surface for the specimen. In the depicted configuration (Fig. 44.1) the specimen is the fourth generation tibia ERP #3402 of the company Sawbones, a two-component composite tibia replica (C) (see Fig. 44.2). It comes with a full 3D CAD model and specified material properties, designed for biomechanical testing. The distal (e.g. lower) part of the tibia is cast integral with epoxy resin in an aluminum housing, which in turn is bolted to a base disk. This buildup provides stability against overturning. High friction tape underneath the disk prevents translation of the whole specimen-setup. Attached to the proximal (e.g. upper) tibia head is an aluminum flange with its milled counterpart. This flange provides the possibility to smoothly introduce forces on the tibia from proximal or anterior/posterior (e.g. simulated body weight or inertial forces) in the position where the knee would be. Additionally, it allows for the installation of the safety ropes.

Fig. 44.1 AMBR mechanical layout with ITEM framework and baseplate (A), force plate (B), specimen setup (C), force redirection system (D), actuator bench (E), MoCap cameras (F)

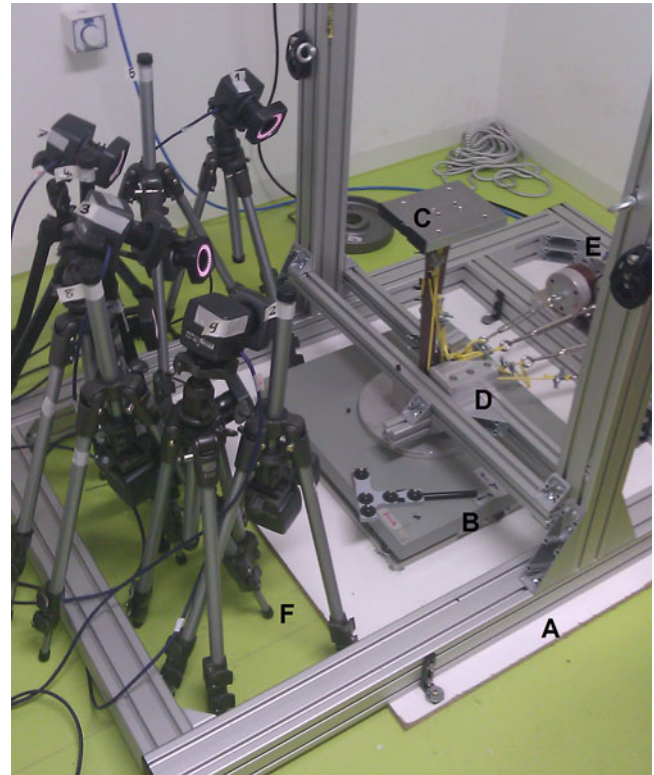
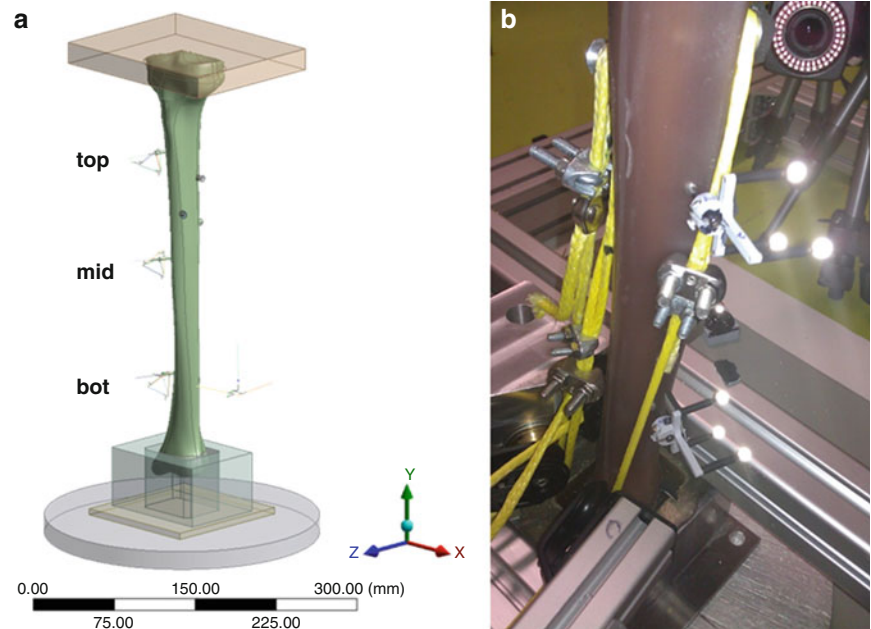
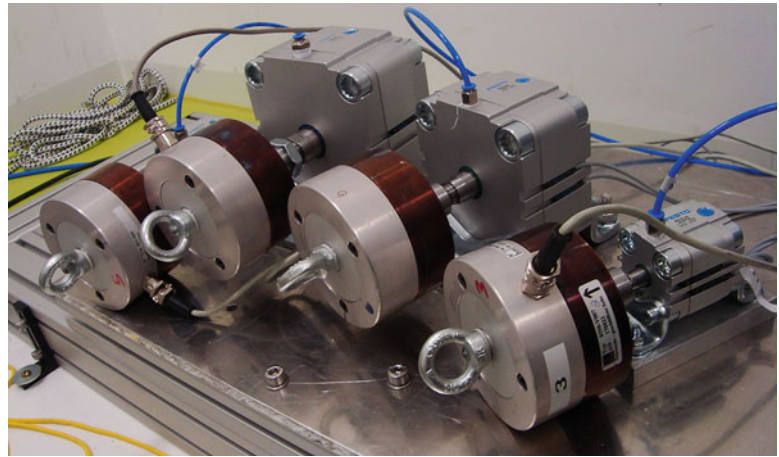


Fig. 44.2 Tibia specimen (a) FE model showing the assembled specimen and the position of the three marker cluster: 'top', 'mid' and 'bot' (b) Sawbones tibia replica with marker cluster mid and bot, attached ropes and pulley system



We decided against the incorporation of joints in this first iteration of the rig to not introduce any unknown and to be able to analyze the effect of single forces on the deformation without the issue of balancing the joint. For the simulated muscle forces an actuator and pulley system are utilized. Four muscles were chosen, which attach directly to the tibia and are the main contributors to its movement, corresponding to other frequently used configuration in IK tool like OpenSim. These are the Soleus, Tibialis Posterior, Tibialis Anterior and Flexor Digitorum Longus muscles. Their contact surfaces and geometrical center, as well as the orientation of the muscle force vector, were determined by anatomical records

Fig. 44.3 Actuator bench with four actuators and load cells



[17]. We inserted a screw on each of these positions as attachment points for the ropes. We use the inner core of 6 mm ropes of the type Coppa 3000 of the brand FSE Robline, supporting high ultimate loads with a minimal internal strain. A pulley system is arranged in a specific way, that the ropes align with the force directions the real muscles would work in (D). The ropes are redirected via the pulleys towards the actuator bench (E) (cf. Fig. 44.3). Manual cable tensioners are intercalated to create the necessary pretension. A load cell is accommodated in front of each actuator with the proper adapter flange, fixed to the actuator with a customized fitting.

44.2.3 Optical Measuring System

Attached to the specimen are three marker clusters, labeled “top”, “mid”, and “bot” according to their location. Each cluster is carrying three high-precision spheres, adding up to a total of nine markers, as seen in Fig. 44.2. These markers have a special retro-reflective surface coating, which allows the MoCap system to track them via infrared pulses. Nine Vicon Bonita 3 cameras with a resolution of 0.3 MP and 240 fps are arrayed around the specimen in an umbrella like configuration (F). While tracking a single marker only reveals its displacement, the arrangement of the markers into cluster spanning plains allows for the calculation of the angles between them and consequently the deformation of the specimen. The optical measurement system thus follows the principles as described by Yang and which was employed in the *in vivo* study yielding our reference deformation data [18].

44.2.4 Mechatronic Design

The realization of the AMBR required the development of a mechatronic system, capable of integrating the mechanics of the rig frame with the different elements operating during regular testing. Therefore, a holistic approach, where actuation, mechanisms, and data gathering elements are combined, is used in order to ensure their proper function and to avoid any sources of disturbance between systems as well as from external sources. The mechatronic design focused on two goals:

- Implementation of a lower leg artificial muscle system capable of contracting and thereby applying forces of the same magnitude and in a similar manner as observed in humans. The actuators will recreate static and semi-static conditions of the human positioning and specific stages of locomotion only. To this end it is only necessary to implement the actuation of the lower leg muscles pulling caudal (e.g. downwards). The usage of actuators capable of a high speed operation for future dynamic tests is advantageous.
- Design a control system using a HMI (Human Machine Interface) that allows the operator to perform biomechanical tests and permits the modification of the force parameters. The HMI should display the necessary information regarding the current state for monitoring purposes as well as to display data and the controls in a graphic, user-friendly manner to facilitate test and evaluation procedures.

Given these design requirements, technologies were investigated and chosen for the rig considering their suitability for performing the required tasks in an effective way.

Table 44.1 Lower leg muscles simulated in the AMBR and their approximate maximum isometric force

Code	Muscle	F _{iso} max (N)
A	M. Soleus	3549
B	M. Tibialis posterior	1588
C	M. Tibialis anterior	905
D	M. Flexor digitorum longus	310

44.2.4.1 Artificial Muscles System

The design and construction of the actuation system is based on muscle biomechanics and the replication of their behavior, in order to manage vital parameters during testing conditions. In the assortment of commercial actuators that display a behavior similar to biological muscles the pneumatic actuators stick out, since they have a contraction mechanism very close to the intended biological model. The option chosen was the compact pneumatic cylinder of the AEVUZ series from Festo AG. & Co. especially designed for pulling applications, discarding the need of further mechanical adaptations.

Four actuators simulating lower leg muscles pulling the tibia bone downwards were installed (Fig. 44.3). As a design criterion the maximum isometric force exerted by the corresponding muscle was chosen. These values were obtained from the OpenSim Gait 2392 model. The list of muscles with their code letters and force magnitudes can be seen in Table 44.1.

44.2.4.2 Control System

As an important part for operating the test rack, a control system was designed, built and tested. The main objective was to enable the operator to manage the rack in an effective manner, for example to apply the desired forces of chosen muscles and to obtain status information of the current procedure in real time.

The main characteristics of the control system are:

- Activate/deactivate the muscle actuators, either simultaneously by user selection, or one at a time.
- Define the force application parameters: magnitude, and initial load cell deviation.
- Obtain and process analogue data from the load cells regarding the force exerted by the actuator, as well as to display information about the status of the actuators through a user-friendly HMI.
- Implement an emergency mechanism to deactivate all outputs when hazardous conditions appear.

With regard to sensing the applied forces by the actuators, load cells were attached to the actuators piston rods. Each of the four cylinders required its own load cell (8531, Burster), with a measuring range of 0–2000 N for three of them and 0–5000 N for one. The load cells are made of high-strength aluminum and consist of foil strain gauges. As the sensor has terminals on both sides for measuring both compression and tension, a special flange was mounted such that the actual tension applied can be read. Coupled with the sensor there is a factory calibrated amplifier of the model 9235. The measurement signals of the sensor, ranging between 0 and 10 mV for bridge connected strain gauges, are amplified to analogue signals of 0–10 V.

The control was designed for the installation of a pair of valves regulating air pressure (force applied) using an ON/OFF control configuration. By determining a set point for the desired force and a regulation window, the control activates and deactivates a set of valves when the pressure magnitude is outside the boundaries of the regulation window, maintaining the force applied within the user specified window. As a communication system capable of handling electric and pneumatic components the EasyPort USB from Festo was implemented. The EasyPort is a process interface used for the bidirectional transmission of process signals from and to a PC. The design and implementation of the control software was oriented to translate the user instructions into the operation of the artificial muscles. The computer interface for the user was developed in LabVIEW 2012 SP1.

44.3 Evaluation

One of the main tasks of this work is to verify the functionality of the systems implemented in the rig. Special tests were performed for each main component of the rig functionality and the resulting data was recorded. Depending on the setup, analyses regarding accuracy, repeatability and reproducibility were made. Once the systems were validated individually, a final integration test was performed to verify the complete functionality of the rig during normal conditions of biomechanical testing.

Table 44.2 Repeatability, reproducibility and accuracy error/bias results for all four actuators (A, B, C, D)

Actuator	Repeatability within trials (%)	Reproducibility between trials (%)	Bias percentage (%)
A	0.35	0.0	1.16
B	1.07	0.11	0.01
C	1.02	0.21	0.01
D	2.44	0.69	0.12

44.3.1 Validation of the Actuation System

In order to validate the performance of the control system, a statistical analysis over a sequence of tests was performed. The physical configuration for testing was an arrangement of mechanical elements connected to the actuator. The verification for each actuator implied the application of a series of forces within their range of operation in an incremental and random order. The desired force introduced to the system was compared to the actual force achieved by the actuator using the converted output of the force sensors. A statistical analysis was performed using Statgraphics Centurion XV software to assess repeatability, reproducibility and accuracy. Results from the analysis were obtained as error/bias percentages, with a low value resembling a high repeatability, reproducibility and accuracy achieved.

The results of the control system for each actuator with respect to repeatability, reproducibility and accuracy can be seen in Table 44.2.

The repeatability and reproducibility percentage expresses the estimation of the total error measurement. The percentages shown are lower than 3 %, demonstrating the high capacity of the control system for repeatability and reproducibility. A remarkable result can be seen for actuator A, where the reproducibility error percentage is 0.0 %. Consequently, for that specific actuator, the influence of the change of force application between trials is null. The bias percentage is low, being slightly higher for actuator A and, up to certain extent, for actuator D. It is possible that the bias percentage is bigger for actuator D because the error difference is high in regard to the small range of force this actuator is capable of generating. For actuator A the higher bias percentage might be a sign of the difficulty in applying high forces to a rigid object, introducing mechanical disturbances. In general, this bias is acceptable, but further improvements should be made to refine the system and not to impede the deformation measured in the specimen due to inaccurate force application.

44.3.2 Validation of the Motion Capture System

The MoCap system is one of the main data gathering components of the rig. It is the mechanism in charge of obtaining significant data to validate the computer model as well as to record deformation in further lower leg biomechanical tests. A verification procedure was carried out in order to assess the accuracy and repeatability of the system by recording known marker displacements along the three spatial axes. The markers movement was controlled using a calibrated caliper with two 5 mm reflective markers attached on the top of the measuring tips and fixed with high stability to the rig frame. The MoCap recorded the chosen variations and the data obtained was processed. A Grubb's outlier test was performed to eliminate data elements resulting from secondary reflections which could introduce errors. In the same way as for the control system, a test on accuracy and repeatability was performed. The marker movement can be recorded with a resolution of 0.01 mm and better, with a bias of 0.33 % and a repeatability error of 0.41 %; both errors being lower than 1 % and allowing to reach the conclusion that the MoCap configuration is appropriate for gathering data of biomechanical tests with the AMBR.

44.3.3 Biomechanical Studies

Utilizing the Sawbones Tibia replica as a specimen a complete functionality test was performed. Excerpts of the main results are presented here for example.

Figure 44.4 shows the displacement of the center of each marker cluster over applied force for the actuator A (M. Soleus). Each point corresponds to a static condition averaged over one second, resulting in a standard deviation of $SD \leq 0.0041$ being not displayed in the figure. Each force step was recorded three times to show the reproducibility of the system.

Fig. 44.4 Displacement over force diagram for actuator A (M. Soleus). Regression line for top in red, mid in green and bot in magenta

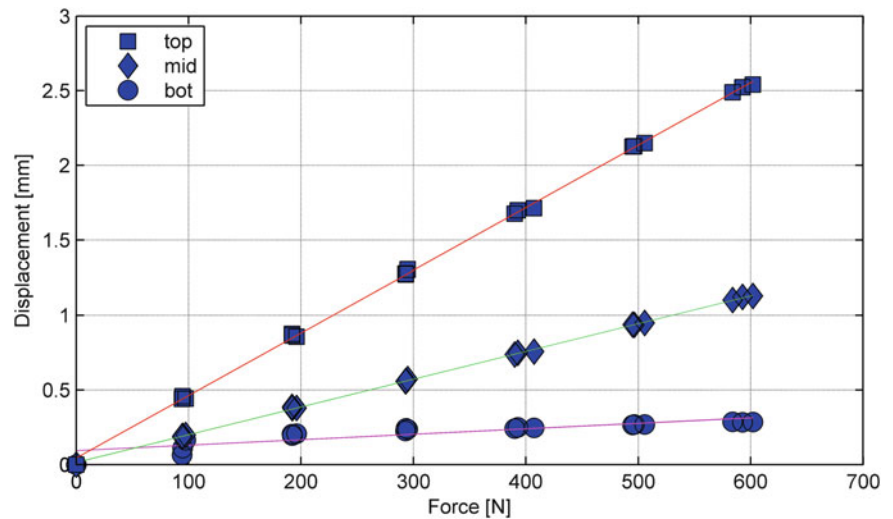
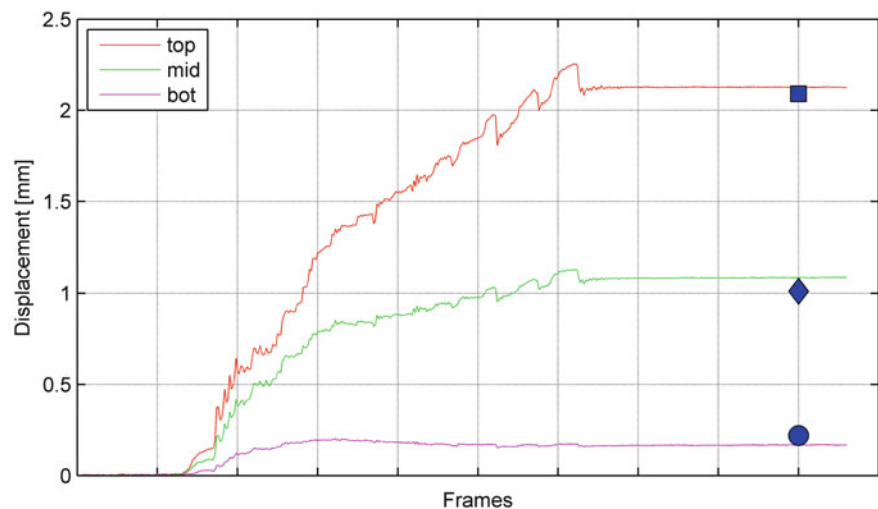


Fig. 44.5 Displacement over time diagram for all four actuators (A, B, C, D) simultaneously. The values for top (square), mid (diamond) and bot (circle) calculated by the FE model with same conditions are added for comparison



The most important finding of these measurements is the linear relationship of force and displacement, represented by the corresponding regression lines. The other three actuators (B, C, D) showed similar results.

The displacement over time diagram can be seen in Fig. 44.5. All four actuators were starting with 100 N of pretension and increased to 25 % of the approximated maximum isometric force of its associated muscle. It was a continuous measurement over the whole time it took the control system to regulate the actuators to the desired forces. When reaching the set points, the control system was disabled and all valves were closed to maintain the current state for a period of time and to prevent disturbances by micro regulations. The depicted values differ from these in Fig. 44.4, since there only one actuator is active, while here all four actuators work together. Integrated into the diagram are three data points resulting from the FE simulation using the model shown in Fig. 44.2a. These points were calculated using the same forces as achieved in the static condition at the end.

While the first two diagrams shown in Figs. 44.4 and 44.5 focused on the mere displacement of the marker cluster, the real strength of the AMBR and the MoCap setup is the ability to measure deformation of the specimen as shown in Fig. 44.6. The data is from the same trial as presented in Fig. 44.5. When comparing the top to the bot cluster and transposing the results into the anatomical coordinate system associated with the tibia, we can determine the bending and rotation of the specimen. Figure 44.6a, b show the bending in the sagittal plain and likewise the coronal plain, while in 6 c the torsion can be seen.

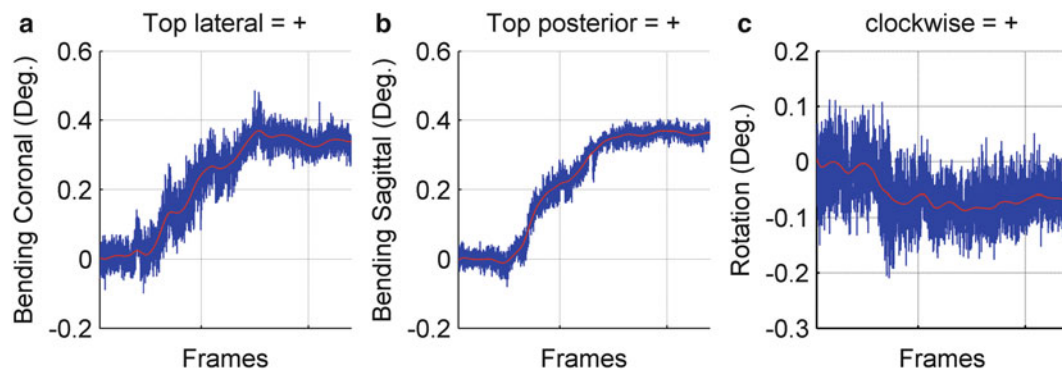


Fig. 44.6 Deformation of the specimen in the three anatomical planes, comparing top cluster to bot, when applying forces with all four actuators (A, B, C, D) simultaneously. *Blue* shows the raw data (deformation angle). The *red line* shows the same data after applying a 2nd order butterworth filter

44.4 Discussion and Outlook

The validation tests performed in the current study indicate that the AMBR can produce significant data on bone deformation and related forces. Our actuation system was successfully verified for applying the appropriate force of the artificial muscles onto the specimen. Furthermore, the data gathering systems are capable of recording information within an acceptable resolution and without being disturbed by external sources. Also, even though the force management (e.g. compressed air control) from valves has a margin of improvement, the application is suitable to test different biomechanical hypothesis of the lower leg kinematics in future studies. Finally, the two main goals, the ability to validate the inverse FE software and the generation of new data, were thus achieved. In particular, comparison between calculated and measured *in vivo* data proved the AMBR to be an adequate platform for biomechanical investigations on the lower leg as an addition, or even replacement for *in vivo* studies.

Emerging from the fulfilled requirement of modularity and the special demands each study entails, the AMBR will undergo future redesigns and improvements. Focus will be set on a more realistic force application onto the specimen. To achieve this, the ropes will be glued to the specimen with an epoxy resin. Therefore, instead of having a bolt screwed into the tibia, damaging it and concentrating the force on one spot, with the new approach the force will be evenly distributed across the anatomical attachment face. Regarding the control system of the rig, an alternate control scheme for managing the force regulation valves will be developed in order to achieve a faster and more stable application of forces. The current design of the rig was focused on static conditions; therefore the contraction time (e.g. speed of force generation) was not a determinant of the actuators chosen. The main priority was the accurate force application during a specific period of time. Nonetheless, the actuators implemented are capable of exerting muscle forces of the required magnitudes at a high speed. Consequently, they can be used for further developments and tests in dynamic conditions, where speed of contraction will be vital for the correct simulation of the musculoskeletal system. Neglecting the influence of the lower limb joints, soft tissue like tendons and ligaments, and even the fibula bone, might have a significant impact on the results. Since the influence of these on the tibia deformation is subject to great controversy, an *ex vivo* study, utilizing cadaverous lower legs, will make use of the AMBR.

References

1. H.M. Frost, Muscle, bone, and the Utah paradigm: a 1999 overview. *J. Bone Miner. Metab.* **18**(6), 305–316 (2000)
2. U. Mittag, A. Kriechbaumer, M. Bartsch, J. Rittweger, Form follows function: a computational simulation exercise on bone shape forming and conservation. *J. Musculoskelet. Neuronal Interact.* **15**(2), 215–226 (2015)
3. T.M. Skerry, The response of bone to mechanical loading and disuse: fundamental principles and influences on osteoblast/osteocyte homeostasis. *Arch. Biochem. Biophys.* **473**, 117–123 (2008)
4. A. Leblanc, V. Schneider, L. Shackelford, S. West, V. Oganov, A. Bakulin, L. Voronin, Bone mineral and lean tissue loss after long duration space flight. *J. Musculoskelet. Neuronal Interact.* **1**, 157–160 (2000)
5. E.S. Orwoll, R.A. Adler, S. Amin, N. Binkley, E.M. Lewiecki, S.M. Petak, S.A. Shapses, M. Sinaki, N.B. Watts, J.D. Sibonga, Skeletal health in long-duration astronauts: nature, assessment, and management recommendations from the NASA bone summit. *J. Bone Miner. Res.* **28**, 1243–1255 (2013)

6. J.D. Sibonga, H.J. Evans, E.R. Spector, M.J. Maddocks, S.A. Smith, L.C. Shackelford, A.D. Leblanc, *What happens to bone health during and after spaceflight?* (Proceedings of the Bone Loss During Spaceflight, Cleveland, OH, 2005)
7. J. Rittweger, D. Felsenberg, Patterns of bone loss in bed-ridden healthy young male subjects: results from the long term Bed rest study in Toulouse. *J. Musculoskel. Neuron Interact.* **3**(4), 290–291 (2003)
8. A. Leblanc, E. Spector, H. Evans, J. Sibonga, Skeletal responses to space flight and the bed rest analog: a review. *J. Musculoskel. Neuron Interact.* **7**, 33 (2007)
9. A.R. Hargens, R. Bhattacharya, S.M. Schneider, Space physiology VI: exercise, artificial gravity, and countermeasure development for prolonged space flight. *Eur. J. Appl. Physiol.* **113**(9), 2183–2192 (2013)
10. L. Shackelford, A. Leblanc, T. Driscoll, H. Evans, N. Rianon, S. Smith, E. Spector, D. Feedback, D. Lai, Resistance exercise as a countermeasure to disuse-induced bone loss. *J. Appl. Physiol.* **97**, 119–129 (2004)
11. P.R. Cavanagh, A.A. Licata, A.J. Rice, Exercise and pharmacological countermeasures for bone loss during long-duration space flight. *Gravit. Space Biol.* **18**, 39–58 (2007)
12. R. Al Nazer, J. Lanovaz, C. Kawalilak, J. Johnston, S. Kontulainen, Direct in vivo strain measurements in human bone—a systematic literature review. *J. Biomech.* **45**, 27–40 (2012)
13. P.-F. Yang, G. Brüggemann, J. Rittweger, What do we currently know from in vivo bone strain measurements in humans. *J. Musculoskel. Neuron Interact.* **11**, 8–20 (2011)
14. C. Disselhorst-Klug, T. Schmitz-Rode, G. Rau, Electromyography and muscle force: Limits in sEMG–force relationship and new approaches for applications. *Clin. Biomech.* **24**(3), 225–235 (2009)
15. S. Delp, F. Anderson, A. Arnold, P. Loan, A. Habib, C. John, E. Guendelman, D. Thelen, OpenSim: open-source software to create and analyze dynamic simulations of movement. *IEEE Trans. Biomed. Eng.* **54**(11), 1940–1950 (2007)
16. P.F. Yang, A. Kriechbaumer, K. Albracht, M. Sanno, B. Ganse, T. Koy, P. Shang, G.P. Brüggemann, L.P. Müller, J. Rittweger, On the relationship between tibia torsional deformation and regional muscle contractions in habitual human exercises in vivo. *J. Biomech.* **48**(3), 456–464 (2015)
17. Sobotta, J. Atlas der Anatomie des Menschen. Publ. by Putz, R., Pabst, R, Freiburg, 21, neu bearbeitete Auflage in einem Band (2004)
18. P.F. Yang, M. Sanno, G.-P. Brüggemann, J. Rittweger, Evaluation of the performance of a motion capture system for small displacement recording and a discussion for its application potential in bone deformation in vivo measurements. *Proc. Inst. Mech. Eng. H J. Eng. Med.* **226**, 838–847 (2012)

Chapter 45

Application of Laser Light on the Development of Equipment for the Study of Proteins

Nydia Tejada Muñoz and Martha Robles-Flores

Abstract The use of the laser technology in medicine has allowed us to expand the knowledge of the cell and its functions. In particular, flow cytometry is a sophisticated equipment, which can do a simultaneous multi-parametric analysis of the physical, and chemical properties of thousands of particles per second. Flow cytometry is routinely used in the diagnosis of health disorders, particularly blood cancers, but it has many other applications in basic research, clinical practice, and clinical trials. Given the extensive available information, flow cytometry was used to study the route by which transduce PKC ζ leads the activation of GSK-3 β , and the physiological significance of its accumulation in the nucleus.

Keywords Flow cytometry • Wnt signaling • GSK-3 β • PKC ζ • Colon cancer

45.1 Introduction

Since the advent of the laser (1960), humanity has seen the unstoppable growing and diversifying the development of all types of lasers, capable of operating over a wide range of wavelengths and increasing high peak powers; the laser systems have led to a broad set of applications that seems to be the key element in present and future investigation.

Lasers have been used in medicine almost from its inception; it is so, that we can now count on new technological processes in the field of surgery, especially handling delicate and dangerous areas, such as the brain or the spinal cord or even the laser systems can be used to correct visual defects, and so many other applications can be stated.

Flow cytometry is a rapid quantitative and objective method of analysis of cells, nuclei, chromosomes, mitochondria or other particles in suspension.

The principle behind this technology consists of passing cells or other particles in suspension, and align one by one in front of a light beam.

The information produced can be grouped into two basic types: the one generated by the light scattering, and the related emission of light by the fluorochromes present in the cell or particle to be excited by the light beam. The detected light signals are transformed into electrical impulses that are amplified, and converted into digital signals that are processed by a computer. It is our interest to compare this technique with biochemical methods of cell analysis, in which an average result for the entire sample is obtained; the flow cytometry is able to provide quantitative information on each particular cell and to identify different subpopulations of cells in the sample, even when they are poorly represented [1, 2].

Because our interest in GSK-3 β protein involved in multiple functions (the Wnt signaling pathway, in protein synthesis, cell proliferation, differentiation, metabolism, cell cycle, apoptosis, and embryonic development), regulating their activity is critical to ensure specificity of signaling pathways [3–5]. To accomplish this, GSK-3 β is subjected to multiple levels of regulation by phosphorylation and other post- translational modifications, their subcellular localization regulation and protein-protein interactions.

The activity of GSK-3 β is significantly inhibited by phosphorylation at Ser 9 its N-terminal; several kinases can phosphorylate that residue as the Akt/PKB protein, PKA, PKC and p90 RSK among others. It is known that this inhibitory phosphorylation of GSK-3 β plays an important role in signaling induced by insulin, and growth factors, but exactly how Wnt ligands suppress the activity of GSK-3 β remains unclear, although an essential step in canonical Wnt pathway is the inhibition of GSK-3 β activity, evidenced by the use of enzyme inhibitor drugs, which mimic the activation of the Wnt pathway. Wnts are known not to induce phosphorylation at Ser 9, but cause the recruitment of GSK-3 β and Axin to the cytosolic fraction of the co-receptor LRP5 that it phosphorylates GSK-3 β , and phosphorylated sites and inhibit GSK-3 β

N.T. Muñoz (✉) • M. Robles-Flores
Department of Biochemistry, Universidad Nacional Autónoma de México, Mexico City, Mexico
e-mail: nydia.tejada@gmail.com

acting as the competitive inhibitors, although with low affinity (K_i of 1.3×10^{-5} M). However, this inhibition is temporary and does not explain how it is maintained for more than 1 h. In this regard, recently Taelman et al. [6] reported that the Wnt ligands, from 15 min post-treatment, cause that the GSK-3 β is internalized in multivesicular bodies “sequestering” the kinase and preventing the phosphorylation of its substrates. Thus, upon binding of the ligand, GSK-3 β accumulates in signalosomes of LRP5 and therefore endocytosis is required for Wnt signaling.

Recently in the laboratory, a novel mechanism of regulation of GSK-3 β in the Wnt signaling pathway through PKC ζ using as model for studying colon cancer was demonstrated. However, it is not clear under what way, Wnt transduces the signal in addition to the functions performed in the nucleus, and the mechanism of translocation. Then, in this paper we focus on studying the technique of flow cytometry.

45.2 Experimental Procedures

45.2.1 Reagents and Antibodies

Antibodies against GSK-3 β were from the following sources: rabbit polyclonal and mouse monoclonal antibody was obtained from Santa Cruz Biotechnology (Sta. Cruz, CA, USA) and from Millipore.

The rabbit monoclonal antibody against Phospho-(Ser) PKC substrate was purchased from Cell Signaling Technology.

45.2.2 Cell Culture

RKO (human colon carcinoma), or SW480 (human colorectal adenocarcinoma) malignant cells, and non-malignant 112CoN (human colon) cells, were all obtained from the American Type Culture Collection (Manassas, VA). RKO and 112CoN cells were maintained in Dulbecco's Modified Eagle's medium (DMEM) supplemented with 10 % fetal bovine serum (FBS), antibiotics (120 mg/mL penicillin and 200 mg/mL streptomycin) and 2 mM L-glutamine. SW480 cells were maintained in DMEM F-12 supplemented with 5 % FBS, antibiotics and 2 mM glutamine. All cells were cultured in a humidified 5 % CO₂ incubator at 37 °C. The human cell lines were authenticated by DNA profiling using short tandem repeat (STR) analysis on an AmpFISTR[®] Identifiler™ PCR Amplification System at “Instituto Nacional de Medicina Genómica” (INMEGEN), México, D.F.

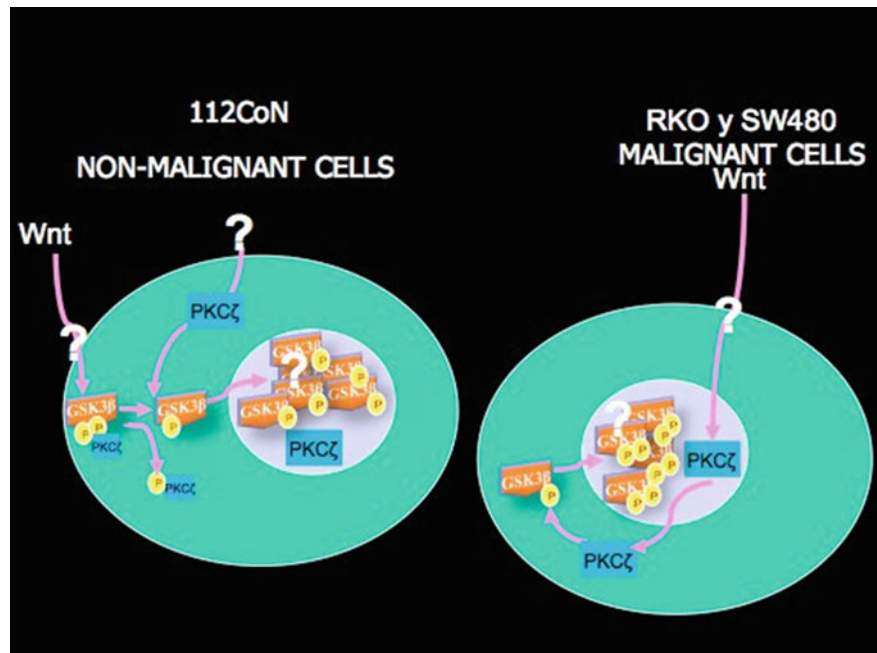
45.2.3 Incubation with Wnt Ligands and Pharmacological Inhibition of PKC ζ

For the pharmacological PKC ζ inhibition in RKO and SW480 cells, serum-starved cells (2 % serum instead of 10 %) were incubated in the absence or presence of the myristoylated PKC ζ -selective inhibitor (20 μ M) for 1 h. Then, cells were incubated in the absence or presence of Wnt3a or Wnt5a ligand (100 ng/mL) for 5 min and cells were then washed and lysed.

45.2.4 Flow Cytometry

Cells were fixed with 2 % paraformaldehyde in FACS buffer (PBS with 4 % fetal bovine serum) and incubated 10 min at 37 °C. The cells were centrifuged at 3000 rpm for 2 min and incubated with absolute methanol for 30 min at 4 °C. After removing the methanol and washing with FACS buffer 1:50 dilution of the primary antibody anti-GSK-3 β , GSK-3 β anti-p-serine 9 1/2/3 anti-AKT and anti-AKT was added p-threonine 308 for 15 min at 4 °C. FACS buffer the cells were washed and incubated in a 1:100 dilution of anti-goat secondary antibody coupled to FITC or anti-rabbit coupled to FITC for 15 min at 4 °C and then washed with FACS buffer. Cells were maintained in buffer for analysis by FACS (FACSCalibur, BD).

Fig. 45.1 Using human colon cell lines, in the laboratory a new mechanism GSK-3 β through PKC ζ was identified. This regulatory mechanism is different in normal and tumor cell lines (this will be published elsewhere), however, is not clear the way by which PKC ζ is activated and the nuclear functions of GSK-3 β



45.3 Results

The effect of stimulation with Wnt ligands revealed a rapid redistribution of GSK-3 β from the cytoplasm to the nucleus in malignant cells, and this correlation between GSK-3 β nuclear and Wnt signaling had not been shown before.

We are investigating the mechanism that GSK-3 β uses to enter and exit the nucleus and the functions in the organelle (Fig. 45.1). As it can be observed in Fig. 45.2, GSK-3 β levels increased with both treatments compared to the control. Importantly in other cellular processes, there are numerous examples showing a partial accumulation of GSK-3 β in the nucleus, and apoptosis [7, 8], replicative senescence, [9] and the S phase of the cell cycle [10]. In human pancreatic tumors there is a redistribution of GSK-3 β , which is overexpressed and accumulated in the nuclei of tumor cell lines, and in most poorly differentiated adenocarcinoma [11].

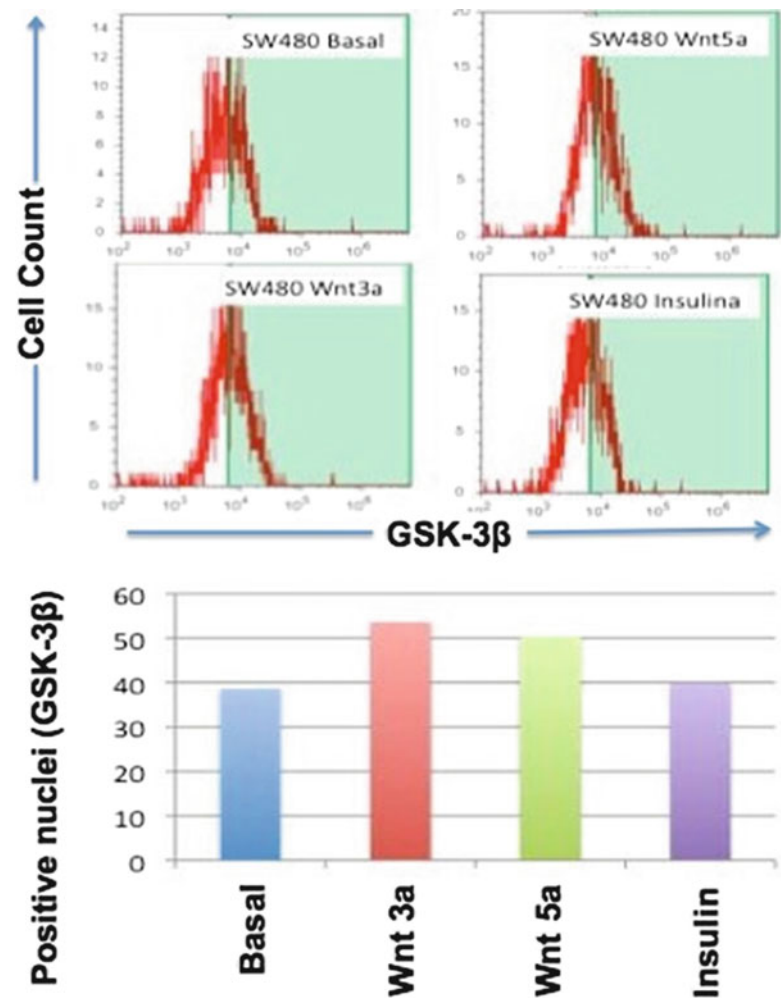
Once in the nucleus, and depending on the cell type, GSK-3 β can phosphorylate substrates such as cyclin D, NFAT, and c-myc.

The import mechanism of GSK-3 β appears to be dependent on a bipartite nuclear localization signal (NLS) [12], while exports under some circumstances require FRAT [13]. Only one report [14] has described a nuclear-cytoplasmic shuttling of GSK-3 β , and so the generality of this observation was previously clear.

45.4 Conclusions

The GSK-3 β is an important therapeutic target in colon cancer so it is fundamental to study the way in which it transduces, and its core functions; as it is reported that both positively and negatively regulates transcription factors. We present experimental evidence that Wnt ligands stimulate the accumulation of GSK-3 β in the nucleus and its functions are being studied.

Fig. 45.2 Quantification of GSK-3 β in the core by flow cytometry. (a) Graph of the amount of nuclear GSK-3 β SW480 cells at baseline, and SW480 cells stimulated with Wnt3a ligand, Wnt5a and insulin. Cells were stimulated (100 ng/mL) ligand Wnt 3a, 5a and insulin (10 mg/L) for 5 min. (b) The amount of nuclear GSK-3 β increases when stimulated with Wnt ligands and stimulate insulin the amount of GSK-3 β is similar to the baseline



References

1. D. Ryan, K. Ren, H. Wu, Single-cell assays. *Biomicrofluidics* **5**, 21501 (2011)
2. S. Gawad, T. Sun, N.G. Green, H. Morgan, Impedance spectroscopy using maximum length sequences: application to single cell analysis. *Rev. Sci. Instrum.* **78**, 054301 (2007)
3. P. Polakis, The oncogenic activation of beta-catenin. *Curr. Opin. Genet. Dev.* **8**, 95–102 (1999)
4. B. Lustig, J. Behrens, The Wnt signaling pathway and its role in tumor development. *J. Cancer Res. Clin. Oncol.* **129**, 199–221 (2003)
5. H. Goto, K. Kawano, I. Kobayashi, H. Sakai, S. Yanagisawa, Expression of cyclin D1 and GSK-3beta and their predictive value of prognosis in squamous cell carcinomas of the tongue. *Oral Oncol.* **38**, 549–556 (2002)
6. V.F. Taelman, R. Dobrowolski, J.L. Plouhinec, L.C. Fuentealba, P.P. Vorwald, I. Gumper, D.D. Sabatini, E.M. De Robertis, Wnt signaling requires sequestration of glycogen synthase kinase 3 inside multivesicular endosomes. *Cell* **143**, 1136–1148 (2010)
7. G.N. Bijur, R.S. Jope, Proapoptotic stimuli induce nuclear accumulation of glycogen synthase kinase-3 beta. *J. Biol. Chem.* **276**(40), 37436–37442 (2001)
8. R.V. Bhat, J. Shanley, M.P. Correll, W.E. Fieles, R.A. Keith, C.W. Scott, C.M. Lee, Regulation and localization of tyrosine216 phosphorylation of glycogen synthase kinase-3beta in cellular and animal models of neuronal degeneration. *Proc. Natl. Acad. Sci. U. S. A.* **97**(20), 11074–11079 (2000)
9. J.W. Zmijewski, R.S. Jope, Nuclear accumulation of glycogen synthase kinase-3 during replicative senescence of human fibroblasts. *Aging Cell* **3**, 309–317 (2004)
10. J.A. Diehl, M. Cheng, M.F. Roussel, C.J. Sherr, Glycogen synthase kinase-3beta regulates cyclin D1 proteolysis and subcellular localization. *Genes Dev.* **12**(22), 3499–3511 (1998)

11. A.V. Ougolkov, M.E. Fernandez-Zapico, V.N. Bilim, T.C. Smyrk, S.T. Chari, D.D. Billadeau, Aberrant nuclear accumulation of glycogen synthase kinase-3 β in human pancreatic cancer: association with kinase activity and tumor dedifferentiation. *Clin. Cancer Res.* **12**, 5074–5081 (2006)
12. G.P. Meares, R.S. Jope, Resolution of the nuclear localization mechanism of glycogen synthase kinase-3: functional effects in apoptosis. *J. Biol. Chem.* **282**(23), 16989–17001 (2007)
13. J. Franca-Koh, M. Yeo, E. Fraser, N. Young, T.C. Dale, The regulation of glycogen synthase kinase-3 nuclear export by Frat/GBP. *J. Biol. Chem.* **277**(46), 43844–43848 (2002)
14. H. Yamamoto, S.K. Yoo, M. Nishita, A. Kikuchi, Y. Minami, Wnt5a modulates glycogen synthase kinase 3 to induce phosphorylation of receptor tyrosine kinase Ror2. *Genes Cells* **12**(11), 1215–1223 (2007)

Chapter 46

Organic Solar Photovoltaic Cells

A. Nava-Vega, Mario Cerda Lemus, Denisse Makoske Ibarra, and Moisés Viloría Sánchez

Abstract In photovoltaic industry the research at solar cells is in continuous development from the innovation at organic molecules until efficient plastics new products have been presented recently, improving efficiencies and costs. In this work we prepared photovoltaic solar organic cells based on the work of J.L. Maldonado et al., where the authors proposed an improvement of the solar cells when it is used fullerene-60 as doped material. We characterized the generated solar cells using the optical fringe projection technique and scanning electron microscope (SEM) imaging, the results gives us 40 μm , for the cells width; and an electric characterization measuring currents of 8 mA.

Keywords Organic • Photovoltaic effect • Profilometry • Electric current and optical characterization

46.1 Introduction

Organic solar cells—organic solar photovoltaic (OPVs) offers many advantages, such as low cost, high throughput production, flexible devices and lightweight products, as well custom-design. As a backward the OPVs still have efficiency values and lifetime expectations low compared to their inorganic counterparts. The most recent National Renewable Energy Laboratory (NREL) certified power conversion of 10.6 % reported by UCLA, and 11.8 % reported by Kyung Hee University [1]. There is a great scientific and technological interest in polymers [2] that present exceptional characteristics, such as flexibility, reachable and low cost fabrication, we implemented an easy and simple method to work with organic solar cells using the methodology reported by J. L. Maldonado [3]. We are looking for a reachable, low cost option to produce organic solar cells, as a proposal to feed different devices, like calculators, watch's, small motors, etc., [4]. Solar-energy conversion has been reported with the use of a hybrid (organic–inorganic) PV Cells [5]. OPVs represent a good option, instead the inorganic custom materials, with limits related to technology, it means, high fabrication cost, difficulties to adapt cells in different applications and non-flexibility of the silica [6]. With a long history, in 1839 the photovoltaic effect was discovered by Alexander-Edmond Becquerel, with contributions of many more until 1905, date that Albert Einstein published his paper explaining the photoelectric effect, the contributions to generated a device to work property did not stopped there, at 1954 researchers at Bell Laboratories discovered the silicon solar cell, which was the first material to directly convert the sunlight into electricity to made work electrical devices. The efficiency of these cells was 4 % to produce 5 mW of electrical energy [6]. In 1986 Tang published an article where a solar cell is based on layers of two organic components with an electric efficiency of 1 % [7]. Organic solar cells was not interesting due the low efficiency, however with Alan Heeger Nobel Chemist prize winner in 2000, awarded by organic photovoltaic research [8], the topic gain attention again and BASF, BOSCH, MERCK y SHOTT industries are working to improve the organic photovoltaic device, which has a 12 % of efficiency, reported by Heliatek [9]. In Sect. 46.2 we give a general overview of the OPVs theory, in Sect. 46.3 we present the details of fabrication, in Sect. 46.4 we have the results and finally in Sect. 46.5 we present a discussion about our work.

A. Nava-Vega (✉) • M.C. Lemus • D.M. Ibarra • M.V. Sánchez
Universidad Autónoma de Baja California, Tijuana, B.C., Mexico C.P. 22420
e-mail: adriana.nava@uabc.edu.mx; mario.cerda@uabc.edu.mx; leilani.makoske@uabc.edu.mx; moises.viloria@uabc.edu.mx

46.2 Theory OPVs

Organic Photovoltaic term refers to solar cells that used an organic component at their production, most of them are doped. The physical principle of function for organic and inorganic cells is based on the electron transference produced by the sunlight incidence, known as photovoltaic effect [10]. The optoelectronics factors are well known form literature, for organic photovoltaic cells the fullerene 60 pretend to improve the current generated in the OPVs.

46.3 OPVs Fabrication Procedure

In the present work, we follow the OPVs fabrication method reported by Maldonado et. al. [3], where all explanation is exposed with detail. As summary, we present at Table 46.1 the material employed at our venture. A semiconductor polymer MEH-PPV with the Fullerene C_{60} enhances the light collected by the OPVs. An ITO coated glasses and wood metal were used as anode and cathode.

46.3.1 Experimental Procedure

Figure 46.1 presents a diagram to prepare the solution 1, with MEH: PPV and solution 2 with fullerene (C_{60}). The solutions keep mixing to have a homogenous final solution. A principal solution (solution 1) is prepared with 29 mg of MEH: PPV in 10 mL of chloroform ($CHCl_3$). By another side, a solution 2 is prepared with 6 mg of C_{60} dissolved in 10 mL of toluene, after

Table 46.1 Material used at PVs production

Materials and reactive
ITO coated glasses
MEH: PPV
C_{60}
Woods metal (melting point = 75 °C)
Chloroform
Toluene
Ethanol

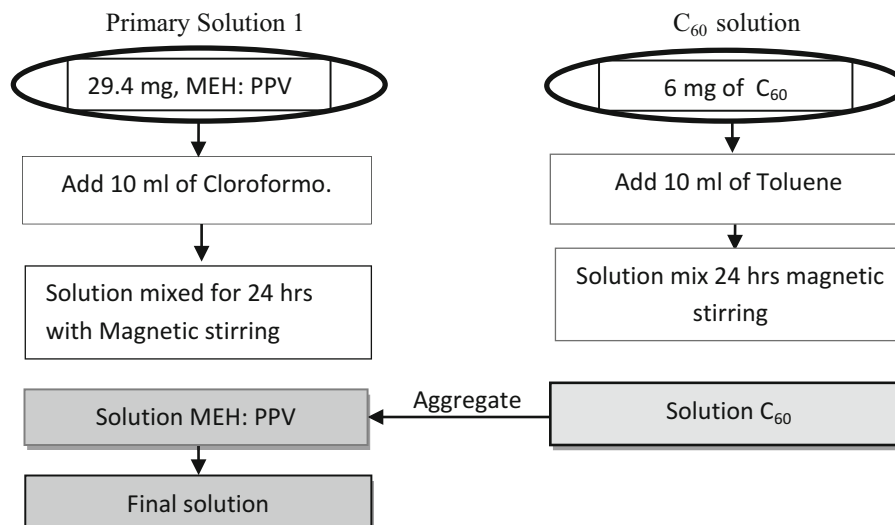


Fig. 46.1 Diagram solution stages

mixing them, a 1 mL of C₆₀ solution is added to the MEH: PPV solution and the new one is mixed again, using a magnetic stirring. It is important to maintain the working area clean and free of dust.

46.3.2 Spin Coating Method

In Fig. 46.2 it is presented graphically the spin coating method. A deposition of organic solution using spin-coating is a very simple and widely used technique to prepare films of uniform thickness. There are four main stages involved in this process: (1) solution pouring (by dropping) the material dissolved in a volatile solvent, it is dripping on the center of a rotating substrate initially; (2) “spin-up”, while the substrate spins, the liquid flows radially driven by the centrifugal force; (3) “spin-off”, liquid that reaches the substrate edge is expelled in drops, as the film thins down; (4) Evaporation, though evaporation occurs at all times from the beginning of the spin coating process, when spin-off is slow and for less volatile solvents, the evaporation becomes the main mechanism of solvents removal and thinning of the film. At Fig. 46.3, a scheme with diagrams of organic layer deposition and a cleaning glass substrate is described. We identified the active area for the ITO electrodes with resistances of 4 and 10 Ω.

Fig. 46.2 Spin-coating technique used to deposit films of organic solution in ITO glass

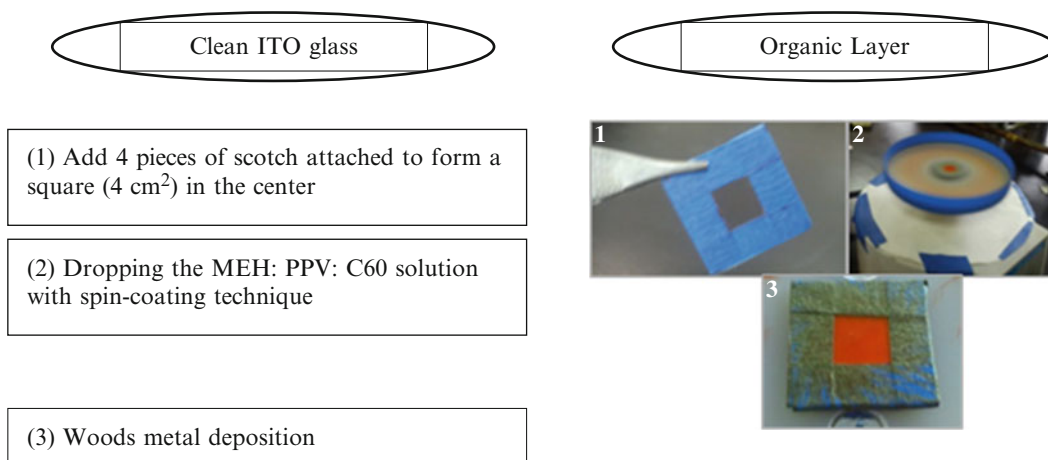
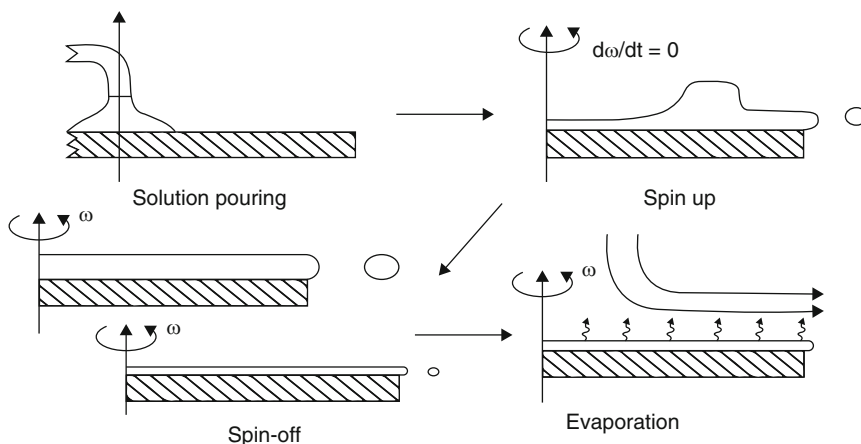


Fig. 46.3 (a) Diagram with sample preparation steps and (b) spin-coating technique used to deposit films of organic solution in ITO glass. OPV cell generated

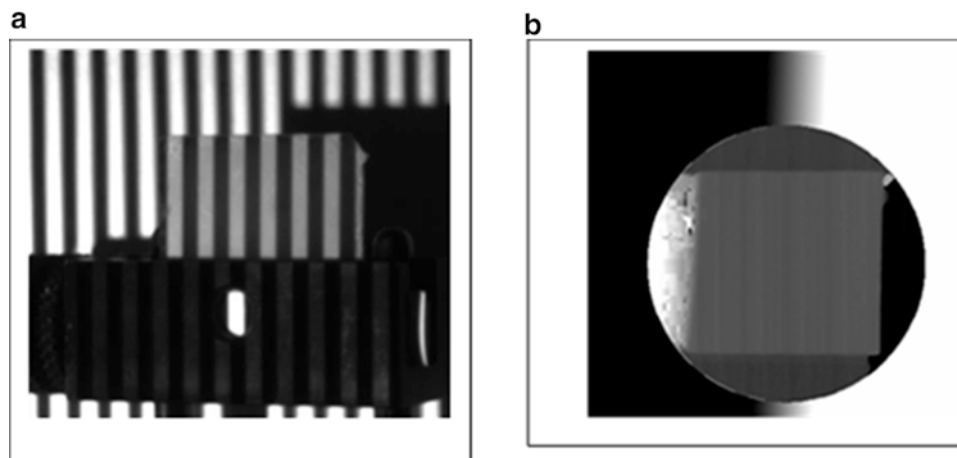
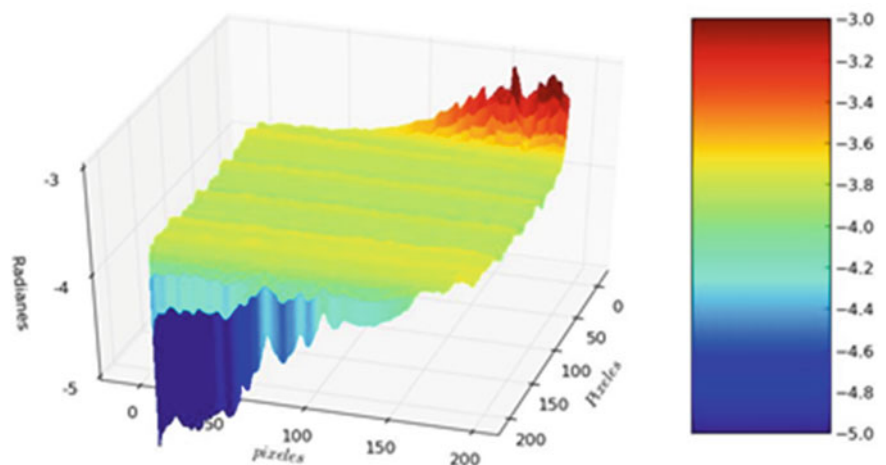


Fig. 46.4 (a) Sinusoidal fringes displayed over OPVs cells without the wood metal deposition, (b) phase of the fringe pattern

Fig. 46.5 Three dimensions phase surface map of Fig. 46.4b. Axis indices are Z radians and X–Y pixels



46.4 Results and Characterization

In Fig. 46.3b we show a final OPV with organic layer deposited on ITO glass, which works as anode; the cathode is the wood metal. We fabricated several OPVs, with variations in the deposition time and rpm motor; samples of OPVs were optically characterized with the fringe projection technique [11, 12]. Figures 46.4 and 46.5 show the projected fringes on the object and phase associated to fringe pattern respectively. Figure 46.6 shows a profile of the sample which was measured using a mechanical profilometer. The tickness of the sample is of $40\ \mu\text{m}$. Corresponding to electrical test, we exposed the all fabricated OPVs at the sunlight, for several days at the maximum solar incidence, with a simple technique, using a Fluke we monitored the current flux, a total of 5 days, and 20 OPVs, between 11:00 and 14 h we measured on April month, notice that the maximum value is 8 mA. Two months later (July) we monitored again the same OPVs cells, noticing that the maximum value now is 5 mA. These measured were made in Tijuana, B.C. (Fig. 46.7).

Fig. 46.6 The thickness of the OPVs is of 40 μm

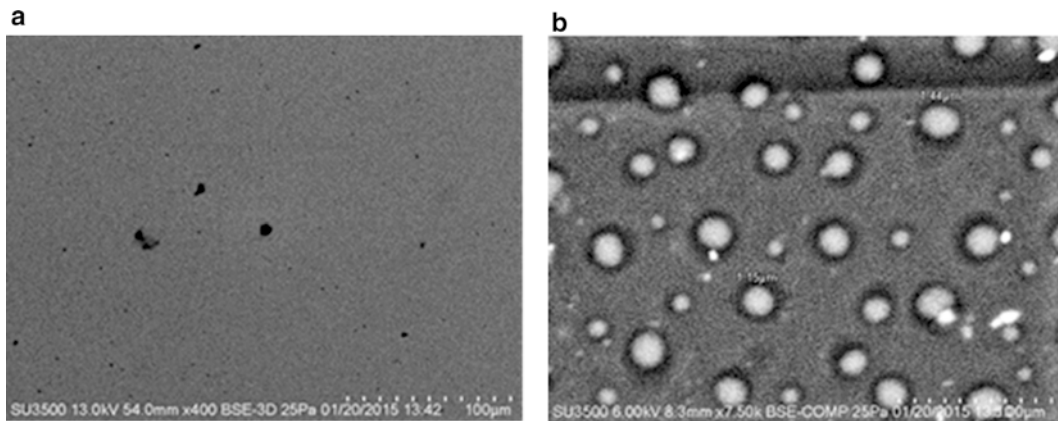
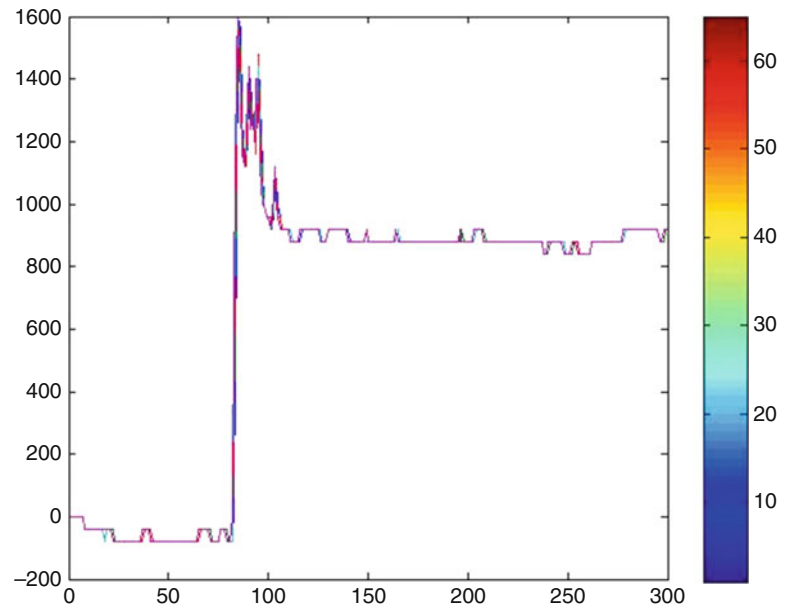


Fig. 46.7 Details of scanning electron microscopy (SEM) to substrate and organics layer images. (a) Zoom out area and (b) zoom in area

46.5 Conclusions

In this work, we reproduce the J.L. Maldonado method [3] to generate OPVs, with some experimental variations; we measured them electrically, with a maximum value of 8 mA that means about a 4 % of efficiency. Optically we characterized the OPVs with a fringe projection technique to test and compare the results with other devices as SEM and a mechanic profilometer. The given results are satisfactory, since we are beginning to experiment with these novel and attractive techniques. Our goal is to offer a simple method to reproduce, improving the results that we already have and calibrate the surface with the optical techniques available at the laboratory.

Acknowledgments A. Nava-Vega thanks to the students that started this process: Juventino Morfin Quintanar, Cecilia Lopez Trujillo, and Grecia Aguilar Herrera. To the technical staff of the SEM, Fabian Alonso and Dr. E. Luna for the digital image processing at fringe projection technique.

References

1. C.J. Brabec, T. Ameri, Solution-processable organic solar cells. *J. Photonics Energy* **5**, 057201 (2015)
2. V. Pecunia, K. Banger, H. Sirringhaus, High-performance solution-processed amorphous-oxide-semiconductor TFTs with organic polymeric gate dielectric. *Adv Electron Mater* **1**(1–2) (2015)
3. J.L. Maldonado, G. Ramos-Ortíz, M.L. Miranda, S. Vázquez-Córdova, M.A. Meneses-Nava, O. Barbosa-García, M. Ortiz-Gutiérrez, Two examples of organic opto-electronic devices: light emitting diodes and solar cells. *Am. J. Phys.* **76**(12), 1130 (2008)
4. H. Ma, A.K.-Y. Jen, L.R. Dalton, Polymer-based optical waveguides: material processing and devices. *Adv. Matter (Weinheim, Ger)* **14**, 1339–1365 (2002)
5. A.F. Nogueira, G. Rumbles, Hybrid organic-inorganic solar cells. *J. Photonics Energy* **5**, 057401 (2015)
6. J. Nelson, *The Principles of Solar Cells* (Imperial College Press, London, 2003). ISBN 978-1-86094-340-9
7. C.W. Tang, Two-layer organic photovoltaic cell. *Appl. Phys. Lett.* **48**, 183–185 (1986)
8. H. Choi, H.-B. Kim, S.-J. Ko, J.Y. Kim, A.J. Heeger, An organic surface modifier to produce a high work function transparent electrode for high performance polymer solar cells. *Adv. Mater.* **27**(5), 892–896 (2015)
9. <http://www.mundoenergia.com/2014/03/26/heliatek-establece-record-de-eficiencia-en-celdas-solares-organicas-con-40-de-transparencia/>
10. S.O. Kasap, *Optoelectronics and Photonics, Principles and Practice* (Prentice Hall, Upper Saddle River, 2001). ISBN 0-201-61087-6
11. D. Malacara, *Optical Shop Testing* (Wiley-Interscience, New York, 1991). ISBN 0-471-52232-5
12. <http://fcqi.tij.uabc.mx>

Chapter 47

Fiber Bragg Gires-Tournois Interferometer Etalons as Fiber Sensor

A. González-García, C.I. Castañeda-Jiménez, N. Rico-Jordan, I. Urbina-Salas, G. González-García, and M.C. Wilson-Herrán

Abstract In this work we report a numerical simulation of a fiber Bragg sensor based on the Gires-Tournois Interferometer as a sensor. This sensor is useful for detection of the high harmonics in an induction electric motor. The high harmonics cause improper working of this type of motor. The sensor is calibrated for a range of ambient temperatures from 25 to 350 °C, but in this work we present a range from −25 to 30 °C.

Keywords Gires-Tournois interferometer • Fiber Bragg grating • Fiber sensor • Pulse laser • Fiber sensor

47.1 Introduction

Advantages are well known when using fiber Bragg gratings, FBG, as sensors and they have been studied in the past years [1]. For example in conventional electrical probes, strain and gauge sensor are useful to perform measurement with improved accuracy and sensitivity immunity to electromagnetic interference. The signal obtained from the FBG sensor is correctly encoded in wavelength domain, and Bragg wavelength shift is sensitive to both temperature and strain. For applications this cross sensitivity is detected and encoded for particular solutions [2–5]. In this work we propose a sensor temperature with high sensibility and applicability in the control of high harmonics that affect the proper working of an induction motor fed by an electric three-phase system.

47.2 Experimental Setup

The fiber Bragg Gires-Tournois sensor used in this work is shown in Fig. 47.1a. We can observe that the sensor is formed by two gratings, one of them is a weak grating (reflectivity ~4 %) and the other one is a strong grating (reflectivity ~99 %). Figure 47.1b shows the schematic diagram of the proposed FBG sensor system, where a broadband source is used, and a pulse generator in the range of 1550 nm as well. The weak and strong gratings are 2 and 4 mm long, respectively (See, Ref. 6). They are separated by 4.1 mm. The pulses from an actively Q-switched pulse laser enters into the system through a circulator and is transmitted to the sensor. A narrow band of the reflected pulse (centered in the Bragg wavelength of 1550 nm), shows that the variations in its spectrum will be depending on the temperature and strain conditions.

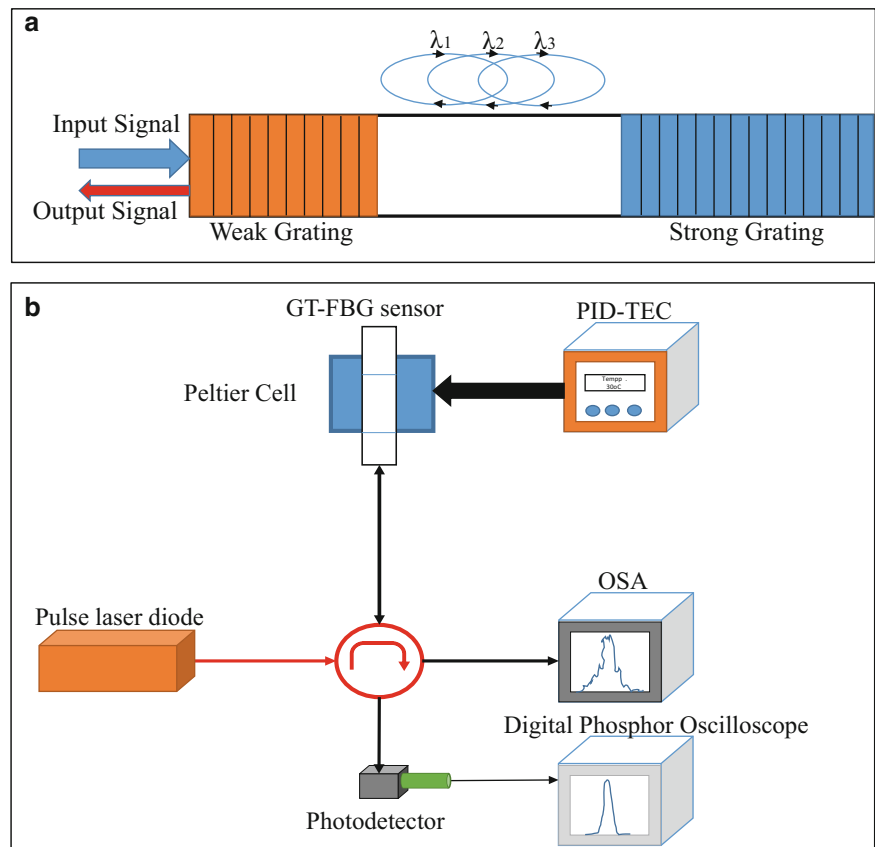
The reflected pulse enters the photodetector (PD) via the circulator. The optical pulse transmitted through the PD is measured by a digital oscilloscope. The precisions of this scheme is related to the precision of an integral-derivative temperature electric controller (PID-TEC) and the scanning amplitude is determined by the resolution of the digital oscilloscope. As the sample signal interferes with noise, it is necessary to choose a suitable filtering technique [6].

A. González-García (✉) • C.I. Castañeda-Jiménez • N. Rico-Jordan • I. Urbina-Salas
Mechatronic Department, Instituto Tecnológico Superior de Guanajuato, Carretera Estatal Guanajuato-Puentecillas, km.,
10.5, Predio el Carmen, C.P. 36262 Guanajuato, Gto., Mexico
e-mail: phd.gonzalezgarcia.a@ieee.org

G. González-García
Chemistry Department, Universidad de Guanajuato, Noria Alta s/n., 36050 Guanajuato, Gto., Mexico
e-mail: gerardog@ugto.mx

M.C. Wilson-Herrán
Physics Department, Facultad de Ciencias Físicas y Matemáticas, Universidad de Chile, Blanco Encalada 2008, Casilla 487-3, Santiago, Chile
e-mail: mario.wilson@ing.uchile.cl

Fig. 47.1 (a) Sensor setup (GTIE) and (b) configuration setup of the sensor system



47.3 Results and Discussion

Following the scheme of Fig. 47.1b, pulses from the laser diode, optical average power of 5 mW, enter through the circulator and then to the fiber Bragg sensor. The FBG sensor has a Gires-Tournois interferometer and a Bragg wavelength of 1550 nm with a bandwidth of 0.2 nm at 3 dB. The reflective pulse is registered by the digital oscilloscope which is controlled by a PD. Using the 3 dB coupler, the reflected Bragg wavelength displacement is simultaneously detected by an optical spectrum analyzer (OSA). A typical spectrum of the laser at 1552 nm is shown in Fig. 47.2.

Figure 47.3 shows the FBG Bragg wavelength displacement detected by the OSA. the maximum displacement is 2.0 nm. The displacement of the spectrum for each wavelength is 0.1 nm/°C.

By considering these results, we think this layout can be potentially used in industrial applications for the analysis of high harmonics in induction synchronous and asynchronous motors. This is part of a future study.

47.4 Conclusion

In conclusion we have demonstrated the relationship between temperature and the wavelength displacement in a fiber Bragg grating, when used as Gires-Tournois interferometer. The results show that we can control the displacement of the wavelength Bragg when related to a certain temperature on the profile of the fiber Bragg grating. This phenomenon can be potentially used in the study of the effect of high harmonics in induction motors.

Fig. 47.2 Spectrum of the pulse diode laser at 1552 nm

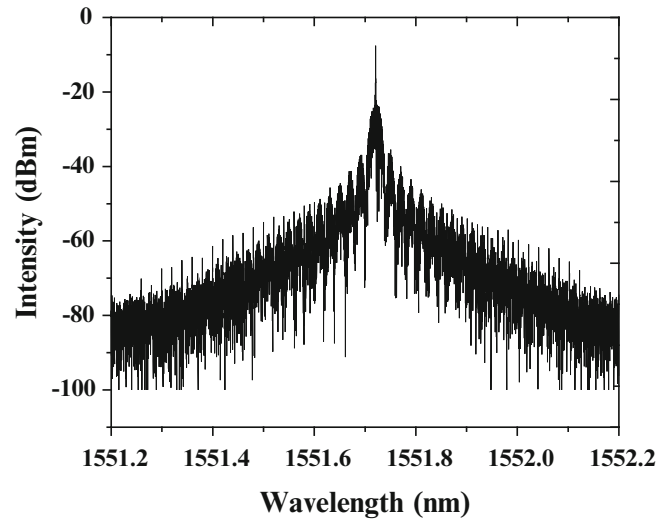
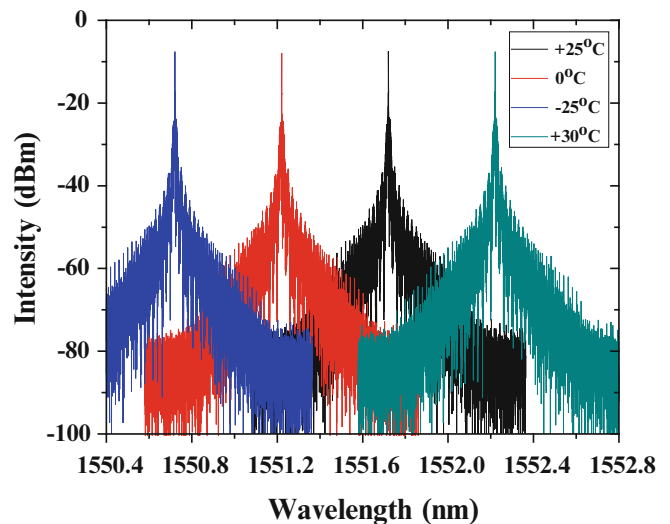


Fig. 47.3 Tunable spectrum of the FBG sensor for a range of temperature from -25 to 30 °C



Acknowledgment This research was supported by the Guanajuato Council for Science (CONCyTEG), A. Gonzalez, and C. Castañeda, acknowledge CONCyTEG project No. 27. M. W. acknowledges FONDECYT project No. 3140387.

References

1. X. Shu, K. Chisholm, J. Mitchell, I. Felmeri, P. Rhead, A. Gillooly, K. Sugden, I. Bennion, Tunable dispersion compensator based on three distributed Gires-Tournois etalons. *Opt. Commun.* **251**, 59–63 (2005)
2. X. Shu, I. Bennion, J. Mitchell, K. Sugden, Tailored Gires-Tournois etalons as tunable dispersion slope compensators. *Opt. Lett.* **9**, 1013–1015 (2004)
3. X.-L. Wang, W.-C. Huang, Y. Zhang, Z.-P. Cai, Design and analysis on a Gires-Tournois resonator based interleaver. *Optoelectron. Lett.* **5**, 51–53 (2009)
4. Y. Zhang, W. Huang, X. Wang, H. Xu, Z. Cai, A novel super-high extinction ratio comb-filter based on cascaded Mach-Zehnder Gires-Tournois interferometers with dispersion compensation. *Opt. Express* **17**, 13685–13699 (2009)
5. Y.K. Lize, M. Summa, P. Wigley, C. Malouin, T.J. Schmidt, P. Day, Tunable high order dispersion compensator for optimized 40 Gb/s performance in 50 GHz channel spacing, *JWA47*, 2009 OSA/OFC/NFOEC (2009)
6. A. Gonzalez-Garcia, O. Pottiez, R. Grajales-Coutiño, B. Ibarra-Escamilla and E.A. Kuzin, Optical pulse compression and amplitude noise reduction using a non-linear optical loop mirror including a distributed Gires-Tournois etalon, *Optics & Laser Technology* **42**, 1103–1111 (2010)

Chapter 48

Cleaning of Tantalum Capacitor Electrode Surface by Laser in Multipulse Regime

A.E. Villarreal, A.K. Frías, F.G. Rendón, T. Flores, L. Ponce, and G. Vázquez-Bautista

Abstract In this paper a method for cleaning tantalum capacitors terminals, using the technique of selective ablation by pulsed laser is proposed. Such ablation is studied by the LIBS technique to characterize capacitors and determine the resin composition and possible contaminants adhered. In addition, OCT measurements are performed to recreate the damage done to the samples.

Keywords Capacitor • Tantalum • LIBS • Multipulse • Nd: YAG laser

48.1 Introduction

Capacitors are electronic devices capable of storing electrical charge. When a voltage is applied by an external source, an effect of electric field occurs therein, and acquires certain amount of electric charge (coulombs) which results in a potential difference between its terminals [1]. These components are used in a wide range of applications and areas such as military aerospace industry, and various equipment ranging from a simple TV to a satellite. Because of it, it is very large demand worldwide. Its typical structure consists of two plates or foils called “frames”, facing and spaced by an insulating material or “dielectric”, which may be air, paper, mica, ceramic, plastic or other insulation [2, 3].

Many of the classic mechanical and chemical cleaning methods used produce some kind of damage on the surface. An example of this is the Sand Blasting (currently used method for cleaning tantalum capacitors), which involves mechanically removing a layer of corrosion on the surface of the object through the collision of sand particles at high speed. The main abrasives are: silica sand, aluminum oxide, silicon carbide, baking soda, glass bead, among others. This method effectively cleans the terminals of the capacitors, but being very abrasive and poorly selective, produces heavy damage to the terminals of the capacitor by weakening or creating problems in its structure [4].

By contrast, laser-based methods have a number of advantages over traditional cleaning methods such as the above, these advantages are: (a) there is no physical contact between the laser and the sample, allowing working with extremely fragile surfaces, (b) the laser beam can be directed with great precision on the surface of the sample, (c) the waste material generated during the laser cleaning process can be easily removed with the help of a flow of high pressure air, (d) it is not necessary to use chemicals. For this reason, the laser is applied as a tool in the restoration and conservation of cultural heritage from the 1980s [5].

The laser cleaning of artworks has been applied mainly in cleaning crust on the rocks and stones, also in paints [6] papers [7, 8], ancient glass with historical importance [9], metal artifacts [10, 11] and also in removing graffiti [12]. Recently, due to the need to control the cleaning process more accurately it has led to the development of laser technology as a diagnostic and characterization [13–15, 25]. In this regard, the laser induced plasma spectroscopy (LIBS) plays an important role in the restoration process because of its many benefits as an analytical technique [16, 17, 26]. This includes multi-elemental characterization of materials, quick analysis without sample preparation, the resolution of the proper depth and the possibility of designing portable systems for applications in situ [18]. Fotakis et al. [19] examined the use of LIBS to oversee the process of laser cleaning limestone of an ancient building. Applying LIBS it is based on the different chemical composition between the black rock fouling covering (black crust) and limestone. As shown, the information obtained by LIBS is very effective in order to control the laser cleaning process and to prevent wear on the rock.

A.E. Villarreal (✉) • A.K. Frías • F.G. Rendón • T. Flores • L. Ponce • G. Vázquez-Bautista
Centro de Investigación en Ciencia Aplicada y Tecnología Avanzada (CICATA) Unidad Altamira del Instituto Politécnico Nacional (IPN), km. 14.5 Carretera Tampico—Puerto Industrial Altamira, C.P. 89600 Altamira, Tamaulipas, Mexico
e-mail: angel.villarreal.1991@gmail.com

In this paper a study is done to demonstrate the potential of LIBS as a cleaning monitoring process, by analyzing the plasma generated by the ablation of surface material of capacitors in an intermediate state of manufacture and resin in the capacitors already completed, in order to determine their composition and behavior by making a series of shots. As further information, damage taken by samples is recreated and measured by the OCT technique.

48.2 Experimental Development

48.2.1 LIBS Facility

For the development of the LIBS technique were available an installation as that shown in Fig. 48.1, which uses a multi-pulsed Nd:YAG laser with a Cr:YAG passive Q-switch, emitting at 1064 nm wavelength. The laser beam is focused on the sample of interest while the generated plasma is collected by a Ocean Optics SR P600-1 m optic fiber coupled to a Ocean Optics USB 4000 UV-VIS spectrometer (spectral range 200–900 nm and optical resolution of 0.35 nm), which processes and transmits the emission spectrum to a PC with the software SpectraSuite.

48.2.2 Samples of Study

Tantalum capacitors such as the one represented in Fig. 48.2 were used as samples. Its dimensions are 8 mm long including the terminals, width of 2.54 mm and the diameter of its terminals is 0.5 mm.

In the manufacturing process, terminals are soldered to the capacitors and are also coated with a resin. In Fig. 48.3 we can observe the image of one completed.

Fig. 48.1 LIBS facility

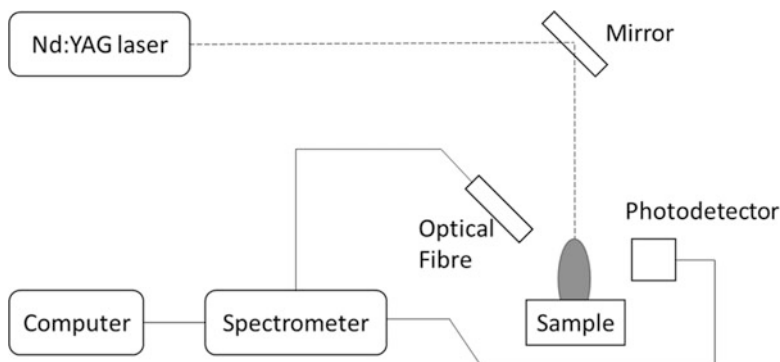


Fig. 48.2 Tantalum capacitor

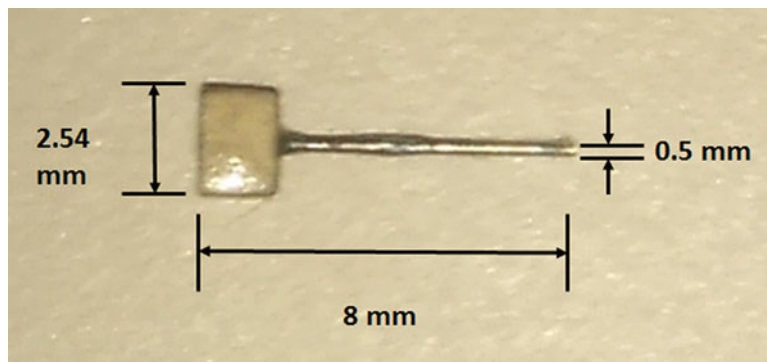


Fig. 48.3 Resin coated capacitor

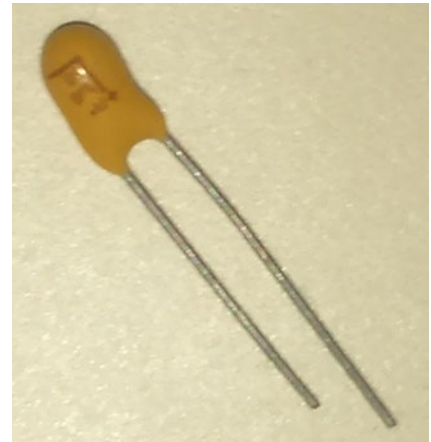
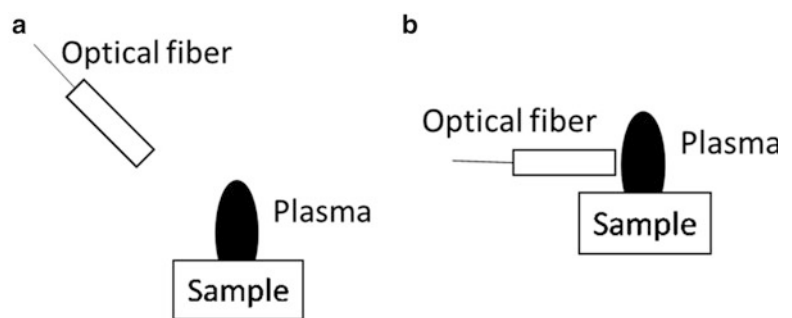


Fig. 48.4 Layout of the fiber relative to the plasma plume, (a) 45°, and (b) 0°



48.2.3 Application of LIBS Technique and Identification of Spectral Lines

A succession of shots were fired with the laser on the sample before and after being coated with resin, in order to define and characterize the emission spectra of the materials involved.

The technique was applied first on the surface of the capacitor to a low energy (15 mJ) with a spot diameter of 1 mm, to obtain low fluence and appreciate the component layers by making a depth analysis. Fiber was placed at 45° with respect to the plasma plume, as shown in Fig. 48.4a.

Once known the composition of the device, we proceeded to analyze the resin on the finished capacitor. Because of the low intensity of the spectra obtained, the working energy was increased to 60 mJ, the optical fiber was positioned at 0° respect to the plasma plume and approached to a minimum distance, as represented in Fig. 48.4b.

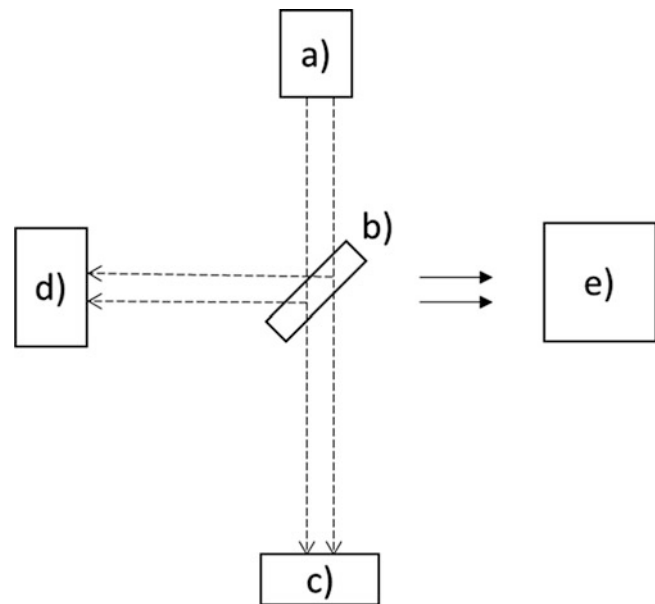
For the identification of spectral lines a comparison with the database of laser technology laboratory IPN-CICATA was done. Also comparisons with the database of the US Army United States Army Research Laboratory were performed [20] and with the National Institute of Standards and Technology (NIST) database [21] were done. To facilitate the work with the latter, the “LIBS Analyzer” software, developed in the laboratory of laser technology were used. In addition, the literature review of other studies that have analyzed the tantalum through LIBS technique was consulted [22–24].

48.2.4 Optical Coherence Tomography

The spectral domain optical coherence tomography (SD-OCT), is a measurement method based on the detection of differences in optical path length. This incorporates a light source with wide spectrum, with a spectrometer, to recreate depth profiles that are achieved by cross-sectional imaging. These cross-sectional images can be used in order to display three-dimensional reconstructions. In Fig. 48.5, a block diagram of the main parts shown.

This measurement method is used to reconstruct images of craters generated by laser ablation, in order to observe the damage done to samples made. The equipment used is the CALLISTO system, Thorlabs, whose central wavelength is 930 nm and its maximum depth resolution is 1.6 mm.

Fig. 48.5 Main parts of an OCT facility: (a) wide spectrum light source, (b) beam splitter lens, (c) sample to be measured, (d) reference (e) detector chamber



48.3 Results and Discussion

48.3.1 Analysis of the Capacitor

A series of ten shots were fired on the component. The emission spectra of generated plasma were collected and proceeded to its identification. With the first shots on the outside surface, silver emission lines corresponding to the wavelengths of 328.17, 337.96, 520.37 and 546.01 nm were found. In Fig. 48.6 the overlap of the two strongest lines after being normalized is illustrated.

As the sample is ablated, the silver lines begin to diminish, while appear and are intensifying the ones corresponding to tantalum at the following wavelengths: 539.91, 593.69 and 648.26 nm. This is represented in Fig. 48.7.

The aforementioned behavior can be seen in Fig. 48.8, where in (a) are shown selected spectra of the sequence performed and on (b) it is represented the graph of the evolution of the silver line at 546.01 nm and the tantalum line at 539.91 nm, with respect to number of shots fired on the sample. It is concluded that there is a thin silver layer covering the tantalum plate.

In Fig. 48.9, OCT images that were taken in order to show the crater generated by laser ablation after the succession of shots are shown. It can be appreciated that penetration on the surface is in the order of microns.

48.3.2 Analysis of the Resin

Just as with the previous case, a succession of shots on a capacitor, but now with the cover resin, was performed. In this case eight shots on the surface were fired. Because the emission spectra were very weak, the collecting fiber was positioned at 0° to the plasma and at a very close distance, as before described.

The trend is illustrated in Fig. 48.10 with selected spectra. In the first six shots, lines from resin and from possible contaminants as a result of the coating process are shown. In the seventh shot total reduction occurs in the spectrum, attributed to two factors. The first is the weak spectrum generated by the resin, the other corresponds to changing the distances between the fiber and the plasma by increased depth of the crater size. In the eighth shot, tantalum spectrum is shown, this being very intense. The fact that the succession from silver to tantalum cannot be observed, may be because in this case as the energy was higher, a higher fluence was achieved, and therefore silver may have been ejected in one shot and at the end only tantalum is observed.

Fig. 48.6 Capacitor LIBS spectra and silver pattern

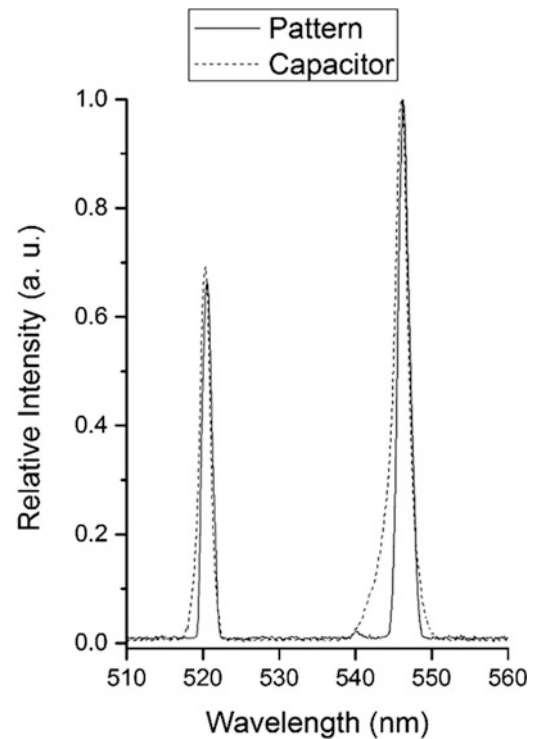
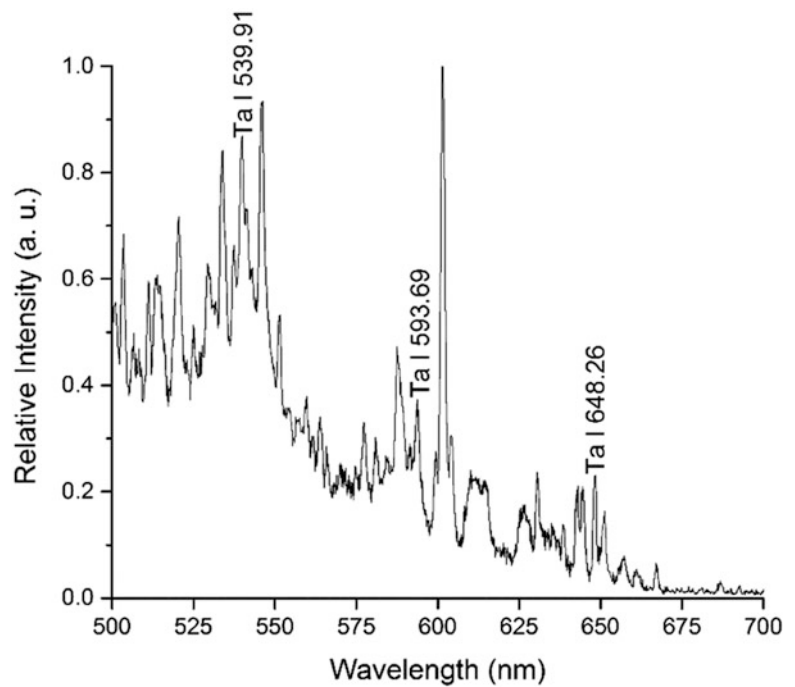


Fig. 48.7 Capacitor LIBS spectrum with tantalum lines



In Fig. 48.11, the lines of the elements identified in the resin are shown. It was selected the spectrum of the sixth shot because there can be appreciated more defined lines.

OCT images of the sample were also taken. They are shown in Fig. 48.12. We can see that the size of the crater is greater because the energy to ablate the resin was higher, corresponding to a higher fluence. The end of the crater is located in the image plane, which is related to that reached the surface of the capacitor, being supported by the LIBS spectrum shown before.

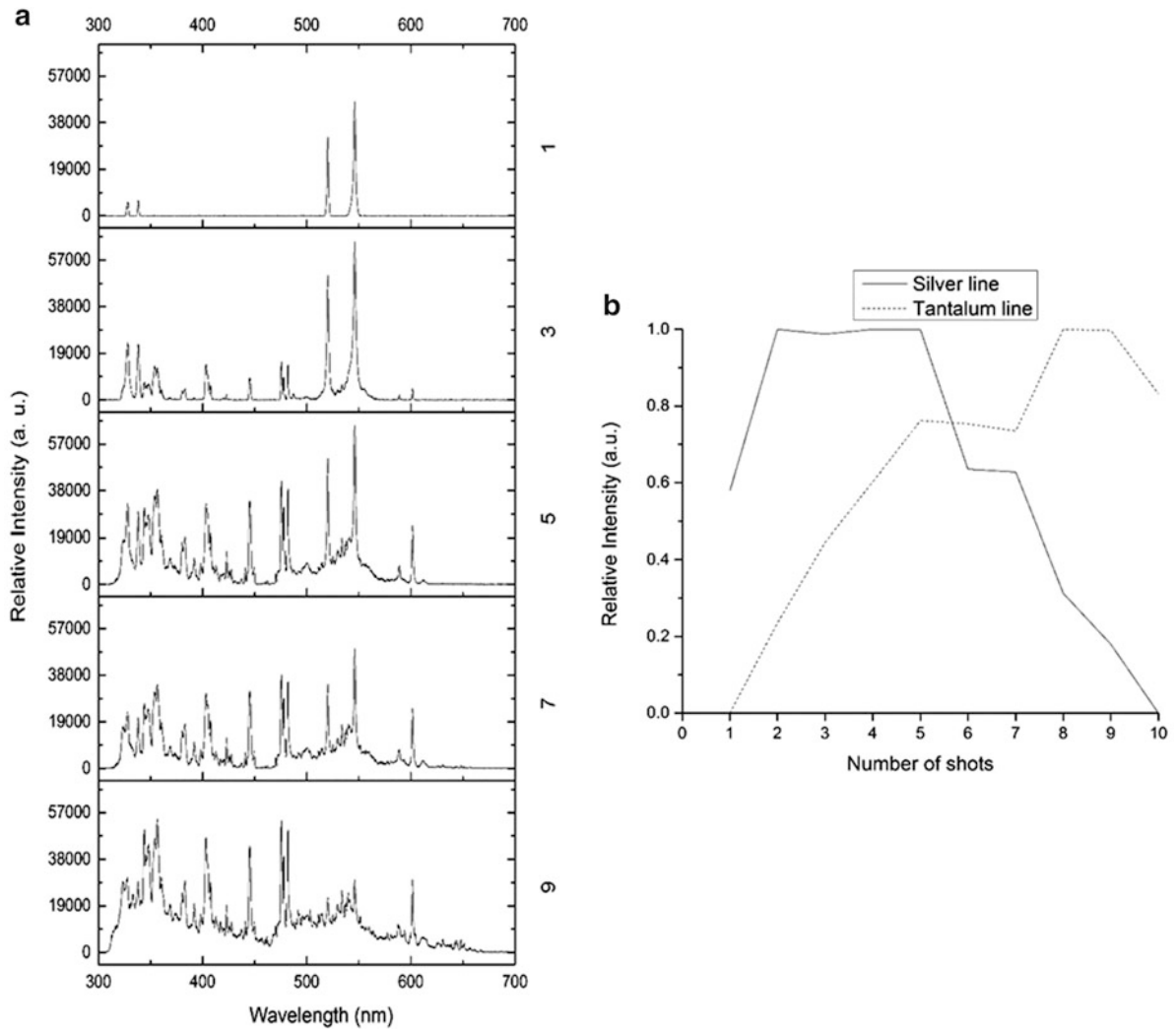


Fig. 48.8 Performance of selected lines of the elements: (a) succession of spectra 1, 3, 5, 7 and 9, (b) comparison of the most intense emission lines of Ta and Ag

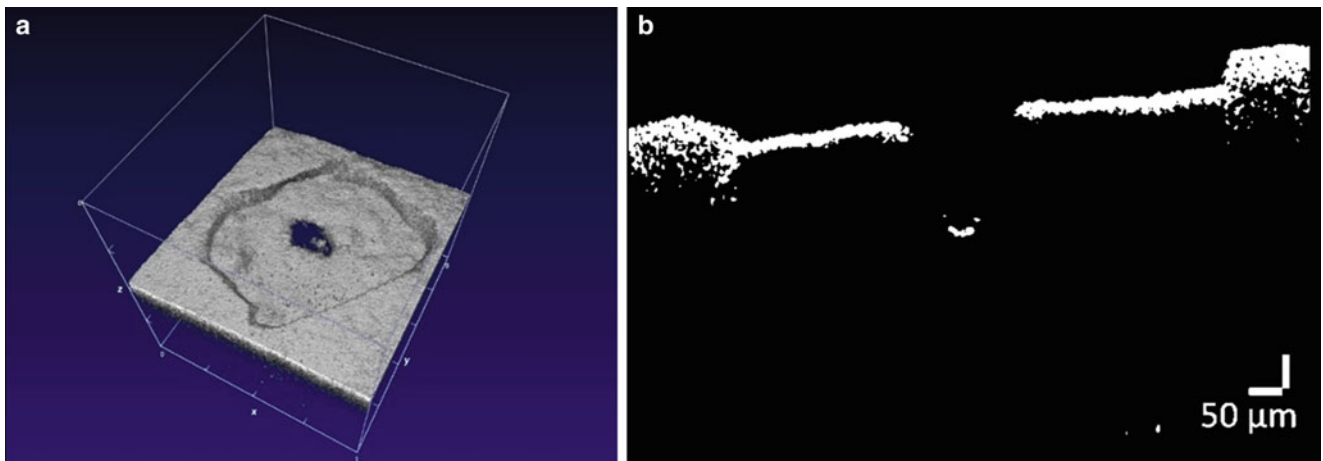


Fig. 48.9 OCT images in 2D and 3D of crater in the capacitor: (a) 3D image generated, (b) 2D image where more depth is appreciated

Fig. 48.10 Sequence of spectra 1, 3, 6, 7 and 8 corresponding to the resin

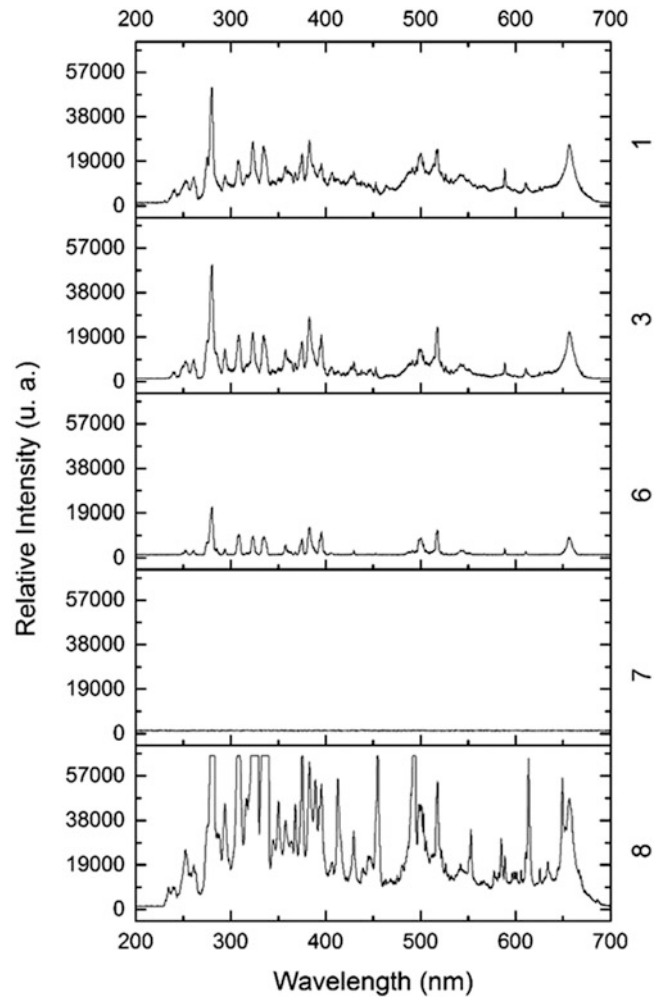
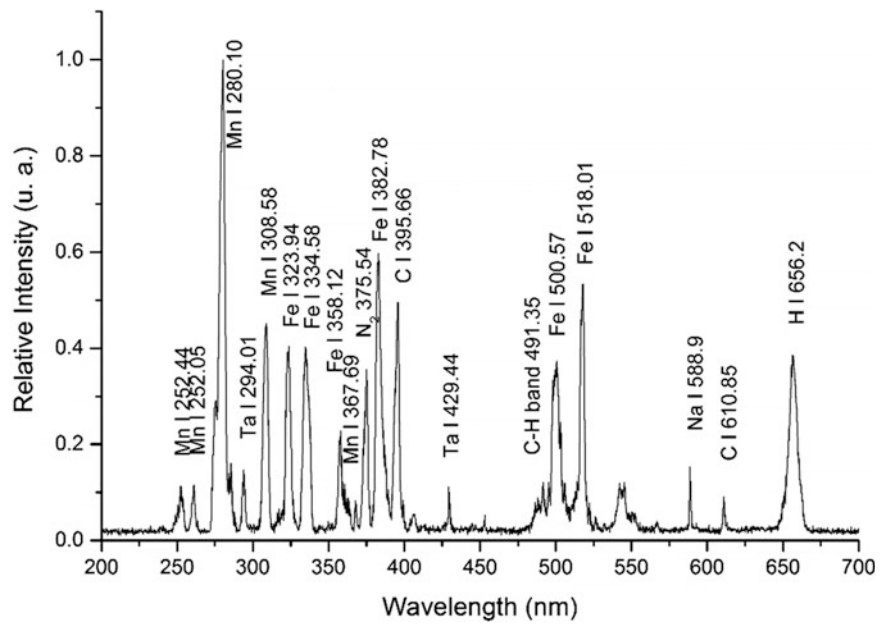


Fig. 48.11 Spectrum of the resin in the sixth shot



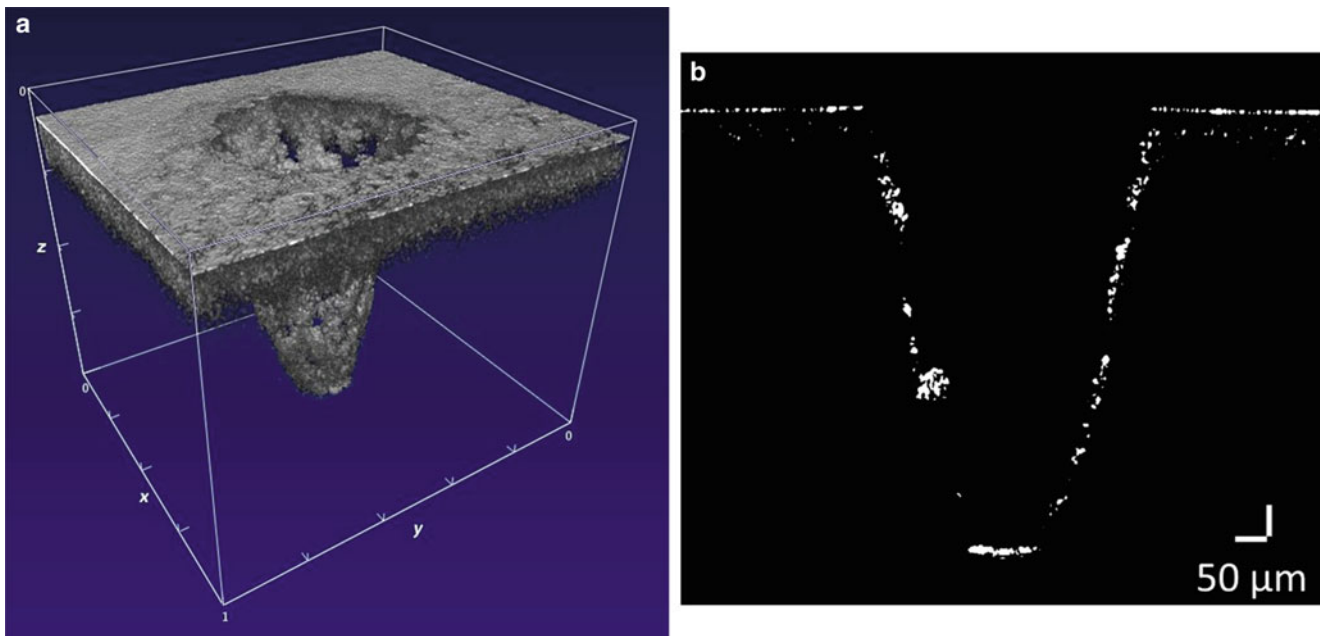


Fig. 48.12 OCT images 2D and 3D from crater in the resin: (a) 3D image generated, (b) 2D image where the surface of the capacitor can be seen in the end of crater

48.4 Conclusions

Elemental analysis was performed by the LIBS technique to tantalum capacitors, in order to monitor the removal process of the resin layer. It was found that the once removed the resin, the capacitor has a composition characterized by the presence of a silver layer covering the tantalum electrode.

In the case of the resin, components that can be defined as potential contaminants during the capacitor manufacturing process, were identified. Due to the weak emission of plasma obtained during ablation of the resin, a configuration was used with the input fiber horizontally relative to the sample and perpendicular to the incidence of the laser, which yielded spectra clearly identifiable peaks.

It was shown that during the process of removing deposited resin on tantalum capacitors with laser, it can be continuously monitored by the LIBS technique, using the same laser source for cleaning and for plasma excitation.

Acknowledgement The authors thank CONACYT and COFAA-IPN for the financial support. This work was supported by project SIP-IPN 20150573.

References

1. A.H. Donate, *Principios de Electricidad y Electrónica III 2aEd* (Marcombo, Barcelona, 2010)
2. J. Bird, *Electrical and Electronic Principles and Technology* (Taylor & Francis, New York, 2010)
3. S.A. Dyer, *Wiley Survey of Instrumentation and Measurement* (Wiley, New York, 2004)
4. F.F. Mazda, *Discrete Electronic Components* (Cambridge University Press, Cambridge, 1981)
5. M. Cooper, *Laser Cleaning in Conservation: An Introduction* (Butterworth-Heinemann, Oxford, 1998)
6. R. Teule, H. Scholten, O.F. van den Brink, R.M.A. Heeren, V. Zafirooulos, R. Hesterman et al., Controlled UV laser cleaning of painted artworks: a systematic effect study on egg tempera paint samples. *J. Cult. Herit.* **4**(Supplement 1), 209–215 (2003)
7. K. Ochocińska, A. Kamińska, G. Śliwiński, Experimental investigations of stained paper documents cleaned by the Nd: YAG laser pulses. *J. Cult. Herit.* **4**(Supplement 1), 188–193 (2003)
8. A. Kaminska, M. Sawczak, K. Komar, G. Śliwiński, Application of the laser ablation for conservation of historical paper documents. *Appl. Surf. Sci.* **253**, 7860–7864 (2007)

9. F. Fekrsanati, S. Klein, J. Hildenhagen, K. Dickmann, Y. Marakis, A. Manousaki et al., Investigations regarding the behaviour of historic glass and its surface layers towards different wavelengths applied for laser cleaning. *J. Cult. Herit.* **2**, 253–258 (2001)
10. E. Drakaki, A.G. Karydas, B. Klinkenberg, M. Kokkoris, A.A. Serafetinides, E. Stavrou et al., Laser cleaning on Roman coins. *Appl. Phys. A* **79**, 1111–1115 (2004)
11. R. Pini, S. Siano, R. Salimbeni, M. Pasquinucci, M. Miccio, Tests of laser cleaning on archeological metal artefacts. *J. Cult. Herit.* **1**(Supplement 1), S129–S137 (2000)
12. S. Chapman, Laser technology for graffiti removal. *J. Cult. Herit.* **1**(Supplement 1), S75–S78 (2000)
13. A. Giakoumaki, K. Melessanaki, D. Anglos, Laser-induced breakdown spectroscopy (LIBS) in archaeological science—applications and prospects. *Anal. Bioanal. Chem.* **387**, 749–760 (2007)
14. K. Melessanaki, V. Papadakis, C. Balas, D. Anglos, Laser induced breakdown spectroscopy and hyper-spectral imaging analysis of pigments on an illuminated manuscript. *Spectrochim. Acta B: Atom. Spectrosc.* **56**, 2337–2346 (2001)
15. F.J. Fortes, M. Cortés, M.D. Simón, L.M. Cabalín, J.J. Laserna, Chronocultural sorting of archaeological bronze objects using laser-induced breakdown spectrometry. *Anal. Chim. Acta* **554**, 136–143 (2005)
16. D.A. Rusak, B.C. Castle, B.W. Smith, J.D. Winefordner, Fundamentals and applications of laser-induced breakdown spectroscopy. *Crit. Rev. Anal. Chem.* **27**, 257–290 (1997)
17. J.D. Winefordner, I.B. Gornushkin, D. Pappas, O.I. Matveev, B.W. Smith, Novel uses of lasers in atomic spectroscopy. Plenary Lecture. *J. Anal. Atom. Spectrom.* **15**, 1161–1189 (2000)
18. F.J. Fortes, J. Cuñat, L.M. Cabalín, J.J. Laserna, In situ analytical assessment and chemical imaging of historical buildings using a man-portable laser system. *Appl. Spectrosc.* **61**, 558–564 (2007)
19. I. Gobernado-Mitre, A.C. Prieto, V. Zafiropulos, Y. Spetsidou, C. Fotakis, On-line monitoring of laser cleaning of limestone by laser-induced breakdown spectroscopy and laser-induced fluorescence. *Appl. Spectrosc.* **51**, 1125–1129 (1997)
20. U. S. Army, United States Army Research Laboratory (ARL) (2010), <http://www.arl.army.mil/www/default.cfm?page=250>
21. U. S. D. o. Commerce, National Institute of Standards and Technology (2010), <http://physics.nist.gov/>
22. S. Khan, S. Bashir, A. Hayat, M. Khaleeq-ur-Rahman, Faizan-ul-Haq, Laser-induced breakdown spectroscopy of tantalum plasma. *Phys. Plasmas* **20**(7), 073104 (2013)
23. K. Novotný, A. Staňková, H. Häkkänen, J. Korppi-Tommola, V. Otruba, V. Kanický, Analysis of powdered tungsten carbide hard-metal precursors and cemented compact tungsten carbides using laser-induced breakdown spectroscopy. *Spectrochim. Acta B: Atom. Spectrosc.* **62**, 1567–1574 (2007)
24. A. Alkhawwam, K. Alnama, A. Jazmati, M.D. Zidan, Characterization of laser induced tantalum plasma by spatio-temporal resolved optical emission spectroscopy. *Optik - Int. J. Light Electr. Opt.* **125**, 2327–2331 (2014)
25. T. Flores, L. Ponce, M. Arronte, E. de Posada, Free-running and Q:Switched LIBS measurements during the laser ablation of Prickle Pears spines. *Optics and Lasers in Engineering*, **47**, 578–583 (2009)
26. L. Moreira Osorio, L.V. Ponce Cabrera, M.A. Arronte García, T. Flores Reyes, I. Ravelo, Portable LIBS system for determining the composition of multilayer structures on objects of cultural value. *Journal of Physics: Conference Series*, **274**, 012093 (2011)

Chapter 49

High Quality Polishing Procedure of Glass Substrates: Application in Integrated Optics

H.E. Lazcano, J.L. Flores, A. Blanco, A. Hernández, R. Nieto, J.L. Martínez, R.A. Torres, G.V. Vázquez, and J.L. Hurtado

Abstract A procedure to polish the edges of glass microscope slides (corning 2947B) for integrated optics is presented in this paper. As usual, the procedure includes six steps: cut of glass substrates, assembly of the glass substrates over a plane surface (blocking), grinding, polishing, disassembly (unblocking) and cleaning. It is possible to fabricate waveguides before or after the polishing procedure. Finally, the outcomes of a practical application are shown. In our opinion, the manufacture of integrated optics devices will increase gradually.

Keywords Polishing • Grinding • Glass slides • Integrated optics • Testplating

49.1 Introduction

Manufacture of integrated optics waveguides, requires substrates with high quality polishing. To achieve that, the setting of the following polishing parameters is important: work surface, abrasive grain size, time and contact pressure. Additionally, in the polish machine, it is important the rotational speed (spindle) and the lateral displacement of the work piece (eccentricity). Also, to verifying the improvement in surface quality, it is advisable to compare it with a flat pattern (to avoid that the surface becomes concave or convex). Polishing the borders between planes is very important because in general, the dimensions of the waveguides are around a few micrometers. The polishing implemented method Polishing allows obtaining many substrates at the same time. After that, using the polished substrates, channel waveguides were fabricated through the laser writing technique [1].

49.2 Materials and Tools

For the polishing process, the following two axes polish machines were used: R. Howard Strasburg, Inc. Model 6UR-2 and polish machine fabricated by CIO technicians. Glass microscope slides were used as substrate (Corning 2947B, 75 × 25 mm, 0.9–1.10 mm thick). The thinnest surface of every slides corresponds to the polished area (25 mm × 1 mm). As abrasives, different grain size of aluminum oxide (Al_2O_3) was use for grinding and 2 μm grain size of cerium oxide (CeO_2) was used for polishing. The procedure sequence was as follows: in the first grinding stage (over metal), 25, 15 and 9 μm were used; then 5 and 3 μm were used over glass. Finally during the polishing stage, over optical pitch (GUGOLZ No. 73), grain of 2 μm was used. Additionally, an electric oven composed by four incandescent light bulbs, was used to heat the wax.

H.E. Lazcano (✉) • J.L. Flores • A. Blanco • A. Hernández • R. Nieto • J.L. Martínez • R.A. Torres • G.V. Vázquez, Ph.D. • J.L. Hurtado
Centro de Investigaciones en Óptica, Loma del Bosque 115, Lomas del Campestre, C.P. 37150 León, Guanajuato, Mexico
e-mail: hugoelh@gmail.com; gvvazquez@cio.mx

49.3 Procedure Details

The proposed polish procedure includes six steps: cut of glass slides, assembly of the glass substrates over a plane surface (blocking), grinding, polishing, disassembly (unblocking) and cleaning. Usually, blocking is a term use in optics that describes the process by which individual optical parts are held in place during manufacture [2]. Therefore, blocking is an action widely used to describe the assembly stage.

49.3.1 Cut of Glass Substrate

To cut the glass slides at the same size, the following procedure was performed: with a stack of ten glass slides a block was made, then using this procedure, in total three blocks were made. After that, the blocks were attached over a flat glass surface. To glue the glass slides to each other, a special heated wax was used, made with beeswax, optical pitch and natural shellac. To improve the blocking, cooling to room temperature is recommended. Figure 49.1 shows details of this process.

49.3.2 Assembly of the Glass Substrates Over a Plane Surface

To polish the glass blocks, it is necessary fixing them on a flat surface. To attach at the polish machine, a flat surface with thread is recommended. For blocking, again heating the wax is necessary and only after cooling at room temperature, it is possible to start the grinding stage. In Fig. 49.2 it is possible to observe images of the blocking processes.

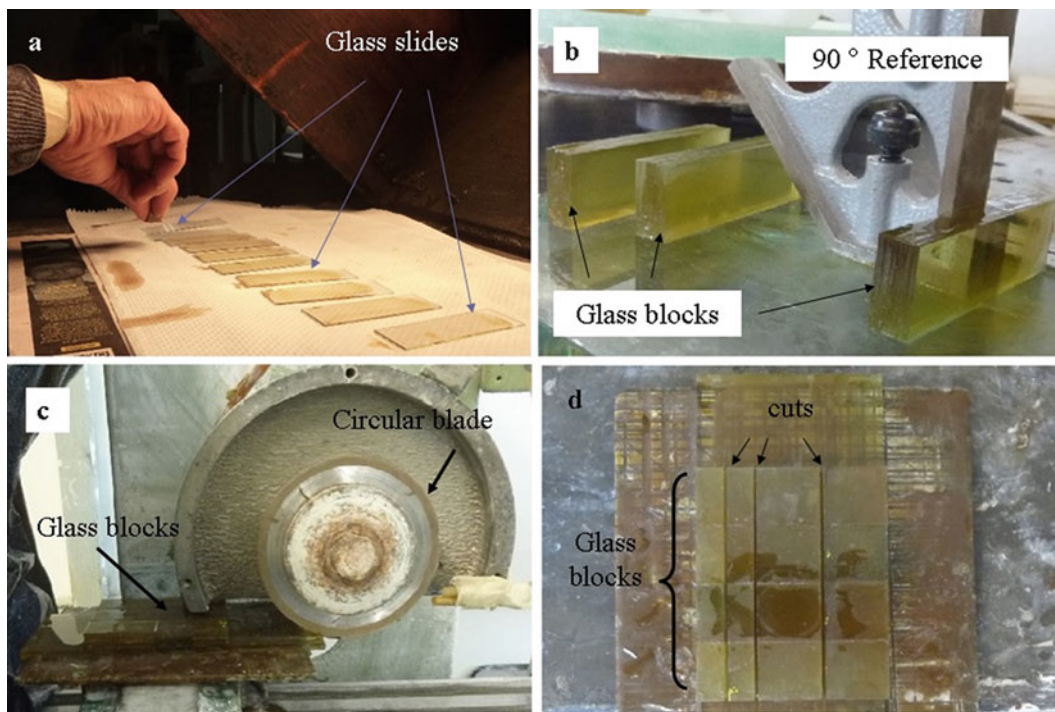


Fig. 49.1 (a) Glass slides were heated and covered with wax before forming the block. (b) Blocks cooling down on a flat base. (c) Detail of the glass blocks during cut processing with diamond blade. (d) Glass blocks after cut process

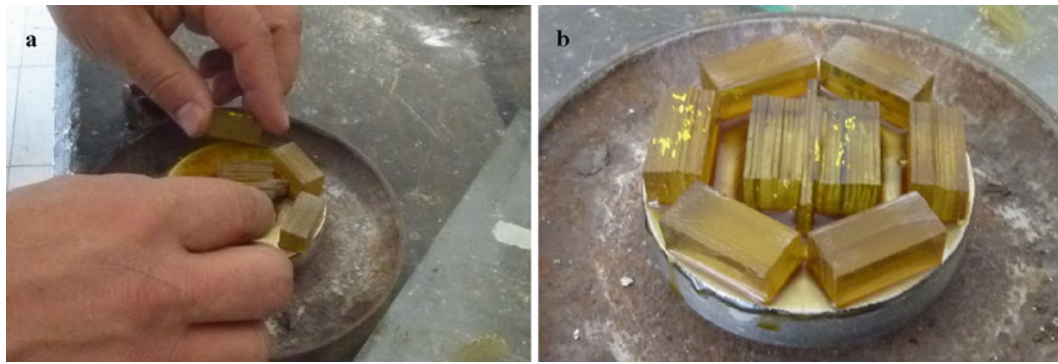


Fig. 49.2 (a) Placing blocks over working plane. (b) Final blocking

Table 49.1 Working time for grinding and polishing processes

Abrasive (μm)		Grinding and polishing time (min)						
		Working piece I		Working piece II		Working piece III		Average
		Surface 1	Surface 2	Surface 1	Surface 2	Surface 1	Surface 2	
Aluminum oxide	25	30	90	90	60	90	60	70
	15	70	60	270	40	270	40	125
	9	50	100	240	180	240	180	165
	5	100	120	90	120	90	120	107
	3	60	130	90	120	90	120	102
Cerium oxide	2	530	590	440	405	465	405	473
Total		840	1090	1220	925	1245	925	1041

49.3.3 Grinding Stage

Grinding is the process of shaping optical materials with free or loose abrasives. The abrasive powder is mixed with water and the grinding is done grinding tools made of cast iron [3]. To initiate this stage, abrasive of $25\ \mu\text{m}$ grain size was used. The abrasive is mixed with water (about one volume of dry abrasive in four volumes of water) to form a slurry [3] that is periodically applied between the grinding tool and the glass workpiece, about one time every 20 s. Additionally, a mass of 1.1 kg was used to press the substrates on the plane. Finally, the working time is not always the same in all the grinding process, because it depends on specific situations as follows: initial quality of the glass surface, tools spins velocity, abrasive supply frequency, and grinding area, among others. Only the continuous assessment of the surface gives the information for setting the required working time. However, as an example, in Table 49.1 information of the working time that we used in grinding and polishing processes are shown. After grinding with abrasive of $25\ \mu\text{m}$, again over metal surface, abrasive of $15\ \mu\text{m}$ and then abrasive of $9\ \mu\text{m}$ were used to continue with the process.

After that, now over a glass surface, abrasive of $5\ \mu\text{m}$ and then $3\ \mu\text{m}$ were used. This stage could be called fine grinding and is a handmade step, without pressure over glass blocks. The movements on the glass surface should be careful, slow and follow a circular path. In Fig. 49.3a it is possible to observe an image of grinding and in Fig. 49.3b fine grinding over a glass surface.

49.3.4 Polishing Stage

The fine ground surfaces become reflective and transparent during the fabrication that is called polishing. In this step, the metallic polishing tools are covered with a viscoelastic material to which an aqueous slurry of a mildly abrasive polishing compound is applied [3]. The polish surface used in this stage was made with optical pitch (Gugolz 73), which requires of the following process to manufacture the polishing surface: First, based on a grinding metallic tool, prepare a mold with a thickness around 2 cm; second, place Gugolz into the mold and heat at melting point ($77\text{--}80\ ^\circ\text{C}$) for a few minutes until the

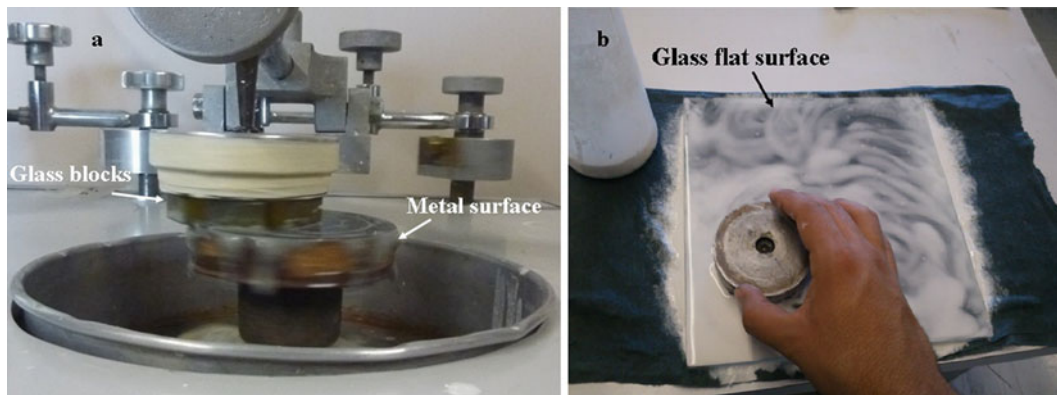


Fig. 49.3 (a) Grinding made with a polish machine fabricated by CIO technicians. (b) Fine grinding over a glass surface

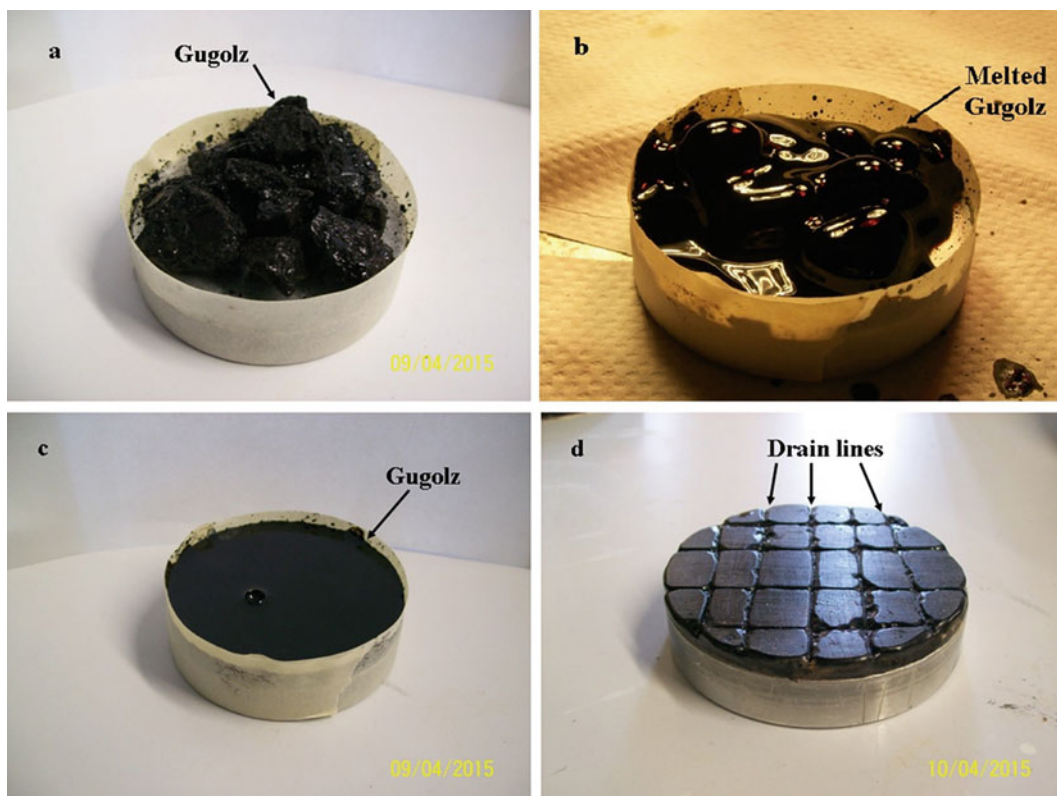


Fig. 49.4 (a) Gugolz before heating. (b) During heating. (c) After heating. (d) Gugolz with drain lines and flat surface

Gugolz has melted and homogeneously distributed; third, allow Gugolz to cool at room temperature. Fourth, with a knife, incise drain lines; finally manufacture a flat Gugolz surface, pressing the Gugolz tool over a flat pattern. Sometimes it is necessary to repeat the third and fourth steps to achieve a really flat surface. In Fig. 49.4, it is possible to observe some images about manufacture of the polishing tool.

Once manufacturing the Gugolz tool, the polishing process was continued, in which cerium oxide (CeO_2) was used as abrasive. This material is one of the primary polishing compounds used today to polish a great variety of optical materials [3]. In Fig. 49.5, it is possible to observe details of the polishing process. Notice that in this stage, the polishing tool is over the workpiece, this configuration improves polishing. Also to enhance this stage, a 1.1 kg mass was used to press the Gugolz tool on the workpiece.

Fig. 49.5 Polishing made with a polish machine fabricated by CIO technicians

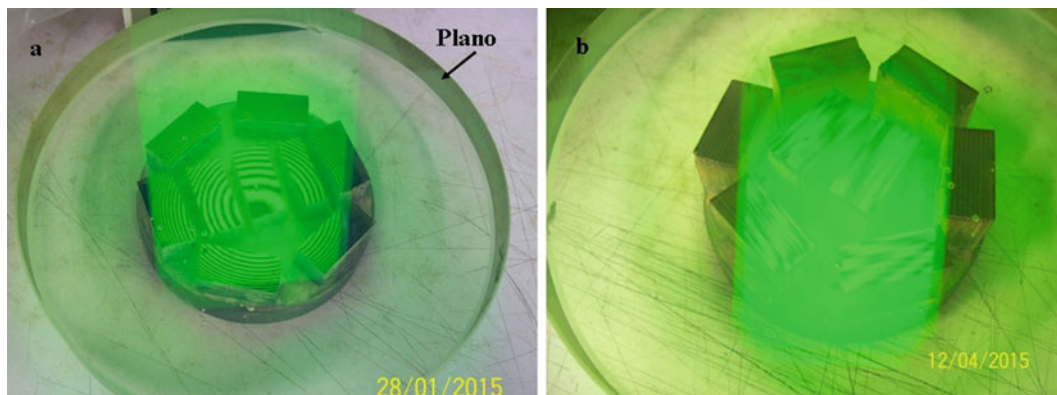
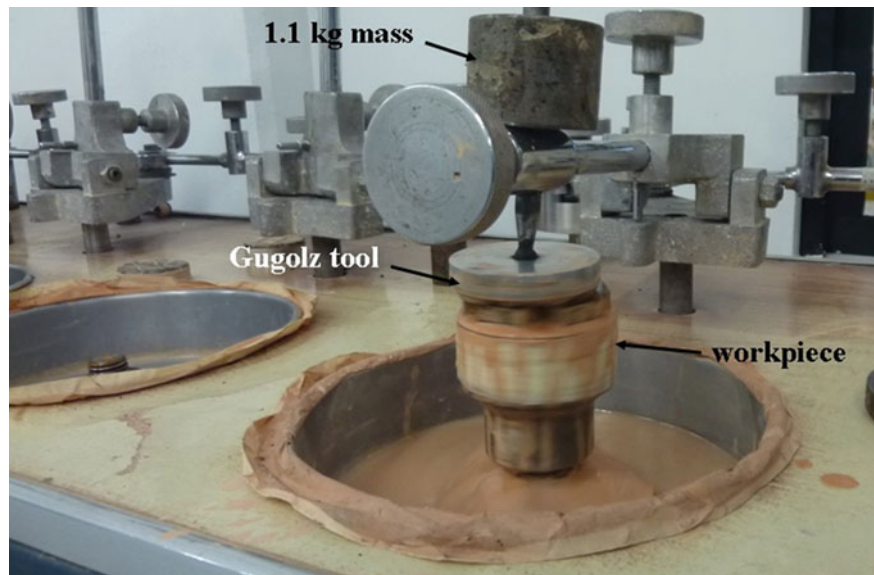


Fig. 49.6 Newton's rings, (a) in working piece II it is possible to observe around 23 rings, that means that the surface is not close to be flat. (b) In working piece III it is possible to observe almost three rings; in this case, the surface is close to be flat

49.3.5 Flatness Testing

Between every step of grinding and polishing processes, assessing flatness is very important to verify that the specified parameters have been achieved. When grinding it is usually enough testing the flatness with a spherometer. The procedure is the following: first, calibrate the spherometer in a flat pattern, second, put the spherometer on the workpiece and take the measurement to determine if the workpiece is concave, convex or flat.

During polishing, testplate testing is the oldest and most commonly method to verify the flatness of optical surfaces during the fabrication phase. Testplate utilizes the interference effect known as Newton's rings or Fizeau fringes [4]. Testplating is also sometimes called contact interferometry because the surfaces of the testplate and the workpiece are in intimate contact [3]. Between both surfaces a very thin air layer is trapped. This thin layer of air has a refractive index of $n = 1.0$. When light falls on such thin transparent layer, the light is reflected from the top and bottom surfaces. The light that is reflected off the top surface precedes the light reflected from the bottom surface by about twice the thickness of the layer. If the phase difference resulting from this optical path difference is exactly one wavelength of the monochromatic light source used, the constructive interference occurs and a light fringe is seen. If the phase difference is one half wavelength then destructive interference occurs and a dark fringe is seen. Fewer rings indicate better flatness. In Fig. 49.6, it is possible to observe Newton's rings in different cases.

49.3.6 Unblocking and Cleaning

To recover the original glass slides disassembling the workpiece is necessary, same as blocking, heating the workpiece is required to melt the wax to separate every glass slide. After that, every slide must be cleaned with solvent, first with thinner and then with acetone. Finally in some cases, there is excess of tartar, which can only be removed with a most precision polishing. In these cases we recommend polishing individual glass slide on a polyurethane foam pad for a few seconds, assessing the surface and repeating if necessary. In Fig. 49.7, it is possible to observe details of the precision polishing over polyurethane foam pad.

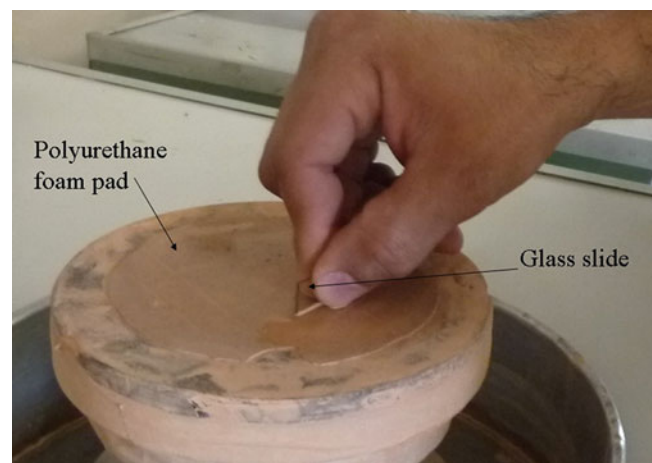
49.4 Results and Discussion

Three workpieces were blocked, for each one, two surfaces were grinded and polished; therefore six times the entire process was made. In Fig. 49.8, it is possible to view pictures of the configuration of every workpiece. Workpiece I includes eight blocks with ten glass slides and one block with eight, in total 88 glass slides were polished ($1.1 \times 2.5 \times 0.1$ cm). Workpiece II includes six blocks with ten glass slides and one central block with 22, in total 82 glass slides were polished ($0.8 \times 2.5 \times 0.1$ cm). Finally workpiece III includes seven blocks with ten glass slides and two central blocks with eleven, in total 82 glass slides were polished ($2 \times 2.5 \times 0.1$ cm). The grand total is 252 glass slides polished.

For each workpiece, it takes in average seven working days to complete all the process in one surface, therefore fourteen working days to complete all the process in one workpiece were required. Regarding grinding above, and only the continuous assessment of the surface gives the information for setting the required working time. However, to give an idea, in Table 49.1 it is possible to observe details of the working time of grinding and polishing processes. Analyzing information in Table 49.1, it is possible to conclude that there is not an exactly recommended working time in every step. However, it is feasible to estimate the minimum and maximum reasonable working times. Additionally, one can appreciate that in average polishing represents almost 50 % of the total working time.

As an example of grinding and polishing processes, in Fig. 49.9 it is possible observe the glass slides surface of one block of the workpiece II after different stages; Fig. 49.9a after cut stage, Fig. 49.9b after grinding with abrasive of $25 \mu\text{m}$, Fig. 49.9c after grinding with abrasive of $15 \mu\text{m}$, Fig. 49.9d after grinding with abrasive of $9 \mu\text{m}$, Fig. 49.9e after grinding with abrasive of $5 \mu\text{m}$ and Fig. 49.9f after polishing with abrasive of $2 \mu\text{m}$.

Fig. 49.7 Precision polishing of an individual glass slide over polyurethane foam pad



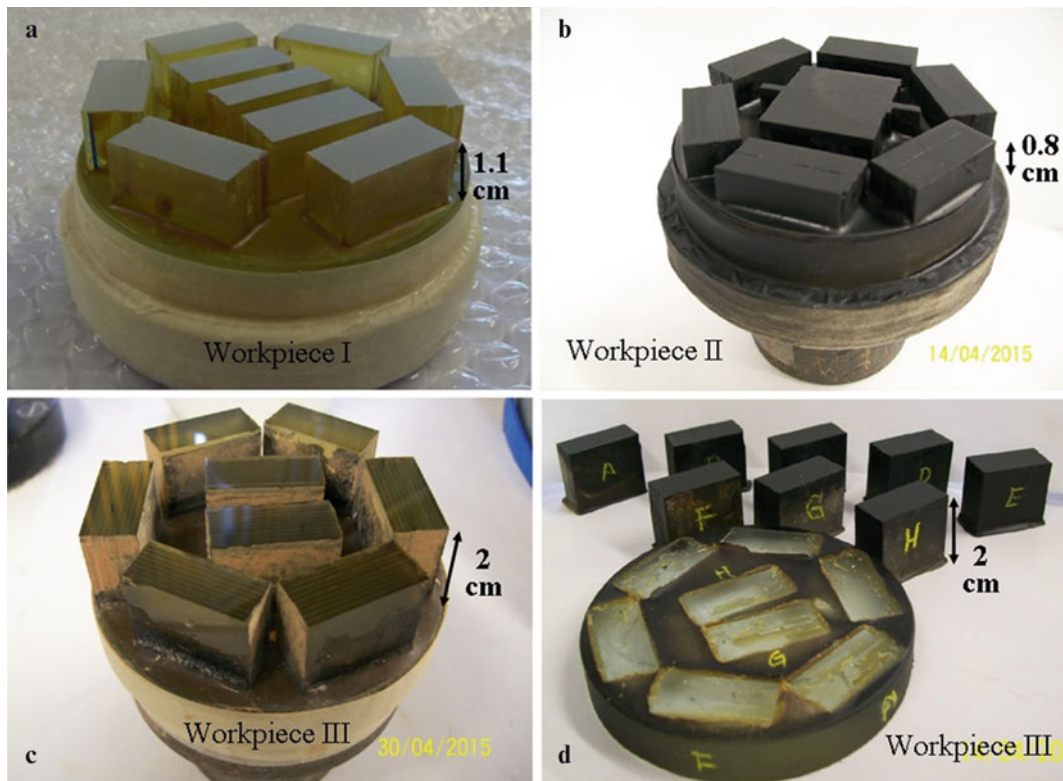


Fig. 49.8 (a) Workpiece I, after grinding. (b) Workpiece II, with protective coating. (c) Workpiece III after polishing. (d) Individual blocks in of workpiece III

The surface quality after polishing with $2\ \mu\text{m}$ CeO_2 abrasive, it is perfect for viewing optical waveguides. Finally in Fig. 49.10, it is possible to observe the polished face of the glass slide and the waveguides manufactured by the writing laser technique. In Fig. 49.10a ten groups of waveguides written at $50\ \mu\text{m}$ deep are shown, six groups written at $100\ \mu\text{m}$ deep, and four groups written at $200\ \mu\text{m}$ deep. In Fig. 49.10b, an amplification of two waveguides written at $50\ \mu\text{m}$ deep is depicted.

49.5 Conclusion

The polishing process is of great importance in order to achieve surfaces with high optical quality. Around 252 glass slides of three different lengths were polished. The quality surface obtained after polishing is perfect for viewing and assessing optical waveguides. One of the main contributions of this work is that it enables the analysis of waveguides on the same day of manufacture, since it is not necessary to polish again the extremes of the glass slides. Another advantage is that several substrates can be processed at the same time, making it an efficient procedure. To guarantee the success of the polishing process, do not forget to assess the surface after every stage.

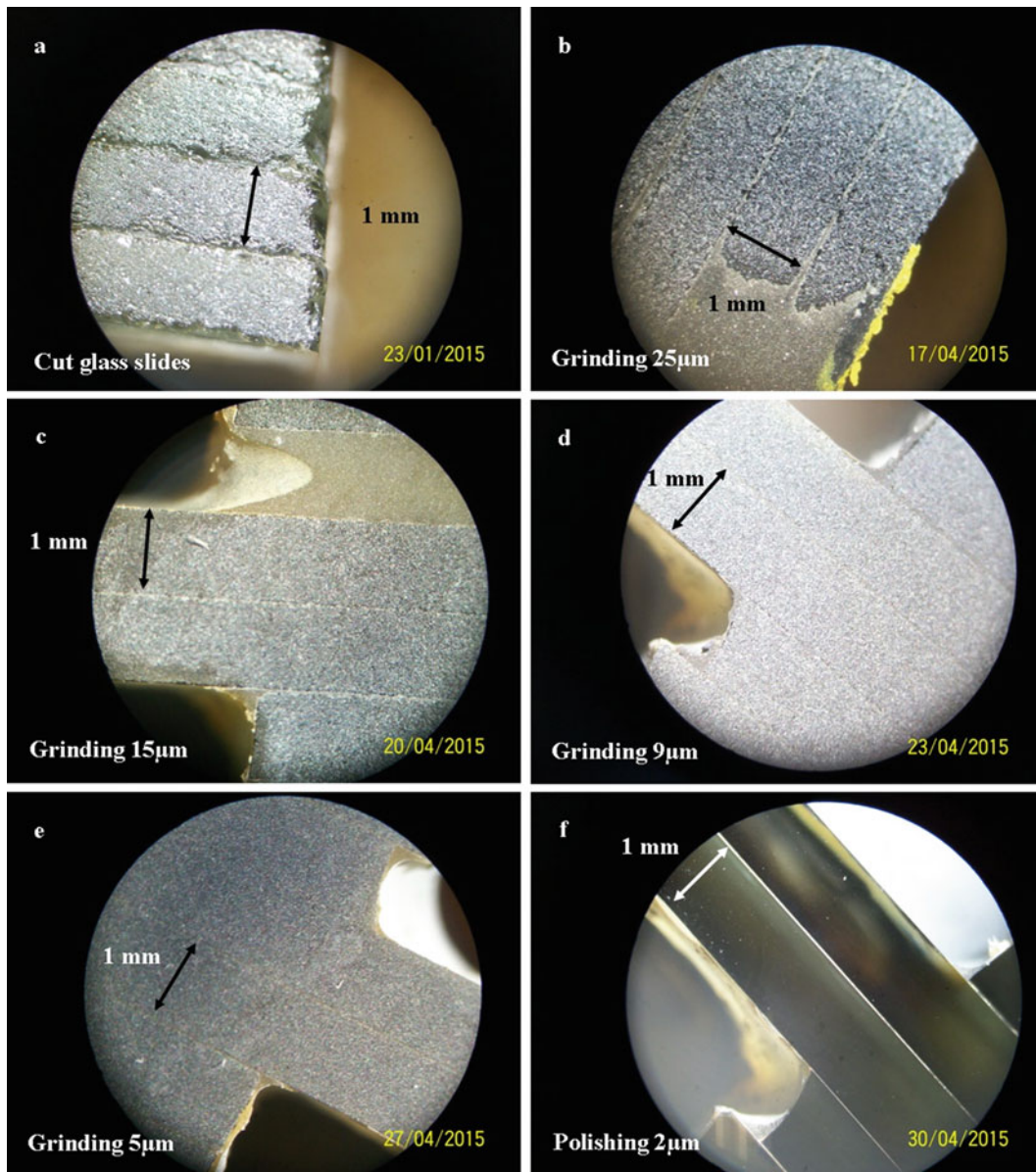


Fig. 49.9 Images after different stages of the second surface of one block of the workpiece II

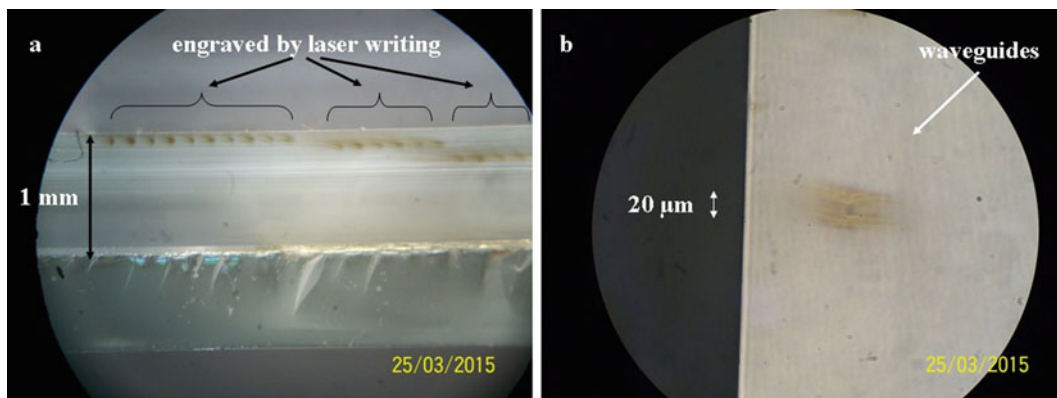


Fig. 49.10 Polished face of glass slide. (a) Waveguides written at 50, 100 and 200 μm deep. (b) Amplification of two waveguides written at 50 μm deep

Acknowledgment H. Lazcano acknowledges the support and encouragement of all the optical shop team members of the “Centro de Investigaciones en Óptica”.

References

1. J.A. Dharmadhikari et al., Writing low-loss waveguides in borosilicate (BK7) glass with a low-repetition-rate femtosecond laser. *Opt. Commun.* **284**, 630–634 (2011)
2. H. Schade, *Procedimientos de Trabajo en Óptica de Taller* (Editorial Reverté, S. A., Barcelona, 1961)
3. H.H. Karow, *Fabrication Methods for Precision Optics* (Wiley, New York, 2004)
4. D. Malacara, *Optical Shop Testing Third Edition*, 3rd edn. (Wiley, New York, 2007)

Index

- A**
- Acousto-optic cell, 2
 - ADAMS
 - finger displacement paths, 276
 - finger positions obtained from, 277
 - simulation, graphical results, 276
 - Adaptive optics (AO) system, 313
 - algorithm simulation, 316
 - analysis, 315
 - calculation, Zernike coefficients, 315
 - control signals, 311
 - DM (*see* Deformable (DM))
 - DM surface, 315, 317
 - elements, 312
 - Matlab, 318
 - process, 315
 - reconstruction and wavefront (WF) correction, 311
 - SH sensor, 312–313
 - static microlens array, 311
 - wavefront, 316
 - Zernike polynomials coefficients, 317
 - Amplified spontaneous emission (ASE)
 - experimental setup, 216
 - methodology, 216–217
 - Sagnac all-fiber interferometer, 215
 - test, reflectance and transmittance signals, 217, 218, 220
 - tuning filter, Bragg grating and long period gratings, 215
 - wavelength, birefringence and fiber length dependence, 215
 - Angle beam inspection, 111
 - Angular resolution, 111
 - ANN. *See* Artificial neural network (ANN)
 - ANSYS® software, 267, 269–271
 - Arduino, 160, 162
 - Artificial muscle biomechanical rig (AMBR), 322–324
 - actuators, 322, 325
 - bone deformation and related forces, 326
 - CAM, 319
 - CT and MRI, 320
 - data gathering systems, 326
 - deformation, 326
 - displacement over time diagram, 325
 - displacement, marker cluster, 325
 - EMG, 319
 - FEM, 320
 - force management, 326
 - force step, 324
 - framework, 320
 - generating data, 320
 - incorporation of joints, 321
 - interactions, 319
 - ITEM framework, 321
 - lack of gravity, 319
 - load cells, 322
 - lower leg muscles, 323
 - mechatronic design, 322, 324
 - control system, 323
 - development, 322
 - implementation, 322
 - OpenSim Gait 2392 model, 323
 - requirements, 322
 - muscle force vector, 321
 - OpenSim, 319, 321
 - optical measuring system, 322
 - redesigns and developments, 326
 - repeatability, reproducibility and accuracy error/bias, 324
 - Sawbones tibia replica, 324
 - speed of contraction, 326
 - static conditions, 326
 - tibia specimen, 320, 321
 - two-component composite tibia replica, 320
 - validation
 - actuation system, 324
 - motion capture system, 324
 - Artificial muscles system, 323
 - Artificial neural network (ANN), 20, 166, 168, 169
 - Atmospheric turbulence, 2
 - Auto-calibration process, 257–262
 - baseline, 258
 - cleaning micro-channel, 259
 - standard solution injection, 259
 - Automated hydrodynamic system, 256, 260
 - Automated LIBE. *See* Laser-induced breakdown spectroscopy (LIBS)
 - Average magnitude and phase, calculation, 4
 - Axis fringe projection
 - calculation, 97
 - diagram, 95, 96
 - divergent illumination, 94
 - 3D surface information, 93
 - equation, 93
 - experimental setup, 95, 96
 - geometry of, 94
 - measurements, 98, 99
 - multiple projectors, 93
 - optical measurement methods, 93

- Axis fringe projection (*cont.*)
 pin-hole camera model, 94
 reference and test object, 97, 98
 shape of, 97, 98
 theater mask, 98, 99
 wavelet analysis, shadows detection, 93
- B**
- Bacillusanthracis (anthrax), 29
 Bacillusglobigii, 29
 Bandpass signal, 3
 Bauschinger effect, 266
 Beam splitter (BS), 118
 Bluetooth LM-058, 257
 Bottom trawl systems, 301
 Bounce control, VCBs, 244–245
 Bragg angle, 45
 Brillouin spectrum, 281
 Broadband viscoelastic spectroscopy (BVS) device, 249
 Buckingham's theorem, 301
 Butterworth low-pass filters (BtwLPF), 77
- C**
- Calibration curve, 20, 21, 25
 Cam, 275, 276
 Cam-follower mechanism, 276
 Carnot cycle, 87
 Carré algorithm, 120
 Chemometric algorithms, 20, 29
 Classic bottom trawl system, 304
 Cleaning micro-channel, 259
 Clinistix[®], 60
 Cobalt spectrophotometric measurement, 257–258
 Collision force, 279
 Collision mechanism, 278
 Color topography, 137–143
 color checker software, 135
 color evaluation
 calibration process, optical devices, 137
 3D reconstruction, 140
 ICP algorithm, model and data, 140, 142
 measurements, 143
 non-calibrated color, 137
 object views, 140, 141
 parameters, experimental setup, 138
 unwrapped phase information, 138, 139
 variations, 139, 140
 wrapped phase of object, 138
 colorimetry, 136
 fringe projection, 135–136
 II Profiler de X-Rite, 135
 Colorimetry, 256, 257
 Complementary metal-oxide-semiconductor (CMOS), 250
 Compression test, 7–10, 17
 Computed tomography (CT), 249
 Computer numerical control (CNC)
 advantage, 200
 automation engineering, 195
 canny edge detector, 198
 3D model and grayscale image, 198
 3D shape recovery, 199
 components layout, fringe projection, 196
 error matrix, surface plots, 199, 200
 fast and fine roughing process, 199, 200
 features, fringe pattern, 198
 indicator E, 199, 200
 inverse engineering, 195
 least-squares algorithm, 196–197
 phase shifting method, 196
 technics, 195
 thresholding, grayscale image, 198, 199
 unwrapping phase, 197
 Control algorithm, 273, 274
 Control system, 273
 Convex mirror, 8
 CrK α radiation, 45
 Crude oil, LIBS, 182
 Arabian oil, 183, 184
 atomic absorption (AA), 181
 atomic emission spectroscopy, 181
 elements, 183, 185
 experimental setup, 182
 heating, 185
 hydrocarbons, 181
 Maya oil, 183, 184
 Nd, YAG, 182
 North Sea oil, 183, 184
 oil exploitation and quality determination, 181
 samples preparation, 182
 spectral lines, 182, 183
Cryptomeria japonica (Japanese cedar), 250
 Cupric nitrate, 23
- D**
- D'Alembert principal, 303
 Data Acquisition Device (NI-USB6008), 119
 Data acquisition system, 212
 DC term, 76
 3D displacement distribution measurement, 191–193
 cantilever
 phase differences, cameras, 191, 193
 photograph, 191, 192
 digital image processing, 187
 grating, phase analysis method, 187
 health monitoring of large structures, 187
 multiple cameras, 189–191
 sampling Moire method, 188–189
 sensitivity, 187
 steel towers, 187
 Dean Index (DI)
 ANN, 166, 168
 control parameters measurement and diagnosis, 166
 Deflectometry, 7
 Deformable (DM)
 Gaussian function, 313
 influence function, 313–315
 modal method, 313
 pseudocode, 315
 surface, 313
 values of voltages, 313
 Deformation matrix, 268
 Degrees of freedom (DOF), 273
 Dental fluorosis
 ANN, 168, 169
 back-propagation, 166, 168, 169
 control parameters measurement and diagnosis, 166
 (*see also* Dean Index (DI))
 diagnostic procedures, 169
 enamel mineralization, 165
 experimental setup, 166–167
 hypomineralization, 165

- medical conditions, 165
 - procedure, control parameters, 167, 168
 - RGB decomposition, 167, 168
 - scales, 166
 - standard deviation, 167
 - techniques, 165
 - visual diagnosis, 168
 - Dextrostix[®], 60
 - Diffraction optical element (DOE), 35, 36
 - Digital holographic microscopy (DHM)
 - identification of microorganisms, 71
 - Lactobacillus casei*, 73
 - optical methods and techniques, 71
 - overlapping/recorded fields, 71
 - phase maps, 71–73
 - transmission, 73
 - Digital holography (DH)
 - amplitude and phase test object, 78
 - amplitude and topography distributions, 81
 - CCD, 76
 - expression, 76
 - filtering process, 77
 - frequency spectrum filtering method, 75
 - ideal filter, 81
 - intensity evolution, 79, 80
 - Michelson interferometer, 76
 - natural diffraction of light, 76
 - off-axis configuration, 75
 - off-axis digital hologram, 78
 - optical imaging system, 79
 - reconstructed amplitude and phase images, 78, 79
 - standard deviation (STD), 81
 - Talbot carpet, sinusoidal gratings, 77, 78
 - Talbot effect, 77, 82
 - twin image, 75
 - virtual image and real image, 75
 - white dashed line, 79–82
 - Digital image processing (DIP), 8, 10, 17, 249, 253
 - Digital speckle pattern interferometry (DSPI), 35–36
 - Distributed sensing, 281
 - Double illumination speckle interferometer, 36
 - 3D printer, 227, 228, 230
 - 3D shape recovery, interferometer
 - beam-splitter cube, 155
 - cube rotation, 156
 - description, 153
 - FireWire digital camera, 156, 157
 - fringe projection technique, 154–155
 - phase-shifting, 156
 - variable resolution, 156
 - wrap phase, 156, 157
- F**
- Electric current and optical characterization. *See* Organic solar photovoltaic (OPV) cells
 - Electromagnetic technology, 56
 - Electromyography (EMG), 319
 - Electronic control, 257
 - Electronic speckle pattern interferometer (ESPI), 7
 - Elliptic-arc-fillet model, 266
 - Energy management system, 256
 - Erbium doped fiber amplifier (EDFA), 216
 - Ergonomic and organic design, 273
 - Escherichia coli*, 30, 31
 - F**
 - Fabrication procedure. *See* Organic solar photovoltaic (OPV) cells
 - Fast Fourier Transform (FFT), 284, 285
 - Fiber Bragg Gires-Tournois sensor
 - accuracy and sensitivity, 341
 - configuration, 342
 - grating, 341
 - photodetector, 341
 - reflective pulse, 342
 - spectrum of the pulse diode laser, 343
 - three-phase system, 341
 - tunable spectrum, 343
 - wavelength displacement, 342
 - wavelength shift, 341
 - Fiber Bragg grating (FBG), 281, 284, 285, 341, 342
 - Fibre optic cable for sensing, 281
 - Filter order, 77
 - Filtering process, 77
 - Finger displacement paths, ADAMS, 276
 - Finite element model (FEM), 250–251, 267
 - capacity flow, 233
 - characteristics, materials, 233, 234, 236
 - failure criterion, 237
 - grain dispenser model, 234, 235
 - granular medium, 233
 - graphic XR control, 234–236
 - hopper, outlet tube, cone, bagging machine, 234
 - materials, 233
 - pilot testing dispenser, 234, 236
 - plastics, 233
 - problems of, 236
 - SolidWorks simulation software, 237
 - stress analysis and displacement, 237, 238
 - test materials, analysis of, 239
 - Flow cytometry, lasers, 329, 330
 - Flow injection analysis, 255
 - Focus zone (FZ), 79
 - Four phase-shifted interferograms, 119
 - Fourier domain imaging, 2, 3
 - Fourier filtering method, 75, 81
 - Fourier spectrum, 72
 - Fourier telescopic, 2, 3
 - Fracture behavior of wood, 249
 - Fragile material fracture, 265
 - Frequency response functions, 248
 - Frequency spectrum filtering method, 76
 - Fresnel diffraction, 16
 - Fringe deflection (FD), 148–150
 - definition, 145
 - displacements, 147
 - schlieren methods, 145
 - synthetic air jet, temperature measurement
 - distribution maps, 150
 - Fourier method, 149
 - Gaussian function, 149
 - generator, 148
 - heated surface, aluminum plate, 148
 - integration process, 149
 - phase values, 149
 - Photron UX100 camera, 148
 - Fringe production, 5
 - Fringe projection, 195, 203
 - robotic arm (*see* Robotic arm CNC (*see* Computer numerical control (CNC)

- G**
- Gaussian beams, 8, 15
 - thin film measurements, 131–134
 - homodyne detector
 - intensity distributions, 133, 134
 - semi-width and centroid, 132–133
 - propagation
 - Fresnel diffraction, 131
 - laser beam, coordinate plane, 131, 132
 - semi-width, 132
 - Gaussian low-pass filters (GLPF), 77
 - Gaussian propagation, 8, 15
 - Gauss-Legendre quadrature, 268
 - Genetic algorithms (GA), 289, 290
 - Gladstone-Dale constant, 87
 - Glass slide, 360
 - Global coordinates, partial derivatives, 268
 - Glucometers, 61
 - GluControl GC300®, 61
 - Glucotrack glucose monitor, 59
 - Glucotrack™, 61
 - ψ -Goniometer, 45
 - Grinding, 355–360
 - GSK-3 β , 329, 332
- H**
- Hand amputation
 - 3D printed hand assembled, 229
 - 3D printing in ABS, 228, 229
 - EMG signals, 227
 - flexible hinges, 228, 229
 - point clouds with imperfections, 228
 - properties, 230
 - prosthetics, 230
 - sectioned with apertures for joints, 228
 - thumb positioned to grasp thin and different objects, 230, 231
 - traditional prosthetic manufacturing methods, 227
 - Headrope and footrope, 301, 303, 305, 306
 - Hole-drilling method, 7, 35, 40
 - Horizontal-path turbulence, 1
 - Human colon carcinoma, 330, 331
 - Hydrodynamic flow system, 256
 - Hydrodynamic forces, 301, 306
- I**
- Ideal low-pass filters (ILPF), 77
 - Image processing, 88
 - INDUSTRIAL PANTOGRAPH computer controlled (CNC), 212
 - Inertial measurement unit (IMU), 114
 - Injection flow system, 256
 - Integrated optics, 355
 - Interferograms, 117
 - Interferometric speckle pattern, 7
 - Inverse FE software program, 320
 - IR absorption region
 - carbonyl group, 298
 - CH group, 297
 - hydroxyl group, 298
 - Isoplanatic patch, 1
- J**
- Japanese cedar (*Cryptomeria japonica*), 250
- K**
- Kinematic simulations, 280
 - Kirchhoff-Fresnel propagation integral, 77
 - K-means method, 26, 27, 32
- L**
- LabVIEW, 273
 - Laser ablation, 29. *See also* Laser-induced breakdown spectroscopy (LIBS); Transparent conductive oxide (TCO) thin films
 - Laser-induced breakdown spectroscopy (LIBS), 19–22, 29, 160–163
 - cleaning monitoring process, 345, 346
 - description, 159
 - echelle spectrometer and ICCD camera, 159
 - experimental setup, 160
 - experimental tests, 163
 - facility, 346
 - hardware, 163
 - Labview, 159
 - restoration process, 345
 - spectra and silver pattern, 349
 - spectral lines, 347
 - spectrum analysis, 162
 - spectrum with tantalum lines, 349
 - visual interface
 - configuration window, 162
 - mapping window, 160, 161
 - positioning window, 160, 161
 - Lasers
 - cell culture, 330
 - development, 329
 - emission of light, 329
 - flow cytometry, 329, 330
 - GSK-3 β , 329, 331
 - light scattering, 329
 - medicine, 329
 - outcomes, 331
 - PKC ζ , 330, 331
 - principle, 329
 - reagents and antibodies, 330
 - Least square method, 269
 - LIBS. *See* Laser-induced breakdown spectroscopy (LIBS)
 - Low Temperature Co-fired Ceramics (LTCC), 256, 257
 - LTCC. *See* Low Temperature Co-fired Ceramics (LTCC)
- M**
- Mach-Zehnder interferometer, 71
 - Mass spectroscopy, 19
 - Mechanics of materials, 9
 - MF-Millipore membrane, 21, 23–25
 - Michelson fiber interferometer, 282
 - Microanalyzer, 257, 258, 260, 261
 - Microanalyzers based on flow injection system, 255
 - Micro-electromechanical (MEMs), 75
 - Microflow injection procedure, 258, 262
 - Microfluidic structure, 261
 - Micro-optical systems (MOEMs), 75
 - Micro-pumps flow rate, 256
 - Microscope objective (MO), 71
 - Miller indices, 44
 - Miniaturization, 256
 - MoCap system, 324
 - Modal testing, 246
 - Modified speckle pattern, 50

Molecular absorption spectrophotometry, 257
 Morphological processing (MP), 113
 Multicommutation techniques to generate flow network, 256
 Multifunction optical measurement system. *See* Transparent
 conductive oxide (TCO) thin films
 Myoelectric signals, 273

N

National Institute of Standards and Technology (NIST), 21, 22, 31
 Neuber's formula, 265
 Neural networks (NN), 22, 30
 Nickel chloride, 23, 24
 8-Node quadrilateral element, 267
 Non-destructive testing (NDT), 114
 Non-invasive glucose monitoring, 57–59
 acoustic properties, 59–60
 in biomedical research, 55
 biosensor technology and digital electronics, 61
 β -cells, 55
 chemical energy, 55
 chemical properties, 56
 Clinistix[®], 60
 Dextrostix[®], 60
 diabetic patients, 62
 electrical properties, 56
 glucometers, 61
 GluControl GC300[®], 61
 GlucoTrack[™], 61
 glycolysis, 55
 micro and nano electronics, 60
 MIR and NIR optical absorption, 60
 multiparametric and hybrid methods, 61, 62
 optical properties
 absorption spectroscopy, 58
 changes of intensity, 57
 fluorescence, 58–59
 medical applications, 57
 polarization, 57–58
 optoelectronic technologies, 60
 Pendra, developed in 2003, 61
 physical properties, 59
 sensitive polarimeter, 61
 thermal properties, 59
 Non-uniform rational B-splines (NURBS), 289, 290, 292
 object representation, 292–293
 surface fitting, 293
 surface representation via GA with SBX, 290, 291
 Notch stress intensity factors (N-SIFs), 265
 NURBS. *See* Non-uniform rational B-splines (NURBS)

O

Ocean Optics fiber, 21
 Ocean Optics USB4000 spectrometer, 30
 OFDR. *See* Optical frequency domain reflectometry (OFDR)
 Optical detection system, 259
 Optical fiber interferometers, 282
 Optical frequency domain analysis, 285, 287
 Optical frequency domain reflectometry (OFDR), 281
 Optical spherical mirror, 7
 Optical time domain reflectometry (OTDR), 281
 Optomechatronics
 data acquisition system, 212
 description, 211

INDUSTRIAL PANTOGRAPH computer controlled (CNC), 212
 industry metal processing, 212
 metrological characteristics, 211
 optical sensors measurement, 212, 213
 Plasma Automation Group, 212
 robotics concept, 212
 SCADA systems, 211
 stress distribution, 212, 213
 Organic solar photovoltaic (OPV) cells, 336, 337
 advantages, 335
 cost, 335
 efficiency, 335
 fabrication procedure
 MEH-PPV, 336
 spin coating method, 337
 fringe projection technique, 339
 history, 335
 material, 336
 measures, 338
 mechanical profilometer, 338
 organic layer deposition, 338
 organics layer images, 339
 power conversion, 335
 sample preparation, 337
 scanning electron microscopy (SEM), 339
 sinusoidal fringes, 338
 solution stages, 336
 spin-coating technique, 337
 theory, 336
 three dimensions phase surface, 338
 Oscillator signal, 4
 OTDR. *See* Optical time domain reflectometry (OTDR)
 Oxidative agents, 295

P

PAST software, 24
 PCB. *See* Printed circuit board (PCB)
 Phase calculation, 119–120
 Phase map, DHM, 71, 72
 Phase shift DSPI (PSDSPI)
 automatic data analysis, 49
 CCD records, 51
 deformations measurement, 49
 DSPI, 50–51
 experimental configuration, 51
 individual pixel intensity variation, 54
 intensity interferograms, 51
 interferometric techniques, 49
 mechanical deformations, 52, 54
 out-of-plane distortions, 54
 phase-shifted interferograms, 51
 phase-stepping and shifting, 49
 piezoelectric transducer, 49
 sinusoidal dependence, 51
 strain concentrations, 49
 unwrapped phase, 52
 Phase-shifted interferograms, 119
 Phase shifting interferometry (PSI), 117
 2π ambiguity, 222
 advantages, 65
 errors, 221
 experimental setup, 222–224
 linear polarizer $P_1(\psi)$, 67
 3.0 Megapixel CMOS sensor, 67

- Phase shifting interferometry (PSI) (*cont.*)
 - microarthropod (collembola), 68
 - non-birefringent samples, 65–66
 - optical system, 66, 67
 - parallel interferograms, 69, 222
 - phase shifting of $\pi/2$, 66
 - RBC, 223
 - ROF algorithm, 221
 - shearograms with π -phased shifts, 65
 - single shearogram, 67
 - techniques of, 65
 - Vargas-Quiroga method, 222
- Photovoltaic effect, 335, 336
- Piezoelectric actuator (PZT), 36
- Piezoelectric micro-pumps, 256
- Piezoelectric transducer, 117
- Pin-hole camera model, 94
- PKC ζ , 330, 331
- Plasma Automation Group, 212
- Plastics, 295
 - degrade, 296
 - zero electrical conductivity, 295
- Point spread function (PSF), 2
- Polarimetry, 57
- Polarization
 - half-wave plates, 49
 - properties, 67
- Polishing, 356
 - blocking, 357
 - CIO technicians, 359
 - flatness testing, 359
 - glass slides, 356, 360, 362
 - glass substrates, 356
 - grinding, 357, 358
 - Gugolz tool, 358
 - high quality, 355
 - materials and tools, 355
 - Newton's rings, 359
 - polyurethane foam pad, 360
 - procedure, 356
 - quality, 361
 - stages, 357–358, 362
 - unblocking and cleaning, 360
 - working time, 357
 - workpiece after grinding, 361
- Polystyrene, 296, 297
- Printed circuit board (PCB), 257
- τ -Profiles, 44
- Prosthesis control systems, 273
- Pulse-echo SONAR, 111
- Pulse-echo technique, 111
- Pulse-echo transducer, 112
- Purkinje images
 - anterior surface of eye, 102
 - areas of interest, 104, 105
 - calculation, 104
 - centroid calculation, 106–108
 - features, 101
 - image segmentation, 104–106
 - infrared LED illumination, 103
 - input data to system, 104
 - intraocular lens misalignment, 101
 - localization, 104
 - non-homogeneous refractive index, 102
 - optical human system, 101, 102
 - PI and PIV over pupil, 103
 - plate, 103
 - pupil, center of, 101
 - simple images process, 102
 - subimage intensities, 104
 - surface of eye, 103, 104
 - system, 103
 - thresholding process, 101, 104, 105
 - vision algorithms, 101
 - workspaces, 104
- R**
- Raman spectroscopy, 57
- Raman Stokes, 281
- Rayleigh backscatter, 281
- Rayleigh distance ($z_{r,dist}$), 77
- Reagents, 257, 261
- Real image, 75
- Refractive index, digital holographic interferometry (DHI), 124–127
 - deviation, 126, 127
 - experimental setup, 124
 - Fourier-transform method, 124, 125
 - full-field index refraction distribution, 126, 128
 - non-destructive methods, 123
 - optical techniques, 123
 - phase measurement
 - glass tube, liquid samples, 124, 125
 - optical path length, 124
 - phase difference maps, 126, 127
 - physical properties, liquids, 123
- Regularized optical flow (ROF) algorithm, 221
- Residual stress, 7, 35, 37–40
- Robotic arm
 - acquisition and image processing, 203
 - Automation Engineering, 203
 - component layout, fringe projection, 204
 - 3D model and grayscale image, 206
 - features, fringe pattern, 206
 - flexibility, 208
 - industrial manufacturing, 207
 - least squares algorithm, 204–205
 - manipulation, 203
 - movements, 206–208
 - orientation, 207
 - spray painting, 206
 - technics, 203
 - unwrapping phase, 206
- ROF. *See* Regularized optical flow (ROF) algorithm
- RS232 serial port adapters, 257
- S**
- Sagnac interferometer (SI), 215
- SBX. *See* Simulated binary crossover algorithm (SBX)
- Schlieren technique
 - atmospheric air at room conditions, 89
 - chromatic crayons, 85, 89
 - CMOS sensor, 88
 - density gradients, 88
 - in fluid flows area, 85
 - isotropic homogeneous media, 85
 - light sources, 85
 - Matlab, 89
 - optical background, 86–87

- refractive index, 88
 - Stirling engine, 86, 87
 - temperature, 89
 - white light LED, 88
 - Z-type Schlieren system, 88
 - Self-imaging, 77
 - Sensing section design, 283
 - Sensing section's reflectors, 282
 - Sensing system, 282
 - Sensor Signal, 284–285
 - Shack-Hartmann (SH) sensor, 311, 312
 - closed loop, 312
 - construction, 313
 - parameters, 313
 - reconstruction matrix, 314
 - WF measures, 312
 - Shearography technique, 65
 - SI. *See* Sagnac interferometer (SI)
 - Simulated binary crossover algorithm (SBX), 289, 290, 292
 - Simultaneous localization and mapping (SLAM), 115
 - Single-mode laser, 117
 - Sinusoid signal, 284
 - Six degrees of freedom (DOF), 273
 - SMD. *See* Surface mounted devices (SMD)
 - SolidWorks simulation software, 237, 239
 - Spatial Fourier components, 1
 - Spatial-frequency-domain imaging, 2
 - Spatial voting and threshold (VT), 112
 - Speckle light pattern, 50
 - Spectral domain optical coherence tomography (SD-OCT), 347
 - Spin coating method, 337
 - Standard solution injection, 259
 - Staphylococcus aureus*, 30, 31
 - Stiffness matrix, 268
 - Stirling engine, 86, 87
 - Stock drive products, 276
 - Straight beam inspection, 111
 - Straight gear, 276
 - Stress concentration factor K_t , 265–267, 270, 271
 - Stress distribution, bolt-nut connectors, 266
 - Stress intensity factors, 265
 - Stress relaxation produces, 35
 - Stress-strain diagrams, 7, 9, 10
 - Stress-strain Young's modulus, 49
 - Styrene polymers, 296
 - Surface mounted devices (SMD), 257
 - Surface representation via NURBS and GA, 290–292
 - Swept-wavelength interferometry (SWI), 281
 - SWI. *See* Swept-wavelength interferometry (SWI)
 - Synthetic air jet, temperature measurement, 145
 - background-oriented schlieren, 145
 - characterization, 145
 - FD (*see* Fringe deflection (FD))
 - ray deflection, 146
- T**
- Talbot effect, 77
 - Talbot plane order (TPO), 77
 - Tantalum capacitors, 346
 - analysis, 348
 - applications and areas, 345
 - cleaning process, 345
 - components, 345
 - laser-based methods, 345
 - LIBS, 345–347, 349, 352
 - manufacturing process, 346
 - mechanical and chemical cleaning methods, 345
 - Nd, YAG laser, 346
 - OCT, 348, 350, 352
 - optical coherence tomography, 347
 - resin, 347–349, 351
 - selection, spectra, 348
 - storage, 345
 - Taylor series, 46, 47
 - TCO thin films. *See* Transparent conductive oxide (TCO) thin films
 - Temperature fields, 88, 89
 - Temperature gradients, 85, 89
 - Tensile test, 250
 - Testplating. *See* Polishing
 - Texas advanced optoelectronic solution (TAOS), 257
 - Thermistors, 285
 - Three-dimensional digital image correlation (3D-DIC) method, 249–251, 253
 - Thresholding process, 104, 105
 - Time-average Fourier telescopy, 1–4
 - Tracheid effect, 249
 - Transducer, 113
 - Transparent conductive oxide (TCO) thin films, 173, 176–178
 - experimental procedure, 175, 176
 - fluorine doped tin oxide (FTO), 177, 178
 - optical microscope, 176, 177
 - optoelectronic products, 173
 - self-assembled multifunction optical measurement system, 175
 - surface profiles
 - Al doped ZnO (AZO), 176, 177
 - indium tin oxide (ITO), 177, 178
 - WLSI (*see* White-light scanning interferometry (WLSI))
 - Trawl door, 301, 303
 - analysis of forces, 303–305
 - balance forces, 308
 - balance moment, 308
 - classic bottom trawl system, 304
 - description, 302–303
 - frame parts dimension, 302
 - INAZTECA, 302, 303, 309
 - mathematical model, 303
 - matrix representation of force, 306
 - objective, 305
 - opening arm dimension, 303
 - warp tension, matrix representation, 306
 - wing parts dimension, 302
 - Trawl fishing gears, 301
 - Triangulation-based fusion (TBF), 113
 - Triaxial strain/stress profiles
 - fundamental equations, 44–45
 - goniometers, 43
 - polycrystalline material, 43
 - simulation, 45–47
 - “sine-square-psi” method, 43
 - Twin image, 75
 - Twyman-Green (TG) interferometer, 117, 118, 120
- U**
- Ultra-low reflectors, 282, 284
 - Ultrasonic arc map (UAM), 112
 - morphological processing, 113
 - spatial voting and threshold, 112
 - triangulation-based fusion, 113

Ultrasonic inspection types, straight and angle beam, 111
 Ultrasonic tomographic technique, 249
 Ultrasound
 diffraction information, 111
 on robotics, 111
 waves propagation, 111
 Ultraviolet Multiprom Eraser, 296
 United States Army Research Laboratory, 21

V

Vacuum circuit breakers (VCBs), 241
 accelerations and forces, 246
 bare vacuum interrupters, 245
 bounce occurrence, 244–245
 collision forces, 243–244
 experiments, 245
 frequency functions, 241
 FRF matrices, 247
 measuring instruments, 245, 246
 medium-voltage systems, 241
 modal testing, 246
 reaction forces, 244, 247, 248
 static contact force, 241
 time integration technique, 242
 vacuum interrupter and parts, 241, 242
 Vargas-Quiroga method, 221, 222
 Vertical-path atmospheric turbulence, 1
 Virtual image, 75
 V-shaped notches, 265

W

Warp tension at trawl door, 306
 Wavelength patterns Ni and Cu, 22
 Wavelength tunability, 119
 White-light scanning interferometry (WLSI)
 light intensity function, 174
 monochromatic fringes, 173
 phase-shifting algorithm (PSA), 173
 self-assembled multifunction optical measurement system, 175
 signal function, 174
 Wireless communication, 257
 Wood, 249
 digital image processing, 249, 253
 factors effect mechanical features, 249
 fiber orientations, 249
 fracture behavior, 249
 irregular fiber orientation, 250
 longitudinal-radial (LR) section, 250
 and MATLAB, 250
 radial-tangential (RT) section, 250
 stiffness, 250
 tensile test, 250
 Worm gear, 276

X

X-ray diffraction, 43

Z

Zero electrical conductivity, 295